

THESIS DISSERTATION

Synthesis and study of the properties of polyaromatic organic compounds of interest in molecular electronics

LUCÍA PALOMINO RUIZ



Departamento de Química Orgánica



UNIVERSIDAD
DE GRANADA

Laboratorio de Electrónica Molecular

instituto
IMdea
nanociencia

Editor: Universidad de Granada. Tesis Doctorales

Autor: Lucía Palomino Ruiz

ISBN: 978-84-1306-827-5

URI: <http://hdl.handle.net/10481/67998>



UNIVERSIDAD
DE GRANADA

instituto
imdea
nanociencia

MEMORIA DE TESIS DOCTORAL

**SÍNTESIS Y ESTUDIO DE LAS PROPIEDADES DE COMPUESTOS
POLIAROMÁTICOS ORGÁNICOS DE INTERÉS EN
ELECTRÓNICA MOLECULAR**

presentada por

LUCÍA PALOMINO RUIZ

para optar al título de

DOCTOR EN QUÍMICA

con mención **INTERNACIONAL**

Granada, 2021



UNIVERSIDAD
DE GRANADA

instituto
imdea
nanociencia

THESIS DISSERTATION

**SYNTHESIS AND STUDY OF THE PROPERTIES OF
POLYAROMATIC ORGANIC COMPOUNDS OF INTEREST IN
MOLECULAR ELECTRONICS**

submitted by

LUCÍA PALOMINO RUIZ

in accordance with the requirements of

DOCTOR EN QUÍMICA

INTERNATIONAL mention

Granada, 2021

Agradecimientos

El trabajo recogido en esta tesis se ha llevado a cabo entre el grupo de “**Materiales Orgánicos Funcionales**” (FQM-367), del Departamento de Química Orgánica de la Universidad de Granada y el grupo de **Electrónica Molecular de la Fundación IMDEA Nanociencia** de Madrid. Ha sido financiado gracias a los siguientes proyectos: **ERC-2015-STG-677023-NANOGRAPHOUT** del Consejo Europeo de Investigación, **PGC2018-101873-A-100** del Ministerio de Economía y Competitividad, **A-FQM-221-UGR18** de la Junta de Andalucía, y **CM-S2018/NMT-4321** del Banco Europeo de Inversiones y de la Comunidad de Madrid.

Esta tesis no hubiera sido posible sin la colaboración, trabajo, ayuda y apoyo de innumerables personas, que han hecho de estos años un viaje lleno de nuevas experiencias y aprendizajes tanto a nivel profesional como personal.

Gracias en primer lugar a mis directoras, las doctoras Araceli González, Teresa González y Alba Millán. Han cumplido sus funciones más allá de lo meramente académico, y han confiado en mí cuando era yo misma quien dudaba. Gracias, **Araceli**, por darme la oportunidad de unirme al grupo y al proyecto Nanographout. Durante este tiempo me he sentido muy orgullosa de formar parte de este equipo. Gracias por hacer lo posible para que yo pudiera participar en las actividades del grupo incluso cuando estaba en Madrid, y gracias infinitas por hacer que la estancia en Bristol fuera posible. **Teresa**, gracias por abrirme las puertas de Imdea Nanociencia y confiarme el día a día con el STM. Gracias también por la paciencia y la energía con la que me enseñaste todo, desde soldar un hilo de oro, hasta hacer las macros de Matlab, pasando por montar un convertidor $I-V$ desde cero. Gracias por estar dispuesta a tirarte al suelo conmigo (literalmente) cada vez que el microscopio daba problemas, y por toda tu ayuda durante la escritura de la tesis. **Alba**, gracias por tu apoyo incondicional, por dejarme llorar cuando lo necesité y por ponerte siempre en mis zapatos. Gracias por ser la mejor mediadora en este equipo de 4 y estar siempre de mi parte, aunque no siempre lo estuvieras. Gracias especialmente por estos últimos meses, en los que has estado al pie del cañón en todos los sentidos y a, tan sólo, un audio de distancia.

Gracias a todos los miembros del grupo FQM-367, por enseñarme el verdadero significado de ser un grupo de investigación, donde todos los componentes son animados a crecer para que el grupo crezca. Gracias por hacer posible este sentimiento de piña, y por convertir en costumbre el celebrar los éxitos de los demás como propios. Fui muy afortunada al encontrar alojamiento en esta casa.

Gracias a **Juan Manuel Cuerva**, mi cuarto director, “el jefe en la sombra”. Ha sido un honor trabajar mano a mano con una mente tan preclara como la tuya. Gracias por esa curiosidad insaciable que intentas despertar en nosotros en cada seminario y en cada visita al laboratorio. Gracias por obligarnos a preguntar, y por enseñarnos a cuestionar constantemente lo que tendemos a dar por sabido.

Gracias a los magníficos **Luis Álvarez de Cienfuegos, José Justicia y Sara P. Morcillo**, cuyos consejos son siempre bienvenidos además de acertados, y a quienes jamás ha faltado una sonrisa o palabra de ánimo que regalarme. Ojalá más tiempo para seguir aprendiendo de vosotros. Justo, confieso que entre los regalos de Navidad siempre escogía el tuyo con la certeza de que sería un libro. Gracias por todos ellos. **Delia**, podrías ser parte de otro grupo, pero nunca dejarás de ser parte de éste. Gracias infinitas por recomendarme para el contrato que me abrió las puertas del departamento. Gracias por tratarme siempre con tanto cariño. **Víctor**, gracias por estar siempre disponible para todos nosotros, es una suerte saber que podemos contar contigo.

Gracias a todos mis compañeros, por ser mucho más que compañeros de trabajo. Sois amigos y familia. A mis Nanografenos, gracias infinitas por hacer del trabajo una fiesta, por aguantar sin protestar (o protestando) a Vanesa Martín sonando a todas horas; por no quejaros de mi voz cantando y recitando a diario; y sobre todo por tener siempre uno y mil abrazos preparados para mí. **Irene**, gracias por ser mi otra mitad del “STM team” y acompañarme en esta aventura de la electrónica molecular. Cómo olvidar nuestros primeros días en Imdea, preguntándonos en qué nos estábamos metiendo cuando soldamos la primera punta de oro. No podíamos imaginar que eso sería lo más fácil de todo lo que se nos venía encima. Te debo muchísimo, probablemente sólo nosotras dos sabemos cuánto. **Carlos**, no hay gracias suficientes para todo lo que te debo. No hay vez que te haya pedido ayuda y no me la hayas brindado, fuera lo que fuera: un espectro, una columna, una placa o la escritura de la tesis. Gracias también por compartir conmigo el

amor por las palabras olvidadas y los poemas de la tierra: *Andaluces de Jaén/aceituneros altivos/decidme en el alma quién/quién levantó los olivos*.¹ **Ana**, bien sabes que no puedes escaparte de aparecer aquí. Gracias por tu sonrisa desde el primer día que me conociste. **Rubén**, eres pura energía y vitalidad desbordante. Gracias por esa naturalidad y espontaneidad que me han hecho replantearme tantas veces el poder que dejamos ejercer sobre nosotros a los convencionalismos sociales. Gracias por protagonizar conmigo esas “escenas de vitrina” en las que tanto hemos discutido, pero que tantos abrazos de reconciliación nos han regalado: *Aún no te has ido y ya te echo de menos. Cuento las horas para vernos de nuevo*.² **Vicente**, creo que tú y tu buen humor habéis sido un punto clave para que los miembros del grupo nos sintamos tan unidos. Gracias por ser ese pegamento, que yo ni siquiera sabía que necesitaba. Llegamos a este grupo a la vez y mientras tú organizabas la primera edición de Priego, a mí me faltaba la confianza para quedarme a dormir allí con vosotros. A veces necesitamos que nos espabilen y nos abran los ojos, y vale más predicar con el ejemplo que dar mil explicaciones. Gracias por ser un verdadero amigo, de los que no sólo te felicitan cuando lo haces bien, sino que además te reprende cuando te equivocas y te llama la atención para que mejores. Sobre todo, gracias por tus abrazos, no sabes cuánto significó ese paso para mí. Ahora sé que no los das a la ligera, y que cada uno de los que he recibido es de valor incalculable. Me siento tremendamente afortunada y agradecida, porque tu amistad ha sido una de las mejores cosas que me han traído estos años. **Miguel Ángel**, gracias por enseñarme a valorar y comprender las dos caras del silencio, hablo del ajeno, pero también del propio. Gracias por los abrazos de antaño, que tantas veces me salvaron. Gracias por los mil favores y recados, sobre todo, de estos últimos meses. Gracias por los grandes temazos musicales que marcaron mi paso por el laboratorio: cómo olvidar los momentos vividos mientras sonaban *Margarita*,³ *In my mind*,⁴ o *Promises*.⁵ Remember, apple of my eye: *Don't stop believin'*.⁶ **Silvia**, mi gallega querida, te considero un regalo. Gracias por ser mi salvavidas cuando sentía que me estaba ahogando. Gracias por cada abrazo y por cada palabra que me mantuvieron a flote. Gracias

¹ Fragmento del poema *Aceituneros de Jaén*, de Miguel Hernández.

² Fragmento de *Aún no te has ido*, canción de Vanesa Martín.

³ Canción de Sergio Dalma

⁴ Canción de Dynoro y Gigi D'Agostino

⁵ Canción de Calvin Harris, Sam Smith y Jessie Reyes.

⁶ Canción de del grupo Journey.

infinitas por todo tu cariño, y por salvar con tu alegría cada domingo de mi tristeza. Me permito mencionar aquí también a **Miguel**, campeón invicto de parchianís y miembro de pleno de derecho de esta familia. Vuestra casa siempre estuvo abierta para mí y no puedo estaros más agradecida. **Fede**, nuestro benjamín, gracias por tu arte, por tu buen ánimo constante y tu sonrisa sincera cada vez que nos vemos. Eres grande y llegarás a serlo aún más (y no lo digo sólo por tu altura). **Sandra**, gracias por tratarme desde el primer momento como si nos conociésemos desde siempre. Gracias por compartir conmigo tus cantigas antes incluso de vernos las caras. **Juanpe**, gracias por ser tan cercano a pesar de haber compartido juntos tan poco tiempo.

Pablo, gracias por ese derroche de talento y arte con el que amenizas cualquier ocasión. Gracias por sintetizar incansablemente cualquier modelo imaginable para el STM, pero, sobre todo, gracias por compartir conmigo tus estaciones: son el paisaje que me devuelve la calma infinita de noches. Escucho y siempre siento *cómo cae la flor de cerezo en la fuente del templo*. Eres increíble y te admiro muchísimo. **Raquel**, mi Sailor Moon particular. Gracias por ser una fuente inagotable de energía positiva, aún en tus días más negros. Jamás te falta la sonrisa y eso siempre es de admirar y agradecer. **Sandra**, gracias por tenerlo todo bajo control dentro y fuera del laboratorio. Merecías, sin duda, el título de organizadora de eventos, porque nadie lo hace (ni lo hará jamás) como tú. Gracias por tu alegría y tus ganas incansables de reír. Estoy segura de que todos soñamos con entrar al laboratorio grande y volver a tenerte allí. **Ana**, gracias por ofrecer tu ayuda siempre de esa forma tan natural. Gracias por traernos de vuelta la coherencia con nosotros, y con el planeta que perdemos a veces. Gracias por esa pasión que lo inunda todo cuando hablas de Disney. Tú sí que eres mágica. **Pili**, *eres luz/ nadie puede hacerte sombra*.⁷ Gracias por tus palabras siempre tan acertadas, gracias por estar siempre pendiente de todos, incluso ahora que estás lejos. Nadie estuvo tan pendiente de mí durante el confinamiento como lo estuviste tú. Gracias de corazón, porque un mensaje en el momento preciso obra milagros. **Karina**, nuestra fotógrafa oficial, gracias por hacer un reportaje digno de una boda en cualquier evento. Incluso cuando las cosas no han ido todo lo bien que se esperaba, nunca has perdido la sonrisa y eso dice muchísimo de ti. Gracias también por compartir con nosotros tus dotes culinarias, esos nachos deliciosos y esos *pancakes* inolvidables para

⁷ Versos del poema *Fe*, de Sara Bueno.

desayunar. ¡Arriba México! **Mari**, estar a tu lado es saborear en los labios la alegría de vivir. Gracias por tener siempre preparados una broma graciosa, una historia curiosa o la canción perfecta para cada momento. Gracias por tu sonrisa y abrazo sinceros en cada uno de mis regresos a Granada. **Arthur**, el mundo necesita más gente como tú. Tu filosofía de vida es admirable y toda una inspiración. Gracias por tu disposición a ayudar siempre y por ese *hoolaaa* tan característico que tanto voy a echar de menos ahora que vas a explorar nuevos continentes. **Rafa**, gracias por compartir con nosotros toda tu sabiduría en los ratos de café, o en las salidas nocturnas. Eres el mejor ejemplo de que en este trabajo se puede ser divertido, festivalero y desenfadado, sin dejar de ser riguroso y serio cuando hay que serlo. Te admiro mucho. **Guille**, aquí siempre tendrás un hueco al que volver. Gracias por ser siempre tan atento conmigo y tenerme una sonrisa reservada. Gracias por tus palabras en la tesis de Irene. Uno nunca sabe lo mucho que puede curar una simple frase cuando el otro está tan herido como yo lo estaba. Gracias de verdad. **Pablo**, qué placer es cruzarse contigo por los pasillos y ver que siempre tienes ese buen humor tan característico. Gracias por estar siempre dispuesto a ayudar y por organizar de forma tan maravillosa los eventos de la Unidad de Excelencia. Vas a dejar el listón altísimo para el siguiente. **Jaime, Jennifer, Marcos, Maria, Sara y Álvaro**, ojalá más tiempo para conocernos mejor.

Mi total agradecimiento al **Centro de Instrumentación Científica de la Universidad de Granada** por permitirnos instalar allí nuestro microscopio. En especial a **Ali**, que nos cedió parte de su espacio.

Gracias a toda la gente de Imdea Nanociencia, por demostrarme que aquella, también era mi casa, y su gente, mi familia. Gracias por hacerme sentir una más en todo momento y por poner a mi alcance todas las herramientas que el centro ofrece. **Jorge**, gracias por esas ganas, esa alegría y ese ímpetu que le pones a todo. Gracias por ayudarme tanto con la electroquímica. Gracias por proponerme mil proyectos locos y entusiastas (una revista de divulgación, la estancia en Japón...), aunque al final no pudiéramos hacer realidad ninguno de ellos. ¡Seguiremos soñando y dando lo mejor! **Ed**, ha sido un placer trabajar contigo y pelearnos juntos con el STM. Gracias por compartir conmigo todos tus trucos y por aportar tu punto de vista, siempre tan acertado, sobre la interpretación de las medidas. Gracias por ser amable y simpático en todo momento. Me encantó perdernos juntos en las calles de Zúrich.

Gracias a mis **Supernanos** por hacerme hueco en sus brazos y darme tierra firme cuando todo lo conocido colapsaba bajo mis pies. Gracias por estar a mi lado cuando más os necesitaba, por inventar planes de la nada cuando no me veáis bien, y por ser mi apoyo constante. **Bea**, doy gracias cada día por haberte conocido y tenerte hoy en mi vida. Gracias por cada consejo, por saber escuchar, por entenderme siempre, y por decirme las cosas como son, incluso cuando no quiero escucharlas. **Ana**, eres aire fresco, tan divertida y risueña. Gracias por demostrarme que la dulzura no está reñida con la fortaleza y la valentía. Chicas, sé que me quedo corta, pero gracias por tanto y tanto. ¡Que nunca nos falten unos buenos mojitos con los que brindar, ya sea para celebrar o para levantar el ánimo!

Adri, marcaste un antes y un después. Gracias por aquella primera visita para invitarme a pizza, y por todas las visitas que han venido después con la única intención de sacarme una sonrisa. Gracias por pasar cada mañana a darme los buenos días con un abrazo y gracias por hacer del almuerzo el momento más loco y divertido de todos. Gracias por cuidar de mí incluso cuando yo estaba en Granada, sintiéndome sola y perdida. Gracias por traerme de vuelta esa confianza en mí misma que voy dejando olvidada por las esquinas. Gracias por cada llamada y por cada idiotez destinada únicamente a hacerme sonreír. Eres único, mi kraken. **Patri**, mi aventurera loca y compañera de planes descabellados. Gracias por preocuparte por la investigadora y por interesarte por la poeta. Gracias por escuchar cada problema, cada verso, y creer en mí. Gracias por esa portada de tesis maravillosa que me has regalado. Tu creatividad y tus ganas de aprender y descubrir cosas nuevas no tiene fin. Llegarás a la luna de un salto y yo estaré allí para verlo. **Patri**, gracias por cada café destinado a hacer tuyos mis problemas, gracias por cada consejo sobre el STM y sobre la vida. Nos debemos un abrazo. **Jenny**, coincidimos poco tiempo en Imdea, pero no olvido que fuiste la primera del grupo en regalarme una sonrisa. Ojalá haberte tenido aquí más tiempo. **Iván**, gracias por esa gracia y esa alegría con la que iluminas allí por donde vas. Contigo las risas están aseguradas. **Gonzalo**, aunque llegaste más tarde, lo hiciste por la puerta grande y ganándote en pocos días el cariño de todos. Gracias por cada “¿cómo estás, muchachilla?” que tantas sonrisas me saca. **Andrea**, gracias por tu dulzura desde el principio, y por mantener el contacto después de dejar Imdea. **Sergio, Joaquim, Ingrid, Manu, Alejandra, Marina, Maite A., Maite M.**, y los **Víctor**, gracias por estar ahí cada día,

haciéndome sentir parte de la familia y acogiéndome en todos vuestros planes, ya sean desayunos, fines de semana en casas rurales, scape-rooms o partidos de fútbol. **Cristina**, gracias por acogerme como a una más de tu grupo en cada celebración. **Ed**, gracias por esos dibujos tan maravillosos, y por apoyar mi faceta poética desde las redes sociales. No sabes lo importante que ha sido saberte cerca estos últimos meses. **Fer**, gracias por ser mi compañero de desayunos de las 8:30. Al volver al laboratorio después de hablar contigo, el día siempre pintaba mejor. **Laura**, gracias por toda tu ayuda con el poder termoeléctrico, y por prestarnos cualquier cosa que hemos necesitado de vuestro laboratorio. Gracias también a **Roberto** y **Juan Carlos**, que han hecho más llevadera cada jornada laboral dándome los buenos días con una sonrisa, y abriéndome las puertas de Imdea y del laboratorio las mil veces que he olvidado la tarjeta.

Gracias a la doctora **Linda Zotti** por estar siempre dispuesta a colaborar con nosotros para los cálculos teóricos. Haces que trabajar contigo sea siempre sencillo. Gracias por ser siempre tan amable conmigo y por acogerme con cariño en todas las actividades de la comunidad. Gracias al profesor **Fernando Martín** y su equipo: **Sandra**, **Cristina** y **Joel**, por su trabajo e implicación en el estudio de las azaborinas. Gracias por todos vuestros consejos y recomendaciones, que hicieron que la publicación quedase redonda. Sandra, especialmente gracias a ti, que has estado siempre dispuesta a pasarme cualquier información o figura que he necesitado. Millones de gracias por tus correcciones para la tesis, y sobre todo por tratarme siempre con tanto cariño.

Many thanks to **Prof. Walther Schwarzacher** for hosting me so kindly during my stay in Bristol. Also thanks for your nice emails during the hard lock-down months. They kept my spirits up! So many thanks to all the members of the group (**Keisha**, **Yang**, **Nathan**, **Aswathi**, **Fred** and **Sarah**) for being so open and cheerful with me. Special thanks to Keisha and Yang, who helped me to become familiar with their STM, and spent their time in sharing with me all the tricks. Also thanks to Nathan, Fred, **Alicja**, **Vahar** and **Daniel** for the “dinner and cinema” sessions. Aswathi and Fred, you were very kind with me not only at Uni, but also at home, sharing everything with me.... Thank you so much! I am very grateful for the time I spent in Bristol, since I can say I was truly happy there.

También me gustaría expresar mi agradecimiento a los doctores **Javier Murciano** y **Francisco Castillo**, mis primeros mentores, quienes han seguido apoyándome aún en la

distancia. A veces sueño que estamos de nuevo juntos en el labo, haciendo cribados con los fagos, picando colonias o preparando librerías. Ambos sois increíbles, os admiro y os quiero. Gracias a **Anamari, Valeria y Sergio** por seguir preocupándoos por mí a pesar de haberme mudado de departamento. Habéis sido unos verdaderos amigos, habéis compartido conmigo vuestros triunfos y también vuestras penas. Parte de mí será siempre *química* gracias a todos vosotros.

Gracias a mis químicas de siempre: **Inma, Alba y Bea**. ¡Cuánto le debo a esta carrera por haberos conocido, y por todos los buenos momentos que hemos pasado! Inma, gracias por cada mensaje, por cada abrazo y por compartir cada poema. Siempre has estado a la luz o a la sombra apoyándome. Espero que la vida nos permita seguir estando cerca. Gracias a mi querido **Ginés**, con quien he compartido tantas comidas que siempre perdemos la cuenta de a quién le toca pagar. Un ratito de desahogo contigo siempre me salva. Gracias infinitas a mi *Review chemistry & Co* (**Gloria, Antonio, Miguel Ángel, Julia y Tomás**), mi quinteto (casi) siempre dispuesto a ver el último estreno, resolver misterios como el mismísimo **Sherlock**, conquistar Poniente (ahora los reinos de papel), disparar balas, robar honores, hacer el gusano, cambiar ladrillos por ovejas y hacer saltar todo por los aires con una bomba. Podremos ser más, pero nunca menos. ¡Que nunca nos falten las ganas de ponernos **Mendos**!

Marta, gracias por estar siempre tan cerca a pesar de estar tan lejos. Desde aquella primera mirada, tus ojos nunca han dejado de transmitirme la confianza que necesitaba, y te estaré siempre agradecida. Eres la persona más valiente que conozco y te admiro infinitamente. *No importa de qué materia sea el lazo que nos une, lo importante es que ese lazo existe.*

Gracias a mi **familia**, grande y extensa, que no deja de creer en mí. Gracias por apoyarme tanto y siempre, a pesar de mis errores y mis caídas. Finalmente, gracias a mis padres y a mi hermana, por ser esa tierra fértil donde todas las semillas florecen. No hay forma humana de agradecer todo lo que habéis hecho por mí. Aun debiéndoslo todo, insistís en que no os debo nada: *esto es amor, quien lo probó lo sabe*.⁸ Gracias por ser mi fuente continua de inspiración.

⁸ Último verso del soneto CXXVI de Lope de Vega

A los que estuvieron,
porque vuestro recuerdo ha caminado junto a mí
en cada paso que me ha traído a este momento.

Mi trabajo
consiste
en un
fluir
i
n
t
e
r
mi
nable
de electrones
que buscan besar los campos de oro
que se vislumbran a la salida de un túnel.

Antes de ser fijado y retenido, sin embargo, el poema es su peso en la red neuronal. Lo que llamamos intuición o idea pesa aún menos, no más que los ligeros electrones que en la mente –esas masas boscosas del interior del cráneo- vuelan de rama en rama como un pájaro gris.

Juan F. Rivero

Resumen

La electrónica molecular es la rama de la ciencia que estudia los fenómenos de transporte electrónico a escala de moléculas individuales. Entre otras cosas, permite explorar el comportamiento de diferentes funciones químicas; buscar estructuras moleculares capaces de emular el funcionamiento de componentes de circuitos electrónicos macroscópicos como cables, transistores, interruptores, etc; y estudiar modelos moleculares pequeños y más accesibles de materiales de mayor área. En los últimos años, la investigación en esta disciplina ha cruzado los límites de la mera electrónica, haciendo posibles estudios de fotovoltaica, termoelectricidad o filtro de spin y abriendo la ventana de funciones y aplicaciones de estos sistemas moleculares a la nanoescala.

Esta tesis doctoral se ha desarrollado de forma complementaria entre dos laboratorios, concretamente el laboratorio FQM-367 del Departamento de Química Orgánica de la Universidad de Granada y el laboratorio de Electrónica Molecular de la Fundación IMDEA Nanociencia en Madrid. En ella, se combinan el diseño y la síntesis de moléculas orgánicas con el estudio de sus propiedades de transporte electrónico mediante la técnica de rotura de uniones con un microscopio de efecto túnel (STM), y con la implementación de mejoras en el equipo de medida. Como parte de la tesis, también se ha llevado a cabo la instalación de un microscopio de efecto túnel en el Centro de Instrumentación Científica de la Universidad de Granada, el cuál fue previamente fabricado en las instalaciones de IMDEA Nanociencia. Finalmente, los estudios realizados se han completado haciendo uso de modelos computacionales que ayudasen a explicar y predecir los resultados experimentales, lo cual ha sido posible gracias a una estrecha colaboración con grupos de expertos en cálculos teóricos. De esta forma, la presente tesis recoge un trabajo interdisciplinar en el que la electrónica molecular ha sido abordada tanto desde un punto de vista químico como físico.

El manuscrito se divide en seis capítulos, al final de cada uno de los cuales se encuentra la sección de referencias correspondiente. En el primero se hace una introducción general a la electrónica molecular, revisando las principales técnicas para realizar medidas de transporte electrónico a nivel unimolecular, explicando qué información nos proporcionan dichas medidas y presentando las bases teóricas de los modelos

desarrollados para estudiar los fenómenos de transporte electrónico en la nanoescala. Igualmente, se incluye una breve revisión de los diferentes elementos de una unión molecular, centrándonos en las posibles aplicaciones de los esqueletos moleculares según las propiedades que exhiben.

La investigación llevada a cabo durante la tesis, se ha desarrollado a lo largo de los siguientes cuatro capítulos (capítulos 2-5), los cuales se estructuran de la siguiente manera: i) Introducción al tema de estudio concreto, ii) Objetivos de la investigación, iii) Resultados y discusión y iv) Conclusiones.

Más concretamente, el capítulo 2 se centra en sistemas moleculares multiestado, diseñados para presentar más de dos valores de conductancia. Como forma novedosa para conseguir esto, se ha propuesto la introducción de un grupo de anclaje en una posición asimétrica del esqueleto molecular. Como prueba de concepto, se ha diseñado un derivado de oligo-*para*-pheniletinileno (*p*-OPE) con un anillo pirimidina en una posición asimétrica. Los resultados demuestran la aparición de dos nuevos caminos de conducción bien diferenciados entre sí, adicionales al camino que va de extremo a extremo, probando así la validez de nuestra propuesta.

El capítulo 3 está dedicado a azaborinas, una familia de heteroarenos sustituidos con nitrógeno y boro, simultáneamente. Esta función química, que aparece frecuentemente en sistemas π -extendidos, da lugar a compuestos isoelectrónicos e isoestructurales a los análogos carbonados, pero introduciendo una polarización de carga en el sistema. En este capítulo se presentan las primeras medidas de conductancia de motivos de aceno incluyendo anillos de azaborina, con la particularidad añadida de que los heteroátomos se encuentran de forma inequívoca en el camino de conducción de los electrones.

El capítulo 4 está dedicado a pequeños hidrocarburos aromáticos policíclicos (PAHs) que presentan curvatura negativa como consecuencia de la presencia de anillos heptagonales en su estructura. En general, los PAHs están suscitando un creciente interés debido a sus propiedades optoelectrónicas únicas. En particular, las propiedades eléctricas de estos sistemas con curvatura negativa no han sido investigadas por el momento, a pesar de poder ser usados como modelos de pequeño tamaño sobre los que explorar el efecto de los anillos heptagonales en el grafeno. En este capítulo se discuten las estrategias

sintéticas para la incorporación de diferentes grupos de anclaje a las estructuras y se presentan las primeras medidas de conductancia para PAHs con curvatura negativa. Finalmente, se incluye un análisis exhaustivo del comportamiento del grupo acetileno terminal como grupo de anclaje, que es usado para comparar los resultados de conductancia de una de estas estructuras curvas con su correspondiente análoga plana.

En el capítulo 5 se detalla el proceso de implementación de un sistema de control electroquímico en el microscopio habitual de medida. Además, se presentan los resultados preliminares para medidas realizadas combinando control electroquímico y electrodos magnéticos.

El capítulo 6 recoge las conclusiones generales de la tesis.

A continuación, se ha incluido una Sección Experimental que contiene, entre otros, una descripción del microscopio usado para las medidas de conductancia unimolecular y los detalles sintéticos para la preparación de las estructuras estudiadas. Finalmente, se ha añadido una lista de Acrónimos y Abreviaturas, además de otra de Publicaciones, tanto derivadas de la tesis como de otras colaboraciones.

Abstract

Molecular electronics is the field of science that studies the electron transport phenomena at the scale of one individual molecule. It allows us to evaluate the effect of different chemical functions; search for molecular structures able to emulate the functioning of components of electronic circuits, such as wires, transistors, switches, etc; and study small and more accessible molecular models of large area materials. In the last years, the research in this field has crossed beyond the limits of mere electronics, making possible studies on photovoltaics, thermoelectricity and spin filtering; broadening the spectra of potential functions and applications for nanoscale molecular systems.

This thesis has been carried out between two complementary laboratories, namely the FQM-367 organic chemistry lab at the *Universidad de Granada* and the molecular electronics lab at the *Fundación IMDEA Nanociencia* in Madrid. It covers the design and synthesis of several novel organic compounds as well as the experimental characterization of their electron transport properties by means of Scanning Tunneling Microscopy Break Junction (STM-BJ) technique, including work in setup improvement implementation. As part of this thesis, a new home-built STM has been developed at *IMDEA Nanociencia* and it has been set up at the *Centro de Instrumentación Científica* from the *Universidad de Granada*. Supplementary collaborations with theoretician groups have expanded the studies, creating models able to explain the experimental observations. Consequently, this thesis comprehends an interdisciplinary research, in which molecular electronics has been tackled from both, chemical and physical points of views.

The manuscript is divided into six chapters, with their corresponding references included at the end of each one. The first chapter consists on a general introduction to molecular electronics, where the principal techniques for single-molecule experiments are collected; the most relevant information they provide is explained; and the theoretical model for understanding the electron transport phenomena in nanoscale molecular systems is presented. Besides, a brief revision of the elements of a molecular junction is included, with special interest on the applications of different molecular backbones according to the properties they exhibit.

Then, the research developed in this doctoral thesis is depicted in the next four chapters (Chapter 2-5). Each of these chapters contains the following sections: i) a background of each specific topic, ii) objectives of the research, iii) results and discussion, and iv) conclusions.

In particular, Chapter 2 is focused on multistate molecular systems, designed for displaying more than two conductance values. The introduction of an in-backbone linker in an asymmetric position of the molecular bridge is proposed as strategy for achieving three different conductance paths in a controlled manner. In particular, an oligo-*para*-phenylethyne (*p*-OPE) derivative, containing a pyrimidine ring in an asymmetric position of the backbone, is used as proof-of-concept for this hypothesis. The results show that this configuration opens two new conduction channels well distinguished from each other in addition to the end-to-end pathway.

Chapter 3 is focused on azaborines, a family of boron–nitrogen heteroarenes. This chemical function appears frequently in π -extended systems like graphene, and leads to isoelectronic and isostructural compounds of the all-carbon analogues, but originating a charge polarization in the system. For the first time, conductance measurements of azaborine-acene derivatives are performed, with the added incentive that heteroatoms are forced to be in the most probable electron pathway.

Chapter 4 is dedicated to small polycyclic aromatic hydrocarbons (PAHs), which exhibit a negative curvature due to the presence of 7-membered rings into their structure. PAHs in general are raising an increasing interest due to their fascinating optoelectronic properties. However, the electrical properties of these curved PAH cores have not been studied yet, in spite of being attractive models for studying the effect of heptagons in graphene. The synthetic strategies for incorporating different anchoring groups into these structures are discussed, and the first conductance measurements of PAHs with negative curvature are presented. Finally, an exhaustive analysis of the behaviour of terminal acetylene groups as anchoring groups is developed, while comparing the conductance of one of the prepared curved PAHs with that of its corresponding planar analogue.

In Chapter 5, the implementation of an electrochemical control system in our STM is detailed. Besides, the preliminary results obtained for simultaneous application of electrochemical control and magnetic electrodes, obtained during a short stay at Bristol University, are presented.

In Chapter 6, a series of general conclusions from the results of the thesis are collected.

Finally, an Experimental Section, containing a description of the STMs used for the single-molecule experiments, as well as the synthetic details for preparing the studied compounds, is included. An Acronyms and Abbreviations section and a List of Publications derived from the thesis results and from other collaborations are added at the end.

TABLE OF CONTENTS

Chapter 1. GENERAL INTRODUCTION

1.1. Molecular electronics	37
1.2. Experimental techniques for single-molecule experiments	40
1.2.1. Break junction technique.....	41
1.2.2. Conductance quantization in atomic metallic contacts.....	43
1.2.3. Single-molecule conductance measurements	45
1.3. Characterization of single-molecule junctions	49
1.3.1. Analysis of <i>G-z</i> traces.....	49
1.3.3. Analysis of conductance traces by multi-parameter vector-based method	50
1.3.4. Current-voltage (<i>I-V</i>) characteristics	53
1.4. Theoretical models for electron transport phenomena	54
1.4.1. Electron conduction at the nanoscale.....	54
1.4.2. Density functional theory and non-equilibrium Green's function (DFT-NEGF) ..	56
1.4.3. Gap correction.....	58
1.5. Elements of a molecular circuit	60
1.5.1. Electrodes.....	60
1.5.2. Anchoring groups	62
1.5.3. Molecular backbone	66
1.6. Beyond conductance measurements	74
1.6.1. Thermoelectricity and thermoelectric effect	74
1.6.2. Gating voltage	76
1.6.3. Magnetic measurements.....	77
1.7. Overview and main goals	79
References	82

Chapter 2. MULTIPLE CONDUCTANCE PATHWAYS IN PYRIMIDINE-BASED OLIGO(PHENYLENEETHYNYLENE) DERIVATIVES

2.1. Introduction	99
2.1.1. Multi-conductance-state systems based on multichannel compounds.....	100
2.1.2. Overview and main implications of previous examples.....	108

2.2. Objectives.....	109
2.3. Results and discussion	111
2.3.1. Molecular design	111
2.3.2. Synthesis	112
2.3.3. Break-junction experiments.....	114
2.3.3.1. Conductance of OPE4-pym.....	115
2.3.3.2. Theoretical models.....	116
2.3.3.3. Conductance of the reference compounds and comparison with the corresponding channels.....	118
2.4. Conclusions.....	129
References.....	130

Chapter 3. EFFECT OF AZABORINE SUBSTITUTION ON THE SINGLE-MOLECULE CONDUCTANCE OF ACENES

3.1. Introduction.....	137
3.1.1. 1,2-azaborines	140
3.1.2. 1,3-azaborines.....	144
3.1.3. 1,4-azaborines	146
3.1.4. Electronic properties of azaborines	150
3.1.5. Overview	153
3.2. Objectives.....	155
3.3. Results and discussion	157
3.3.1. Molecular design	157
3.3.2. Synthesis	159
3.3.3. Break-junction experiments.....	160
3.3.3.1. Effect of 1,4 BN substitution in anthracene scaffold: conductance of CCA and BNA	161
3.3.3.2. From terphenyl to anthracene: unravelling the effect of the lateral rings ...	164
3.3.3.3. 1,4-BN substitution in larger acenes: conductance of BNP	166
3.3.3.4. Clustering analysis of <i>G-z</i> traces for CCA, BNA and BNP.....	167
3.3.3.5. Demonstrating the acene-gold interaction hypothesis	171
3.3.4. Theoretical modelling.....	172
3.4. Conclusions.....	177
References.....	178

Chapter 4. ELECTRON TRANSPORT THROUGH CURVED HEPTAGON-CONTAINING NANOGRAFENES

4.1. Introduction.....	189
4.1.1. Preparation of nanographenes	192
4.1.1.1. Top-down methods	192
4.1.1.2. Bottom-up methods.....	193
4.1.1.3. In-solution synthesis of purely hexagonal nanographenes.....	194
4.1.1.4. Nanographenes containing odd-membered rings.....	201
4.1.1.5. Synthetic strategies for nanographenes containing heptagons.....	204
4.1.2. Nanographenes for electronic applications	206
4.2. Objectives.....	215
4.3. Results and discussion	217
4.3.1. Molecular design	217
4.3.2. Synthesis	219
4.3.3. Break junction experiments.....	226
4.3.3.1. Effect of the linker on the conductance of 7-HBCs	227
4.3.3.2. Conductance of 7-oliphenylene	231
4.3.3.3. Effect of the 7-membered ring and analysis of terminal acetylenes as linkers	233
4.4. Conclusions.....	241
References.....	242

Chapter 5. MOLECULAR-JUNCTION STUDIES UNDER ELECTROCHEMICAL CONTROL

5.1. Introduction.....	255
5.1.1. Electrochemical gating of a single molecule	258
5.1.2. BJ experiments with electrodes made of metals different from gold.....	264
5.1.3. Measurements with magnetic electrodes.....	266
5.1.4. Overview	271
5.2. Objectives.....	273
5.3. Results and discussion	275

5.3.1. Implementation of the electrochemical control system into the <i>IMDEA Nanociencia</i> setup.....	275
5.3.1.1. Designing the electrochemical cell.....	275
5.3.1.2. Electrode preparation.....	276
5.3.1.3. The electric circuit.....	281
5.3.2. Experiments with ferromagnetic electrodes under electrochemical conditions at the University of Bristol.....	283
5.3.2.1. University of Bristol setup.....	283
5.3.2.2. Electrode preparation.....	285
5.3.2.3. The experiments.....	288
5.4. Conclusions.....	291
References.....	292

Chapter 6. GENERAL CONCLUSIONS

6.1. General Conclusions.....	303
Experimental Section.....	307
Acronyms and Abbreviations.....	351
List of Publications.....	355
Annexes.....	357

**CHAPTER 1:
GENERAL INTRODUCTION**

1.1. Molecular electronics

Molecular electronics is the field of science that investigates the electronic and thermal transport properties of circuits in which individual molecules (or assemblies of them) are used as basic building blocks.¹ This involves to understand the flux of electrons to and through single molecules in atomic or nano-size junctions, and entails notable experimental and theoretical difficulties. From a theoretical perspective, the electron transport phenomena in nanosystems is not governed by the same rules as macroscopic ones, being necessary a quantum mechanical approach to describe it. Concerning the experimental side, questions like *how to attach molecules to electrodes?*, *how to create atomic-sized junctions?*, *how to keep these junctions stable?*, *which are the electrode requirements?* and *how to struggle with large fluctuations in experimental data?* have been, and still are, open challenges.²

It is difficult to establish a clear date for the beginning of molecular electronic as an independent research field, but it is clear that its development has been the result of different contributions from experimental physicists, electrical engineers, and computational, physical and synthetic chemists along years.³ In view of the social demands of miniaturization of electronic devices, and the physical limits given by the Moore's Law^a (Figure 1.1) in the context of silicon-based devices, individual molecules were soon considered the smallest elements for a promising new generation of devices. In 1974, Aviram and Ratner published the first theoretical discussion of electron transport through a single molecule, which could act as a rectifier.⁴ In the 80s, the development of the scanning tunnelling microscope (STM),⁵ and later the atomic force microscope (AFM),⁶ provided tools able to manipulate single molecules. However, preliminary measurements of the electrical properties of single molecules were not a reality until 1997, when Tour and co-workers reported the conductance of benzene-1,4-dithiolate, connected between stable and proximal metallic gold contacts at room temperature.⁷ Later, Lindsay and co-workers pointed out the need of reproducible measurement.⁸ In this direction, Tao's group started to apply the experimental procedure and the same statistical analysis already being

^a Moore's Law predicts a doubling of the performance and functionality of digital electronics about every two years. Nevertheless, this growing trend is anticipated to flatten by 2025, as a consequence of the physical limits of space and capacity of silicon-based electronic devices.

used for the study of atomic metallic junctions,^b achieving the desired reproducibility.⁹ From that moment, important knowledge about electron transport itself has been collected, but also the electrical properties of different families of molecules have been investigated. Importantly, the development of the non-equilibrium Green's function approach in the early 21st century led to more reliable junction modelling, with remarkably good agreements between calculations and experiments.¹

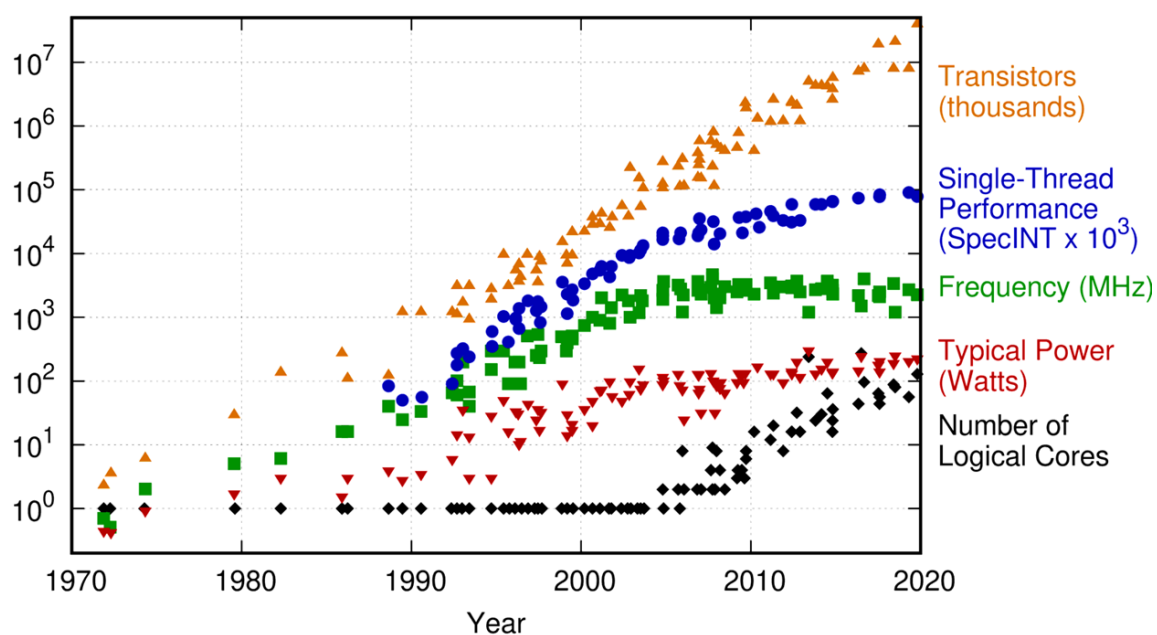


Figure 1.1. Moore's Law. 'Microprocessor trend data', in particular for transistors (orange), single-thread performance (blue), frequency (green), power (red) and logical cores (black). The units in y-axis are indicated for each data set. Original data up to year 2010 collected and plotted by M. Horowitz, F. Labonte, O. Shacham, K. Olukotum, L. Hammond, and C. Batten. Plot data collected for 2010-2019 by K. Rupp. Creative Commons Attribution 4.0 International Public License^c

However, the fabrication of operative single-molecule devices, able to compete against silicon ones, has not been already achieved due to their low conductance, which involves a very limited application capacity. Nowadays, pointing to the next technological revolution, individual molecules are considered as possible silicon microelectronics complements rather than competitors, since they open a wide range of potential functionalities not existent for macroscopic circuits.³ Currently, the field is still progressing,

^b The creation and analysis of atomic metallic junctions are detailed in section 1.2.2.

^c Figure 1.1, raw data and license available at K. Rupp Webpage (<https://www.karlrupp.net/2018/02/42-years-of-microprocessor-trend-data/>).

gaining fundamental knowledge about transport phenomena and thermal conduction at the nanometric scale, where the physics is completely dominated by quantum mechanical effects. It offers the possibility to explore the electrical properties of new molecules, investigating the role of different chemical functions and molecular properties, such as aromaticity, on the electron transport. Due to that, the research in the field has crossed beyond the limits of mere electronics, towards spin filtering,¹⁰ photovoltaics¹¹ and thermoelectricity,¹² among others. Importantly, it had also permitted to shed light into the electron transport and transfer mechanisms involved in natural processes, such as photosynthesis, respiration and neural communication.¹

1.2. Experimental techniques for single-molecule experiments

Different experimental techniques have been used for the measurement of the electrical resistance R associated to a single molecule. In all cases, it is necessary to incorporate the molecule into an electric circuit and force the electron flux to and through it. Ohm's law establishes that the current I is proportional to the applied voltage V , being the electrical conductance G the constant of proportionality between them.

$$I = GV = \frac{1}{R}V \quad (\text{Eq.1.1})$$

Since the conductance corresponds to the inverse of the electrical resistance, it is extended the use of this parameter for describing the electrical conduction through a single-molecule. To determine the conductance of a single molecule, it is mandatory (i) to provide a signature to identify that the measured conductance corresponds to a single-molecule junction, (ii) to ensure that the molecule is properly attached to both electrodes, and (iii) to perform the measurement in a well-defined environment.¹³ Considering that, the desired configuration of single-molecule junctions is depicted in Figure 1.2, with a molecule fully extended between two metallic electrodes. In order to provide a good molecule-electrode contact, two binding groups (also called linkers or anchors) are located at both ends of the molecule.

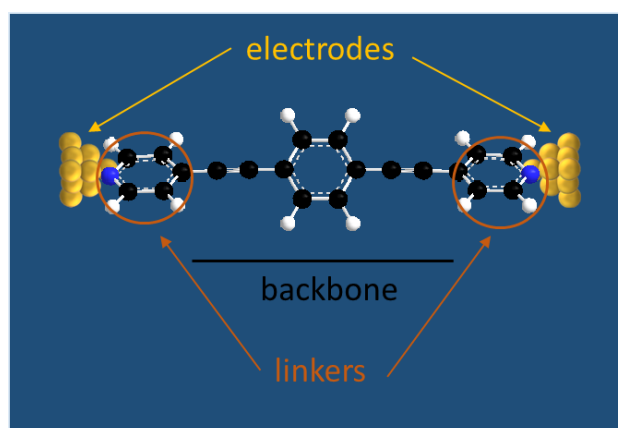


Figure 1.2. Molecular junction consisting of a single molecule wired between two metallic electrodes by means of two linkers or anchoring groups, which permit the molecule-electrode interaction.

Several techniques are able to provide the aforementioned configuration, such as break junction, electro migration or contact conductive probe AFM. Basis and functioning of all of them can be found in literature, as well as specific examples of experimental studies conducted with them.^{13,14} Among them, break-junction technique, based on repetitive mechanical formation and rupture of metallic atomic contacts, is the most broadly employed and it has been the one used for the single-molecule experiments developed during this thesis. In the next section, the bases of this technique are detailed.

1.2.1. Break junction technique

Given the difficulty to fabricate electrodes separated by a nanogap and able to fit molecules precisely, an extended strategy is making cycles of bringing two electrodes together until forming a metallic contact and separating them apart mechanically, leaving two clean atomically sharp electrodes. Two different instruments have been preferably used for applying this technique: (i) a mechanically controllable break junction (MCBJ) device and (ii) a scanning tunneling microscope (STM). Although these two instruments seem very different, they permit to create atomic and molecular junctions with the same characteristics, being comparable the results obtained with them.

Mechanically controllable break junction (MCBJ)

The schematic top and side views of the assembly of a MCBJ are depicted in Figure 1.3a, while a real picture of the top view of one of its earliest examples is shown in Figure 1.3b.

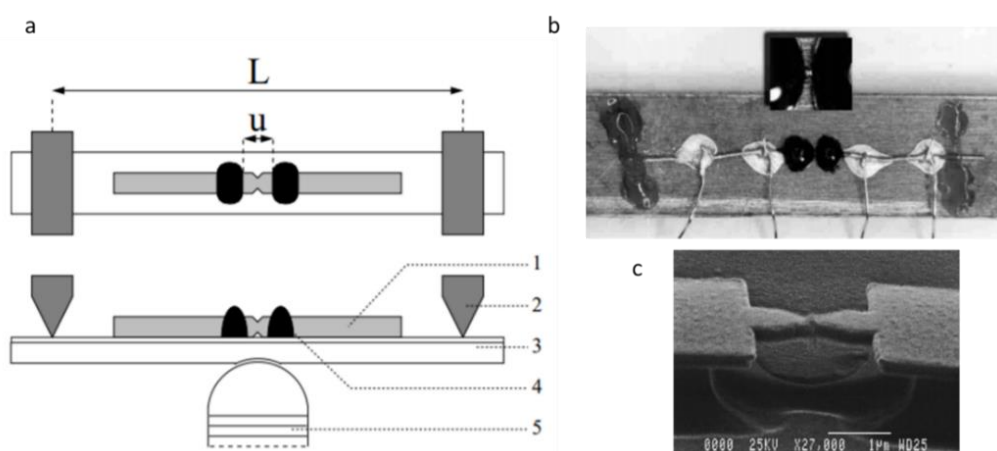


Figure 1.3. (a) Schematic top and side views of the assembly of a MCBJ with the metal wire (1), two holders for fixing the substrate (2), bending substrate (3), drops of epoxy adhesive for fixing the wire (4) and the

EXPERIMENTAL TECHNIQUES FOR SINGLE-MOLECULE EXPERIMENTS

piezoelectric tube (5). **(b)** Top view of a MCBJ set up with metallic wires. **(c)** Scanning electron microscope picture of a modern MCBJ device fabricated by electron beam lithography. **(a)** and **(b)** Reproduced with permission of ref.¹⁵ Copyright © 2003 Elsevier Science B.V. All rights reserved. **(c)** Reproduced with permission of ref.¹⁶ Copyright © 1996 managed by AIP Publishing.

Its functioning is based on the break of a thin metal wire with a middle notch, into a pair of facing electrodes. To do so in a controlled way, the ends of the wire are fixed on top of a flexible substrate which is bent using a three-points bending mechanism. It is pushed in the middle part with a rod connected to a mechanical gear until the wire breaks and two clean fracture atomically sharp electrodes surfaces are exposed. The fracture surfaces can be brought back into contact by relaxing the force on the substrate.¹⁵ In 1996, Urbina and co-workers proposed the use of electron beam lithography for fabricating this kind of contacts in a reproducible manner and controlling the neck geometry (Figure 1.3c).¹⁶ In this way, the system became more stable and less sensitive to external vibrations.

Scanning tunnelling microscope (STM)

It consists of a sharp metallic tip placed in proximity to a metallic surface, close enough to establish a tunneling current when a bias voltage is applied between them (Figure 1.4a). The tip acts as a probe able to measure the current along the substrate surface, arranged perpendicular to it. The STM functioning is based on the quantum tunneling effect, in other words, on the ability of electrons to cross from a region of the space (1) to another (2), when they are separated by a potential barrier V_0 , as schematically depicted in Figure 1.4b. In classical mechanics, the electron transmission can only occur when the electron energy E is higher than V_0 . However, in quantum mechanics, it exists a finite probability, known as transmission probability (T), for the electron to cross through the potential barrier even when E is lower than V_0 . When a potential difference is applied between STM tip and substrate, the distance between them (z axis) defines the dimension of the potential barrier that electrons have to surpass for going from an electrode to the other. This transmission decays exponentially with the barrier width L (distance between the electrodes) and it is able to originate an electric current known as tunneling current. The exhaustive control of the movement of the tip along the x , y , and z axes, with resolution even on the picometers or below, is achieved by means of assembling it to a piezoelectric element, which suffer mechanical deformation when a voltage is applied. Although the conventional used of the STM is the surface topography scanning with atomic resolution, it also allows the creation

of atomic metallic junctions of the same nature of those of the MCBJ device. This is done by repeatedly moving the STM tip, into and out of contact with the substrate electrode, in the z axis. In the process, the current value is used as a guide to know when the circuit is closed and when it is open. As advantage over the MCBJ, the break junction technique base in STMs (STM-BJ) permits to collect thousands of conductance traces in a short time, allowing to perform highly reliable statistical analysis.

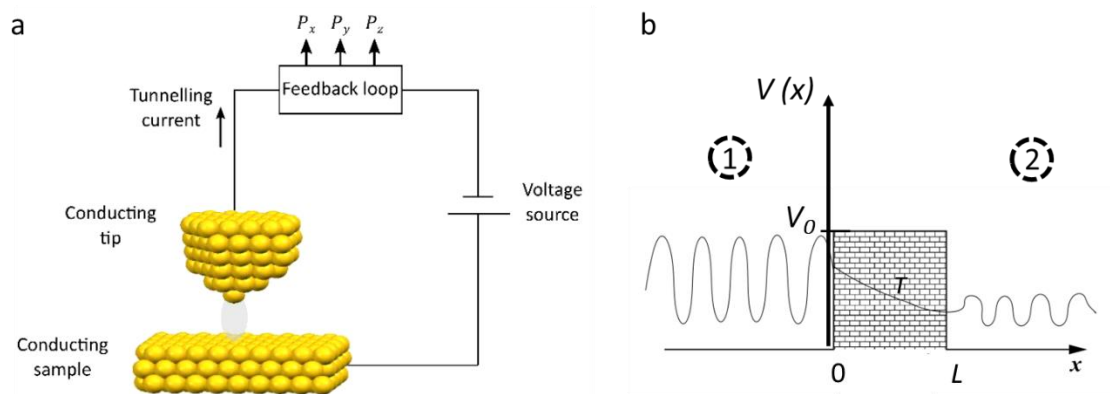


Figure 1.4. (a) Working principle and main components of a STM. Reproduced from ref.¹⁷ (b) Scheme of the tunneling effect. It exists a probability of transmission T for the electron from region 1 to region 2, through a potential barrier V_0 of width L . Adapted from ref.¹

1.2.2. Conductance quantization in atomic metallic contacts

The break junction technique was firstly used for studying electron tunnelling phenomena¹⁸ and demonstrating the conductance quantization in atomic metallic contacts.¹⁹ The stretching process of an electrode contact is schematically depicted in Figure 1.5a. The analysis of the current recorded during the repeated breaking process of metallic contacts revealed a stepwise fashion, in which every step concurred at nearly multiples of the same value. This behaviour can be appreciated in the conductance versus distance (G - z) curve, shown in Figure 1.5b, which corresponds to the breaking of a gold contact. These steps, also called plateaus, were found to be due to the breaking of the metallic contact atom by atom. The conductance values at which the steps occur are specific of each metal. In particular, they are related to the atomic orbitals contributing to

EXPERIMENTAL TECHNIQUES FOR SINGLE-MOLECULE EXPERIMENTS

electron conduction.^d In the case of monovalent metals (Cu, Ag, Au and the alkali metals Li, Na and K), plateaus tend to have a sloping profile for the higher conductance values when the contact size is large; while they are well-defined and almost horizontal for the lowest conductance values when the contact consists in a few atoms.¹⁵ Every plateau ends with a sharp jump toward the next, decreasing the conductance in the order of the quantum unit G_0 ($G_0 = 2e^2/h = 77.5 \times 10^{-6}$ S). The last plateau at $1 G_0$ corresponds to a contact consisting in just one atom, so that, its rupture is a proof for the total breakage of the contact. When the last atomic contact breaks, the atoms of both electrodes, previously suffering tension due to the stretching, shrink abruptly in a relaxation mechanism that involves atomic rearrangements. This produces a significant abrupt decay of conductance just after the $1G_0$ plateau (Figure 1.5c, region 2). Then, as the separation of electrodes continues, the current decreases nearly exponentially with such separation in the tunnelling regime (Figure 1.5d, region 3). Finally, the current arrives to the noise level (Figure 1.5d, region 4).

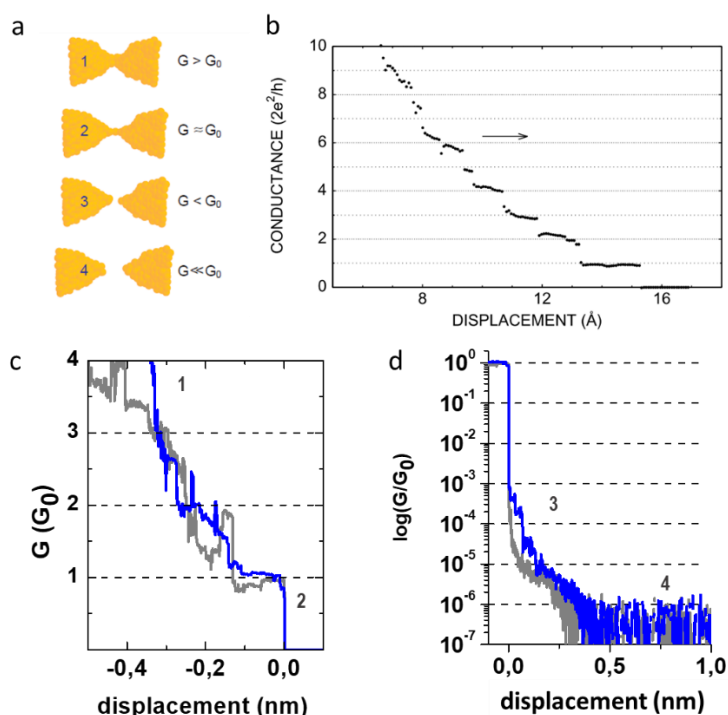


Figure 1.5. Stretching of a gold contact. **(a)** Four particular situations can be distinguished: 1) formation of a neck due to the stretching of the electrodes, 2) the contact between electrodes is reduced until being formed just by one atom, 3) when the contact finally breaks, the electrode suffer a retraction due to the previous stretching tension and a tunnelling current is flowing between them, 4) the electrode separation carries on up to a distance out of the tunnelling regime. **(b)** Conductance curve for the rupture of a gold

^d The theory of the electric conduction in this kind of systems at the nanoscale is detailed later in section 1.4.1.

contact. During the stretching of a gold contact, the conductance decreases in a stepwise fashion, where every step occurs at multiple of G_0 . **(c)** Linear representation of two G - z traces where plateaus not occur at every multiple of G_0 . The G - z regions corresponding to situations 1 and 2 of panel a have been signalized. **(d)** Logarithmical representation of the same two G - z traces displayed in panel c, between $(G/G_0) = 1$ and $(G/G_0) = 0$. The G - z regions corresponding to situations 3 and 4 of panel a have been signalized. **(c)** reproduced with permission of ref.²⁰ Copyright ©1995 American Physical Society.

Since each trace reflects an individual breakage process and the atomic structure of the electrodes can change from junction to junction, strong conductance fluctuations are observed from trace to trace. Then, a statistical data analysis is carried out on sets of large number of individual G - z traces in order to capture the full complexity of the system.²¹

The standard manner to summarise the recorded traces is to plot one-dimensional (1D) histograms of G (Figure 1.6). In these 1D histograms, the number of counts measured in fixed G intervals is accumulated. This means that peaks are found at that G values corresponding to the aforementioned plateaus. Besides, the higher the number of conductance traces used for building the histograms, the more apparent these peaks will be. As example, in Figure 1.6 it is shown the 1D histograms of gold contacts built with 3000, 6000, 9000, and 12000 traces.²²

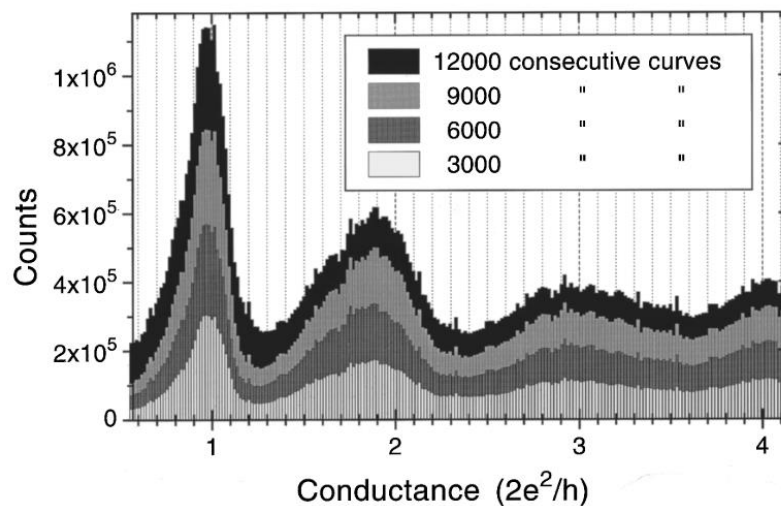


Figure 1.6. 1D Conductance histogram for gold contacts. The intensity of the peaks depends on the number of curves used for building the histograms. Reproduced with permission of ref.²² Copyright © 2003 Elsevier Science B.V. All rights reserved.

1.2.3. Single-molecule conductance measurements

EXPERIMENTAL TECHNIQUES FOR SINGLE-MOLECULE EXPERIMENTS

In 1997, Tour and collaborators reported for the first time the use of the MCBJ for conductance measurements of molecular junctions.⁷ They exposed the electrodes to a solution containing benzenedithiol and, after evaporation of the solvent, they measured a finite current between the electrodes. This current was attributed to the electron transport through benzenedithiol molecules, even though it was not still clear how many molecules were involved in the conduction and whether the molecules were bound to both electrodes. In the next years, large disparities in the electron transport were reported for identical or very similar molecules, until 2001, when Lindsay and collaborators highlighted the enormous importance of the molecule–electrode bonding.⁸ They immersed a gold substrate in a solution of octanethiol molecules in which a small amount of octanedithiol molecules had been incorporated. These molecules created a monolayer onto the gold surface, being the octanedithiol molecules dispersed randomly between the octanethiol ones. The protruding thiols of dithiolated molecules could be functionalized with gold nanoparticles. Using a conducting AFM, they probed that nonbonded contacts to the octanethiol monolayer were at least four orders of magnitude more resistive, less reproducible and had a different voltage dependence than bonded contacts through the Au-functionalized octanedithiol (Figure 1.7a).

In 2002, Weber and co-workers applied a fixed voltage across the electrodes during the closing of the metallic contacts, and recorded the current.²³ Initially, the current grew exponentially due to electron tunneling across the gap. When the gap was decreased to a certain width, the current locked sometimes into a stable value or plateau, not clearly dependent on the gap width (Figure 1.7b).

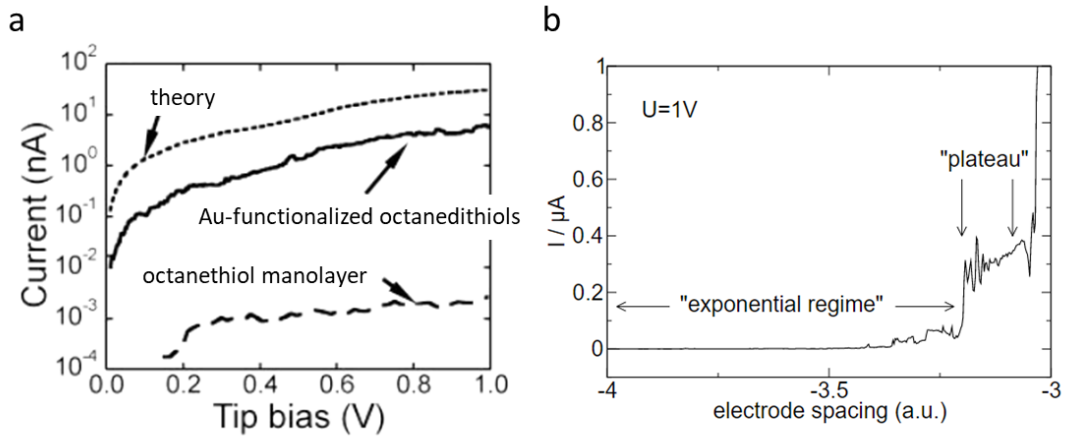


Figure 1.7. (a) Current (on a log scale) as a function of voltage calculated from first principles with no adjustable parameters (dashed line), measured for a bonded single molecule (solid line), and for a nonbonded contact to the surrounding octanethiol matrix (broken line) (noise-dominated data at low bias are suppressed). Adapted with permission of ref.⁸ Copyright © 2001, The American Association for the Advancement of Science. **(b)** Closing behaviour while establishing a metal–molecule–metal contact. While decreasing the distance between electrodes, the current is recorded (at a constant bias voltage of 1 V). After a region of exponential increase, the current suddenly displays a stable value (plateau), due to a molecular bridge. Reproduced with permission of ref.²³ Copyright © 2002 Elsevier Science B.V. All rights reserved.

In 2003, Xu and Tao used for the first time a STM for measuring the conductance of molecular junctions, with the same strategy previously used for studying atomic metallic contacts.⁹ In other words, the authors performed repeated formation and breakage of metallic contacts, but in this case, the substrate was previously exposed to a solution of the target molecule, namely 4,4'-bipyridine. Then, they analysed the G - z traces recorded for the stretching and observed often new steps at $G < G_0$ values (Figure 1.8b). These plateaus were assigned to the formation of molecular bridges able to postpone the breaking point of the junction, as shown in Figure 1.8a.

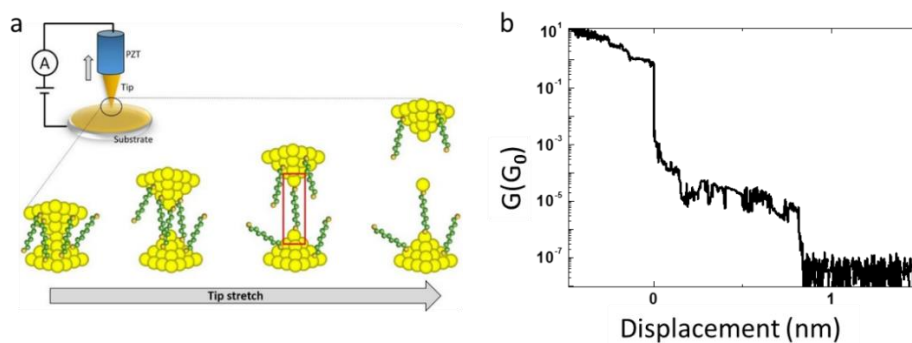


Figure 1.8. (a) Working principle of STM-BJ technique. Reproduced from ref.²⁴ **(b)** G - z trace of a molecular junction.

EXPERIMENTAL TECHNIQUES FOR SINGLE-MOLECULE EXPERIMENTS

Using this methodology with both, STMs and MCBJ devices, the conductance for a plethora of molecules has been successfully measured. An important factor to consider is that both instruments allow establishing a relationship between the length of plateaus and the separation between the electrodes (gap width). Considering the bridge configuration, with the molecule extended between the electrodes, such distance should depend on the length of the molecule involved in the junction. Therefore, the comparison of the stretching length with the known length of the molecule permits to check that the conductance signal is not due to oligomeric forms, and even elucidate the molecule geometry in the junction. However, they do not provide absolute certainty about the number of molecules in the junction, as this information cannot be extracted from the conductance value or the breakdown distance. In this sense, the STM allows to carry out a previous scanning of the electrode surface in order to avoid areas with self-assembled islands or monolayers. Therefore, single-molecule junction can be favoured by selecting low-coverage areas.²¹ Besides, it is possible to move the STM tip from one area of the surface to a fresh one during the measurements.¹³ For long measuring times, the use of STM is preferred, since the lifetime of the sample is directly related with the stability of the molecules of interest. Otherwise, MCBJ technique is selected when a fixed gap size is required for long periods, as it provides higher junction stability.

1.3. Characterization of single-molecule junctions

1.3.1. Analysis of G - z traces

Similarly as for atomic contacts, the general characterization of molecular junctions is based on the analysis of the G - z traces, which permits to obtain the most probable conductance value for the junction. Strong trace-to-trace conductance variations are also observed in this case, considering that not only the atomic structure of the electrodes can change from junction to junction, but also that a molecule can interact with the electrodes from different geometries.

In addition to the 1D conductance histograms previously explained, conductance versus electrode distance (2D) histogram are also built (Figure 1.9). For 2D histograms, it is important the conductance-distance alignment of the traces at the z point where the conductance of each trace reached G_0 (just when the last metallic contact is broken). Once the traces are aligned, it is built by accumulating the number of counts measured in fixed $\log(G/G_0)$ - z intervals from the traces, using a colour scale to symbolize the number of counts in each $\log(G/G_0)$ - z interval. A relevant appreciation is the use of $\log G$ rather than G for the representation of 1D and 2D histograms. This was proposed by Calame and co-workers,²⁵ being rapidly accepted as the proper representation, since the logarithmical scale permits a better identification of the molecular signal due to a better overview from the single-atom contact to the tunneling.

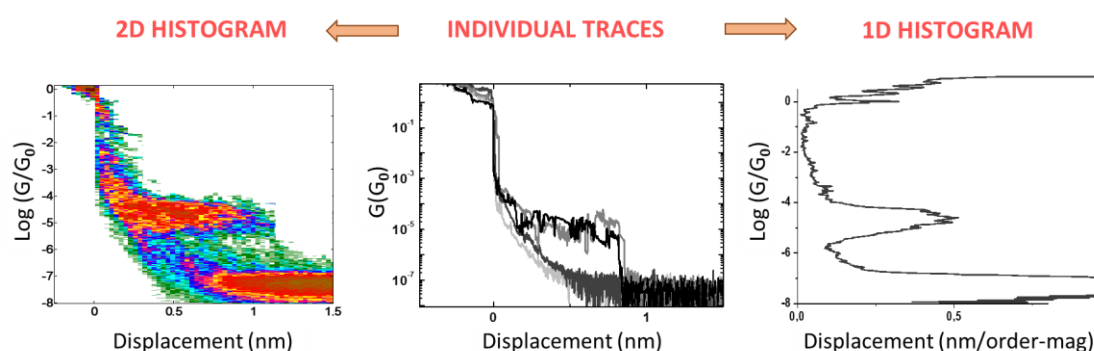


Figure 1.9. Formation of 1D and 2D histograms from the collected individual G - z traces.

1.3.2. Detection of plateaus and extraction of the conductance value

Considering that not all collected G - z traces display molecular plateaus, the separation of such traces from those presenting just tunnelling was proposed.²⁵ The 1D and 2D

CHARACTERIZATION OF SINGLE-MOLECULE JUNCTIONS

histograms built from only the traces displaying plateaus allow a better characterization of the molecular signal, since a more accurate assessment of the length of plateaus and the conductance value can be carried out. The conductance value is commonly extracted from 1D histograms, using a Gaussian fit to calculate the main value of the peak generated by the presence of plateaus. Although this value is given as the more probable conductance for the junction, the peaks have a width related with the range of conductance values at which the molecular signal can occur, which is generally about one order of magnitude.

2D histograms not only contain conductance information, but also plateau-length information. Besides, they provide the profile of plateaus, which can reveal information about additional processes or interactions taking place while the stretching of the electrodes.

The building of plateau-length histograms can provide useful information for identifying the most probable geometry of the molecule in the junction. The analysis of distances can also reveal the presence of more than one conduction pathways in the molecule and/or evidence the formation of oligomers.

1.3.3. Analysis of conductance traces by multi-parameter vector-based method

The direct histogram-based analysis, described above, presents certain deficiencies: i) it has a strong focus on the most abundant class of signals and sub-populations in the data may remain unnoticed; ii) different breaking events can promote molecular signals of very similar conductance value, being hard (even impossible) to distinguish them. Albrecht and collaborators proposed the use of vector-based classification algorithms to distinguish different molecular signatures within the collected data,^{26,27} as this analysis methodology had already demonstrated to be a powerful tool for categorizing data in fields such as neuroscience.^{28,29} For a current (or conductance) versus distance trace, this method considers the N current values as a vector X_n ($n=1, \dots, N$) in which each value is related with M distance observations. This results in a data matrix $X_{n,m}$ ($n=1, \dots, N$; $m=1, \dots, M$) for each trace. The $|\Delta X|$ between two vector points can be used as a measure for similarity between different data sets m and m' . If X_m and $X_{m'}$ are identical, then ΔX_m is zero; if they are very different, ΔX_m is large. After calculating all combinations of distances between the M data sets, a probability criterion may then be used to classify the traces. Since this distance-based criterion seems to be insufficient in many cases, an N -component vector R is

included in the system as reference, corresponding to exponentially decaying current–distance values, which mimic the experimental data without molecular binding events. In this context, it is possible to calculate the $|\Delta X|$ between every trace and the R vector, which permits to distinguish between traces differing from the reference vector in distinct ways and detect events which occur in low ratios of appearance.²⁷ It is worth mentioning that this classification method does not provide any physical interpretation of the data, and therefore, every group of classified data is then analysed independently using the well-known histogram-based methodology.

More recently, Perrin and collaborators reported a reference-free variation of this vector-based method,³⁰ in which each G - z trace is transformed into an image, more specifically into a 2D histogram. Then, each 2D histogram is converted into a feature vector, obtaining as many vectors as individual breaking curves. This transformation is exemplified in Figure 1.10.

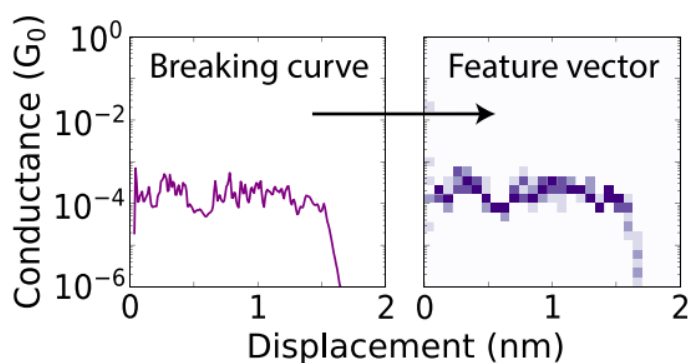


Figure 1.10. Transformation of a breaking trace into a vector, which can be represented as an individual 2D histogram. Adapted with permission of ref.³⁰ Copyright © 2019 managed by AIP Publishing.

Importantly, a specific region of interest has to be defined in order to reduce as much as possible the high-dimensional spaces that are generated. To focus on the behaviour of the traces after the breaking of the junction, it can be selected a conductance range between the noise-floor value and G_0 , and an electrode displacement range according to the calculated junction distance for the molecule fully extended between the electrodes.

Probing the potential of this method, the authors used the clustering algorithm *K-means++* (available in the Scikit-Learn Python library) over the vectors obtained for the conductance traces for oligophenylethynylene junctions. Next, they employed a principal component

CHARACTERIZATION OF SINGLE-MOLECULE JUNCTIONS

method analysis, obtaining three different clusters, which were used to construct the corresponding 2D histograms (Figure 1.11). They found that each cluster corresponded to a different breaking behaviour, obtaining three classes of G - z traces. Class 1 corresponded to traces no displaying molecular signal (Figure 1.11b). Class 2 corresponded to sloping and short plateaus at high conductance values (Figure 1.11c). Class 3 corresponded to flat and long plateaus at low conductance values (Figure 1.11d).

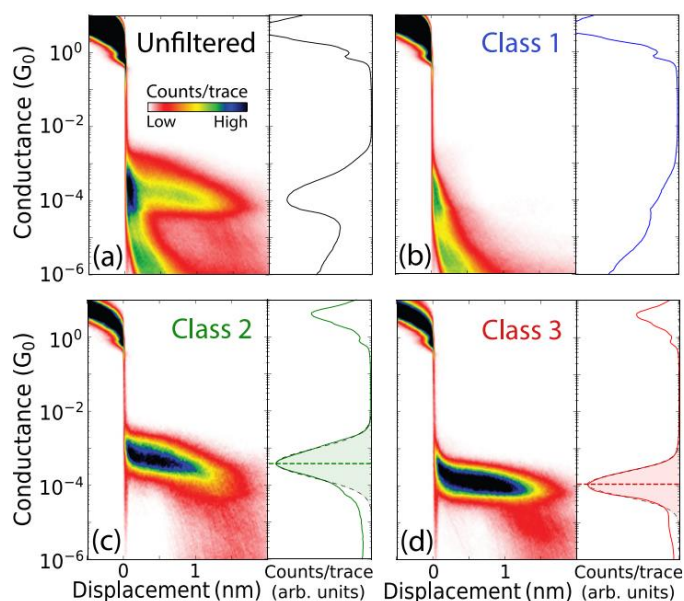


Figure 1.11. Operating of classification algorithms for G - z traces. **(a)** 2D and 1D conductance histograms built from all the breaking curves for an oligophenylethynylene junction, corresponding to 41916 traces.

(b)–(d) 2D and 1D conductance histograms built from the breaking curves of three different classes obtained with the vector-based classification method. Class 1 **(b)** corresponds to traces no displaying molecular signal; class 2 **(c)** corresponds to sloping and shorter plateaus at higher conductance values; and class 3 **(d)** corresponds to flat and longer plateaus at lower conductance values. The horizontal green/red dashed lines in the 1D histograms of **(c)** and **(d)**, respectively, correspond to the mean of the log-normal distribution fits for the conductance peaks. Reproduced with permission of ref.³⁰ Copyright © 2019 managed by AIP Publishing.

These methods have been also used to distinguish different conduction pathways in multiconductance-state systems.³¹ In addition, they have demonstrated their potential not only for revealing breaking events with low-rate of appearance, but also for a more accurate determination of the molecular conductance since the obtained peaks are narrower and more symmetric.³⁰

1.3.4. Current-voltage (I - V) characteristics

Current-voltage (I - V) characteristics can also be studied in molecular junctions by means of applying voltage cycles while the molecule is wired between the electrodes, this is, while the molecular plateau in the G - z trace remains (Figure 1.12). In this sense, the more stable the molecule-electrode interaction, the easier to record I - V curves, being the optimization of the signal-to-noise-ratio essential for these measurements.

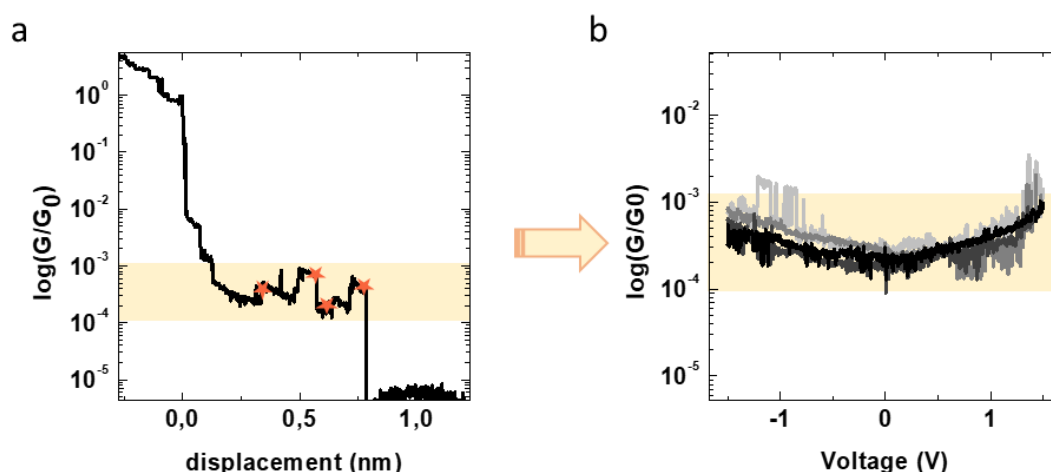


Figure 1.12. I - V curves are recorded along the molecular plateau. **(a)** G - z trace displaying a plateau, along which four I - V cycles have been measured (stars). **(b)** Four I - V traces recorded in the same plateau, between 1.5 and -1.5 V. (As current (I) is related with the conductance (G) through the formula $I=GV$, these curves can also be plotted using conductance instead of the current in the y-axis).

The treatment of I - V curves is similar to that described for G - z traces. Thousands of current-voltage cycles are recorded, generally several of them in each plateau that appear in the G - z traces. The 2D histograms are built from all these I - V curves. The behaviour of the I - V curves is generally related to the HOMO-LUMO gap, so the more higher the curvature of the I - V s, the closer in energy the HOMO or LUMO are. The asymmetry on the I - V s is usually related with different coupling of the molecule with the right and left electrodes, as usually occurs for asymmetric molecules.

1.4. Theoretical models for electron transport phenomena

1.4.1. Electron conduction at the nanoscale

As mentioned before, the electrical conduction in macroscopic wires is described by Ohm's law. For a given sample, G increases linearly with the transverse area S and it is inversely proportional to its length L :

$$G = \sigma \frac{S}{L} \quad (\text{Eq.1.2})$$

where σ is the conductivity of the sample, which is specific for each material. In these cases, electrons take a random path through the material due to scattering. In contrast, charge transport at the nanoscale, in which the length or width of the material are of the same order of magnitude of that of the electrons, takes place *via* ballistic transport, where electrons propagate coherently. It happens in metallic nanowires but also in 2D materials. In the ballistic transport regime the conductance can be described by the Landauer formula, which can be presented in the following form:

$$G = \frac{2e^2}{h} \sum_{n=1}^N T_n \quad (\text{Eq.1.3})$$

In this equation, there are N different transmission channels, each of which contributes certain transmission T_n to the total conductance. The prefactor $2e^2/h$ is the conductance quantum, denoted G_0 :

$$G_0 = \frac{2e^2}{h} \approx 77.5 \times 10^{-6} \quad (\text{Eq.1.4})$$

The quantum conductance corresponds to an electric resistance of $1/G_0 \sim 12.9 \text{ k}\Omega$, associated to the resistance at the interfaces between the electrodes and the ends of the molecule; in other words, between the macroscopic leads and the material of limited dimensions. When the material with limited dimensions is a single molecule, we refer as to molecular junctions, whose configuration was shown in Figure 1.2. In this case, the

molecular levels constitute the conduction channels that electrons follow from one electrode to the other.

The energy diagram of a molecular junction is depicted in Figure 1.13, where the metallic electrodes have continuous electronic states, filled up to Fermi level (E_F), and the molecular channels are represented by their HOMO (Highest Occupied Molecular Orbital) and LUMO (Lowest Unoccupied Molecular Orbital). Although many molecular orbitals can participate in the electronic transport, these frontier orbitals have the main contribution (Figure 1.13a). The transmission probability in the junction strongly depends on the energetic alignment of the molecular orbital with respect to the metal Fermi level. Due to its hybridization with the band energy levels of the metal electrodes, the molecular orbitals change their position and suffer a broadening (Figure 1.13b), which gives rise to the transmission function depicted between the electrodes. Note that the higher probability of transmission occurs at energies related to the original HOMO and LUMO molecular orbitals. When a bias voltage V is applied to one of the electrodes, its energy level is modified ($E_F + eV$) and a tunnelling current is forced to break through the molecule (Figure 1.13c). This tunnelling current allows to explore the electrical properties of the molecular junction, such as the conductance G and the current-voltage I - V behaviour. Remarkably, for long molecules, the electron transport has been proposed to occur by means of a hopping mechanism, in which electrons are localized at certain molecular orbitals of the molecular backbone and hop between them (Figure 1.13d).¹

Thanks to first-principles methods, normally based on density functional theory (DFT), in combination with non-equilibrium Green's function techniques (NEGF), the alignment of the molecular levels with the metal states can be modelled and the electrical properties of single-molecule junctions predicted. In this sense, theory provides information concerning the nature of the relevant orbitals, the most favorable binding geometry and possible interference effects.²¹ However, it has to be considered that the theoretical models are based on a simplified picture of the molecule–electrode junctions, since the real shape of the electrodes and the geometry of the molecule are not trivial and can change during the real experiments.

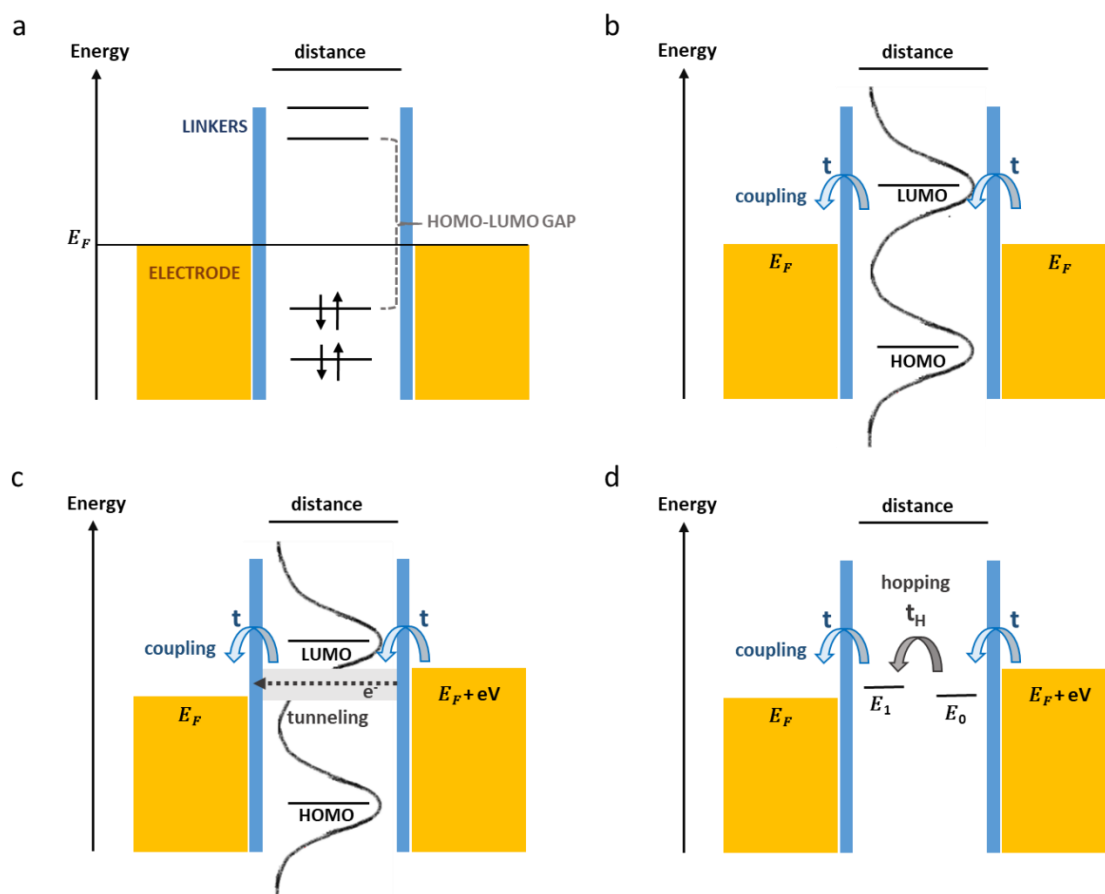


Figure 1.13. Schematic energy levels for a molecular junction. **(a)** Energy level of the molecular orbitals with respect to the Fermi Energy before coupling with the electrodes. The linkers act as a potential barrier. **(b)** Alignment of the molecular energy levels with respect to the E_F and broadening of the orbitals, resulting into a continuous transmission probability, which is higher at those energies related with the original molecular orbitals HOMO and LUMO. **(c)** Application of a bias voltage V to one of the contacts. The Fermi level is modified and a tunnelling current flows through the molecule. **(d)** Hopping mechanism. Here, it is depicted a two-state model, where the two states are coupled via a hopping t_H .

1.4.2. Density functional theory and non-equilibrium Green's function (DFT-NEGF)

DFT provides information about the standard ground state of finite systems, like molecules or atomic clusters. Also related properties can be predicted, such as molecular structure, vibrational frequencies, atomization energies, dipole moments, and ionization and affinity energies. Since molecular junctions are neither finite nor periodic, the application of DFT is complicated. Moreover, the application of a bias voltage between the electrodes involves a driving out of equilibrium, which is out of the DFT scope. Therefore, to describe the transport properties of nanoscale junctions, DFT is usually combined with NEGF techniques.¹

The application of those models starts with the optimization of the minimum energy molecular geometry, which further allows to extract the topologies and the energetic alignment of the frontier molecular orbitals (HOMO and LUMO). Next, the optimized molecule is allocated between the electrodes, giving rise to molecular junctions, which are divided into three parts: the left (L) and right (R) electrodes and a central part that contains the molecular bridge and metallic screening layers (Figure 1.14). Remarkably, several trends for the modelling of the molecule-electrode interfaces are nowadays considered: pyramidal electrodes or flat surfaces with adatoms, depending on the most probably shape of electrodes, which generally is related to the anchoring group.

The charge density of the system is computed, in terms of a density matrix, both in equilibrium conditions and considering the shift of the chemical potential of the electrodes caused by the applied bias voltage. These models permit to obtain the probability of transmission as a function of the energy.

Although DFT-NEGF is the theoretical approach with the largest impact in molecular electronics, it has its limitations. Since the transport often proceeds through the tails of the molecular orbitals closest to the Fermi energy, small errors in the position of those levels can lead to large errors in the transport properties. In this sense, the intrinsic approximations made in the DFT-NEGF method can also be responsible for discrepancies between experiment and theory, such as insufficient description of the electronic correlation or *in situ* atomic rearrangements that may involve significant conductance variations. Since the most theoretical studies are restricted to the analysis of a few idealized geometries, the comparison of these results with the experiment should be taken with caution. The use of DFT-based molecular dynamics is also extended nowadays, since it provides a very valuable insight into the mechanism of junction formation and most favorable contact geometries (Figure 1.15).³²

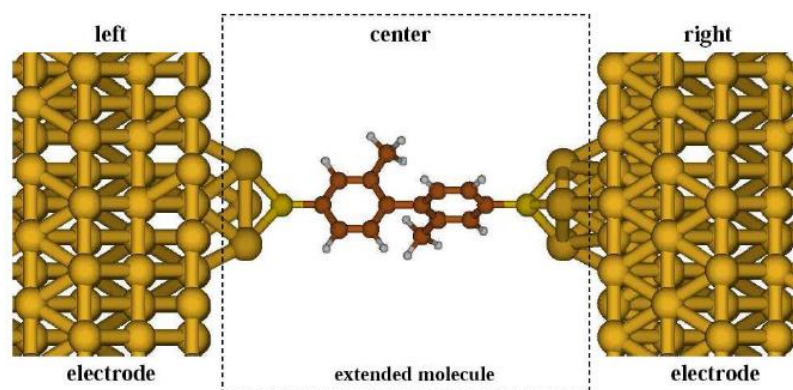


Figure 1.14. Schematic representation of a molecular junction. Three regions are distinguished: the left and right semi-infinite electrodes and the central region that contains the extended molecule and part of the electrodes. Reproduced from ref.¹

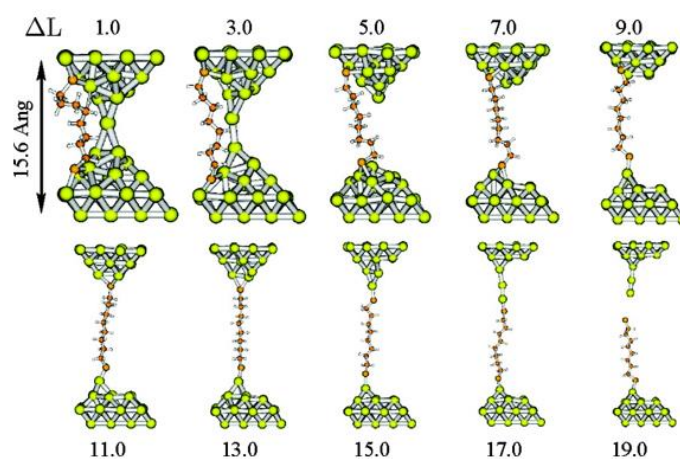


Figure 1.15. Snapshots of the formation of an octanedithiol molecular junction simulated using DFT-based molecular dynamics. Reproduced with permission of ref.³² Copyright © 2009, American Chemical Society. Short movies of the molecular dynamic are also available in the Supporting Information of ref.³²

1.4.3. Gap correction

Theory is generally in good qualitative agreement with the experimental results, being able to predict the conductance trend in a family of compounds. However, clear quantitative discrepancies between them are common, predicting the theoretical models higher values than the experimental ones, and being the differences especially significant for low-bias conductance. This fact has been attributed to intrinsic deficiencies of the DFT functionals, which tend to underestimate the HOMO–LUMO gap.³³ In order to overcome such known

deficiencies, the self-energy corrected DFT+ Σ approach is typically applied and it has been demonstrated to improve the agreement with experimental conductance values.^{34,35,36}

In brief, this correction is based on a shift of the HOMO and LUMO levels toward opposite directions, which promotes an opening of the gap and gives rise to a modified molecular Hamiltonian. This new Hamiltonian is incorporated to the system and DFT is conducted as usual, obtaining a corrected conductance value lower than the previous one and, in general, in better agreement with the experimental conductance.³³

1.5. Elements of a molecular circuit

Each component of a single-molecule junction plays a key role on the conductance experiments, not only on the final value, but also in other aspects of the measurements. It is possible to distinguish three different components: i) electrodes, ii) anchoring or linking groups, and iii) molecular backbone (Figure 1.16). In this section, a brief discussion about their influence on the conductance has been included, considering the fundamental findings in the field to date.

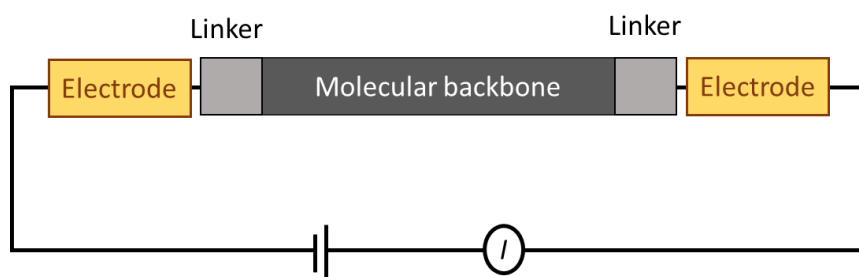


Figure 1.16. Components of a molecular junction.

1.5.1. Electrodes

Although several metals have been used as electrode (Pt, Ag, Cu...), in this kind of measurements, gold is the most common electrode material because of its inertness, which favours more consistent and reproducible single-molecule conductance experiments and allows their development under ambient conditions. Others metals, which suffer oxidation processes in presence of oxygen, originate an oxide layer on the electrode surface that hinders a clean formation of metal–molecule–metal junctions. Those metals, such as Ni, Cu and Fe, require the use of ultra-high-vacuum systems, inert atmosphere or electrochemical control for avoiding or removing the oxide layer. This fact adds a greater complexity to the experiments.

As previously explained, the Fermi Energy level (E_F) of the metal is a key factor in the conductance value, since E_F deeply influences the molecule-metal coupling. Therefore, junctions formed with the same molecule but different metallic electrodes have been reported to have distinct conductance value, due to the different E_F of the metals.^{37,38} As example, Figure 1.17 summarizes the results obtained by Kim for 4,4'-diaminobiphenyl junctions with Ni, Au and Ag (Figure 1.17b) and the schematic energy alignment for each

junction (Figure 1.17c).³⁸ The conductance value obtained for Ag junctions was lower, since its E_F was in the middle region between HOMO and LUMO. The E_F of Ni and Au were closer to the HOMO level, giving rise to higher conductance values.

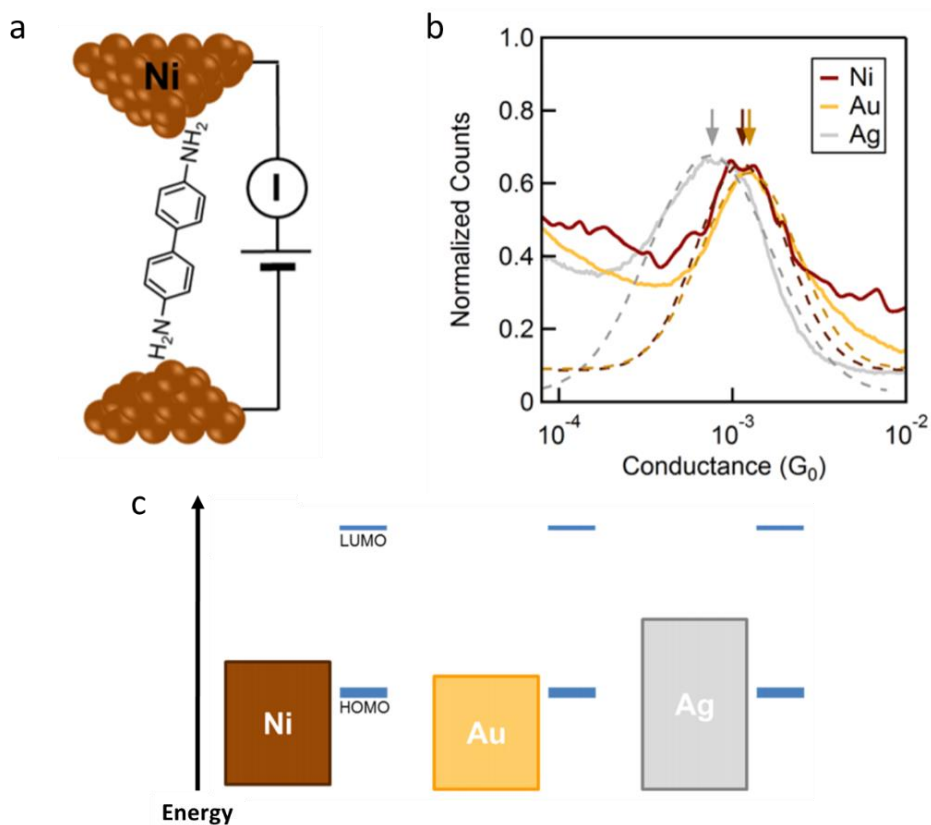


Figure 1.17. Conductance value depends on the metal electrode used in the junction. **(a)** Schematic 4,4'-biaminobiphenyl junction. **(b)** 1D histograms for the junction with Ni, Au and Ag. **(c)** Energy diagram indicating the molecular HOMO-LUMO gap, relative to the Ni, Au and Ag Fermi level. Reproduced from ref.³⁸ Copyright © 2014, Korean Chemical Society.

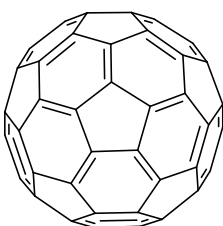
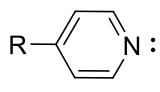
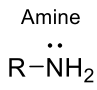
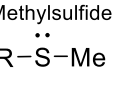
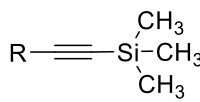
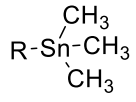
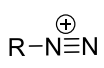
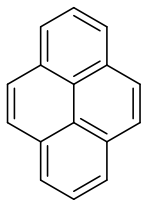
Another important factor in conductance experiments seems to be the shape of the electrodes. Although break-junction techniques generally involve at least one of the electrodes with pyramidal shape, theoretical models predict higher conductance values for systems in which both electrodes have a flat configuration.³⁹

The measurements of the electron transport properties of the molecules studied in this thesis have been performed using Au (Chapters 2, 3 and 4) and Ni (Chapter 5) electrodes.

1.5.2. Anchoring groups

The anchors or linkers are the functional groups or molecular points through which the molecule is attached to the electrodes. Generally, two linkers are introduced at both ends of the molecule in order to achieve a junction configuration in which it is fully extended between the electrodes. Although the molecule-metal bonding is weak in comparison with the typical molecular bonds, it strongly influences the amount of charge transfer, the broadening of the HOMO–LUMO and their final position with respect to the Fermi level.²¹ The metal-molecule coupling is typically produced by means of donor–acceptor (dative) interactions or covalent bonds and depends on both the metal and the group used as linker. In Table 1.1, the most common linker groups used for gold electrodes have been collected and classified depending on the nature of their interaction with the metal.

Table 1.1. Most common linker groups classified depending on the kind of interaction with the electrodes.

Dative anchors		Covalent anchors
π donors	Lone pair donors	
 <p>C₆₀</p>	<p>Pyridine</p>  <p>Cyano</p> $R-C\equiv N:$ <p>Isocyanate</p> $R-N=C:$ <p>Amine</p>  <p>Methylsulfide</p> 	<p>Thiol</p> $R-SH \xrightarrow{Au} R-S-Au$ <p>Trimethylsilyl</p>  $\xrightarrow[Au]{TBAF} R\equiv Au$ <p>Organotin</p>  $\xrightarrow{Au} R-Au$ <p>Diazonium</p>  $\xrightarrow[Au]{+e^-} R-Au$
 <p>Pyrene</p> <p>Aromatic surfaces in general</p>		

Among the anchors, the most frequently used are groups incorporating sulphur atoms ($-SH$, $-SMe$) and nitrogen atoms (pyridine, $-NH_2$, $-C\equiv N$). In the case of nitrogen groups, the interaction takes place through the lone pair of electrons, giving rise to dative coordination bonding. In contrast, when sulphur is the atom involved in the coupling, a covalent bond ($-SH$) or a dative bond ($-SMe$) can be formed between the linker and the metal. Other linkers such as π -conjugated hydrocarbons⁴⁰ and fullerenes,^{41,42} have also been used as linkers, since their π -donor character gives rise to a dative bonding with the metal.

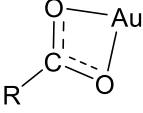
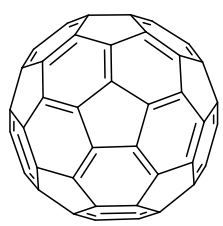
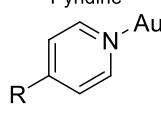
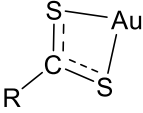
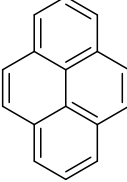
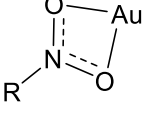
In-situ formation of covalent Au–C bonds has also been reported through different terminal groups:

- i) Transmetalation of C–SnR₃: This method has been used for the *in situ* cleavage of terminal C–SnMe₃ bonds, in order to obtain covalent Au–arene and Au–alkane contacts.⁴³ Note that for obtaining the desired cleavage, the most reactive Sn–C bond must be the one between the Sn and the backbone.⁴⁴
- ii) Desilylation of terminal trimethylsilylacetylene (TMS–C≡C) groups: This method is based on the addition of tetrabutylammonium fluoride (Bu₄NF) to a solution of the target molecules protected with TMS–.⁴⁵ A disadvantage of this method is the generation of Bu₄N⁺ electrolytes, which may produce an ionic current between the electrodes able to mask the signal of low-conductance molecules. Remarkably, it has been reported recently that terminal acetylenes can interact directly with gold electrodes, avoiding the deprotection step and the resulting ionic currents.⁴⁶
- iii) Electroreduction of diazonium salts: Initially, this approach seemed attractive since covalent Au–C contacts could be generated (irreversibly) on demand by increasing the reduction potential;⁴⁷ however, diazonium salts are known to be thermally unstable and, in many cases, explosive. For that reason, this method is currently in disuse.⁴⁸

A different classification of the anchors has been proposed, according to the number of atoms involved in the binding: i) monodentate, ii) bidentate, and iii) multidentate anchor groups (Table 1.2).

ELEMENTS OF A MOLECULAR CIRCUIT

Table 1.2. Most common linker groups classified depending on the number of atoms involved in the binding

Monodentate		Bidentate	Multidentate
Thiol $R-S-Au$	Methylsulfide $R-S(Me)-Au$	Carboxylic acid 	C_{60} 
Amine $R-N(H)_2-Au$	Pyridine 	Dithiocarboxylic acid 	Pyrene 
Cyano $R-C#N-Au$	Selenol $R-Se-Au$	Nitro 	Aromatic surfaces in general
Isocyanate $R-N=C-Au$	Diazonium $R-N#N^+-Au$		
Trimethylsilyl $R-Si(CH_3)_3-Au$	Organotin $R-Sn(CH_3)_3-Au$		

As mentioned before, the nature of the linker affects the conductance value. It has been reported several examples in which the change of linker involves the change of the orbital controlling the conduction. In particular, Erbe and collaborators studied tolane molecules attached to gold contacts by means of different anchors, namely thiol, amine, nitro and cyano groups.⁴⁹ They found that, for these junctions, the HOMO dominates the transport for linkers with electron-donating character (thiol and amine), and the LUMO dominates the transport for linkers with electron-withdrawing character (nitro and cyano).

Understanding the behaviour of each linker is of special interest in order to establish trends of conductance values. Agraït and co-workers studied amine and thiol anchor groups for alkanes of different length.⁵⁰ One of the main aspects they found was the different behaviour of the gold electrodes with each linker. It was observed that amines did not modify the gold breaking dynamics, obtaining the normal gold jump-out-of-contact. The junction separation at breakdown point was also comparable with the length of the molecule. In contrast, the thiol terminated alkanes strongly modified the gold breaking dynamics, giving rise to junctions with apparent stretching distances significantly longer

than the corresponding amines, which indicated mobilisation of gold atoms in the contact (Figure 1.18).

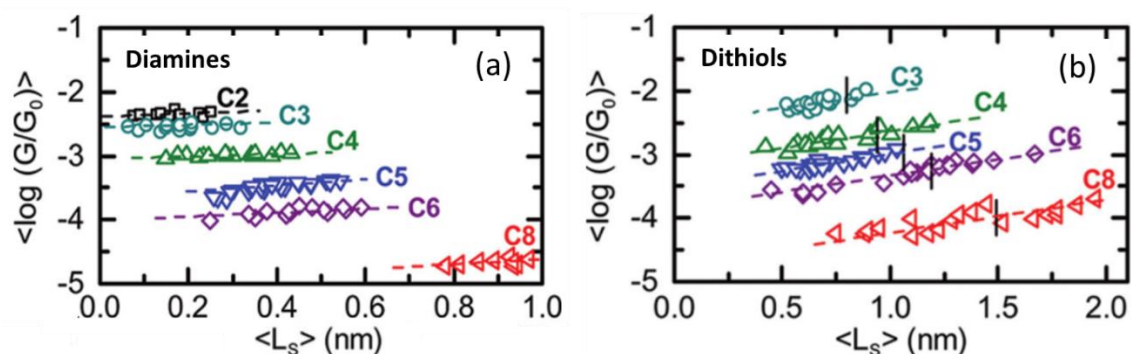


Figure 1.18. Variation of conductance ($\log(G/G_0)$) with breakdown distances (L_s) for different alkane chains presenting amines (a) and thiols (a) as linkers. Dashed-lines are guides for the eye and the vertical lines in the bottom panel correspond to the theoretical length of the molecules. Reproduced with permission of ref.⁵⁰ Copyright © 2011, American Chemical Society

In this context, Leary and collaborators proposed the formation of oligomeric gold–thiolate units during the stretching when thiol groups are used as anchors.⁵¹ Some of the possible configurations are collected in Figure 1.19. Interestingly, this increase of the junction length for the same molecules presenting –SMe linkers was not observed, concluding that the formation of those oligomeric gold–thiolate units was favoured by thiols groups.⁵¹

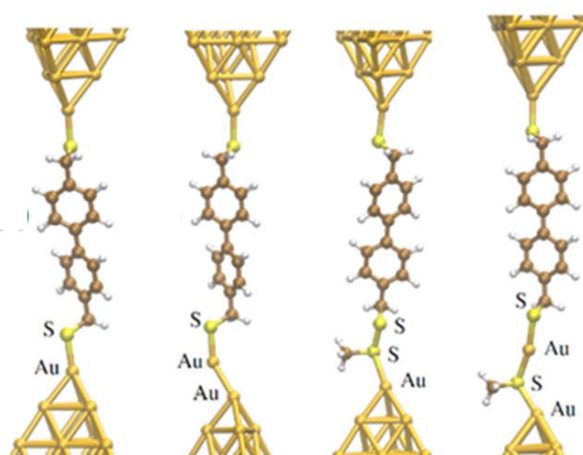


Figure 1.19. Different possible geometries including adatoms for dithiolated molecular junctions. In the two last geometries the CH_3 group replaces a full target molecule. Biphenyl backbone has been used as example. Reproduced with permission of ref.⁵¹ Copyright © 2018, American Chemical Society

In this thesis, –SMe groups have been the preferable linkers, since this is as extensively studied group, whose behaviour in single-molecule junctions is well-established.

Nevertheless other groups have been also explored, particularly in Chapter 4, where an exhaustive analysis of the terminal acetylene group as linker is included.

1.5.3. Molecular backbone

The molecular backbone is defined as the pathway through which charge flows from one anchor to another.⁴⁸ The variety of possible molecular backbones is almost unlimited since any chemically reasonable structure can be prepared by means of synthetic chemistry. As mentioned before, a proper attachment to the electrodes is generally achieved introducing two anchoring groups to the backbone. However, there are cases, particularly with molecules presenting aromatic surfaces such as acenes and fullerenes, in which the linkers are not needed.⁵²⁻⁵⁴

Molecular backbones are typically classified according to their behaviour or function within an electronic circuit. Some examples of these functions are given below.

Rectifiers consists of an acceptor π -system (A-system) and a donor π -system (D-system), separated by a tunnelling bridge. Due to this disposition, they are able to give rise to D-A junctions. The distance between the acceptor and donor units is a key factor in these systems, since if they are too far apart, then they will not communicate and if they are too close, a new single mixed ground state will form, precluding the rectification. Rectifiers present a characteristic asymmetric I - V profile since the molecular orbitals have an asymmetric charge distribution, which involves a different coupling to the left and right electrodes. Therefore, the current is lower for the side with the weaker coupling, while the current shifts toward the chemical potential of the electrode that is better coupled.¹ In this sense, rectification can also be achieved by the direct use of distinct anchors in each end of the molecule,⁵⁵ or simply by using different metals as electrodes.⁵⁶

Aviram and Ratner were the pioneers on proposing the used of single molecules as rectifiers.^e In 1974, they explained how a modified charge-transfer salt could operate as a traditional diode in electrical circuits.⁴ However, this idea was considered just a theoretical hypothesis that could not be tested experimentally. The first real nanosystems having a rectifying behaviour consisted in Langmuir-Blodgett monolayers or self-assembled

^e In fact, this is the first proposal using a single molecule as an electronic component.

monolayers formed by 10^{14} to 10^{15} molecules measured in parallel. Between 1997 and 2006, Metzger's group reported several monolayers of different structures able to act as rectifiers.⁵⁷ I - V curves characteristics of one of them are shown in Figure 1.20, where it can be noticed that the current is very much higher for the chemical potential of the right electrode. Remarkably, the same group proposed later that the rectification observed in those systems was due to the aliphatic chain rather than the donor- π -acceptor part according to tight-binding calculations.⁵⁸

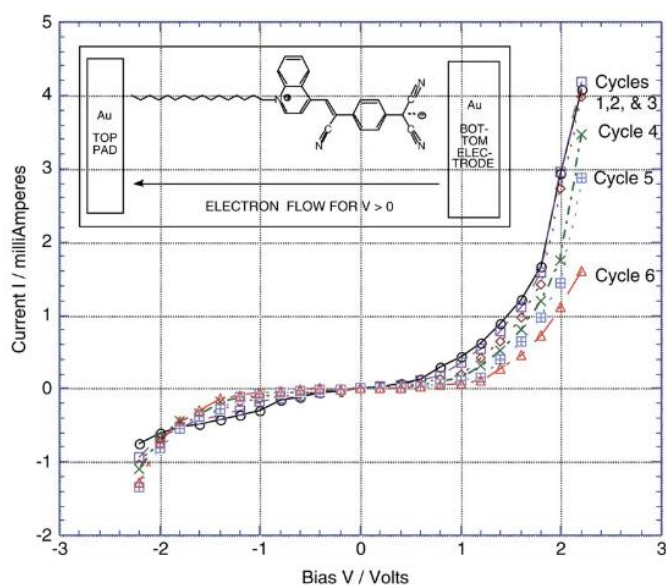


Figure 1.20. I - V characteristics reveal the rectifying behaviour of the system. Reproduced with permission of ref.⁵⁹ Copyright © 2003, American Chemical Society

Rectification behaviour at the single-molecule level was explored later by means of MCBJ and STM break-junction techniques.^{55,60-63} The rectification ratio (RR) is the difference of current, in absolute value, obtained at the same potential at positive and negative sign ($RR = |I(V)/I(-V)|$). For those molecules, the RR ranged from 1.2 to 10.⁶⁴ Several fully theoretical studies have been also developed for different structures, obtaining rectification ratios in the same range of values, for both D- π -A systems and D- σ -A systems.^{65,66} Later, Liu and coworkers proposed a tandem rectifier, in which two single D- σ -A rectifiers were coupled via a π -bridge.⁶⁷ Using NEGF approach, they obtained that the rectification ratio of this tandem was about 20 times higher than that of the single rectifier.

ELEMENTS OF A MOLECULAR CIRCUIT

Switches are able to shift between two or more stable states (in this case, conductance values), by means of an external and controllable stimulus. Multi-conductance state systems are relevant in molecular electronics due to their promising applications in high-density data storage.⁶⁸ A possible way for improving data storage potential is to increase the number of memory states in each cell. This means going beyond binary systems and searching for molecules having more than two output signals: 0, 1, 2, 3, 4... In this context, the practical utility of multi-state systems resides in conductance values in the range allowed by the detection limits, but different enough to be easily distinguishable. The existence of several (two or more) electrical responses for a single molecule lies in intrinsic (chemical, structural, conformational, electronic...) molecular changes, which should be promoted by an external stimulus. Switches have been extensively studied in molecular electronics, finding in literature examples of multi-conductance-state systems based on redox,^{68,69} light-driven⁷⁰ and proton transfer⁷¹ processes or combination of them.⁷²

Wires are the elementary building block for nanoscale devices, since they serve as a channel for electrons. Oligomeric backbones, such as oligophenyleneimine (OPI),⁷³ oligo(phenylene)ethynylenes (OPE),⁷⁴ oligonaphthalene-fluoreneimine (ONI)⁷⁵ and oligophenylenetriazole (OPT),⁷⁶ among others, have received special attention, being the coupling between monomers a key factor in the conductance of all of them. Its ability to transport electrons has been evaluated by comparing how their conductance decreases with increasing their length. The parameter used for that is the β decay factor, which is extracted from the conductance plotting on a semi-logarithmic scale against the molecular length (L) of the oligomer, using the following formula:

$$G = G_c e^{-\beta L} \quad (\text{Eq.1.5})$$

where G_c is the contact conductance of the molecular wire junction.⁷⁷ β values depend on the coupling strength between monomer units. Backbones that are strongly conjugated have a shallow conductance decay: the lower β values for an oligomer family, the more effective at charge transporting it is. The study of several families of oligomeric wires has revealed interesting information. Thus, for example, since alkane chains ($-\text{[CH}_2\text{]}_n-$) do not have strongly conjugated bonds, they present high β values (0.84 \AA^{-1}). Although

permethyloligosilanes ($-\text{[SiMe}_2\text{]}_n-$) are their structural analogues, they are able to transport charge more effectively (β values 0.39 \AA^{-1}) because Si–Si σ bonds are more strongly conjugated than C–C σ bonds, probably because their bonding orbitals are larger in size and higher in energy.⁴⁸ In Figure 1.21, it has been collected the conductance of several oligomeric families, (OPI, OPE, OPT and ONI). It is appreciable that for longer oligomers in the series, the conductance decays smoothly or even remains constant. This suggests that, for these families, the transport mechanisms is changing along the series, going from tunnelling to hopping.⁷⁸

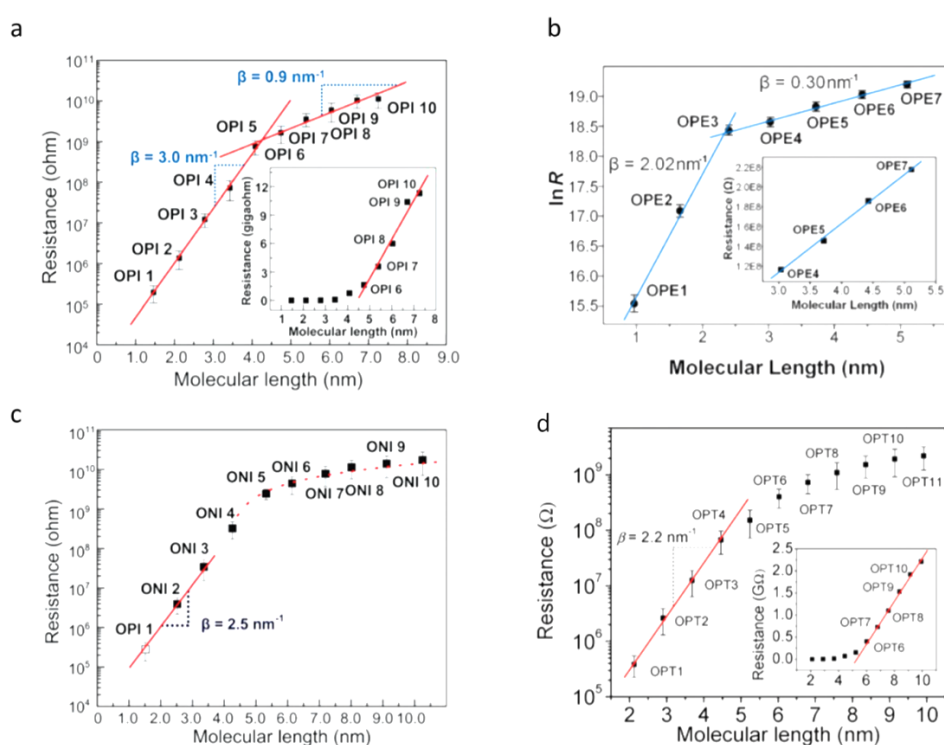


Figure 1.21. Resistance vs molecular length graphics for four different families. **(a)** OPI, **(b)** OPE, **(c)** ONI and **(d)** OPT. In these examples, it is appreciable a change in the electron transport mechanism from tunnelling to hopping, by means of a change in the slope (β values). **(a)** Reproduced with permission of ref.⁷³ Copyright © 2008, American Association for the Advancement of Science. **(b)** Reproduced with permission of ref.⁷⁴ Copyright © 2010, American Chemical Society. **(c)** Reproduced with permission of ref.⁷⁵ Copyright © 2010, American Chemical Society. **(d)** Reproduced with permission of ref.⁷⁶ Copyright © 2009, American Chemical Society. Adaptations taken from ref.⁷⁸

Molecular wires consisting in oligocarbynes are also of special interest. This family comprises cumulenes, formed by successive double bonds, and polyynes (also called oligoynes) formed by alternating single and triple bonds. Interestingly, Venkataraman and collaborators reported recently that the conductance for cumulenes increases with

ELEMENTS OF A MOLECULAR CIRCUIT

length,⁷⁹ in contrast to polyynes and the others aforementioned oligomeric families (Figure 1.22).

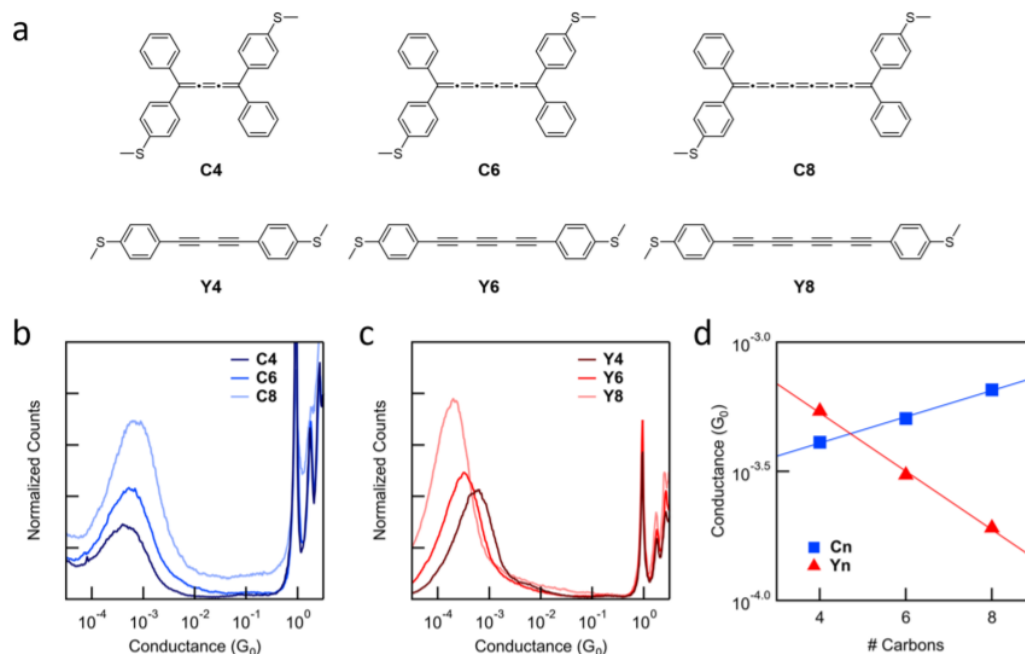


Figure 1.22. (a) Series of cumulenes and polyynes investigated by Venkataraman and collaborators. (b) 1D histograms of the cumulene series measured at 100 mV. (c) 1D histograms of polyynes series measured under the same conditions. (d) Conductance determined for cumulenes (blue) and polyynes (red) as a function of the number of carbons in the chain. Reproduced with permission of ref.⁷⁹ Copyright © 2020, American Chemical Society

Other families exhibiting interesting properties are pyridine end-capped cyclopentadithiophene-vinylene oligomers, recently studied by Venkataraman and co-workers,⁸⁰ presenting large transport to distances as large as 5 nm.

Finally, it is worthy to highlight the last investigations on rotaxane-like molecular wires, considering the complexity of these systems.^{81,82} Nichols and collaborators found a slight increase of the conductance for a rotaxane system in comparison with that of the dumbbell, which was a pyridine end-capped oligoyne wire.⁸²

For all these different functions (wires, rectifiers, switches...), there are several factors related with the molecular backbone that highly influence the conductance, such as the substituents, able to tune the electron-acceptor or electron-withdrawing behaviour of

different regions along the molecule; the torsion angles, which influences the coupling between planar units; and the aromaticity of conjugated structures.

- Dihedral angles: when a molecule is formed by one or more phenyl rings or other aromatic surfaces, the angles between them, as well as the angles with the linkers highly influences the conductance. As experimentally and theoretically demonstrated, a higher conductance is obtained for molecules with lower dihedral angles, since the conjugation between the aromatic motifs is more effective. For example, studying a series of substituted biphenyl derivatives,^{83,84} it was found that the greater the twist between phenyl rings, the less conjugation and conductance value (Figure 1.23).

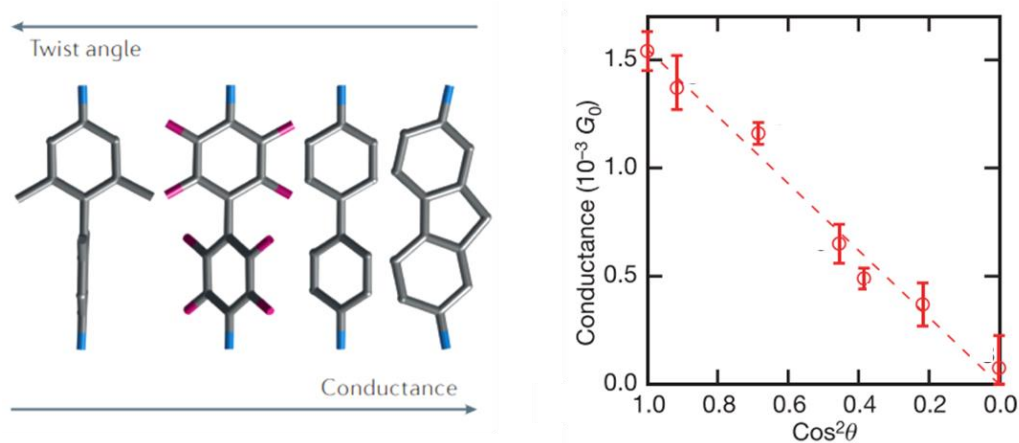


Figure 1.23. Conductance decreases with an increasing twist angle between biphenyl rings. The experimental values in red correspond to different biphenyl derivatives measured in ref.⁸³ which present different twist angle. Reproduced from ref.⁸³ Copyright © 2006, Nature Publishing Group.

- Effect of substituents: The effect of substituents in the conductance can be distinct for different molecules. Thus for example, in the particular case of 1,4-diaminobenzene-based molecular wires, different substituents were introduced at the 2-, 3-, 5- and 6-positions. Steigerwald and collaborators demonstrated that electron-donating groups (–Me and –OMe) originate an increase in conductance, whereas electron-withdrawing groups (–CF₃, –Br, –Cl and –F) promote the reverse effect.⁸⁵ Remarkably, in certain systems, variations of the substituent groups can promote changes in the torsion angles, involving conductance decreases as previously described in Figure 1.23.

ELEMENTS OF A MOLECULAR CIRCUIT

- Aromaticity: it is a term that groups together a collection of physicochemical properties determining specific features of cyclic or polycyclic π -electron molecules. For defining a molecule to be aromatic, some criteria have to be accomplished:

- i) it has to be cyclic or polycyclic
- ii) its bond lengths exhibit very low bond lengths alternation
- iii) it should be more stable than its acyclic analogue
- iv) when it is submitted to an external magnetic field, a current is induced into the ring, displaying an increased diamagnetic susceptibility and chemical shifts of exocyclic protons in ^1H NMR spectra toward low field.
- v) substitution reactions take place more easily than addition reactions.

Different aromatic indexes have been used to compare the aromatic character of conjugated molecules, based on energetic and geometric criteria, among others. The most commonly used are i) harmonic oscillator model of aromaticity (HOMA), introduced by Krygowski and Kruszewski, improving the first approach by Julg and Françoise;⁸⁶ and ii) nucleus independent chemical shift (NICS), introduced by Schleyer and collaborators.⁸⁷

HOMA: it is an index directly based on the molecular geometry, namely on the bond lengths, since strongly aromatic compounds are related to non-alternant bond lengths or very weak variations. Then, the variance of the perimeter bond lengths is compared with a hypothetical optimal bond length R_{opt} , calculated for the fully-aromatic structure.

NICS: it is a magnetic aromaticity criterion, defined as the negative of the absolute magnetic current that flows along the ring when a magnetic field is applied, calculated at any point of the molecule. This shielding is usually calculated at the center of any of the rings (NICS(0)zz), however nowadays it is more extended the calculation of the out-of-plane component of the magnetic shielding. For that, it is calculated the NICS(X)zz, where X is the distance in Å above the molecular plane.

Remarkably, the more negative the NICS values is, the more aromatic the molecule. The effect of aromaticity on the conductance have been a controversial topic,⁸⁸ since the conductance have been demonstrated to decrease with the aromaticity in a considerable number of cases,⁸⁹⁻⁹² whereas, it has been reported to increase in others.⁹³ Besides, when a strong coupling between anchor and electrodes exists, this coupling dominates the conductance. Therefore, small structural changes involving variations in aromaticity are

then statistically insignificant for the final conductance value. In those cases, conductance is considered to be independent of aromaticity.⁹⁴

Importantly, in most of the systems, several of these effects (angles, substituents and aromaticity) can be present at the same time, acting on each other. For example, the substituents introduced in a conjugated core can be decisive for the aromaticity of the structure, making possible to use them as strategy for tuning the conductance. In the same way, bulky substituents generally involve higher torsion angles, affecting not only the conductance value, but also other properties such as the rectification behaviour.⁹⁵

For the different molecular backbones investigated in this thesis, several of these factors have been found to have a strong influence on the conductance values obtained.

1.6. Beyond conductance measurements

The experiments explained above, consisting in the creation of metallic nanojunctions, also allow exploring other parameters and effects, besides conductance, related with the transport at the nanoscale. The application of a gate voltage, a temperature gradient or a magnetic field usually involves substantial changes in transport that have major implications for fundamental understanding of the processes at the nanoscale.^{96,97} In such cases, it has been already demonstrated that both, experimental setups and theoretical modeling, need to be adapted to new requirements.

In this section some of those complementary studies (namely thermoelectric effect, electrochemical gating and magnetic measurements) are overviewed, considering their potential for future research and applications according to the advances already made, as well as the experimental modifications required for conducting those measurements.

1.6.1. Thermoelectricity and thermoelectric effect

Thermoelectricity is the combination of thermal and charge transport. When the two sides of a junction are at different temperatures, T_1 and T_2 , a voltage difference, $V_1 - V_2$, proportional to the temperature difference, appears (Figure 1.24). The constant of proportionality that relates both terms is the thermopower or Seebeck coefficient (S), following the next equation:

$$V_1 - V_2 = -S(T_1 - T_2) \quad (\text{Eq.1.6})$$

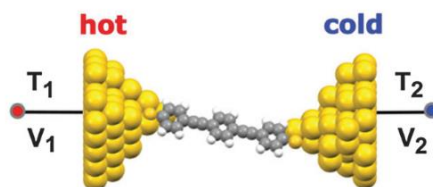


Figure 1.24. Schematic disposition of the elements of a molecular junction for thermopower measurement. Reproduced from ref. ¹² with permission from The Royal Society of Chemistry.

In order to make possible thermopower measurements, it is mandatory to reach a reliable temperature difference between the two sides of the junction. The implementation of an

accurate temperature control system into an MCBJ device or an STM is not trivial, since temperature drops and temperature gradients due to thermovoltages in all conducting materials have to be taken into account.

Several techniques have been proposed for measuring thermopower, being such proposed by Agraït and collaborators¹² the most advantageous, since it allows the simultaneous measurement of thermopower and conductance. It is based on the shift of the point at which the I - V curves cross the voltage axis. As $\Delta V = -S\Delta T$, S can be obtained as the slope of the voltage at the crossing point of I - V s for different ΔT .

Thermopower measurements can also provide additional information about the transport, such as if E_F is closer to the HOMO or closer to the LUMO. In fact there is no other specific method for determining that with certainty. In this sense, the sign of the Seebeck coefficient (S) of molecular junctions can indicate this relative position,^{98,99} as shown in Figure 1.25. When E_F is closer to HOMO level, electrons flow towards the hot side, giving rise to a positive value for the Seebeck coefficient ($S > 0$), while when E_F is closer to the LUMO level, electrons flow towards the cold side and the Seebeck coefficient has a negative value ($S < 0$).¹²

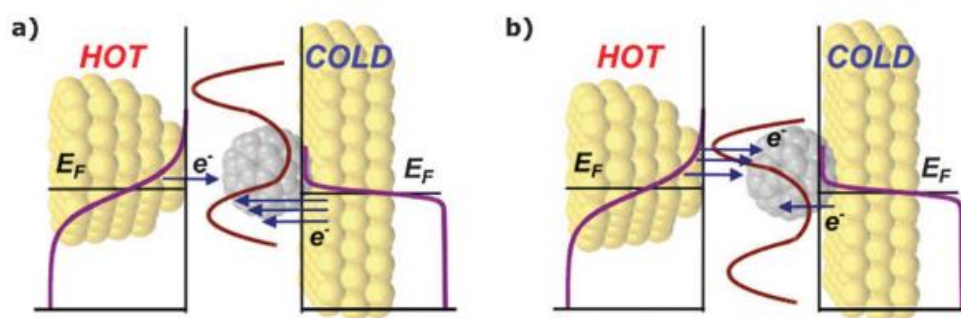


Figure 1.25. The sign of S is related with the alignment of the E_F and the HOMO and LUMO levels. **(a)** When the HOMO level is closer to the E_F , electrons flow towards the hot side and $S > 0$. **(b)** When the LUMO level is closer to the E_F , electrons flow towards the cold side and $S < 0$. Reproduced from ref.¹² with permission from The Royal Society of Chemistry.

Importantly, understanding the electronic response to a temperature difference in a single-molecule junction is not limited to correlate different molecular backbones and linkers with the Seebeck coefficient; this information can be applied for the design of devices with a high thermoelectric efficiency, improving the conversion of wasted heat into usable electricity through the thermoelectric effect.⁹⁶

1.6.2. Gating voltage

The incorporation of a third electrode (gate electrode) into the system has allowed the modulation of the transport properties of single-molecule junctions, since it permits the application of a gate voltage able to tune the alignment between the E_F and the molecular orbitals HOMO and LUMO. This three-electrode disposition is based on the transistor configuration, where the usual two electrodes involved in the junction would correspond to the drain and source electrodes, while the third one would act as a gate. The implementation of the gate electrode is not trivial, as it has to be placed very close to the junction in order to achieve a large enough gate field. A back-gate has been used for static techniques, using a conventional solid-state device configuration, but also combined with measurements in liquid,¹⁰⁰ while the use of electrochemical gate has been preferred for BJ techniques with both, MCBJ and STM.¹⁰¹ For the electrochemical gating, the three-electrode configuration becomes into a four-electrode configuration (Figure 1.26), since two additional electrodes are needed: a reference (RE) and a counter (CE); while the two electrodes responsible for the generation of the junction are both considered as working electrodes.

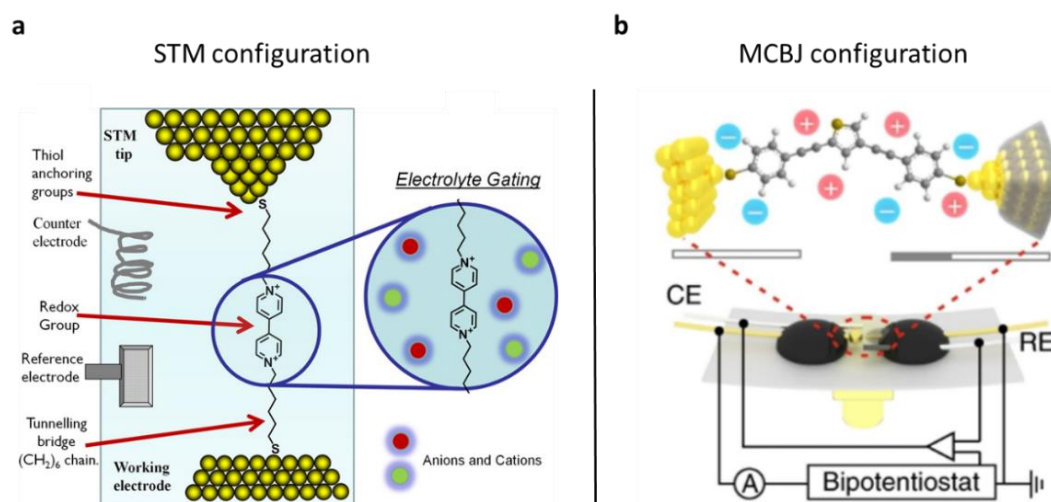


Figure 1.26. Disposition of the electrodes for electrochemical control. **(a)** STM; **(b)** MCBJ. **(a)** Reproduced with permission of ref.¹⁰² Copyright © 2015, American Chemical Society. **(b)** Reproduced with permission of ref.¹⁰³ Copyright © 2019, Springer Nature

The presence of a bipotentiostat allows the independent gating of each one of the working electrodes with respect to the reference, while the bias voltage between them is maintained. The four electrodes have to be allocated in an electrochemical cell and be immersed in an electrolyte solution which enables the electrochemical control of the system.

Besides modulating the E_F level, the electrochemical gating has demonstrated to be an efficient tool for different approaches:

- i) Investigating the electron transport of electrochemically active molecules, by means of applying a potential for keeping them in oxidized and/or reduced state, as well as by exploring the conductance at potentials around the oxidation and/or reduction peaks.^{104–107} In those cases, the response obtained from the molecular junctions depend on the electrolyte, typically aqueous solutions or ionic liquids.
- ii) A careful control of the oxidation state of metallic electrodes that tend to oxidize in ambient conditions, such as nickel, cobalt or iron.^{108–110} The use of such metals is of special interest as they have magnetic properties and open the door to carry out transport measurements with magnetized electrodes. A more detailed explanation of those experiments is given in the next section.

1.6.3. Magnetic measurements

The use of magnetic metal electrodes for single-molecule junctions is allowing the investigation of the spin transport behavior of different structures. The main inconvenience of these experiments is that, as indicated above in section 1.5.1, it is necessary to avoid the metal oxidation, or to establish a strategy for *in-situ* removing the oxide layer from the metal surface. In this sense, the combination of magnetic electrodes with electrochemical control seems to be a good strategy for carrying out these experiments, as electrochemistry allows both, removing any oxide layer formed in the surface of the electrodes and maintaining them in the desired oxidation state. Nevertheless, the application of a magnetic field have been used not only for magnetizing electrodes, but

BEYOND CONDUCTANCE MEASUREMENTS

also for investigating magnetoresistance behavior in junctions formed with Au¹¹¹ and Ni¹¹² electrodes.

Concerning the magnetic field exposition, two different methods have been reported:

- i) Application of the magnetic field during the break-junction experiments.^{111,113} This method entails an extra difficulty as the location of the magnet close enough of the junctions is not trivial, and could originate the heating of the electrodes. However, it would permit to control the direction of the field, parallel or perpendicular to the junction.
- ii) Magnetizing the electrodes before the experiments.^{114,115} This method simplifies the measurement itself but adds the need to test the electrodes before and after the experiments, in order to ensure that the magnetization remains.

In Chapter 5, we describe the implementation of an electrochemical control system into our homebuilt STM and presented the results of our preliminary studies with magnetic electrodes.

1.7. Overview and main goals

Since its birth, molecular electronics has been an active field of research which has provided fundamental knowledge about the electron and thermal transport at the nanoscale, shedding light on the keys for developing more efficient electronic devices, devices for particular applications, and even single-molecule-based devices. This field has been the ideal experimental and theoretical platform for studying the electrical properties of very different molecules, as long as they contain appropriate binding sites for being wired within an electric circuit. It has demonstrated that molecules are able to emulate the functioning of different components of macroscopic circuits, and even exhibiting unexpected ones.

Although several techniques have been developed along years, break junction is, at the moment, the most extended one for studies at the single-molecule level. It provides reproducible and reliable results, being possible to use different instruments. Molecular electronics has taken advantage of the ability of synthetic chemistry for preparing multitude of compounds whose structure can be controlled by means of carefully designed routes. Working together, it has been possible to investigate the electron transport through novel structures, chemical functions still unexplored from an electrical perspective, and even small molecules which could be used as models for exploring their structurally related large-area materials.

Crossing beyond the limits of mere electronics, toward spintronic, photovoltaics, and thermoelectricity, has been other of the great achievements of the field in the last years. In this sense, electrochemical gating have demonstrated to be an useful tool for tuning the electrical properties of junctions, being the external stimulus able to induce conductance changes by means of modifying the E_F level and carrying the molecules to different oxidation states. Besides, it offers the possibility of using metals sensitive to oxidation in controlled conditions, making possible to carry out magnetic experiments with metals such as nickel or iron.

Taking all that into account, the main goals during this thesis, have been:

- i) To design a strategy for obtaining a multi-conductance state molecule, having well-defined and distinguishable states. Although there is a considerable

OVERVIEW AND MAIN GOALS

amount of research reporting junctions able to display several conductance values, only few of them focused on achieving this in a controlled manner. (Chapter 2 is dedicated to this goal).

- ii) To study two different families that remain almost unexplored from a molecular electronics perspective: azaborines and negatively curved nanographenes.

Azaborines are a family of heteroaromatic compounds, in which two carbon atoms in one (or several) of the rings have been substituted by nitrogen and boron. Remarkably, this simultaneous doping or substitution, can occur in three distinct relative positions: 1,2-, 1,3- and 1,4. Although it has been demonstrated that these three possible configurations exhibit different stability, reactivity and optical properties, the electronic transport properties of these compounds remains practically unexplored. Azaborines are isoelectronic with the all-C analogues. This means that the number of electrons involved in the system is the same for both. In this way, they maintain the topology of the parent scaffold, but inducing a certain charge polarization in the ring. (Chapter 3 is focused on this family).

Nanographenes are molecules of small size but with the same basic structure of graphene, this is, a monolayer of carbon atoms in hexagonal arrangement. The incorporation of heptagonal rings in their structure induces a negative curvature through which the electron transport has not been investigated yet. Remarkably, the synthesis and study of these distorted structures is receiving an special attention nowadays, since several structures exhibiting promising optoelectronics properties have been reported to date. (Chapter 4 is focused on this family).

Besides, both, azaborines and heptagon-containing nanographenes, involve an additional interest, since they can be used as model for investigating defects in graphene by extrapolation from these smaller and easy-to-handle analogues. In particular, azaborines can be used to investigate the local effects of B-N doping, while heptagon-containing nanographenes, can shed light about the effect of

heptagons, one of the structural defects more frequently found in large-area graphene.

- iii) To carry out the implementation of an electrochemical control system in our homebuilt STM, which will allow to tune the E_F level, study electrochemically active molecules and use metals such as iron or nickel for magnetic experiments. (Chapter 5 is dedicated to this process).

In order to achieve these goals, we have used synthetic chemistry for designing and preparing the target molecules, whose electrical properties have been measured by means of the break junction technique, using a homebuilt STM. The bases of this technique have been already presented in this Chapter 1, while a description of the experimental setups is given in the Experimental Section. Although a detailed background corresponding to each topic has been included later in every chapter, we decided to present in brief the different topics here, with the hope of facilitating the reading and highlighting, in advance, the reasons for finding them of interest for this field.

REFERENCES

References

- (1) Cuevas, J. C.; Escheer, E. *Molecular Electronics an Introduction to Theory and Experiment (World Scientific)*; **2010**. <https://doi.org/10.1142/7434>.
- (2) Ratner, M. A Brief History of Molecular Electronics. *Nat. Nanotechnol.* **2013**, *8*, 378–381. <https://doi.org/10.1038/nnano.2013.110>.
- (3) Choi, H.; Mody, C. C. M. The Long History of Molecular Electronics: Microelectronics Origins of Nanotechnology. *Soc. Stud. Sci.* **2009**, *39*, 11–50. <https://doi.org/10.1177/0306312708097288>.
- (4) Aviram, A.; Ratner, M. A. Molecular Rectifiers. *Chem. Phys. Lett.* **1974**, *29*, 277–283. [https://doi.org/10.1016/0009-2614\(74\)85031-1](https://doi.org/10.1016/0009-2614(74)85031-1).
- (5) Binnig, G.; Rohrer, H.; Gerber, C.; Weibel, E. Tunneling through a Controllable Vacuum Gap. *Appl. Phys. Lett.* **1982**, *40*, 178–180. <https://doi.org/10.1063/1.92999>.
- (6) Binnig, G.; Quate, C. F.; Gerber, C. Atomic Force Microscope. *Phys. Rev. Lett.* **1986**, *56*, 930–934. <https://doi.org/10.1103/PhysRevLett.56.930>.
- (7) Reed, M. A.; Zhou, C.; Muller, C. J.; Burgin, T. P.; Tour, J. M. Conductance of a Molecular Junction. *Science* **1997**, *278*, 252–254. <https://doi.org/10.1126/science.278.5336.252>.
- (8) Cui, X. D.; Primak, A.; Zarate, X.; Tomfohr, J.; Sankey, O. F.; Moore, A. L.; Moore, T. A.; D. Gust; Harris, G.; Lindsay, S. M. Reproducible Measurement of Single-Molecule Conductivity. *Science* **2001**, *294*, 571–574. <https://doi.org/10.1126/science.1064354>.
- (9) Xu, B.; Tao, N. J. Single-Molecule Resistance Measured by Repeated Formation of Molecular Junctions. *Science* **2003**, *301*, 1221–1223. <https://doi.org/10.1126/science.1087481>.
- (10) Peng, J.; Zhou, W. X.; Chen, K. Q. High-Efficiency Spin Filtering in Salophen-Based Molecular Junctions Modulated with Different Transition Metal Atoms. *Phys. Lett. A* **2014**, *378*, 3126–3130. <https://doi.org/10.1016/j.physleta.2014.09.015>.

- (11) Mohamad, M.; Ahmed, R.; Kanoun, A. A.; Shaari, A.; Goumri-Said, S. Designing a Molecular Device for Organic Solar Cell Applications Based on Vinazene: I-V Characterization and Efficiency Predictions. *Sol. Energy* **2016**, *140*, 124–129. <https://doi.org/10.1016/j.solener.2016.10.028>.
- (12) Rincón-García, L.; Evangeli, C.; Rubio-Bollinger, G.; Agraït, N. Thermopower Measurements in Molecular Junctions. *Chem. Soc. Rev.* **2016**, *45*, 4285–4306. <https://doi.org/10.1039/C6CS00141F>.
- (13) Chen, F.; Hihath, J.; Huang, Z.; Li, X.; Tao, N. J. Measurement of Single-Molecule Conductance. *Annu. Rev. Phys. Chem.* **2007**, *58*, 535–564. <https://doi.org/10.1146/annurev.physchem.58.032806.104523>.
- (14) Mantooth, B. A.; Weiss, P. S. Fabrication, Assembly, and Characterization of Molecular Electronic Components. *Proc. IEEE* **2003**, *91*, 1785–1802. <https://doi.org/10.1109/JPROC.2003.818320>.
- (15) Agraït, N.; Yeyati, A. L.; van Ruitenbeek, J. M. Quantum Properties of Atomic-Sized Conductors. *Phys. Rep.* **2003**, *377*, 81–279. [https://doi.org/10.1016/S0370-1573\(02\)00633-6](https://doi.org/10.1016/S0370-1573(02)00633-6).
- (16) Van Ruitenbeek, J. M.; Alvarez, A.; Piñeyro, I.; Grahmann, C.; Joyez, P.; Devoret, M. H.; Esteve, D.; Urbina, C. Adjustable Nanofabricated Atomic Size Contacts. *Rev. Sci. Instrum.* **1996**, *67*, 108–111. <https://doi.org/10.1063/1.1146558>.
- (17) Rincón García, L. Conductance, Thermopower and Thermal Conductance Measurements in Single-Molecule Junctions and Atomic Contacts, **2019**. PhD dissertation, Universidad Autónoma de Madrid
- (18) Moreland, J.; Ekin, J. W. Electron Tunneling Experiments Using Nb-Sn “Break” Junctions. *J. Appl. Phys.* **1985**, *58*, 3888–3895. <https://doi.org/10.1063/1.335608>.
- (19) Muller, C. J.; van Ruitenbeek, J. M.; de Jongh, L. J. Conductance and Supercurrent Discontinuities in Atomic-Scale Metallic Constrictions of Variable Width. *Phys. Rev. Lett.* **1992**, *69*, 140–143. <https://doi.org/10.1103/PhysRevLett.69.140>.
- (20) Brandbyge, M.; Schiøtz, J.; Sørensen, M. R.; Stoltze, P.; Jacobsen, K. W.; Nørskov, J.

REFERENCES

- K.; Olesen, L.; Laegsgaard, E.; Stensgaard, I.; Besenbacher, F. Atom-Sized Wires Between Two Metals. *Phys. Rev. B* **1995**, *52*, 8499–8514.
- (21) Leary, E.; La Rosa, A.; González, M. T.; Rubio-Bollinger, G.; Agraït, N.; Martín, N. Incorporating Single Molecules into Electrical Circuits. the Role of the Chemical Anchoring Group. *Chem. Soc. Rev.* **2015**, *44*, 920–942. <https://doi.org/10.1039/c4cs00264d>.
- (22) Costa-Krämer, J. Conductance Quantization at Room Temperature in Magnetic and Nonmagnetic Metallic Nanowires. *Phys. Rev. B* **1997**, *55*, R4875–R4878. <https://doi.org/10.1103/PhysRevB.55.R4875>.
- (23) Weber, H. B.; Reichert, J.; Weigend, F.; Ochs, R.; Beckmann, D.; Mayor, M.; Ahlrichs, R.; Löhneysen, H. V. Electronic Transport through Single Conjugated Molecules. *Chem. Phys.* **2002**, *281*, 113–125. [https://doi.org/10.1016/S0301-0104\(02\)00343-9](https://doi.org/10.1016/S0301-0104(02)00343-9).
- (24) Wang, K. Modulation and Control of Charge Transport through Single Molecule Junctions, 2016.
- (25) González, M. T.; Wu, S.; Huber, R.; Van Der Molen, S. J.; Schönenberger, C.; Calame, M. Electrical Conductance of Molecular Junctions by a Robust Statistical Analysis. *Nano Lett.* **2006**, *6*, 2238–2242. <https://doi.org/10.1021/nl061581e>.
- (26) Inkpen, M. S.; Lemmer, M.; Fitzpatrick, N.; Milan, D. C.; Nichols, R. J.; Long, N. J.; Albrecht, T. New Insights into Single-Molecule Junctions Using a Robust, Unsupervised Approach to Data Collection and Analysis. *J. Am. Chem. Soc.* **2015**, *137*, 9971–9981. <https://doi.org/10.1021/jacs.5b05693>.
- (27) Lemmer, M.; Inkpen, M. S.; Kornysheva, K.; Long, N. J.; Albrecht, T. Unsupervised Vector-Based Classification of Single-Molecule Charge Transport Data. *Nat. Commun.* **2016**, *7*, 12922. <https://doi.org/10.1038/ncomms12922>.
- (28) Naselaris, T.; Kay, K. N.; Nishimoto, S.; Gallant, J. L. Encoding and Decoding in FMRI. *Neuroimage* **2011**, *56*, 400–410. <https://doi.org/10.1016/j.neuroimage.2010.07.073>.
- (29) Haxby, J. V.; Connolly, A. C.; Guntupalli, J. S. Decoding Neural Representational

- Spaces Using Multivariate Pattern Analysis. *Annu. Rev. Neurosci.* **2014**, *37*, 435–456. <https://doi.org/10.1146/annurev-neuro-062012-170325>.
- (30) Cabosart, D.; El Abbassi, M.; Stefani, D.; Frisenda, R.; Calame, M.; Van der Zant, H. S. J.; Perrin, M. L. A Reference-Free Clustering Method for the Analysis of Molecular Break-Junction Measurements. *Appl. Phys. Lett.* **2019**, *114*, 143102. <https://doi.org/10.1063/1.5089198>.
- (31) El Abbassi, M.; Zwick, P.; Rates, A.; Stefani, D.; Prescimone, A.; Mayor, M.; Van Der Zant, H. S. J.; Dulić, D. Unravelling the Conductance Path through Single-Porphyrin Junctions. *Chem. Sci.* **2019**, *10*, 8299–8305. <https://doi.org/10.1039/c9sc02497b>.
- (32) Paulsson, M.; Krag, C.; Frederiksen, T.; Brandbyge, M. Conductance of Alkanedithiol Single-Molecule Junctions: A Molecular Dynamics Study. *Nano Lett.* **2009**, *9*(1), 117–121. <https://doi.org/10.1021/nl802643h>.
- (33) Zotti, L. A.; Bürkle, M.; Pauly, F.; Lee, W.; Kim, K.; Jeong, W.; Asai, Y.; Reddy, P.; Cuevas, J. C. Heat Dissipation and Its Relation to Thermopower in Single-Molecule Junctions. *New J. Phys.* **2014**, *16*, 015004. <https://doi.org/10.1088/1367-2630/16/1/015004>.
- (34) Quek, S. Y.; Venkataraman, L.; Choi, H. J.; Louie, S. G.; Hybertsen, M. S.; Neaton, J. B. Amine - Gold Linked Single-Molecule Circuits: Experiment and Theory. *Nano Lett.* **2007**, *7*, 3477–3482. <https://doi.org/10.1021/nl072058i>.
- (35) Widawsky, J. R.; Darancet, P.; Neaton, J. B.; Venkataraman, L. Simultaneous Determination of Conductance and Thermopower of Single Molecule Junctions. *Nano Lett.* **2012**, *12*, 354–358. <https://doi.org/10.1021/nl203634m>.
- (36) Miguel, D.; Álvarez De Cienfuegos, L.; Martín-Lasanta, A.; Morcillo, S. P.; Zotti, L. A.; Leary, E.; Bürkle, M.; Asai, Y.; Jurado, R.; Cárdenas, D. J.; Rubio-Bollinger, G.; Agraït, N.; Cuerva, J. M.; González, M. T. Toward Multiple Conductance Pathways with Heterocycle-Based Oligo(Phenyleneethynylene) Derivatives. *J. Am. Chem. Soc.* **2015**, *137*, 13818–13826. <https://doi.org/10.1021/jacs.5b05637>.
- (37) Ko, C. H.; Huang, M. J.; Fu, M. D.; Chen, C. H. Superior Contact for Single-Molecule Conductance: Electronic Coupling of Thiolate and Isothiocyanate on Pt, Pd, and Au.

REFERENCES

- J. Am. Chem. Soc.* **2010**, *132*, 756–764. <https://doi.org/10.1021/ja9084012>.
- (38) Kim, T. Conductance of a Single Molecule Junction Formed with Ni, Au, and Ag Electrodes. *J. Korean Chem. Soc.* **2014**, *58*, 513–516. <https://doi.org/10.5012/jkcs.2014.58.6.513>.
- (39) Herrer, L.; Ismael, A.; Martín, S.; Milan, D. C.; Serrano, J. L.; Nichols, R. J.; Lambert, C.; Cea, P. Single Molecule vs. Large Area Design of Molecular Electronic Devices Incorporating an Efficient 2-Aminepyridine Double Anchoring Group. *Nanoscale* **2019**, *11*, 15871–15880. <https://doi.org/10.1039/c9nr05662a>.
- (40) Jenkins, S. J. Aromatic Adsorption on Metals via First-Principles Density Functional Theory. *Proc. R. Soc. A* **2009**, *465*, 2949–2976. <https://doi.org/10.1098/rspa.2009.0119>.
- (41) Martin, C. A.; Ding, D.; Sørensen, J. K.; Bjørnholm, T.; Van Ruitenbeek, J. M.; Van Der Zant, H. S. J. Fullerene-Based Anchoring Groups for Molecular Electronics. *J. Am. Chem. Soc.* **2008**, *130*, 13198–13199. <https://doi.org/10.1021/ja804699a>.
- (42) Leary, E.; González, M. T.; Van Der Pol, C.; Bryce, M. R.; Filippone, S.; Martín, N.; Rubio-Bollinger, G.; Agraït, N. Unambiguous One-Molecule Conductance Measurements under Ambient Conditions. *Nano Lett.* **2011**, *11*, 2236–2241. <https://doi.org/10.1021/nl200294s>.
- (43) Cheng, Z. L.; Skouta, R.; Vazquez, H.; Widawsky, J. R.; Schneebeli, S.; Chen, W.; Hybertsen, M. S.; Breslow, R.; Venkataraman, L. In Situ Formation of Highly Conducting Covalent Au-C Contacts for Single-Molecule Junctions. *Nat. Nanotechnol.* **2011**, *6*, 353–357. <https://doi.org/10.1038/nnano.2011.66>.
- (44) Batra, A.; Kladnik, G.; Gorjizadeh, N.; Meisner, J.; Steigerwald, M.; Nuckolls, C.; Quek, S. Y.; Cvetko, D.; Morgante, A.; Venkataraman, L. Trimethyltin-Mediated Covalent Gold-Carbon Bond Formation. *J. Am. Chem. Soc.* **2014**, *136*, 12556–12559. <https://doi.org/10.1021/ja5061406>.
- (45) Hong, W.; Li, H.; Liu, S. X.; Fu, Y.; Li, J.; Kaliginedi, V.; Decurtins, S.; Wandlowski, T. Trimethylsilyl-Terminated Oligo(Phenylene Ethynylene)s: An Approach to Single-Molecule Junctions with Covalent Au-C σ -Bonds. *J. Am. Chem. Soc.* **2012**, *134*,

- 19425–19431. <https://doi.org/10.1021/ja307544w>.
- (46) Bejarano, F.; Olavarria-Contreras, I. J.; Droghetti, A.; Rungger, I.; Rudnev, A.; Gutiérrez, D.; Mas-Torrent, M.; Veciana, J.; Van Der Zant, H. S. J.; Rovira, C.; Burzurí, E.; Crivillers, N. Robust Organic Radical Molecular Junctions Using Acetylene Terminated Groups for C-Au Bond Formation. *J. Am. Chem. Soc.* **2018**, *140*, 1691–1696. <https://doi.org/10.1021/jacs.7b10019>.
- (47) Hines, T.; Díez-Pérez, I.; Nakamura, H.; Shimazaki, T.; Asai, Y.; Tao, N. Controlling Formation of Single-Molecule Junctions by Electrochemical Reduction of Diazonium Terminal Groups. *J. Am. Chem. Soc.* **2013**, *135*, 3319–3322. <https://doi.org/10.1021/ja3106434>.
- (48) Su, T. A.; Neupane, M.; Steigerwald, M. L.; Venkataraman, L.; Nuckolls, C. Chemical Principles of Single-Molecule Electronics. *Nat. Rev. Mater.* **2016**. <https://doi.org/10.1038/natrevmats.2016.2>.
- (49) Zotti, L. A.; Kirchner, T.; Cuevas, J. C.; Pauly, F.; Huhn, T.; Scheer, E.; Erbe, A. Revealing the Role of Anchoring Groups in the Electrical Conduction through Single-Molecule Junctions. *Small* **2010**, *6*, 1529–1535. <https://doi.org/10.1002/sml.200902227>.
- (50) Arroyo, C. R.; Leary, E.; Castellanos-Gómez, A.; Rubio-Bollinger, G.; González, M. T.; Agraït, N. Influence of Binding Groups on Molecular Junction Formation. *J. Am. Chem. Soc.* **2011**, *133*, 14313–14319. <https://doi.org/10.1021/ja201861k>.
- (51) Leary, E.; Zotti, L. A.; Miguel, D.; Márquez, I. R.; Palomino-Ruiz, L.; Cuerva, J. M.; Rubio-Bollinger, G.; González, M. T.; Agraït, N. The Role of Oligomeric Gold-Thiolate Units in Single-Molecule Junctions of Thiol-Anchored Molecules. *J. Phys. Chem. C.* **2018**, *122*, 3211–3218. <https://doi.org/10.1021/acs.jpcc.7b11104>.
- (52) Kihira, Y.; Shimada, T.; Matsuo, Y.; Nakamura, E.; Hasegawa, T. Random Telegraphic Conductance Fluctuation at Au-Pentacene-Au Nanojunctions. *Nano Lett.* **2009**, *9*, 1442–1446. <https://doi.org/10.1021/nl803284t>.
- (53) Evangeli, C.; Gillemot, K.; Leary, E.; González, M. T.; Rubio-Bollinger, G.; Lambert, C. J.; Agraït, N. Engineering the Thermopower of C₆₀ Molecular Junctions. *Nano Lett.* **2013**, *13*, 2141–2145. <https://doi.org/10.1021/nl400579g>.

REFERENCES

- (54) Lee, S. K.; Ohto, T.; Yamada, R.; Tada, H. Thermopower of Benzenedithiol and C₆₀ Molecular Junctions with Ni and Au Electrodes. *Nano Lett.* **2014**, *14*, 5276–5280. <https://doi.org/10.1021/nl502305e>.
- (55) Van Dyck, C.; Ratner, M. A. Molecular Rectifiers: A New Design Based on Asymmetric Anchoring Moieties. *Nano Lett.* **2015**, *15*, 1577–1584. <https://doi.org/10.1021/nl504091v>.
- (56) Kushmerick, J. G.; Pollack, S. K.; Yang, J. C.; Naciri, J.; Holt, D. B.; Ratner, M. A.; Shashidhar, R. Understanding Charge Transport in Molecular Electronics. *Ann. N. Y. Acad. Sci.* **2003**, *1006*, 277–290. <https://doi.org/10.1196/annals.1292.019>.
- (57) Metzger, R. M. Unimolecular Rectifiers: Present Status. *Chem. Phys.* **2006**, *326*, 176–187. <https://doi.org/10.1016/j.chemphys.2006.02.026>.
- (58) Krzeminski, C.; Delerue, C.; Allan, G.; Vuillaume, D.; Metzger, R. M. Theory of Electrical Rectification in a Molecular Monolayer. *Phys. Rev. B - Condens. Matter Mater. Phys.* **2001**, *64*, 1–6. <https://doi.org/10.1103/PhysRevB.64.085405>.
- (59) Metzger, R. M. Unimolecular Electrical Rectifiers. *Chem. Rev.* **2003**, *103*, 3803–3834. <https://doi.org/10.1021/cr020413d>.
- (60) Weigend, F.; Elbing, M.; Ochs, R.; Koentopp, M.; Fischer, M.; Ha, C. Von; Evers, F.; Weber, H. B.; Mayor, M. A Single-Molecule Diode. *Proc. Natl. Acad. Sci. U. S. A.* **2005**, *102*, 8815–8820. <https://doi.org/10.1073/pnas.0408888102>.
- (61) Morales, G. M.; Jiang, P.; Yuan, S.; Lee, Y.; Sanchez, A.; You, W.; Yu, L. Inversion of the Rectifying Effect in Diblock Molecular Diodes by Protonation. *J. Am. Chem. Soc.* **2005**, *127*, 10456–10457. <https://doi.org/10.1021/ja051332c>.
- (62) Díez-Pérez, I.; Hihath, J.; Lee, Y.; Yu, L.; Adamska, L.; Kozhushner, M. A.; Oleynik, I. I.; Tao, N. Rectification and Stability of a Single Molecular Diode with Controlled Orientation. *Nat. Chem.* **2009**, *1*, 635–641. <https://doi.org/10.1038/nchem.392>.
- (63) Wang, W.; Yu, L. Intramolecular Hydrogen Bonding Assisted Charge Transport through Single Rectifying Molecule. *Langmuir* **2011**, *27*, 2084–2087. <https://doi.org/10.1021/la104002s>.

- (64) Tsuji, Y.; Staykov, A.; Yoshizawa, K. Molecular Rectifier Based on π - π Stacked Charge Transfer Complex. *J. Phys. Chem. C* **2012**, *116*, 2575–2580. <https://doi.org/10.1021/jp209547a>.
- (65) Stokbro, K.; Taylor, J.; Brandbyge, M. Do Aviram - Ratner Diodes Rectify? *J. Am. Chem. Soc.* **2003**, *125*, 3674–3675. <https://doi.org/10.1021/ja028229x>.
- (66) Staykov, A.; Nozaki, D.; Yoshizawa, K. Theoretical Study of Donor- π -Bridge-Acceptor Unimolecular Electric Rectifier. *J. Phys. Chem. C* **2007**, *111*, 11698–11705. <https://doi.org/10.1021/jp072600r>.
- (67) Liu, H.; Wang, N.; Li, P.; Yin, X.; Yu, C.; Gao, N.; Zhao, J. Theoretical Investigation into Molecular Diodes Integrated in Series Using the Non-Equilibrium Green's Function Method. *Phys. Chem. Chem. Phys.* **2011**, *13*, 1301–1306. <https://doi.org/10.1039/c0cp00118j>.
- (68) Li, H.; Xu, Q.; Li, N.; Sun, R.; Ge, J.; Lu, J.; Gu, H.; Yan, F. A Small-Molecule-Based Ternary Data-Storage Device. *J. Am. Chem. Soc.* **2010**, *132*, 5542–5543. <https://doi.org/10.1021/ja910243f>.
- (69) Chan, H.; Wong, H. L.; Ng, M.; Poon, C. T.; Yam, V. W. W. Switching of Resistive Memory Behavior from Binary to Ternary Logic via Alteration of Substituent Positioning on the Subphthalocyanine Core. *J. Am. Chem. Soc.* **2017**, *139*, 7256–7263. <https://doi.org/10.1021/jacs.7b00895>.
- (70) Dulić, D.; van der Molen, S. J.; Kudernac, T.; Jonkman, H. T.; de Jong, J. J. D.; Bowden, T. N.; van Esch, J.; Feringa, B. L.; van Wees, B. J. One-Way Optoelectronic Switching of Photochromic Molecules on Gold. *Phys. Rev. Lett.* **2003**, *91*, 207402. <https://doi.org/10.1103/PhysRevLett.91.207402>.
- (71) Auwärter, W.; Seufert, K.; Bischoff, F.; Ecija, D.; Vijayaraghavan, S.; Joshi, S.; Klappenberger, F.; Samudrala, N.; Barth, J. V. A Surface-Anchored Molecular Four-Level Conductance Switch Based on Single Proton Transfer. *Nat. Nanotechnol.* **2012**, *7*, 41–46. <https://doi.org/10.1038/nnano.2011.211>.
- (72) Ye, C.; Peng, Q.; Li, M.; Luo, J.; Tang, Z.; Pei, J.; Chen, J.; Shuai, Z.; Jiang, L.; Song, Y. Multilevel Conductance Switching of Memory Device through Photoelectric Effect.

REFERENCES

- J. Am. Chem. Soc.* **2012**, *134*, 20053–20059. <https://doi.org/10.1021/ja305354y>.
- (73) Choi, S. H.; Kim, B.; Frisbie, C. D. Electrical Resistance of Long Conjugated Molecular Wires. *Science* **2008**, *320*, 1482–1486. <https://doi.org/10.1126/science.1156538>.
- (74) Choi, S. H.; Risko, C.; Ruiz Delgado, M. C.; Kim, B.; Brédas, J. L.; Frisbie, C. D. Transition from Tunneling to Hopping Transport in Long, Conjugated Oligo-Imine Wires Connected to Metals. *J. Am. Chem. Soc.* **2010**, *132*, 4358–4368. <https://doi.org/10.1021/ja910547c>.
- (75) Luo, L.; Frisbie, C. D. Length-Dependent Conductance of Conjugated Molecular Wires Synthesized by Stepwise “Click” Chemistry. *J. Am. Chem. Soc.* **2010**, *132*, 8854–8855. <https://doi.org/10.1021/ja103239b>.
- (76) Lu, Q.; Liu, K.; Zhang, H.; Du, Z.; Wang, X.; Wang, F. From Tunneling to Hopping: A Comprehensive Investigation of Charge Transport Mechanism in Molecular Junctions Based on Oligo(*p*-PhenyleneEthynylene)s. *ACS Nano* **2009**, *3*, 3861–3868. <https://doi.org/10.1021/nn9012687>.
- (77) Khoo, K. H.; Chen, Y.; Li, S.; Quek, S. Y. Length Dependence of Electron Transport through Molecular Wires—a First Principles Perspective. *Phys. Chem. Chem. Phys.* **2015**, *17*, 77–96. <https://doi.org/10.1039/c4cp05006a>.
- (78) Luo, L.; Choi, S. H.; Frisbie, C. D. Probing Hopping Conduction in Conjugated Molecular Wires Connected to Metal Electrodes. *Chem. Mater.* **2011**, *23*, 631–645. <https://doi.org/10.1021/cm102402t>.
- (79) Zang, Y.; Fu, T.; Zou, Q.; Ng, F.; Li, H.; Steigerwald, M. L.; Nuckolls, C.; Venkataraman, L. Cumulene Wires Display Increasing Conductance with Increasing Length. *Nano Lett.* **2020**, *20*, 8415–8419. <https://doi.org/10.1021/acs.nanolett.0c03794>.
- (80) Guijarro, F. G.; Rivero, S. M.; Gunasekaran, S.; Arretxea, I.; Ortiz, R. P.; Caballero, R.; Crux, P. de la; Langa, F.; Venkataraman, L.; Casado, J. Synthesis and Electronic Properties of Pyridine End-Capped Cyclopentadithiophene-Vinylene Oligomers. *RSC Adv.* **2020**, *10*, 41264–41271. <https://doi.org/10.1039/d0ra08220a>.
- (81) Zhang, W.; Gan, S.; Vezzoli, A.; Davidson, R. J.; Milan, D. C.; Luzyanin, K. V.; Higgins,

- S. J.; Nichols, R. J.; Beeby, A.; Low, P. J.; Li, B.; Niu, L. Single-Molecule Conductance of Viologen-Cucurbit[8]Uril Host-Guest Complexes. *ACS Nano* **2016**, *10*, 5212–5220. <https://doi.org/10.1021/acsnano.6b00786>.
- (82) Milan, D. C.; Krempe, M.; Ismael, A. K.; Movsisyan, L. D.; Franz, M.; Grace, I.; Brooke, R. J.; Schwarzacher, W.; Higgins, S. J.; Anderson, H. L.; Lambert, C. J.; Tykwinski, R. R.; Nichols, R. J. The Single-Molecule Electrical Conductance of a Rotaxane-Hexayne Supramolecular Assembly. *Nanoscale* **2017**, *9*, 355–361. <https://doi.org/10.1039/c6nr06355a>.
- (83) Venkataraman, L.; Klare, J. E.; Nuckolls, C.; Hybertsen, M. S.; Steigerwald, M. L. Dependence of Single-Molecule Junction Conductance on Molecular Conformation. *Nature* **2006**, *442*, 904–907. <https://doi.org/10.1038/nature05037>.
- (84) Mishchenko, A.; Vonlanthen, D.; Meded, V.; Bürkle, M.; Li, C.; Pobelov, I. V.; Bagrets, A.; Viljas, J. K.; Pauly, F.; Evers, F.; Mayor, M.; Wandlowski, T. Influence of Conformation on Conductance of Biphenyl-Dithiol Single-Molecule Contacts. *Nano Lett.* **2010**, *10*, 156–163. <https://doi.org/10.1021/nl903084b>.
- (85) Venkataraman, L.; Park, Y. S.; Whalley, A. C.; Nuckolls, C.; Hybertsen, M. S.; Steigerwald, M. L. Electronics and Chemistry: Varying Single-Molecule Junction Conductance Using Chemical Substituents. *Nano Lett.* **2007**, *7*, 502–506. <https://doi.org/10.1021/nl062923j>.
- (86) Kruseewski, J. .; Krygowski, T. M. A Quantum-Chemical Approach to the Chemical Definition of Aromaticity. *Tetrahedron Lett.* **1970**, *4*, 319–324. [https://doi.org/10.1016/S0040-4039\(00\)61818-X](https://doi.org/10.1016/S0040-4039(00)61818-X).
- (87) Schleyer, P. von R.; Maerker, C.; Dransfeld, A.; Jiao, H.; van Eikema Hommes, N. J. R. Nucleus-Independent Chemical Shifts: A Simple and Efficient Aromaticity Probe. *J. Am. Chem. Soc.* **1996**, *118*, 6317–6318. <https://doi.org/10.1021/ja960582d>.
- (88) Zhang, G. P.; Xie, Z.; Song, Y.; Wei, M. Z.; Hu, G. C.; Wang, C. K. Is There a Specific Correlation between Conductance and Molecular Aromaticity in Single-Molecule Junctions? *Org. Electron.* **2017**, *48*, 29–34. <https://doi.org/10.1016/j.orgel.2017.05.032>.

REFERENCES

- (89) Chen, W.; Li, H.; Widawsky, J. R.; Appayee, C.; Venkataraman, L.; Breslow, R. Aromaticity Decreases Single-Molecule Junction Conductance. *J. Am. Chem. Soc.* **2014**, *136*, 918–920. <https://doi.org/10.1021/ja411143s>.
- (90) Xie, Z.; Ji, X. L.; Song, Y.; Wei, M. Z.; Wang, C. K. More Aromatic Molecular Junction Has Lower Conductance. *Chem. Phys. Lett.* **2015**, *639*, 131–134. <https://doi.org/10.1016/j.cplett.2015.09.017>.
- (91) Fujii, S.; Marqués-González, S.; Shin, J. Y.; Shinokubo, H.; Masuda, T.; Nishino, T.; Arasu, N. P.; Vázquez, H.; Kiguchi, M. Highly-Conducting Molecular Circuits Based on Antiaromaticity. *Nat. Commun.* **2017**, *8*, 15984. <https://doi.org/10.1038/ncomms15984>.
- (92) Yin, X.; Zang, Y.; Zhu, L.; Low, J. Z.; Liu, Z.-F.; Cui, J.; Neaton, J. B.; Latha Venkataraman; Campos, L. M. A Reversible Single-Molecule Switch Based on Activated Antiaromaticity. *Sci. Adv.* **2017**, *3*, eaao2615. <https://doi.org/10.1126/sciadv.aao2615>.
- (93) Gil-Guerrero, S.; Ramos-Berdullas, N.; Mandado, M. Can Aromaticity Enhance the Electron Transport in Molecular Wires? *Org. Electron.* **2018**, *61*, 177–184. <https://doi.org/10.1016/j.orgel.2018.05.043>.
- (94) Yang, Y.; Gantenbein, M.; Alqorashi, A.; Wei, J.; Sangtarash, S.; Hu, D.; Sadeghi, H.; Zhang, R.; Pi, J.; Chen, L.; Huang, X.; Li, R.; Liu, J.; Shi, J.; Hong, W.; Lambert, C. J.; Bryce, M. R. Heteroatom-Induced Molecular Asymmetry Tunes Quantum Interference in Charge Transport through Single-Molecule Junctions. *J. Phys. Chem. C* **2018**, *122*, 14965–14970. <https://doi.org/10.1021/acs.jpcc.8b03023>.
- (95) Valdiviezo, J.; Palma, J. L. Molecular Rectification Enhancement Based on Conformational and Chemical Modifications. *J. Phys. Chem. C* **2018**, *122*, 2053–2063. <https://doi.org/10.1021/acs.jpcc.7b12780>.
- (96) Aradhya, S. V.; Venkataraman, L. Single-Molecule Junctions beyond Electronic Transport. *Nat. Nanotechnol.* **2013**, *8*, 399–410. <https://doi.org/10.1038/nnano.2013.91>.
- (97) Bergfield, J. P.; Ratner, M. A. Forty Years of Molecular Electronics: Non-Equilibrium

- Heat and Charge Transport at the Nanoscale. *Phys. Status Solidi B* **2013**, *250*, 2249–2266. <https://doi.org/10.1002/pssb.201350048>.
- (98) Paulsson, M.; Datta, S. Thermoelectric Effect in Molecular Electronics. *Phys. Rev. B - Condens. Matter Mater. Phys.* **2003**, *67*, 1–4. <https://doi.org/10.1103/PhysRevB.67.241403>.
- (99) Reddy, P.; Jang, S. Thermoelectricity in Molecular Junctions. *Science* **2007**, *315*, 1568–1572. <https://doi.org/10.1126/science.1137149>.
- (100) Knopfmacher, O.; Tarasov, A.; Fu, W.; Wipf, M.; Niesen, B.; Calame, M.; Schönenberger, C. Nernst Limit in Dual-Gated Si-Nanowire FET Sensors. *Nano Lett.* **2010**, *10*, 2268–2274. <https://doi.org/10.1021/nl100892y>.
- (101) Li, X.; Xu, B.; Xiao, X.; Yang, X.; Zang, L.; Tao, N. Controlling Charge Transport in Single Molecules Using Electrochemical Gate. *Faraday Discuss.* **2006**, *131*, 111–120. <https://doi.org/10.1039/b505666g>.
- (102) Osorio, H. M.; Catarelli, S.; Cea, P.; Gluyas, J. B. G.; Hartl, F.; Higgins, S. J.; Leary, E.; Low, P. J.; Martín, S.; Nichols, R. J.; Tory, J.; Ulstrup, J.; Vezzoli, A.; Milan, D. C.; Zeng, Q. Electrochemical Single-Molecule Transistors with Optimized Gate Coupling. *J. Am. Chem. Soc.* **2015**, *137*, 14319–14328. <https://doi.org/10.1021/jacs.5b08431>.
- (103) Bai, J.; Daaoub, A.; Sangtarash, S.; Li, X.; Tang, Y.; Zou, Q.; Sadeghi, H.; Liu, S.; Huang, X.; Tan, Z.; Liu, J.; Yang, Y.; Shi, J.; Mészáros, G.; Chen, W.; Lambert, C.; Hong, W. Anti-Resonance Features of Destructive Quantum Interference in Single-Molecule Thiophene Junctions Achieved by Electrochemical Gating. *Nat. Mater.* **2019**, *18*, 364–369. <https://doi.org/10.1038/s41563-018-0265-4>.
- (104) Baghernejad, M.; Zhao, X.; Baruël Ørnsø, K.; Füg, M.; Moreno-García, P.; Rudnev, A. V.; Kaliginedi, V.; Vesztergom, S.; Huang, C.; Hong, W.; Broekmann, P.; Wandlowski, T.; Thygesen, K. S.; Bryce, M. R. Electrochemical Control of Single-Molecule Conductance by Fermi-Level Tuning and Conjugation Switching. *J. Am. Chem. Soc.* **2014**, *136*, 17922–17925. <https://doi.org/10.1021/ja510335z>.
- (105) Capozzi, B.; Chen, Q.; Darancet, P.; Kotiuga, M.; Buzzeo, M.; Neaton, J. B.; Nuckolls, C.; Venkataraman, L. Tunable Charge Transport in Single-Molecule Junctions via

REFERENCES

- Electrolytic Gating. *Nano Lett.* **2014**, *14*, 1400–1404. <https://doi.org/10.1021/nl404459q>.
- (106) Nichols, R. J.; Higgins, S. J. Single Molecule Nanoelectrochemistry in Electrical Junctions. *Acc. Chem. Res.* **2016**, *49*, 2640–2648. <https://doi.org/10.1021/acs.accounts.6b00373>.
- (107) Xiao, X.; Nagahara, L. A.; Rawlett, A. M.; Tao, N. Electrochemical Gate-Controlled Conductance of Single Oligo(PhenyleneEthyne)s. *J. Am. Chem. Soc.* **2005**, *127*, 9235–9240. <https://doi.org/10.1021/ja050381m>.
- (108) Catarelli, S. R.; Higgins, S. J.; Schwarzacher, W.; Mao, B. W.; Yan, J. W.; Nichols, R. J. Ionic Liquid Based Approach for Single-Molecule Electronics with Cobalt Contacts. *Langmuir* **2014**, *30*, 14329–14336. <https://doi.org/10.1021/la503077c>.
- (109) Brooke, R. J.; Jin, C.; Szumski, D. S.; Nichols, R. J.; Mao, B. W.; Thygesen, K. S.; Schwarzacher, W. Single-Molecule Electrochemical Transistor Utilizing a Nickel-Pyridyl Spinterface. *Nano Lett.* **2015**, *15*, 275–280. <https://doi.org/10.1021/nl503518q>.
- (110) Brooke, R. J.; Szumski, D. S.; Vezzoli, A.; Higgins, S. J.; Nichols, R. J.; Schwarzacher, W. Dual Control of Molecular Conductance through pH and Potential in Single-Molecule Devices. *Nano Lett.* **2018**, *18*, 1317–1322. <https://doi.org/10.1021/acs.nanolett.7b04995>.
- (111) Hayakawa, R.; Karimi, M. A.; Wolf, J.; Huhn, T.; Zöllner, M. S.; Herrmann, C.; Scheer, E. Large Magnetoresistance in Single-Radical Molecular Junctions. *Nano Lett.* **2016**, *16*, 4960–4967. <https://doi.org/10.1021/acs.nanolett.6b01595>.
- (112) Yamada, R.; Noguchi, M.; Tada, H. Magnetoresistance of Single Molecular Junctions Measured by a Mechanically Controllable Break Junction Method. *Appl. Phys. Lett.* **2011**, *98*, 053110. <https://doi.org/10.1063/1.3549190>.
- (113) Horiguchi, K.; Sagisaka, T.; Kurokawa, S.; Sakai, A. Electron Transport through Ni/1,4-Benzenedithiol/Ni Single-Molecule Junctions under Magnetic Field. *J. Appl. Phys.* **2013**, *113*. <https://doi.org/10.1063/1.4800530>.

- (114) Aragonès, A. C.; Aravena, D.; Cerdá, J. I.; Acís-Castillo, Z.; Li, H.; Real, J. A.; Sanz, F.; Hihath, J.; Ruiz, E.; Díez-Pérez, I. Large Conductance Switching in a Single-Molecule Device through Room Temperature Spin-Dependent Transport. *Nano Lett.* **2016**, *16*, 218–226. <https://doi.org/10.1021/acs.nanolett.5b03571>.
- (115) Aragonès, A. C.; Medina, E.; Ferrer-Huerta, M.; Gimeno, N.; Teixidó, M.; Palma, J. L.; Tao, N.; Ugalde, J. M.; Giralt, E.; Díez-Pérez, I.; Mujica, V. Measuring the Spin-Polarization Power of a Single Chiral Molecule. *Small* **2017**, *13*, 1602519. <https://doi.org/10.1002/sml.201602519>.

**CHAPTER 2:
MULTIPLE CONDUCTANCE PATHWAYS IN PYRIMIDINE-
BASED OLIGO(PHENYLENEETHYNYLENE) DERIVATIVES**

2.1. Introduction

Many different compounds able to form multiple molecular junctions of different conductance have been reported in literature. The existence of several (two or more) electrical responses for a single molecule lies in intrinsic (chemical, structural, conformational, electronic...) molecular changes, which should be promoted by an external stimulus. Redox,^{1,2} light-driven,³ proton transfer processes⁴ or even a combination of them⁵ have been used for originating this external stimulus and switching between two or more conductance states. In those cases, the measurement device should be attached to systems able to provide potential (gate-voltage), electrochemical, photoelectric, magnetic field or electric field control, depending on the external stimulus to be applied. Particular cases are those in which the conductance value for a junction varies due to a mechanical stimulus applied using the electrodes. This occurs when the molecules contain different conduction channel along the molecular backbone, due to additional binding sites to the typical two end linkers. If the additional anchor points interact efficiently with the electrodes, it is possible to choose the electron conduction pathway by controlling to which particular anchor site the electrode binds. In other words, a switch between different conductance states can be modulated *via* compression-stretching of the molecular junction. This concept, initially proposed by Venkataraman and co-workers in 2011,⁶ was later named by Kiguchi and collaborators as “*switch of anchor*” in 2014.⁷ Considering that the additional conduction pathways are shorter and of higher G than the corresponding end-to-end pathway, this kind of multichannel compounds can be considered as molecular potentiometers,⁶ since the total resistance (typical end-to-end pathway) can be fractionated (shorter pathways). However, obtaining two different conductance values is not enough anymore, since a potentiometer requires at least three different resistance values. In this sense, the rational creation of new channels in a controlled way is as important as searching for strategies which produce systems with more than two different conductance states. In the next section, we discuss the most relevant contributions on this kind of multi-conductance-states systems based on multichannel compounds.

It is important to highlight that systems presenting several conductance states due to reasons different from the addition of specific binding sites on the backbone have been also reported in literature. For example, due to different geometries for the electrode-

INTRODUCTION

linker coupling, as it happens for pyridine terminated molecules;⁸⁻¹⁰ or due to uncontrollable and undesirable interactions of the electrodes with the substituents, as reported Van der Zant and collaborators for a family of porphyrin derivatives.¹¹ In addition, molecules presenting “through-space” channels¹²⁻¹⁴ and systems consisting of several channels in parallel^{14,15} have been kept out of the following review, in spite of being multichannel compounds, since they do not provide the required configuration for their use as potentiometer.

2.1.1. Multi-conductance-state systems based on multichannel compounds

Venkataraman and co-workers reported in 2011, the first molecule able to provide two well-distinguishable conductance values, between which it was possible to perform a switch *via* controlling the movement of the piezoelectric.⁶ In particular, the molecules consisted in polyene chains, including cyano-groups on the molecular backbone in order to enhance the molecular stability. Single-molecule experiments revealed two different molecular signals at two different conductance values. The lower conductance state, producing flat and long plateaus, was in good agreement with the molecule fully extended between the electrodes. For the higher conductance state, a sloping profile in which the conductance dramatically decreased with the distance was found. So that, the authors hypothesized that the electrodes were directly interacting with the olefin backbone until the distance between them was sufficiently large for switching to an extended configuration (Figure 2.1a). Finally, they demonstrated that the rational switching between these two states was possible by compressing and elongating the junction (Figure 2.1b and 2.1c), probing that a single-molecule circuit can function as a potentiometer, in this case of only two possible conductance values.

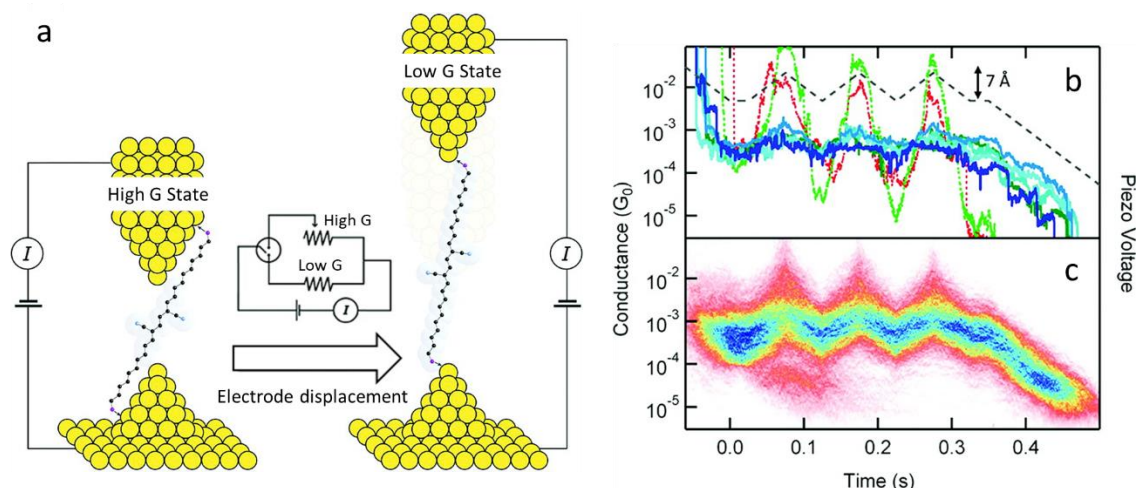


Figure 2.1. (a) Schematic depiction of an oligoene break junction, in the high G configuration and low G configuration. (b) G traces showing conductance changing continuously and reversibly between the two conductance states, as the piezo voltage is modulated (black line). (c) 2D histogram constructed from more than 1500 G traces obtained *via* compression and elongation of the junction. Fitting the average slope of the different sections of the piezo ramp shows that the conductance grows and decays exponentially with a factor of $0.2/\text{\AA}$ throughout the measurement, emphasizing the reproducibility of the potentiometer behavior. Adapted from ref.⁶ Copyright © 2011, American Chemical Society

In 2013, the same group carried out conductance studies of a family of silicon-containing molecular wires (Figure 2.2a).¹⁶ The molecules under study incorporated differently substituted silanes in the middle of the backbone: dimethylsilane, silacyclopentane or silacyclobutane. Only the molecule with a single silacyclobutane and without substituents in the rings (marked with a blue square), originated a second conduction pathway of high G due to an electrode-silacycle interaction (Figure 2.2b and 2.2c). Interestingly, they did not observe molecular junction formation for the reference compound for the high G pathway (marked with a green square), an analogue without one of the end linkers. This effect could be indicating that this second end linker is contributing to the stabilization of the junction responsible for the high G plateaus.

INTRODUCTION

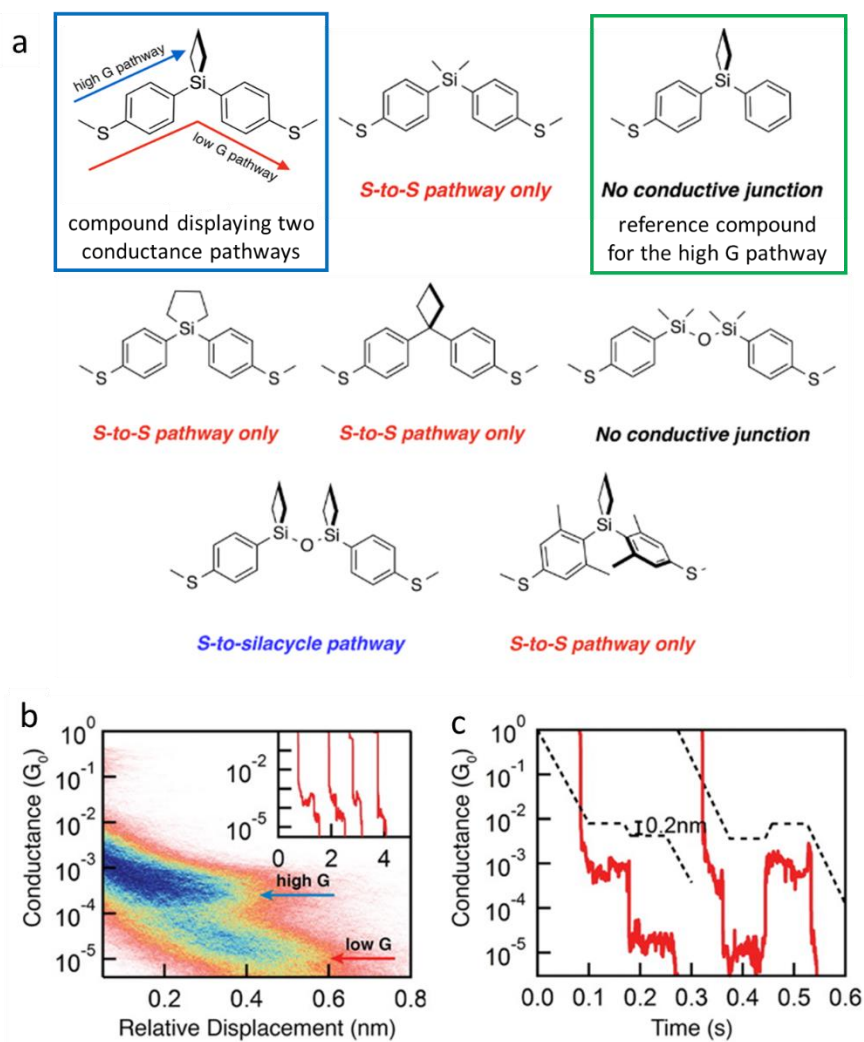


Figure 2.2. (a) Molecules under study. (b) 2D histogram of the first molecule (marked in a blue square) built from 5000 traces (some of them are shown in the inset). (c) Single-junction elongation (left) and compression traces (right) showing switching events. The black dotted line denotes the piezoelectric motion while the red solid line shows the conductive response. Reproduced with permission of ref.¹⁶ Copyright © 2013, American Chemical Society.

Agrait and Martín groups studied fluorene systems covalently connected to two bulky C_{60} moieties as binding groups. First, in 2011, they reported three distinguishable conductance values for the bifluorene junction shown in Figure 2.3a.¹⁷ Later, in 2015, for the single-fluorene analogue system,¹⁸ they only detected two different conductance states (Figure 2.3b). The high G state was attributed to the electron tunneling through a single C_{60} unit (Figure 2.3c), while the low G state was attributed to the fully extended molecule, in which each electrode interacts with one of the C_{60} moieties (Figure 2.3d). The switching between both states was achieved by modulating the pressure exerted by the STM tip.

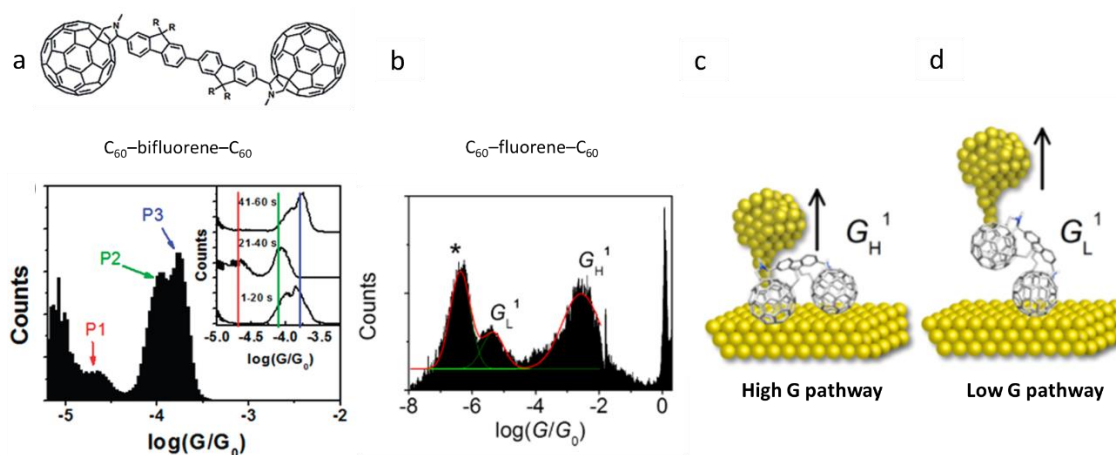


Figure 2.3. (a) 1D histogram built from the retraction curves recorded for the C₆₀-bifluorene-C₆₀ junction. Three conductance states (P₁, P₂ and P₃) are distinguished. Adapted from ref.¹⁷ Copyright © 2011, American Chemical Society. (b) 1D histogram built from the retraction curves for C₆₀-fluorene-C₆₀ junctions, recorded at $\log(G_{\text{trigger}}/G_0) = -1.0$. (c) Configuration responsible of the high G pathway, and (d) configuration responsible of the low G pathway. Adapted from ref.¹⁸ Copyright © 2015, American Chemical Society.

Also in 2015, our group studied the conductance of a family of oligo(phenyleneethynylenes), consisting on three rings, in which the central unit were a heterocycle.¹⁹ It was evaluated the ability of pyridine, pyrimidine and thiophene, in inner positions of the backbone, for interacting with the electrodes and creating a new conduction channel. The results showed that only the pyrimidine-containing OPE was able to give rise to the additional linker-heterocycle pathway (Figure 2.4a), producing plateaus shorter and of higher G (Figure 2.4b, blue trace) than those of the end-to-end pathway (Figure 2.4b, red trace). For further confirmation of the pyrimidine ring as responsible for the high G plateaus, a structural analogue for the pyrimidine-linker pathway was used as reference compound. The experiments for such reference compound probed that both, the conductance value and the plateau length, were in good agreement with those observed for the high G state of the pyrimidine-containing OPE.

INTRODUCTION

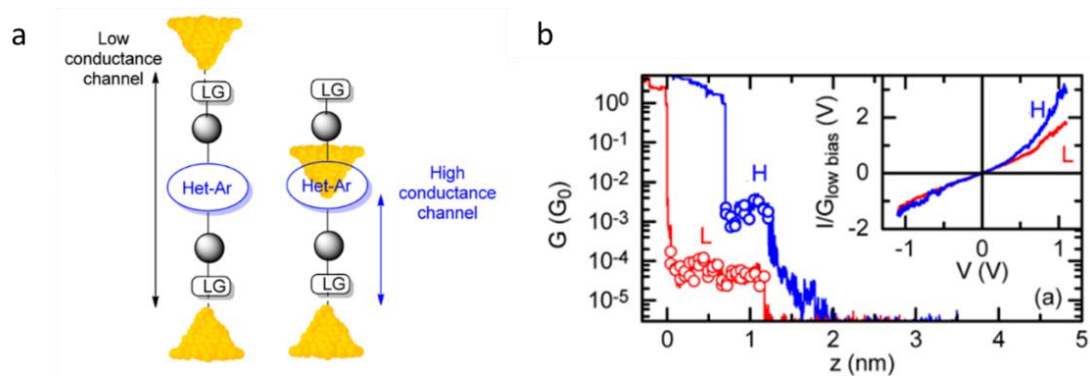


Figure 2.4. (a) High and low conductance channels in pyrimidine-based OPEs with three rings. (b) Two G - z traces for pyrimidine-based OPE displaying high G plateaus (blue trace) low G plateaus (red trace). The empty circles indicate the positions at which I - V for each plateau have been collected (inset). Reprinted with permission of ref.¹⁹ Copyright © 2015, American Chemical Society

A series of donor–acceptor (D–A) ladder-type heteroacenes were studied by Yu and collaborators in 2018.²⁰ These molecules contained up to 24 fused rings and were functionalized with thiol anchoring groups. The authors found that an additional charge-transport pathway appeared when these heteroacenes included benzothiadiazole (BTD) or benzoselenadiazole (BSD) units in the central position (Figure 2.5a). They probed that the origin of this new conductance signal was the result of the interaction of the electrodes with the middle groups, using the comparison with reference compounds in which the end-to-end pathway was suppressed by eliminating one of the end thiols (Figure 2.5b).

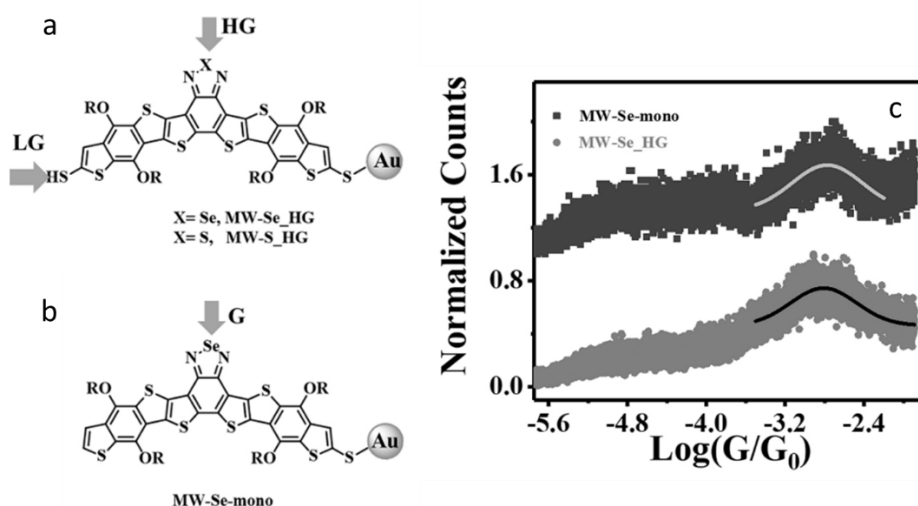


Figure 2.5. (a) Two conducting pathways of S- and Se-substituted ladder molecules. (b) The analogue with only one thiol group displayed a single conductance pathway. (c) Conductance histogram of both structures with Se substitution. Reproduced with permission of ref.²⁰ Copyright © 2018 Wiley-VCH Verlag GmbH & Co. KGaA, Weinheim.

Hong and co-workers presented an interesting case in 2020.²¹ The authors demonstrated that an external electric field (EEF) is able to induce a switching in the connectivity in single-molecule junctions. The molecules under study are oligo(phenyleneethynylene) derivatives with three rings. The side rings were connected with the central pyridine unit in *meta* position each one with respect to the other, and with respect to the nitrogen atom (Figure 2.6). They used trifluoroacetic acid (TFA) for *in-situ* protonating the pyridine ring, what involved a significant enhancement of its dipole moment. In this way, the applied electric field favours the interaction between the gold electrode and the pyridinium unit. They observed that as they increased the electric field, the percentage of the lower conductance state decreased progressively until being near to zero. Besides, at low electric fields both states could be obtained, but the end-to-end configuration, related with the lower conductance signal, was favoured. The novelty of this work abides first, in the combination of mechanical stimulus with the application of an external electric field as strategy for switching between both possible connectivities in the molecule; and second, in the possibility of the complete suppression of one of the conductance pathways (Figure 2.6).

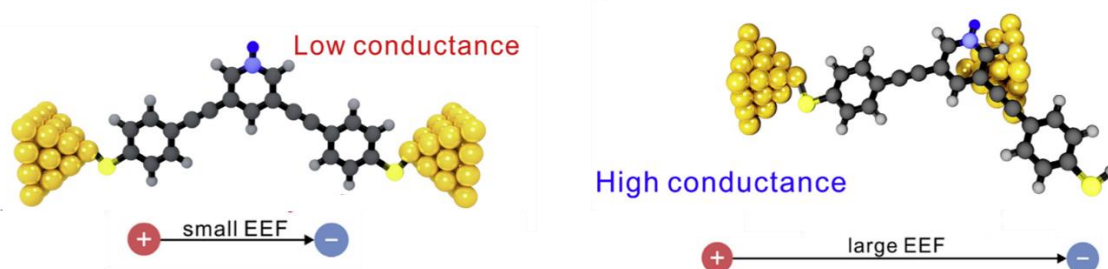


Figure 2.6. External electric field (EEF) is able to block one of the two possible connectivities in this oligo(phenyleneethynylene) derivative. Reproduced from ref.²¹ under the terms of the Creative Commons CC-BY license.

Nakamura and collaborators presented the first molecule with three conduction pathways in 2014.⁷ It was a quaterthiophene-based molecular wire protected *via* an insulating layer which prevented the conductance signals due to intermolecular interactions (Figure 2.7a). This molecule displayed different conductance signals (Figure 2.7b), depending on the combination of thiophene groups interacting with the electrodes. In this way, they could distinguish the conductance signals due to bithiophene (red pathway T1–T1), terthiophene (green pathway T1–T2) and quaterthiophene (blue pathway T2–T2).

INTRODUCTION

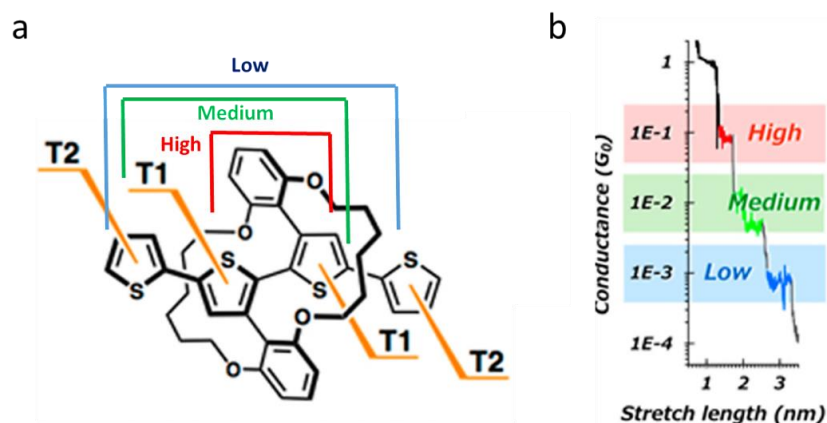


Figure 2.7. (a) Structure of the quaterthiophene-based molecular wire. (b) G - z trace showing plateaus corresponding with the three different conduction channels: High G channel (red line), Medium G channel (green line), and low G channel (blue line). Adapted with permission from ref.⁷ Copyright © 2014, American Chemical Society

In 2016, Kiguchi and co-workers reported a tripyridyl-triazine in which each heterocyclic ring could behave as an independent binding site by itself.²² The authors observed three different signals at different G regimes. They associated the higher conductance signal with the interaction of both electrodes with the central ring in a sandwich disposition (Figure 2.8a). The middle one was related to one electrode interacting with the central ring and the other interacting with one of the pyridyl rings (Figure 2.8b). The signal of lower conductance was proposed to be due to the interaction of the electrodes with two different pyridyl rings (Figure 2.8c). They supported this hypothesis with the analysis of plateau lengths for each group of signals (Figure 2.8d).

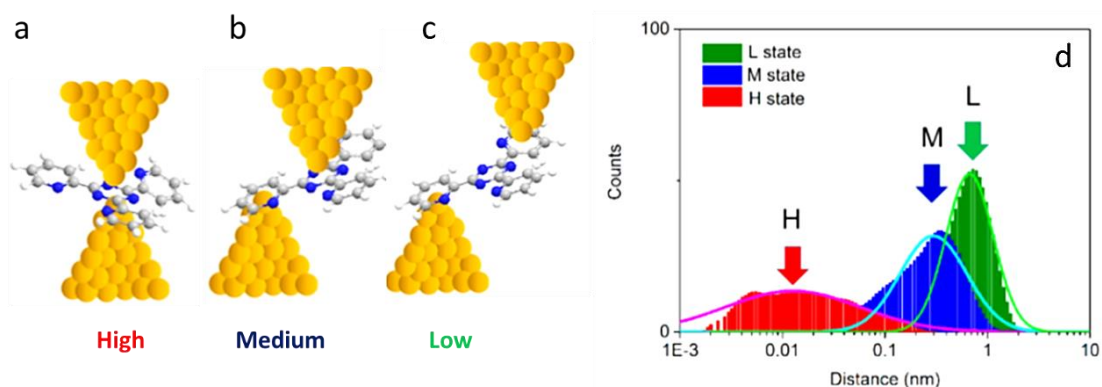


Figure 2.8. Schematic configuration for a tripyridyl-triazine molecular junctions in (a) H, (b) M, and (c) L conductance states. Blue balls represent N atoms. (d) Distribution of the gap distance of the high, middle, and low conductance states for the single tripyridyl-triazine molecular junctions. Reprinted from ref.²² Copyright © 2016, American Chemical Society

In 2017, Venkatramani and collaborators reported the electron-transport result for (4',4''''-(1,4-phenylene)-bis(3,2':6',3''-terpyridine)).²³ In this molecule (Figure 2.9a), every pyridyl group can provide multiple contact points with the electrodes. The multiple anchoring points in the linkers could originate 61 possible circuits within a single molecular junction (some of them are shown in Figure 2.9b). Due to the complexity of the system, the electric response did not allow to distinguish discrete conductance values that could be unambiguously related with specific conduction pathways. However, the authors used theoretical calculation in an attempt to guess the conductance value for the different connectivities, and determine in which percentage and conductance range along the G - z traces they were possibly contributing (Figure 2.9c).

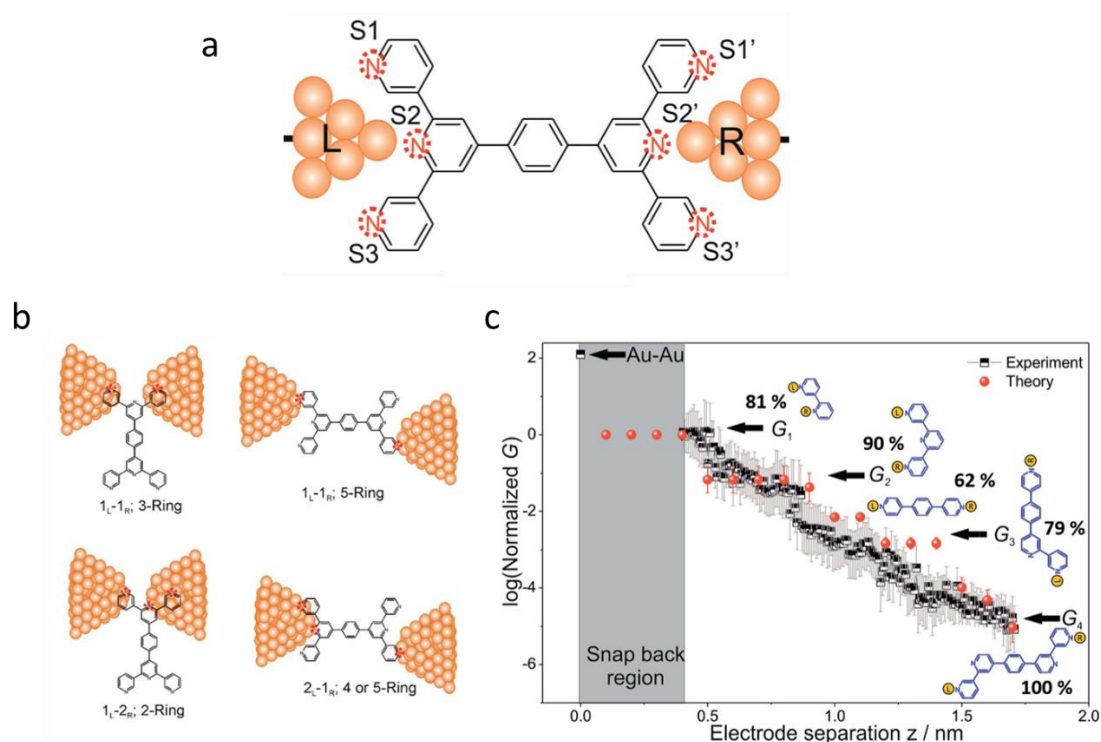


Figure 2.9. Example of molecule with more than three different conduction pathways. (a) Molecule in the junction. (b) Some of the 61 possible circuits depending on the heteroatoms interacting with the electrodes. (c) Conductance response for the molecule. Reproduced with permission of ref.²³ Published by The Royal Society of Chemistry.

2.1.2. Overview and main implications of previous examples

The previous examples let us to draw the following conclusions:

- The presence of heteroatoms along the molecular backbone is the most extended strategy for creating additional conduction pathways.^{7,16,19–22} However, an efficient interaction with the electrodes is not always achieved, due to structural limitations.^{16,19,20} In particular for obtaining two well-differentiated conduction pathways the repeated use of symmetric molecules bearing an heteroatom is observed. In these systems, the heteroatom acts as efficient anchor point located in the middle of the molecular backbone.^{16,19,20,21}
- Plateau-length distributions for the different conductance groups can be used as a guide for relating the conductance signals with the conduction pathway that originates them.
- The comparison of conductance values and plateau lengths of the multichannel compound with those of reference compounds, which recreate the independent pathways, is highly desirable in order to further confirm the origin of each signal.
- Considering the relevance of achieving more than two conduction pathways in the same system, we have found that only two compounds displaying three conductance values have been reported.^{7,22} In addition, as the number of possible conduction pathways increases, it is more probable to find indistinguishable conductance states.²³ In this sense, the potential use of these multichannel compounds as potentiometers is related with their ability to display well-defined and easily distinguishable pathways. Considering that the conductance signals have a typical width of one order of magnitude, the goal of the field should not be the infinitely increase of the number of possible conduction pathways in a system, but to achieve the maximum number of conduction pathways with conductance values different enough.

2.2. Objectives

According to the information collected in the background section and taking into account the previous knowledge of the group about multichannel compounds, we hypothesized that an asymmetrical allocation of the inner anchor point could originate two additional conduction pathways to that of the end-to-end configuration, giving a total of three conductance channels. Additionally, we searched for a strategic design that warranties that the resulting three conductance values are well separated.

Based on this hypothesis the following objectives were proposed:

1. To design a simple proof-of-concept molecule for our hypothesis, incorporating a motif able to act as inner anchor point in an asymmetrical position with respect to the end anchoring groups.
2. To synthesize the designed molecule and study its electron transport properties.
3. To synthesize reference structures for recreating each pathway and study their electric properties.
4. To evaluate the validity of the hypothesis: the potential of asymmetry for creating more than one additional conduction pathways, considering the results of the electron transport studies.

2.3. Results and discussion

2.3.1. Molecular design

Given the experience of our group working with oligo(phenyleneethynylene)s (OPEs) concerning to both synthesis^{24–26} and single-molecule experiments,^{19,27} we considered them as the ideal backbone for testing our hypothesis. On the one hand, they present a non-intricate basic structure, consisting of benzene rings connected by means of acetylene moieties. On the other hand, this is an extensively studied family in molecular electronics, also by other groups.^{28–30} In particular, our group previously demonstrated that the *p*-OPE bearing –SMe group as linkers, shown in Figure 2.10a, was able to display two well-spaced conductive channels, as consequence of the efficient interaction of the central pyrimidine ring with the electrodes. In that sense, a longer *p*-OPE, presenting the pyrimidine ring in an asymmetric position (Figure 2.10b), was proposed as a natural proof-of-concept for testing our hypothesis.

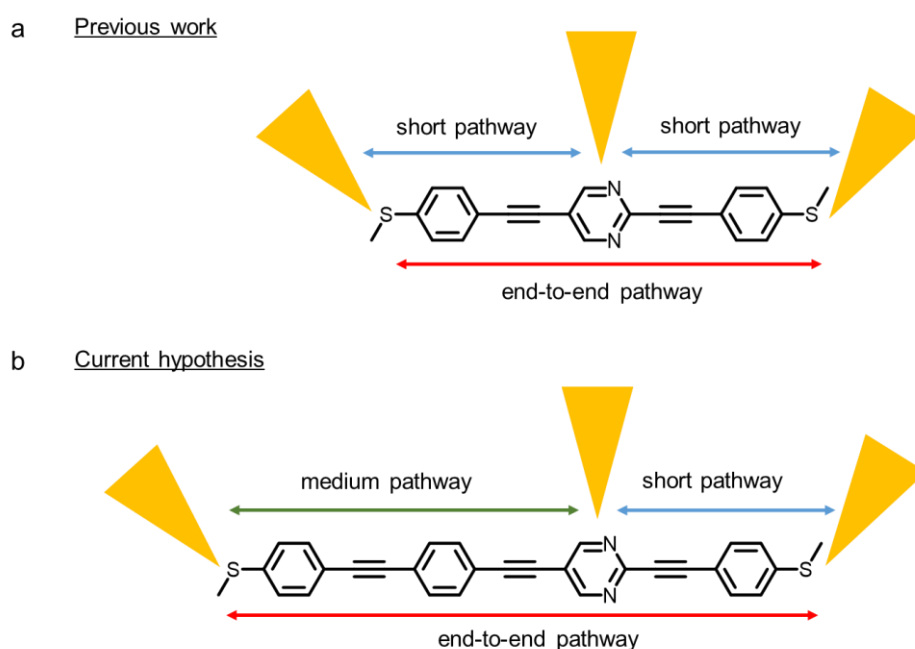


Figure 2.10. (a) Pyrimidine-containing *p*-OPE derivative presenting two different conduction pathways. (b) Proposed pyrimidine-containing *p*-OPE derivative and its hypothetical conduction pathways.

Several reference compounds (see Figure 2.11), were also designed for recreating each proposed conduction pathway of our target *p*-OPE (**1**). Compound **2** was proposed as

RESULTS AND DISCUSSION

reference for the short pathway, while **3** was proposed as reference for the medium one. **4** seemed the most direct reference compound for the end-to-end pathway, however this compound resulted to be highly insoluble, precluding its purification and a full characterisation. So that compound **5** was envisioned as a more easy-to-handle reference for this channel.

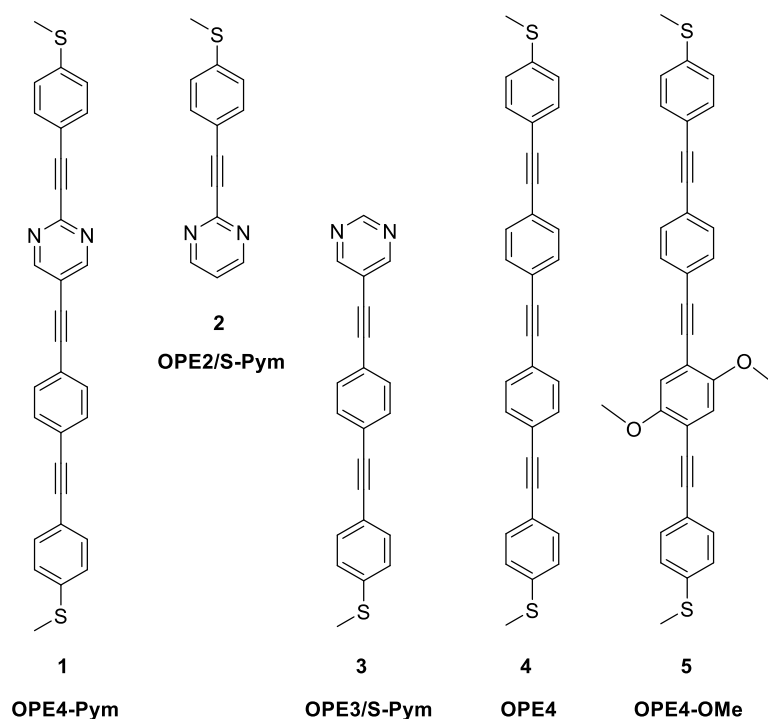


Figure 2.11. Synthesized *p*-OPE (**1**) and reference compounds for its possible short (**2**), medium (**3**) and long (**4** and **5**) pathways. More recognizable names have been assigned to these compounds for clarity in the discussion of the break-junction experiments.

2.3.2. Synthesis

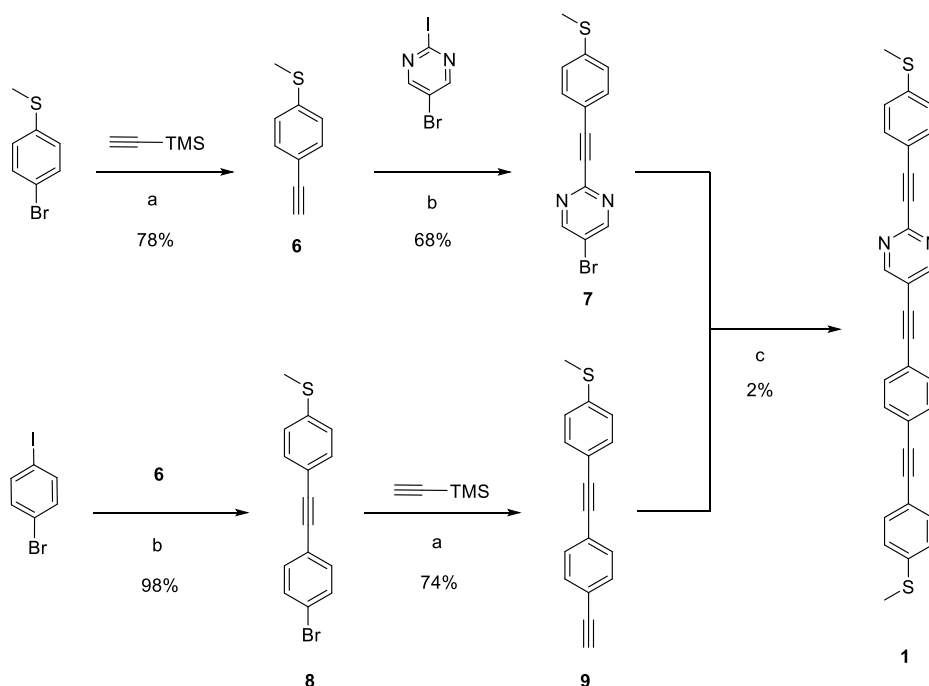
The synthetic strategy for preparing the designed pyrimidine-containing *p*-OPE **1** and its reference compounds **2**, **3**, **4**, and **5** are based on iterative Sonogashira cross-coupling reactions.³¹ The specific synthetic route for preparing the designed pyrimidine-containing *p*-OPE **1** depicted in Scheme 2.1, while the routes toward the reference compounds **2**, **3**, **4**, and **5** are collected in Scheme 2.2.^a In general, intermediate building blocks were obtained in moderate to good yield. The low yield observed in the final coupling steps is

^a The synthesis of compounds **1-5** was carried out in collaboration with Dr. Pablo Reiné.

attributed to the low solubility of the final products. Note the additional deprotection step when the alkyne coupling partner was trimethylsilylacetylene (TMSA), and the use of $\text{PtBu}_3\cdot\text{HBF}_4$ as ligand was required when the halide derivative involved in the Sonogashira coupling was $\text{Ar}-\text{Br}$ instead of $\text{Ar}-\text{I}$. Remarkably this reaction was compatible with the cross-coupling occurring selectively in the iodine position when aryl bromide is also available (synthesis of molecules **7** and **10**). Moreover, the one-pot Sonogashira cross-coupling methodology, reported by Grieco and co-workers for symmetrical bisarylethynylenes,³² was used for the synthesis of compound **10** (condition b, Scheme 2.2). The key of that strategy is the addition of 1,8-diazabicyclo[5.4.0]undec-7-ene (DBU) and substoichiometric amounts of water, which permits the *in-situ* deprotection of TMSA and the second coupling step.

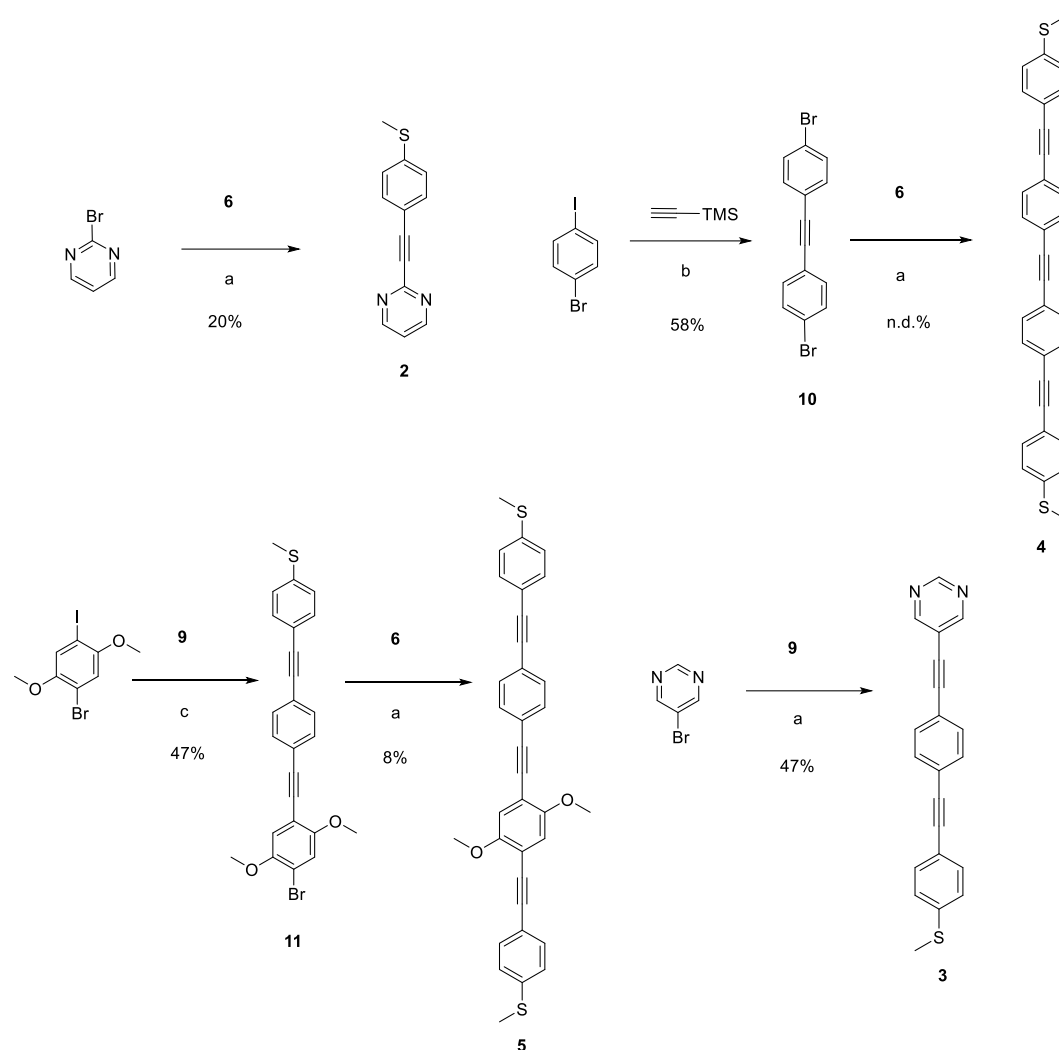
The building blocks and final compounds **1-5** were purified by flash chromatography and their structure confirmed by ^1H - and ^{13}C -Nuclear Magnetic Resonance (NMR). Compound **4** was an exception, as its high insolubility precluded an appropriate characterization. Experimental details of the synthesis of compounds **1-5** are available in the Experimental Section, and NMR spectra of final products are collected in the Annexes.

Synthetic route toward designed *p*-OPE **1**



Scheme 2.1. (a) (i) $\text{Pd}(\text{CH}_3\text{CN})_2\text{Cl}_2$, $\text{PtBu}_3\cdot\text{HBF}_4$, CuI , $i\text{Pr}_2\text{NH}/\text{THF}$, rt, 16 h. (ii) Bu_4NF , THF , rt, 2 h; (b) $\text{Pd}(\text{PPh}_3)_2\text{Cl}_2$, CuI , $\text{Et}_3\text{N}/\text{THF}$, rt, 16 h; (c) $\text{Pd}(\text{CH}_3\text{CN})_2\text{Cl}_2$, $\text{PtBu}_3\cdot\text{HBF}_4$, CuI , $i\text{Pr}_2\text{NH}/\text{THF}$, rt, 16 h.

Synthetic routes toward reference compounds 2, 3, 4 and 5



Scheme 2.2. (a) $\text{Pd}(\text{CH}_3\text{CN})_2\text{Cl}_2$, $\text{PtBu}_3 \cdot \text{HBF}_4$, CuI , $i\text{Pr}_2\text{NH}/\text{THF}$, rt, 16 h; (b) $\text{Pd}(\text{PPh}_3)_2\text{Cl}_2$, CuI , DBU , H_2O , acetonitrile, 60°C , 16 h. (c) $\text{Pd}(\text{PPh}_3)_2\text{Cl}_2$, CuI , $\text{Et}_3\text{N}/\text{THF}$, rt, 16 h;

2.3.3. Break-junction experiments

For higher clarity when showing and discussing the electron transport experimental results, we assigned more recognizable names to the target molecules, namely: **OPE4-pym** for molecule 1, **OPE2/S-pym** for molecule 2, **OPE3/S-pym** for molecule 3, **OPE4** for molecule 4 and **OPE4-OMe** for molecule 5, as indicated in Figure 2.11.

For the break-junction experiments, gold on quartz plates for break junction experiments were previously cleaned as described in the Experimental Section, and immersed for 15-20 min in DCM solutions of the corresponding compounds, with initial concentrations between 10^{-4} and 10^{-3} mM. The target compounds were measured applying a 0.16 bias

voltage, and using 1×10^8 V/A and 4.5×10^{10} V/A amplification gains in the STM circuit, with a protection resistor of $2 \times 10^6 \Omega$ in series. This combination allowed us to explore a range in conductance $G=I/V$ of 8 orders of magnitude between $10 G_0$ and $10^{-7} G_0$. Several rounds of measures were recorder for each compound. The raw conductance-distance (G - z) traces for each one were subjected to the searching plateaus process described in the Experimental Section, and the corresponding 1D and 2D histograms built from the traces displaying plateaus.

2.3.3.1. Conductance of OPE4-pym

The 2D histogram obtained for all the traces displaying plateaus (22% of the total traces) for **OPE-4pym** is shown in Figure 2.12a. It clearly shows that indeed our proposed compound successfully gives rise to three well-separated conductance clouds of different length. In particular, it displayed molecular signals at three different conductance regions, roughly at $\log(G/G_0) = -2$, $\log(G/G_0) = -4$, and $\log(G/G_0) = -6$. A further clustering-based separation was next performed over these traces, in order to obtain clear separated profiles for these three detected molecular signals. The 1D histograms of differentiated groups are collected in Figure 2.12b, while their independent 2D histograms are shown in Figures 2.12c-d. Three well-differentiated sets of plateaus were found. The high conductance signal represented the 37% of the total traces, the middle conductance signal involved the 26%, and the lower conductance group was formed by the 37% remaining. The observed peaks in the 1D histograms are quite symmetric, despite the corresponding signals in the 2D histograms have a certain sloping profile. The superimposition of the peaks shows that just a minimum overlap occurs between the three signals, making them easily distinguishable. The conductance for each group was calculated as the main value of their corresponding peaks using a Gaussian fit, obtaining the following values: $\log(G/G_0) = -5.8 \pm 0.37$ for the low conductance group; $\log(G/G_0) = -4.2 \pm 0.52$ for the middle conductance group; and $\log(G/G_0) = -2.2 \pm 0.21$ for the high conductance group. The error is given by the half width at half maximum (HWHM) of the Gaussian fit.

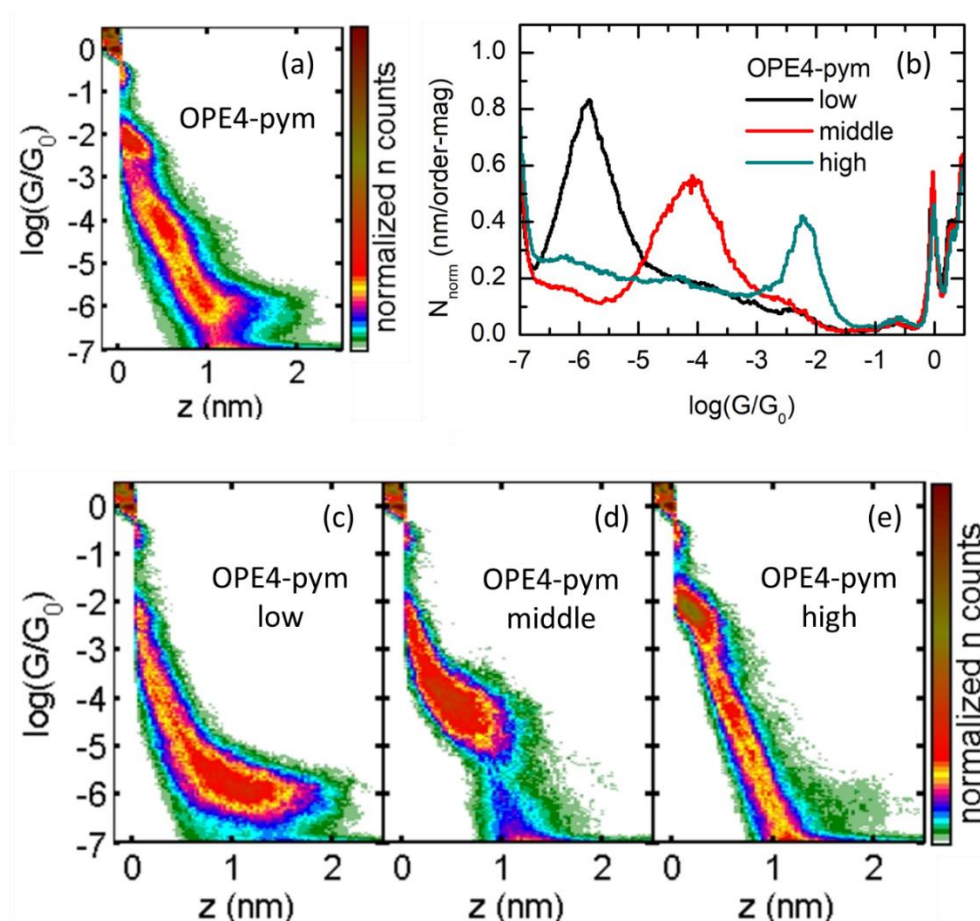


Figure 2.12. (a) 2D histogram built from all the traces (2593 curves) displaying plateaus for **OPE4-pym**. (b) 1D histograms for the three sets of plateaus found after the clustering-based analysis, and (c-e) the independent 2D histogram of these groups. Low G plateaus 37%, middle G plateaus 26% and high G plateaus 37%.

2.3.3.2. Theoretical models

Dr. Linda Zotti, from *Universidad Autónoma de Madrid*, investigated the possible geometries for the molecular junction with **OPE4-pym** responsible for each conductance signal, and obtained the corresponding transmission spectra. The gold–molecule–gold junction was built by placing the relaxed structure of the gas-phase molecule between two Au clusters of 35 and 242 atoms, respectively. The low-bias transmission of the junction was then computed using the Landauer formalism and Green’s function techniques, as described in section 1.4. The main investigated geometries have been summarized in Figure 2.13. Geometry **a** corresponds to the fully extended molecule between the electrodes, by connecting the molecule to gold through the –SMe group on each side. In

geometry **b**, the long branch of **OPE4-Pym** is connected to the upper electrode *via* the sulphur of the $-SMe$ group, while short branch is physisorpted on a lateral face of the lower gold electrode. The reversed situation, in which the long branch is physisorpted on the lower electrode, is represented in geometry **d**. Finally, geometry **c** was obtained by relaxing the gold top atom. This geometry is very similar to geometry **b**, but involving an additional Au–N bond (zoomed-in detail in Figure 2.13c). Such configuration has been considered indeed possible, given the rugosity of real gold electrodes, as well as the remarkable flexibility of gold. Importantly, in geometries **b**, **c** and **d**, it was observed that the junction was stabilized due to the physisorption of the branch lying on the lower electrode.

The transmission curves, calculated for the aforementioned geometries are also shown in Figure 2.13. The lowest conductance value ($3.4 \times 10^{-4} G_0$) is given by geometry **a**, because of its longer Au–Au distance (2.95 nm). The corresponding curve (green line) also shows the highest energy-alignment for both HOMO and LUMO, as a result of the stronger and symmetrical binding through sulphur on both sides. For geometries **b** and **c**, both transmission curves (blue and orange lines, respectively) and conductance values ($1.1 \times 10^{-3} G_0$ and $1.5 \times 10^{-3} G_0$, respectively) are pretty similar, despite the aforementioned differences in the Au–heterocycle bond. Finally, geometry **d** yields the highest conductance value ($3.5 \times 10^{-3} G_0$), because of the very short Au–Au distance (0.87 nm).

Considering these theoretical models, geometry **a**, corresponding to the proposed long pathway can be related to the obtained low G signal for **OPE4-Pym**; geometries **b** and **c**, both corresponding to the proposed medium pathway, can be related with the observed middle G signal; and geometry **d**, corresponding to the proposed short pathway, can be related with the detected high G signal. The trend for the calculated G values for the different geometries is in good agreement with that of the experimentally observed G states. However, theoretical G values tend to be higher than the corresponding experimental ones, as it happens for the low and middle G signals, due to the well-known conductance overestimation arising from the DFT inaccuracies. Then, these theoretical models support that the three hypothesized conduction channels for **OPE4-pym** are able to give rise to stable junctions

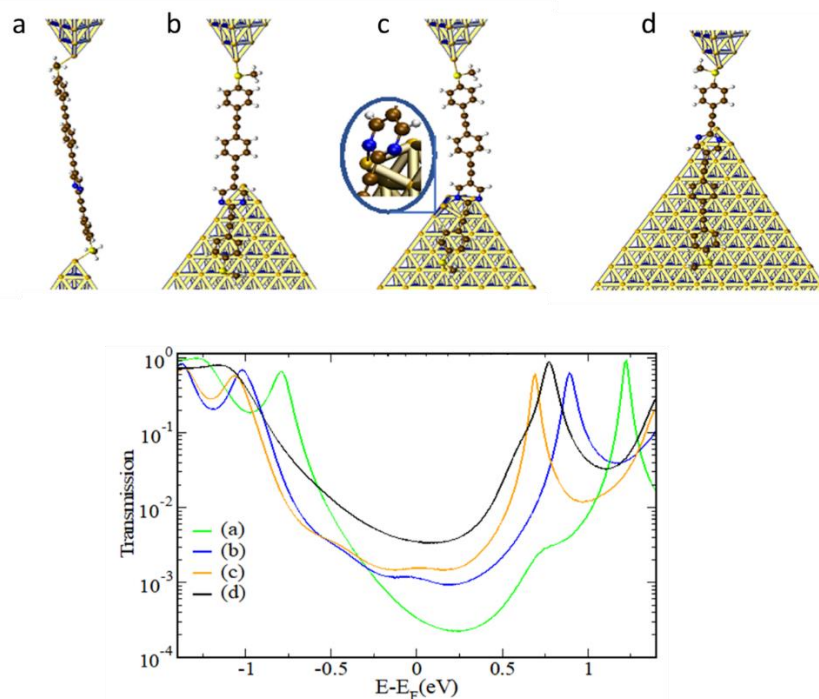


Figure 2.13. (a-d) Binding geometries analyzed for **OPE4-pym** and their corresponding transmission curves.

2.3.3.3. Conductance of the reference compounds and comparison with the corresponding channels

For further investigate the origin of the molecular signals observed in **OPE4-Pym** and evaluate their correspondence with the proposed pathways, the transport properties of the prepared reference compounds were studied, and both their conductance and plateau lengths were compared with those observed in **OPE4-pym**.

Single-molecule experiments performed for **OPE2/S-pym**, the reference structure for the short pathway, gave rise to 9% of *G*-*z* traces displaying plateaus. Two different molecular signals were observed, which could be easily separated using again the clustering analysis. The independent 2D and 1D histograms for these two peaks are shown in Figure 2.14. The first group, constituting the 22% and denoted **OPE2/S-pym 1**, presented a higher conductance (brown line) than the second group (orange line), constituting the 78% remaining and denoted **OPE2/S-pym 2**. For a better comparison, the 2D histogram of the high conductance signal found for **OPE4-pym** is also shown (Figure 2.14c) and the 1D histogram superimposed (black line) in Figure 2.14d. It can be noticed that the peak

corresponding to **OPE4-pym**, appears indeed at a conductance value between the two groups for **OPE2/S-pym**. The plateau-length distributions for these three signals (Figure 2.14e) are in good agreement, concurring, at the end of the distribution, on the same distance. Note that the expected Au-Au distance for this junction is marked as a red vertical line in Figure 2.15e.^b

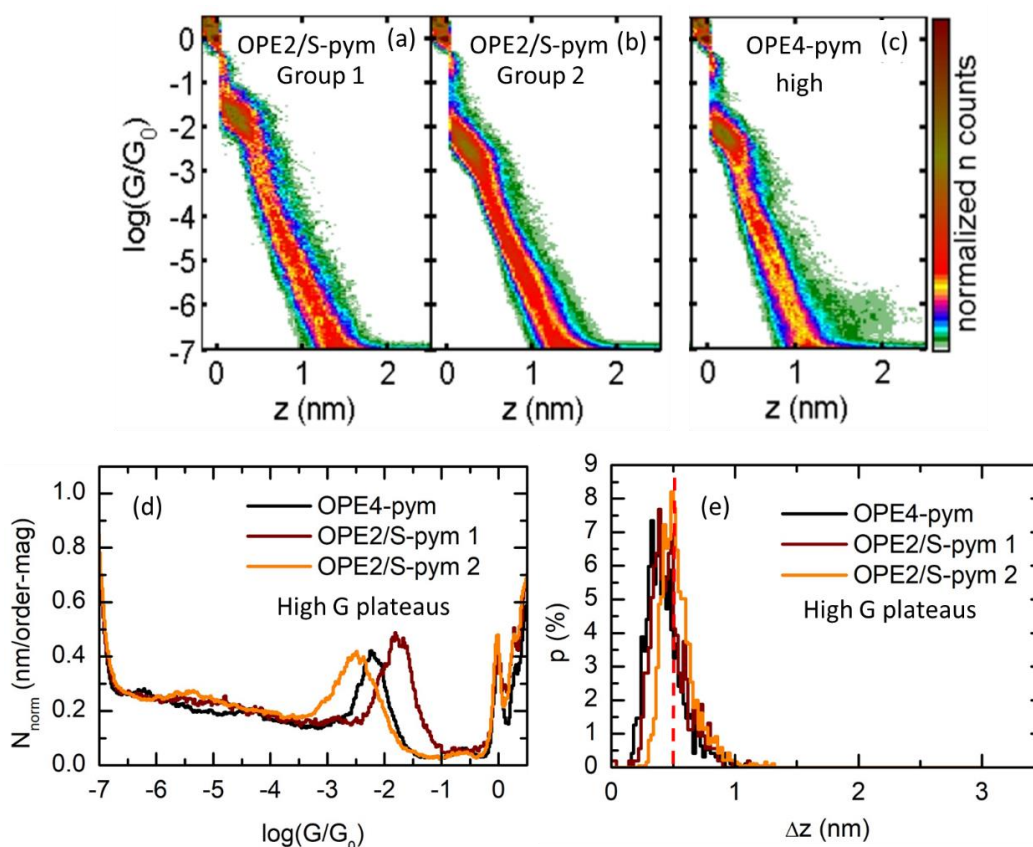


Figure 2.14. (a) and (b) 2D histograms for the two sets of differentiated molecular signal obtained for **OPE2/S-pym**. Group 1 (a) comprises 22% of the traces displaying plateaus (534), while group 2 (b) comprises the remaining 78% (1854). (c) 2D histogram for the high G group obtained for **OPE4-pym**. (d) 1D histograms corresponding to the same groups of traces used for building 2D histograms (a-c). (e) Plateau-length distributions for the traces used for building 2D histograms (a-c). The corrected Au–Au distance has been marked with a red vertical line (0.5 nm).

^b This value has been calculated as the theoretical Au–Au distance (0.9 nm) minus an interval of 0.4 nm, which compensates the effect of the electrode retraction after the gold contact breaks. This correction has been considered for all Au-Au distances marked in the plateau-length distributions.

RESULTS AND DISCUSSION

Although the origin of the two different sets of signals observed for **OPE2/S-Pym** is not clear, both the low percentage of total traces displaying plateaus (9%) and their practically same plateau-length distributions discard the possibility of one of them being due to several molecules in the junction. Otherwise, this effect seems very similar to that observed for pyridine-linked compounds, which display two different sets of signals, particularly well-differentiated for short molecules as bipyridine.^{8,10,33} We therefore hypothesize that the two groups can be originated by two binding configurations of the pyrimidine group, one with more overlap with the gold electrode than the other.

The 1D and 2D histograms obtained for **OPE3/S-pym**, the proposed reference compound for the medium G channel, are shown in Figure 2.15. They are built from 1221 traces displaying plateaus, corresponding to the 32% of the total traces. A broad molecular signal is detected, giving rise to a clear peak in the 1D histogram at $\log(G/G_0) \simeq -5.1 \pm 0.38$. The superimposition of this histogram with that of the middle G group for **OPE4-pym**, revealed a shift toward lower values for the peak of the reference. Remarkably, the plateau-length distribution for both groups was in perfect agreement, concurring the end of the distributions at the expected Au-Au distance (~ 1.3 nm), as shown in Figure 2.15d.

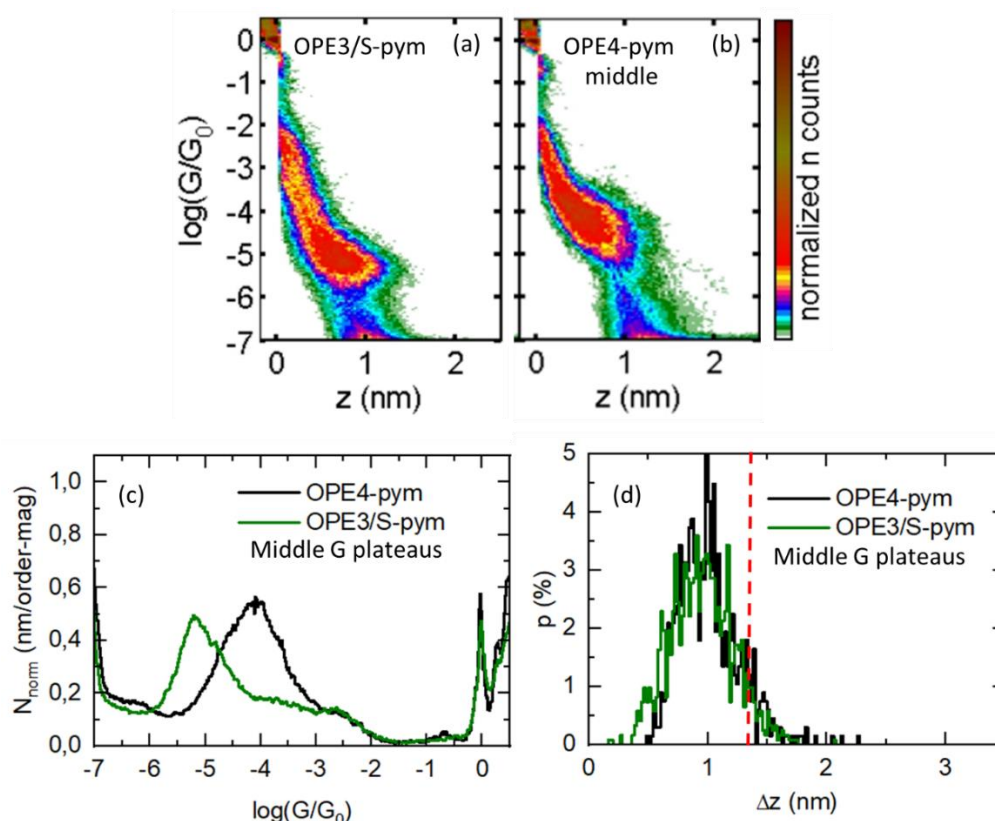


Figure 2.15. (a) 2D histogram for OPE3/S-pym, built from 1221 traces displaying plateaus. (b) 3D histogram for the middle conductance group of OPE4-pym. (c) 1D histogram for OPE3/S-pym (green line), and for the middle conductance group of OPE4-pym (black line). (d) Plateau-length distributions for the traces used for building the histograms (a-b). The corrected Au–Au distance has been marked with a red vertical line (1.3 nm).

Since the distance for the plateaus were in agreement, the junction for OPE3/S-pym was also computationally modelled in order to find the origin for the observed conductance differences between its experimental conductance value and that of the middle *G* group of OPE4-pym. The obtained geometry for the junction (noted as geometry **e**), and the calculated transmission curve are shown in Figure 2.16. In this figure, geometry **b** for OPE4-pym and its transmission curve have been added for a better comparison. For both configurations, the upper electrode is connected to the molecule *via* the –SMe group, while the lower electrode is interacting with the pyrimidine ring. However, the stabilization originated by the short branch onto the gold cannot occur for the OPE3/S-pym. The lack of this additional stabilization is translated into a decreased in the calculated conductance for geometry **e**, in comparison with that of geometry **b**, as the transmission curves revealed. This trend is compatible with the experimental observations, as the conductance of OPE3/S-pym is shifted toward lower values with respect that of the middle *G* plateaus for

RESULTS AND DISCUSSION

OPE4-pym. Interestingly, the same effect was previously observed by our group while studying the previously mentioned *p*-OPE with two different channel.¹⁹ In that work, the conductance of the short channel was found to be higher than that of the corresponding reference compound, in spite of the distances for the plateaus of both groups being the same. Then, these calculations, points out to the branch lying on the electrode, as responsible for, not only a mechanical junction stabilization, but also an increase on conductance with respect the independent pathway.

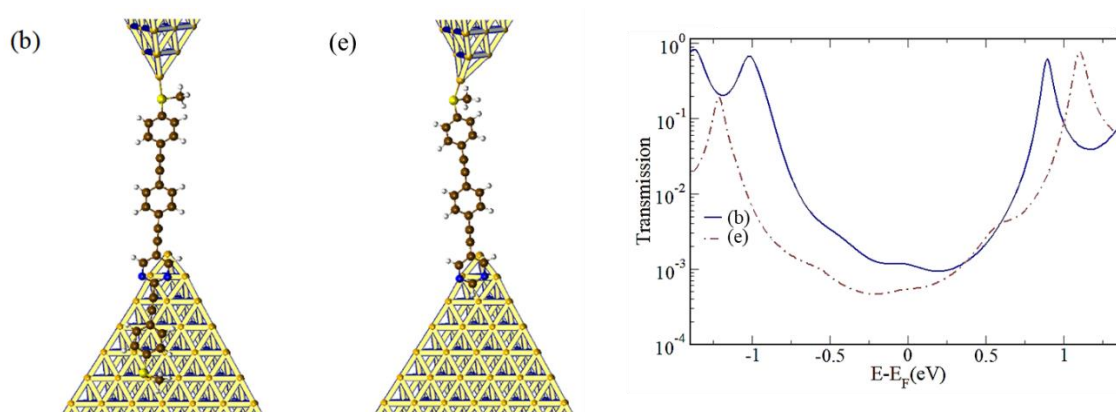


Figure 2.16. Binding geometries for **OPE3/S-pym** (e) and its corresponding transmission curve (grey dotted line). Geometry **b** for **OPE4-pym** and its transmission curve (blue line) have been added for a better comparison.

Importantly, if we extend this explanation to what observed for **OPE2/S-pym**, **OPE2/S-pym 2** would correspond to a configuration closer to that, occurring for **OPE4-pym**, as it presents a slight shift toward lower conductance values with respect to that of the high *G* pathway for **OPE4-pym**, due to the lack of the extra branch physisorpted onto the electrode in the junction.

Finally, **OPE4** was proposed as the reference compound for the longer pathway for **OPE4-pym**. In this case, the final synthetic step gave rise to a highly insoluble precipitate. By sonication, we could dissolved a minimum amount of the precipitate, which was subjected to high-performance liquid chromatography (HPLC). In the purified fraction, it was possible to confirm the presence of the desired compound by ¹H-NMR and HRMS. Having these evidences, we use this solution (of unknown concentration) for preparing a sample and performing conductance experiments. Plateaus were detected in the 70% of the total

traces. Two different sets of plateaus, centered at $\log(G/G_0) = -4.1 \pm 0.61$ and $\log(G/G_0) = -5.9 \pm 0.41$, were found. Their independent 2D histograms are shown in Figure 2.17a and 2.17b. The 1D histogram of the lowest conductance signal was in good agreement with that of the low G plateaus for **OPE4-pym** and the end of the plateau-length distribution of both groups concurred on ~ 2.3 nm (Figure 2.17d). In contrast, the origin of the shorter set of plateaus occurring at a higher conductance for **OPE4** is not clear. We propose several hypotheses, namely the possible interaction of the inner rings with the electrodes, as previously reported for other unsubstituted OPEs.¹⁹ Another possibility is the presence of remaining byproducts able to interact with the electrodes, giving rise to stable molecular junctions. However, G - z traces displaying this high G plateau tend to also display the lower one, as observed in Figure 2.17a. This is generally a signal of two different processes occurring during the stretching of the electrodes in the same molecular junction. So we consider this second option improbable.

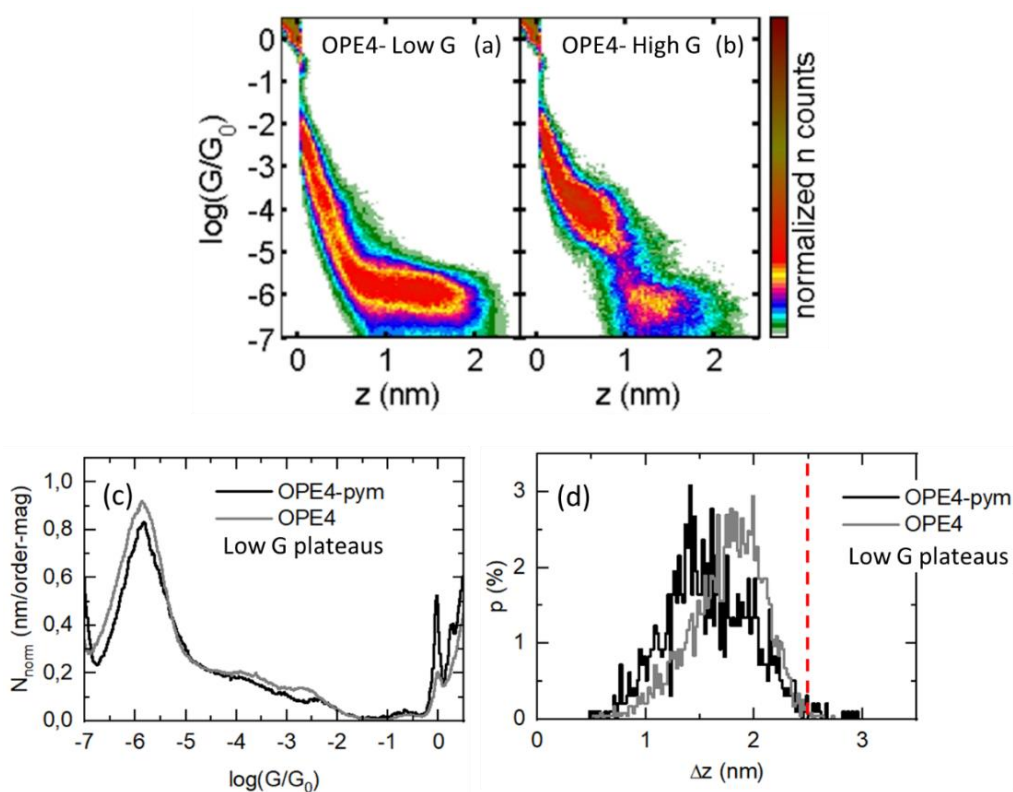


Figure 2.17. (a) and (b) 2D histograms for the two molecular signals detected for **OPE4**, at low and high conductance value, respectively. (c) 1D histogram for the low conductance plateaus **OPE4** (grey line) and the low conductance group of **OPE4-pym** (black line). (d) Plateau-length distributions for the traces used for building the 1D histograms of (c). The corrected Au–Au distance has been marked with a red vertical line (2.5 nm).

RESULTS AND DISCUSSION

A more soluble model of OPE4-pym is OPE4-OMe. As can be seen in Figure 2.11, this structure is based on an identical molecular backbone, but incorporating two –OMe groups in one of the inner rings in order to increase the solubility. Additionally, previous studies on OPES, demonstrated that the incorporation of –OMe groups in the internal rings of this wires precluded their undesirable interaction with the electrodes.²⁷ This molecule was successfully synthesized and purified and single-molecule experiments performed. For this molecule, different behaviour was found for high and low rate of traces displaying plateaus. These two behaviours are shown in Figure 2.18. For high rates of traces displaying plateaus (80%), the clustering-based analysis allowed to distinguish three groups of plateaus (A, B and C) in the same conductance range. Groups B and C, were formed by sloping plateaus, while group A was formed by flat plateaus. In contrast, for low rates of traces displaying plateaus (20%), the clustering-based analysis allowed to distinguish only two groups of plateaus (A and B). Group A was formed again by flat plateaus, but in this case, the second group detected was formed by traces in which broken plateaus appears eventually after the current has arrived to the noise level, originating a small current jump from the noise level to the plateau, and from the plateau again to the noise level. Since group A was present in both, high and low rates of traces displaying plateaus (Figure 2.19a), and it was formed by flat plateaus, this group was attributed to the molecular signal corresponding to a single-molecule fully extended between the electrodes. In contrast, the groups of sloping plateaus, only appearing at high rates of traces displaying plateaus, and which gave rise to slightly higher conductance values (as shown in Figure 2.19b), they were attributed to junctions with several molecules between the electrodes. In fact, this effect has been previously reported in literature for OPEs.^{19,27}

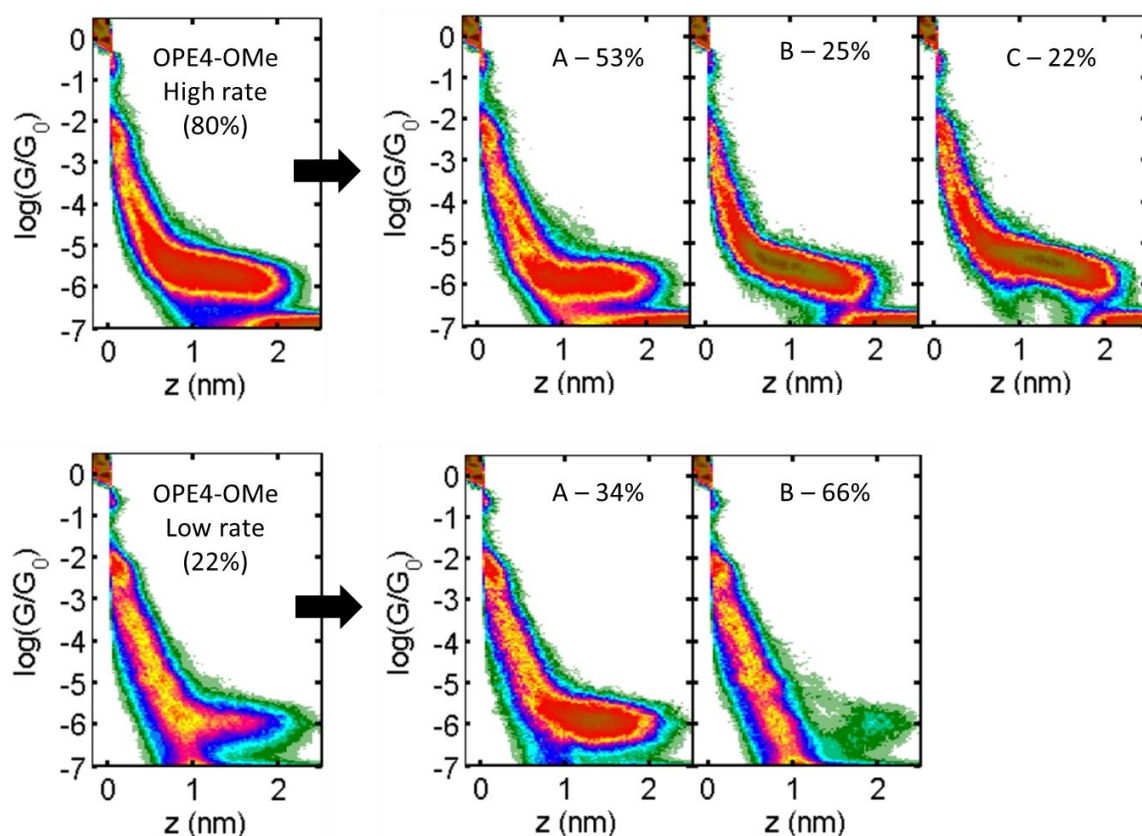


Figure 2.18. 2D histograms for OPE4-OMe obtained with high and low rate of traces displaying plateaus (80% and 22%, respectively). The clustering-based analysis allowed to identify two groups of sloping plateaus for the sets of high rate, which did not occur at low rates, being attributed to junction with more than one molecule between the electrodes.

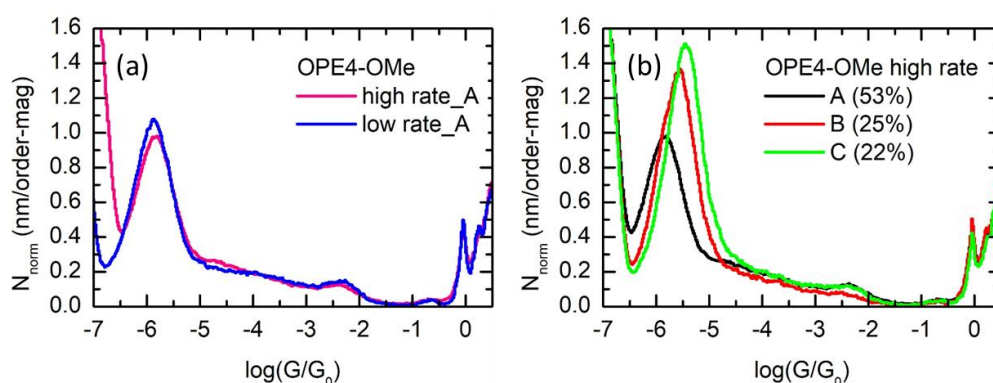


Figure 2.19. (a) 1D histograms of group A obtained for OPE4-OMe at high (blue line) and low (pink line) rates of plateaus displaying plateaus, and formed by flat plateaus. (b) 1D histograms of groups A (black line), B (red line) and C (green line) detected for the high rate of traces displaying plateaus sets for OPE4-OMe. The peaks of groups B and C, constituted by sloping plateaus, are shifted toward higher conductance values than that of group A, formed by flat plateaus.

RESULTS AND DISCUSSION

Taking into account these results, the 1D histogram of group A for **OPE4-OMe**, attributed to just one molecule in the junction (blue line), was compared with those obtained for the groups of lower G for **OPE4** (grey line) and **OPE4-pym** (black line) in Figure 2.20a. The plateau-length distribution of these groups, which is shown in Figure 2.20b, was in perfect agreement not only between them but also with the expected Au–Au distance for a molecule fully extended between the electrodes (marked with a vertical line).

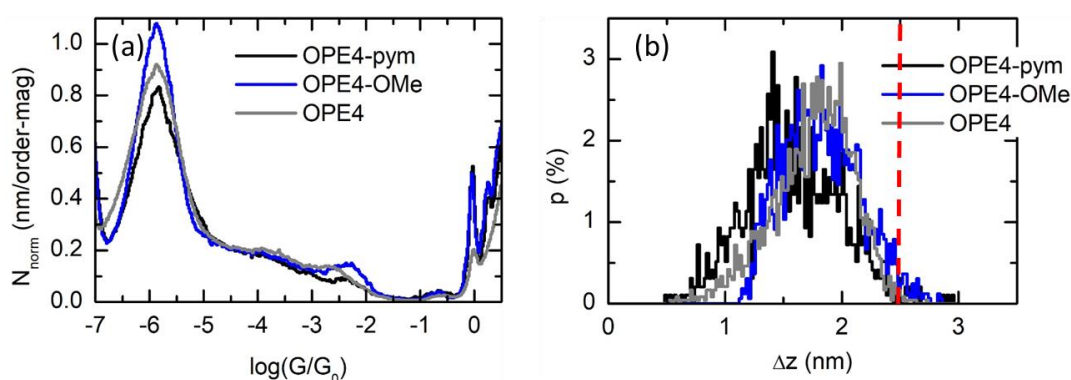


Figure 2.20. (a) 1D histogram for the low G groups of **OPE4-pym** (black line), **OPE4** (grey line) and group A for **OPE4-OMe**, (blue line). (b) Plateau-length distributions for the traces used for building the 1D histograms of (a). The corrected Au–Au distance has been marked with a red vertical line (2.5 nm).

Finally, the experimental values obtained for the different signals for **OPE4-Pym** and the studied reference compounds are collected in Table 2.1.

Table 2.1 Experimental conductance values obtained for the different signals for OPE4-Pym and the studied reference compounds

Different molecular signals for OPE4-Pym ($\log G/G_0$)		Reference compounds ($\log G/G_0$)	
Low G	-5.8 ± 0.37	OPE4	-5.9 ± 0.41
		OPE4-OMe	-5.9 ± 0.32
Middle G	-4.1 ± 0.52	OPE3/S-Pym	-5.1 ± 0.38
High G	-2.2 ± 0.21	OPE2/S-Pym	-2.5 ± 0.22

Considering the results of this chapter, we can summarize that we have successfully prepared a molecule which present three well-differentiated conductance states, at $\log(G/G_0) = -5.8 \pm 0.37$, $\log(G/G_0) = -4.1 \pm 0.52$ and $\log(G/G_0) = -2.2 \pm 0.21$, respectively. The molecular signals contributing to each conductance value, also display plateaus of different lengths. In this sense, the low G signal was in good agreement with the expected distance for the molecule fully extended between the electrodes. The comparison with reference compounds allowed demonstrating that the high and middle G signals agreed in both, conductance and length with the corresponding proposed channels, due to the interaction of the electrodes with the pyrimidine ring. Therefore, the asymmetric allocation of this in-backbone binding group allowed the well-differentiated conductance values and plateau lengths related to the two new conduction channels, additional to the usual linker-to-linker pathway.

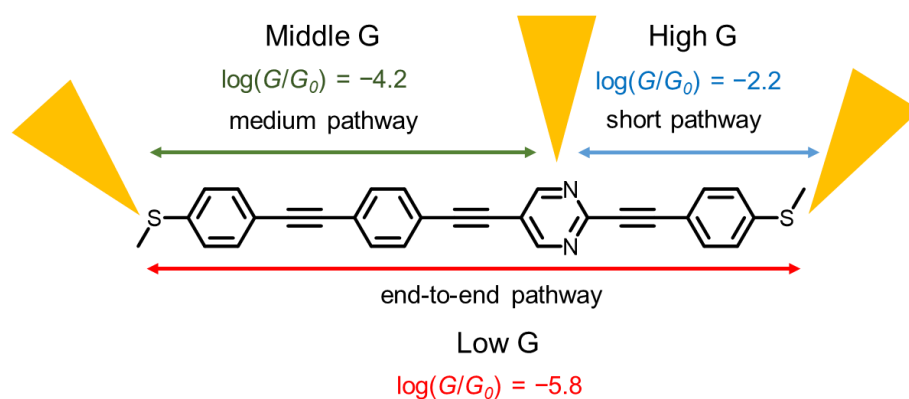


Figure 2.21. The pyrimidine-based *p*-OPE prepared is able to give rise to three well differentiated conductance values due to different conduction channels along the molecular backbone.

2.4. Conclusions

Based on the results of this chapter, the following conclusions can be drawn:

- A new strategy for obtaining multi-conductance state molecules, with well-defined and distinguishable states, based on asymmetry, has been proposed. An oligo-*para*-phenyleneethynylene (*p*-OPE) derivative incorporating a pyrimidine ring in an asymmetric position was synthesized as proof-of-concept.
- Single-molecule experiments revealed three different conductance values for this pyrimidine based-OPE.
- The origin of the observed signals was investigated using theoretical models in combination with the experimental measurements of reference compounds able to recreate each proposed channel.
- The pyrimidine ring was found to be responsible for creating two new conduction channels, additional to the end-to end-pathway, while its asymmetric position was responsible for the well-separated and distinguishable conductance value for each channel.
- It was found that in-bone *G* channels can present a slightly higher conductance value than the corresponding models, revealing that being part of the multi-conductance system involves an increase in conductance with respect to the independent pathway, which is related with a mechanical stabilization due to the physisorption of the pendant backbone-piece onto the electrodes.

References

- (1) Li, H.; Xu, Q.; Li, N.; Sun, R.; Ge, J.; Lu, J.; Gu, H.; Yan, F. A Small-Molecule-Based Ternary Data-Storage Device. *J. Am. Chem. Soc.* **2010**, *132*, 5542–5543. <https://doi.org/10.1021/ja910243f>.
- (2) Chan, H.; Wong, H. L.; Ng, M.; Poon, C. T.; Yam, V. W. W. Switching of Resistive Memory Behavior from Binary to Ternary Logic via Alteration of Substituent Positioning on the Subphthalocyanine Core. *J. Am. Chem. Soc.* **2017**, *139*, 7256–7263. <https://doi.org/10.1021/jacs.7b00895>.
- (3) Dulić, D.; van der Molen, S. J.; Kudernac, T.; Jonkman, H. T.; de Jong, J. J. D.; Bowden, T. N.; van Esch, J.; Feringa, B. L.; van Wees, B. J. One-Way Optoelectronic Switching of Photochromic Molecules on Gold. *Phys. Rev. Lett.* **2003**, *91*, 207402. <https://doi.org/10.1103/PhysRevLett.91.207402>.
- (4) Auwärter, W.; Seufert, K.; Bischoff, F.; Ecija, D.; Vijayaraghavan, S.; Joshi, S.; Klappenberger, F.; Samudrala, N.; Barth, J. V. A Surface-Anchored Molecular Four-Level Conductance Switch Based on Single Proton Transfer. *Nat. Nanotechnol.* **2012**, *7*, 41–46. <https://doi.org/10.1038/nnano.2011.211>.
- (5) Ye, C.; Peng, Q.; Li, M.; Luo, J.; Tang, Z.; Pei, J.; Chen, J.; Shuai, Z.; Jiang, L.; Song, Y. Multilevel Conductance Switching of Memory Device through Photoelectric Effect. *J. Am. Chem. Soc.* **2012**, *134*, 20053–20059. <https://doi.org/10.1021/ja305354y>.
- (6) Meisner, J. S.; Kamenetska, M.; Krikorian, M.; Steigerwald, M. L.; Venkataraman, L.; Nuckolls, C. A Single-Molecule Potentiometer. *Nano Lett.* **2011**, *11*, 1575–1579. <https://doi.org/10.1021/nl104411f>.
- (7) Kiguchi, M.; Ohto, T.; Fujii, S.; Sugiyasu, K.; Nakajima, S.; Takeuchi, M.; Nakamura, H. Single Molecular Resistive Switch Obtained via Sliding Multiple Anchoring Points and Varying Effective Wire Length. *J. Am. Chem. Soc.* **2014**, *136*, 7327–7332. <https://doi.org/10.1021/ja413104g>.
- (8) Quek, S. Y.; Kamenetska, M.; Steigerwald, M. L.; Choi, H. J.; Louie, S. G.; Hybertsen, M. S.; Neaton, J. B.; Venkataraman, L. Mechanically Controlled Binary Conductance

- Switching of a Single-Molecule Junction. *Nat. Nanotechnol.* **2009**, *4*, 230–234. <https://doi.org/10.1038/nnano.2009.10>.
- (9) Liu, Z.; Ding, S. Y.; Chen, Z. Bin; Wang, X.; Tian, J. H.; Anema, J. R.; Zhou, X. S.; Wu, D. Y.; Mao, B. W.; Xu, X.; Ren, B.; Tian, Z. Q. Revealing the Molecular Structure of Single-Molecule Junctions in Different Conductance States by Fishing-Mode Tip-Enhanced Raman Spectroscopy. *Nat. Commun.* **2011**, *2*. <https://doi.org/10.1038/ncomms1310>.
- (10) Baghernejad, M.; Zsolt Manrique, D.; Li, C.; Pope, T.; Zhumaev, U.; Pobelov, I.; Moreno-García, P.; Kaliginedi, V.; Huang, C.; Hong, W.; Lambert, C.; Wandlowski, T. Highly-Effective Gating of Single-Molecule Junctions: An Electrochemical Approach. *Chem. Commun.* **2014**, *50*, 15975–15978. <https://doi.org/10.1039/c4cc06519k>.
- (11) El Abbassi, M.; Zwick, P.; Rates, A.; Stefani, D.; Prescimone, A.; Mayor, M.; Van Der Zant, H. S. J.; Dulić, D. Unravelling the Conductance Path through Single-Porphyrin Junctions. *Chem. Sci.* **2019**, *10*, 8299–8305. <https://doi.org/10.1039/c9sc02497b>.
- (12) Chen, L.; Wang, Y.-H.; He, B.; Nie, H.; Hu, R.; Huang, F.; Qin, A.; Zhou, X.-S.; Zhao, Z.; Tang, B. Z. Multichannel Conductance of Folded Single-Molecule Wires Aided by Through-Space Conjugation. *Angew. Chem. Int. Ed.* **2015**, *127*, 4305–4309. <https://doi.org/DOI:10.1002/anie.201411909>.
- (13) Zhen, S.; Mao, J. C.; Chen, L.; Ding, S.; Luo, W.; Zhou, X. S.; Qin, A.; Zhao, Z.; Tang, B. Z. Remarkable Multichannel Conductance of Novel Single-Molecule Wires Built on Through-Space Conjugated Hexaphenylbenzene. *Nano Lett.* **2018**, *18*, 4200–4205. <https://doi.org/10.1021/acs.nanolett.8b01082>.
- (14) Shen, P.; Huang, M.; Qian, J.; Li, J.; Ding, S.; Zhou, X. S.; Xu, B.; Zhao, Z.; Tang, B. Z. Achieving Efficient Multichannel Conductance in Through-Space Conjugated Single-Molecule Parallel Circuits. *Angew. Chem. Int. Ed.* **2020**, *59*, 4581–4588. <https://doi.org/10.1002/anie.202000061>.
- (15) Okazawa, K.; Tsuji, Y.; Yoshizawa, K. Understanding Single-Molecule Parallel Circuits on the Basis of Frontier Orbital Theory. *J. Phys. Chem. C* **2020**, *124*, 3322–3331. <https://doi.org/10.1021/acs.jpcc.9b08595>.

RESULTS AND DISCUSSION

- (16) Su, T. A.; Widawsky, J. R.; Li, H.; Klausen, R. S.; Leighton, J. L.; Steigerwald, M. L.; Venkataraman, L.; Nuckolls, C. Silicon Ring Strain Creates High-Conductance Pathways in Single-Molecule Circuits. *J. Am. Chem. Soc.* **2013**, *135*, 18331–18334. <https://doi.org/10.1021/ja410656a>.
- (17) Leary, E.; González, M. T.; Van Der Pol, C.; Bryce, M. R.; Filippone, S.; Martín, N.; Rubio-Bollinger, G.; Agraït, N. Unambiguous One-Molecule Conductance Measurements under Ambient Conditions. *Nano Lett.* **2011**, *11*, 2236–2241. <https://doi.org/10.1021/nl200294s>.
- (18) Moreno-García, P.; La Rosa, A.; Kolivoška, V.; Bermejo, D.; Hong, W.; Yoshida, K.; Baghernejad, M.; Filippone, S.; Broekmann, P.; Wandlowski, T.; Martín, N. Charge Transport in C₆₀-Based Dumbbell-Type Molecules: Mechanically Induced Switching between Two Distinct Conductance States. *J. Am. Chem. Soc.* **2015**, *137*, 2318–2327. <https://doi.org/10.1021/ja511271e>.
- (19) Miguel, D.; Álvarez De Cienfuegos, L.; Martín-Lasanta, A.; Morcillo, S. P.; Zotti, L. A.; Leary, E.; Bürkle, M.; Asai, Y.; Jurado, R.; Cárdenas, D. J.; Rubio-Bollinger, G.; Agraït, N.; Cuerva, J. M.; González, M. T. Toward Multiple Conductance Pathways with Heterocycle-Based Oligo(Phenyleneethynylene) Derivatives. *J. Am. Chem. Soc.* **2015**, *137*, 13818–13826. <https://doi.org/10.1021/jacs.5b05637>.
- (20) Cai, Z.; Zhang, N.; Awais, M. A.; Filatov, A. S.; Yu, L. Synthesis of Alternating Donor–Acceptor Ladder-Type Molecules and Investigation of Their Multiple Charge-Transfer Pathways. *Angew. Chem. Int. Ed.* **2018**, *57*, 6442–6448. <https://doi.org/10.1002/anie.201713323>.
- (21) Tang, C.; Zheng, J.; Ye, Y.; Liu, J.; Chen, L.; Yan, Z.; Chen, Z.; Chen, L.; Huang, X.; Bai, J.; Chen, Z.; Shi, J.; Xia, H.; Hong, W. Electric-Field-Induced Connectivity Switching in Single-Molecule Junctions. *iScience* **2020**, *23*, 100770. <https://doi.org/10.1016/j.isci.2019.100770>.
- (22) Iwane, M.; Fujii, S.; Nishino, T.; Kiguchi, M. Single Tripyridyl-Triazine Molecular Junction with Multiple Binding Sites. *J. Phys. Chem. C* **2016**, *120*, 8936–8940. <https://doi.org/10.1021/acs.jpcc.5b12728>.

- (23) Seth, C.; Kaliginedi, V.; Suravarapu, S.; Reber, D.; Hong, W.; Wandlowski, T.; Lafalet, F.; Broekmann, P.; Royal, G.; Venkatramani, R. Conductance in a Bis-Terpyridine Based Single Molecular Breadboard Circuit. *Chem. Sci.* **2017**, *8*, 1576–1591. <https://doi.org/10.1039/c6sc03204d>.
- (24) Reiné, P.; Justicia, J.; Morcillo, S. P.; Mazzeo, G.; García-Fernández, E.; Rodríguez-Diéguez, A.; Álvarez de Cienfuegos, L.; Abbate, S.; Cuerva, J. M.; Longhi, G.; Miguel, D. Exploring Potentialities and Limitations of Stapled *O*-Oligo(Phenyleneethynylene)s (*o*-OPEs) as Efficient Circularly Polarized Luminescence Emitters. *Chirality* **2018**, *30*, 43–54. <https://doi.org/10.1002/chir.22774>.
- (25) Reiné, P.; Ortuño, A. M.; Resa, S.; Álvarez de Cienfuegos, L.; Blanco, V.; Ruedas-Rama, M. J.; Mazzeo, G.; Abbate, S.; Lucotti, A.; Tommasini, M.; Guisán-Ceinos, S.; Ribagorda, M.; Campaña, A. G.; Mota, A.; Longhi, G.; Miguel, D.; Cuerva, J. M. OFF/ON Switching of Circularly Polarized Luminescence by Oxophilic Interaction of Homochiral Sulfoxide-Containing *o*-OPEs with Metal Cations. *Chem. Commun.* **2018**, *54*, 13985–13988. <https://doi.org/10.1039/c8cc08395a>.
- (26) Reine, P.; Campaña, A. G.; Alvarez De Cienfuegos, L.; Blanco, V.; Abbate, S.; Mota, A. J.; Longhi, G.; Miguel, D.; Cuerva, J. M. Chiral Double Stapled: *O*-OPEs with Intense Circularly Polarized Luminescence. *Chem. Commun.* **2019**, *55*, 10685–10688. <https://doi.org/10.1039/c9cc04885e>.
- (27) González, M. T.; Zhao, X.; Manrique, D. Z.; Miguel, D.; Leary, E.; Gulcur, M.; Batsanov, A. S.; Rubio-Bollinger, G.; Lambert, C. J.; Bryce, M. R.; Agraït, N. Structural versus Electrical Functionalization of Oligo(Phenylene Ethynylene) Diamine Molecular Junctions. *J. Phys. Chem. C* **2014**, *118*, 21655–21662. <https://doi.org/10.1021/jp506078a>.
- (28) Lu, Q.; Liu, K.; Zhang, H.; Du, Z.; Wang, X.; Wang, F. From Tunneling to Hopping: A Comprehensive Investigation of Charge Transport Mechanism in Molecular Junctions Based on Oligo(*p*-Phenylene Ethynylene)s. *ACS Nano* **2009**, *3*, 3861–3868. <https://doi.org/10.1021/nn9012687>.

RESULTS AND DISCUSSION

- (29) Lu, Q.; Yao, C.; Wang, X.; Wang, F. Enhancing Molecular Conductance of Oligo(*p*-Phenylene Ethynylene)s by Incorporating Ferrocene into Their Backbones. *J. Phys. Chem. C* **2012**, *116*, 17853–17861. <https://doi.org/10.1021/jp2119923>.
- (30) Hong, W.; Li, H.; Liu, S. X.; Fu, Y.; Li, J.; Kaliginedi, V.; Decurtins, S.; Wandlowski, T. Trimethylsilyl-Terminated Oligo(Phenylene Ethynylene)s: An Approach to Single-Molecule Junctions with Covalent Au-C σ -Bonds. *J. Am. Chem. Soc.* **2012**, *134*, 19425–19431. <https://doi.org/10.1021/ja307544w>.
- (31) Chinchilla, R.; Nájera, C. Recent Advances in Sonogashira Reactions. *Chem. Soc. Rev.* **2011**, *40*, 5084–5121. <https://doi.org/10.1039/c1cs15071e>.
- (32) Mio, M. J.; Kopel, L. C.; Braun, J. B.; Gadzikwa, T. L.; Hull, K. L.; Brisbois, R. G.; Markworth, C. J.; Grieco, P. A. One-Pot Synthesis of Symmetrical and Unsymmetrical Bisarylethynes by a Modification of the Sonogashira Coupling Reaction. *Org. Lett.* **2002**, *4*, 3199–3202. <https://doi.org/10.1021/ol026266n>.
- (33) Kamenetska, M.; Quek, S. Y.; Whalley, A. C.; Steigerwald, M. L.; Choi, H. J.; Louie, S. G.; Nuckolls, C.; Hybertsen, M. S.; Neaton, J. B.; Venkataraman, L. Conductance and Geometry of Pyridine-Linked Single-Molecule Junctions. *J. Am. Chem. Soc.* **2010**, *132*, 6817–6821. <https://doi.org/10.1021/ja1015348>.
- (34) Ke, G.; Duan, C.; Huang, F.; Guo, X. Electrical and Spin Switches in Single-molecule Junctions. *InfoMat* **2020**, *2*, 92–112. <https://doi.org/10.1002/inf2.12068>.

**CHAPTER 3:
EFFECT OF AZABORINE SUBSTITUTION ON THE
SINGLE-MOLECULE CONDUCTANCE OF ACENES**

3.1. Introduction

Azaborines are particular heteroaromatic molecules in which a CC unit has been replaced by its isosteric BN unit (Figure 3.1a). The first synthetic molecule incorporating B-N covalent bonds embedded in an aromatic structure was borazine, prepared in 1926 by Stock and Pohland by a reaction of diborane and ammonia.¹ This molecule consists of a hexagonal ring alternating B and N atoms (Figure 3.1b). It is commonly known as “inorganic benzene” as the number of π electrons is the same as in benzene, and the length of all B–N bonds is equivalent. Remarkably, borazine has been studied both experimentally and theoretically for decades, without achieving any consensus about its degree of aromaticity.²

A single CC/BN substitution in a benzene ring can lead to three possible isomers, namely 1,2-azaborines, 1,3-azaborines and 1,4-azaborines (Figure 3.1b). The CC/BN isosterism arises from the fact that both units provide the same valence electron count (that is, eight). In the CC unit, each carbon contributes with four valence electrons, while in the BN unit, boron has three and nitrogen has five. In this case, two electrons provided by the nitrogen atom compensate the electron deficiency at the boron.³ This electron donation promotes a unique polarization in the aromatic ring, being not trivial the relative BN-position, which influences the stability and the aromatic character of the resulting structure.⁴

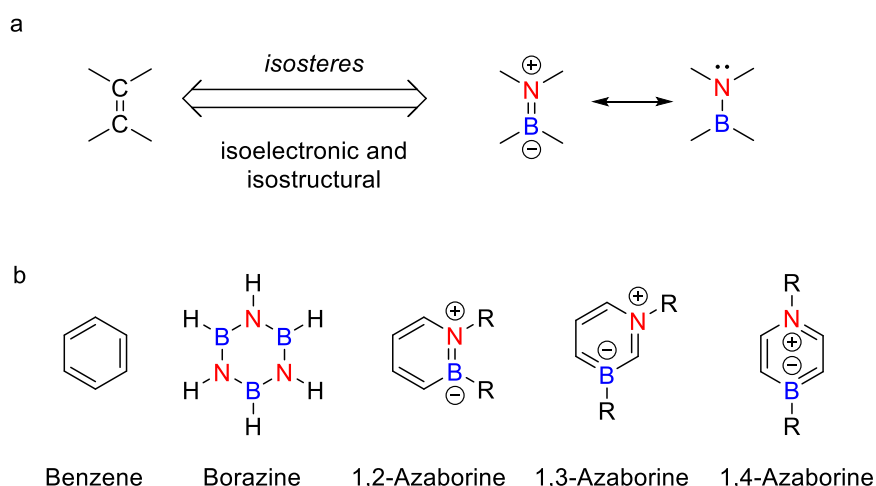


Figure 3.1. (a) Isoelectronic relationship between CC and BN. (b) Isomeric forms of BN substituted aromatic ring.

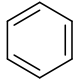
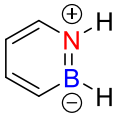
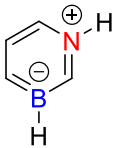
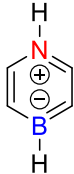
INTRODUCTION

Computational predictions suggest that the 1,2-isomer is the thermodynamically most stable isostere, followed by the 1,4- and then 1,3-isomer.⁴ This trend has been explained in based on the number and nature of CC and BN bonds in the ring. The 1,2-isomer has two CC double bonds and one BN double bond, being the most stable. The 1,4-isomer is the next in the series, with two CC double bonds, but no BN bond. Finally, the least stable is the 1,3-isomer, containing only one CC double bond and no BN bond.⁵ Not surprisingly, this agrees with the number of examples of the three different BN-regioisomers synthesized in literature: while we can find a notable amount of synthesized and characterized 1,2- and 1,4-azaborine compounds, the number of reported 1,3-azaborine derivatives is scarce.^{6,7}

Pati and collaborators gave different aromatic index values for 1,2-dihydrido-1,2-azaborine, 1,4-dihydrido-1,4-azaborine and 1,3-dihydrido-1,3-azaborine; and compared them with those obtained for benzene.⁸ The HOMA, NICS(0)_{zz} and NICS(1)_{zz} values obtained by these authors are collected in Table 3.1. The results clearly show that all-carbon analogues are always more aromatic than the BN-isosteres. Nevertheless, among the BN, the aromaticity seems to decrease with the stability, being the energetically most stable 1,2-dihydrido-1,2-azaborine the less aromatic, followed by 1,4-dihydrido-1,4-azaborine and 1,3-dihydrido-1,3-azaborine, the most aromatic isomer. Recently, Udagawa and Iwaki have provided new calculations of HOMA and NICS(1)_{zz} for the three isosteres (also shown in Table 3.1), extracting the same conclusions despite obtaining values slightly different to the previous ones.⁹ This trend has been explained based on the charge separation, which promotes a higher delocalization, that is, the largest aromaticity, in the 1,3-azaborine isomer. In contrast, in 1,2-azaborine, the electron delocalization is disrupted by the polarity of the BN bond, while the atom distribution in 1,4-isomers favours a directional π -electron delocalization rather than cyclic. In this sense, 1,4-azaborines have been considered as push-pull π -electron systems rather than π -aromatic molecules.⁵

**CHAPTER 3: EFFECT OF AZABORINE SUBSTITUTION
ON THE SINGLE-MOLECULE CONDUCTANCE OF ACENES**

Table 3.1. Aromaticity indexes for C₆H₆, 1,2-dihydrido-1,2-azaborine, 1,3-dihydrido-1,3-azaborine and 1,4-dihydrido-1,4-azaborine, collected from ref.⁸ and ref.⁹

Molecule	HOMA		NICS(0) _{zz}		NICS(1) _{zz}	
	Pati 2011	Udagawa 2020	Pati 2011	Udagawa 2020	Pati 2011	Udagawa 2020
	0.97	0.989	-14.51	-	-28.85	-29.50
	0.71	0.793	-4.28	-	-20.08	-20.29
	0.74	0.802	-9.86	-	-24.90	-25.17
	0.51	0.627	-3.54	-	-19.46	-19.64

BN/CC isosterism encloses a great potential to expand the chemical space of organic compounds, allowing the preparation of BN-heterocycle motifs. Azaborines are also perfect candidates to be embedded in the core of nanographenes, since they maintain the original topology of the all-carbon analogues.¹⁰⁻¹² Therefore, the introduction of BN units in PAHs can be used for tuning the physicochemical properties of the parent structures through minimum structural changes, as well as a strategy for obtaining reliable and more easily-handle models for studying the larger doped 2D-analogues. In that sense, an increasing interest on azaborines has raised in last decades, promoting a development of novel and efficient synthetic strategies toward BN-doped PAHs and allowing studies about their properties and potential applications.¹¹ Some interesting achievements in the azaborine field are summarized in the next sections.

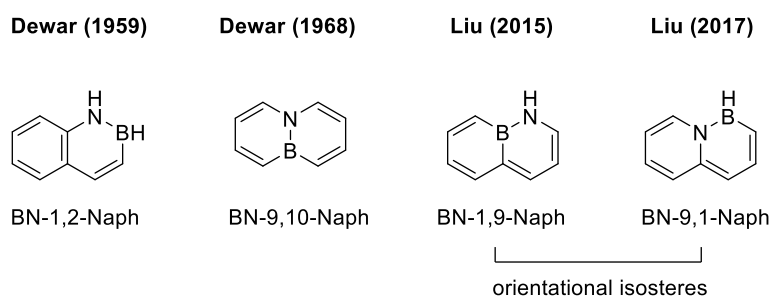
INTRODUCTION

3.1.1. 1,2-azaborines

In the synthesis of 1,2-azaborines, the pioneer works of Dewar's group in the synthesis of BN-naphthalenes: BN-1,2-naphthalene¹³ and BN-9,10-naphthalene¹⁴ (Scheme 3.1A) are remarkable. However, the low yield (0.2%) for the latter through the proposed route rendered it inaccessible until 2014, when Fang and collaborator used a modern ring-closing metathesis/oxidation protocol for obtaining it in higher yields (Scheme 3.1B).¹⁵ This route starts from diallylaminoboron dichloride **I**, which can be easily prepared by the reaction of BCl₃ and diallylamine. Subsequent allylation with allyl-MgBr, followed by ring-closing metathesis using Grubbs' catalyst, affords the BN-bicycle **III**. A dehydrogenation step with DDQ gives rise to the desired BN-naphthalene **IV**. Diverse halogenated derivatives **V** were also obtained by the authors through halogenation *via* electrophilic aromatic substitution, which takes place exclusively at the α -carbon positions next to boron. The halogenated derivative is then a viable substrate for further structure expansion by another electrophilic aromatic substitution (**VI**) Suzuki–Miyaura (**VII**), Sonogashira (**VIII**) or Heck (**IX**) cross-coupling reactions.

CHAPTER 3: EFFECT OF AZABORINE SUBSTITUTION
ON THE SINGLE-MOLECULE CONDUCTANCE OF ACENES

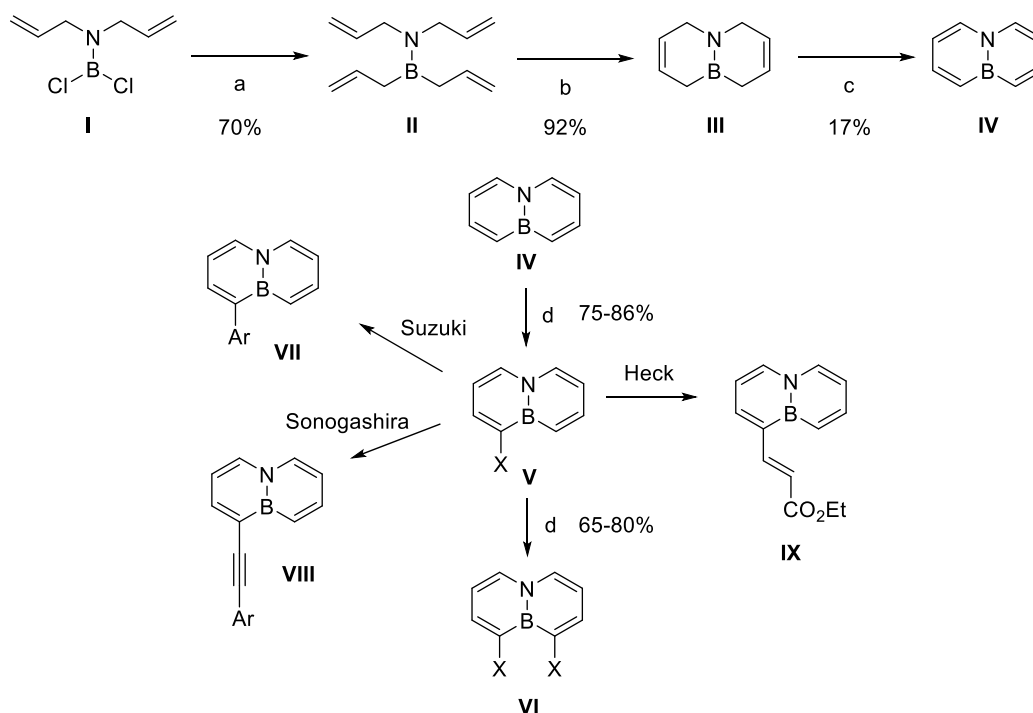
A) BN-doped naphthalene regioisosteres



Non-synthesized BN-doped naphthalene isosteres



B) Fang's synthetic route toward BN-9,10-naphthalene and BN-9,10-naphthalene derivatives



Scheme 3.1. (A) BN-doped naphthalene regioisosteres. (B) Synthesis of BN-9,10-naphthalene and BN-9,10-naphthalene derivatives reported by Fang and co-workers.¹⁵ (a) allyl-MgBr; (b) $(\text{C}_3\text{P})_2\text{Cl}_2\text{Ru}=\text{CHPh}$, CH_2Cl_2 ; (c) DDQ, hexane, 60 °C; (d) NXS, AlCl_3 . X = Cl, Br, I.

Liu and collaborators successfully achieved the synthesis of BN-1,9-naphthalene¹⁶ and BN-9,1-naphthalene¹⁷ in 2015 and 2017, respectively (Scheme 3.1A). However, the

INTRODUCTION

parent isosteres, BN-2,3-naphthalene and BN-2,1-naphthalene, have not been synthesized yet,¹⁸ despite the great diversity of derivatives of the latter that have been reported to date.^{19,20}

Liu and co-workers provided UV-Vis absorption spectra of the four BN-naphthalene isosteres synthesized to date (Figure 3.2a), as well as excitation energies associated with the HOMO-LUMO transitions calculated using TD-DFT (Figure 3.2b).¹⁷ The comparison of the UV-Vis absorption spectra demonstrates appreciable different optical responses depending on the position of the B-N units in the naphthalene scaffold, exhibiting the orientational isomers BN-1,9-Naph (orange trace) and BN-9,1-Naph (red trace) more similar electronic transitions than the other BN naphthalene counterparts. Theoretical HOMO-LUMO energy gaps showed very similar values for the couple of orientational isomers (BN-1,9-Naph/BN-9,1-Naph and BN-1,2-Naph/BN-2,1-Naph). Therefore, unlike position, orientation does not seem to origin a deep impact on the optical properties.

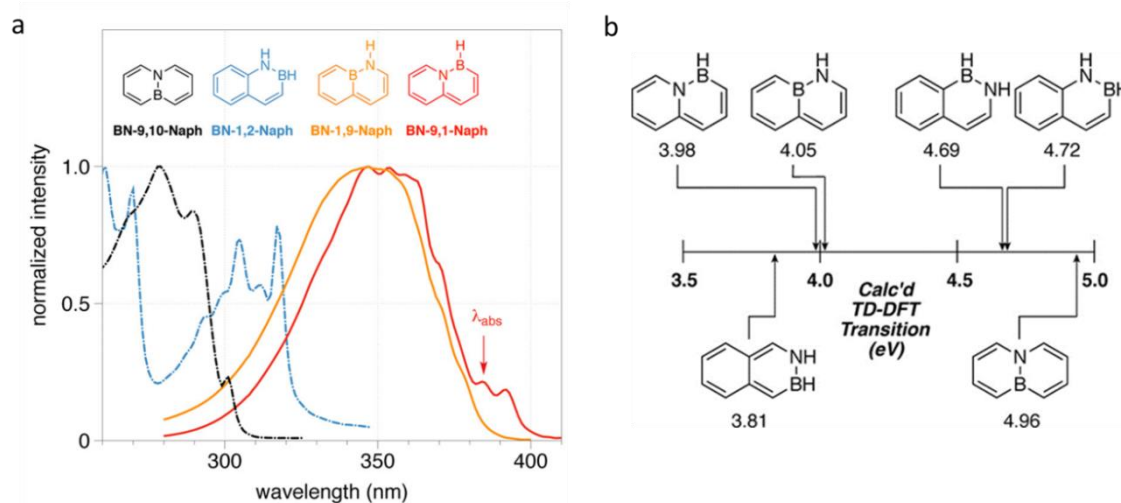
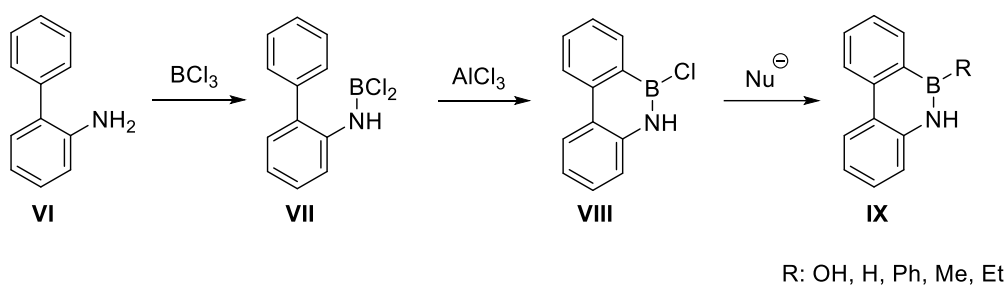


Figure 3.2. (a) UV-Vis absorption spectra of BN-naphthalenes in cyclohexane. (b) TD-DFT excitation energies associated with the HOMO-LUMO transition of BN-naphthalenes calculated at the CAM-B3LYP/6-311G(d,p) level. (This figure is an unofficial adaptation of part of an article that appeared in an ACS publication. ACS has not endorsed the content of this adaptation or the context of its use.¹⁷)

Dewar's group also reported the synthesis of the first BN-substituted phenanthrenes in 1958, namely 9,10-azaboraphenanthrenes.²¹ As shown in Scheme 3.2, the reaction of 2-phenylaniline **VI** with BCl_3 , followed by treatment with AlCl_3 , gave rise to the Friedel-Craft product **VIII**. A family of BN-substituted phenanthrene derivatives **IX** was obtained by means of reaction between compound **VIII** and various nucleophiles.



Scheme 3.2. Synthesis of 9,10-azaboraphenanthrene derivatives.²¹

The effect of the 9,10-BN substitution in phenanthrenes with respect to the all-carbon analogue (Figure 3.3a) was explored by UV-Vis spectroscopy (Figure 3.3b). The position of the main absorption bands was similar in both spectra, but a remarkable increase in the α -band intensity was observed. This effect was attributed to the elimination of the molecular orbital degeneracy present in the all-carbon phenanthrene, when the BN unit is introduced in the system. Later, Parvez and collaborators studied the fluorescence of both compounds, in addition to that of another BN isostere: 4a,4b-azaboraphenanthrene²² (Figure 3.3c). Phenanthrene exhibited emission mainly in the UV region with a relatively low quantum yield ($\phi_F = 0.09$). The replacement of the two carbon atoms at the peripheral 9,10-positions with the BN unit resulted in a blue-shifted emission. In sharp contrast, when the BN unit occupied the internal 4a,4b-positions, the emission spectrum showed a significant bathochromic shift. Remarkably, in both cases the quantum yield increases ($\phi_F = 0.61$ and 0.58 , respectively, versus 0.09 for phenanthrene). This comparison demonstrated the efficiency of BN substitution in modulating the optical properties of polycyclic aromatics, and revealed that the position of the BN unit in the same scaffold can involve important changes in the properties.

INTRODUCTION

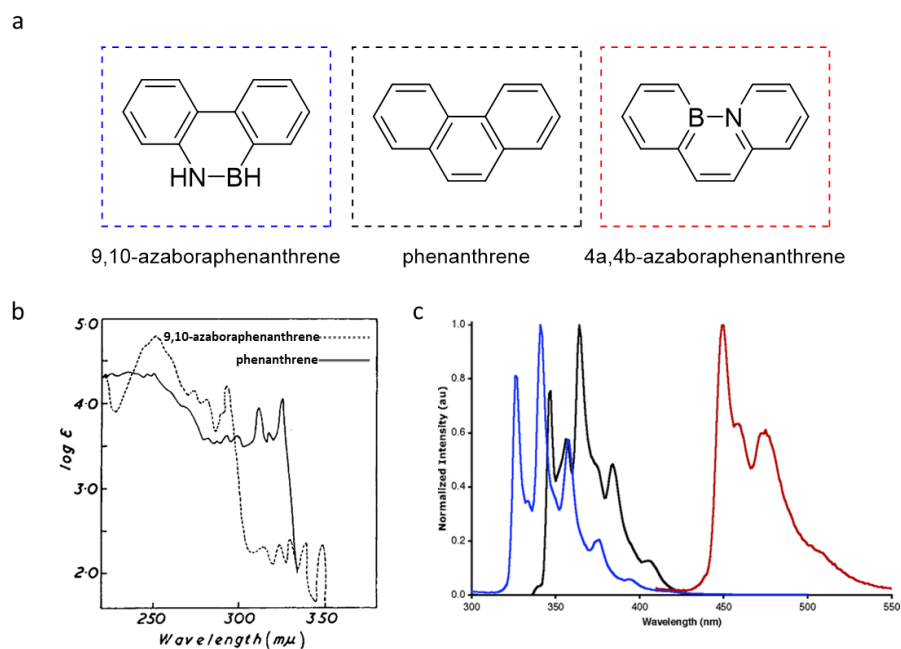


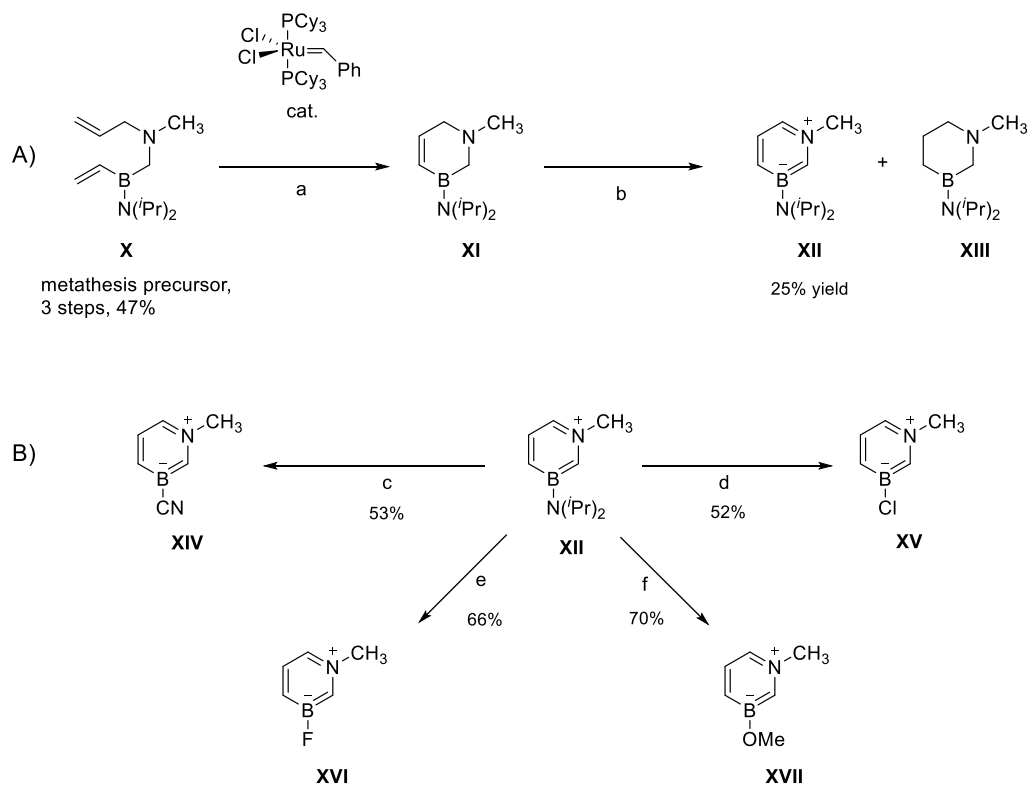
Figure 3.3. (a) Structures of 9,10-azaboraphenanthrene (blue), phenanthrene (black) and 4a,4b-azaboraphenanthrene (red). (b) Ultraviolet spectra of 9,10-azaboraphenanthrene (—), and phenanthrene (- - -). Adapted from ref.²¹ with permission from The Royal Society of Chemistry. (c) Fluorescence emission spectra of phenanthrene (black line), 4a,4b-azaboraphenanthrene (red line), and 9,10-azaboraphenanthrene (blue line) in cyclohexane. Reproduced with permission from ref.²² Copyright © 2007 American Chemical Society

More recently, larger PAHs containing 1,2-azaborines have been reported, presenting different number of BN units,^{23,24} oligomeric structure¹² or even curved structure.²⁵ The most relevant contributions, including synthetic strategies and properties evaluation can be found in reviews such as those provided in references ^{10,23,26,27}.

3.1.2. 1,3-azaborines

In 2011 Liu and co-workers reported the synthesis of the first 1,3-azaborine derivatives, based on ring-closing metathesis (Scheme 3.3A).²⁸ In this case, the metathesis occurs between the N-allyl and B-vinyl groups of **X**, an acyclic intermediate previously prepared. For an efficient ring-closing metathesis reaction, the nitrogen lone pair needs to be protected to avoid catalyst degradation. Then the metathesis product is deprotonated with DBU to afford the 1,3-azaborine heterocycle **XI**. A final Pd/C-mediated dehydrogenation reaction gives rise to a mixture of the desired 1,3-azaborine derivative **XII** and the reduced byproduct **XIII**. Using this compound as starting material, a series of

1,3-azaborine derivatives functionalized at the boron position has been also synthesized (Scheme 3.3B).²⁹



Scheme 3.3. (A) Synthetic route toward an 1,3-azaborine derivative. (B) Substitution reactions for obtaining different B-substituted derivatives. Reagent conditions: (a) (i) CF₃SO₃H, CH₂Cl₂, -30 °C to rt, 10 min; (ii) cat., 24 h; (iii) DBU; (b) Pd/C, benzene, 120 °C, 16 h; (c) TMSCN, MeOH/THF, 24 h; (d) HCl, THF, rt, 24 h; (e) HF·Py, THF, rt, 30 min; (f) MeOH, HCl, THF, rt, 24 h; PCy₃=tricyclohexylphosphine, Py=pyridine, TMS=trimethylsilyl.

Liu and collaborators also studied the electronic structure of N-Me-1,3-BN-toluene³⁰, and compared it with those of pristine toluene and N-Me-1,2-BN-toluene. From this analysis, they concluded that both, 1,2- and 1,3-BN substitutions, promote a destabilization of the HOMO, going from -8.84 eV for toluene to -8.0 eV and to -8.45 eV, for 1,2 and 1,3-BN-toluene respectively. These differences also suggests a different reactivity for 1,2 and 1,3-azaborines, but it has been scarcely explored from an experimental perspective, since the synthesis of 1,3-azaborines to date is limited to monocyclic cores.^{28,29,31}

INTRODUCTION

3.1.3. 1,4-azaborines

The earliest example of a 1,4-azaborine was reported in 1961 by Maitlis,³² (Figure 3.4a, XVIII) *via* reaction of the dilithium derivative XXII with dibutyl(phenylboronate) (Figure 3.4b). In 1992, Clark and collaborators continued the studies on 1,4-BN-anthracene scaffolds, obtaining the X-ray structure of N-methyl-B-mesityldibenzo-1,4-azaborine (Figure 3.4a, XIX).³³ Later, Kawashima and co-workers synthesized the pentacene-like analogue XX³⁴ and obtained its X-ray structure. The comparison of X-ray structural parameters of anthracene- and pentacene-like molecules, shows that the dihedral angle between the mesitylene group and the azaborine ring is slightly larger for the pentacene-like derivative. Moreover, the bent angle of lateral rings respect to the BN-doped central one is also different (15° for pentacene and 9° for anthracene). However, Kawashima and collaborators concluded that these differences between the two molecular structures may come from the crystal packing, as DFT calculations predicted almost the same geometries around the central azaborine ring for both compounds.³⁴ The authors also compared the absorption and emission spectra of these two molecules. Pentacene-like azaborine shows an absorption maximum at 519 nm, which is red-shifted from that of anthracene-like azaborine (405 nm). That indicates a decrease in the HOMO-LUMO energy gap, probably due to the elongation of the π -system. Concerning the emission maxima, it is also appreciable a bathochromic shift of the absorption maximum for pentacene-like azaborine. Remarkably, the fluorescence quantum yield for pentacene-like derivative ($\phi_F = 0.29$ at 524 nm) was lower than that for anthracene-like one ($\phi_F = 0.48$ at 421 nm).

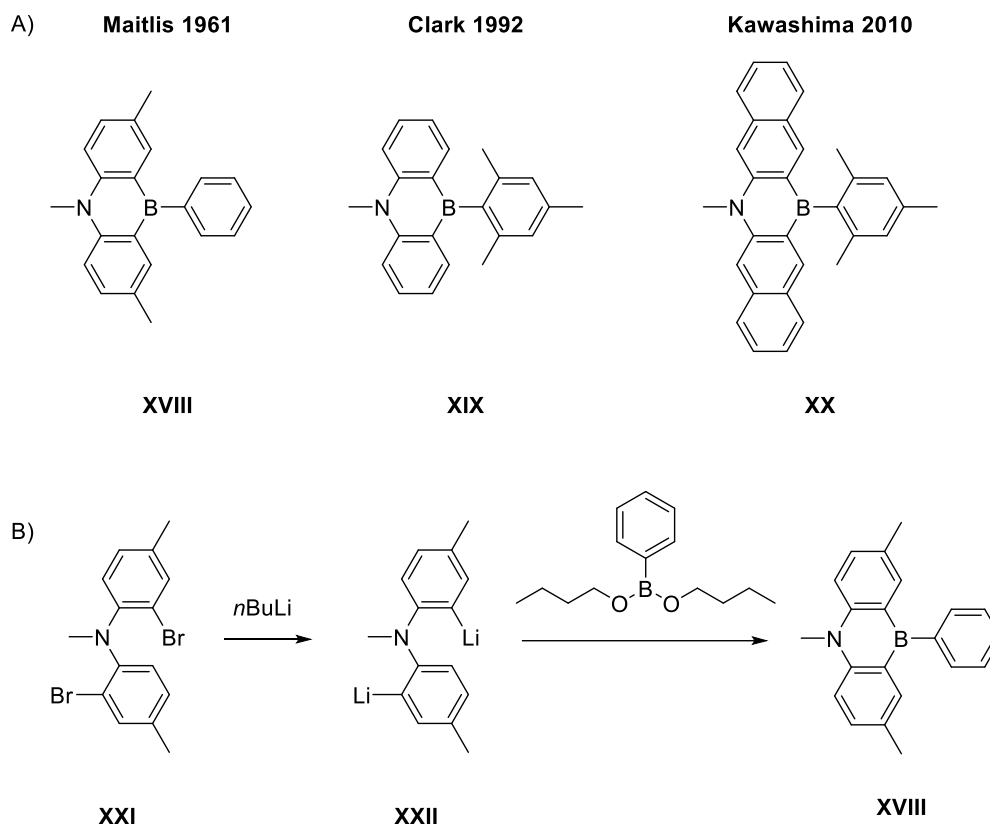


Figure 3.4. (A) Examples of 1,4-azaborine derivatives. (B) Synthetic route for 1,4-azaborine derivatives used by Maitlis in 1961.³²

Kawashima and collaborators developed the synthesis and study of larger acenes (pentacene and heptacene) containing several 1,4-BN units^{35,36} (molecules **XXIII**, **XXIV** and **XXV** in Figure 3.5). Their optical absorption and emission responses were evaluated and compared with those of the BN anthracene analogue (molecule **XXVI** in Figure 3.5). As shown, the absorption band of anthracene **XXVI** and *meta*-type pentacene molecule **XXIII** are located almost at the same wavelength, revealing weak or no π -conjugation between the two neighbouring azaborine units in molecule **XXIII**. The absorption maxima of *para*-type pentacene molecule **XXIV** is red-shifted in comparison with the *meta*-analogue **XXIII**, what indicates a more extended π -conjugation. In this way, the relative orientation of the BN units in acene scaffolds may deeply influence the properties. The fluorescence spectra of heptacene-like molecule **XXV** shows two emission maxima, unlike the other compounds, although the origin of the second peak remains unknown. The obtained quantum yield for *para*-type molecule **XXIV** ($\phi_F = 0.69$) was higher than that of *meta*-type

INTRODUCTION

analogue **XXIII** ($\phi_F = 0.21$), suggesting that the incorporation of 1,4-BN units in alternate orientations could give rise to efficient molecules for light-emitting devices.

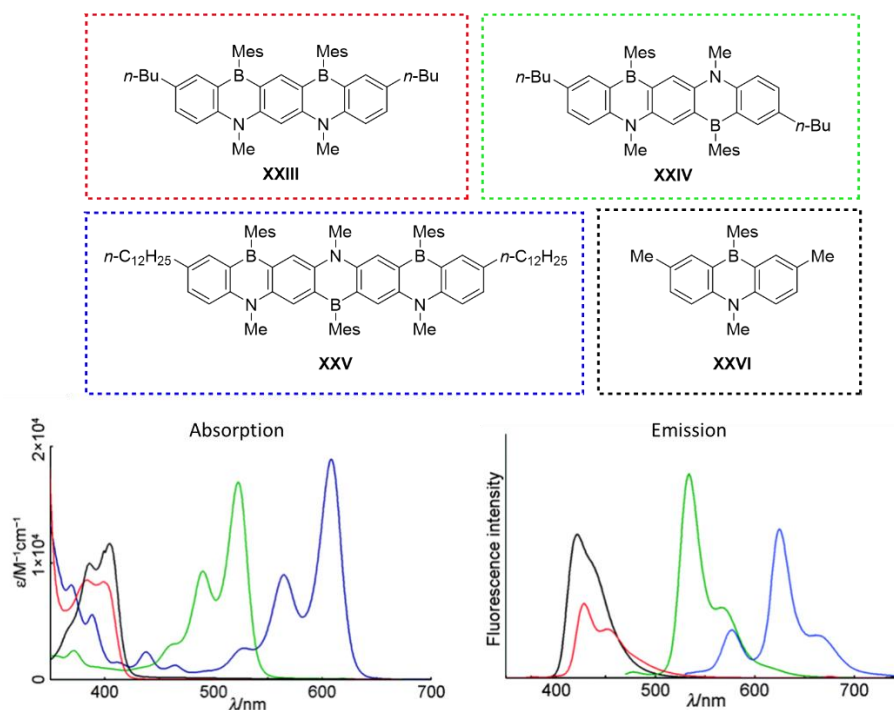
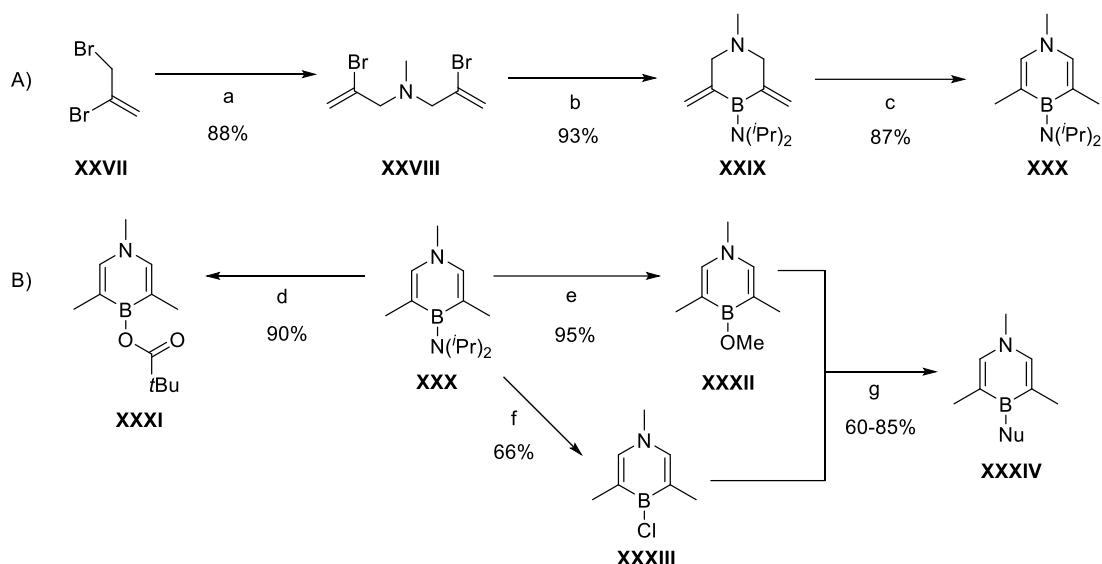


Figure 3.5. Acene-like 1,4-azaborine derivatives prepared by Kawashima and collaborators and their UV-Vis and fluorescence spectra in cyclohexane (Red: **XXIII**, Green: **XXIV**, Blue: **XXV**, Black: **XXVI**). Spectra reproduced with permission of ref.³⁶ Copyright © 2006 American Chemical Society

Liu's group recently presented a synthetic approach to substituted monocyclic 1,4-azaborines.³⁷ As shown in Scheme 3.4A, this route is based on metal-halogen exchange of the dibromide **XXVIII**, followed by quenching with iPr_2NBCl_2 , giving rise to the 6-membered BN-heterocycle **XXIX**. Isomerization of the exocyclic double bonds in presence of Ru(II) catalyst produces the desired target **XXX**, which can be derivatized in an easy manner for preparing a plethora of 1,4-azaborines functionalized at the boron position (Scheme 3.4B). Using this methodology, the authors synthesized a series of functionalized terphenyls (Figure 3.6, **XXXVIII** and **XXXIX**), presenting a 1,4-azaborine units in the central ring. The study of the optical properties (UV-Vis and fluorescence) revealed that when two functional groups of different nature (donor/acceptor) are incorporated in B and N positions, the exhibited properties are highly dependent on the placement of these groups. In this way, the specific location of the donor/acceptor groups on 1,4-azaborines

has a dramatic impact on the optical properties, in contrast to what happens with the all-carbon counterparts (XXXV and XXXVI), where the relative placement of the donor/acceptor groups in *para*-position does not involve considerable changes in the optical responses.



Scheme 3.4. (A) Synthetic sequence for monocyclic 1,4-azaborines. (B) Functionalization possibilities at the boron atom of 1,4-azaborines. Reagent conditions: (a) K_2CO_3 , MeNH₂, MeCN, reflux; (b) (i) *t*BuLi, (ii) *i*Pr₂NBCl₂; (c) HRuCl(CO)(PPh₃)₃, toluene, 110 °C; (d) pivalic acid, CH₂Cl₂, rt, 2 h; (e) MeOH, CH₂Cl₂, rt, 2 h; (f) HCl, CH₂Cl₂, rt, 2 h; (g) Nu, THF. (Nu= EtMgBr, CH₂=CHMgBr, CH₂=CHCH₂MgBr, PhMgBr, mesityllithium, PhOLi, Et₃BLiH, *i*Pr₂NLi).

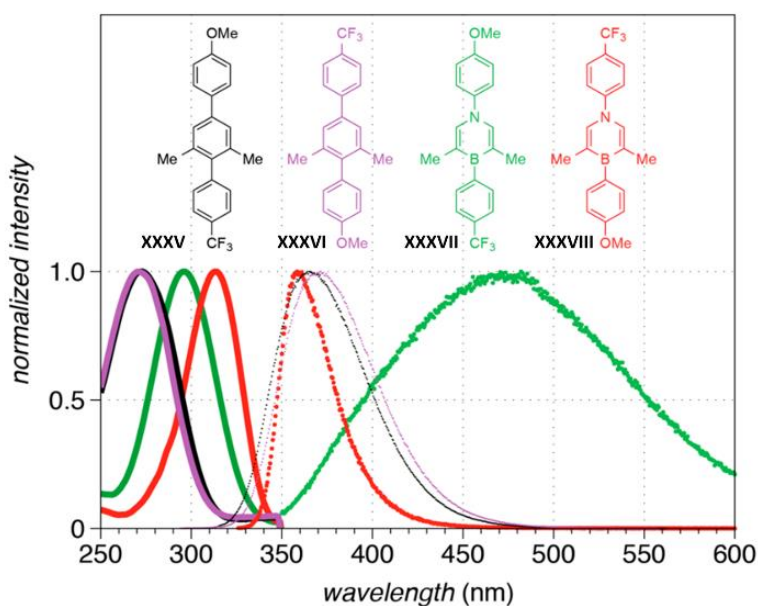


Figure 3.6. Normalized absorption (solid lines) and emission (dotted traces) spectra for two inversely substituted 1,4-azaborines (green and red); and their all-carbon analogues (black and purple, respectively). Reproduced with permission of ref.³⁷ Copyright © 2016 American Chemical Society

INTRODUCTION

3.1.4. Electronic properties of azaborines

In spite of the raising interest of azaborines and their probed power for tuning the properties of the all-carbon parent structures, the effect of the BN-doping on electron transport has not been well defined yet.

At the single-molecule level, azaborines remain almost unexplored. Only a BN-phenanthrene derivative has been recently studied by STM-BJ technique.³⁸ Wan and collaborators carried out conductance experiments of a 9-aza-10-boraphenanthrene derivative (a 1,2-azaborine derivative) incorporating pyrimidine rings as linkers (Figure 3.7a). The results were compared with those of the corresponding all-C analogue, and the authors found that these isoelectronic structures presented a conductance value in the same order of magnitude, between $\log(G/G_0) = -4$ and $\log(G/G_0) = -5$, being slightly higher for the BN-doped structure. Figure 3.7b shows the 1D histograms of both compound for a better comparison.

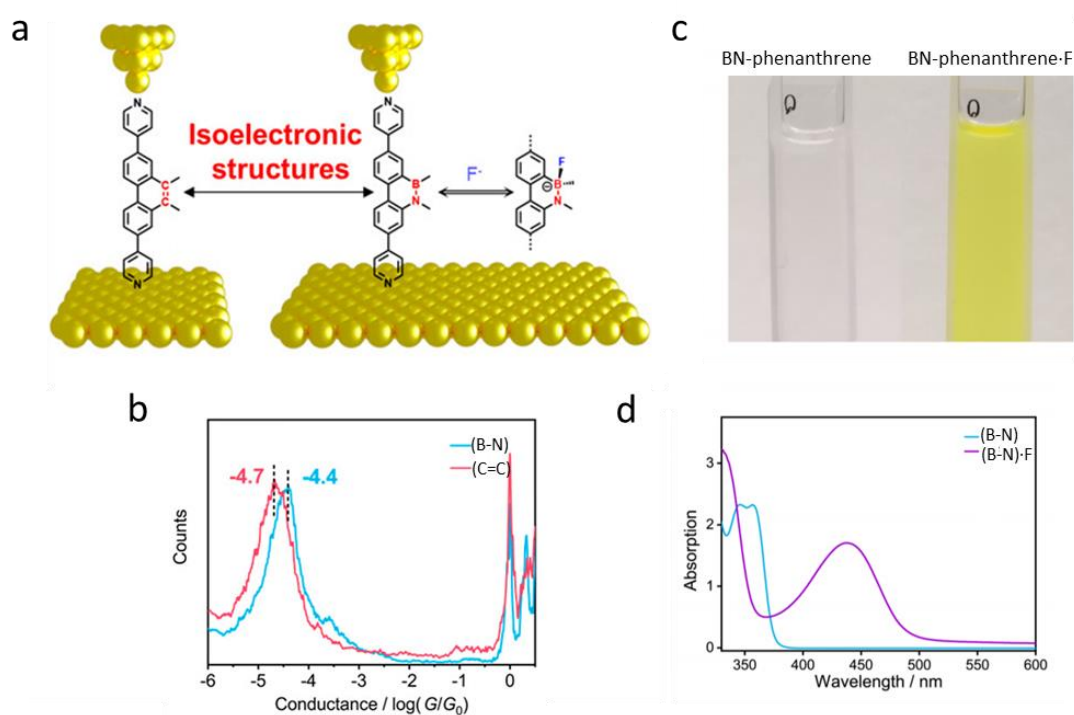


Figure 3.7. (a) Graphical representation of the metal-molecule-metal junctions in the conductance experiments for the molecules of interest. (b) Representative conductance traces for both molecules. (c) Visual colour change after the formation of the B–F coordinated species in a mixture 1:4 THF:TMB. (d) Absorbance spectra of BN-phenanthrene and B–F coordinated phenanthrene derivative. Adapted with permission of ref.³⁸ Copyright © 2020 American Chemical Society

Additionally, and considering the electron-accepting character of azaborines due to the vacant p-orbital of the boron,³⁵ they originated the B–F coordinated specie by adding tetrabutylammonium fluoride (Bu₄NF). The formation of B–F coordination bond was followed by colorimetric change in the solution (Figure 3.7c), obtaining a UV-Vis spectra with a new largely red-shifted absorption band (Figure 3.7d). Remarkably, the conductance of the coordinated specie was four times lower than that of the F-free azaborine derivative. Quantum transport calculations revealed that the formation of the B–F coordination bond rearranges the local molecular structure, leading to a substantial change of the electronic structure of BN derivatives with a significant shift of the LUMO toward higher energy levels.

This abovementioned study is only the first step toward understanding the effect of azaborine substitution in the electron transport, since 1,3- and 1,4- azaborine isomers remain completely unexplored. The electronic properties for the three azaborine isomers in the relative 1,2-, 1,3- and 1,4-positions are expected to be different, since their aromaticity and stability are also different. In addition, for each series of these isomers, distinct positions for both, the BN unit and the substituents, give rise to compounds exhibiting clearly different optical responses, as shown in the previous sections. Therefore, it is expected to find also different electron transport properties for compounds with different substituents, even with the same relative (1,2-, 1,3- and 1,4-) BN position.

Concerning heteroaromatic compounds in general, the particular position of the heteroatoms with respect to the most favourable electron pathway is of special interest regarding their impact on the electronic properties. If they are located in the most favourable conduction pathway, the heteroatoms are forced to participate in the molecular orbitals responsible of the conduction, while if they are placed in positions further away from such path, the electron conduction takes place through the eigenchannels already accessible in the pristine all-carbon analogues, assuming a minimum participation of the heteroatoms on the electron conduction. It is possible a third situation, that occurs when heteroatoms are placed laterally with respect to the electron pathway, being difficult to determine their real participation on the electron conduction. This is the case for the 1,2-BN-phenanthrene already studied: the

INTRODUCTION

heteroatoms are not placed in the direct end-to-end pathway, but the ring they are part of does.³⁸ In this sense, molecules containing oxygen, sulphur or nitrogen, among others, have been experimentally studied too.^{39–41} Remarkably, the greater effect of the presence of heteroatoms has been observed in wires with π - σ - π backbone, where the sigma moiety is a single heteroatom⁴² or a sequence of them.⁴³ In both cases, despite not being embedded into the aromatic system, heteroatoms have a strong impact in the conductance, since they are unequivocally in the electron path and due to its difference in size, polarizability and electronegativity with respect to carbon atoms.

A good method for evaluating the impact of the heteroatoms on the electronic properties is the comparison with the corresponding all-C analogues. However, in most of the studies found in literature about the electron transport of heteroatom-containing molecules, the parent hydrocarbons are not always reported. This absence is probably due to such studies are more interested on the electronic properties of these compounds themselves, rather than the evaluation of the specific modifications that the heteroatoms promote on the properties.

Taking into account these exposed considerations, to unambiguously assess the effect of the BN substitution in the electronic transport through PAHs, it can be said that the experimental approach should ideally meet the following three criteria:

- (i) Heteroatoms should be embedded in the π -core.
- (ii) Heteroatoms should be located into the most favorable electron-conduction pathway.
- (iii) Comparison with the corresponding all-carbon analogues is highly desirable.

3.1.5. Overview

Azaborines have the potential of expand the physicochemical space of PAHs, as they can present different aromaticity, reactivity and properties of that of the parent hydrocarbons while maintain their original topology due to the CC/BN isosterism. The properties exhibited by these compounds can change depending on three considerations:

- (i) The relative position 1,2, 1,3 or 1,4 of the B and N atoms within the ring.
- (ii) The specific position of the substitution within the molecule.
- (iii) The presence and position of additional substituents.

Considering that, the potential of azaborines almost rise to infinity, highlighting that more extensive research in the field is still needed.

Already studied azaborine systems have revealed that 1,3-azaborines are the most aromatic but less stable isomer, while 1,2-azaborines are the less aromatic but more stable isomer. 1,4-azaborines are a particular case, where the directional π -electron delocalization originated by the heteroatoms, gives rise to a push-pull π -electron systems rather than aromatic.

While the reactivity and optical properties of azaborines are the main topic of most of the research already done in the field, their electron transport properties at the single-molecule scale have been scarcely investigated, existing in literature just one recent example (2020) of a 1,2-azaborine derivative. One of the reasons of lacking studies can be the synthetic efforts needed, not only for the incorporation of B and N in the structures, but also for the introduction of the anchoring groups required for this kind of experiments.

In this context, a proper starting point seems to be the study of the electron transport properties of different azaborine cores, as well as those of their parent hydrocarbons, in order to establish the impact of the substitution. In this sense, it should be considered that the heteroatom participation on the conduction would be maximized if they are unambiguously place in the most favorable electron path. Although the three regioisomers 1,2, 1,3 and 1,4 have been equally understudied, the particular polarization

INTRODUCTION

of the latter, as a push-pull system, seem to be the most interesting from the electronic perspective.

3.2. Objectives

According to the information collected in the background section, the next objectives were proposed:

1. To design, synthesize and characterize a 1,4-BN-functionalized arene incorporating linker groups to establish single-molecule junction between gold electrodes, allowing the development of single-molecule conductance experiments. In the designed compound, heteroatoms must be unequivocally located in the electron path.
2. To design, synthesize and characterize the corresponding heteroatom-free analogue, enabling a direct comparison of the properties of both structures.
3. To evaluate the effect of the CC-to-BN substitution in the electron-transport properties of PAHs by means of single-molecule conductance experiments.

3.3. Results and discussion

3.3.1. Molecular design

Taking into account the relative position of B and N in 1,4 azaborines, as well as the relevance of (i) incorporating anchoring groups into the structures and (ii) ensuring the presence of boron and nitrogen in the electron path, acene scaffolds seemed to be the ideal targets, since they allow locating the linkers directly in N and B positions. In this configuration, shown in Figure 3.8, the electrons are forced to pass through both heteroatoms, while they remain embedded in the fully conjugated structure. Besides, the electron properties of the corresponding hydrocarbons are also of special interest in molecular electronics due to its high charge-carrier mobility, which has been reflected in its good performance in organic devices such as OLEDs, OFETs and OPVs.^{44,45}

Heteroatoms in the electron path

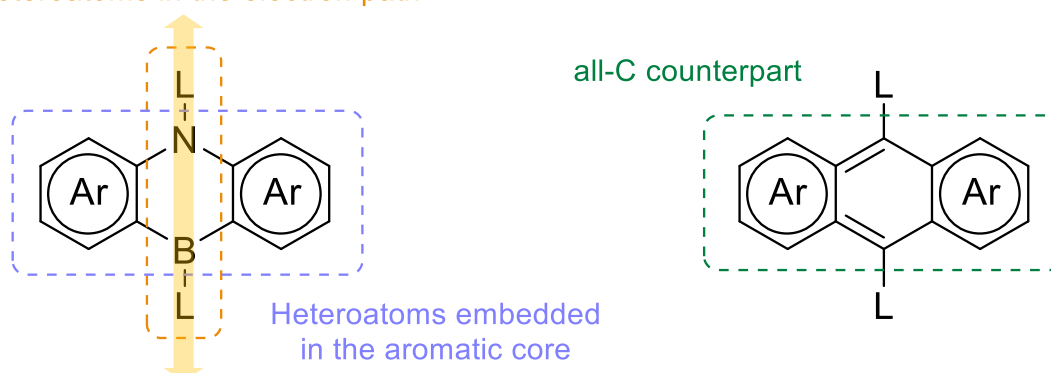


Figure 3.8. Design: 1,4-azaborine in acene motifs ensures to meet the three criteria mentioned in section 3.1.4 since (i) boron and nitrogen are embedded in a fully conjugated structure, (ii) a smart location of linkers ensures the electrons passing through both, nitrogen and boron atoms; and (iii) they have synthetically accessible all-C counterparts.

However, electronic properties of acene motifs at the single-molecule scale have been scarcely investigated to date.^{46–51} In addition, only a few of those studies considered the incorporation of anchors to the acene scaffold,^{46–48} while in the rest, the lack of specific anchoring groups hinders the determination of the exact binding geometries that are originating the conductance signals.^{49–51} The reason of so few number of studies focussed in single-molecule conductance of acenes (particularly from pentacene onwards) is probably their stability, since as the π -skeleton of acenes is extended, their stability

RESULTS AND DISCUSSION

dramatically decreases, precluding their isolation and the development of the corresponding experiments. Although there is not a consensus on the origin of such instability, it seems to be related with the increasing biradical character of the ground states of acenes as their size increases.^{52,53} In this sense, it has been recently demonstrated that the presence of BN units in these scaffolds promotes an improvement of their stability, upon exposure to oxygen and light.⁵⁴ This effects could be attribute to the absence of quasi-degenerate ground state in azaborines³⁴ and could be used as strategy for preparing larger acene derivatives, stable enough for studying their unimolecular conductance or even to make possible their implementation in single-molecule electronic devices.

In this context, we proposed the preparation of the molecules depicted in Figure 3.9. Firstly, as one of the shorter compounds in the acene series, an all-C anthracene including linker groups (**CCA**); and the corresponding 1,4-azaborine analogue (**BNA**). The comparison of the conductance of both molecules would be used for elucidating the direct effect of the BN substitution in the electron transport. Secondly, the pentacene-like counterpart (**BNP**) in order to study if the laterally enlargement of the acene scaffold respect to the conduction pathway promotes changes in the conductance value. In this case, the direct comparison with the all-C analogue is not possible, since this structure, namely 6,13-diphenylpentacene, has been reported to have a lifetime in the presence of oxygen and light of only 8.5 minutes in CH₂Cl₂ solution.⁵⁵

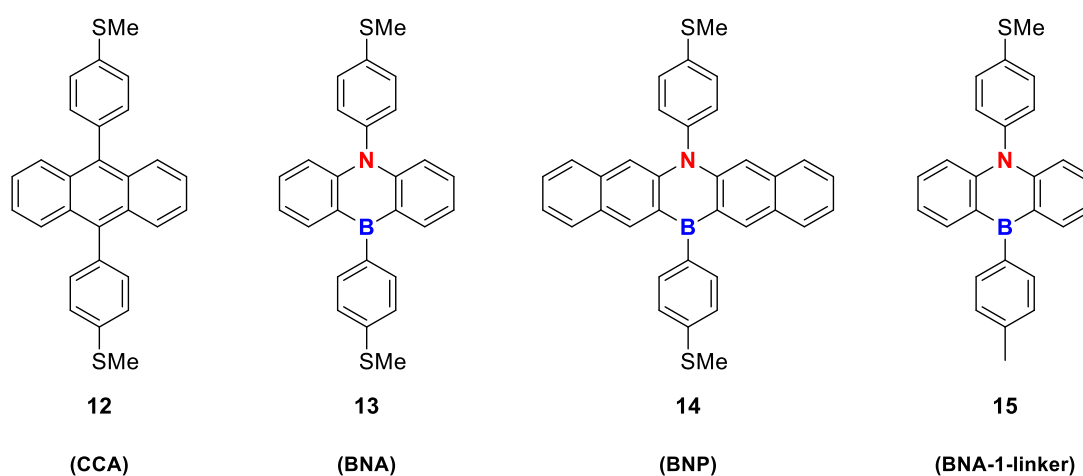
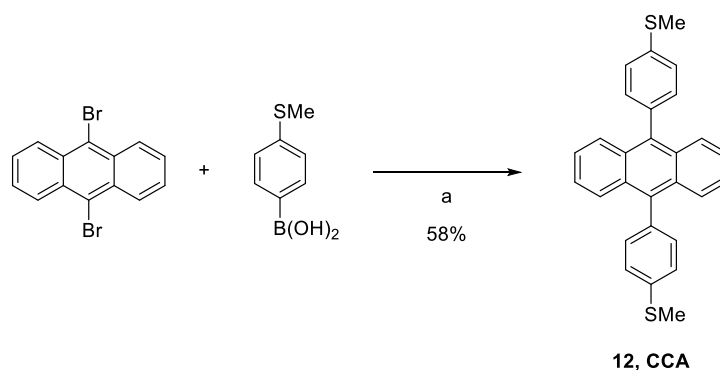


Figure 3.9. Target molecules. In parentheses the names given for clarity along the discussion of results.

Finally, a BN-anthracene analogue including a single linker group (**BNA-1-linker**). The reasons for preparing and measuring the conductance of this molecule are explained in section 3.3.4. All these compounds were designed including thiomethyl (–SMe) groups as linkers, which are well-known to provide a good contact between metallic electrodes in STM-BJ,^{56,57} and additional benzene rings as spacers.

3.3.2. Synthesis

The synthetic strategy used for preparing compound **CCA** is depicted in Scheme 3.5. It is based on a double Suzuki coupling between dibromide anthracene and 4-(methylthio)phenylboronic acid, by means of Pd(OAc)₂ catalyst, affording compound **CCA** in good yield.

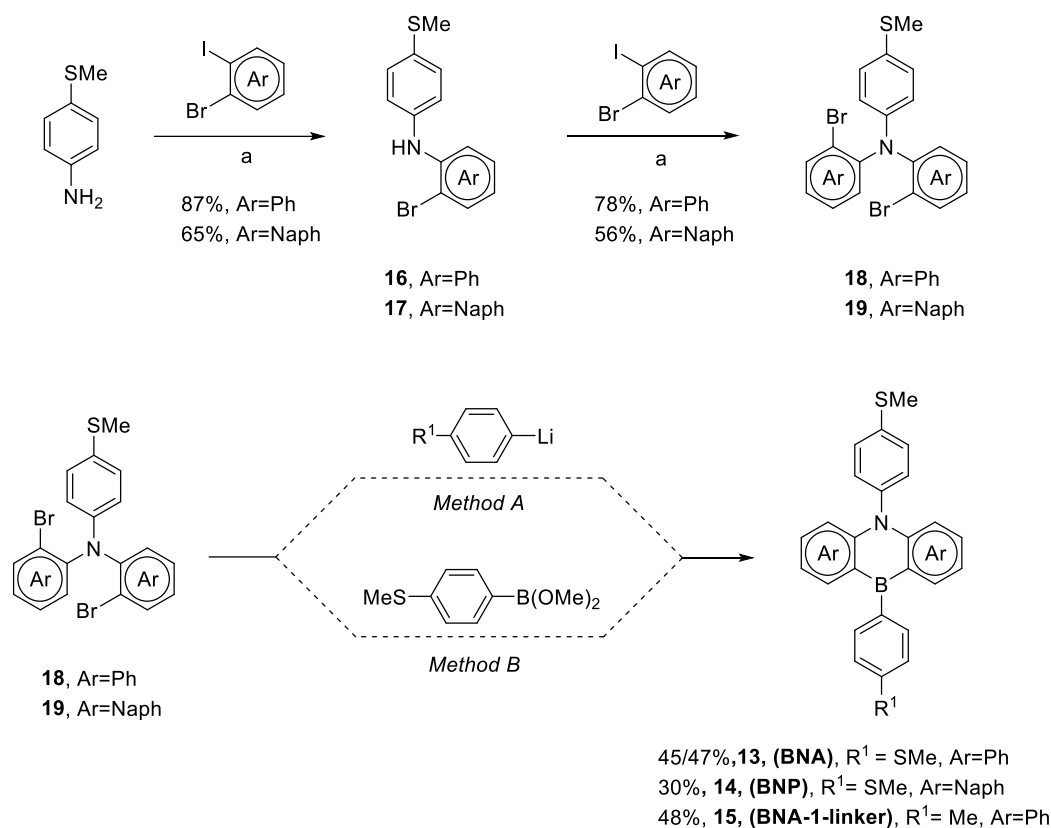


Scheme 3.5. Synthetic route toward compound **CCA**. Reagent conditions: **(a)** Pd(OAc)₂, K₂CO₃, Bu₄NBr, Toluene/H₂O, 70 °C, 18 h.

The preparation of compounds **BNA**, **BNP**, and **BNA-1-linker** was carried out following the synthetic route shown in Scheme 3.6. Two consecutive Buchwald-Hartwig cross-coupling reactions over 4-(methylthio)aniline using the appropriate dihaloarene gave rise to dibromide derivatives **18** and **19**, respectively in good yields. A final lithiation-boration step afforded the BN-doped anthracenes **BNA** and **BNA-1-linker** and the BN-doped pentacene **BNP** in reasonable yields. Remarkably, two different methods were used for the last reaction. Method A was successfully employed for the synthesis of **BNA**, however, it did not work in the case of **BNP**. Therefore, Method B was developed in particular for the preparation of **BNP**. Since it involved an easier purification of the final product, it was also used for preparing a second batch of **BNA**, demonstrating a wider scope than Method

RESULTS AND DISCUSSION

A. Experimental details of the compounds prepared are available in the Experimental Section, and the NMR spectra of the target compounds collected in the Annexes.



Scheme 3.6. Synthetic routes used for preparing compounds **BNA**, **BNP** and **BNA-1-linker**. Reagent conditions: **(a)** Pd(dba)₂, PtBu₃·HBF₄, tBuONa; **Method A:** (i) *n*-BuLi, (ii) B(OMe)₃, (iii) lithiated arene; **Method B:** (i) *n*-BuLi, (ii) dimethyl (4-(methylthio)phenyl)boronate.

3.3.3. Break-junction experiments

The gold on quartz plates for break junction experiments were previously cleaned as described in the Experimental Section. Then, they were immersed for 15-20 min in DCM solutions of the corresponding molecules, with concentrations between 10⁻⁴ and 10⁻³ mM. Compounds **CCA**, **BNA** and **BNP** were measured applying a 0.16 bias voltage, and using 1 × 10⁸ V/A and 4.5 × 10¹⁰ V/A amplification gains in the STM circuit, with a protection resistor of 2 × 10⁶ Ω in series. This combination allowed us to explore a range in conductance $G=I/V$ of 8 orders of magnitude between 10 G_0 and 10⁻⁷ G_0 . Several rounds of measurements were recorded for each compound. The raw conductance-distance ($G-z$) traces for each one were subjected to the searching plateaus process described in

detail in the Experimental section. The corresponding 1D and 2D histograms were built from the traces displaying plateaus.

3.3.3.1. Effect of 1,4 BN substitution in anthracene scaffold: conductance of CCA and BNA

The 2D histograms obtained for compounds **CCA** and **BNA** are shown in Figure 3.10a and 3.10b, respectively. They presented a similar shape, with a broad and sloping conductance signal. This sloping profile is usually associated with an important interaction of the core of the molecules with the gold electrodes as the molecules slide over them during the pulling process. The presence of several molecules in parallel between the electrodes can also contribute to it. It is easy to think that both processes can be favoured by the presence of the extended acene, since aromatic surfaces have been reported to interact with gold efficiently.⁵⁸ This profile gave rise to asymmetric peaks in the corresponding 1D histograms, which are superimposed in Figure 3.10c for a better comparison. Although the conductance peaks of both compounds were located between $\log(G/G_0) = -5$ and -6 , it was appreciable a slightly shift of conductance towards lower values for **BNA**. The analysis of the plateau-length distributions is shown in Figure 3.10d. The expected plateau-length for these molecular junctions is depicted as a vertical grey line. This value was obtained after the subtraction of an interval of 0.4 nm to the calculated (S-S) molecular distance (1.48nm), compensating the effect of the electrode retraction after the gold contact breaks. For both molecules, the end of the Gaussian distribution concurred with the expected molecular length, therefore it could conclude that equivalent molecular junctions are being formed for **CCA** and **BNA**, corresponding to molecules fully extended between the gold electrodes. In this way, we probed that the 1,4-BN substitution in the central ring, not only permits the electron transport through the molecules, but also leads to a molecular conductance of the same order of magnitude as that for the all-carbon structure.

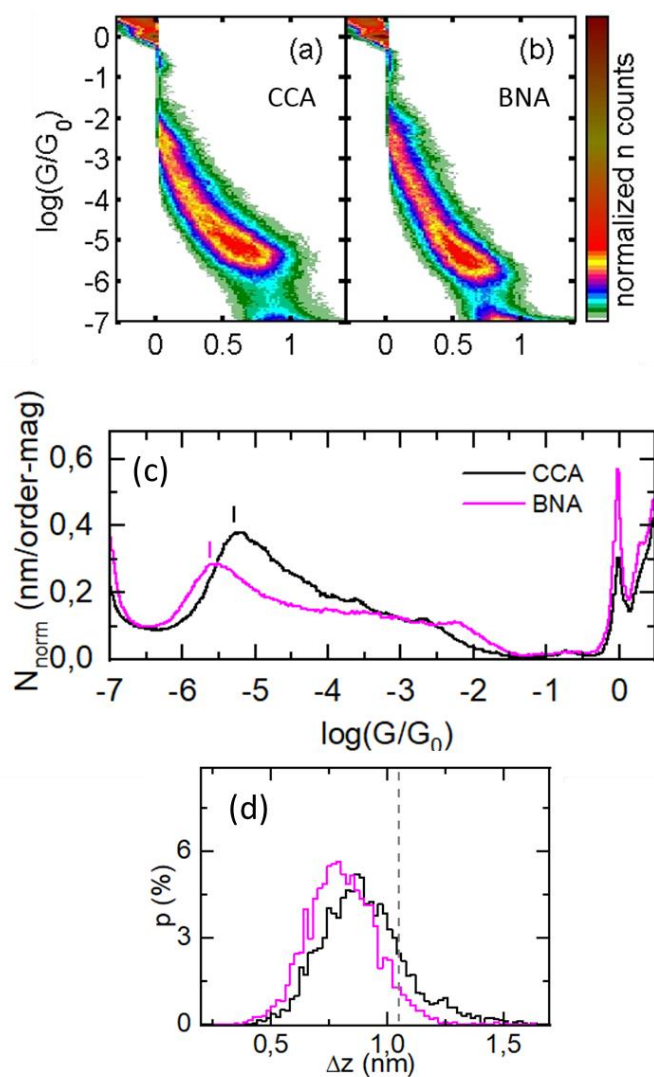


Figure 3.10. 2D histograms of compounds (a) CCA and (b) BNA, built from all traces displaying plateaus. (c) 1D histograms of compounds CCA (black line) and BNA (pink line). The middle point of the conductance peaks are marked with a vertical line. (d) Plateau-length distributions, where the grey line corresponds to the expected length of plateaus for the S-S distance.

Current vs Voltage curves for calculating the rectification ratio (RR)

As explained in Chapter 1 (section 1.5.3.), the I - V characteristics of asymmetric molecules can reveal rectification behaviour. In the case of these BN-doped molecules, the position of the heteroatoms and the polarization of charges could contribute to such effect, favoring the electron transport in one direction of the molecule respect to the other. To study this possibility, a second break-junction experiment was carried out for **BNA** and current vs voltage (I - V) curves were recorded. The motion of the electrodes was stopped during the opening process each 0.07 nm and the voltage was ramped between +1 V and -1 V. Both the up-ramp and down-ramp I - V curves were collected. The identification of

traces displaying plateaus was conducted as previously explained and we selected those I - V curves recorded along plateaus in the range between $\log(G/G_0) = -6$ and -4.5 . Figure 3.11a shows an example of a conductance trace recorded in this way, with circles indicating the positions at which I - V curves were obtained. The corresponding I - V curves for such trace are displayed in Figure 3.11b.

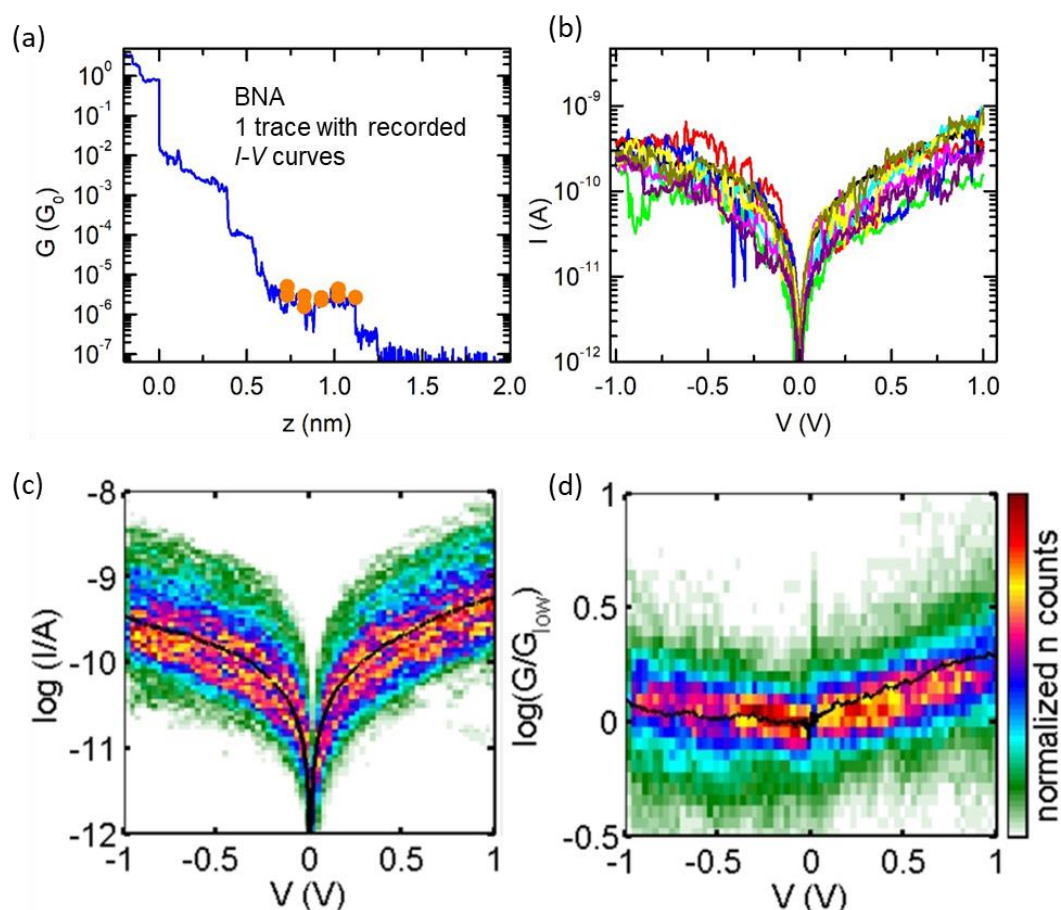


Figure 3.11. (a) Example of a conductance trace for **BNA** displaying a plateau along which I - V curves are recorded. Orange circles indicate the position where the motion of the electrodes was paused and I - V curves were recorded. (b) Corresponding I - V curves recorded along the conductance trace shown in (a). (c) 2D histograms of $\log(I)$ - V and (d) 2D histogram of $\log(G/G_{low})$ - V curves, built from all the traces displaying plateaus. The average curve is superimposed in black over the histogram in both figures. In order to see the average asymmetry in the curves, they were first flipped to have the branch of higher current of all curves at positive bias voltages. In both figures, the log difference between the values at $+1$ and -1 V is around 0.25, which translates in a rectification ratio of 1.8 in the linear scale.

Gathering the I - V curves from all the conductance traces with plateau, the 2D histogram of Figure 3.11c was built, where the average I - V curve is superimposed. In order to see clearly the typical I - V curve asymmetry in the histogram, we flipped first the I - V curves to

RESULTS AND DISCUSSION

have the branch of higher current always at positive bias voltages. We found out that a 48% of the I - V curves needed to be flipped. This value is indeed close to the theoretical 50% that we expect as there should not be any preferential orientation of the molecules or their binding respect to the STM tip and substrate. In addition, we obtained the corresponding G - V curves by calculating $G = I/V$ for each point, and scaled these by the conductance value at low bias voltage values, G_{low} . The latter was obtained fitting a polynomial to the interval (-0.2 V, 0.2 V) of the I - V curves. Figure 3.11d shows the corresponding 2D histogram of these scaled curves, again with their average curve superimposed. In order to quantify the asymmetry of the I - V curves, we determined the rectification ratio (RR) at ± 1 V. As reminder RR corresponds to the ratio between the current at a given positive bias voltage and the corresponding current at the reversed bias voltage. We obtained an average RR value of 1.8 ± 0.7 , which agrees with the difference between the values at +1 and -1V for the average curves in the log scale of approximately 0.25 in both Figures 3.11.c and 3.11.d. This RR value is only slightly larger than that previously reported for fully symmetric compounds,^{39,59} and similar to that observed in N-phenylbenzamide derivatives,⁶⁰ where the dependence of the rectification factor with the strength of the molecule's linking group is demonstrated. This result is also consistent with the transmission curves displayed later in the section 3.3.4, with the gold Fermi level being practically at the center of a wide HOMO-LUMO gap.

3.3.3.2. From terphenyl to anthracene: unravelling the effect of the lateral rings

We observed nevertheless that the conductance of both anthracene-like compounds **CCA** and **BNA** was nearly two orders of magnitude smaller than that of the equivalent *p*-terphenyl derivative (4,4''-bis(methylthio)-1,1':4',1''-terphenyl),^a as can be seen in Figures 3.12a and 3.12b.⁶¹ This molecule presents a very similar S-S distance, since its difference with **CCA** consists in the addition of two lateral rings in the central core, going from benzene to anthracene. Plateau-length distributions were indeed essentially the same (Figure 3.12c). Very likely, the reason for the smaller conductance of **CCA** is the higher

^a The corresponding data for the terphenyl compound, analogue to **CCA**, were previously used in an already published work in collaboration with Nazario Martin's group during the development of the present thesis. Such work corresponds to reference ⁶¹ and it is also available in the List of Publications.

dihedral angle (70.3°) between the bulky central part of the molecule and the thiomethylphenyl rings in comparison with those of *p*-terphenyl (33.8°),^b according to the theoretical calculations exposed later in this chapter.

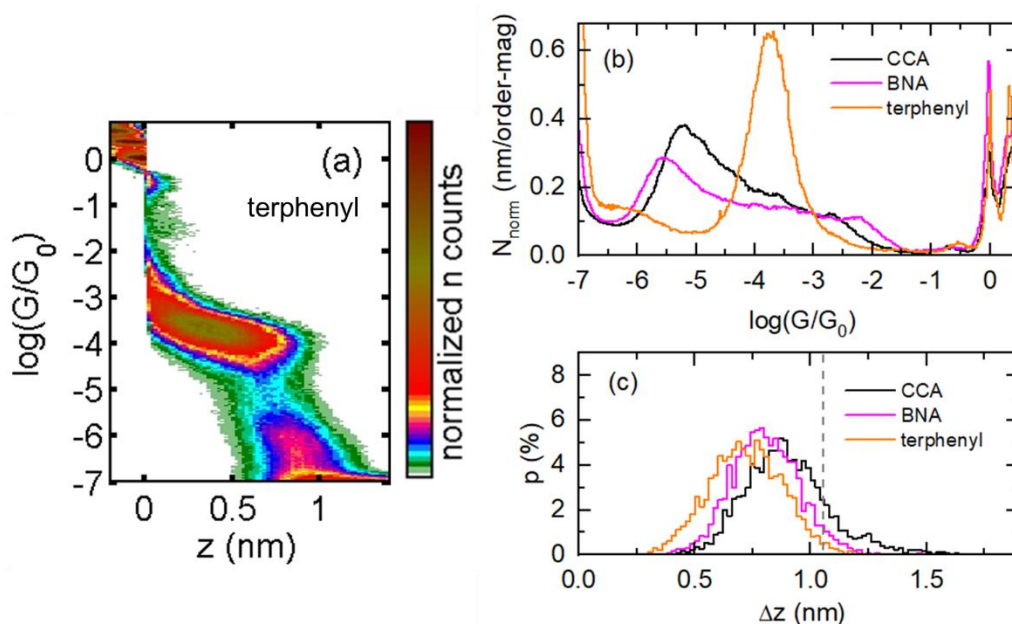


Figure 3.12. (a) 2D histogram for *p*-terphenyl. (b) 1D histograms and (c) plateau-length distributions for CCA, BNA and *p*-terphenyl. The vertical grey line marks the expected plateau length for the S-S distance.

In addition to the conductance value, a clear difference in the shape of the conductance peaks can be appreciated in Figure 3.12a, since *p*-terphenyl traces display flatter plateaus, which produce a symmetric and narrow peak in the 1D histogram between $\log(G/G_0) = -4$ and -3 (Figure 3.12b). On the other hand, the plateaus for CCA traces fall down toward lower conductance values as the separation between the electrodes increases, so that the main signal spreads over two orders of magnitude. Remarkably, these conductance values are compatible with previous conductance measurements for benzene and naphthalene diamine analogues to CCA⁶² (Figure 3.13) in which the conductance decreases for the more extended compound, as it presents a higher dihedral angle.

^b A general discussion about the effect of dihedral angles in the conduction pathway was presented in Chapter 1, section 1.5.3. Theoretical calculations for these compounds, including the dihedral angles are described in section 3.4.

RESULTS AND DISCUSSION

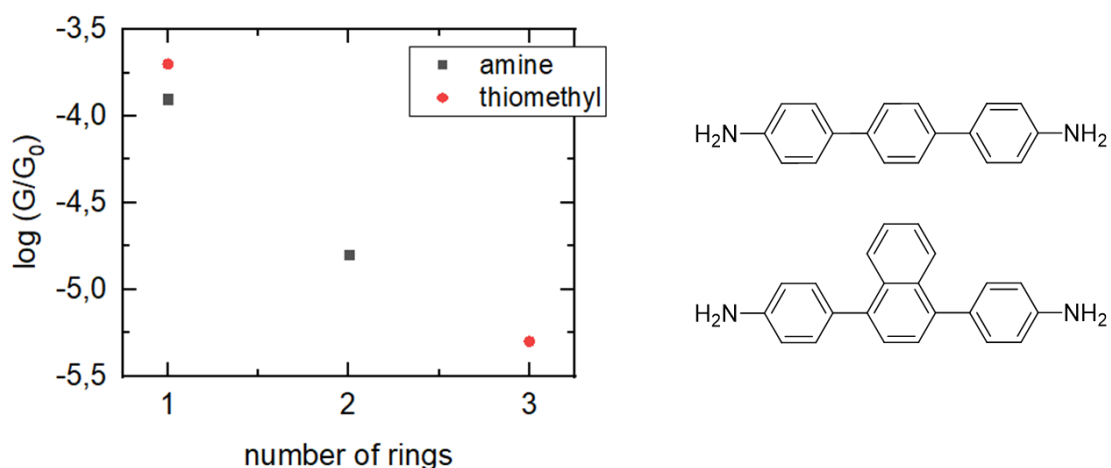


Figure 3.13. Conductance vs number of rings for benzene and anthracene cores with thiomethyl linkers (red circles); and benzene and naphthalene cores with amine linkers (black squares). Data for the amine molecules taken from ref.⁶²

3.3.3.3. 1,4-BN substitution in larger acenes: conductance of BNP

The 2D histogram for **BNP**, shown in Figure 3.14a, displays a well-defined flat cloud of high conductance between $\log(G/G_0) = -4$ and $\log(G/G_0) = -5$. This signal clearly extends to shorter distances than those for the previous compounds, suggesting that it does not correspond to a linker-to-linker configuration.

However, a second broader cloud is also noticeable at lower conductance values. A better assessment of these two signals was achieved after separating the G - z traces in two groups: traces displaying conductance plateaus above and below $\log(G/G_0) = -5$. The independent 2D histograms for both groups are shown in Figure 3.14b and 3.14c, while the corresponding 1D histograms and plateau length distributions can be found in Figures 3.14e and 3.14f, respectively. Some individual G - z traces are depicted in Figure 3.14d. They show that the conductance signal below $\log(G/G_0) = -5$ is due to clear plateaus. This signal constituted only 20% of the total traces, but both, conductance and plateau-length, were in the range of those of **CCA** and **BNA**. Therefore, this set of plateaus could be assigned to **BNP** molecular junctions with the molecule fully extended between the electrodes.

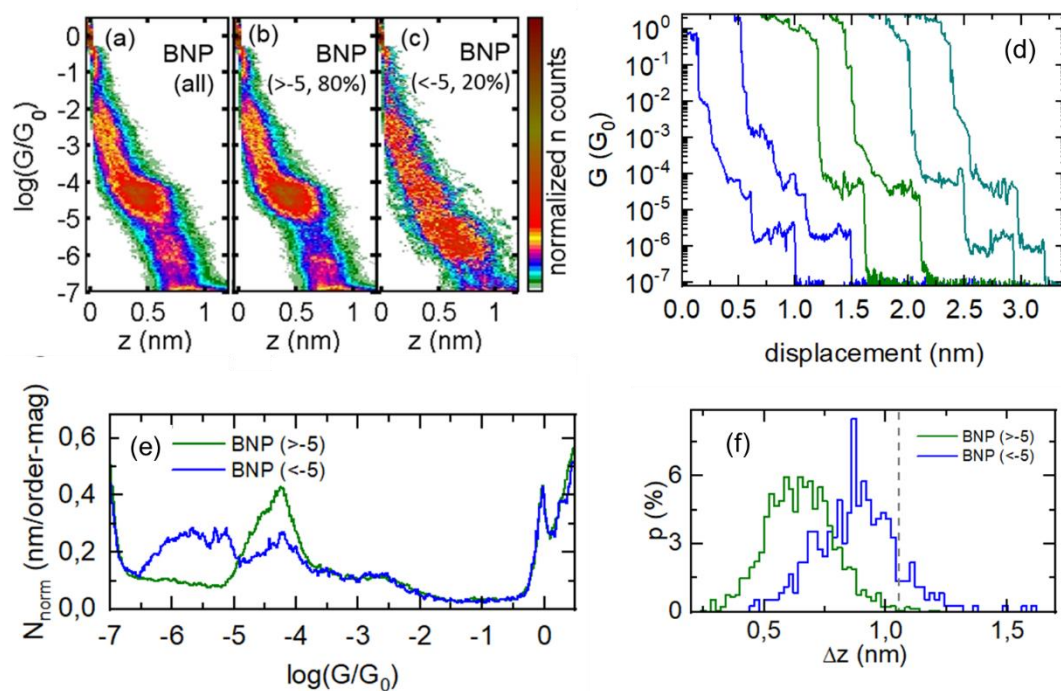


Figure 3.14. (a) 2D histogram for compound **BNP**. (b) and (c) Independent 2D histograms of the two groups separated for **BNP**: traces displaying plateaus above $-5 \log(G/G_0)$ and traces displaying plateaus below $-5 \log(G/G_0)$, respectively. (d) Individual G - z traces for **BNP**. Three different behaviours are shown: only displaying plateaus at the lower conductance region (blue traces), only displaying plateaus at the higher conductance region (green traces) and displaying plateaus at both higher and lower conductance regions (cyan traces). (e) 1D histograms for all traces of **BNP** and the two groups obtained from the separation of this traces. (f) Plateau-length distribution for both groups, where the grey line corresponds to the expected length of plateaus for the S-S distance.

As explained before, the main signal for **BNP** (80% of the total traces) appeared at a higher conductance values and it was constituted by G - z traces displaying shorter plateaus. For further investigate the conductance of **BNP**, a clustering separation analysis was additionally carried out. The results of such analysis are exposed in the next section.

3.3.3.4. Clustering analysis of G - z traces for CCA, BNA and BNP

A clustering-based analysis were carried out for G - z traces of **CCA**, **BNA** and **BNP**, using only those traces previously identified as displaying plateaus for each compound.^c During the analysis, different numbers of blind subdivisions were explored in the algorithm. A visual analysis of the different sets allowed us to identify three significant different traces profiles, whose 2D and 1D histograms are displayed in Figures 3.15 and 3.16 respectively. In Figure 3.15, the histograms in the first column correspond to the higher occurring-rate

^c The bases of this kind of analysis can be found in Chapter 1, section 1.3.3.

RESULTS AND DISCUSSION

group of plateaus for each compound. The second column gathers those traces with more sloping plateaus (or less defined profiles in the case of **BNP**, third row). The third column shows the histograms of the traces with plateaus also in the minority conductance value. For **BNP**, this column contains traces displaying two plateaus, which agree with the two different conductance regions distinguished in the last section. For **BNA** and **CCA**, this column contains the histograms built from traces displaying plateaus at higher conductance values than the main signal. Probably because of their low occurring rate, this last group for **BNA** and **CCA** had remained imperceptible in the previous analysis, hidden in the tunneling background. For a better assessment of the distance of those signals, a gray vertical line indicating the expected plateau-length for the fully extended molecules between the electrodes is also shown in the histograms. This subdivision process revealed that the higher conductance signal, detected for **BNP**, was also present in **BNA** and **CCA** (Figure 3.15c and 3.15f), concluding that for the three studied compounds, **CCA**, **BNA** and **BNP**, plateaus can appear at two different conductance values.

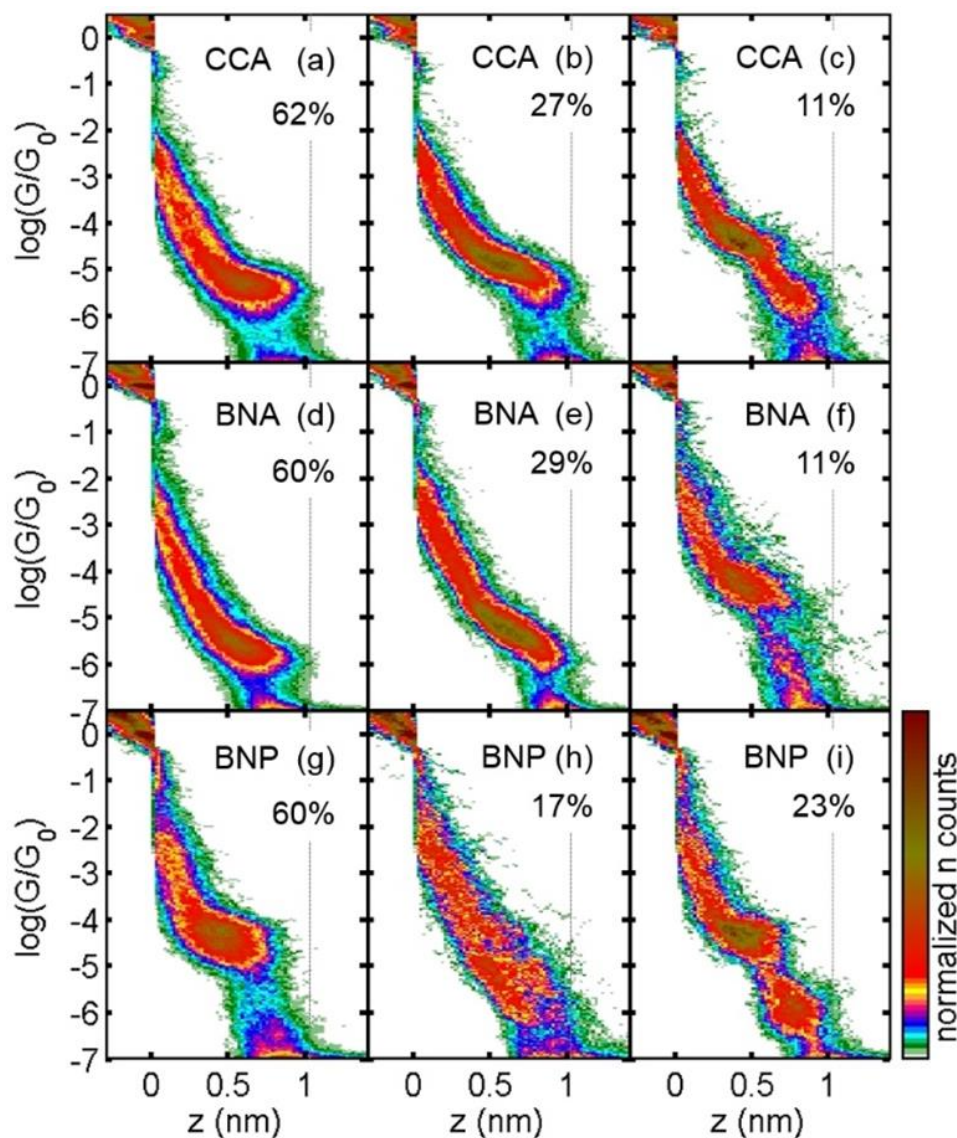


Figure 3.15. 2D Histograms of three groups of traces separated using a clustering process for CCA (a-c), BNA (d-f) and BNP (g-i).

Figure 3.16 shows the 1D histograms for every group of CCA, BNA and BNP, being the group of lower conductance in black, that of higher conductance in blue, and the remaining group in green. The first group (black lines) came from plateaus occurring between $\log(G/G_0) = -6$ and -5 , that reached the expected molecular-junction length for the fully extended compound between the electrodes, as shown in the plateau-length distributions of Figure 3.17. This separation also facilitated the extraction of a reliable typical molecular-junction conductance value from this group of traces. For that, a Gaussian was fitted to their symmetric peak in the corresponding 1D histograms (red dashed lines in Figure 3.16). The extracted conductance values are indicated in the top of

RESULTS AND DISCUSSION

the corresponding peaks, being the conductance values ordered as follows:

$$G_{CCA} > G_{BNA} > G_{BNP}.$$

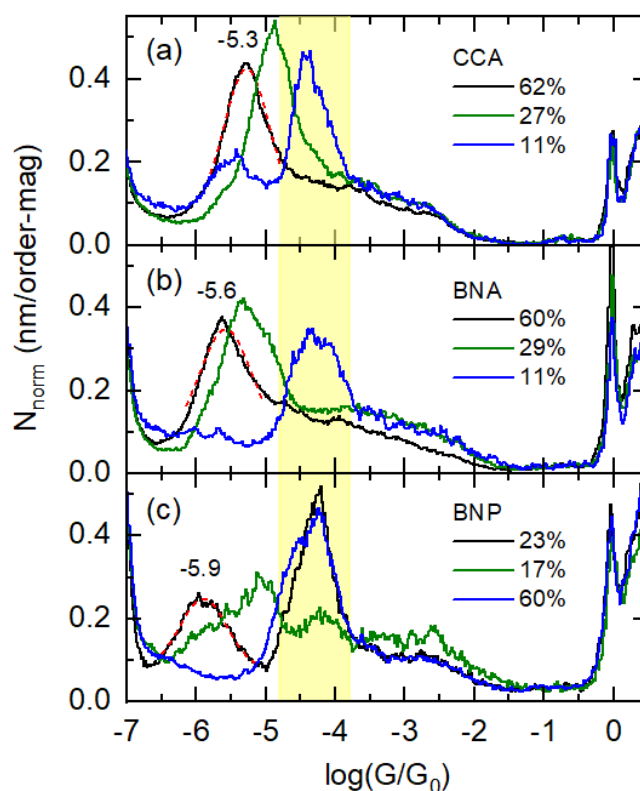


Figure 3.16. Conductance histograms of three groups of traces separated using a clustering process for **CCA (a)**, **BNA (b)** and **BNP (c)**. The Gaussian curve fitted to the lowest conductance peak for each compound is shown as a red dashed line, while its mean $\log(G/G_0)$ value is indicated on its top. The light-yellow band marks the conductance interval of the highest peak common to the three compounds, probably due to junctions with molecules interacting from the middle acene to one of the electrodes.

The second group (blue lines), common to all three compounds, is due to plateaus occurring between $\log(G/G_0) = -5$ and -4 (Figure 3.16), and typically 0.2 nm shorter than the corresponding to the fully extended molecule in the junction (See plateau-length distribution in Figure 3.17b). The shorter length of those plateaus, encouraged us to hypothesize that it could be due to junctions in which the molecules are not fully extended between the electrodes. Significantly, while the peak of lower conductance moves towards lower values according to the abovementioned trend, the peak at higher conductance stays rather constant. Only the occurring rate changes, being only a 10 % for **CCA** and **BNA**, while it represents the majority of the plateaus for **BNP** ($\approx 80\%$), showing that this kind of interaction seems to be favored for pentacene in contrast to anthracene.

As the distance is basically the same in the three molecules, the interaction originating these shorter plateaus seems to be due to one of the electrodes not interacting with the linker ($-SMe$), but directly with the acene itself. In this way, as the pentacene core involves a higher electron density, this interaction is favoured, increasing its occurring rate with respect the anthracene. An extra demonstration of this hypothesis is included in the next section.

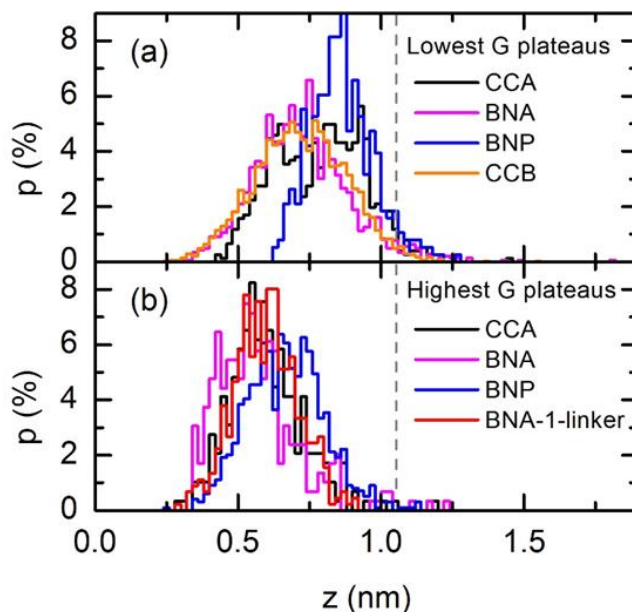


Figure 3.17. Plateau-length distribution for different groups of traces separated using a clustering process for compounds **CCA**, **BNA** and **BNP**. **(a)** Plateau-length distribution for the lowest conductance peaks, corresponding to histograms (a), (d) and (i) in Figure 3.15 (length interval between $G=0.5$ and $5 \cdot 10^{-7} G_0$).

The plateau-length distribution for **CCB** has been also added for comparison. **(b)** Plateau-length distribution for the highest conductance peak, corresponding to histograms (c), (f) and (g) in Figure 3.15 (length interval between $G=0.5$ and $8 \cdot 10^{-6} G_0$). The plateau-length distribution for **BNA-1-linker** has been also added for comparison.

3.3.3.5. Demonstrating the acene-gold interaction hypothesis

In order to probe the hypothesis consisting in the acene core as responsible for the higher conductance signal detected in **CCA**, **BNA** and **BNP**, single-molecule conductance measurements for compound **BNA-1-linker** were carried out. In this molecule, one of the terminal thiomethyl groups has been replaced by a methyl group, hindering the molecule full extension between the electrodes, *via* the minimum structural change in the target scaffold. The break-junction experiments resulted in a conductance signal that perfectly

RESULTS AND DISCUSSION

fitted in value (Figure 3.18) and length (Figure 3.17b, red line) with that generated by the shorter plateaus of **BNP**, **BNA** and **CCA**.

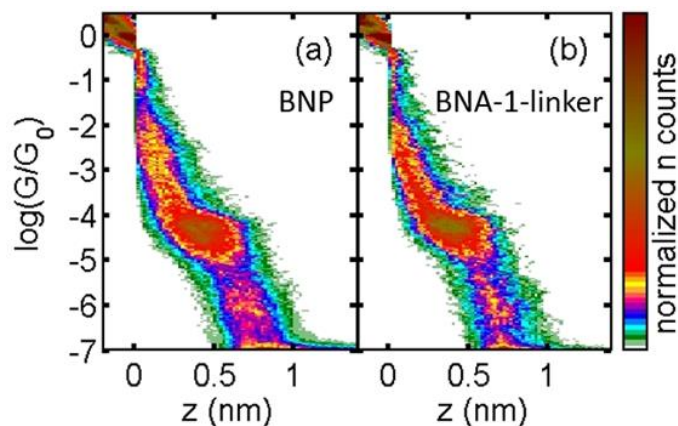


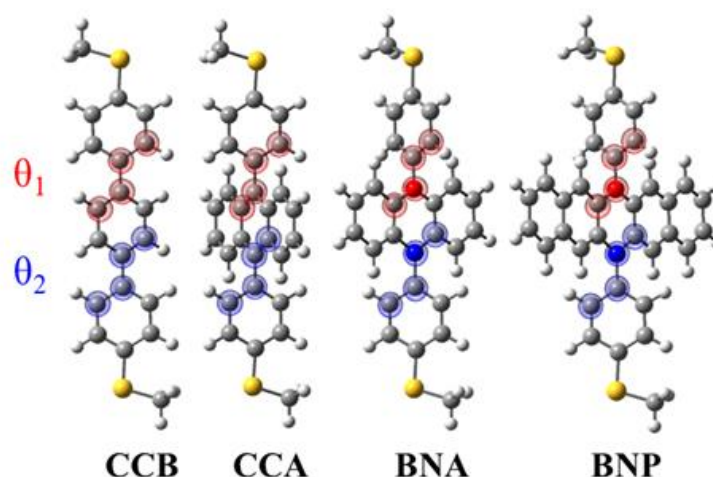
Figure 3.18. 2D conductance histogram for (a) **BNP** and (b) **BNA-1-linker**.

3.3.4. Theoretical modelling

In order to rationalize these experimental results, a collaboration with Fernando Martín's group from *Universidad Autónoma de Madrid* was developed.^d First-principles conductance simulations of the single-molecule **CCA**, **BNA**, and **BNP** junctions, with molecules fully extended between electrodes, were performed. Firstly, it was simulated the full relaxed geometry of each isolated molecule using Density Functional Theory (DFT) implemented in the code Gaussian09.⁶³ The optimized geometries were visualized as shown in Figure 3.19. From the analysis of these optimized structures, it was found that the dihedral angles in both sides of the acene motif are the same for the all-C molecules **CCB** and **CCA**, while they are different for the BN-doped molecules **BNA** and **BNP**. Interestingly, the change from benzene to anthracene in the central core involves a non-planar conformation, reducing the conjugation and the π -coupling between the two separate π -systems. Concerning the BN-doped molecules, the thiomethyl phenyl group next to the nitrogen atom is really close to be perpendicular (90°) to the acene central

^d More specifically, Dr. Sandra Rodríguez and Joel G. Fallaque (thesis in progress) were the direct responsible for carrying out the calculations.

core, while the same dihedral angle in the all-carbon counterpart (**CCA**) takes a value around 70°.



	Gas Phase				Single Molecule Junction			
	CCB	CCA	BNA	BNP	CCB	CCA	BNA	BNP
θ_1	33.8°	70.3°	90.1°	90.2°	33.1°	69.9°	90.9° (90.2°)	91.3° (90.4°)
θ_2	33.8°	70.3°	53.8°	53.6°	33.3°	69.8°	53.7° (53.5°)	53.7° (52.6°)

Figure 3.19. Schematic representation of the optimized geometries for **CCB**, **CCA**, **BNA** and **BNP** fully relaxed without any restriction. The dihedral angles between the central core and the thiomethyl phenyl groups have been highlighted and collected in the table. For molecules **CCB**, **CCA**, **BNA** and **BNP** in the gas phase, and in the single-molecule-junction, values for the (T-N-B-S)/ (T-B-N-S) polarizations are given outside/ inside parentheses, respectively.

Once the geometries were optimized, a combination of DFT and non-equilibrium Green's function (NEGFs) methodology was implemented in the TransSIESTA code²² in order to provide accurate energy positions of molecular states with respect to the junction Fermi level. Importantly, asymmetrical electrodes were modelled (Figure 3.20a), using a pyramidal electrode as tip and a flat surface with a gold adatom as substrate. Therefore, as BN and NB polarizations of the azaborine molecules with respect to the junction are equally probable in the experiment, we took into account both tip-N-B-substrate (T-N-B-S) and tip-B-N-substrate (T-B-N-S) orientations. The calculated transmission functions were very similar for both orientations in the energy window that is experimentally accessible with the applied bias voltage (0.16 V), which was in agreement with the *I-V* curve profiles analysed for **BNA** before, in section 3.3.2.1. The transmission functions for

RESULTS AND DISCUSSION

molecules **CCA**, **BNA** and **BNP** junctions, considering (T-N-B-S) and (T-B-N-S) orientations, are collected in Figure 3.20b. It can be observed a conductance reduction when going from **CCA** to **BNA** and **BNP** (Table 3.2), in agreement with the experimental results. As explained before, the change of dihedral angles due to the BN-substitution could be responsible for such conductance reduction for **BNA** and **BNP** in comparison with **CCA**. However the slightly different behaviour of **BNA** and **BNP** cannot be explained by differences in the angles, since the enlargement of the acene scaffold do not involve a change in the dihedral angles, as the optimized geometries (Figure 3.19) reveal.

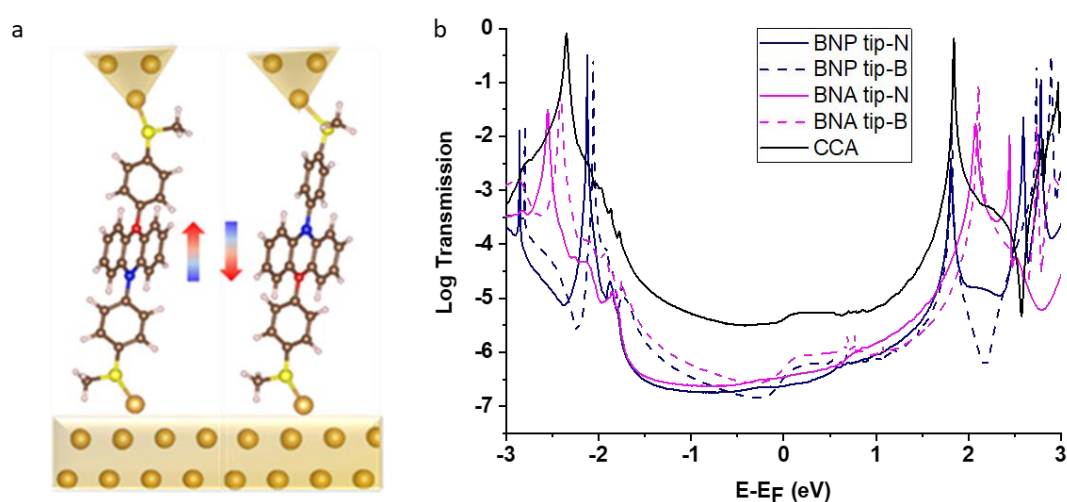


Figure 3.20. (a) Single molecule models for the **BNA** polarized junctions: T-N-B-S (left) and T-B-N-S (right). N: red; B: blue (b) Energy transmission function for compounds: **CCB** (orange), **CCA** (black), **BNA** (pink), and **BNP** (blue), in the T-N-B-S (solid line) and T-B-N-S (dashed line) polarization scenario.

Table 3.2. Calculated and experimentally measured conductance values ($\log(G/G_0)$) in the single molecule-junctions, and NICS (1.7)zz indexes for the central ring (in ppm) for **CCA**, **BNA** and **BNP**. Values for the (T-B-N-S) polarization are in parentheses.

Compound	CCA	BNA	BNP
$\log(G/G_0)_{DFT+\Sigma}$	-5.39	-6.46 (-6.30)	-6.62(-6.45)
$\log(G/G_0)_{exp.}$	-5.30 ± 0.31	-5.60 ± 0.33	5.90 ± 0.40
NICS(1.7)zz	-23.57	-12.54	-9.09

The role of aromaticity: calculation of Nuclear-Independent Chemical Shifts (NICS)

In an effort to understand the role of aromaticity in the conductance values, the Nucleus-Independent Chemical Shift (NICS) index have been calculated for each individual fused ring in **CCA**, **BNA** and **BNP**. Only out-of-plane contributions were evaluated, namely at 1.7 Å above the molecular plane (NICS (1.7)zz), which has been established as the optimal height where the π -contributions are of interest.^{64,65} Note here that, as explained in the General Introduction, the more negative NICS values, the more aromatic is the molecule. The calculated values (Table 3.3, FR column) show that the central ring, through which conductance mainly takes place, suffers a considerable loss of aromaticity after BN-substitution. Similarly, a slight decrease in aromaticity is obtained when going from **BNA** to **BNP**. Considering the trend for the conductance values and the latter results, it can be conclude that the aromaticity is playing a key role, as a higher aromaticity gives rise to a lower conductance. However, it is difficult to quantify this role, since the dihedral angles are clearly also taking part in the decrease of conductance. Therefore, additional conductance/NICS calculations were performed, in which the aforementioned angles in BN-substituted species are set to be identical to that of the all-carbon counterpart **CCA** (70.3°).

Table 3.3. Calculated NICS (1.7)zz indexes for **CCA**, **BNA** and **BNP** for the T-B-N-S polarization, considering both, fully relaxed (FR) and constrained dihedral angles (CDA) configurations. (T-B-N-S) polarization values are in parenthesis.

Ring	FR			CDA	
	CCA	BNA	BNP	BNA	BNP
Lateral ₁	---	---	-20.16 (-20.66)	---	-20.42 (-20.81)
Adjacent ₁	-19.53	-21.12 (-19.87)	-21.28 (-21.61)	-21.45 (-19.68)	-21.12 (-22.08)
Central	-24.53	-12.21 (-12.35)	- 8.61 (-8.28)	-12.34 (-12.42)	-8.68 (-8.91)
Adjacent ₂	-21.74	-19.86 (-21.03)	-21.86 (-21.06)	-19.66 (-21.43)	-21.93 (-21.24)
Lateral ₂	---	---	-20.48 (-20.31)	---	-20.92 (-20.32)

The results, show that the general conductance variation trend still remains, as shown in the transmission curves obtained for the forced structures (Figure 3.21), and considering that the calculated NICS values do not change from the relaxed to the forced structures (Table 3.3, FR column vs CDA column). This suggests that approximately half of the

RESULTS AND DISCUSSION

difference in the logarithm of the conductance between **CCA** and the BN-doped compounds can be accounted for by the angle variation, while the combination of experimental and theoretical data highlight the important effect of the aromaticity on the conductance of these compounds.

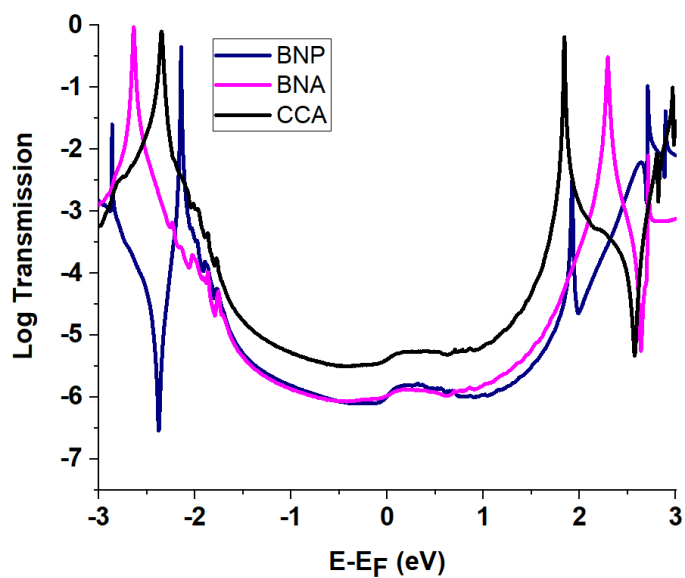


Figure 3.21. Energy transmission function for compounds **BNA** (pink), and **BNP** (blue) in a conformation in which the dihedral angles between rings are forced to be identical to that of the all-carbon counterpart **CCA** (black). Only curves for the T-N-B-S orientation are shown.

3.4. Conclusions

Based on the obtained results for this chapter, the following conclusions can be drawn:

- A smart design allowed the preparation of 1,4-azaborine anthracene-like derivative (**BNA**) incorporating linkers in positions that ensure the presence of the heteroatoms in the most favourable electron pathway
- The all-C anthracene counterpart (**CCA**), involving the same basic electron pathway, was also synthesized in order to facilitate a direct evaluation of the effect of the BN substitution.
- The same BN substitution was used as strategy for synthesizing the analogue 1,4-azaborine pentacene-like derivative (**BNP**). Remarkably, this BN analogue shows higher stability in ambient conditions than its highly unstable all-C counterpart which allowed the characterization of its electron properties.
- Single-molecule conductance of **BNA**, **BNP** and **CCA** were performed using the break-junction technique.
- The comparison of experimental results for **CCA** and **BNA** demonstrated that the 1,4-azaborine substitution in acene scaffolds gives rise to slightly lower conductance values, but still in the same order of magnitude, than that for the all-C analogue, being this results in agreement with the theoretical observed trend.
- The comparison of experimental results for **CCA** and its *p*-terphenyl-like counterpart revealed that the enlargement of the central unit, going from benzene to anthracene, involves a decrease of conductance of two orders of magnitude, pointing the theoretical studies at the constriction of dihedral angles as an important factor on this decrease.
- The results for **BNP** allowed to conclude that the laterally enlargement of the acene core from anthracene to pentacene does not have a remarkable influence in the conductance value.
- Calculated NICS (1.7)_{zz} indexes revealed that the CC-to-BN substitution involves a reduction of aromaticity in the corresponding ring that is an important cause for the slight decrease in the conductance of doped **BNA** and **BNP** with respect to pristine **CCA**.

REFERENCES

References

- (1) Stock, A.; Pohland, E. Borwasserstoffe, I. X.: $B_3N_3H_6$. *Ber. Dtsch. Chem. Ges.* **1926**, *59*, 2215–2223. <https://doi.org/10.1002/cber.19260590907>.
- (2) Islas, R.; Chamorro, E.; Robles, J.; Heine, T.; Santos, J. C.; Merino, G. Borazine: To Be or Not to Be Aromatic. *Struct. Chem.* **2007**, *18*, 833–839. <https://doi.org/10.1007/s11224-007-9229-z>.
- (3) Campbell, P. G.; Marwitz, A. J. V.; Liu, S. Y. Recent Advances in Azaborine Chemistry. *Angew. Chem. Int. Ed.* **2012**, *51*, 6074–6092. <https://doi.org/10.1002/anie.201200063>.
- (4) Baranac-Stojanović, M. Aromaticity and Stability of Azaborines. *Chem. Eur. J.* **2014**, *20*, 16558–16565. <https://doi.org/10.1002/chem.201402851>.
- (5) Baranac-Stojanović, M. Triplet-State Structures, Energies, and Antiaromaticity of BN Analogues of Benzene and Their Benzo-Fused Derivatives. *J. Org. Chem.* **2019**, *84*, 13582–13594. <https://doi.org/10.1021/acs.joc.9b01858>.
- (6) Bélanger-Chabot, G.; Braunschweig, H.; Roy, D. K. Recent Developments in Azaborinine Chemistry. *Eur. J. Inorg. Chem.* **2017**, 4353–4368. <https://doi.org/10.1002/ejic.201700562>.
- (7) Giustra, Z. X.; Liu, S. Y. The State of the Art in Azaborine Chemistry: New Synthetic Methods and Applications. *J. Am. Chem. Soc.* **2018**, *140*, 1184–1194. <https://doi.org/10.1021/jacs.7b09446>.
- (8) Ghosh, D.; Periyasamy, G.; Pati, S. K. Density Functional Theoretical Investigation of the Aromatic Nature of BN Substituted Benzene and Four Ring Polyaromatic Hydrocarbons. *Phys. Chem. Chem. Phys.* **2011**, *13*, 20627–20636. <https://doi.org/10.1039/c1cp22104c>.
- (9) Iwaki, R. A.; Udagawa, T. Effect of Heteroatoms on Aromaticity Analyzed by Geometric, Magnetic, and Electronic Criteria. *Chem. Phys. Lett.* **2020**, *745*, 137271. <https://doi.org/10.1016/j.cplett.2020.137271>.
- (10) Huang, J.; Li, Y. BN Embedded Polycyclic π -Conjugated Systems: Synthesis,

- Optoelectronic Properties, and Photovoltaic Applications. *Front. Chem.* **2018**, *6*, 341. <https://doi.org/10.3389/fchem.2018.00341>.
- (11) Dosso, J.; Battisti, T.; Ward, B. D.; Demitri, N.; Hughes, C. E.; Williams, P. A.; Harris, K. D. M.; Bonifazi, D. Boron–Nitrogen-Doped Nanographenes: A Synthetic Tale from Borazine Precursors. *Chem. Eur. J.* **2020**, *26*, 6608–6621. <https://doi.org/10.1002/chem.201905794>.
- (12) Chen, Y.; Chen, W.; Qiao, Y.; Lu, X.; Zhou, G. BN-Embedded Polycyclic Aromatic Hydrocarbon Oligomers: Synthesis, Aromaticity, and Reactivity. *Angew. Chem. Int. Ed.* **2020**, *59*, 7122–7130. <https://doi.org/10.1002/anie.202000556>.
- (13) Dewar, M. J. S.; Dietz, R. New Heteroaromatic Compounds. Part III. 2,1-Borazaro-Naphthalene (1,2-Dihydro-1-Axa-2-Boranaphthalene). *J. Chem. Soc.* **1959**, 2728–2730. <https://doi.org/10.1039/JR9590002728>.
- (14) Dewar, M. J. S.; Jones, R. New Heteroaromatic Compounds. XXVIII. Preparation and Properties of 10,9-Borazaronaphthalene. *J. Am. Chem. Soc.* **1968**, *90*, 2137–2144. <https://doi.org/10.1021/ja01010a601>.
- (15) Sun, F.; Lv, L.; Huang, M.; Zhou, Z.; Fang, X. Palladium-Catalyzed Cross-Coupling Reactions of 4a,8a-Azaboranaphthalene. *Org. Lett.* **2014**, *16*, 5024–5027. <https://doi.org/10.1021/ol502339h>.
- (16) Brown, A. N.; Li, B.; Liu, S. Y. Negishi Cross-Coupling Is Compatible with a Reactive B-Cl Bond: Development of a Versatile Late-Stage Functionalization of 1,2-Azaborines and Its Application to the Synthesis of New BN Isosteres of Naphthalene and Indenyl. *J. Am. Chem. Soc.* **2015**, *137*, 8932–8935. <https://doi.org/10.1021/jacs.5b05879>.
- (17) Liu, Z.; Ishibashi, J. S. A.; Darrigan, C.; Dargelos, A.; Chrostowska, A.; Li, B.; Vasiliu, M.; Dixon, D. A.; Liu, S. Y. The Least Stable Isomer of BN Naphthalene: Toward Predictive Trends for the Optoelectronic Properties of BN Acenes. *J. Am. Chem. Soc.* **2017**, *139*, 6082–6085. <https://doi.org/10.1021/jacs.7b02661>.
- (18) Stojanović, M.; Baranac-Stojanović, M. Mono BN-Substituted Analogues of Naphthalene: A Theoretical Analysis of the Effect of BN Position on Stability,

REFERENCES

- Aromaticity and Frontier Orbital Energies. *New J. Chem.* **2018**, *42*, 12968–12976. <https://doi.org/10.1039/c8nj01529e>.
- (19) Wisniewski, S. R.; Guenther, C. L.; Andreea Argintaru, O.; Molander, G. A. A Convergent, Modular Approach to Functionalized 2,1-Borazaronaphthalenes from 2-Aminostyrenes and Potassium Organotrifluoroborates. *J. Org. Chem.* **2014**, *79*, 365–378. <https://doi.org/10.1021/jo402616w>.
- (20) Liu, X.; Wu, P.; Li, J.; Cui, C. Synthesis of 1,2-Borazaronaphthalenes from Imines by Base-Promoted Borylation of C-H Bond. *J. Org. Chem.* **2015**, *80*, 3737–3744. <https://doi.org/10.1021/jo5029437>.
- (21) Dewar, M. J. S.; Kubba, V. P.; Pettit, R. New Heteroaromatic Compounds. Part I. 9-Aza-10-Bora-Phenanthrene. *J. Chem. Soc.* **1958**, 3073 – 3076. <https://doi.org/10.1039/JR9580003073>.
- (22) Bosdet, M. J. D.; Jaska, C. A.; Piers, W. E.; Sorensen, T. S.; Parvez, M. Blue Fluorescent 4a-Aza-4b-Boraphenanthrenes. *Org. Lett.* **2007**, *9*, 1395–1398. <https://doi.org/10.1021/ol070328y>.
- (23) Fu, Y.; Zhang, K.; Dmitrieva, E.; Liu, F.; Ma, J.; Weigand, J. J.; Popov, A. A.; Berger, R.; Pisula, W.; Liu, J.; Feng, X. NBN-Embedded Polycyclic Aromatic Hydrocarbons Containing Pentagonal and Heptagonal Rings. *Org. Lett.* **2019**, *21*, 1354–1358. <https://doi.org/10.1021/acs.orglett.9b00057>.
- (24) Ishibashi, J. S. A.; Marshall, J. L.; Mazière, A.; Lovinger, G. J.; Li, B.; Zakharov, L. N.; Dargelos, A.; Graciaa, A.; Chrostowska, A.; Liu, S. Y. Two BN Isosteres of Anthracene: Synthesis and Characterization. *J. Am. Chem. Soc.* **2014**, *136*, 15414–15421. <https://doi.org/10.1021/ja508813v>.
- (25) Wang, X. Y.; Zhuang, F. D.; Wang, R. B.; Wang, X. C.; Cao, X. Y.; Wang, J. Y.; Pei, J. A Straightforward Strategy toward Large BN-Embedded π -Systems: Synthesis, Structure, and Optoelectronic Properties of Extended BN Heterosuperbenzenes. *J. Am. Chem. Soc.* **2014**, *136*, 3764–3767. <https://doi.org/10.1021/ja500117z>.
- (26) Wang, X. Y.; Wang, J. Y.; Pei, J. BN Heterosuperbenzenes: Synthesis and Properties. *Chem. Eur. J.* **2015**, *21*, 3528–3539. <https://doi.org/10.1002/chem.201405627>.

- (27) Stępień, M.; Gońka, E.; Żyła, M.; Sprutta, N. Heterocyclic Nanographenes and Other Polycyclic Heteroaromatic Compounds: Synthetic Routes, Properties, and Applications. *Chem. Rev.* **2017**, *117*, 3479–3716. <https://doi.org/10.1021/acs.chemrev.6b00076>.
- (28) Xu, S.; Zakharov, L. N.; Liu, S. Y. A 1,3-Dihydro-1,3-Azaborine Debuts. *J. Am. Chem. Soc.* **2011**, *133*, 20152–20155. <https://doi.org/10.1021/ja2097089>.
- (29) Xu, S.; Mikulas, T. C.; Zakharov, L. N.; Dixon, D. A.; Liu, S. Y. Boron-Substituted 1,3-Dihydro-1,3-Azaborines: Synthesis, Structure, and Evaluation of Aromaticity. *Angew. Chem. Int. Ed.* **2013**, *52*, 7527–7531. <https://doi.org/10.1002/anie.201302660>.
- (30) Chrostowska, A.; Xu, S.; Lamm, A. N.; Mazière, A.; Weber, C. D.; Dargelos, A.; Baylère, P.; Graciaa, A.; Liu, S. Y. UV-Photoelectron Spectroscopy of 1,2- and 1,3-Azaborines: A Combined Experimental and Computational Electronic Structure Analysis. *J. Am. Chem. Soc.* **2012**, *134*, 10279–10285. <https://doi.org/10.1021/ja303595z>.
- (31) Li, J.; Daniliuc, C. G.; Mück-Lichtenfeld, C.; Kehr, G.; Erker, G. Multi-Component Synthesis of Rare 1,3-Dihydro-1,3-azaborinine Derivatives: Application of a Bora-Nazarov Type Reaction. *Angew. Chem. Int. Ed.* **2019**, *58*, 15377–15380. <https://doi.org/10.1002/anie.201909530>.
- (32) Maitlis, P. M. New Heteroaromatic Compounds. Part IX. Some 10,9-Borazaroanthracenet. *J. Chem. Soc.* **1961**, 425–429. <https://doi.org/10.1039/JR9610000425>.
- (33) Kranz, M.; Hampel, F.; Clark, T. N-Methyl-B-Mesityldibenzo-1,4-Azaborinine: The First Experimental Structure of a 1,4-Aza Borinine Derivative. *J. Chem. Soc.* **1992**, 1247–1248.
- (34) Agou, T.; Arai, H.; Kawashima, T. Synthesis, Structure, and Properties of a Dinaphthoazaborine. *Chem. Lett.* **2010**, *39*, 612–613. <https://doi.org/10.1246/cl.2010.612>.
- (35) Agou, T.; Sekine, M.; Kobayashi, J.; Kawashima, T. Synthesis and Reactivity of a

REFERENCES

- Bis(Dimesitylboryl)Azaborine and Its Fluoride Sensing Ability. *Chem. Commun.* **2009**, No. 14, 1894–1896. <https://doi.org/10.1039/b818505k>.
- (36) Agou, T.; Kobayashi, J.; Kawashima, T. Syntheses, Structure, and Optical Properties of Ladder-Type Fused Azaborines. *Org. Lett.* **2006**, *8*, 2241–2244. <https://doi.org/10.1021/ol060539n>.
- (37) Liu, X.; Zhang, Y.; Li, B.; Zakharov, L. N.; Vasiliu, M.; Dixon, D. A.; Liu, S.-Y. A Modular Synthetic Approach to Monocyclic 1,4-Azaborines. *Angew. Chem. Int. Ed.* **2016**, *55*, 8333–8337. <https://doi.org/10.1002/anie.201602840>.
- (38) Zhao, Z.-H.; Wang, L.; Li, S.; Zhang, W.-D.; He, G.; Wang, D.; Hou, S.-M.; Wan, L.-J. Single-Molecule Conductance through an Isoelectronic B-N Substituted Phenanthrene Junction. *J. Am. Chem. Soc.* **2020**, *142*, 8068–8073. <https://doi.org/10.1021/jacs.0c00879>.
- (39) Chen, W.; Li, H.; Widawsky, J. R.; Appayee, C.; Venkataraman, L.; Breslow, R. Aromaticity Decreases Single-Molecule Junction Conductance. *J. Am. Chem. Soc.* **2014**, *136*, 918–920. <https://doi.org/10.1021/ja411143s>.
- (40) Klausen, R. S.; Widawsky, J. R.; Su, T. A.; Li, H.; Chen, Q.; Steigerwald, M. L.; Venkataraman, L.; Nuckolls, C. Evaluating Atomic Components in Fluorene Wires. *Chem. Sci.* **2014**, *5*, 1561–1564. <https://doi.org/10.1039/c4sc00064a>.
- (41) Ismael, A. K.; Wang, K.; Vezzoli, A.; Al-Khaykane, M. K.; Gallagher, H. E.; Grace, I. M.; Lambert, C. J.; Xu, B.; Nichols, R. J.; Higgins, S. J. Side-Group-Mediated Mechanical Conductance Switching in Molecular Junctions. *Angew. Chem. Int. Ed.* **2017**, *56*, 15378–15382. <https://doi.org/10.1002/anie.201709419>.
- (42) Wang, Y. H.; Huang, H.; Yu, Z.; Zheng, J. F.; Shao, Y.; Zhou, X. S.; Chen, J. Z.; Li, J. F. Modulating Electron Transport through Single-Molecule Junctions by Heteroatom Substitution. *J. Mater. Chem. C* **2020**, *8*, 6826–6831. <https://doi.org/10.1039/d0tc00256a>.
- (43) Su, T. A.; Li, H.; Klausen, R. S.; Widawsky, J. R.; Batra, A.; Steigerwald, M. L.; Venkataraman, L.; Nuckolls, C. Tuning Conductance in π - σ - π Single-Molecule Wires. *J. Am. Chem. Soc.* **2016**, *138*, 7791–7795.

<https://doi.org/10.1021/jacs.6b04394>.

- (44) Naibi Lakshminarayana, A.; Ong, A.; Chi, C. Modification of Acenes for N-Channel OFET Materials. *J. Mater. Chem. C* **2018**, *6*, 3551–3563. <https://doi.org/10.1039/c8tc00146d>.
- (45) Anthony, J. E. The Larger Acenes: Versatile Organic Semiconductors. *Angew. Chem. Int. Ed.* **2008**, *47*, 452–483. <https://doi.org/10.1002/anie.200604045>.
- (46) Quinn, J. R.; Foss, F. W.; Venkataraman, L.; Hybertsen, M. S.; Breslow, R. Single-Molecule Junction Conductance through Diaminoacenes. *J. Am. Chem. Soc.* **2007**, *129*, 6714–6715. <https://doi.org/10.1021/ja0715804>.
- (47) Kaliginedi, V.; Moreno-García, P.; Valkenier, H.; Hong, W.; García-Suárez, V. M.; Buitter, P.; Otten, J. L. H.; Hummelen, J. C.; Lambert, C. J.; Wandlowski, T. Correlations between Molecular Structure and Single-Junction Conductance: A Case Study with Oligo(Phenylene-Ethynylene)-Type Wires. *J. Am. Chem. Soc.* **2012**, *134*, 5262–5275. <https://doi.org/10.1021/ja211555x>.
- (48) Liu, Y.; Ornago, L.; Carlotti, M.; Ai, Y.; El Abbassi, M.; Soni, S.; Asyuda, A.; Zharnikov, M.; van der Zant, H. S. J.; Chiechi, R. C. Intermolecular Effects on Tunneling through Acenes in Large-Area and Single-Molecule Junctions. *J. Phys. Chem. C* **2020**, *124*, 22776–22783. <https://doi.org/10.1021/acs.jpcc.0c05781>.
- (49) Kihira, Y.; Shimada, T.; Matsuo, Y.; Nakamura, E.; Hasegawa, T. Random Telegraphic Conductance Fluctuation at Au-Pentacene-Au Nanojunctions. *Nano Lett.* **2009**, *9*, 1442–1446. <https://doi.org/10.1021/nl803284t>.
- (50) Liu, C.; Kaneko, S.; Komoto, Y.; Fujii, S.; Kiguchi, M. Highly Conductive Single Naphthalene and Anthracene Molecular Junction with Well-Defined Conductance. *Appl. Phys. Lett.* **2015**, *106*, 103103. <https://doi.org/10.1063/1.4914501>.
- (51) Yelin, T.; Korytár, R.; Sukenik, N.; Vardimon, R.; Kumar, B.; Nuckolls, C.; Evers, F.; Tal, O. Conductance Saturation in a Series of Highly Transmitting Molecular Junctions. *Nat. Mater.* **2016**, *15*, 444–449. <https://doi.org/10.1038/nmat4552>.
- (52) Bendikov, M.; Duong, H. M.; Starkey, K.; Houk, K. N.; Carter, E. A.; Wudl, F.

REFERENCES

- Oligoacenes: Theoretical Prediction of Open-Shell Singlet Diradical Ground States. *J. Am. Chem. Soc.* **2004**, *126*, 7416–7417. <https://doi.org/10.1021/ja048919w>.
- (53) Yang, Y.; Davidson, E. R.; Yang, W. Nature of Ground and Electronic Excited States of Higher Acenes. *Proc. Natl. Acad. Sci. U. S. A.* **2016**, *113*, E5098–E5107. <https://doi.org/10.1073/pnas.1606021113>.
- (54) Zhuang, F.; Sun, Z.; Yao, Z.; Chen, Q.; Huang, Z.; Yang, J.; Wang, J.; Pei, J. BN-Embedded Tetrabenzopentacene: A Pentacene Derivative with Improved Stability. *Angew. Chem. Int. Ed.* **2019**, *58*, 10708–10712. <https://doi.org/10.1002/anie.201905601>.
- (55) Kaur, I.; Jia, W.; Kopreski, R. P.; Selvarasah, S.; Dokmeci, M. R.; Pramanik, C.; McGruer, N. E.; Miller, G. P. Substituent Effects in Pentacenes: Gaining Control over HOMO-LUMO Gaps and Photooxidative Resistances. *J. Am. Chem. Soc.* **2008**, *130*, 16274–16286. <https://doi.org/10.1021/ja804515y>.
- (56) Leary, E.; La Rosa, A.; González, M. T.; Rubio-Bollinger, G.; Agraït, N.; Martín, N. Incorporating Single Molecules into Electrical Circuits. the Role of the Chemical Anchoring Group. *Chem. Soc. Rev.* **2015**, *44*, 920–942. <https://doi.org/10.1039/c4cs00264d>.
- (57) Su, T. A.; Neupane, M.; Steigerwald, M. L.; Venkataraman, L.; Nuckolls, C. Chemical Principles of Single-Molecule Electronics. *Nat. Rev. Mater.* **2016**, *1*, 16002. <https://doi.org/10.1038/natrevmats.2016.2>.
- (58) Moreno-García, P.; La Rosa, A.; Kolivoška, V.; Bermejo, D.; Hong, W.; Yoshida, K.; Baghernejad, M.; Filippone, S.; Broekmann, P.; Wandlowski, T.; Martín, N. Charge Transport in C60-Based Dumbbell-Type Molecules: Mechanically Induced Switching between Two Distinct Conductance States. *J. Am. Chem. Soc.* **2015**, *137*, 2318–2327. <https://doi.org/10.1021/ja511271e>.
- (59) Guo, S.; Hihath, J.; Díez-Pérez, I.; Tao, N. Measurement and Statistical Analysis of Single-Molecule Current-Voltage Characteristics, Transition Voltage Spectroscopy, and Tunneling Barrier Height. *J. Am. Chem. Soc.* **2011**, *133*, 19189–19197. <https://doi.org/10.1021/ja2076857>.

- (60) Koepf, M.; Koenigsmann, C.; Ding, W.; Batra, A.; Negre, C. F. A.; Venkataraman, L.; Brudvig, G. W.; Batista, V. S.; Schmuttenmaer, C. A.; Crabtree, R. H. Controlling the Rectification Properties of Molecular Junctions through Molecule-Electrode Coupling. *Nanoscale* **2016**, *8*, 16357–16362. <https://doi.org/10.1039/c6nr04830g>.
- (61) Sacchetti, V.; Ramos-Soriano, J.; Illescas, B. M.; González, M. T.; Li, D.; Palomino-Ruiz, L.; Márquez, I. R.; Leary, E.; Rubio-Bollinger, G.; Pauly, F.; Agraït, N.; Martín, N. Effect of Charge-Assisted Hydrogen Bonds on Single-Molecule Electron Transport. *J. Phys. Chem. C* **2019**, *123*, 29386–29393. <https://doi.org/10.1021/acs.jpcc.9b06850>.
- (62) Quinn, J. R.; Foss, F. W.; Venkataraman, L.; Breslow, R. Oxidation Potentials Correlate with Conductivities of Aromatic Molecular Wires. *J. Am. Chem. Soc.* **2007**, *129*, 12376–12377. <https://doi.org/10.1021/ja0745097>.
- (63) Frisch, M. J.; Trucks, G. W.; Schlegel, H. B.; G. E., S.; Robb, M. A.; Cheeseman, J. R.; Scalmani, G.; Barone, V.; Petersson, G. A.; Nakatsuji, H.; Li, X.; Caricato, M.; Marenich, A. V.; Bloino, J.; Janesko, B. G.; Gomperts, R.; Mennucci, B.; Hratchian, H. P.; Ortiz, J. V.; Izmaylov, A. F.; Sonnenberg, J. L.; Williams-Young, D.; Ding, F.; Lipparini, F.; Egidi, F.; Goings, J.; Peng, B.; Petrone, A.; Henderson, T.; Ranasinghe, D.; Zakrzewski, V. G.; Gao, J. N.; Rega, G. Gaussian Inc., Wallingford CT. **2016**.
- (64) Stanger, A. Obtaining Relative Induced Ring Currents Quantitatively from NICS. *J. Org. Chem.* **2010**, *75*, 2281–2288. <https://doi.org/10.1021/jo1000753>.
- (65) Gershoni-Poranne, R.; Stanger, A. The NICS-XY-Scan: Identification of Local and Global Ring Currents in Multi-Ring Systems. *Chem. Eur. J.* **2014**, *20*, 5673–5688. <https://doi.org/10.1002/chem.201304307>.

CHAPTER 4:
ELECTRON TRANSPORT THROUGH CURVED
HEPTAGON-CONTAINING NANOGRAFHENES

4.1. Introduction

Nanographenes are graphene fragments ranging from 1 to 100 nm, according to the classification proposed by K. Müllen and co-workers and shown in Figure 4.1.¹ This term includes different structures such as polycyclic aromatic hydrocarbons (PAHs), graphene quantum dots (GQDs) and graphene nanoribbons (GNRs). With the same basic structure of graphene, the skeleton of these molecules is also based in a network of fused benzene rings. Each C atom presents sp^2 hybridization and is directly bonded with other three identical atoms through σ -bonds. The sp^2 hybridization leads to a trigonal planar structure and the non-hybridized p orbital, perpendicular to the σ bonds, takes part on a π -bond that gives rise to a delocalized π orbital along the surface. In particular, hexa-*peri*-hexabenzocoronene (HBC), a PAH consisting in 13 fused benzene rings and its related structures are considered the smallest type of possible nanographenes.

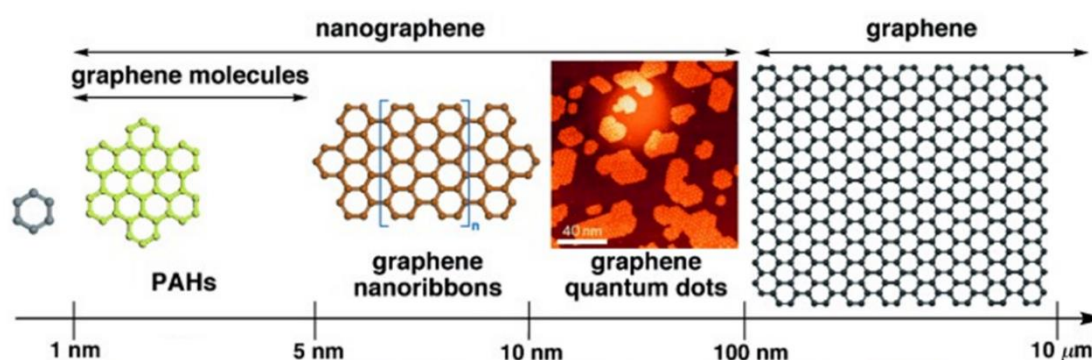


Figure 4.1. Graphene terminology defined according to the size scale of the materials. Reproduced with permission from ref.¹ Copyright © 2012 WILEY-VCH Verlag GmbH & Co. KGaA, Weinheim

Although graphene molecules are a well-known family in chemistry, the interest in these structures has increased in recent decades as they can serve as model systems for studying graphene. In this sense, nanographenes have been suggested to be better candidates for nanoelectronics than graphene since they have non-zero bandgaps due to their reduced size. This is in contrast to graphene, a semiconductor of zero bandgap, whose applicability in digital-logic-based electronics is reduced, as devices could not be switched off.² This growing interest has entailed a great synthetic effort focussed on the

INTRODUCTION

development of strategies for preparing ever larger and more intricate well-defined nanographenes, with great potential in nanoelectronics, optoelectronics and spintronics.

Another strategy for opening the bandgap in graphene is the introduction of topological defects in its structure. Those defects can be deliberately generated by electronic beam impacts or chemical treatment, but may also appear unexpectedly during its growth and/or processing. Defects break the integrity and symmetry of graphene lattices, modifying their topology, creating curvature and changing the electronic structure of graphene, what, consequently, alters its mechanical, thermal, optical and electrical properties.³ In this sense, the synthesis and study of nanographenes incorporating defects in a controlled manner can help in the establishment of unequivocal defect-properties relationships in graphene-like structures. This information might be useful for a controlled tuning of nanographenes properties, as well as for elucidating the influence of those defects in defective large-area graphene.

Microscopy techniques, such as transmission electron microscopy (TEM) and scanning tunneling microscopy (STM) have provided images of defective graphene with atomic resolution, revealing the existence of different kinds of defect which have been extensively reviewed.⁴⁻⁷ Structural defects can be classify in different ways. They can be extrinsic or intrinsic, depending on if the crystalline order is perturbed with or without the presence of foreign atoms, respectively. Another way to classify them is depending on their distribution and situation in the sheet: zero-dimensional (point) or one-dimensional (line) defects. Between the most common defects, it highlights:

- i) Dopants, which can substitute a C atom or interact with the lattice using the third dimension (Figure 4.2a). Nitrogen and boron are the most frequent dopants since they can form three chemical bonds, replacing any carbon atom. The doping with metals is also of interest, as it means an injection of charge into the electron system of graphene.
- ii) Non-hexagonal rings (pentagons, heptagons and octagons, among others and combinations of them), whose formation is originated by point defects such as C adatoms (Figure 4.2b), vacancies (Figure 4.2c) or even just odd rearrangements of the C atoms in the hexagonal lattice (Figure 4.2d). They can also be originated as consequence of line defects such as disclinations

(Figure 4.2e). Note that the formation of non-hexagonal rings usually promotes distortion on the lattice, leading to curved structures.

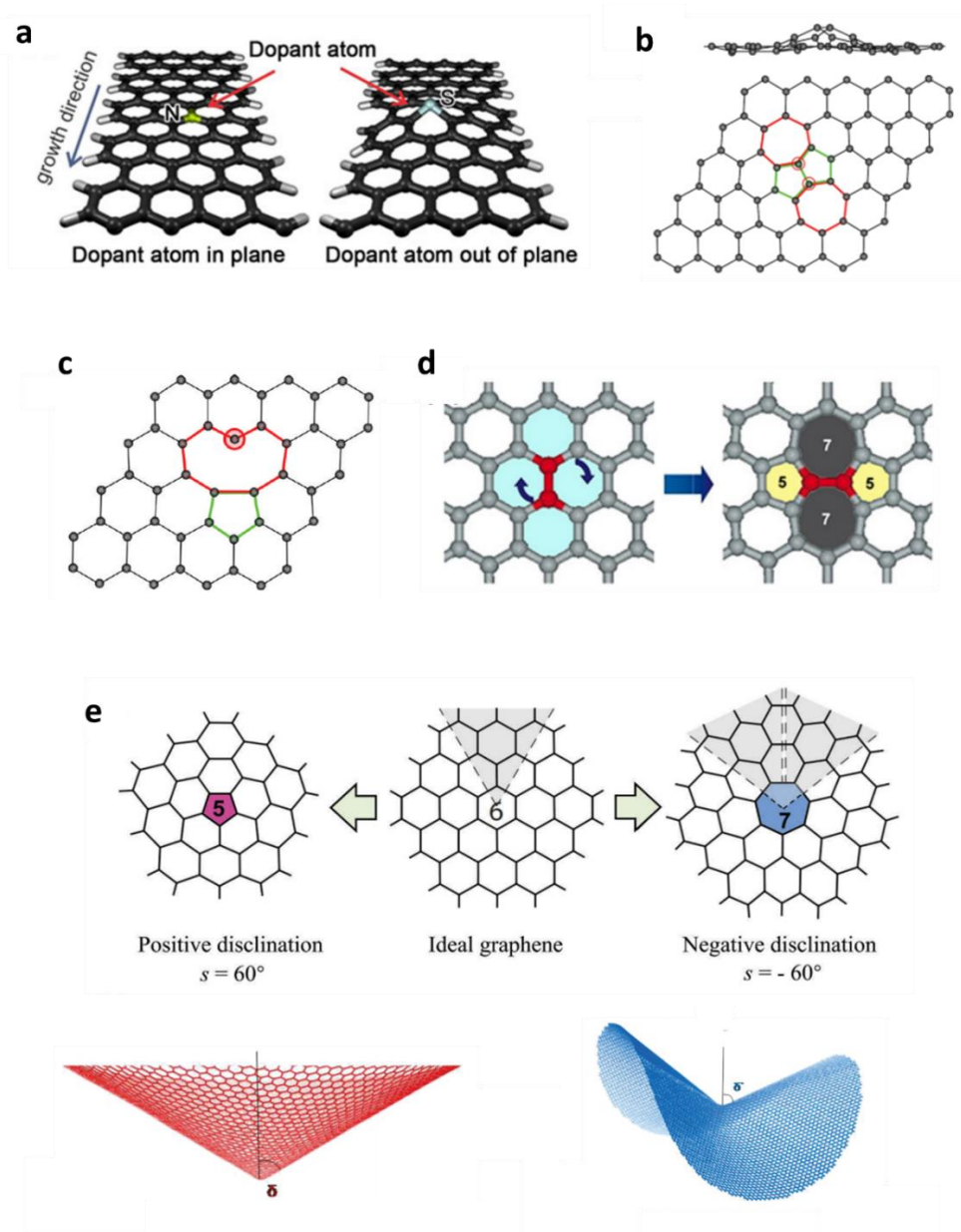


Figure 4.2. Some of the structural defects found in graphene. **(a)** Dopants in and out of plane. **(b-d)** non-hexagonal rings formed by a C adatom, a vacancy and rearrangement of C atoms without any introduction or removal, respectively. **(e)** Non-hexagonal rings originated by disclinations, topological defects obtained by removing and adding a semi-infinite wedge to a perfect graphene lattice. Positive disclinations originate 5-membered rings and involved a positive curvature in the lattice. Negative disclinations originate 7-membered rings and involved a negative curvature in the lattice. Panels **(a)** and **(d)** are reproduced with permission of ref.³ Copyright © 2012 IOP Publishing Ltd. Panels **(b)** and **(c)** are reproduced with permission of ref.⁵ Copyright © 2010 American Chemical Society. Panel **(e)** have been composed from images used with permission of ref.⁴ Copyright © 2010 American Physical Society and ref.⁸ Copyright © 2010 American Chemical Society.

INTRODUCTION

Since the azaborine-acenes scaffolds studied in Chapter 3 can be considered as simple BN-doped nanographenes, this chapter is focused on nanographenes containing non-hexagonal rings, more specifically 7-membered rings.

4.1.1. Preparation of nanographenes

Nanographenes can be prepared by top-down or bottom-up methodologies. Those two terms make reference to the nature of the starting material. Top-down strategies use macroscopic starting materials, involving a dimensional reduction of the precursors, for example from 2D graphene or carbon nanotubes (CNTs) to smaller graphene molecules. Bottom-up strategies are based on the use of molecular building blocks such as low molecular weight hydrocarbons, involving a dimensional increase of the precursors.

4.1.1.1. Top-down methods

GQDs are typically prepared by cutting graphene sheets into nanoscale graphene fragments by means of electron-beam lithography. It permits the preparation of small graphene fragments with desired geometries, but it requires complex processes that hinder the projection of this technique on a large scale. However, GQDs have been obtained in large quantities, using a hydrothermal method to cut graphene sheets into ~10 nm-sized flakes, by cage-opening of fullerenes (C₆₀) or fragmentation of double-walled CNTs through chemical oxidation.⁹

In the case of GNR, the two major top-down methods for its fabrication are cutting graphene sheets by nanolithography (scanning tunnelling microscopy, electron-beam lithography and helium-ion-beam lithography) and unzipping of CNTs.¹⁰ GNRs with various widths (~2–60 nm) were also successfully achieved by sonicating expanded graphite in a 1,2-dichloroethane solution of poly(*m*-phenylene)-co-(2,5-dioctoxy-*p*-phenylenevinylene) (PmPV).⁹

However, the precision in the obtained structures depends on the resolution of the technique. For example, in electron-beam lithography the resolution results in an effective beam width from 15 to 20 nm, what is very wide considering that the C–C bond length in graphene is ~0.1 nm.¹¹ Therefore, achieving atomically precise and uniform

graphene nanostructures, especially with sizes and/ or widths as narrow as 1–3 nm, by means of top-down methods still represents a challenge.

4.1.1.2. Bottom-up methods

Bottom-up strategies are characterized by affording an exquisite control of edges, size and shape of the final nanostructures. The versatility of bottom-up methods also allows inclusion of non-hexagonal rings^{12–14}, dopants^{13,15,16} and helical moieties^{17,18} on nanographenes, in a controlled manner and at selected positions. Therefore, novel structures presenting remarkable distortion and twists have been successfully prepared, as well as heteroatom-doped scaffolds tuning the optoelectronic properties to the pristine structures without changing the conjugated skeleton. In this sense, those defective structures can result in reliable models for studying the influence of those defects in graphene properties.

Within the bottom-up strategies for the chemical synthesis of nanographenes, two different methodologies can be found: on-surface and in-solution synthesis. The first one commonly requires sublimation of previously prepared precursors in conditions of ultra-high vacuum (UHV), reaching pressures of up to 10^{10} bars. Next, it is required the adsorption of precursors onto a metallic surface.¹⁹ The final step on the on-surface synthesis is to provide the required energy to induce the desired chemical reaction. The energy is usually thermal, although the metallic surface can act as catalyst, reducing the amount of energy needed to trigger the reactions. In any case, the required temperature directly depends on the desired reactions. On-surface synthesis has resulted a powerful tool especially for the preparation of a plethora of nanoribbons with different shapes and lengths (Figure 4.3).^{20,21}

Concerning the in-solution synthesis, a major problem to overcome is the low solubility of final nanographene molecules. However, as in-solution strategies permit a smart design of the synthetic route toward the final structure, alkyl chains can be introduced into the periphery of the molecule in order to increase the solubility and avoid aggregation processes.

INTRODUCTION

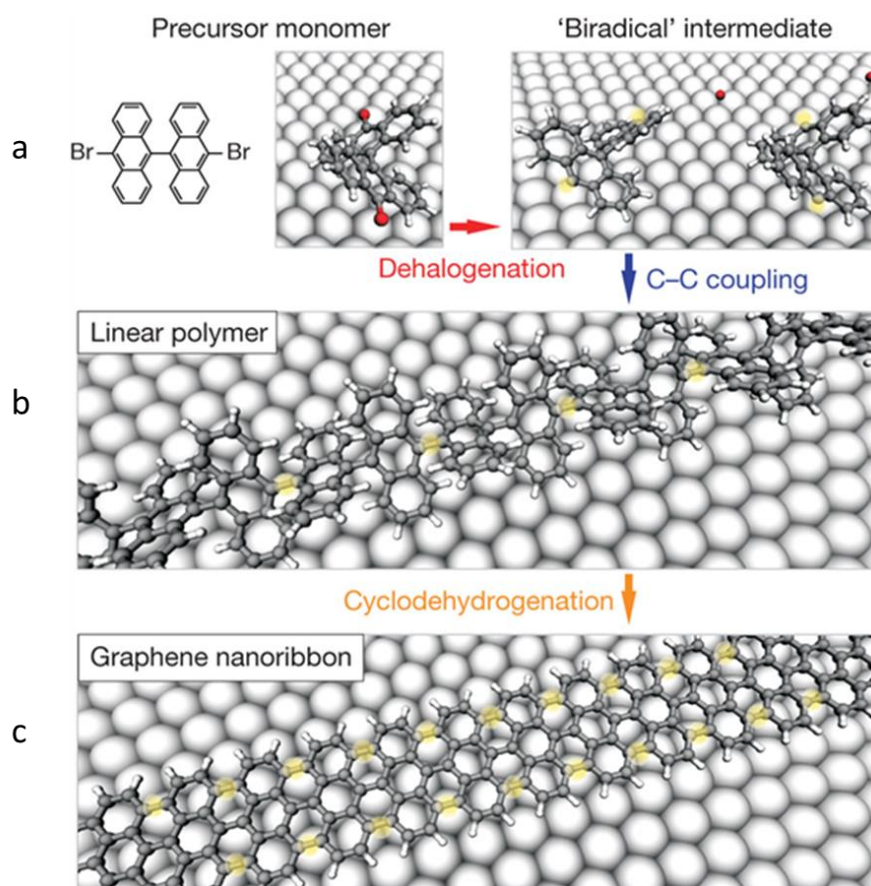


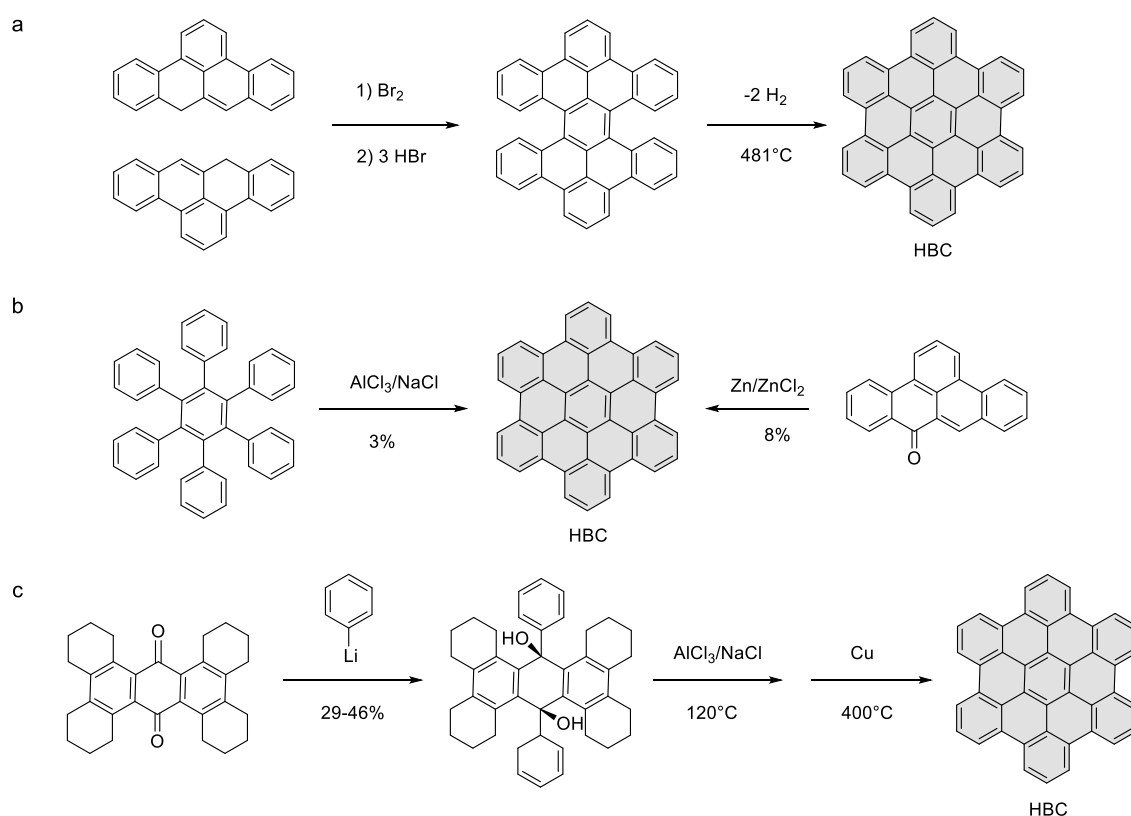
Figure 4.3. Basic steps for the surface-assisted synthesis of graphene nanoribbons, using as example the synthesis of an armchair nanoribbon from precursor 10,10'-dibromo-9,9'-bianthryl. **(a)** Dehalogenation during adsorption of the precursor monomers. **(b)** Formation of linear polymers by covalent interlinking of the dehalogenated intermediates. **(c)** Formation of fully aromatic GNRs by cyclodehydrogenation. Adapted with permission from ref. ²⁰ Copyright © 2010 Springer Nature.

The molecules studied on this chapter were prepared by means of bottom-up in solution methods. Therefore, the next sections are dedicated to the main synthetic strategies for the in-solution preparation of planar and distorted nanographenes from simple and small starting materials.

4.1.1.3. In-solution synthesis of purely hexagonal nanographenes

A great variety of reactions have been used for the synthesis of PAHs since the first works developed by the groups of Scholl^{22,23} and Clar^{24,25} at the beginning of the last century. Indeed, it is common to find in literature that several approaches toward the same aromatic core have been reported along years, as new methodologies were developed or different starting materials become accessible. This evolution can be easily

appreciated in the case of hexa-*peri*-hexabenzocoronene (HBC). For this scaffold, it is possible to find synthetic routes based on very diverse reactions.²⁶ The first proposed approaches toward HBC are shown in Scheme 4.1. One of them was presented by Clar and co-workers in 1959,²⁴ *via* dimerization of dibenzo-*peri*-naphthene (Scheme 4.1a). Practically at the same time, Halleux and collaborators reported two completely different methods toward HBC²⁷ (Scheme 4.1b), using i) cyclodehydrogenation of hexaphenylbenzene by treatment with AlCl₃ and NaCl, or ii) self-condensation of dibenz[1,9;2,3]anthrone using the combination Zn/ZnCl₂. In 1986, Schmidt and co-workers presented a new approach, based on the addition of organometallic compounds to benzoquinone derivatives, as shown in Scheme 4.1c. The product was subsequently cyclized in melt AlCl₃/NaCl and then subjected to aromatization with Cu toward the desired HBC structure.²⁸



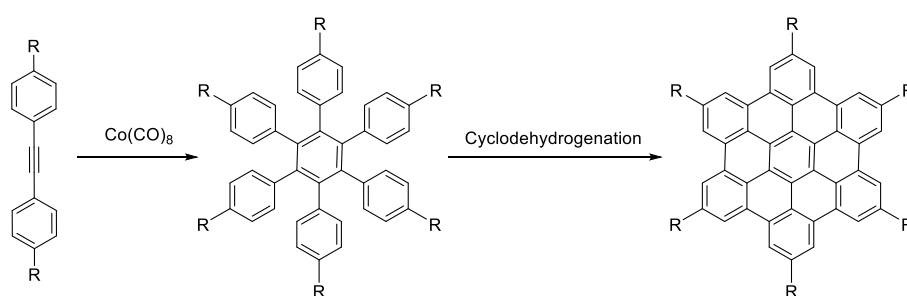
Scheme 4.1. First approaches toward HBC

INTRODUCTION

Nowadays, the general method for the preparation of HBC-based nanographenes is based in two key steps: i) formation of oligophenylene precursors of various sizes and shapes by means of either cyclotrimerization reaction of suitable building blocks or Diels–Alder reaction, followed by ii) cyclodehydrogenation reaction for the planarization and aromatization of the oligophenylene precursors, using Lewis acids/oxidants. These methods are described below:

- Preparation of oligophenylene precursors *via* alkyne cyclotrimerization reaction.

The cyclotrimerization reaction of functionalized diphenylacetylenes precursors constitutes a case of [2+2+2] cycloaddition. It is mediated by cobalt, rhodium or iridium complexes of type CpML_2 ($\text{L} = \text{CO}, \text{PR}_3, \text{alkenes}$),²⁹ however the used of $\text{Co}_2(\text{CO})_8$ is also very commonly reported³⁰ and it usually requires heating. The versatility of this strategy is based on the easy access to different substituted diphenylacetylenes by commonly used palladium-catalyzed cross-coupling methods such Sonogashira reactions. In Scheme 4.2 it is shown the synthesis of symmetric HBC derivatives *via* cyclotrimerization of three molecules of the same symmetric diphenylacetylene, which ultimately results in a nanographene with six identical R– groups. Similarly, the use of diphenylacetylenes with different substituents has been also reported, with the subsequent formation of mixtures of the corresponding regioisomers.³¹

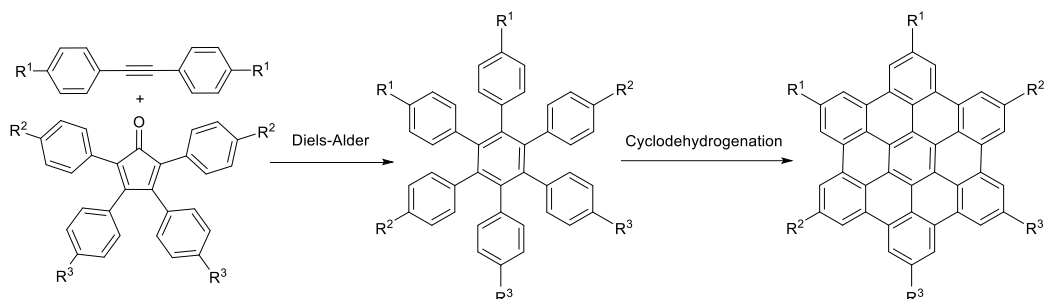


Scheme 4.2. Synthesis of HBC-based nanographenes by alkyne cyclotrimerization.

- Preparation of oligophenylene precursors *via* Diels–Alder reaction.

Diels–Alder reaction is preferred in synthetic routes toward HBC cores with different R– groups at the periphery, in order to avoid mixture of products. It consists in an

intermolecular [4+2] cycloaddition of a diphenylacetylene and a tetraphenylcyclopentadienone, both suitably substituted (Scheme 4.3).

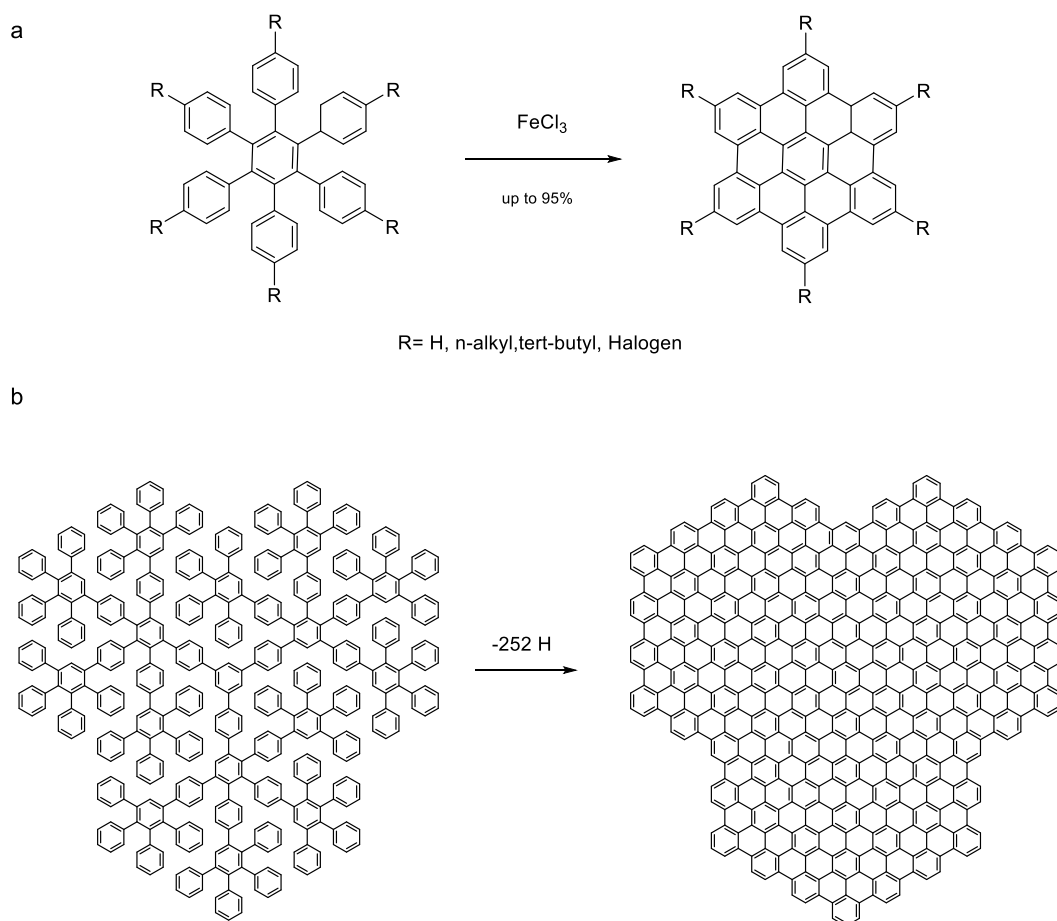


Scheme 4.3. Synthesis of HBC-based nanographenes by Diels-Alder reaction.

- Oxidative cyclodehydrogenation reaction of oligophenylenes:

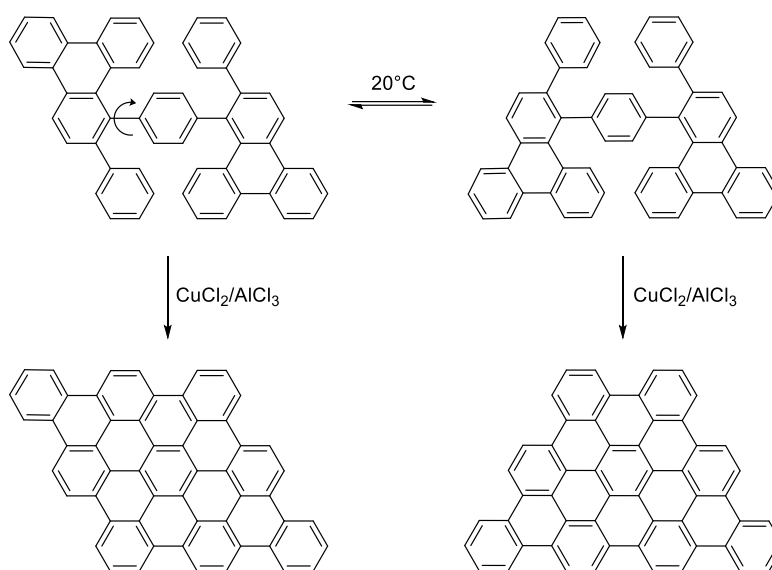
An oxidative cyclodehydrogenation reaction is the required final step in the synthetic routes toward graphene molecules, since it allows the planarization of the final structures via formation of the missing C–C bonds between the rings of the dendritic oligophenylenes. The formation of these C–C bonds has been accomplished in different oxidative conditions, such as treatment with a Lewis acid (AlCl_3 or FeCl_3), or combination of oxidants with acids (2,3-dichloro-5,6-dicyano-*p*-benzoquinone (DDQ) + triflic/methanesulfonic acid). However, the use of FeCl_3 is one the most extended method (Scheme 4.4a). Also known as Scholl or Scholl-type reaction, cyclodehydrogenation reaction has been extensively used and it was successfully employed by Müllen and co-workers for forming as many as 126 new C–C bonds in a single step (Scheme 4.4b).³²

INTRODUCTION

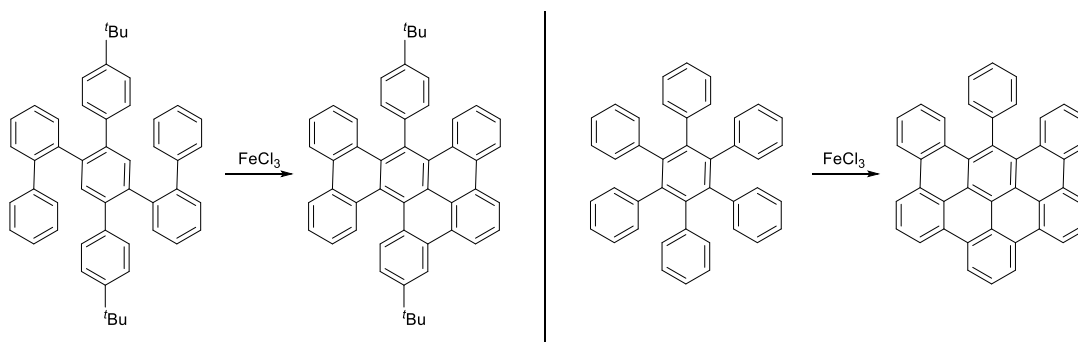


Scheme 4.4. Oxidative cyclodehydrogenation, final step toward nanographene molecules of different shapes and sizes.

The main disadvantage of Scholl reaction is that it can also promote the reversible Friedel-Crafts alkylation in certain conditions. Therefore, cases of dealkylation, migration of the alkyl chains or even chlorination of the aromatic system have been detected. In an attempt for minimizing those undesirable events, the use of the weaker Lewis acid FeCl_3 is preferred instead AlCl_3 .³¹ Other characteristic of Scholl reaction is that the selectivity cannot be guarantee if several stable conformations of the oligophenylene scaffold are possible. Thus, for example in Scheme 4.5 the same oligophenylene might lead to different PAHs. Remarkably, the nature of the substituents seems to govern this reaction, as different partially fused compounds can be originated depending on the present substituents and their position, as shown in Scheme 4.6.³³



Scheme 4.5. Formation of different nanographene molecules from an oligophenylene derivatives with several possible conformations.



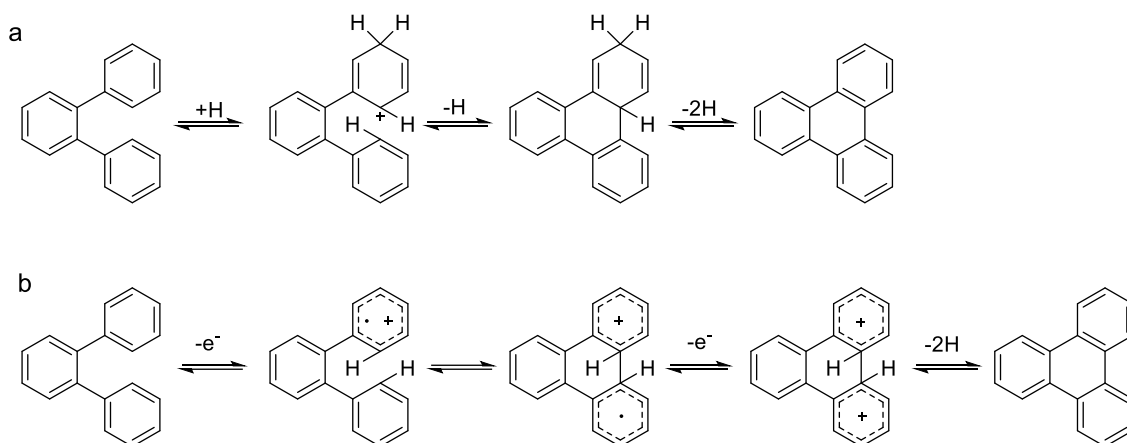
Scheme 4.6. Formation of partially fused intermediates during Scholl reaction.

Two different mechanisms have been proposed for this reaction: a) the arenium cation mechanism and b) the cationic radical mechanism.³⁴ The arenium cation mechanism is based on a first protonation of the aromatic compound generating the mentioned arenium cation which is a strong σ -electrophile. This cation can react with a neighbour aromatic ring creating a new C–C bond, followed by deprotonation. Finally, a dehydrogenation step is needed, obtaining the reaction product (Scheme 4.7a).

The second suggested mechanism entails the formation of a radical cation after the monoelectronic oxidation of the substrate. Firstly, a radical cation is formed by

INTRODUCTION

monoelectronic oxidation, followed by the formation of a new C–C bond with a neighbour aromatic ring. Subsequently, a monoelectronic oxidation occurs to form a dicationic specie. This double charged specie evolves to the final product by losing two hydrogen atoms (Scheme 4.7b).



Scheme 4.7. Proposed mechanisms for Scholl reaction: **(a)** arenium cation mechanism and **(b)** the cationic radical mechanism.

This methodology based on Diels–Alder or cyclotrimerization reaction followed by cyclodehydrogenation reaction has been successfully applied not only for HBCs, but also for nanographenes in general, allowing the preparation of graphene molecules of different molecular sizes, shapes and symmetries. In the literature, several book chapters and reviews can be found,^{26,35} where the most striking routes and structures to date are collected. Remarkably, some of them are specially dedicated to GNR,³⁶ nanographenes containing odd-membered rings^{37,38} and heteroatom-containing nanographenes.^{39,40}

4.1.1.4. Nanographenes containing odd-membered rings

The presence of non-hexagonal rings induces distortions on the aromatic surface of nanographenes, bending the sp^2 network and leading to curved nanographenes. However, different types of curvature can be observed depending of the number of C atoms (n) in the non-hexagonal rings. Rings with $n=3-5$ originate a bowl-shaped structure, namely positive curvature, while rings with $n=7-16$ lead to saddle-shaped structures, namely negative curvature.⁴¹ The curvature of PAHs containing non-planar rings can be calculated as follows: the interior of the non-hexagonal ring has to be subdivided into triangles, concurring these triangles at a common vertex. If the sum of the interior angles of these triangles is larger than 360° , the curvature is negative (saddle type); and if the sum is less than 360° , the curvature is positive (bowl type).⁴² The simplest molecules where we can observe this effect are $[n]$ circulenes, a family of PAHs consisting in a n -sided ring fully surrounded by fused six-membered benzenoid rings. In the case of $[6]$ circulene (commonly known as coronene), it does not present curvature as the central ring is hexagonal (Figure 4.4).

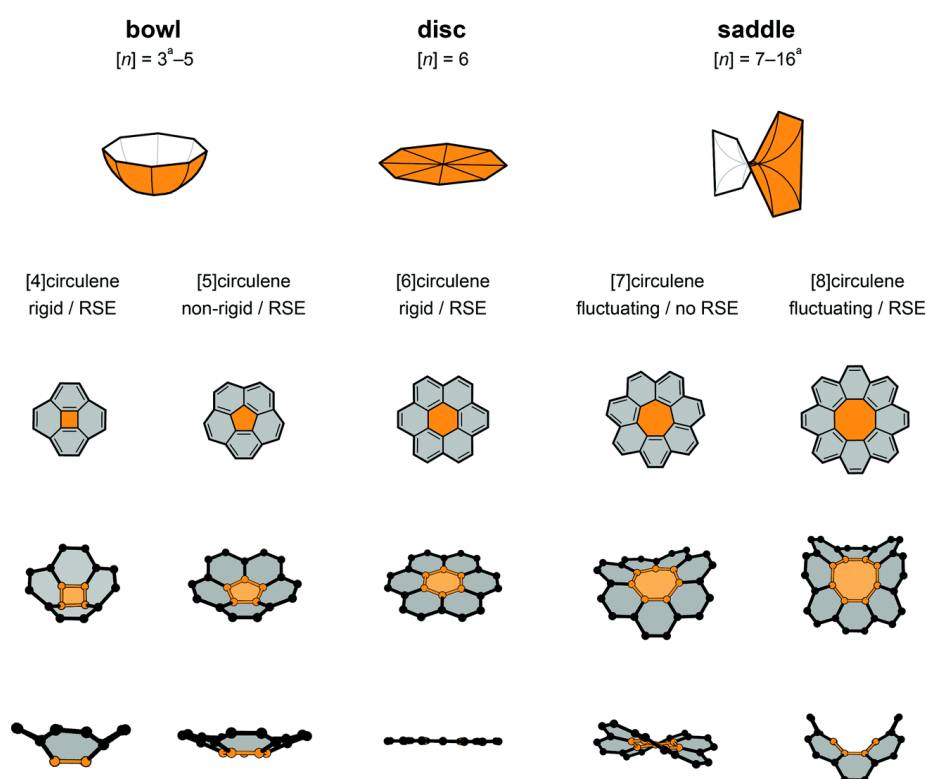
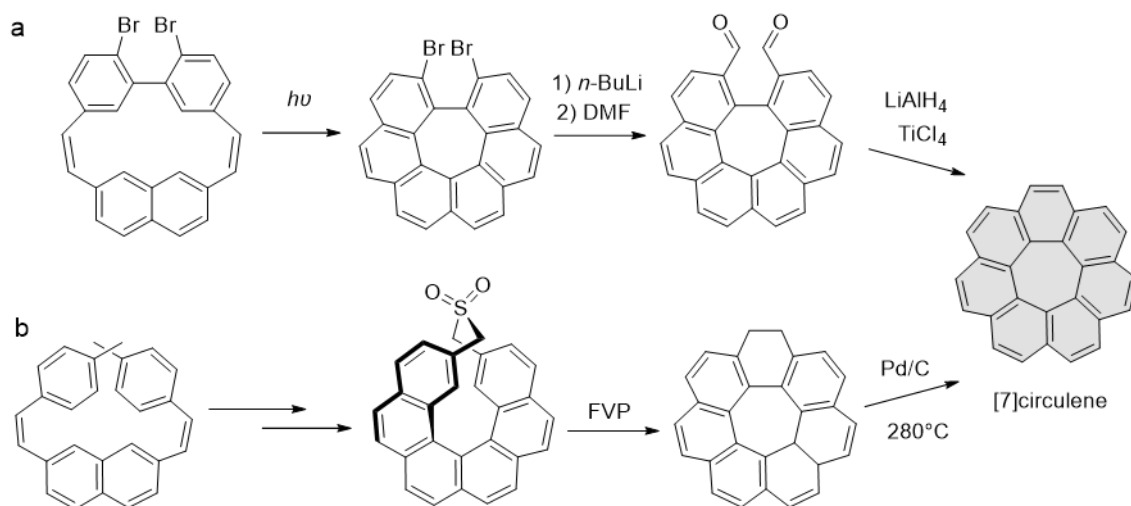


Figure 4.4. Schematic illustration of $[n]$ -circulenes and their curvature. RSE = relative strain energy. Reproduced with permission from ref.⁴¹. Copyright © 2017 Royal Society of Chemistry.

INTRODUCTION

The structural calculations for [3]circulene showed that it presents such a high strain energy that it is not synthetically feasible. The strain energy for [4]circulene is also high, explaining the failures in the different attempts to prepare it.⁴³ However, the synthesis of the latter has been possible including substituents at the periphery.⁴⁴ [5]circulene received a especial attention since it can be found in fullerene fragments and carbon nanotubes end caps. The first synthesis of [5]circulene, also known as corannulene, was reported in 1966,⁴⁵ however until 1971 the experimental details were not published.⁴⁶ Flash vacuum pyrolysis (FVP), quickly emerged as an effective method for the synthesis of corannulene and corannulene-based structures, highlighting the works developed by Scott's group.⁴⁷ However, FVP has a major limitation: starting materials must be robust enough to survive to the required temperature to sublime them into the gas phase, what limits the range of functionalities that can be included on the corannulene scaffold. Siegel's works^{48,37} gave the solution to that problem, using in-solution methods, which employ milder reaction conditions. In that sense, corannulene has been extensively used as a core scaffold for the synthesis of larger nanographenes, as it can be derivatized in a well-defined manner and prepared on a multigram scale.^{37,49}

In the case of larger [n]circulenes, [7]circulene was successfully prepared in 1983 *via* photocyclization of biphenylnaphthalene cyclophane, followed by the formation of the final benzene ring to complete the [7]circulene (Scheme 4.8a).⁵⁰ The X-ray diffraction confirmed the expected saddle-shaped geometry. An alternative synthesis was proposed in 1996, in which the formation of both the central heptagonal ring and the last peripheral benzene ring was accomplished in a single step using FVP method (Scheme 4.8b).⁵¹ A related extended [7]circulene-based nanographene was also reported recently by Miao and coworkers using a synthetic sequence based on ring expansion/Diels-Alder/Scholl reactions.⁵²



Scheme 4.8. Synthetic routes for [7]circulene.⁵³

[8]circulene has not been synthesized yet, probably because of the existence of unstable structural points which coincide with double bonds outside of sextets, according to Clar representation⁵⁴ (Figure 4.5). Indeed, [8]circulene derivatives in which no double bonds exist outside of sextets has been successfully synthesized, both all-carbon such as tetrabenzo[8]circulene^{54,55,56} and heterocyclic [8]circulene derivatives.^{53,52}

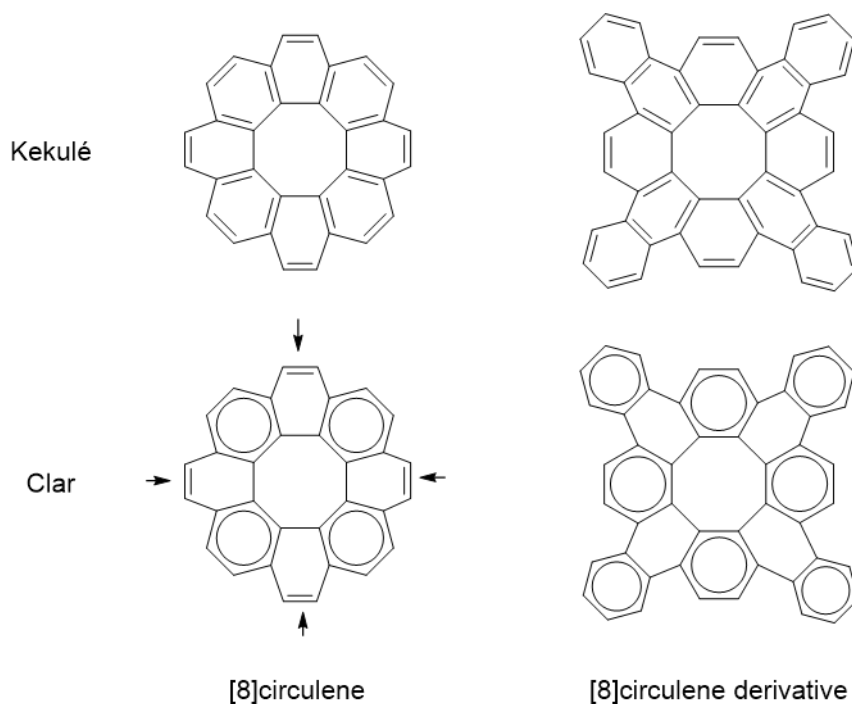


Figure 4.5. Kekulé and Clar representation for [8]circulene and a derivative in which benzene rings are fused in the periphery of the molecule. Arrows in Clar representation mark instability points due to double bonds outside of sextets.⁵⁴

INTRODUCTION

Beyond [n]circulenes and [n]circulene-based molecules, other nanographenes containing non-hexagonal rings have been also reported. In particular, PAHs containing odd-membered rings have received an especial attention due to the distortion of their structure and their remarkable opto-electronic properties. In addition, the synthesis of these distorted structures entails a challenge by itself.

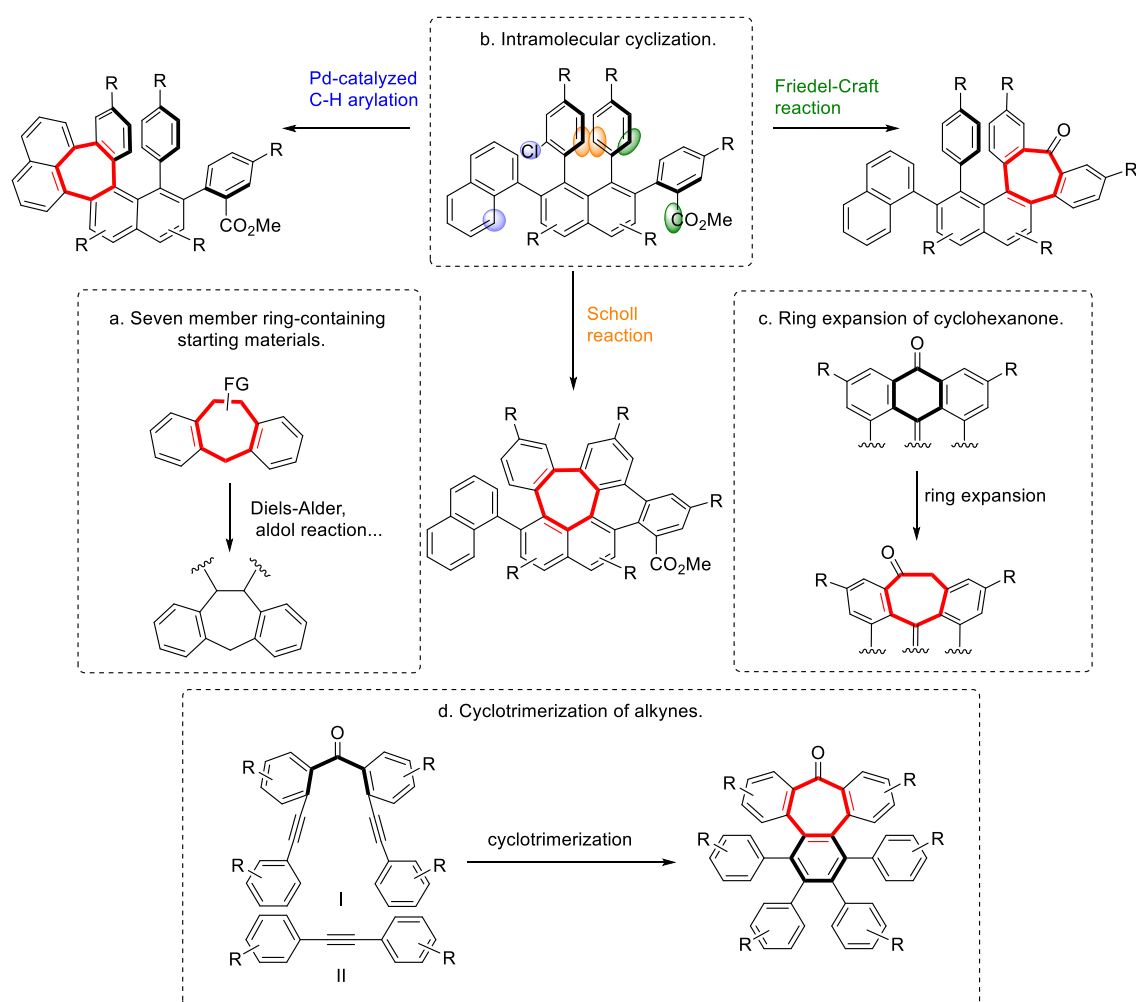
Nanographenes containing 5-membered rings have been extensively synthesized and studied, existing in the literature a considerable number of different structures containing pentagons. However, the synthesis of heptagon-containing nanographenes remained almost unexplored until the last decade. Since this chapter is particularly devoted to the study of nanographenes with heptagons, the main strategies developed to date for preparing nanographenes containing 7-membered rings are exposed in the next section.

4.1.1.5. Synthetic strategies for nanographenes containing heptagons

The key step for the synthesis of heptagon-containing nanographenes is the generation of the heptagonal carbocycle at a controlled position. From the perspective of organic synthesis, four different strategies have been mainly used to date for creating 7-membered carbocycles into nanographenes (Scheme 4.9):

- Using starting materials that already contain 7-membered carbocycles (Scheme 4.9a), creating the surrounding aromatic backbone in the following steps.^{57,58}
- By intramolecular cyclization via Scholl reaction, Friedel-Craft reaction or Pd-catalyzed C–H arylation (Scheme 4.9b). Remarkably, Scholl reaction does not require any previous functionalization in the substrate. However, the outcome of the reaction is not always easily predictable, entailing a disadvantage for the synthesis of well-defined structures especially in the case of distorted nanographenes. In contrast, although functionalized precursors are required, the outcome of the reaction is better predicted for both Friedel-Craft reaction and Pd-catalyzed C–H arylation.^{58,59}
- Via ring expansion of cyclohexanone derivatives (Scheme 4.9c). This strategy was recently reported (2018) by Miao and co-workers, using trimethylsilyldiazomethane (TMSCHN₂).⁶⁰

- Through Co(0)-mediated cyclotrimerization of alkynes (Scheme 4.9d). This methodology was developed some years ago (2017) by our research group.¹⁴ It was inspired by the previously mentioned cyclotrimerization-dehydrogenation sequence for the synthesis of purely hexagonal nanographenes, but joined to a smart selection of starting materials that allows the creation of the 7-membered ring. The major advantage is the use of simple and accessible starting materials, as well as the formation of the 7-membered carbocycle and the required polyphenylene aromatic backbone in one single step. Additionally, the versatility of the method allows the use of a variety of precursors with functional groups in different positions, what permits an easy further expansion of the structure.



Scheme 4.9. Synthetic methodologies toward 7-membered carbocycles. Adapted from ref.³⁸

INTRODUCTION

4.1.2. Nanographenes for electronic applications

Nanographenes are highly attractive compounds for electronic and optoelectronic applications because their properties can be tuned through synthetic modification of their sizes and topologies, affecting their HOMO–LUMO gaps and charge carrier mobilities. Their capacity for stacking due to their extended aromatic surface has been also leveraged for application in solar cells, creating stacks oriented “face-on” relatively to the surface, and organic field-effect transistors (OFETs), with stacks in “edge-on” orientation.⁶¹

On the other hand, the idea of single-molecule devices based on nanographenes was proposed by Müllen and Rabe in 2008,⁶¹ as the properties of these devices could be systematically tuned by means of controlled organic synthesis. In the same direction, Chen and Tao highlighted in 2009 the necessity of studying the electron transport through the many molecular structures between graphene and benzene.⁶² As explained in section 1.5.2, the presence of anchoring groups is highly desirable in molecules for electronic applications, since it allows to manage the electron conduction through a preferred orientation of the molecule, as well as to ensure well-defined molecule-electrode contacts.

Single-molecule conductance of nanographenes

Only few single-molecule conductance studies of nanographenes or related PAHs have been experimentally performed and reported in literature. In 2005, Tao and collaborators presented the results of break junction experiments for perylene tetracarboxylic diimide (PTCDI).⁶³ In this work, PTCDI was wired to two gold electrodes (source and drain) via gold-thiol bonds. A large gate field was achieved using an electrochemical gate in which the gate voltage (V_g) was applied between the source and a gate in electrolyte solution (Figure 4.6a).

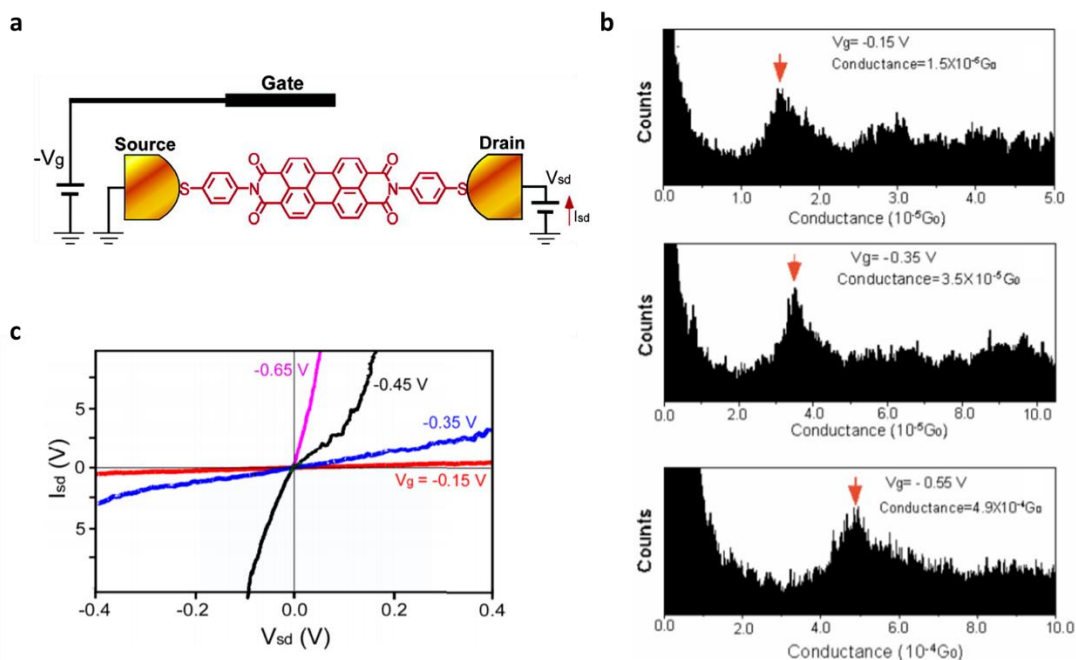


Figure 4.6. (a) Schematic single-molecule junction for PTCDI in a three-electrode cell with an electrochemical gate. (b) Conductance histograms of PTCDI molecular junctions formed in 0.01 M NaClO₄ at various gate voltages. Arrows mark the main peak corresponding for a single-molecule. (c) Linear scale plots of I - V curves at various gate voltages. Adapted from ref.⁶³ Copyright © 2005 American Chemical Society.

Molecular junctions were created using the STM break-junction technique, and conductance histograms were constructed with 1000 individual G - z traces. As shown in Figure 4.6b, the conductance peak corresponding to a single molecule shifted toward higher conductance values when increasing the gate voltage. Finally, I - V curves were recorded for different gate voltages (Figure 4.6c). They presented a linear dependence with the bias voltage (V_{sd}) when $V_g > \sim -0.4$ V, but became increasingly non-linear when $V_g < \sim -0.4$ V.

In 2010, also Tao's group studied the transport properties of nanoscale graphene-type OFETs prepared following a bottom-up approach (Figure 4.7).⁶⁴ They synthesized two HBC derivatives: the first one with branched lateral chains and amines as linkers; and the second one with longer alkyl chains and thiols as terminal groups, separated from the coronene core by an additional benzene ring. They studied the electron transport through them as a function of electrochemical gate voltage, using again a STM to bridge HBC molecules between the electrodes *via* the introduced anchoring groups. As electrolyte, the ionic liquid 1-butyl-3-methylimidazolium hexafluorophosphate was used.

INTRODUCTION

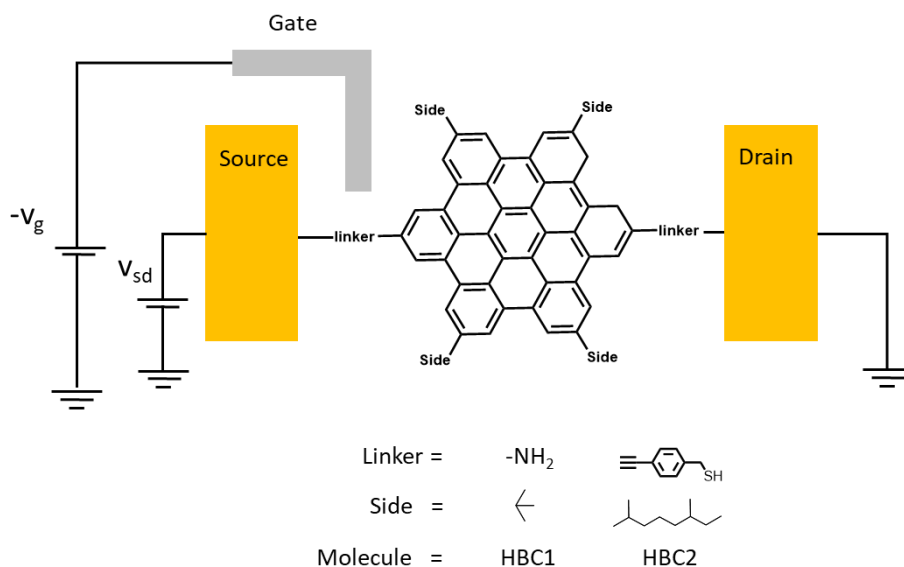


Figure 4.7. Representation of a single HBC molecule FET. Two HBC derivatives were studied. Adapted from ref⁶⁴.

The resulting conductance histograms, build from ~ 1000 individual traces, are shown in Figure 4.8. They obtained different conductance value for both molecules, being the lowest for HBC2. This lower conductance was attributed to the longer distance between anchoring groups compared with that of HBC1. The increase of the electrode-electrode distance is also notable since the plateaus displayed in the I - z traces are longer for the HBC2 (Figures 4.8b and 4.8c). Concerning to the gate voltage effect, they observed an increase of conductance with more negative gate voltages (Figure 4.9a), the same trend previously observed for PTCDI.⁶³ Additionally, temperature-dependent transport measurements were carried out (Figure 4.9b). They found that the conductance values for HBC molecules were insensitive to temperature within the experimental accessible temperature window (25–50 °C).

A final switching behaviour test allowed to calculate an on/off ratio of about 50, which is larger than those of most graphene-based FETs fabricated using top-down approaches. In general, on/off ratios in OFETs are presumed to be increased by more stable electrode-molecule contacts and larger backbones, however, the understanding of the size dependence in extended aromatic systems has not been clarified yet, with some studies pointing out that the HOMO–LUMO gap of large PAHs could be inversely proportional to the molecular length.⁶⁴

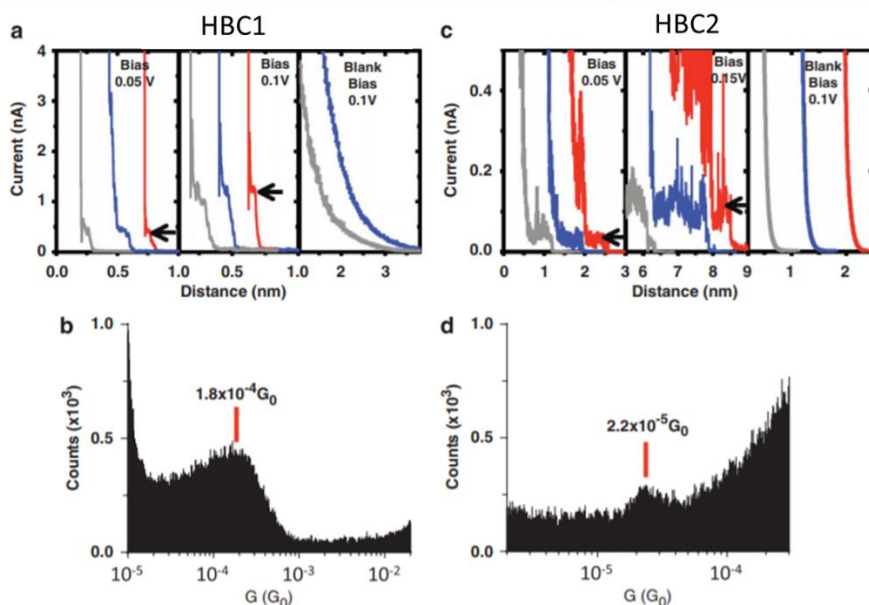


Figure 4.8. Current-distance traces for HBC1 **(a)** and HBC2 **(c)** at different bias voltage. **(b)**, **(d)** 1D histograms for them, respectively. Reproduced with permission from ref.⁶⁴ Copyright © 2010 Springer Nature

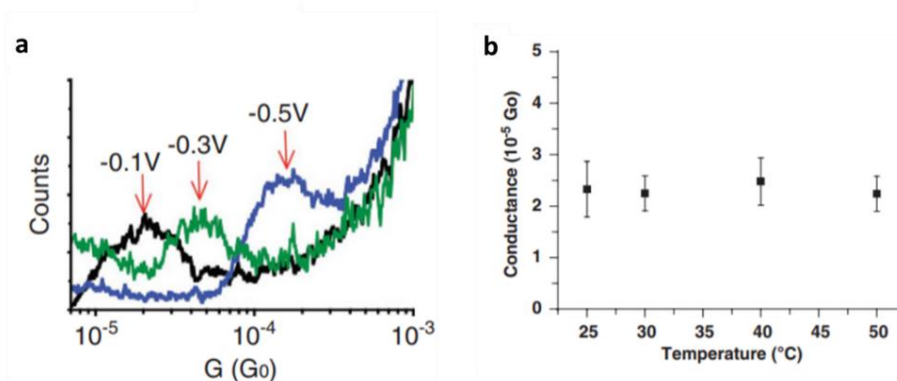


Figure 4.9. **(a)** Gate-voltage dependence of the conductance for HBC2. **(b)** Temperature-dependent transport measurements showed conductance independence with temperature. Adapted with permission of ref.⁶⁴ Copyright © 2010 Springer Nature

The position of the linkers in the same nanographene core also seems to change the transport properties dramatically, as diverse theoretical studies revealed.^{65,66} However, to the best of our knowledge, only one study deals with this topic from an experimentally perspective. This is the case of the anthanthrene derivatives studied by Liu and collaborators in 2015⁶⁷ and depicted in Figure 4.10a and 4.10b. Here, an MCBJ setup was employed to perform electron transport experiments of both structures, being the conductance histograms obtained for them shown in Figure 4.10c and 4.10d. They found

INTRODUCTION

that single-molecule conductance of short-axis-contacted anthanthrene is notable higher than that of its long-axis-contacted analogue.

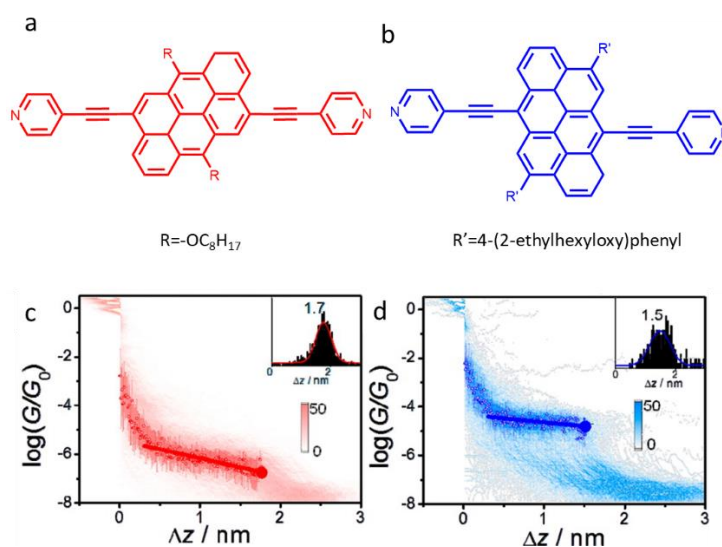


Figure 4.10. Anthanthrene derivatives of study. **(a)** Long-axis-contacted and **(b)** Short-axis-contacted. **(c)**, **(d)** 2D conductance histograms for long-axis-contacted and short-axis-contacted, respectively. Insets: Stretching distance distributions determined from $0.1G_0$ to $10^{-7} G_0$ **(c)** and from $0.1G_0$ to $10^{-5.9} G_0$ **(d)**. Adapted from ref.⁶⁷ Copyright © 2015, American Chemical Society

Trying to determine the ratio between both conductance values, they observed that two different ratios could be obtained depending on the way of determining the conductance value. When they compared the conductance at the mid-point of the peaks in the 1D histograms, they obtained a ratio of 32, but when the value was extracted from the final point of plateaus in the 2D histograms (solid red and blue circles in Figure 4.10c and 4.10d), the conductance ratio between the molecules was ~ 79 . At that point the length of plateaus concurs with the length of the fully stretched molecules in the junctions (taking into account the retraction of the tip). In base of these results, and using density functional theory (DFT) combined with nonequilibrium Green's functions (NEGF), the group developed a "magic ratio rule" (MRR) for predicting conductance ratios for the same graphene core depending on the position of linkers. They provided tables of quantum numbers or magic integers (Mii') that capture the contribution of connectivity to the electrical conductance of graphene-like cores, when one electrode is connected to an "unprimed" site i and the other is connected to a "primed" site i' , being those sites the carbon atoms in the structure. The prediction of conductance ratios *via* the MRR tables, establishes that "the ratio of conductances of two molecules is equal to the square of the

ratio of their magic integers". The MRR table for the studied anthanthrene core is presented in Figure 4.11b, as well as the correspondence of every carbon atom in the structure with those i and i' sites (Figure 4.11a).

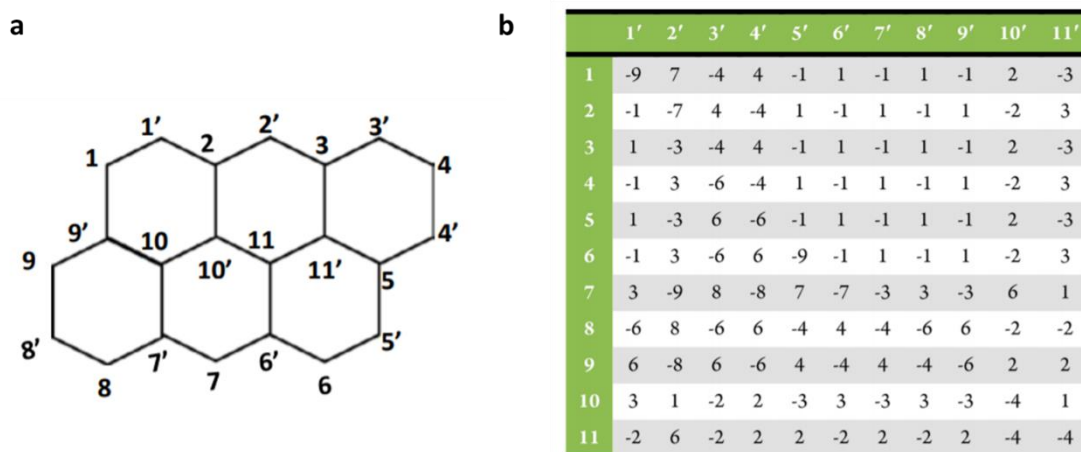


Figure 4.11. (a) Primed and unprimed sites i for C atoms in anthanthrene, and (b) magic ratio rule table. Adapted from ref. ⁶⁷ Copyright © 2015, American Chemical Society

Using the nomenclature of Figure 4.11a, long-axis-contacted molecule had an MI of $M_{15'} = -1$, while that corresponding of short-axis-contacted molecule was $M_{72'} = -9$. Therefore, the calculated conductance ratio was $(-9/-1)^2 = 81$, which is really close to that one experimentally obtained (79).

Also in 2015, this group applied again the MRR calculations to pyrene cores presenting linkers in different positions, and obtained a good agreement with both experiment data and DFT calculations.⁶⁸ In this way, the MRR calculations seems to be an effective manner to predict conductance ratios for different linker positions in the same purely hexagonal and all-carbon graphene core.⁶⁶⁻⁶⁸ However its effectiveness and accuracy has not been proved yet for curved and heteroatom-containing nanographenes, where the assignation of primed and unprimed sites is not trivial.

Concerning curved nanographenes, a few theoretical studies can be found in literature, all of them focussed on corannulene derivatives. In 2015, Baldrige and co-workers investigated charge transport in corannulene junctions using NEGF.⁶⁹ The junctions were designed with a functionalized corannulene unit assembled between two carbon

INTRODUCTION

nanotubes used as electrodes (CNT-[linker]-molecule-[linker]-CNT). The effects of different hybridized anchoring groups and molecule functionalization, among others, were evaluated. Three types of anchoring groups (sp , sp^2 and sp^3) were designed, as depicted in Figure 4.12a. Only slight modulation in quantum conductance was found between the sp - and sp^2 -hybridized linkers. However, insertion of completely saturated linkers broke the π -conjugation through the junction, decoupling the molecule from the electrodes. The sp^3 linker group showed a general reduction in conductance along the whole energy range, being the calculated transmission spectrum drastically different from that of the other two cases (Figure 4.12b). Using an identical sp carbon-carbon triple bond linker, they established new junctions in which the central corannulene core presented different functionalizations. The calculated transmission spectra of several functionalized structures were compared with that of pristine corannulene, as observed in Figure 4.12c-e. The calculation revealed that i) the enlargement of the aromatic core entailed an opening of the gap, and ii) the presence of fluorine groups ($-F$ and $-CF_3$) represents a reduction of the gap, more notable as the number of these groups increases.

On the other hand, cyclopentadienyl (Cp) and corannulene Fe complexes were the spotlight of the work developed by Sun and collaborators in 2018, which used a combination of DFT and NEGF theoretical calculations.⁷⁰ Corannulene acting as a ligand can provide four different binding sites on each side of the curved surface for the attachment of the CpFe fragment. After a geometry optimization of all possible CpFe-corannulene derivatives, they found that the most stable are CpFe- η^6 (exo)-corannulene, CpFe- η^6 (endo)-corannulene, and CpFe- η^5 (exo)-corannulene, shown in Figure 4.13. Diphenylacetylene was linked to two opposite sides of the CpFe-corannulene complexes and single-molecule junctions were built. The calculated I - V curves for these compounds revealed notable higher conductance values for the third derivative, demonstrating that the coordination position has a significant influence on the transport properties. Remarkably, a spin filter effect appeared in η^6 *exo* and *endo* isomers. The corresponding spin polarization is close to 100% for both derivatives in the considered bias region (0–1V), what indicates that they can be considered as “perfect” spin filters.

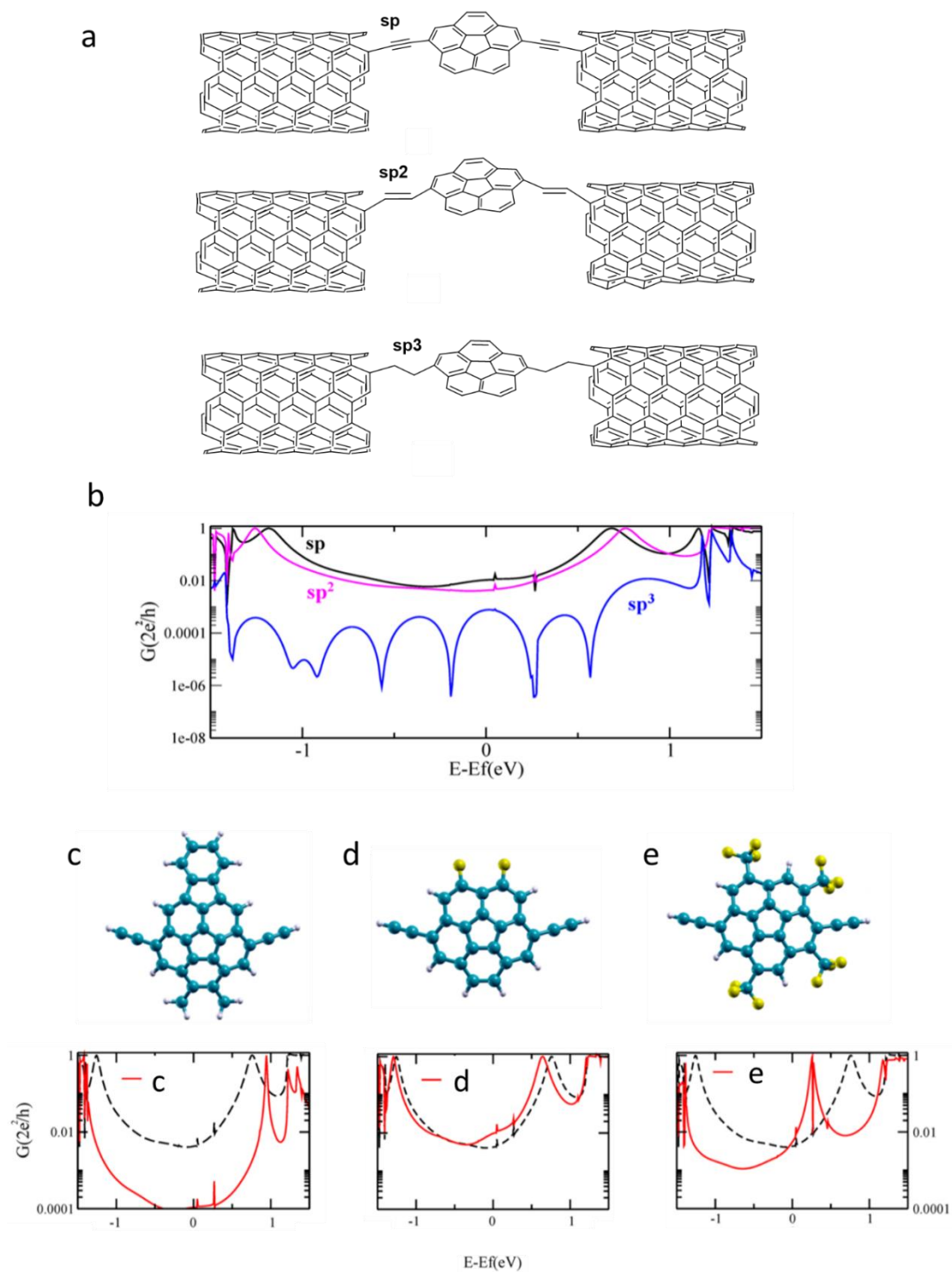


Figure 4.12. (a) Prototype junctions consisting of 1,6- diethynylcorannulene linked to (5,5)-CNT through sp, sp² and sp³ carbon atoms. (b) Transmission spectra of the sp, sp² and sp³ hybridized molecular junctions. (c), (d) and (e) structure and transmission spectra of different fractionalized corannulenes (yellow balls are fluorine atoms). Adapted from ref.⁶⁹ Copyright © 2015 American Chemical Society

INTRODUCTION

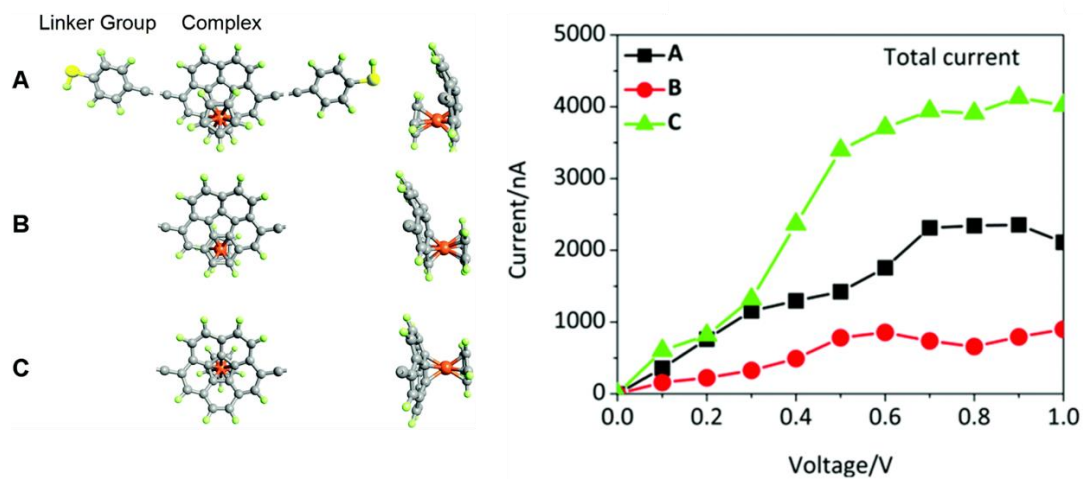


Figure 4.13. CpFe-corannulene derivatives and the calculated I-V curves. Adapted with permission of ref.⁷⁰
Copyright © 2015 American Chemical Society

Those theoretical results highlight the potential of curved PAHs, not only for mere electronic applications, but also in spintronics and emphasized the necessity of experimental studies which complement and demonstrate those predictions.

4.2. Objectives

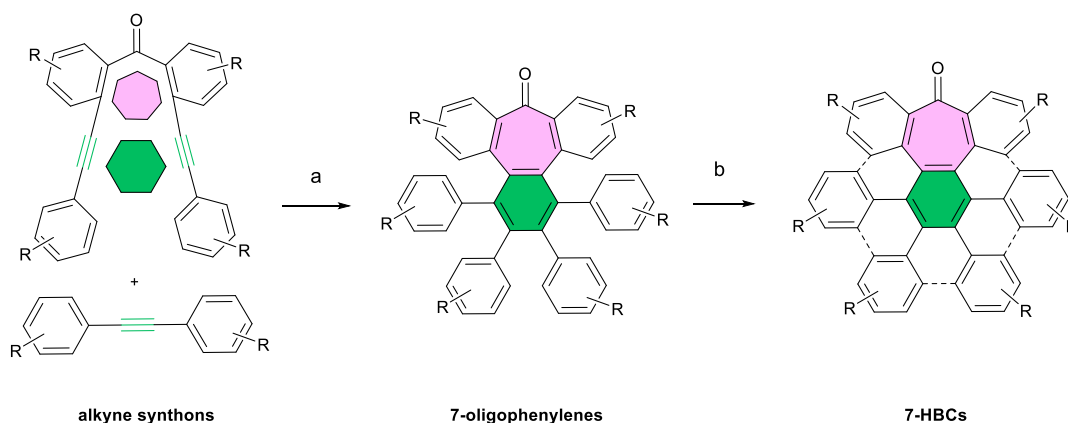
According to previous knowledge of the group about the preparation of curved heptagon-containing nanographenes, and taking into account the information collected in the background section, the following objectives were proposed:

1. To synthesize and characterize curved HBC-like nanographenes incorporating 7-membered carbocycles (hept-HBC) with different anchoring groups, which permit the single-molecule conductance experiments.
2. To synthesize and characterize a defective-free HBC analogue incorporating one of the anchoring groups previously employed.
3. To carry out single-molecule conductance experiments for the synthesized molecules using the STM break-junction technique.
4. To study the effect of different anchors on the conductance of curved hept-HBC molecules.
5. To evaluate the effect of 7-membered rings on the electron transport properties of HBC-like molecules.

4.3. Results and discussion

4.3.1. Molecular design

The synthetic strategy developed by our group¹⁴ for the preparation of heptagon-containing HBC-like nanographenes (7-HBCs), which was described in section 4.1.1.3, is an optimum methodology toward the incorporation of anchoring groups into distorted aromatic cores, as it allows the introduction of diverse functional groups in selected positions. It is based on a sequence of intermolecular Co-mediated cyclotrimerization of alkynes and cyclodehydrogenation reactions, in which the starting materials govern the structure of the final compounds (Scheme 4.10). These alkynes can be easily prepared from simple precursors *via* Sonogashira cross-coupling reactions. Importantly, the cyclotrimerization reaction is compatible with the presence of different functional groups in the alkyne synthons, which can serve for a further expansion of the structures, including the introduction of adequate anchoring groups. The ketone dialkyne derivative is the key compound in this strategy, as it leads to the formation of the 7-membered carbocycle on the edge of the HBC-based nanographenes, while the carbonyl group can be also used for further functionalisation.



Scheme 4.10. Synthetic route toward heptagon-containing HBC-based nanographenes. **(a)** Co-mediated cyclotrimerization reaction. **(b)** cyclodehydrogenation reaction.

Remarkably, the curvature induced by the presence of the 7-membered ring leads to highly soluble compounds.¹⁴ Therefore, the incorporation of large alkyl chains for increasing the solubility are not imperiously required.

RESULT AND DISCUSSION

Heptagon-containing dendritic oligophenylenes (7-oligophenylenes) are synthesized, as intermediate compounds in the route towards the 7-HBC molecules, as Scheme 4.10 shows. Both structures only differ on 5 C–C bonds, but they are fundamental for the expansion of the aromatic surface going from the oligophenylenes to the fully conjugated 7-HBC cores. In this sense, the comparison of the conductance for these two types of structures, can shed light on the understanding of the effect of aromaticity on the electron transport. So that, the preparation of these 7-oligophenylenes, incorporating anchoring groups was also proposed.

Finally, for the evaluation of the effect of the 7-membered rings on the electron transport, we considered a planar HBC core incorporating anchoring groups in the appropriate positions, as the most reliable defective-free analogue. As remainder, the low solubility of this structures requires the introduction of additional alkyl chains. Although alternative synthetic routes towards HBC derivatives have been proposed in literature (see section 4.1.1.3.), the Diels-Alder/cyclodehydrogenation combination seems to be preferable here (see Scheme 4.3), since at least two of the solubilizing-alkyl chains have to be substituted by the corresponding anchoring groups.

Thus, the molecular cores of interest for this chapter are collected in Figure 4.14, namely the heptagon-containing HBC-like cores (**7-HBC**), the heptagon-containing dendritic oligophenylenes (**7-oliphe**), and the planar HBC cores (**HBC**).

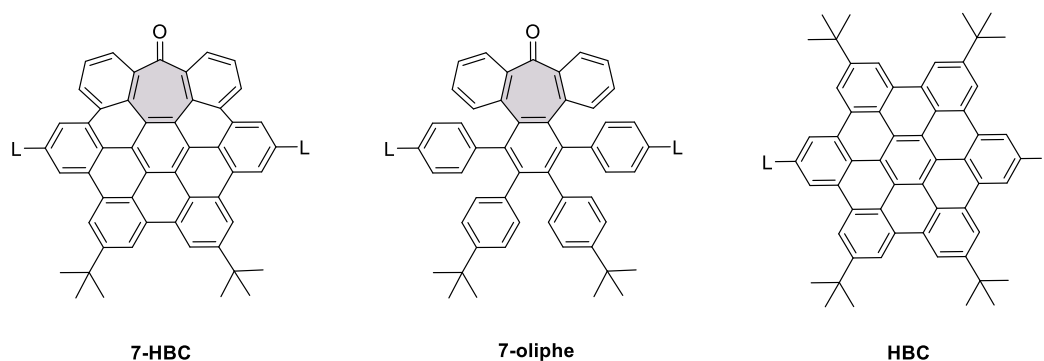
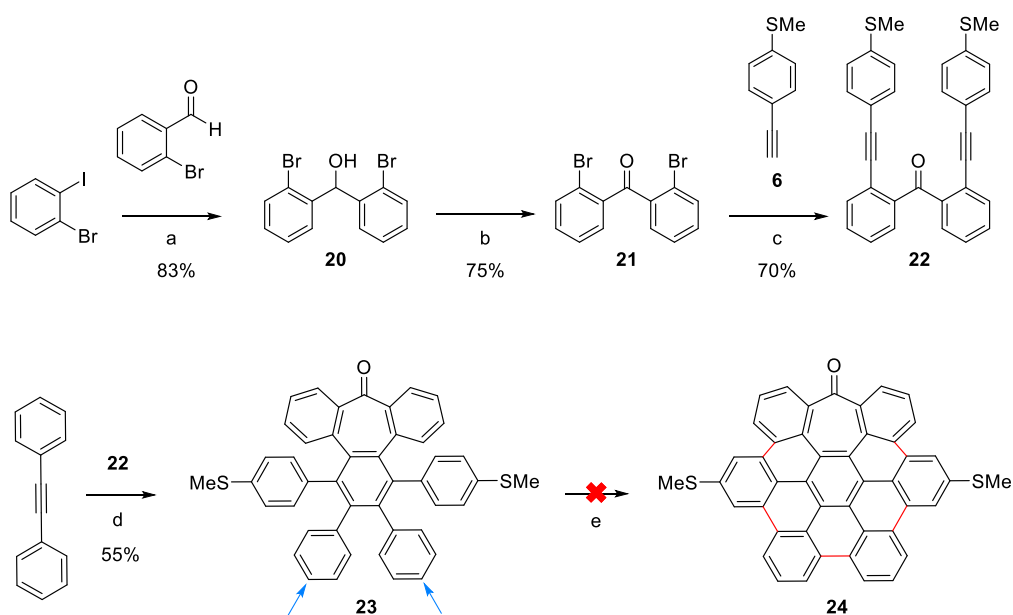


Figure 4.14. Target cores of interest. (L=linker group)

4.3.2. Synthesis

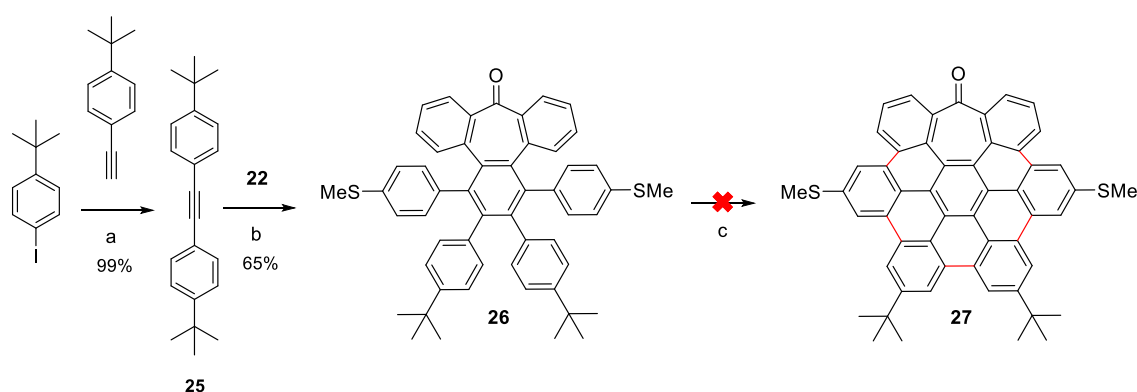
As explained in Chapter 1, section 1.5.2, the choice of anchoring group is an important point in the evaluation of the electron transport properties of a particular system, since the conductance value and the length of plateaus obtained for the same core can change depending on the chosen one.⁷¹ Since the electron transport through curved nanographenes has been scarcely investigated (see section 4.1.2.1), and specifically heptagon containing nanographenes have not been explored at all, we proposed the use of –SMe groups, since their effectiveness as linkers has been widely demonstrated, and their behaviour is well-known. Then, we started the synthesis of **24** (Scheme. 4.11) with an iodine/magnesium exchange in commercial 2-bromoiodobenzene by addition of turbo-Grignard reagent (*i*PrMgCl·LiCl), followed by the nucleophilic attack over 2-bromobenzaldehyde. Subsequent oxidation of the obtained secondary alcohol **20** with Dess-Martin periodinane afforded the resulting 2,2'-dibromobenzophenone (**21**). Double Sonogashira coupling of **21** with previously synthesized alkyne **6** gave rise to dialkyne **22** in good yield. The subsequent cobalt-catalyzed [2+2+2] alkyne cyclotrimerization reaction of **22** with commercial diphenylacetylene afforded the oligophenylene **23** but, unfortunately, the final cyclodehydrogenation promoted by the oxidant/acid combination 2,3-dichloro-5,6-dicyanobenzoquinone (DDQ)/ methanesulfonic acid, did not take place.



Scheme 4.11. (a) *i*PrMgCl·LiCl, THF, –78 °C to rt, 16 h; (b) DMP, CH₂Cl₂, rt, 16 h; (c) PdCl₂(CH₃CN)₂, CuI, PtBu₃·HBF₄, THF, *i*Pr₂NH, rt, 16 h; (d) Co₂(CO)₈, Dioxane, 110 °C, 16 h (e) DDQ/MeSO₃H, DCM, 0 °C.

RESULT AND DISCUSSION

In fact, activating groups like –OMe, very similar to –SMe, were previously reported as effective *o,p*-directors in this reactions.³³ This means that the formation of C–C bonds in *ortho* and *para* positions, with respect the –OMe groups, is favored as they are activated, while the reaction is hindered in *meta* positions (the desired positions here), as they are deactivated. Nevertheless, the group successfully achieved in the past different structures analogue to **24**, which incorporated –OMe functions instead of –SMe in the desired positions.^{72,73} The methodology consisted in the incorporation of *t*-butyl groups as activating group in strategic positions of the oligophenylene (Scheme 4.11, arrows in **23**), in combination with the use of stronger reaction conditions for the cyclodehydrogenation (different acid). In sight of those results, we tackled the synthesis of **27**. We prepared the new oligophenylene **26**, obtained after cyclotrimerization of dialkyne **22** and **25**. Nevertheless, the result for the treatment of **26** with DDQ and trifluoromethanesulfonic acid (CF₃SO₃H), was again the same, and any C–C bond was formed.^a

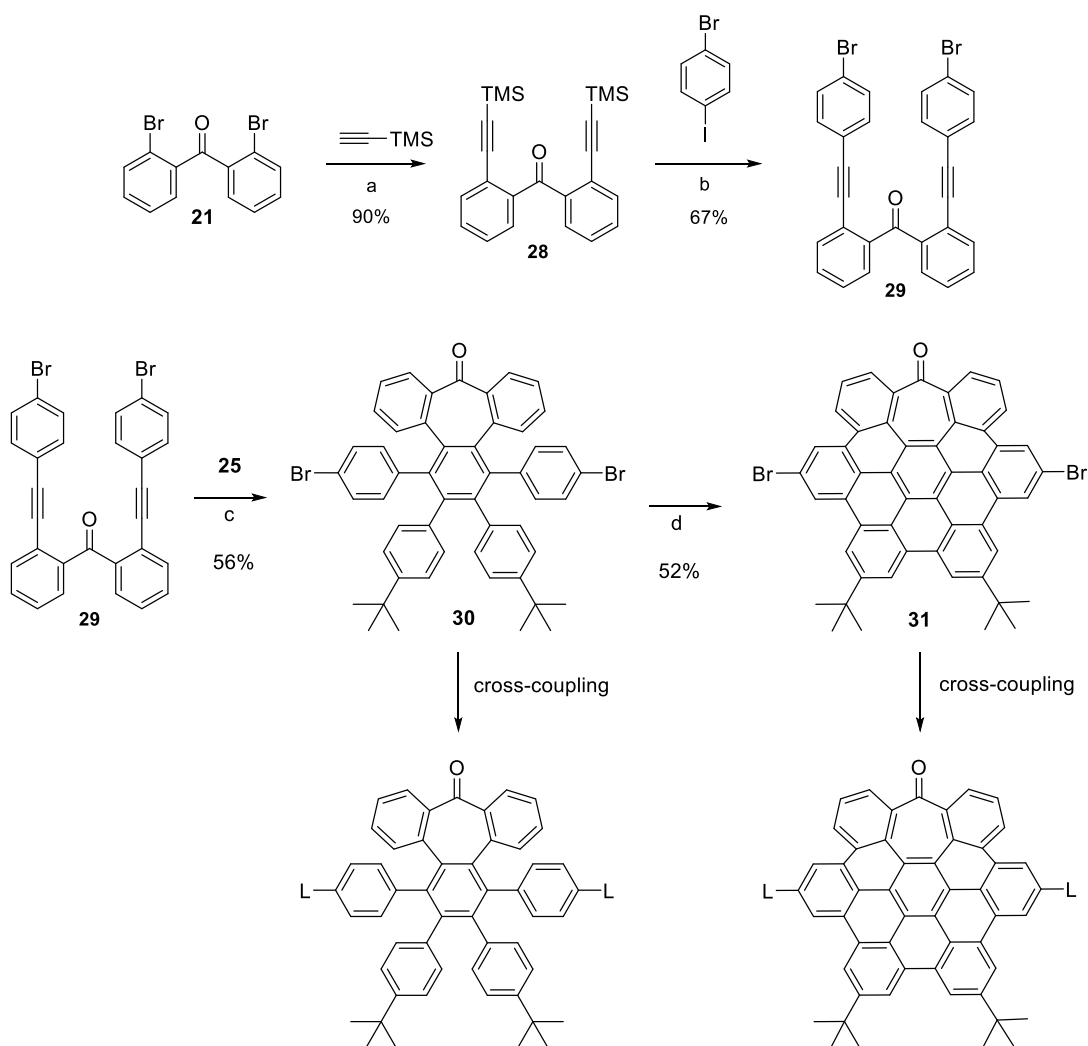


Scheme 4.12. (a) PdCl₂(PPh₃)₂, CuI, Et₃N, THF, rt, 16 h; (b) Co₂(CO)₈, toluene, 110 °C, 16 h; (c) DDQ, CF₃SO₃H, CH₂Cl₂, 0 °C, 10 min.

These failed experiments demonstrated the strong effect of the –SMe groups into the rings, which is able to totally prevent the cyclodehydrogenation reaction in the desired positions. Then, we decided to move on a different strategy in order to introduce the linkers in a straightforward manner.

^a For the dehydrogenation reactions over **23** and **26**, FeCl₃ conditions were also tested in the group with the same negative results.

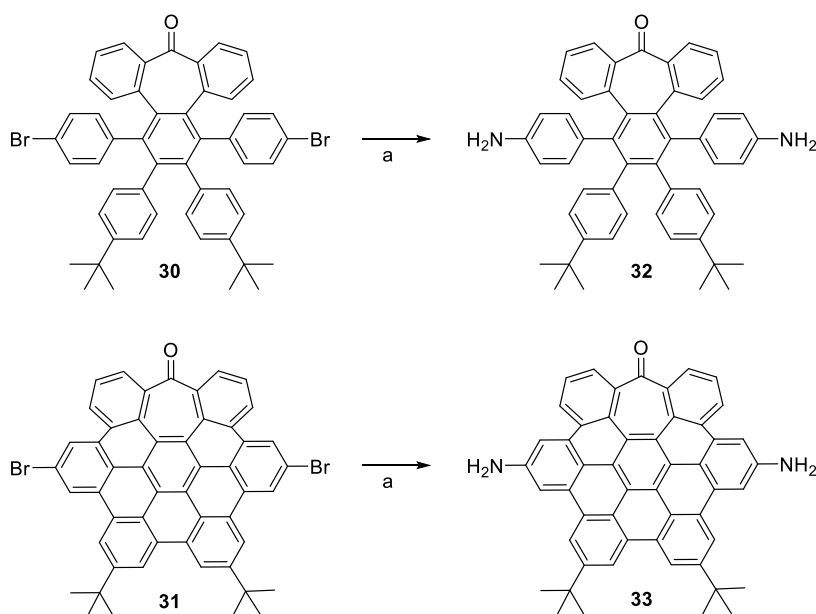
Following the same reaction sequence as before, we prepare the dibromide oligophenylene **30** (Scheme 4.13), a versatile intermediate that can take part in different cross-coupling reactions. In this way different linkers can be included in the oligophenylene core. The synthesis of **30** started with the preparation of dialkyne derivative **28** from double Sonogashira cross-coupling of dibenzophenone **21** with trimethylsilylacetylene (TMSA). Compound **28** was then coupled with 1-bromo-4-iodobenzene through a modified Sonogashira cross-coupling reaction involving an *in situ* alkyne deprotection,⁷⁴ affording the dibromide derivative **29**. This compound **29** was subjected to alkyne cyclotrimerization with diphenylacetylene **25**, giving rise to the desired oligophenylene **30**. Moreover, compound **30** reacts under Scholl reaction conditions to give compound **31**, again suitable for cross-coupling reactions for introducing different linkers.



Scheme 4.13. (a) TMSA, PdCl₂(CH₃CN)₂, CuI, PtBu₃-HBF₄, THF, *i*Pr₂NH, rt, 16 h; (b) 1-bromo-4-iodobenzene, PdCl₂(PPh₃)₂, CuI, Et₃N, DBU, THF, H₂O, 70 °C, 16 h; (c) Co₂(CO)₈, toluene, 110 °C, 16 h; (d) DDQ, CF₃SO₃H, CH₂Cl₂, 0 °C, 10 min.

RESULT AND DISCUSSION

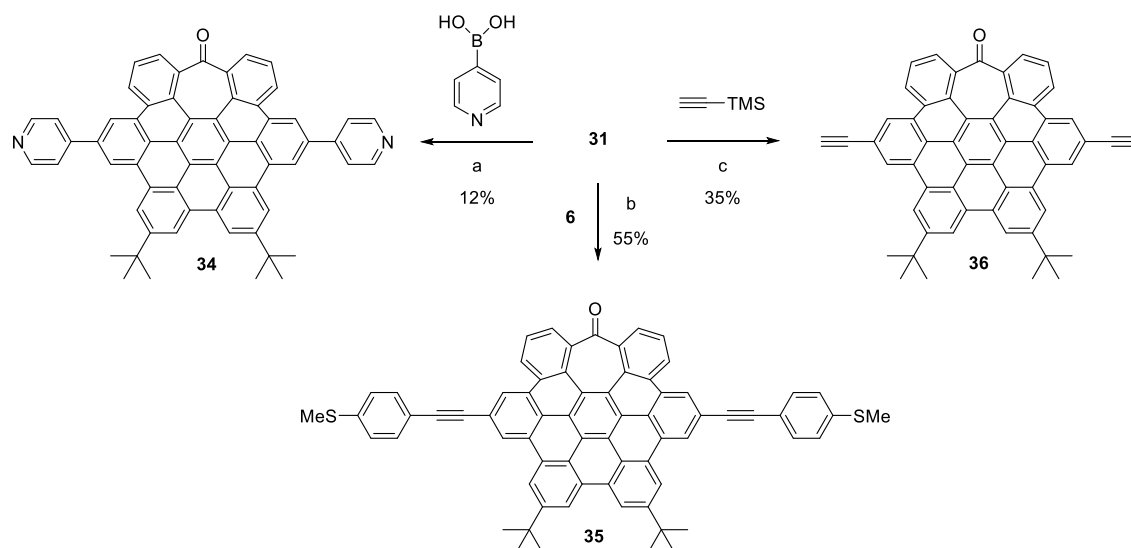
Having synthesized key intermediates **30** and **31**, firstly, we tackled the preparation of the amine derivatives **32** and **33** (Scheme 4.14). Amines are again extensively used anchoring groups, which behavior is well-known. Additionally, the single-molecule conductance of the planar analogue to diamine 7-HBC **33** was reported by Tao and collaborators,⁶⁴ as highlighted in section 4.1.2.1. In this sense, the comparison of the single-molecule experiments for both structures could shed light on the effect of the 7-membered ring on the electron transport. Both, **32** and **33**, were prepared by Buchwald-Hartwig amination reaction with *t*-butyl carbamate over **30** and **31**, respectively, followed by treatment with TFA.



Scheme 4.14. (a) (i) *t*-butyl carbamate, Pd(dba)₂, PtBu₃·HBF₄, *t*BuONa, toluene, 115 °C, 16 h; (ii) TFA, CH₂Cl₂, 30 min.

However, both compounds were air-sensitive, being impossible to maintain their structural integrity. So that, we discarded the use of free amines as linkers and decided to use pyridine instead. Thus, pyridine-containing 7-HBC **34** (Scheme 4.15) was prepared *via* Suzuki cross-coupling reaction of **31** with 4-pyrimidylboronic acid. Finally, using again the versatile dibromide **31**, we prepared compound **35** by means of double Sonogashira cross-coupling with **6**; and compound **36** through double Sonogashira coupling with TMSA, followed by deprotection with tetrabutylammonium fluoride (TBAF). These 7-HBC

structures were obtained in moderate to good yields, and their structure were confirmed by ^1H - and ^{13}C -NMR. In such way we were able to introduce a pyridine ring, a terminal alkyne and a SMe-bearing fragment and increase our linker's scope.



Scheme 4.15. **a)** 4-pyridine-boronic acid, K_2CO_3 , $\text{Pd}(\text{PPh}_3)_4$, toluene, H_2O , $100\text{ }^\circ\text{C}$, 16 h; **b)** $\text{PdCl}_2(\text{CH}_3\text{CN})_2$, CuI , $\text{PtBu}_3\cdot\text{HBF}_4$, THF, $i\text{Pr}_2\text{NH}$, $70\text{ }^\circ\text{C}$, 16 h; **c)** (i) $\text{PdCl}_2(\text{CH}_3\text{CN})_2$, CuI , $\text{PtBu}_3\cdot\text{HBF}_4$, THF, $i\text{Pr}_2\text{NH}$, rt, 16 h; (ii) TBAF, THF, 2 h.

Due to the growth of low-quality crystals, those compounds could not be characterized by X-ray crystallography. However, the distortion and negative curvature of this kind of 7-HBCs have been extensively studied previously in our group (Figure 4.15).¹⁴

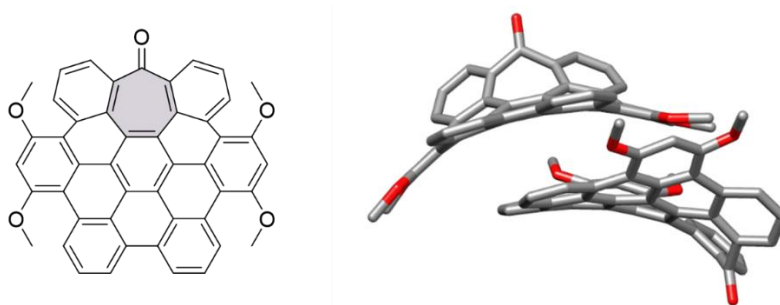
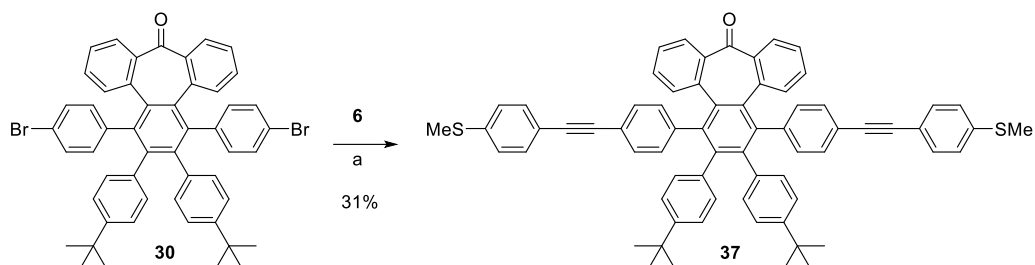


Figure 4.15. X-ray diffraction structure of a similar 7-HBC, where the saddle type curvature can be appreciated. Reproduced with permission of ref.⁷²

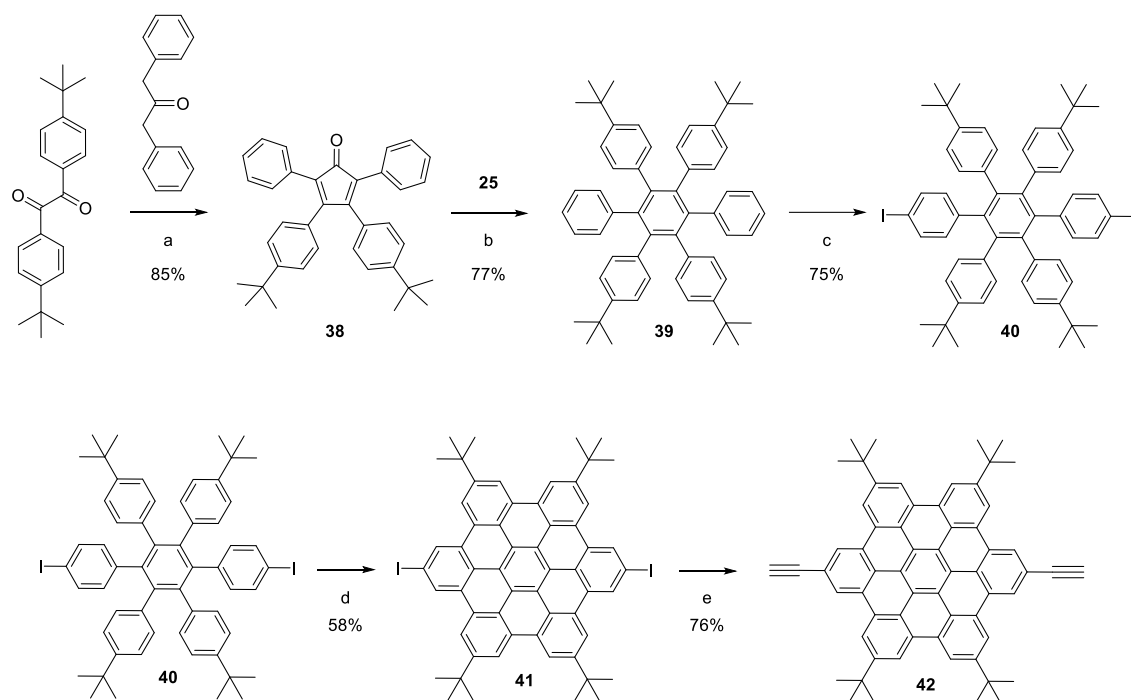
RESULT AND DISCUSSION

Concerning the 7-oligophenylenes, we decided to focus on **37**, the dendritic analogue of **35**, which was prepared *via* double Sonogashira cross-coupling reaction of **30** and **6** in a moderated yield.



Scheme 4.16. a) PdCl₂(CH₃CN)₂, CuI, PtBu₃·HBF₄, THF, *i*Pr₂NH, 70 °C, 16 h.

Our next objective was to prepare the planar HBCs. The synthesis of this class of compounds involves important limitations due to the low solubility of the molecules. Considering that, we only could obtain HBC **42** (Scheme 4.17), the planar analogue of 7-HBC **36**, that present terminal acetylene groups as linkers. The synthesis started with aldol condensation between 1,2-bis(4-(tert-butyl)phenyl)ethane-1,2-dione and 1,3-diphenylpropan-2-one, giving cyclopentadienone **38** in high yield. Diels-Alder reaction of **38** with previously prepared diphenylacetylene **25** led to hexaphenylbenzene derivative **39**. This compound **39** was submitted to iodination on the available positions *via* reaction with phenyliodine bis(trifluoroacetate) (PIFA) and iodine, originating compound **40** in moderate yield. A subsequent cyclodehydrogenation reaction by treatment with FeCl₃ afforded the corresponding diiodo HBC derivative **41**. Final coupling of **41** with TMSA, followed by deprotection in the presence of TBAF, gave rise to the desired HBC **42**.

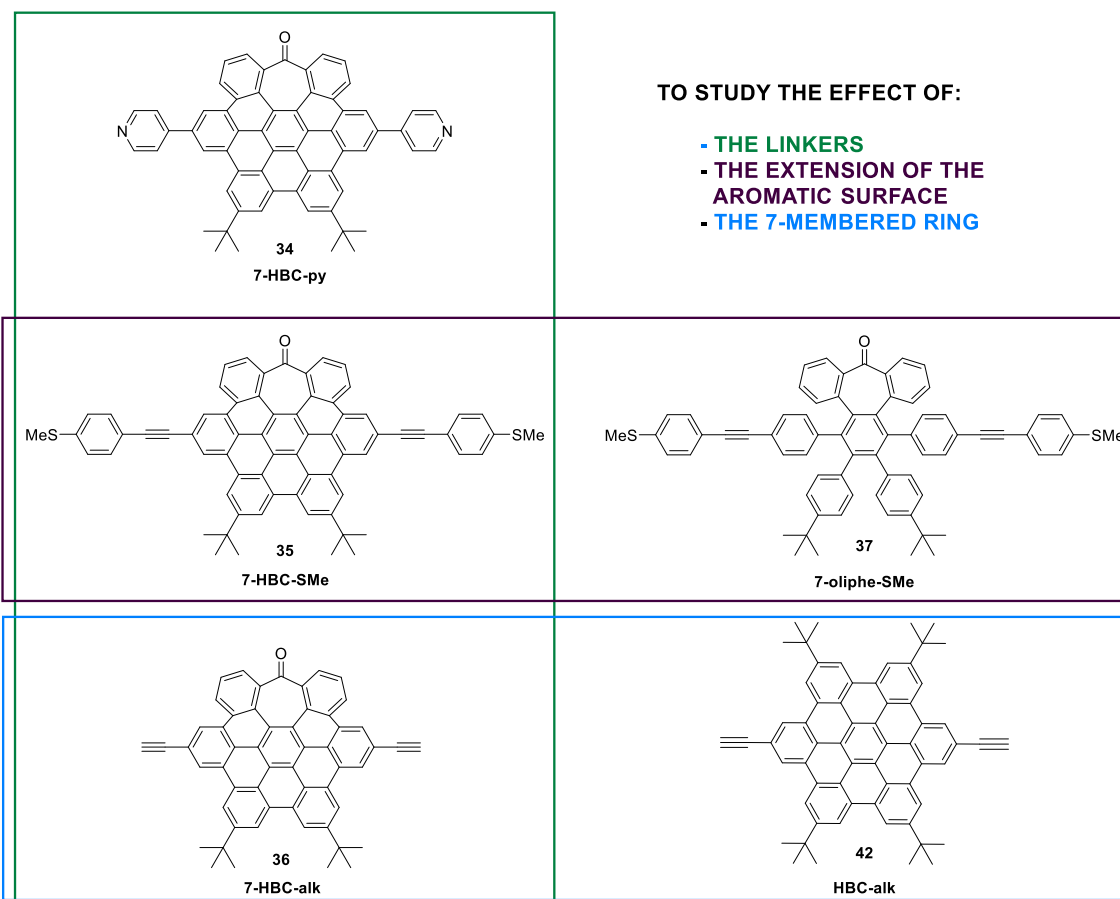


Scheme 4.17. (a) KOH, EtOH, reflux, 15 min; (b) Ph₂O, reflux, 16 h; (c) PIFA, I₂, CH₂Cl₂, rt, 72 h; (d) FeCl₃, CH₂Cl₂, CH₃NO₂, 0 °C to rt, 16 h; (e) (i) TMSA, Pd(PPh₃)₄, CuI, Et₃N, THF, 16 h; (ii) TBAF, THF, 2 h.

In the following scheme, a summary of the synthesized molecules is shown.^b The prepared compounds **34**, **35** and **36** permit the study of the effect of different linkers on this 7-HBC core. These compounds are shown all together in a green rectangle and renamed as follows in order to easily relate each compound with its corresponding linker: **7-HBC-Py**, **7-HBC-SMe** and **7-HBC-alk**, respectively. The comparison between **7-HBC-SMe** and its 7-membered containing dendritic oligophenylene analogue **37** (**7-oliphe-SMe**), which are shown together in a purple rectangle, permits to study the effect of the extension of the aromatic surface. Finally, the comparison between **7-HBC-alk** and its planar HBC analogue **42** (**HBC-alk**), which are depicted together in a blue rectangle, allows to study the effect of the negative curvature due to the presence of the 7-membered ring.

^b Dr. Rubén Tapia, Dr. Irene R. Marquez, Dr. Silvia Castro Fernández and Dr. Vicente García Jiménez contributed to the preparation of the of HBCs and 7-HBCs molecules discussed along the section.

RESULT AND DISCUSSION



Scheme 4.18. The collection of synthesized molecules allows to study the effect of: (i) the linkers (green square), (ii) the extension of the aromatic surface (purple square) and (iii) the 7-membered ring (brown square) on the conductance.

4.3.3. Break junction experiments

Gold on quartz plates were cleaned as described in the Experimental Section, and immersed for 15-20 min in DCM solutions of the corresponding molecules, with concentrations between 10^{-4} and 10^{-3} mM. Different combinations of gains were used, allowing to explore a conductance range in concordance with each molecule. *G-z* traces for compounds **7-HBC-SMe**, and **7-HBC-Py** were recorded applying a 0.16 bias voltage, while 0.2 bias voltage were used for **7-oliphe-SMe**, **7-HBC-alk** and **HBC-alk**. The raw conductance-distance (*G-z*) traces for each compound were subjected to the searching plateaus process described in the Experimental Section and the corresponding 1D and 2D histograms were built from the traces displaying plateaus. In the case of compounds **HBC-**

alk and 7-HBC-alk, an additional clustering-based analysis was needed, which was developed using the individual 2D histograms of the each trace displaying plateaus.

4.3.3.1. Effect of the linker on the conductance of 7-HBCs

2D and 1D histograms obtained for compounds 7-HBC-Py, 7-HBC-SMe and 7-HBC-alk are shown in Figure 4.16. Compound 7-HBC-Py displayed a well-defined molecular signal which originated a narrow and highly symmetric peak in the 1D histogram centered at $\log(G/G_0) = -5.7 \pm 0.23$. Compound 7-HBC-SMe displayed a broad molecular signal at lower conductance, centered at $\log(G/G_0) = -6.1 \pm 0.42$. Compound 7-HBC-alk gave rise to a sloping signal that started over $\log(G/G_0) = -3$ and finished about $\log(G/G_0) = -5$. Additionally, this compounds also displayed a small cloud at lower conductance but at the same length at which the main signal ended. This striking profile originated a broad and asymmetrical peak in the 1D histogram.

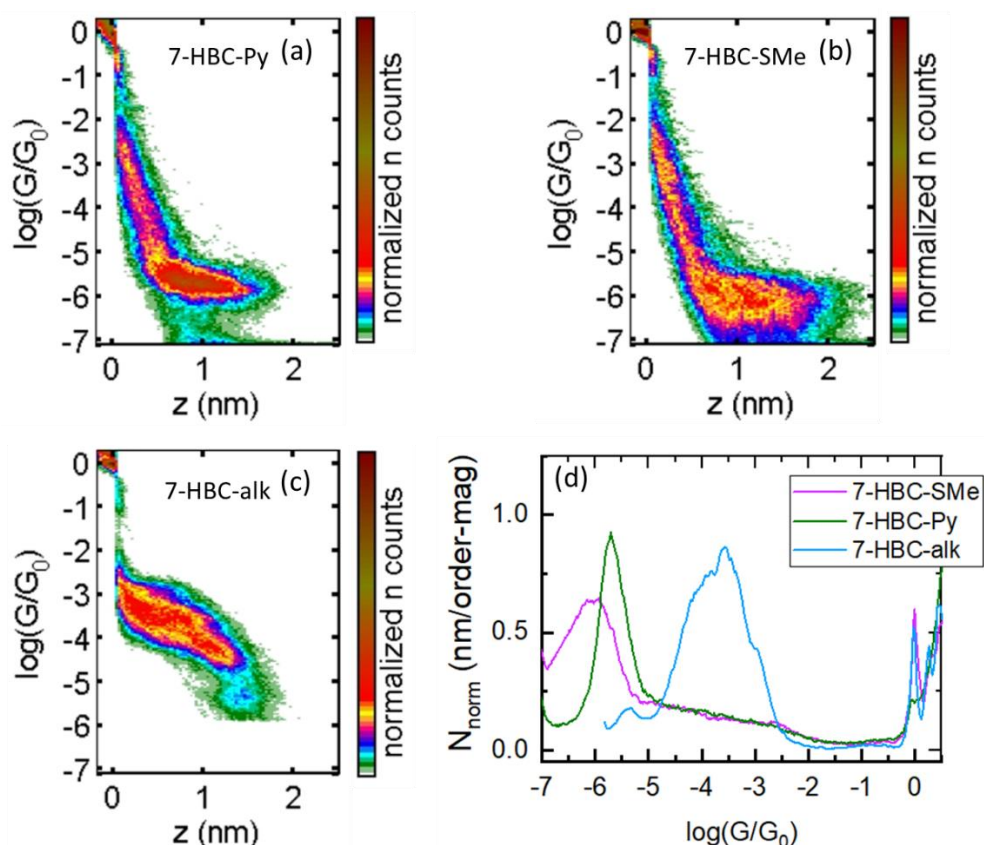


Figure 4.16. (a)-(c) 2D histograms of compounds 7-HBC-Py, 7-HBC-SMe and 7-HBC-alk, respectively. (d) 1D histograms of the same compounds (7-HBC-SMe, pink line), (7-HBC-Py, green line) and (7-HBC-alk, blue line). Histograms are built from 645, 1214 and 965 curves displaying plateaus, representing rates of success of 40%, 17% and 5%, respectively.

RESULT AND DISCUSSION

Some representative individual G - z traces for compounds **7-HBC-SMe**, **7-HBC-Py** and **7-HBC-alk** are shown in Figure 4.17. The traces are shifted in z for a better comparison. Flat plateaus were found for **7-HBC-SMe** and **7-HBC-Py**. The observed plateau-length distribution for these two compounds is also shown in Figure 4.17d, where the expected length of plateaus for the linker-to-linker distance is marked with a vertical line. These values are calculated as the molecular distance between the linking points, namely from the middle Au–L bond of one side to the other, once an interval of 0.4 nm is subtracted to compensate the electrode retraction after the gold contact breaks.

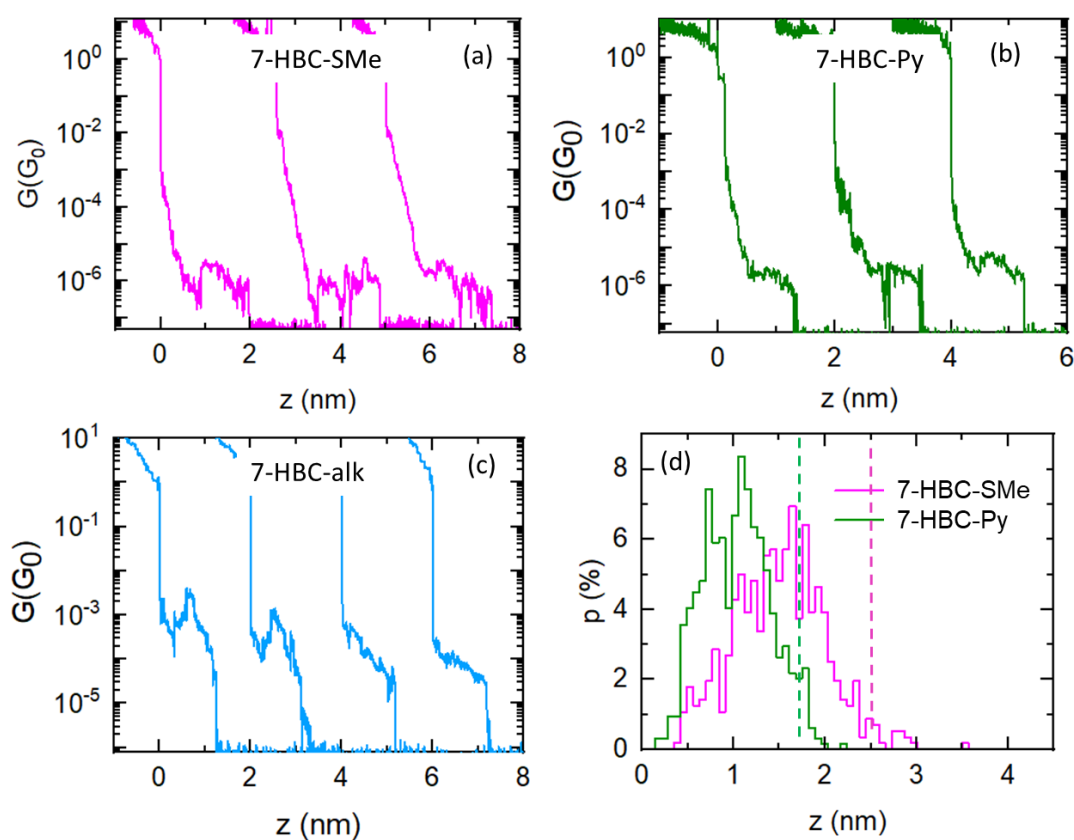


Figure 4.17. (a)–(c) Individual G - z traces for compounds **7-HBC-SMe**, **7-HBC-Py** and **7-HBC-alk**, respectively. (d) Distribution of the traces length for compounds **7-HBC-SMe** (pink line) and **7-HBC-Py** (green line). The expected molecular distances are marked as dashed lines.

Plateaus for compound **7-HBC-SMe** appeared in a wide conductance range, being responsible for the broad signal previously highlighted in the 1D and 2d histograms. The plateau length distribution shows that plateaus (Figure 4.17d, pink line) reach the expected length value (2.5 nm), although they tend to break at shorter distances. The traces in Figure 4.17a are examples of this behavior. The individual G - z traces for

compound **7-HBC-Py** (Figure 4.17b) were found highly reproducible, displaying plateaus in a very narrow conductance range, and originating a well-defined signal in the 1D and 2D histograms. The tail of the plateau-length distribution (Figure 4.17d, green line) agreed with the expected distance (1.75 nm). In the case of **7-HBC-alk**, different behaviors for the *G*-*z* traces were found. Examples of some individual *G*-*z* traces are shown in Figure 4.17c, where clearly curved plateaus, as well as sloping plateaus, can be distinguished. Given the evident presence of different kinds of plateaus, and considering the striking profile displayed in the 1D and 2D histograms, a clustering-based method was used for a further investigation on this molecule. This analysis, conducted over both **7-HBC-alk** and **HBC-alk** is detailed later in section 4.3.3.3. Nevertheless, in advance, we can say that the most frequent group, formed by traces displaying the flattest plateaus, is in agreement with the expected plateau length (marked as a blue vertical line in Figure 4.17d) and presents a typical conductance of $\log(G/G_0) = -3.5 \pm 0.23$.

As summary for these results, the experimental conductance values for **7-HBC-SMe**, **7-HBC-Py** and **7-HBC-alk** have been collected in table 4.1. Not surprisingly, a clear increase in the conductance value is observed as the molecule length decreases. Nevertheless, there is not a linear correlation between the conductance and the distance, due to the additional effect of the different coupling occurring in each case.

Table 4.1. Theoretical Au-Au distance for junctions with the molecules fully extended between the electrodes and experimental conductance values.

	Au-Au distance (nm)	$\text{Log}(G/G_0)_{\text{EXP}}$
7-HBC-SMe	2.5	-6.1 ± 0.42
7-HBC-Py	2.0	-5.7 ± 0.23
7-HBC-alk	1.7	-3.5 ± 0.23

Besides conductance, the different linkers have also involved different rates of *G*-*z* traces displaying plateaus, despite very similar conditions were used for preparing the samples (mM solutions and times of immersion). The higher rate was obtained for **7-HBC-SMe** (40%), followed by **7-HBC-Py** (15%). Finally, for **7-HBC-alk**, it was observed a 5% of traces

RESULT AND DISCUSSION

displaying plateaus, which could not be enhanced even by using more concentrated solutions for preparing the sample or by increasing the times of immersion.

Importantly, the conductance of a planar HBC analogue of **7-HBC-SMe** was reported by Tao and collaborators in 2010,⁶⁴ as discussed in section 4.1.2. This HBC molecule presents thiols as linkers instead of $-SMe$ groups, and also an additional C atom between the benzene ring and the linker (Figure 4.18).

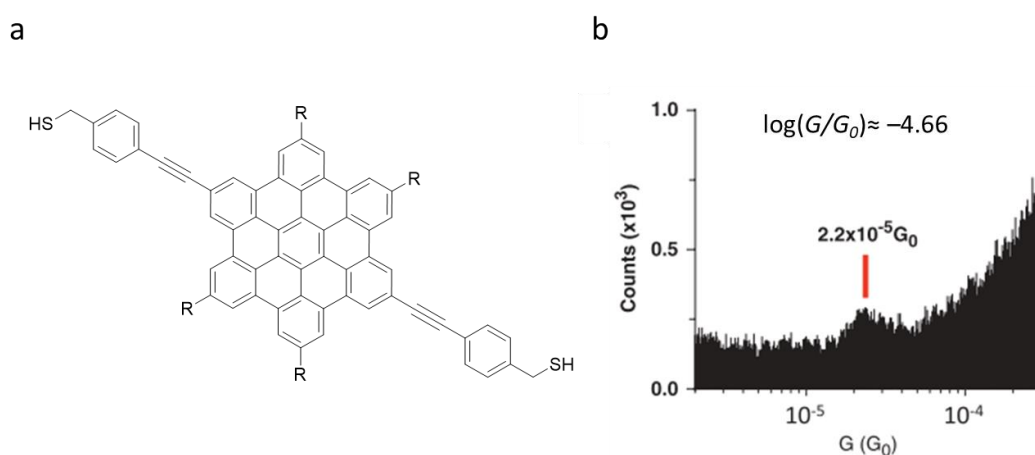


Figure 4.18. (a) Structure of the planar HBC analogue of **7-HBC-SMe**, reported by Tao and collaborators. (b) 1D histogram obtained for the compound, where the typical conductance value has been marker.

Although these two structural difference involve a certain effect on the conductance value, their influence have been studied previously in literature. Therefore, using the reported conductance value for the HBC analogue depicted in Figure 4.18, it is possible to estimate the expected conductance for the planar analogue of **7-HBC-SMe**, without the extra C atom at each side and displaying $-SMe$ groups as linkers. The comparison between them could help us to understand the effect of the curvature on the electron transport. On the one hand, according to previous studies, the presence of these extra C atoms at each side involves a conductance decrease of more than one order of magnitude (for example, going from $\log(G/G_0) \approx -1.96$ for benzenedithiol to $\log(G/G_0) \approx -3.22$ for benzenedimethanethiol).⁷⁵ On the other hand, the effect of having thiol- or thiolate-terminated molecules has been reported to be milder (for example, going from $\log(G/G_0) \approx -4$ for [1,1'-biphenyl]-4,4'-diyldimethanethiol to $\log(G/G_0) \approx -4,2$ for 4,4'-

bis((methylthio)methyl)-1,1'-biphenyl).⁷⁶ Considering the influence of these two effects, we can expect the conductance of the most direct planar analogue of **7-HBC-SMe** to be higher than that reported by Tao and coworkers for their HBC. This means, at least, a conductance difference of two orders of magnitude between the planar and the curved structures, involving, in fact, an important effect of the negative curvature on the conductance. Further discussion about the influence of the curvature on the transport for these HBC-like cores is included later in section 4.3.3.3, where the conductance for **7-HBC-alk** and **HBC-alk** is compared.

4.3.3.2. Conductance of 7-oliphenylene

Figure 4.19a shows the 2D histogram for compound **7-oliphe-SMe**. It could be noticed a molecular signal that started below $\log(G/G_0) = -6$ and extends toward out of the limits of the experimental conductance window. In spite of its low conductance and proximity to the bottom, plateaus are easily detectable due to their flat shape, as the individual G - z traces demonstrate (Figure 4.19b). Besides, the length of the longest plateaus agrees with the expected distance (2.5 nm), which is marked in the plateau-length distribution as a vertical line (Figure 4.19d). The impossibility of obtaining the complete profile of the conductance peak does not allow the reliable assignment of the conductance value for this compound. However, a general comparison with its π -extended counterpart is possible, being their 1D histograms and plateau-length distributions superimposed in Figure 4.19c and 4.19d, respectively. The conductance of compound **7-oliphe-SMe** seemed to be, at least, one order of magnitude lower than that of compound **7-HBC-SMe**, as it can be noticed from the comparison of their 1D histograms (Figure 4.19c). This trend agreed with the one observed in the transmission curves calculated for these compounds (Figure 4.20), which predicted a conductance difference of one and a half order of magnitude. This difference between the two compounds may be due to two main effects related with the formation of the 5 C–C bonds from **7-oliphe-SMe** to **7-HBC-SMe**: (i) the minimization of the dihedral angles between rings in the linker-to linker pathway, going from almost 45° in the **7-oliphe-SMe** to near zero in **7-HBC-SMe**; and (ii) the enlargement of the conjugated surface in the 7-HBC structure. The length of longest plateaus found

RESULT AND DISCUSSION

for both compounds is practically the same and in agreement with their expected linker-to linker distances.

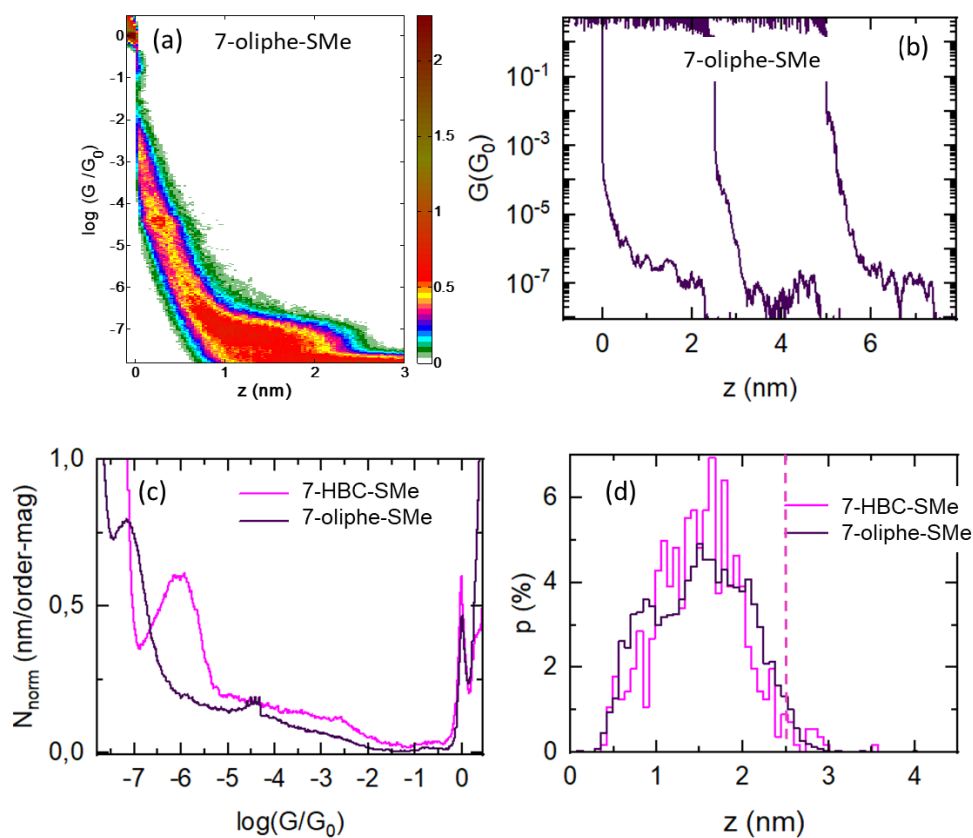


Figure 4.19. (a) 2D histogram for compound **7-oliphe-SMe**, built from all the traces displaying plateaus (2765 curves, 58% rate of success). (b) Representative traces displaying plateaus. (c) 1D histogram of compounds **7-HBC-SMe** (pink line) and **7-oliphe-SMe** (purple line). (d) Plateau-length distribution for both compounds.

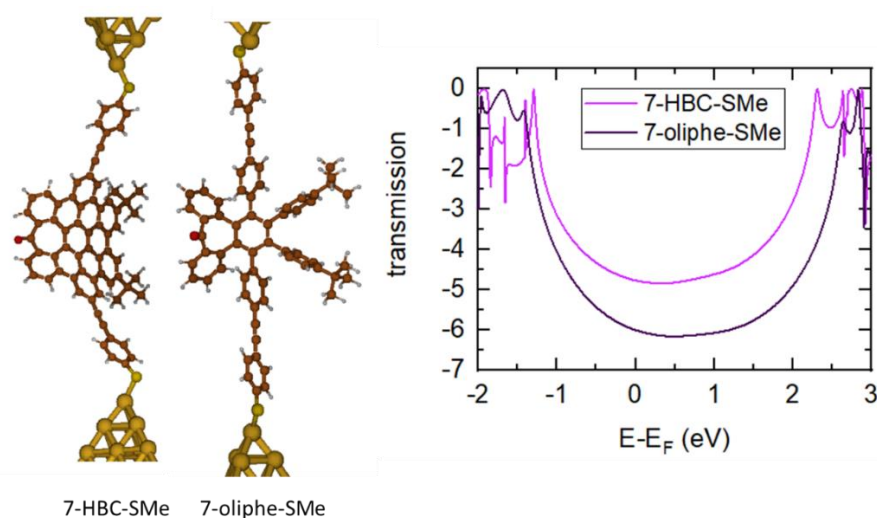


Figure 4.20. Geometries for **7-HBC-SMe** and **7-oliphe-SMe** molecules fully extended between the electrodes and transmission spectrum for **7-HBC-SMe** (pink line) and **7-oliphe-SMe** (purple line), calculated by Dr. Linda Zotti, from the *Universidad Autónoma de Madrid*.

4.3.3.3. Effect of the 7-membered ring and analysis of terminal acetylenes as linkers

In order to investigate the effect of the 7-membered ring in the electron transport about the nanographene, the results of the single-molecule experiments for **7-HBC-alk** were compared with those for **HBC-alk**. As previously explained, these compounds present terminal acetylene groups as linkers. This linker has demonstrated to produce a good interaction with gold electrodes, but its behaviour is not still well understood, since different profiles for the junctions with this linker have been reported (Figure 4.21).^{68,77,78} In this sense, in addition to the direct comparison of **7-HBC-alk** and **HBC-alk**, a thorough analysis of the behaviour of terminal acetylene as linker has been carried out.

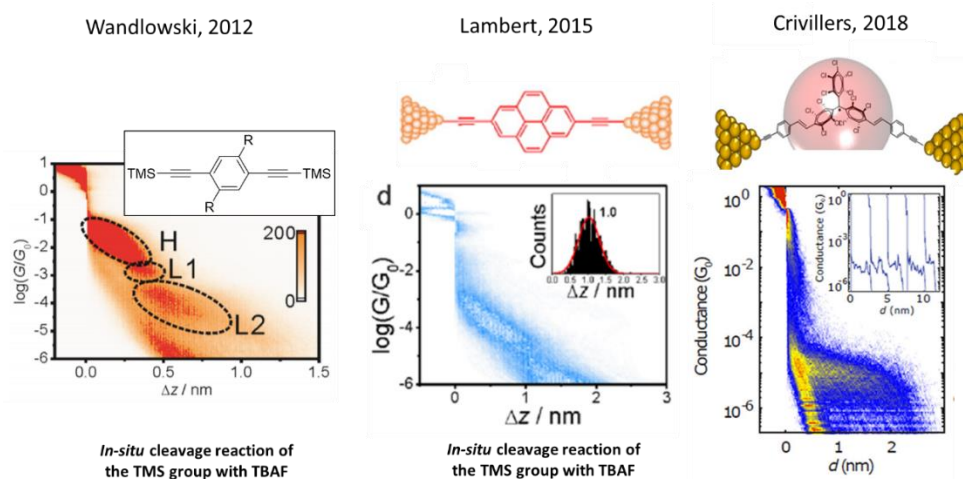


Figure 4.21. Profile of breaking traces for different junctions with terminal acetylenes as linkers. Adapted with permission from ref.^{68,77,78}

The single-molecule experiments for both **7-HBC-alk** and **HBC-alk** gave rise to a low rate of traces displaying plateaus (5% and 4%, respectively), which was not increased after increasing the concentration of the solution used for preparing the sample. The 2D and 1D histograms built from the traces displaying plateaus are collected in Figure 4.22. The histograms for both compounds are very similar, indicating the presence of several molecular signals between $\log(G/G_0) = -2$ and -6 , as the individual G - z traces for **7-HBC-alk** shown in Figure 4.17c previously revealed. In order to separate the traces according to their different breaking profiles, an additional clustering analysis was conducted over

RESULT AND DISCUSSION

the traces displaying plateaus for both compounds. The results obtained from this analysis are collected in Figure 4.23.

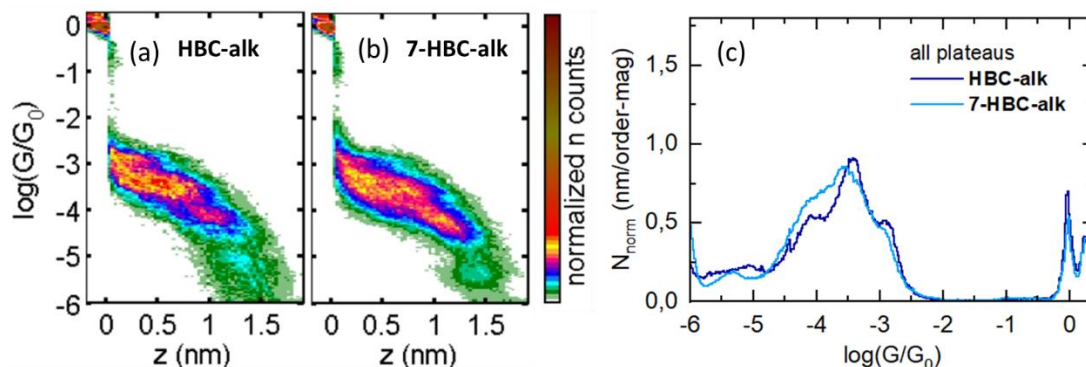


Figure 4.22. (a) 2D histogram built from all the traces displaying plateaus (629) for **HBC-alk**. (b) 2D histogram built from all the traces displaying plateaus (1274) for **7-HBC-alk**. (c) 1D histograms built from the same traces used for (a) and (b).

The clustering-based analysis allowed to distinguish between three different profiles (A, B, C) for the G - z traces recorded for both **HBC-alk** and **7-HBC-alk** (Figure 4.23a and 4.23b, respectively). Group A is formed by traces displaying flat and short plateaus at high conductance values. Group B consists of traces displaying longer plateaus at lower conductance. For both groups A and B, the plateaus are generally followed by a sloping tail. Group C collects the traces displaying more sloping plateaus. The independent 1D histograms for groups A, B and C for **HBC-alk** and **7-HBC-alk** are shown in Figure 4.23c and 4.23d, respectively. The peaks corresponding to the groups A concurred at the same main conductance value, namely $\log(G/G_0) \approx -2.9 \pm 0.13$. The peaks corresponding to groups B also concurred at the same value for both compounds ($\log(G/G_0) \approx -3.5 \pm 0.23$). The profile for group C is quite different in these compounds, despite consisting of sloping plateaus, since their slope and length is different, as shown in the corresponding 2D histograms. The plateau-length distributions for groups A and B are depicted in Figures 4.23e and 4.23f, respectively. Importantly, these values have been extracted at the end of the flat plateaus, avoiding the contribution of the tails. The plateau lengths for groups B are in perfect agreement, concurring the ends of the Gaussian distributions at the same value. However, a clear difference in length can be appreciated for plateaus in groups A.

The plateau-length distribution extends towards 1.25 nm in the case of 7-HBC-alk, while group A for HBC-alk displays shorter plateaus (up to 1 nm).

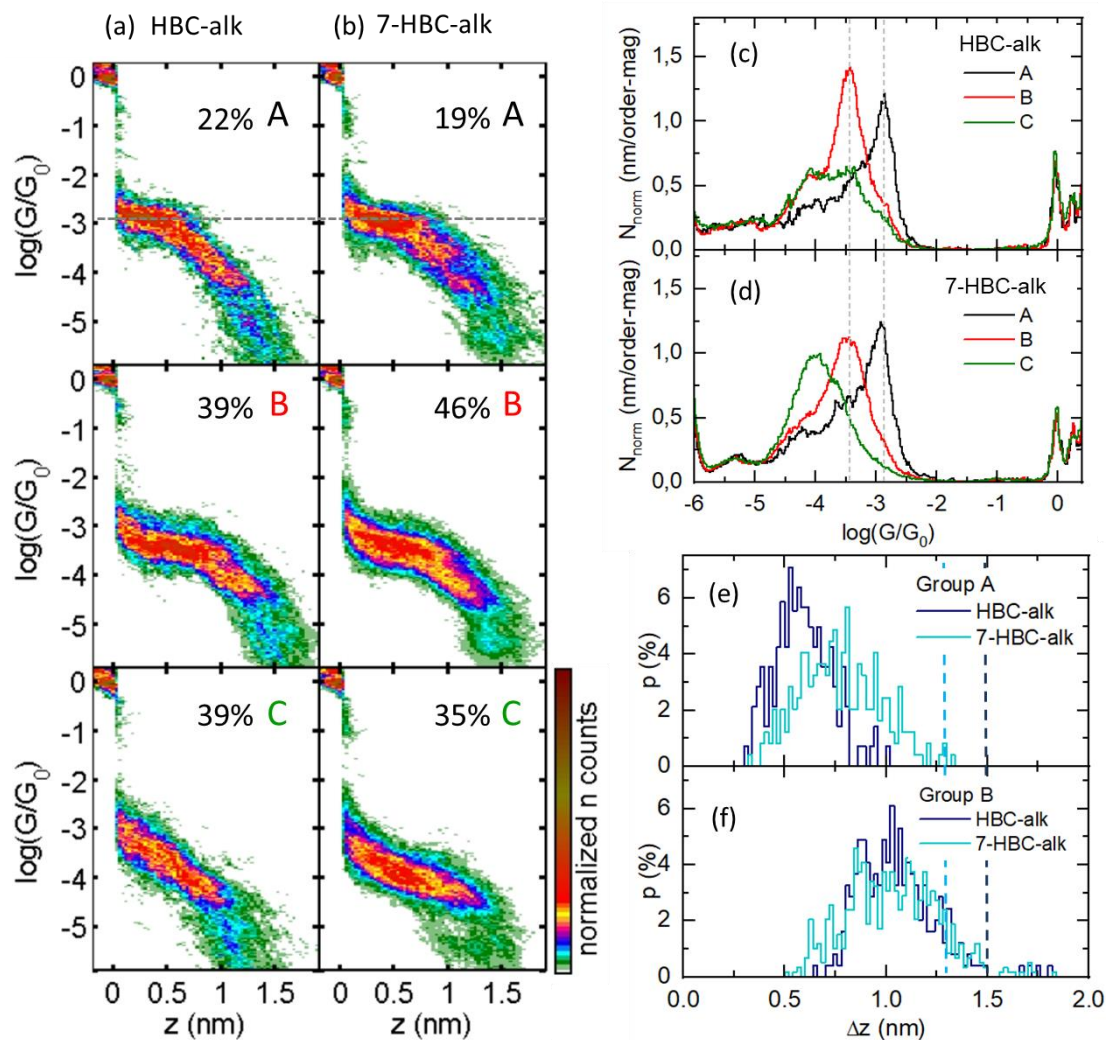


Figure 4.23. (a) 2D histograms for the three groups of breaking profiles (A, B and C) found for HBC-alk. (b) 2D histograms for the three groups of breaking profiles (A, B and C) found for 7-HBC-alk. (c) Independent 1D histograms of the groups A (black line), B (red line) and C (green line) found for HBC-alk. (d) Independent 1D histograms of the groups A (black line), B (red line) and C (green line) found for 7-HBC-alk. (e) Plateau-length distributions for traces in group A for HBC-alk (dark blue) and 7-HBC-alk (light blue). (f) Plateau-length distributions for traces in group B for HBC-alk (dark blue) and 7-HBC-alk (light blue).

Additional plateau-length distributions, shown in Figure 4.24, were built taking into account the effect of the tails. In this figure, the expected plateau length for the junctions of 7-HBC-alk (1.3 nm) and HBC-alk (1.5 nm) have been marked with a vertical blue line. For 7-HBC-alk, the distributions for the tails of the three groups are very similar, extending in each case up to 2 nm (Figure 4.24b). Considering that the expected plateau length for

RESULT AND DISCUSSION

the molecule fully extended between the electrodes is 1.28 nm, it seems clear that the tails are promoted by an additional process occurring during the stretching of the junction. For **HBC-alk**, the tails (Figure 4.24d) also extend toward considerable longer distances than those of the flat regions (Figure 4.24c), nevertheless not as much as in the previous case with respect the expected plateau length (1.47 nm). A possible explanation for this extension of the junction toward higher distances after the flat region can be related with a strong C-Au binding, able to mobilize Au atoms from the electrodes before the final breakage of the junction, as previously proposed in literature.⁷⁹ This hypothesis is also supported by the noticeable island occurring at $\log(G/G_0) < -5$, which is particularly visible in the 2D histogram built from all the traces displaying plateaus for **7-HBC-alk**, shown in Figure 4.22. This signal is due to a distance range in which the junctions usually break, independently of the kind of plateau displayed at higher conductance values.

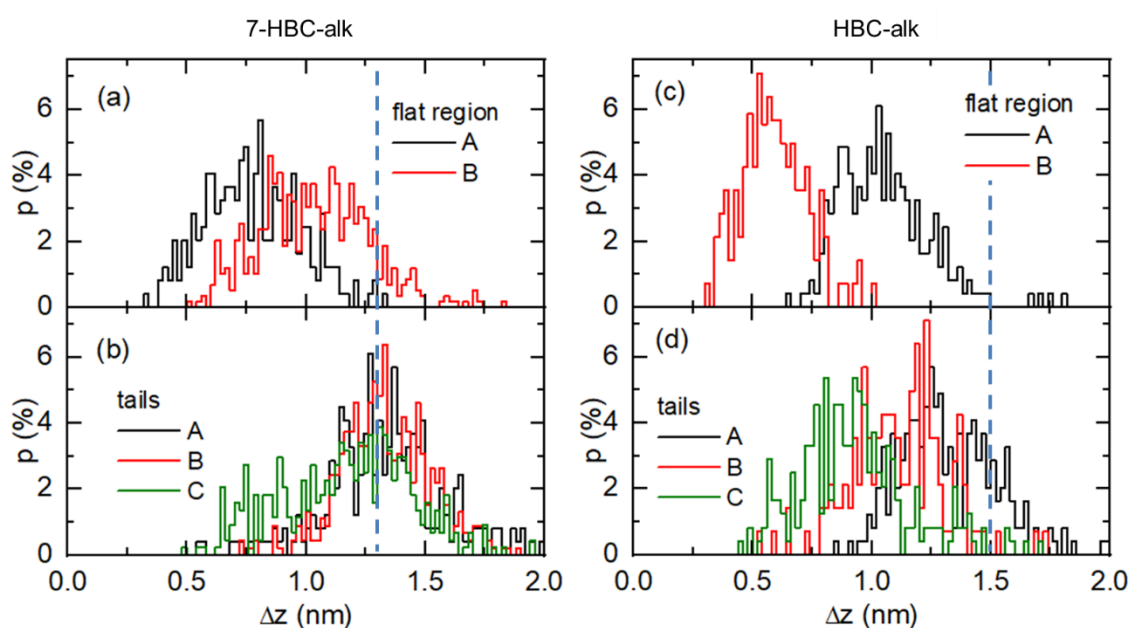


Figure 4.24. Plateau-length distributions for groups A, B and C found for **7-HBC-alk** (a-b) and **HBC-alk** (c-d), analysing separately the length at the end of the flat region ((a) and (c), respectively) and that of the tails ((b) and (d), respectively). The expected plateau length is marked as a vertical blue line.

Taking into account the expected plateau distances, the high G plateaus (group A) in both compounds are especially shorter. However, the flat profiles point at a stable junction occurring similarly in both cases. Two different possibilities have been considered. First,

the electrodes interacting with the extended aromatic surface, and secondly, the interaction with the triple bond itself, instead of the terminal C atoms. Interestingly, the direct metal- π coupling has been previously reported.^{80,81} In this case, the geometry responsible for those plateaus could evolve toward a more extended geometry for the molecule in the junction before the breakage point, while the separation of the electrodes continues. This could explain the 2D histogram of group A for **7-HBC-alk** (Figure 4.23b), where additional conductance regions seems particularly probable once the higher G plateaus end.

In general, the profile observed here for these compounds, agrees well with the reported complex and sloping profiles for this linking group (see Figure 4.21). In the study of Crivillers and co-workers, where a clear flat conductance cloud is reported (Figure 4.21c), the plateaus are so close to their detection limit that we cannot rule out a sloping behavior after the plateaus.

A further separation could be carried out for **7-HBC-alk** traces in group B. Within this group, three different profiles were found, as shown in Figure 4.25. Group BA presents sloping plateaus even before the tail (Figure 4.25b). Group BB displays flat plateaus followed by the sloping tail (Figure 4.25c). Group BC is formed by traces displaying flat plateaus without tail (Figure 4.25d). In consequence, this last group gives rise to a highly symmetric peak in the 1D histogram, without the noticeable shoulder present in the 1D histograms of groups BA and BB (Figure 4.25e). The plateau-length distributions for these three groups were again analysed at the end of the plateau region (Figure 4.25f) and the ends of the tails (Figure 4.25g). The expected plateau length for the molecule fully extended between the electrodes is marked with a vertical blue line. Again it can be seen that the flat plateaus of groups BB and BC are in good agreement with the expected distance for the molecular junction, while the tails of groups BA and BB extend toward higher distances.

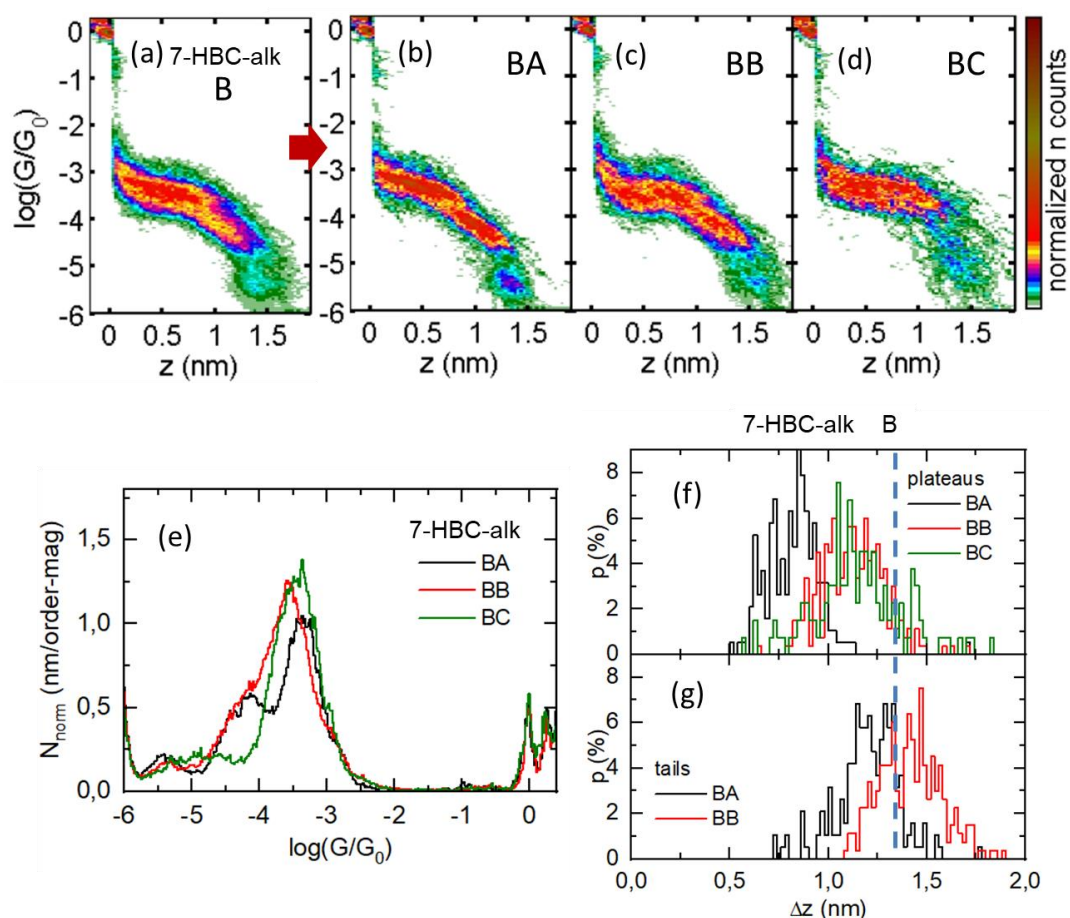


Figure 4.25. (a) 2D histogram built from the 7-HBC-alk traces in group B. A further clustering analysis allows to distinguish three different groups: 7-HBC-alk BA (b) 7-HBC-alk BB (c) and 7-HBC-alk BC (d). (e) Independent 1D histograms of the three groups. (f) Plateau-length distribution at the end of the flatter region. (g) Plateau-length distributions at the tails.

Taking into account this analysis for 7-HBC-alk and HBC-alk traces, we can conclude that the flat-plateau regions observed in group B correspond to a molecule fully extended between the electrodes, while the shorter and higher G plateaus observed in group A are due to an interaction between the gold and the π -surface (aromatic core or triple bonds) along the molecular backbone. Additionally, the tails reveal mobility of the electrode gold atoms during the stretching. Therefore, no particular influence on the conductance has been experimentally detected for the 7-membered ring, neither the negative curvature. The calculated transmission curves for both compounds supported these experimental findings (Figure 4.26), since almost identical curves were obtained for 7-HBC-alk and HBC-alk. It particularly highlights that the calculated HOMO–LUMO gap is exactly the same for both structures. Interestingly, this result is in contrast to that aforementioned in section

4.3.3.1 for **7-HBC-SMe** and its planar analogue. It is also in contrast to the reported HOMO–LUMO gap for large-area graphene, where an opening of the gap has been calculated for graphene containing structural defects.⁸² This fact could point to the gap being more influenced by the strong C–Au coupling rather than the curvature, in the case of **7-HBC-alk**.

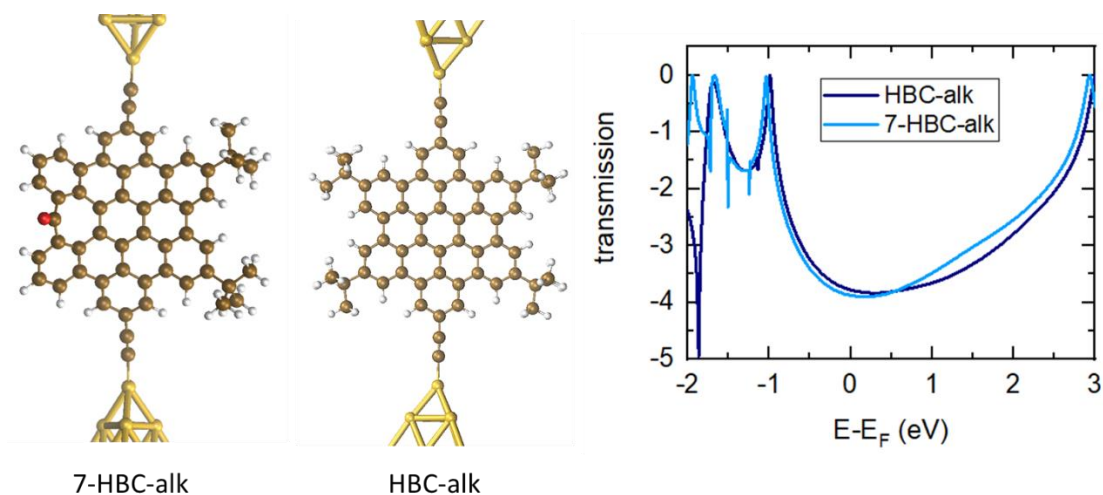


Figure 4.26. Geometries for **7-HBC-alk** and **HBC-alk** molecules fully extended between the electrodes, and comparison of the transmission curves for both compounds. Transmission curves were calculated by Dr. Linda Zotti, from *Universidad Autónoma de Madrid*.

Since no remarkable change on the conductance has been observed for the acetylene-terminated HBCs, but the experimental conductance values for other differently terminated HBCs suggest a certain effect of the curvature, it is required to compare the transport properties of other negatively curved nanographenes with that of their planar analogues prior to obtain a final conclusion for this topic. Nevertheless, this work can be considered the first step toward the unrevealing of the influence of the negative curvature on the electron transport properties of nanographenes.

4.4. Conclusions

Based on the obtained results for this chapter, the following conclusions can be drawn:

- A versatile synthetic methodology has allowed us the preparation of curved HBC-like molecules which incorporate a 7-membered ring in one of the edges, presenting functionalities such as thiomethyl, pyridyl and terminal acetylene, able to act as anchoring groups for single-molecule conductance experiments.
- The studies about the influence of the anchoring groups on the conductance of these hept-HBC compounds show that the conductance increases by reducing the distance between the linkers and the aromatic core.
- The study of the conductance of a dendritic oligophenylene synthetic precursor has demonstrated that the extension of the aromatic surface, based on the formation of 5 C–C bonds, involves an increase in the conductance of more than one order of magnitude.
- An exhaustive analysis of the conductance traces obtained using terminal acetylenes as binding group has been carried out, revealing the presence of flat and shorter plateaus due to interaction with the π -surface of the core, plateaus corresponding with the molecule extended between the electrodes and mobilization of atoms on the electrodes before the complete breakage of the junction.
- The effect of the curvature on the conductance of these structures has been evaluated by comparison with the planar HBC counterpart, revealing that the distortion, promoted by the presence of a heptagonal ring on the edge, does not modify the electron conduction, at least with alkyl binding groups, with strongly couple to the electrodes.

REFERENCES

References

- (1) Chen, L.; Hernandez, Y.; Feng, X.; Müllen, K. From Nanographene and Graphene Nanoribbons to Graphene Sheets: Chemical Synthesis. *Angew. Chem. Int. Ed.* **2012**, *51*, 7640–7654. <https://doi.org/10.1002/anie.201201084>.
- (2) Geim, A. K.; Novoselov, K. S. The Rise of Graphene. *Nat. Mater.* **2007**, *6*, 183–191. <https://doi.org/10.1038/nmat1849>.
- (3) Terrones, H.; Lv, R.; Terrones, M.; Dresselhaus, M. S. The Role of Defects and Doping in 2D Graphene Sheets and 1D Nanoribbons. *Rep. Prog. Phys* **2012**, *75*. <https://doi.org/10.1088/0034-4885/75/6/062501>.
- (4) Yazyev, O. V; Louie, S. G. Topological Defects in Graphene: Dislocations and Grain Boundaries. *Phys. Rev.* **2010**, *81*, 195420. <https://doi.org/10.1103/PhysRevB.81.195420>.
- (5) Banhart, F.; Kotakoski, J.; Krasheninnikov, A. V. Structural Defects in Graphene. *ACS Nano* **2011**, *5*, 26–41. <https://doi.org/10.1021/nn102598m>.
- (6) Tian, W.; Li, W.; Yu, W.; Liu, X. A Review on Lattice Defects in Graphene: Types Generation Effects and Regulation. *Micromachines* **2017**, *8*, 163. <https://doi.org/10.3390/mi8050163>.
- (7) Yang, G.; Li, L.; Ng, M. C. Structure of Graphene and Its Disorders: A Review. *Sci. Technol. Adv. Mater.* **2018**, *19*, 613–648. <https://doi.org/10.1080/14686996.2018.1494493>.
- (8) Liu, Y.; Yakobson, B. I. Cones, Pringles, and Grain Boundary Landscapes in Graphene Topology. *Nano Lett.* **2010**, *10*, 2178–2183. <https://doi.org/10.1021/nl100988r>.
- (9) Wang, X.; Akimitsu, N.; Müllen, K. Precision Synthesis versus Bulk-Scale Fabrication of Graphenes. *Nat. Rev.* **2017**, *2*, 0100.
- (10) Xu, W.; Lee, T. W. Recent Progress in Fabrication Techniques of Graphene Nanoribbons. *Mater. Horizons* **2016**, *3*, 186–207.

<https://doi.org/10.1039/c5mh00288e>.

- (11) Tour, J. M. Top-down versus Bottom-up Fabrication of Graphene-Based Electronics. *Chem. Mater.* **2014**, *26*, 163–171. <https://doi.org/10.1021/cm402179h>.
- (12) Zuzak, R.; Pozo, I.; Englund, M.; Garcia-Lekue, A.; Vilas-Varela, M.; Alonso, J. M.; Szymonski, M.; Guitián, E.; Pérez, D.; Godlewski, S.; Peña, D. Synthesis and Reactivity of a Trigonal Porous Nanographene on a Gold Surface. *Chem. Sci.* **2019**, *10*, 10143–10148. <https://doi.org/10.1039/c9sc03404h>.
- (13) Skidin, D.; Eisenhut, F.; Richter, M.; Nikipar, S.; Krüger, J.; Ryndyk, D. A.; Berger, R.; Cuniberti, G.; Feng, X.; Moresco, F. On-Surface Synthesis of Nitrogen-Doped Nanographenes with 5-7 Membered Rings. *Chem. Commun.* **2019**, *55*, 4731–4734. <https://doi.org/10.1039/C9CC00276F>.
- (14) Márquez, I. R.; Fuentes, N.; Cruz, C. M.; Puente-Muñoz, V.; Sotorrios, L.; Marcos, M. L.; Choquesillo-Lazarte, D.; Biel, B.; Crovetto, L.; Gómez-Bengoña, E.; González, M. T.; Martín, R.; Cuerva, J. M.; Campaña, A. G. Versatile Synthesis and Enlargement of Functionalized Distorted Heptagon-Containing Nanographenes. *Chem. Sci.* **2017**, *8*, 1068–1074. <https://doi.org/10.1039/c6sc02895k>.
- (15) Draper, S. M.; Gregg, D. J.; Madathil, R. Heterosuperbenzenes: A New Family of Nitrogen-Functionalized, Graphitic Molecules. *J. Am. Chem. Soc.* **2002**, *124*, 3486–3487. <https://doi.org/10.1021/ja017394u>.
- (16) Takase, M.; Enkelmann, V.; Sebastiani, D.; Baumgarten, M.; Müllen, K. Annularly Fused Hexapyrrolohexaazacoronenes: An Extended π System with Multiple Interior Nitrogen Atoms Displays Stable Oxidation States. *Angew. Chem. Int. Ed.* **2007**, *46*, 5524–5527. <https://doi.org/10.1002/anie.200701452>.
- (17) Cruz, C. M.; Márquez, I. R.; Mariz, I. F. A.; Blanco, V.; Sánchez-Sánchez, C.; Sobrado, J. M.; Martín-Gago, J. A.; Cuerva, J. M.; Maçôas, E.; Campaña, A. G. Enantiopure Distorted Ribbon-Shaped Nanographene Combining Two-Photon Absorption-Based Upconversion and Circularly Polarized Luminescence. *Chem. Sci.* **2018**, *9*, 3917–3924. <https://doi.org/10.1039/C8SC00427G>.

REFERENCES

- (18) Castro-Fernández, S.; Cruz, C. M.; Mariz, I. F. A.; Márquez, I. R.; Jiménez, V. G.; Palomino-Ruiz, L.; Cuerva, J. M.; Maçôas, E.; Campaña, A. G. Two-Photon Absorption Enhancement by the Inclusion of a Tropone Ring in Distorted Nanographene Ribbons. *Angew. Chem. Int. Ed* **2020**, *59*, 7139. <https://doi.org/10.1002/ange.202000105>.
- (19) Méndez, J.; López, M. F.; Martín-Gago, J. A. On-Surface Synthesis of Cyclic Organic Molecules. *Chem. Soc. Rev.* **2011**, *40*, 4578–4590. <https://doi.org/10.1039/c0cs00161a>.
- (20) Cai, J.; Ruffieux, P.; Jaafar, R.; Bieri, M.; Braun, T.; Blankenburg, S.; Muoth, M.; Seitsonen, A. P.; Saleh, M.; Feng, X.; Müllen, K.; Fasel, R. Atomically Precise Bottom-up Fabrication of Graphene Nanoribbons. *Nature* **2010**, *466*, 470–473. <https://doi.org/10.1038/nature09211>.
- (21) Narita, A.; Feng, X.; Müllen, K. Bottom-up Synthesis of Chemically Precise Graphene Nanoribbons. *Chem. Rec.* **2015**, *15*, 295–309. <https://doi.org/10.1002/tcr.201402082>.
- (22) Scholl, R.; Seer, C.; Weitzenboock, R. Perylen, Ein Hoch Kondensierter Aromatischer Kohlenwasserstoff C₂₀H₁₂. *Chem. Ber.* **1910**, *43*, 1910.
- (23) Scholl, R.; Seer, C. Abspaltung Aromatisch Gebundenen Wasserstoffs Und Verknüpfung Aromatischer Kerne Durch Aluminiumchlorid. *Liebigs Ann. Chem.* **1912**, *394*, 1912.
- (24) Clar, E.; Ironside, C. T.; Zander, M. The Electronic Interaction between Benzenoid Rings in Condensed Aromatic Hydrocarbons. 1 : 12-2 : 3-4 : 5-6 : 7-8 : 9-10 : 11-Hexabenzocoronene, 1 : 2-3 : 4-5 : 6-10 : 11-Tetrabenzoanthanthrene, and 4 : 5-6 : 7-11 : 12-13 : 14-Tetrabenzoperopyrene. *J. Chem. Soc.* **1959**, 142–147.
- (25) Clar, E.; schmidt, W. Localised vs Delocalised Molecular Orbitals in Aromatic Hydrocarbons. *Tetrahedron* **1979**, *35*, 2673–2680. [https://doi.org/10.1016/0040-4020\(79\)87049-0](https://doi.org/10.1016/0040-4020(79)87049-0).
- (26) Siegel, J. S.; Wu, Y.-T. Polyarenes I. In *Topics in Current Chemistry*; **2014**, 349. <https://doi.org/10.1007/978-3-662-43379-9>.

- (27) Halleux, A.; Martin, R. H.; King, G. S. D. 129. Syntheses Dans La Serie Des Derives Polycycliques Aromatiques Hautement Condenses. L'hexabenz-1,12; 2,3; 4,5; 6,7; 8,9; 10,11-Coronene, Le Tetrabenz-4,5; 6,7; 11,12; 13,14-Peropyrene et Le Tetrabenz-1,2; 3,4; 8,9; 10,11-Bisanthene. *Helv Chim Acta* **1958**, *XLI*, 1177–1183. <https://doi.org/10.1002/hlca.19580410502>.
- (28) Hendel, W.; Khan, Z. H.; Schmidt, W. Hexa-Peri-Benzocoronene, a Candidate for the Origin of the Diffuse Interstellar Visible Absorption Bands ? *Tetrahedron* **1986**, *42*, 1127–1134. [https://doi.org/10.1016/S0040-4020\(01\)87517-7](https://doi.org/10.1016/S0040-4020(01)87517-7).
- (29) Agenet, N.; Gandon, V.; Vollhardt, K. P. C.; Malacria, M.; Aubert, C. Cobalt-Catalyzed Cyclotrimerization of Alkynes: The Answer to the Puzzle of Parallel Reaction Pathways. *J. Am. Chem. Soc.* **2007**, *129*, 8860–8871. <https://doi.org/10.1021/ja072208r>.
- (30) Yamamoto, Y. Recent Advances in Intramolecular Alkyne Cyclotrimerization and Its Applications. In *Current Organic Chemistry*; **2005**; *9*, 503–519. <https://doi.org/10.2174/1385272053544399>.
- (31) Müller, M.; Kübel, C.; Müllen, K. Giant Polycyclic Aromatic Hydrocarbons. *Chem. Eur. J.* **1998**, *4*, 2099–2109. [https://doi.org/10.1002/\(SICI\)1521-3765\(19981102\)4:11<2099::AID-CHEM2099>3.0.CO;2-T](https://doi.org/10.1002/(SICI)1521-3765(19981102)4:11<2099::AID-CHEM2099>3.0.CO;2-T).
- (32) Simpson, C. D.; Mattersteig, G.; Martin, K.; Gherghel, L.; Bauer, R. E.; Räder, H. J.; Müllen, K. Nanosized Molecular Propellers by Cyclodehydrogenation of Polyphenylene Dendrimers. *J. Am. Chem. Soc.* **2004**, *126*, 3139–3147. <https://doi.org/10.1021/ja036732j>.
- (33) King, B. T.; Kroulík, J.; Robertson, C. R.; Rempala, P.; Hilton, C. L.; Korinek, J. D.; Gortari, L. M. Controlling the Scholl Reaction. *J. Org. Chem.* **2007**, *72*, 2279–2288. <https://doi.org/10.1021/jo061515x>.
- (34) Grzybowski, M.; Sadowski, B.; Butenschön, H.; Gryko, D. T. Synthetic Applications of Oxidative Aromatic Coupling—From Biphenols to Nanographenes. *Angew. Chem. Int. Ed.* **2020**, *59*, 2998–3027. <https://doi.org/10.1002/anie.201904934>.
- (35) Narita, A.; Wang, X. Y.; Feng, X.; Müllen, K. New Advances in Nanographene

REFERENCES

- Chemistry. *Chem. Soc. Rev.* **2015**, *44*, 6616–6643. <https://doi.org/10.1039/c5cs00183h>.
- (36) Yoon, K. Y.; Dong, G. Liquid-Phase Bottom-up Synthesis of Graphene Nanoribbons. *Mater. Chem. Front.* **2020**, *4*, 29–45. <https://doi.org/10.1039/c9qm00519f>.
- (37) Wu, Y. T.; Siegel, J. S. Aromatic Molecular-Bowl Hydrocarbons: Synthetic Derivatives, Their Structures, and Physical Properties. *Chem. Rev.* **2006**, *106*, 4843–4867. <https://doi.org/10.1021/cr050554q>.
- (38) Márquez, I. R.; Castro-Fernández, S.; Millán, A.; Campaña, A. G. Synthesis of Distorted Nanographenes Containing Seven- and Eight-Membered Carbocycles. *Chem. Commun.* **2018**, *54*, 6705–6718. <https://doi.org/10.1039/c8cc02325e>.
- (39) Stępień, M.; Gońka, E.; Żyła, M.; Sprutta, N. Heterocyclic Nanographenes and Other Polycyclic Heteroaromatic Compounds: Synthetic Routes, Properties, and Applications. *Chem. Rev.* **2017**, *117*, 3479–3716. <https://doi.org/10.1021/acs.chemrev.6b00076>.
- (40) Wang, X. Y.; Yao, X.; Narita, A.; Müllen, K. Heteroatom-Doped Nanographenes with Structural Precision. *Acc. Chem. Res.* **2019**, *52*, 2491–2505. <https://doi.org/10.1021/acs.accounts.9b00322>.
- (41) Rickhaus, M.; Mayor, M.; Juriček, M. Chirality in Curved Polyaromatic Systems. *Chem. Soc. Rev.* **2017**, *46*, 1643–1660. <https://doi.org/10.1039/c6cs00623j>.
- (42) Pun, S. H.; Miao, Q. Toward Negatively Curved Carbons. *Acc. Chem. Res.* **2018**, *51*, 1630–1642. <https://doi.org/10.1021/acs.accounts.8b00140>.
- (43) Christoph, H.; Grunenberg, J.; Hopf, H.; Dix, I.; Jones, P. G.; Scholtissek, M.; Maier, G. MP2 and DFT Calculations on Circulenes and an Attempt to Prepare the Second Lowest Benzolog, [4]Circulene. *Chem. Eur. J.* **2008**, *14*, 5604–5616. <https://doi.org/10.1002/chem.200701837>.
- (44) Bharat, R. B.; Bally, T.; Valente, A.; Cyrański, M. K.; Dobrzycki, Ł.; Spain, S. M.; Rempała, P.; Chin, M. R.; King, B. T. Quadrannulene: A Nonclassical Fullerene Fragment. *Angew. Chem. Int. Ed.* **2010**, *49*, 399–402.

<https://doi.org/10.1002/anie.200905633>.

- (45) Barth, W. E.; Lawton, R. G. Dibenzo[ghi,mno]Fluoranthene. *J. Am. Chem. Soc.* **1966**, *88*, 380–381. <https://doi.org/10.1021/ja00954a049>.
- (46) Barht, W.; Lawton, R. The Synthesis of Corannulene. *J. Am. Chem. Soc.* **1971**, *2*, 1730–1745.
- (47) Tsefrikas, V. M.; Scott, L. T. Geodesic Polyarenes by Flash Vacuum Pyrolysis. *Chem. Rev.* **2006**, *106*, 4868–4884. <https://doi.org/10.1021/cr050553y>.
- (48) Jon Seiders, T.; Baldrige, K. K.; Siegel, J. S. Synthesis and Characterization of the First Corannulene Cyclophane. *J. Am. Chem. Soc.* **1995**, *34*, 273.
- (49) Muzammil, E. M.; Halilovic, D.; Stuparu, M. C. Synthesis of Corannulene-Based Nanographenes. *Commun. Chem.* **2019**, *2*. <https://doi.org/10.1038/s42004-019-0160-1>.
- (50) Yamamoto, K.; Harada, T.; Nakazaki, M. Synthesis and Characterization of [7]Circulene. *J. Am. Chem. Soc.* **1983**, *105*, 7171–7172.
- (51) Yamamoto, K.; Sonobe, H.; Matsubara, H.; Sato, M.; Okamoto, S.; Kitaura, K. Convenient New Synthesis of [7]Circulene. *Angew. Chem. Int. Ed.* **1996**, *35*, 69–70.
- (52) Pun, S. H.; Wang, Y.; Chu, M.; Chan, C. K.; Li, Y.; Liu, Z.; Miao, Q. Synthesis, Structures, and Properties of Heptabenzo[7]Circulene and Octabenzo[8]Circulene. *J. Am. Chem. Soc.* **2019**, *141*, 9680–9686. <https://doi.org/10.1021/jacs.9b03910>.
- (53) Hensel, T.; Andersen, N. N.; Plesner, M.; Pittelkow, M. Synthesis of Heterocyclic [8]Circulenes and Related Structures. *Synlett* **2016**, *27*, 498–525. <https://doi.org/10.1055/s-0035-1560524>.
- (54) Miller, R. W.; Duncan, A. K.; Schneebeli, S. T.; Gray, D. L.; Whalley, A. C. Synthesis and Structural Data of Tetrabenzo[8]Circulene. *Chem. Eur. J.* **2014**, *20*, 3705–3711. <https://doi.org/10.1002/chem.201304657>.
- (55) Feng, C. N.; Kuo, M. Y.; Wu, Y. T. Synthesis, Structural Analysis, and Properties of [8]Circulenes. *Angew. Chem. Int. Ed.* **2013**, *52*, 7791–7794. <https://doi.org/10.1002/anie.201303875>.

REFERENCES

- (56) Sakamoto, Y.; Suzuki, T. Tetrabenz[8]Circulene: Aromatic Saddles from Negatively Curved Graphene. *J. Am. Chem. Soc.* **2013**, *135*, 14074–14077. <https://doi.org/10.1021/ja407842z>.
- (57) Luo, J.; Xu, X.; Mao, R.; Miao, Q. Curved Polycyclic Aromatic Molecules That Are π -Isoelectronic to Hexabenzocoronene. *J. Am. Chem. Soc.* **2012**, *134*, 13796–13803. <https://doi.org/10.1021/ja3054354>.
- (58) Cheung, K. Y.; Xu, X.; Miao, Q. Aromatic Saddles Containing Two Heptagons. *J. Am. Chem. Soc.* **2015**, *137*, 3910–3914. <https://doi.org/10.1021/jacs.5b00403>.
- (59) Kawai, K.; Kato, K.; Peng, L.; Segawa, Y.; Scott, L. T.; Itami, K. Synthesis and Structure of a Propeller-Shaped Polycyclic Aromatic Hydrocarbon Containing Seven-Membered Rings. *Org. Lett.* **2018**, *20*, 1932–1935. <https://doi.org/10.1021/acs.orglett.8b00477>.
- (60) Pun, S. H.; Chan, C. K.; Luo, J.; Liu, Z.; Miao, Q. A Dipleiadiene-Embedded Aromatic Saddle Consisting of 86 Carbon Atoms. *Angew. Chem. Int. Ed.* **2018**, *57*, 1581 – 1586. <https://doi.org/10.1002/anie.201711437>.
- (61) Müllen, K.; Rabe, J. P. Nanographenes as Active Components of Single-Molecule Electronics and How a Scanning Tunneling Microscope Puts Them to Work. *Acc. Chem. Res.* **2008**, *41*, 511–520. <https://doi.org/10.1021/ar7001446>.
- (62) Li, Z.; Smeu, M.; Rives, A.; Maraval, V.; Chauvin, R.; Ratner, M. A.; Borguet, E. Towards Graphyne Molecular Electronics. **2015**. <https://doi.org/10.1038/ncomms7321>.
- (63) Xu, B.; Xiao, X.; Yang, X.; Zang, L.; Tao, N. Large Gate Modulation in the Current of a Room Temperature Single Molecule Transistor. *J. Am. Chem. Soc.* **2005**, *127*, 2386–2387. <https://doi.org/10.1021/ja042385h>.
- (64) Diez-Perez, I.; Li, Z.; Hihath, J.; Li, J.; Zhang, C.; Yang, X.; Zang, L.; Dai, Y.; Feng, X.; Muellen, K.; Tao, N. Gate-Controlled Electron Transport in Coronenes as a Bottom-up Approach towards Graphene Transistors. *Nat. Commun.* **2010**, *1*, 31. <https://doi.org/10.1038/ncomms1029>.

- (65) Martín-Lasanta, A.; Miguel, D.; García, T.; López-Villanueva, J. A.; Rodríguez-Bolívar, S.; Gómez-Campos, F. M.; Buñuel, E.; Cárdenas, D. J.; Cienfuegos, L. Á.; Cuerva, J. M. Influence of the Number of Anchoring Groups on the Electronic and Mechanical Properties of Benzene-, Anthracene- and Pentacene-Based Molecular Devices. *ChemPhysChem* **2012**, *13*, 860–868. <https://doi.org/10.1002/cphc.201100582>.
- (66) Lambert, C. J.; Liu, S. X. A Magic Ratio Rule for Beginners: A Chemist's Guide to Quantum Interference in Molecules. *Chem. Eur. J.* **2018**, *24*, 4193–4201. <https://doi.org/10.1002/chem.201704488>.
- (67) Geng, Y.; Sangtarash, S.; Huang, C.; Sadeghi, H.; Fu, Y.; Hong, W.; Wandlowski, T.; Decurtins, S.; Lambert, C. J.; Liu, S. X. Magic Ratios for Connectivity-Driven Electrical Conductance of Graphene-like Molecules. *J. Am. Chem. Soc.* **2015**, *137*, 4469–4476. <https://doi.org/10.1021/jacs.5b00335>.
- (68) Sangtarash, S.; Huang, C.; Sadeghi, H.; Sorohhov, G.; Hauser, J.; Wandlowski, T.; Hong, W.; Decurtins, S.; Liu, S. X.; Lambert, C. J. Searching the Hearts of Graphene-like Molecules for Simplicity, Sensitivity, and Logic. *J. Am. Chem. Soc.* **2015**, *137*, 11425–11431. <https://doi.org/10.1021/jacs.5b06558>.
- (69) Zoppi, L.; Ferretti, A.; Baldrige, K. K. Tuning Electron Transport through Functionalized C₂₀H₁₀ Molecular Junctions. *J. Chem. Theory Comput.* **2015**, *11*, 4900–4910. <https://doi.org/10.1021/acs.jctc.5b00592>.
- (70) Jiang, Y.; Xu, X.; Hu, Y.; Zhang, G.; Liang, Z.; Li, W.; Jiang, Y.; Sun, X. A Computational Study on a Multimode Spin Conductance Switching by Coordination Isomerization in Organometallic Single-Molecule Junctions. *Phys. Chem. Chem. Phys.* **2018**, *20*, 20280–20286. <https://doi.org/10.1039/c8cp02914h>.
- (71) Arroyo, C. R.; Leary, E.; Castellanos-Gómez, A.; Rubio-Bollinger, G.; González, M. T.; Agraït, N. Influence of Binding Groups on Molecular Junction Formation. *J. Am. Chem. Soc.* **2011**, *133*, 14313–14319. <https://doi.org/10.1021/ja201861k>.
- (72) Marquez, I. Desarrollo de Nuevas Metodologías Sintéticas Utilizando Sistemas Multimetalicos, **2017**. Thesis dissertation, Universidad de Granada.

REFERENCES

- (73) Cruz, C. M. Design, Synthesis and Physical Properties Evaluation of Heptagon-Containing Distorted Nanographenes, **2020**. Thesis dissertation, Universidad de Granada.
- (74) Mio, M. J.; Kopel, L. C.; Braun, J. B.; Gadzikwa, T. L.; Hull, K. L.; Brisbois, R. G.; Markworth, C. J.; Grieco, P. A. One-Pot Synthesis of Symmetrical and Unsymmetrical Bisarylethyne by a Modification of the Sonogashira Coupling Reaction. *Org. Lett.* **2002**, *4*, 3199–3202. <https://doi.org/10.1021/ol026266n>.
- (75) Xiao, X.; Xu, B.; Tao, N. J. Measurement of Single Molecule Conductance: Benzenedithiol and Benzenedimethanethiol. *Nano Lett.* **2004**, *4*, 267–271. <https://doi.org/10.1021/nl035000m>.
- (76) Leary, E.; Zotti, L. A.; Miguel, D.; Márquez, I. R.; Palomino-Ruiz, L.; Cuerva, J. M.; Rubio-Bollinger, G.; González, M. T.; Agraït, N. The Role of Oligomeric Gold-Thiolate Units in Single-Molecule Junctions of Thiol-Anchored Molecules. *J. Phys. Chem. C.* **2018**, *122*, 3211–3218. <https://doi.org/10.1021/acs.jpcc.7b11104>.
- (77) Hong, W.; Li, H.; Liu, S. X.; Fu, Y.; Li, J.; Kaliginedi, V.; Decurtins, S.; Wandlowski, T. Trimethylsilyl-Terminated Oligo(Phenylene Ethynylene)s: An Approach to Single-Molecule Junctions with Covalent Au-C σ -Bonds. *J. Am. Chem. Soc.* **2012**, *134*, 19425–19431. <https://doi.org/10.1021/ja307544w>.
- (78) Bejarano, F.; Olavarria-Contreras, I. J.; Droghetti, A.; Rungger, I.; Rudnev, A.; Gutiérrez, D.; Mas-Torrent, M.; Veciana, J.; Van Der Zant, H. S. J.; Rovira, C.; Burzurí, E.; Crivillers, N. Robust Organic Radical Molecular Junctions Using Acetylene Terminated Groups for C-Au Bond Formation. *J. Am. Chem. Soc.* **2018**, *140*, 1691–1696. <https://doi.org/10.1021/jacs.7b10019>.
- (79) Frei, M.; Aradhya, S. V.; Hybertsen, M. S.; Venkataraman, L. Linker Dependent Bond Rupture Force Measurements in Single-Molecule Junctions. *J. Am. Chem. Soc.* **2012**, *134*, 4003–4006. <https://doi.org/10.1021/ja211590d>.
- (80) El Abbassi, M.; Zwick, P.; Rates, A.; Stefani, D.; Prescimone, A.; Mayor, M.; Van Der Zant, H. S. J.; Dulić, D. Unravelling the Conductance Path through Single-Porphyrin Junctions. *Chem. Sci.* **2019**, *10*, 8299–8305. <https://doi.org/10.1039/c9sc02497b>.

- (81) Meisner, J. S.; Ahn, S.; Aradhya, S. V.; Krikorian, M.; Parameswaran, R.; Steigerwald, M.; Venkataraman, L.; Nuckolls, C. Importance of Direct Metal- π Coupling in Electronic Transport through Conjugated Single-Molecule Junctions. *J. Am. Chem. Soc.* **2012**, *134*, 20440–20445. <https://doi.org/10.1021/ja308626m>.
- (82) Repetsky, S. P.; Vyshyvana, I. G.; Kruchinin, S. P.; Bellucci, S. Influence of the Ordering of Impurities on the Appearance of an Energy Gap and on the Electrical Conductance of Graphene. *Sci. Rep.* **2018**, *8*. <https://doi.org/10.1038/s41598-018-26925-0>.

**CHAPTER 5:
MOLECULAR-JUNCTION STUDIES
UNDER ELECTROCHEMICAL CONTROL**

5.1. Introduction

The development of the Electrochemical Scanning Tunneling Microscopy (ECSTM)¹ expanded the potential of the STM, allowing the study of electrode-electrolyte interfaces *in situ*, as well as the monitoring of redox processes at the surface of the sample electrode. Despite the same elements as in a standard STM setup can be observed in the ECSTM setup, this new configuration required the implementation of three additional elements: i) an electrochemical control system, ii) an electrochemical cell, and iii) probes compatible with the electrochemical conditions. The main elements of an ECSTM are schematically depicted in Figure 5.1. The most usual configuration consists in a three-electrode cell. In a first approach (Figure 5.1a), the substrate is considered as a working electrode, whose potential is controlled by means of a potentiostat with respect to a reference electrode, while the current flows between the working and the counter electrodes.²

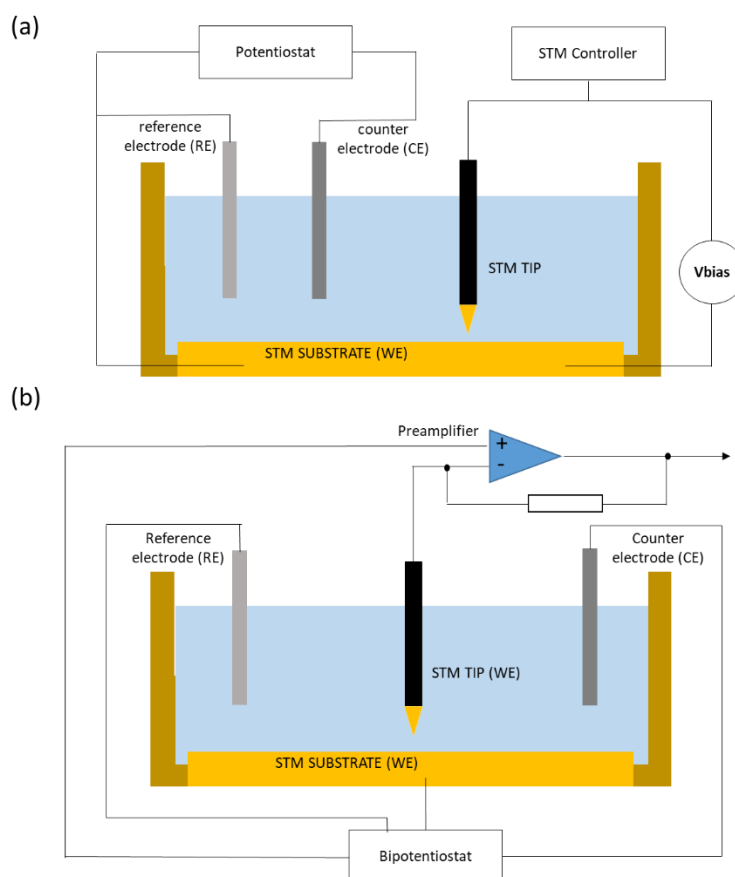


Figure 5.1. ECSTM configuration based on a three-electrode system. **(a)** Initial approach and **(b)** bipotentiostate configuration. Adapted from ref.²

INTRODUCTION

In ECSTM, the current arriving to the tip has other contributions in addition to the tunneling current, namely faradaic currents created by the electrochemical reactions and charge-discharge processes at the electrode/electrolyte interface.² If the addition of these two components is larger than the set-point tunneling current, the STM measurement will no longer be possible. However, as faradaic/capacitive currents are directly proportional to the exposed area of the electrode, they can be minimized by insulating the most of the tip surface except from its apex. Several strategies and materials have been proposed in the literature for coating purposes, such as apiezon wax,³⁻⁷ melt glass,⁸ copolymers,^{9,10} silicon¹¹ and electrophoretic paintings,¹²⁻¹⁴ among others.

Important improvements to this first ECSTM configuration have been developed, such as the use of different tips depending on the sample and the kind of processes under study (Figure 5.2) and the introduction of the bipotentiostat approach, in which both, tip and sample potentials, are independently controlled with respect to the reference electrode (Figure 5.1b).

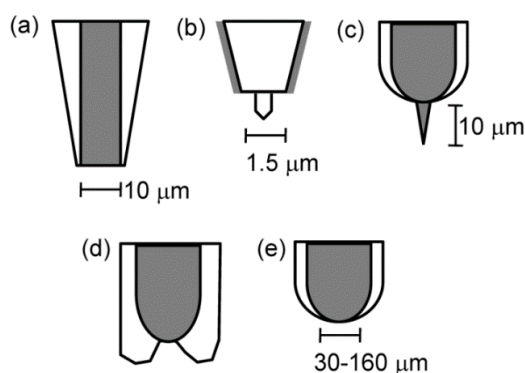


Figure 5.2. Schematics of the shapes of different microelectrodes used in scanning probe microscopy. Reproduced from ref.²

The electrochemical control in the STM was not only a breakthrough for scanning purposes, but it also proved to be useful and applicable to observe single-molecule charge transport, with special impact on biosciences, as these liquid electrolytic conditions allows to investigate biomolecules involved in live redox-processes *in-situ*. It has been the case of biological macromolecules like DNA and redox proteins.¹⁵ On the

one hand, charge transfer in DNA is fundamental for investigations on oxidative damage and its repair, while a step forward understanding the protein electron transport processes has been the study of proteins like azurin, cytochrome and stellacyanin, as well as small protein fragments surrounding the redox centers of interest.¹⁵

The fundamentals of the electron transport experiments under electrochemical control is that it allows the use of the electrochemical potential for applying a gating voltage to the system. This possibility is highly attractive since it has been shown that the conductance of a single molecule can be modulated using a gate electrode, similarly to conventional field effect transistors (FETs). Different ways of applying this gate configuration have been proposed in recent years (Figure 5.3):

Back gate: this approach consists in allocating the source and drain on a solid substrate, such as Si or Al substrate covered by a thin oxide layer (Figure 5.3a). The main disadvantage of this approach is that a new device has to be built for each experiment, involving the modification of the source and drain distances according to the system of interest, and requiring the use of nanofabrication facilities. Besides, significant variations from device to device have been reported.¹⁶⁻¹⁸

Electrochemical gate: this approach uses an electrolyte as medium for applying the gate voltage using a third electrode also immersed in the electrolyte (Figure 5.3b). The most common configuration consists of a reference and counter electrode, as explained above for the ECSTM. As electrolyte, ionic liquids and electrolytic aqueous solutions have been used. This approach provides both an effective and a highly reproducible gating platform.¹⁸⁻²¹

Other gates: as chemical reactions, bonding formation and structural changes in the molecules under study (Figure 5.3c) can involve changes on the electron transport properties, they have been considered as potential gating or tuning methods.^{22,23}

Between them, electrochemical gate seems to be the most versatile option for several reasons. Firstly, it allows adjusting the most convenient potential window according to the studied system by selecting different electrodes and electrolytes; and secondly, it has demonstrated to be compatible with the break-junction technique conducted with both, mechanically controllable devices and scanning tunneling microscope.

INTRODUCTION

The most relevant advances and contributions in this topic are reviewed in the next sections.

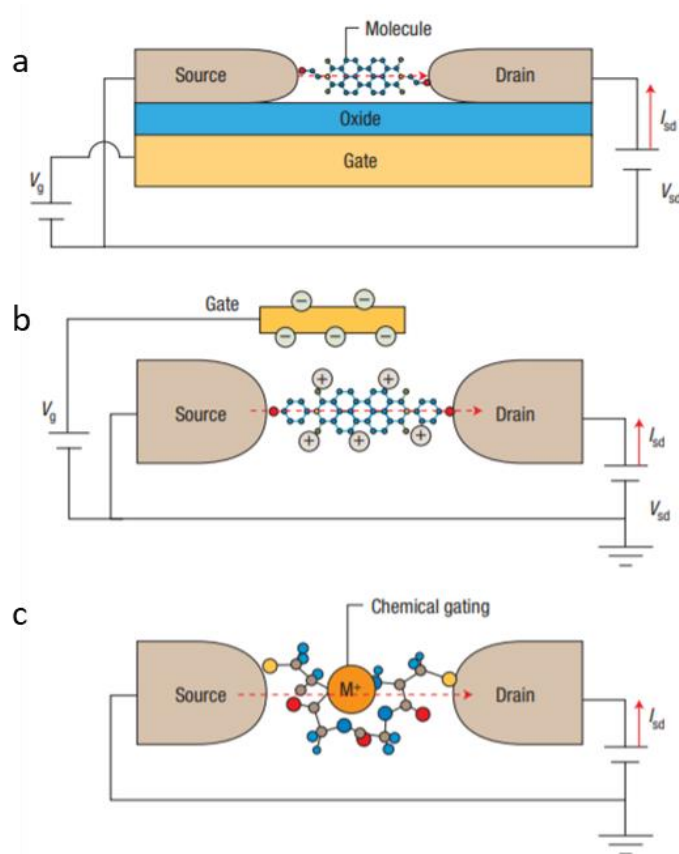


Figure 5.3. Controlling current through a molecule using different gates. **(a)** Back gate using an oxidized Si gate. **(b)** Electrochemical gate with reference electrode inserted in the electrolyte (the counter electrode is not drawn). **(c)** Chemical gate: reversible chemical event, such as binding, reaction, doping or complexation. Reproduced with permission of ref.²⁴ Copyright © 2006 Nature Publishing Group.

5.1.1. Electrochemical gating of a single molecule

The idea of an “electrochemical gate” to control charge transport in molecular electronics was introduced by Wrighton and collaborators, who reported the fabrication of a chemically derivatized microelectrode array that could function as a transistor when it was immersed in an electrolyte solution.²⁵ A further development was carried out by Tao, who used an ECSTM configuration to study the tunneling through a protoporphyrin (PP) and Fe(III)–protoporphyrin (FePP) adsorbed on a highly ordered pyrolytic graphite (HOPG) electrode.⁴ It was observed an enhanced tunneling current at the FePP positions at the

potentials where the Fe(III) is reversibly reduced to Fe(II) (-0.48 V), while the current remained constant at the PP positions (Figure 5.4a-e). This fact was attributed to a higher proximity between the Fermi level of the metal electrode and the lowest unoccupied molecular level (LUMO) of FePP, in comparison with the HOMO and LUMO levels of PP. As shown in Figure 5.4k, the electrode E_F is just in the middle of the PP HOMO-LUMO gap, far away from both levels. In this way, the gate potential applied is insufficient for promoting a significant current variation at the position occupied by these molecules. In contrast, when the gate potential is near to the Fe(III)/Fe(II) reduction potential, the Fermi level begins to align to the FePP LUMO. This gating effect was translated into a peak in the apparent height vs potential plot, as shown in Figure 5.4l. This work had a remarkable relevance, since the power of the electrochemical gating for tune the properties of redox-active molecules was demonstrated, but also the potential of STM for identifying two different molecules with very similar shape and size, based on their different redox properties.

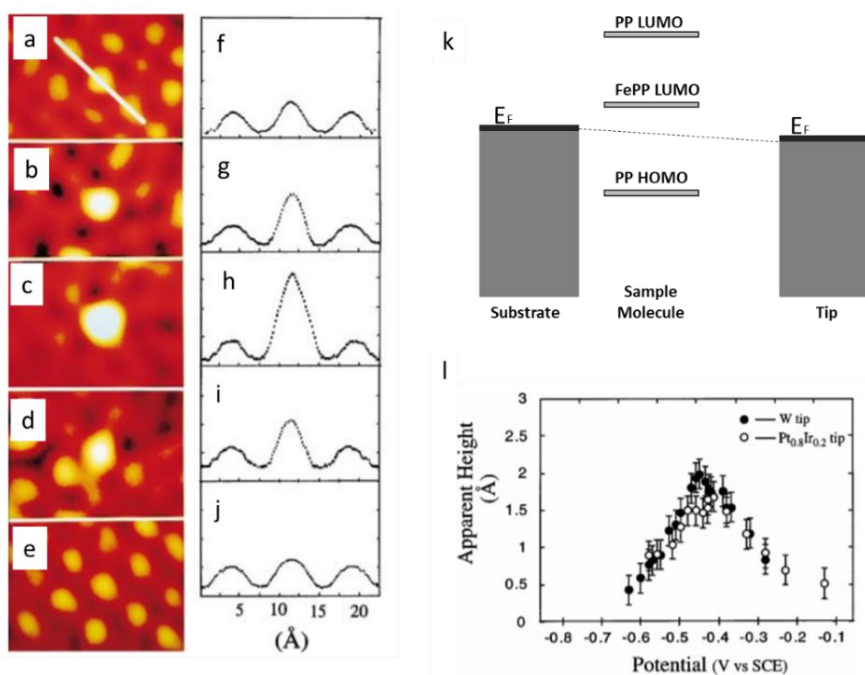


Figure 5.4. (a-e) STM image of an FePP molecule embedded in an ordered array of PP molecules at 20.15, 20.30, 20.40, 20.55, and 20.65 V, respectively; and (f-j) their corresponding cross sections along the white line indicated in (a). (k) Position of the HOMO and LUMO level of PP and FePP with respect to the E_F of the electrodes. (l) Apparent height of FePP relative to PP as a function of the substrate potential, recorded with both, Pt 0.8-Ir 0.2 tip (open circles), and W tip (filled circles). (a-j) and (l) are reproduced with permission of ref.⁴ Copyright ©1996 American Physical Society

INTRODUCTION

This gating based on redox reactions was later employed for controlling the alignment between the electrodes E_F and the molecular HOMO and LUMO in BJ experiments, allowing the tuning of the electron transport properties of the molecular junctions. Redox-active molecules are particularly interesting in this context, since they offer addressable energy states in an electrochemically accessible potential window. The electrochemical active molecular systems studied to date are very varied, including viologens,^{20,26–30} pyrrolo-tetrathiafulvalenes,^{28,31} oligoanilines,^{32,33} ferrocene complexes,^{34,35} substituted oligo(phenyleneethynyls) (OPEs),^{19,36} and perylenes,^{18,37} among others. A comparison between the results reported in those studied reveals that the electrochemical gate voltage response is highly variable even for the same molecules in different conditions. For example, two possible profiles have been reported for the plot of single-molecule conductance against applied electrochemical potential.²¹ The first one consists in a mild increase or decrease of the conductance with the electrochemical potential, without noticeable defined peaks. This phenomenon is known as “soft gating”.²⁰ The second one consists in a clear peak centered at the potential corresponding to the redox switching of the target molecule. These two different behaviors have been found for the same viologens at electrolytic aqueous solutions and ionic liquids, respectively (Figure 5.5).

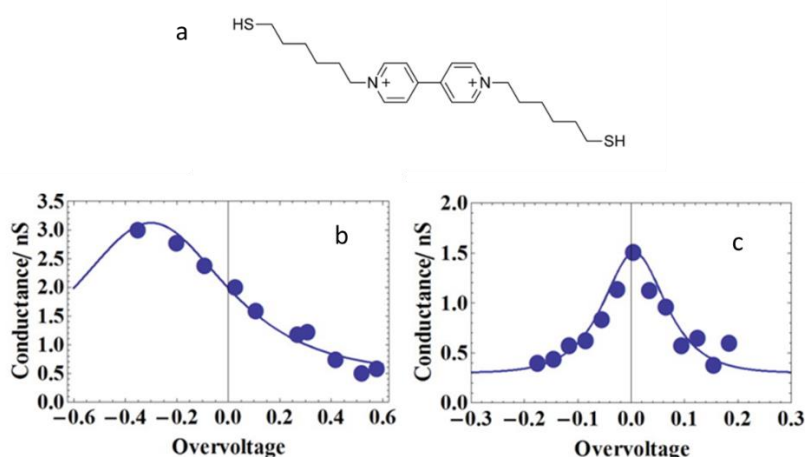


Figure 5.5. Plot of the single molecule conductance data for viologen 1²⁺ (a) versus the gate voltage in (b) aqueous electrolytic solution and (c) ionic liquid. Adapted with permission of ref.²¹ Copyright © 2015, American Chemical Society

Similar to what mentioned for FePP (Figure 5.4I), those different conductance vs overvoltage profiles are due to the gating voltage inside or outside the redox-active potential region,³⁸ but also to different alignment between the molecular and metal energy levels, which can change for the same molecule depending on the experimental conditions. Therefore, the peak-profile can be understood by the alignment illustrated in Figure 5.6. As the energy for the redox reaction is swept from an out-of-resonance condition (a) into the “Fermi window” defined by the two metal electrodes (b), the conductance increases. As the energy levels move out of this resonance condition (c), the conductance decreases again.³¹ As a result, a conductance maximum is obtained at the potential that produces the better alignment of the oxidized and reduced states with the “Fermi window”.

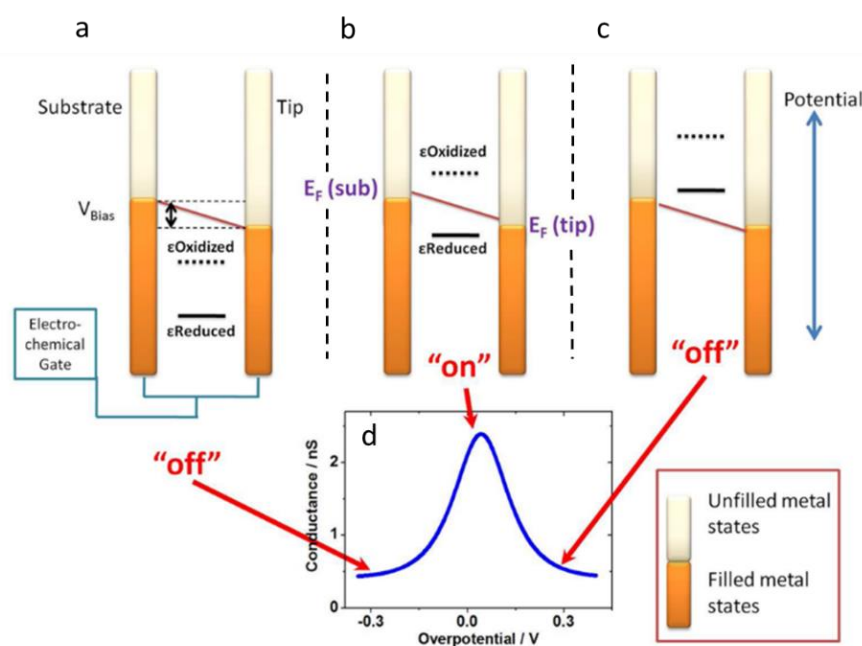


Figure 5.6. Alignment for negative (a), zero (b) and positive (c) overpotentials, producing a peak in the conductance vs overpotential plot (d). Reproduced with permission of ref.³¹ Copyright © 2012 American Chemical Society.

Most recently, the electrochemical gating has been also used for investigating non-redox molecules,^{39–42} since it can modulate the alignment of the conducting orbital relative to the metal Fermi energy, independently of the existence of redox reactions. This is the case of bipyridine (4,4'-BPY), studied by Wandlowski and collaborators.^{39,41} They carried out STM-BJ experiments in a 0.05 M KClO₄ solution, applying a 120 mV gate potential

INTRODUCTION

with respect to a Hg/Hg₂SO₄ (MSE) electrode, and observed three different sets of signals for these junctions. They are marked in the 1D histogram (Figure 5.7b) as L (low), M (middle) and H (high).^a A shift of the conductance toward higher values for the L, M and H sets of signals was observed, as more negative gate potentials were applied. This trend, shown in Figure 5.7c, was related with an approach of the E_F toward the LUMO of 4,4'-BPY from an initial medium position with respect to the HOMO–LUMO gap. The movement of energetic levels is illustrated in Figure 5.7a, and corresponds with the aforementioned “soft gating” profile. In Figure 5.7c, a cyclic voltammetry (CV) of the system at pH 5.8 and in 0.05 M KClO₄ is also depicted. Importantly, at this pH, the molecules are assumed to be non-protonated. The peaks observed in the CV, marked as a and b, were attributed to changes in the orientation of 4,4'-BPY on the Au(111) surface, according to previous studies, and not to redox events. Remarkably, at very negative potentials, the surface coverage was found to decrease by a factor of 2, reducing the rate of success for the formation of molecular junctions.

^a Au-pyridyl contacts give rise to two well-known different conductance values, which are related to different binding geometries.^{64,65} Therefore, the third and high conductance set of signals here has been attributed to junctions due to more than one molecule between tip and substrate. Note that at very negative potentials, this signal disappears, since the probability that two molecules bridge the gap decreases as the surface coverage decreases.

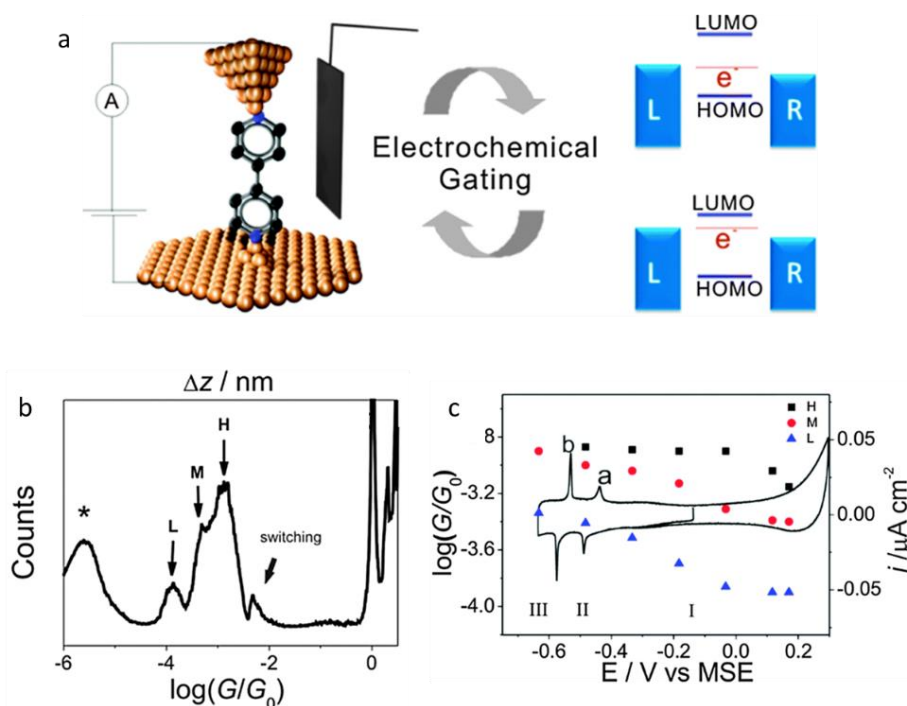


Figure 5.7. (a) 4,4'-BPY junction at electrochemical conditions and changes in the alignment between the electrode E_F and the HOMO and LUMO molecular levels, promoted by the electrochemical gating. (b) 1D histogram built from individual G traces for 4,4'-BPY junctions, recorded at pH 5.8 and in 0.05 M KClO_4 . The asterisk marks the noise level, and the small spike at $\log(G/G_0)=-2.2$ is an artefact due to the amplifier. (c) Shift of the conductance toward higher values as more negative gate potential are applied, and CV of the system recorded at pH 5.8 and in 0.05 M KClO_4 . Regions noted as I, II and III corresponds to different molecular orientation on the gold surface. Reproduced from ref.⁴¹ with permission from The Royal Society of Chemistry.

4,4'-BPY was later studied by Brooke and collaborators in different electrolyte solutions, and using a polypyrrole (PPy) quasi-reference electrode.⁴² These experimental conditions include acidic and basic solutions, involving both, non-protonated and protonated forms of 4,4'-BPY. They obtained a similar trend in all cases (Figure 5.8), in agreement with the previous results, and concluding that conductance seems to be non-sensitive to these changes of the experimental conditions, neither pH.

INTRODUCTION

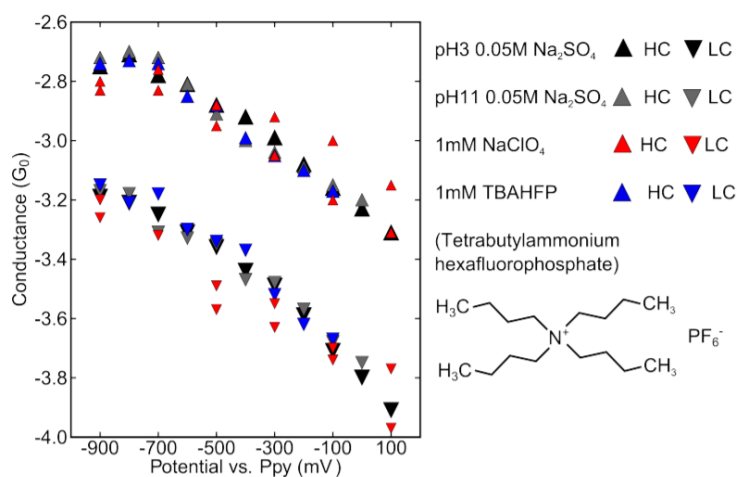


Figure 5.8. Conductance of Au-4,4'-BPY-Au junctions measured in different solutions plotted as a function of gate voltage. Reproduced with permission of ref.⁴² Copyright © 2015, American Chemical Society

Bipyridine derivatives, such as 1,2-bis(4-pyridyl)ethylene, have been also studied under electrochemical conditions, obtaining the same gating behavior that the parent 4,4'-BPY.^{40,42} Additionally, it was demonstrated that high or low conductance states could be favoured depending on both the solution pH and the electrochemical gate voltage.⁴³

5.1.2. BJ experiments with electrodes made of metals different from gold

As explained in Chapter 1, the use of different metals as electrodes can involve changes in the conductance for the junctions created with the same molecule, due to different alignments between the molecular HOMO and LUMO levels and the corresponding E_F . In this sense, comparing the gate effect of junctions created with different metals can be of interest. For example, Brooke and collaborators, obtained a more pronounced gate effect for 4,4'-BPY junctions created with Ni electrodes than the observed for junctions with Au electrodes (Figure 5.9).

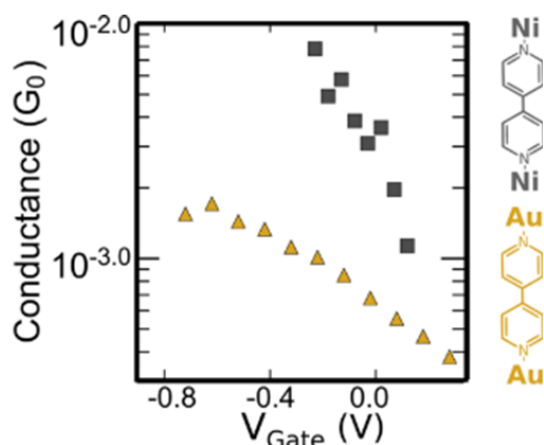


Figure 5.9. Gate effect in Au–4,4′-BPY–Au junctions (golden triangles) and Ni–4,4′-BPY–Ni junctions (black squares), at pH 3, 0.05 M Na₂SO₄ aqueous solution, using a Pt electrode as counter and a PPy quasi-reference electrode. Reproduced with permission of ref⁴² Copyright © 2015, American Chemical Society

Electrochemistry also permits the control of the redox state of the metals used as electrodes, allowing the BJ experiments using metals that suffer oxidation at ambient conditions. That is the case of nickel, cobalt, copper or iron. Taking into account that the surface of the substrate is considerably larger than that of the tip, some strategies focus on preventing the oxidation of such electrodes have been proposed. An example is the well-known “template-stripping” technique, which has been extensively used for fabricating electrodes of inert metals such as Ag, Au, Pd, or Pt.^{44,45} In 2017, Nijhuis and collaborators used this technique for fabricating Ni electrodes.⁴⁶ Although it has been mostly used for devices based on self-assembled monolayers (SAMs), it can be also used for preparing electrodes for BJ-STM experiments. This technique, schematically depicted in Figure 5.10, is based on the deposition of nickel by e-beam evaporation, onto a clean and ultra-smooth Si/SiO₂ layer. The Ni is next covered with a glass plate by means of an optical adhesive.^b The advantage of these home-fabricated substrates is that the Si/SiO₂ layer serves as a protective barrier, which avoids contamination and oxidation of the metal surface, as it can be removed just before the experiments.

^b An inert atmosphere was used during the process in order to prevent the nickel oxidation.

INTRODUCTION

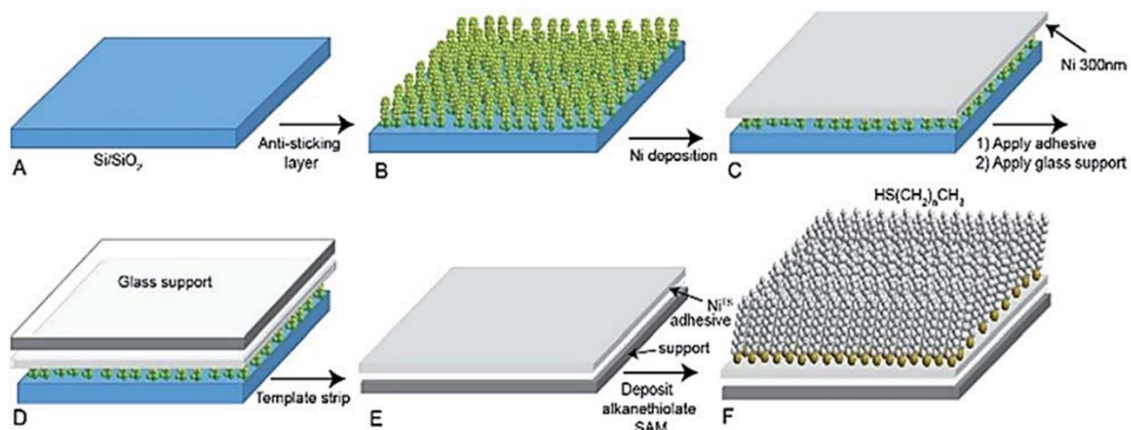


Figure 5.10. Fabrication process of template-stripped Ni electrodes coated with a SAM. **(A)** On a clean Si/SiO₂ surface **(B)** anti-sticking polymer was deposited, followed by **(C)** e-beam deposition of 300 nm Ni. **(D)** Glass supports were glued on the Ni surface using photocurable optical adhesive. **(E)** After curing of the adhesive, the nickel film, with its glass support, was lifted off to expose an ultra-flat Ni film (at N₂ atmosphere). **(F)** The Ni surface was then immediately transferred into a solution of n-alkanethiolates in order to form a SAM. Reproduced with permission from ref.⁴⁶ published by The Royal Society of Chemistry.

Independently of the method for substrate fabrication, and if they have been preserved at inert atmosphere, the use of the electrochemical control permits to perform an *in-situ* cyclic voltammetry (CV) prior to carry out the experiments, ensuring the cleaning of the surface and the removal of any possible oxide layer.

5.1.3. Measurements with magnetic electrodes

Metals like nickel, copper or iron have the additional interest of being magnetizable materials, allowing BJ experiments for magnetic measurements. In these metals, there is a spin-dependent density of states at both sides of the junction, and the conductance depends on the spin direction. In addition, the number of occupied states with spin up does not have to be equal to the number of occupied states with spin down. The atomic contacts breakage of such metals was studied by Costa-Krämer,⁴⁷ among others, obtaining a considerably more complex situation than those of diamagnetic metals like gold. While Au breaking-curve histograms show well-defined peaks (as discussed in Chapter 1 and shown in Figure 5.11), for Ni, Co and Fe, the histograms are flat, despite the individual conductance curves present well-defined steps. This effect have been

attributed to a different plastic behavior at the nanoscale in comparison with Au, in addition to the loss of the spin degeneracy.⁴⁷

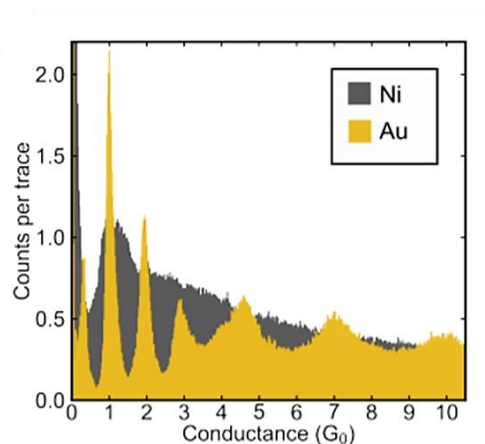


Figure 5.11. 1D conductance histograms for Au-Au and Ni-Ni contacts. Reproduced with permission of ref. ⁴² Copyright © 2015, American Chemical Society

The BJ experiments with magnetizable metals are receiving an increasing interest since they can be used for investigating the spin-dependent transport in individual molecules. In this context, chiral molecules are particularly interesting targets, as the phenomenon known as chirality-induced spin selectivity (CISS) can occur.⁴⁸ This CISS phenomenon in chiral structures involves that the transport of one of the electronic spins is favoured over the other. Naaman and co-workers developed the pioneering work, in which they showed that nanoscale junctions formed by trapping few DNA molecules between an Au nanoparticle and an Ni ferromagnetic surface display current asymmetries as a function of the direction of the Ni magnetic polarization.⁴⁹

With those experiments in mind, BJ experiments while junctions are exposed to a magnetic field, have been proposed.⁵⁰ Nevertheless, the required configuration involves practical difficulties, related to the assembling of not only the electrochemical control system, but also the magnet and its own control system. An alternative, successfully applied by Aragonès and coworkers, is taking advantage of the ferromagnetic properties of the metals.^{51,52} Ferromagnetic materials present the ability of maintaining (at least partially) the magnetization even out of the influence of the external magnetic field. In the context of BJ experiments, this means that the electrodes can be magnetized prior to the measurements, keeping their magnetic properties while the experiments are carried

INTRODUCTION

out. For ensuring the reliability of this approach, the authors monitored the magnetization of a Ni tip before and after single-molecule transport measurements, using SQUID (Superconductor Quantum Interference Device) experiments. They tested the negative (α) and positive (β) magnetization of Ni tips by means of increasing exposure times of the tip near a commercial magnet, obtaining progressively larger tip magnetizations (Figure 5.12a-c) until a saturation value reached at 2 hours. Remarkably, about the 80% of the initial Ni tip magnetization still remained after single-molecule junction experiments (Figure 5.12d).

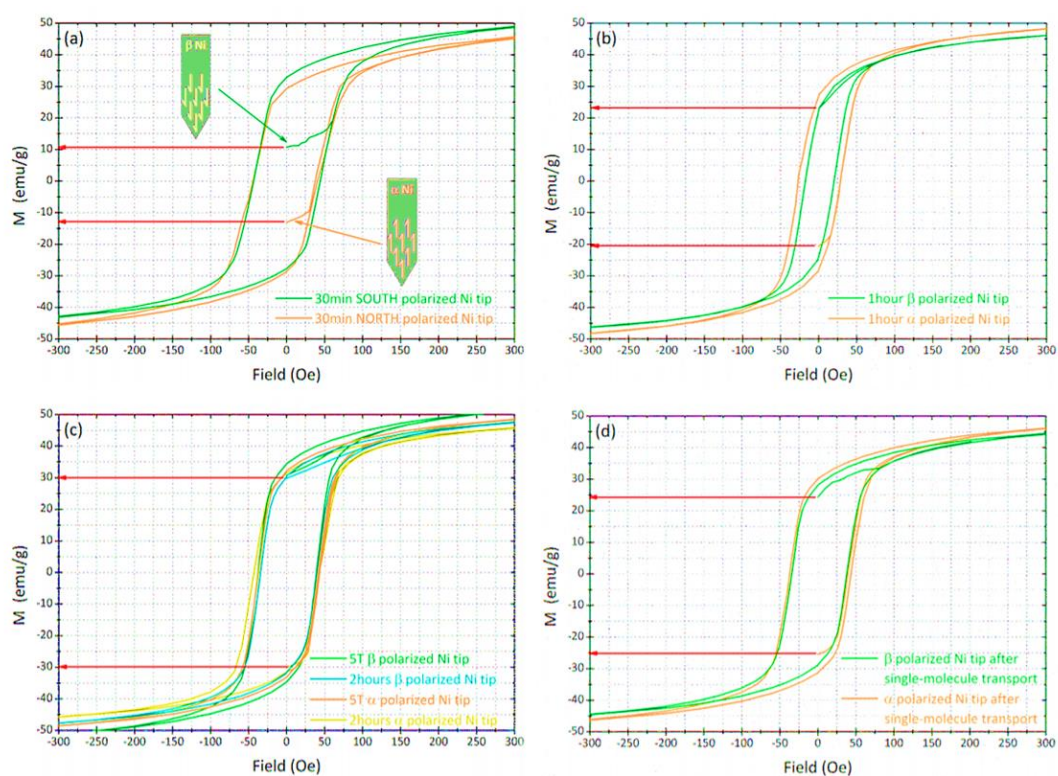


Figure 5.12. SQUID measurements of magnetized Ni tips. **(a-c)** Magnetization times of 30 minutes, 1 hour and 2 hours, respectively. **(d)** Measurements of 2 hours magnetized Ni tips after single-molecule transport experiments. Reproduced with permission of ref.⁵² Copyright © 2016, American Chemical Society

Other particularities of the experiments carried out by these authors are i) the lack of electrochemical control despite the employment of nickel tips and ii) the use of gold substrates. The Ni tip is pushed and pulled into a gold substrate. Due to the more pliable behavior of gold, the tip apex is covered by gold, giving rise to Au-Au contacts (distinguishable for the presence of peaks at multiples of G_0 in the 1D histograms), while

the magnetization of the Ni tip remains. The authors demonstrated that oxidation can be minimized, but not fully prevented, by means of preserving the tips under inert atmosphere, obtaining only a slight increased oxidation of the Ni tip apex after the single-molecule experiments (Figure 5.13).

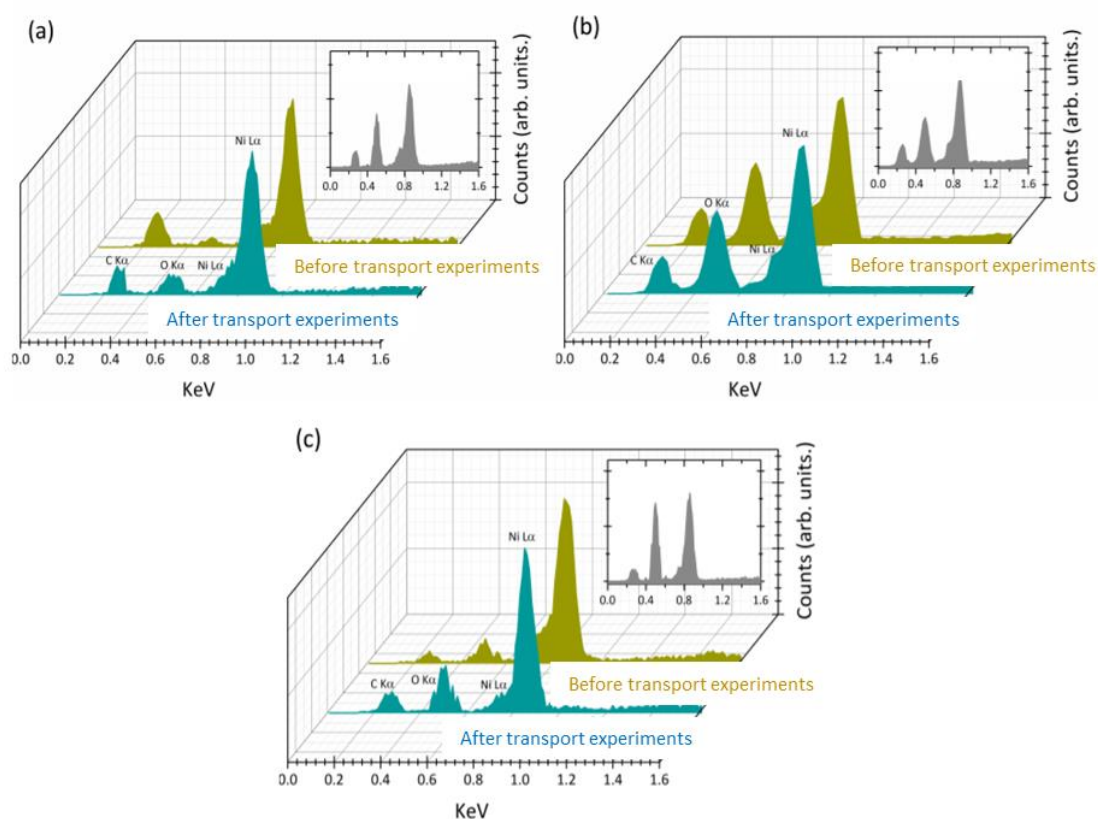


Figure 5.13. Energy Dispersive Spectroscopy (EDS) spectra for the apex of Ni tips before and after single-molecule experiments: **(a)** freshly cut tips, **(b)** non-preserved tips and **(c)** preserved tip under inert atmosphere. Figure insets are EDS results in a point away from the tip apex. Reproduced with permission of ref.⁵² Copyright © 2016, American Chemical Society

Using this approach, Aragonès and collaborators continued the investigation on the spin-polarization power of chiral helical peptides.⁵¹ The authors studied a peptide (Figure 5.14) built with all-D and all-L amino acid, obtaining two different isomers of opposite chirality (D_{peptide} and L_{peptide} , respectively). They observed that the negative polarization was favoured for the D_{peptide} (Figure 5.14a), while the positive one was favoured for the L_{peptide} (Figure 5.14b). Interestingly, the highest conductance value was obtained for L_{peptide} with positive spin polarization of the Ni tip.

INTRODUCTION

Those studies have demonstrated that single molecules can act as spin filters, highlighting their potential as circuit components in spintronic devices.

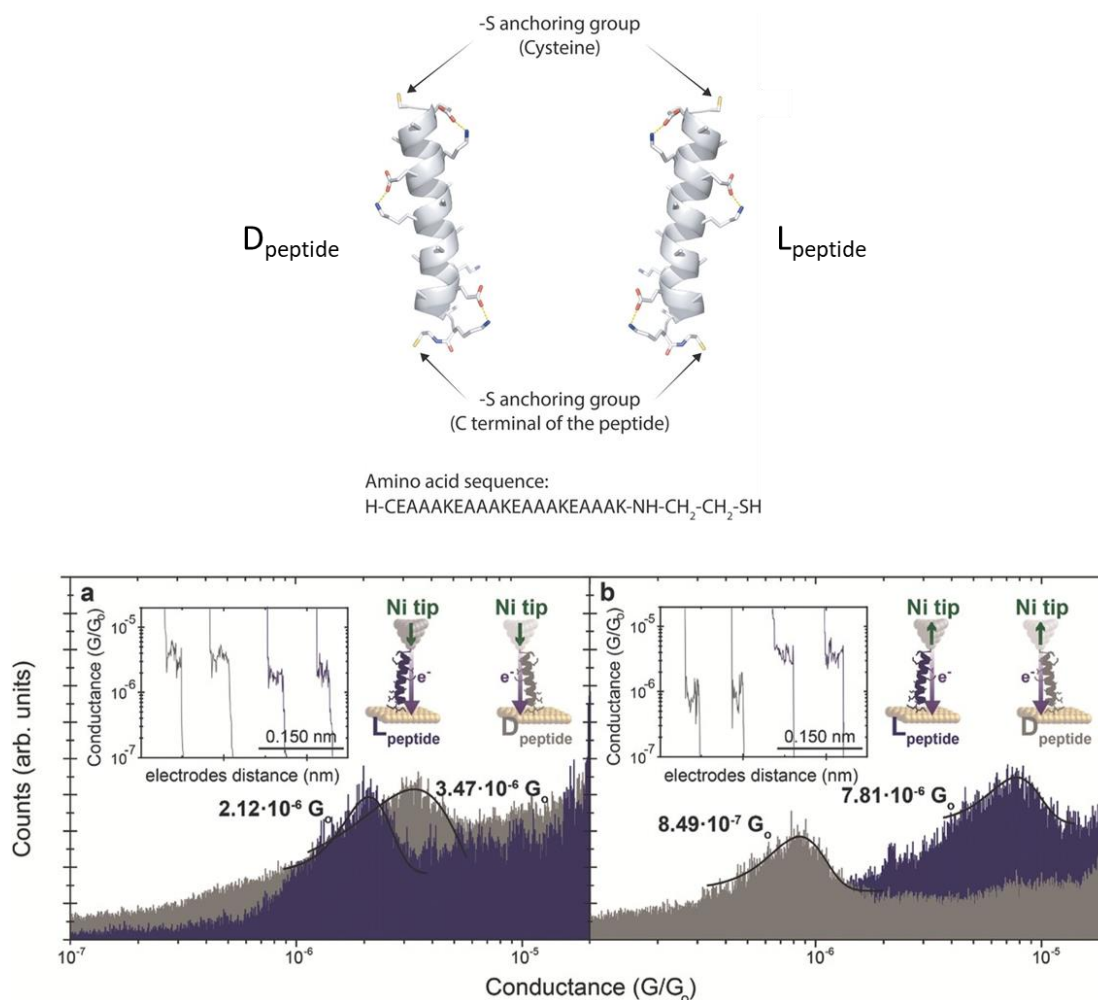


Figure 5.14. Amino acid sequence and 1D histograms for the corresponding L and D peptides under spin down (a) and up (b) Ni magnetic polarizations (bias was set to +50 mV). The short green arrows indicate the Ni-tip magnetization direction while the violet arrows indicate the electron injection direction. Insets show representative conductance versus distance traces. Reproduced with permission of ref.⁵¹ © 2016 WILEY-VCH Verlag GmbH & Co. KGaA, Weinheim.

Using Ni magnetic electrodes, benzenedithiol (BDT) junctions have been also studied,^{53,54} revealing promising results in the context of magnetoresistance. Nevertheless, no agreement was found for the results of such studies, possibly as a consequence of the very different experimental conditions. Yamada and co-workers performed single-molecule experiments at room temperature, applying a magnetic field parallel to the junction,⁵³ while Horiguchi and collaborators used cryogenic and vacuum conditions,

applying a magnetic field perpendicular to the junction.⁵⁴ Remarkably, in these experimental works no precautions were taken against the oxidation of the Ni electrodes.

5.1.4. Overview

The incorporation of the electrochemical control during the development of BJ experiments has allowed extending the applicability of this kind of single-molecule experiments in different ways:

- The application of an electrochemical gate potential permits the modulation of the alignment between the molecular energy levels and the E_F of the electrodes, tuning the electron transport properties of a given junction.
- Additionally, this electrochemical gating is the perfect strategy for investigating redox-active molecules with different oxidation states accessible within the electrochemical potential window.
- The electrochemical control can be used for preventing/avoiding the oxidation of the electrodes when metals such as Cu, Ni, Co or Fe are used, being such metals of special interest for experiments with magnetic electrodes.

Importantly, the use of magnetic electrodes is fundamental in order to search for molecules with potential applications on spintronic. In this context, several configurations have been proposed, including i) the simultaneous application of electrochemical control and magnetic fields during the BJ experiments; ii) the magnetization of the electrodes prior to the BJ experiments; and iii) the combination of the previous magnetization of the electrodes with the preservation of the electrodes at inert atmosphere until the experiments, instead of applying the electrochemical control.

Each one of these options presents advantages and disadvantages, which might be considered depending on the particularities of the experiments, such as the systems under study and the experimental setup available.

5.2. Objectives

Considering the potential of the electrochemical control for BJ experiments, as shown throughout the information collected in the Introduction, and within the context of a 3-month stay in the group of Professor Schwarzacher at the University of Bristol, the following objectives were established:

1. To incorporate an electrochemical control system into our homebuilt STM and to tune it up.
2. To carry out benzenedithiol single-molecule experiments with clean ferromagnetic electrodes under electrochemical conditions, in collaboration with the group of Professor Schwarzacher from the University of Bristol.

5.3. Results and discussion

5.3.1. Implementation of the electrochemical control system into the *IMDEA Nanociencia* setup

The process for the implementation of an electrochemical control system into our homebuilt STM required very different tasks. The most relevant, which are related with the design of the cell, the introduction of new modules into the electric circuit and the preparation of the electrodes, are described in the next sections.

5.3.1.1. Designing the electrochemical cell

The assembly of the electrochemical control system was performed into the already existing homebuilt STM described in the Experimental Section and which is located at the Molecular Electronics Lab at IMDEA Nanociencia. In order to preserve the stable configuration of the STM body and head, an electrochemical cell as small as possible was designed. Besides, the employment of reference electrodes such as MSE and SCE (traditionally used in electrochemistry) was discarded, in favor of customized microelectrodes, fabricated from commercial metal wires (as they are extensively used in literature for nanoelectrochemistry).

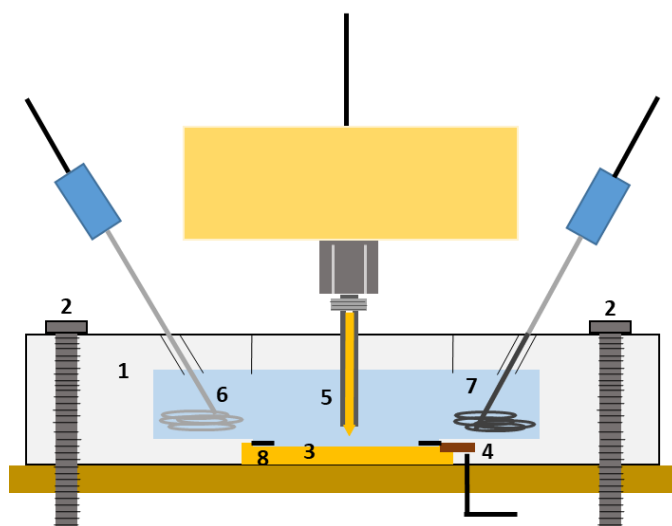


Figure 5.15. Schematic representation of the electrochemical cell especially designed for the homebuilt STM. **1)** PEEK tray. **2)** Screws for holding the cell to the STM table. **3)** STM substrate. **4)** Copper electrode for the electric contact of the substrate. **5)** Modified STM tip for measurements under electrochemical conditions. **6)** Counter electrode. **7)** Reference electrode. **8)** O-ring for avoiding leakage phenomena.

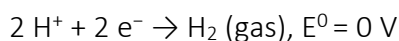
RESULTS AND DISCUSSION

The designed cell is schematically depicted in Figure 5.15. The tray (1) was a short cylinder made of PEEK (polyether ether ketone), with a big central hole for accommodating the STM tip and substrate. Four screws (2) are used for holding the tray to the table and fixing the substrate (3) into the center of the hole. An o-ring (8) between the tray and the substrate guarantees the tightness of the whole system and avoids leakages. The substrate is connected to the electric circuit through a copper electrode (4), which is not exposed to the electrolyte. The STM tip (5) has to be insulated for the experiments under electrochemical conditions, following a procedure explained later in this section. The tray presents two additional communicated holes for accommodating the counter (6) and the reference (7) electrodes, being properly fixed and immersed in the solution, but separated enough for preventing them to touch each other. Although the specific electrodes and electrolyte can be modified according to the requirements of each particular experiment, Pt wire as counter and Pt wire coated with polypyrrole (PPy) as reference is a usual combination found in literature for aqueous electrolytes. The preparation protocol of PPy electrodes can be found in the Experimental Section.

5.3.1.2. Electrode preparation

As explained in the introduction, the minimization of faradaic currents created by the electrochemical reactions and charge-discharge processes at the electrode/electrolyte interfaces can be achieved by insulating the tip as much as possible. In order to allow the repeated formation of metallic contacts between tip and substrate, the best geometry is to get a sharp tip prepared by electrochemical etching, followed by coating of the tip with an insulating material except for the very apex. The combination of these processes gives rise to tips only exposed to the electrolytic solution at the apex, where the diameter is minimum. The solvents, times and potentials applied for the etching depend of the tip material (gold, nickel, tungsten, cobalt...), and they are detailed below. As special consideration, tips used for experiments under electrochemical conditions are longer than those used in dry measurements, since it is necessary to keep the tip holder and STM head high enough away from the electrolytic solution, avoiding any contact with the liquid.

Etching Au tips: The setup needed for the electrochemical etching of Au tips is shown in Figure 5.16, and comprises an adjustable DC voltage generator, connected to a Pt ring, which acts as cathode electrode. The gold wire that we want to etch is located in the center of the Pt ring, also connected to the DC supplier and acting as anode electrode. Both electrodes are immersed in an HCl/MeOH solution (1:1). The electrochemical etching is a redox process between gold and water in acidic environment. The main electrochemical redox couples are:



Gold atoms at the wire surface are oxidized becoming either Au(I) or Au(III), which in presence of Cl^- ions, precipitate as gold chloride. The oxidation produces a neck in the gold wire, which is progressively reduced. When the weight of the lower part of the wire exceeds the tensile strength of the neck, it breaks and the current drops to zero, finishing the etching. While the gold oxidation occurs at the anode, H^+ ions are reduced at the platinum wire surface, generating H_2 , which is easily detected as an intense bubbling. Given a gold wire of certain diameter and a Pt ring, the time required for the etching, as well as the conical shape of the tip, depends on the constant voltage applied. As the etching process occurs at the interface between the solution and the air, where a meniscus is formed around the gold wire, this methodology can be used for sharpening two tips at the same time (above and below the meniscus). Nevertheless, the tip formed below the meniscus suffers a certain loss of material due to the electrochemical process, giving rise to tips of less diameter. Besides, it falls to the bottom of the cell when the etching finishes (drop-off point), and, in our experience, the manipulation required for collecting it usually ends in unreliable tips. A constant voltage (V) is applied during the process, while the current decreases progressively to zero. Although 10 V is a common voltage used for gold tips for STM imaging and Raman spectroscopy, we use 3 V, since it gives rise to a larger cone in the apex of the tip, which is better for break-junctions experiments, as it is explained later in this section. By applying 3 V, the initial current is around 4×10^{-4} A, and the required etching time (current arriving to zero) between 2 and

RESULTS AND DISCUSSION

3 minutes. Finally, the etched tips are rinsed in distilled water in order to eliminate the salts from the solution, and later in ethanol to remove any organic contaminant.

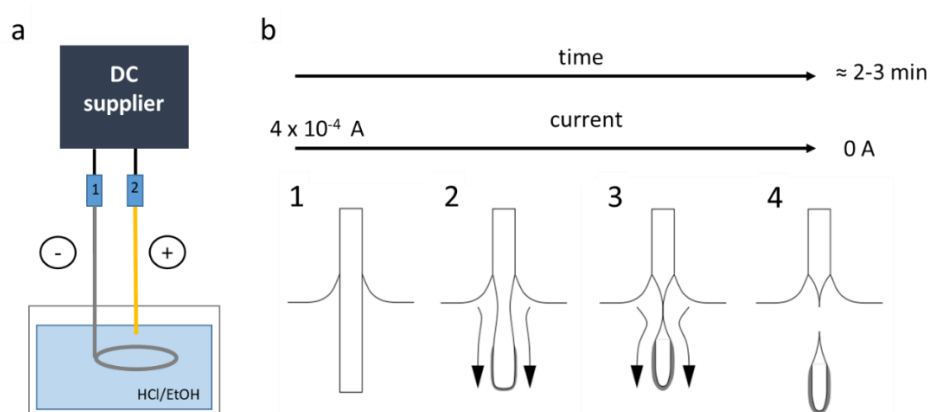


Figure 5.16. (a) Setup for etching Au tips. 1. Cathode electrode. 2. Anode electrode. (b) Tip sharpening during the etching process. Adapted from Ref.⁵⁵

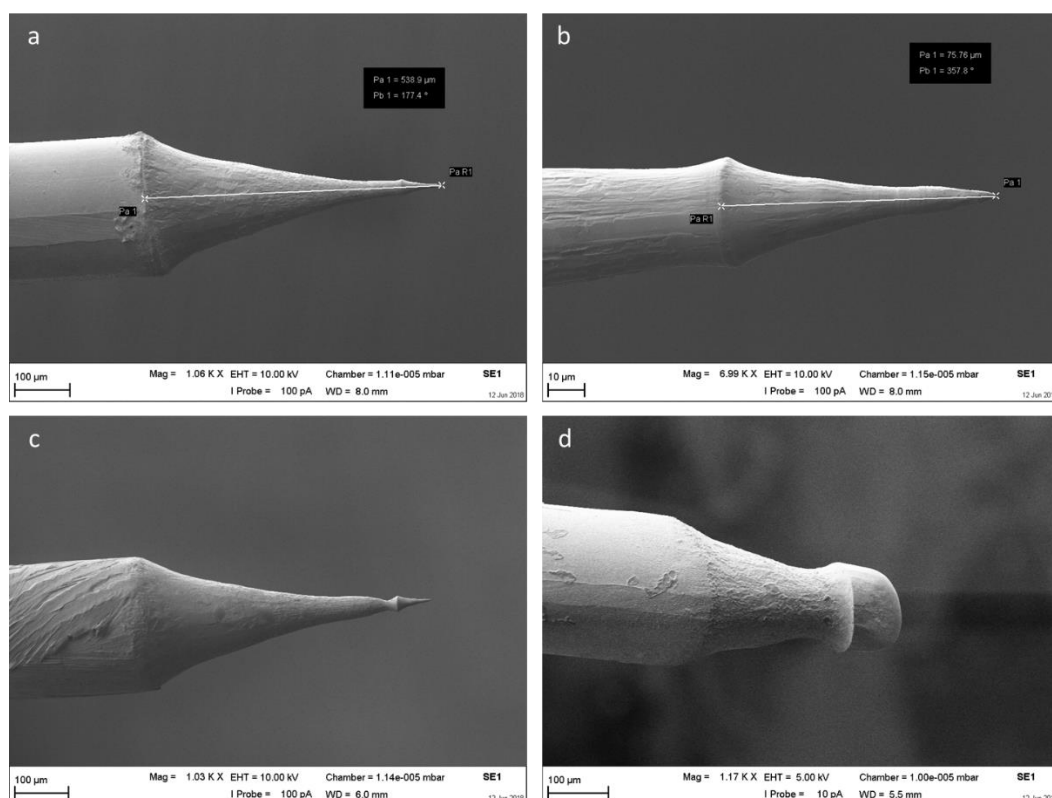


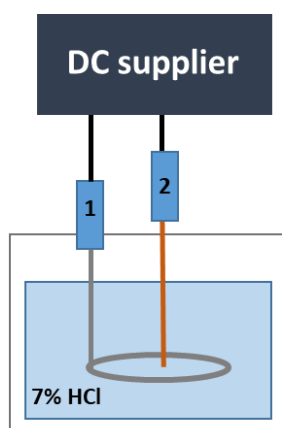
Figure 5.17. SEM images of electrochemically etched gold tips. (a-b) Tip with the desirable shape at two different zoom. (c-d) Obtained tips with undesirable shapes. The drumstick shaped tips (d), eventually obtained, reveal a failed etching process due to the immersion of a too long piece of wire into the etching solution. Images courtesy of Beatriz L. Rodilla.

Some scanning electron microscopy (SEM) pictures of the tips, collected in Figure 5.17, allow a detailed characterization of the final shape of the tips. It also reveals that undesirable tip shapes can also be obtained (Figure 5.17 c-d). We observed the drumstick shape quite often, which has also been previously reported in literature,^{56,57} not only for gold, but also for tungsten and nickel tips, and seems to be related to having a too long piece of the gold immersed in the liquid. As the length of the immersed wire increases, the neck of the wire suffers a higher stress just before the drop-off, what can cause this kind of rearrangement of the apex after the rupture.⁵⁵

Etching Ni tips: The methodology is quite similar to that used for Au etching,⁵⁸ and required the same kind of setup (Figure 5.18). In this case, the anode is a Ni wire, and the electrochemical solution is a hydrochloric aqueous solution. For the etching, a constant 5 A current is applied, which drops to zero when the process finishes. The etching takes about a minute. Finally, the etched tips are rinsed in distilled water in order to eliminate any NiCl₂ deposited on the surface, and then in ethanol to remove possible organic contaminants. The reaction occurring at the anode involves the formation of NiCl₂, while in the cathode H₂ is generated:

at the anode:
$$\text{Ni (solid)} + 2 \text{Cl}^- \rightarrow 1\text{e}^- + \text{NiCl}_2 \text{ (precipitate)}$$

at the cathode:
$$2 \text{H}^+ + 2 \text{e}^- \rightarrow \text{H}_2 \text{ (gas)}$$



1. Pt ring
2. Ni wire

Figure 5.18. Setup for the electrochemical etching of Ni tips. The cathode electrode is a Pt ring (1), and the Ni wire acts as anode (2).

RESULTS AND DISCUSSION

Insulating the tips: the most used coating for preparing tips for BJ experiments is apiezon wax, which is solid at room temperature and electrochemically inert. The followed procedure was based on those described in literature.³ The setup is depicted in Figure 5.19a. It consists in a hairpin shaped soldering, held in a clamp stand, and a manual micrometer to which the etched tip is assembled. The soldering is heated around 100 °C and the apiezon applied to the hot surface. The soldering surface keeps covered by wax, while the heat prevents the solidification. The tip is then coated by passing it several times through the slit of the hairpin. The tip is removed and the wax allowed to cool down to room temperature for some minutes. Surface tension prevents the molten wax from entirely coating the sharp apex of the tip leaving a small metallic area exposed after hardening. Although this general protocol seems to be employed for coating all kind of tips, we found that the gold tips are easily fully coated. This means that no current was recorded when they were assembled into the STM circuit. In order to avoid this phenomenon, the gold tips were coated with the soldering vertically hold while the tip is moved horizontally. This configuration avoided the coating of the very end apex of the tip, as shown in Figure 5.19b-d, while enough surface was coated for reducing the faradaic currents arriving to the tip.

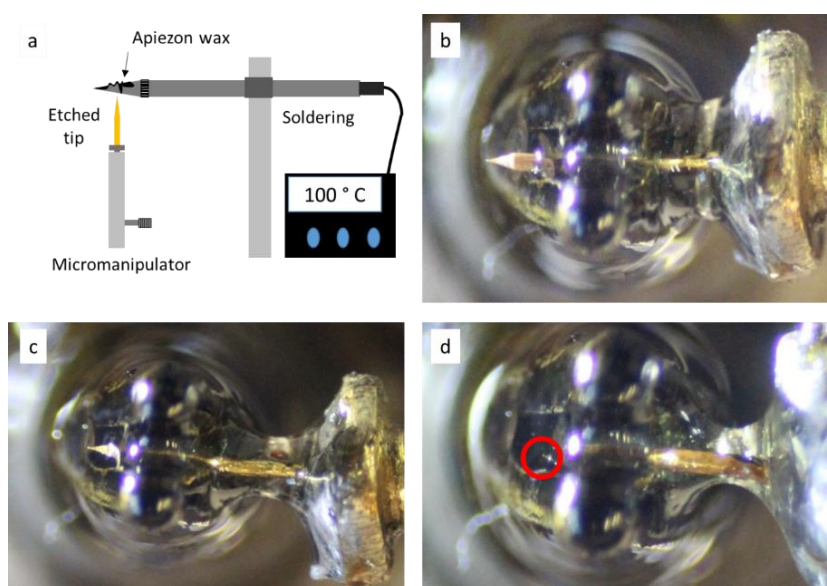


Figure 5.19. (a) Setup for coating tips. (b-d) Pictures of the slightly modified process for coating gold tips, which are not totally passed through the soldering. The red circle in (d) marks the apex of the tip, which is not coated with wax. Note that in the pictures, the apiezon wax, which is black, has been substituted with silicon for clarity.

The tips prepared with the sequence etching-coating were found to be able to measure tunneling currents as low as $G = 10^{-5} G_0$ with a bias voltage of 0.1 in optimal conditions, which is the lower-limit value found in literature for the BJ experiments under electrochemical conditions. However, generally only one of every three prepared tips was good enough for performing this kind of experiments, being this rate of success in agreement with the previous experience of other groups. Importantly, the time of measurement with these tips, under electrochemical conditions, is shorter than for the directly cut wires working in air. The repeated push and pull process can cause deformation in the exposed metal apex, as well as certain damage in the coating, involving a slow but noticeable increase in the conductance background, and hence, a reduction of the conductance working window. Considering that this can leave out the molecular signature, we considered that the electrochemical control limits the molecular junctions that we can study to those with conductance values higher than $G = 10^{-4} G_0$.

5.3.1.3. The electric circuit

The electrochemical control requires the incorporation of two additional modules into the STM circuit. Firstly, a second I - V converted for the reading of the electrochemical current, and secondly a bipotentiostat. As explained in the Section 5.1., the introduction of the bipotentiostat approach was an important improvement, since it permits the independent control of both tip and substrate potentials, with respect to the reference electrode, and hence, to establish a controlled voltage decay between the tip and the substrate. Therefore, a simple homemade bipotentiostat circuit, as well as a new I - V converted, similar to that reported in the literature,⁵⁹ were incorporated into the circuit.

The described configuration allows to record at the same time the tunneling current (current at the tip of reduced area to make ionic/capacitive current minimal) and the electrochemical current (current at the substrate of large area so that the ionic/capacitive current dominates while the tunneling current is negligible). Using this configuration, we could carry out simultaneously cyclic voltammetry of clean gold tip and substrate while keeping a constant bias voltage between them, obtaining their corresponding independent CVs, which are collected in Figure 5.20 b (experimental conditions detailed

RESULTS AND DISCUSSION

in the figure caption). In this case, as we do not want to record any tunneling current, we adjust the amplification gain at the tip to be able to follow the low electrochemical current also at the tip during the voltamogram. Note the significant difference in magnitude of both currents due to their different exposed area, demonstrating the effectiveness of the tip coating. In fact, we see that the exposed area at the tip is 1000 times smaller than that of the substrate.

The shape of the cycles is rather different, since it is well known, that, even in the same conditions, the CV profile is dependent of the atomic order in the surface of the sample, as well as the cleanliness of the electrolyte-sample interface.^{60,61} The oxidation peak is more marked in the substrate cycle than in the tip cycle, while the reduction peak is in both clearly noticeable. A slight shift toward higher positive potentials is also noticeable for the reduction peak in the substrate cycle. This shift is due to the applied V_{bias} (0.05 V) between the electrodes.

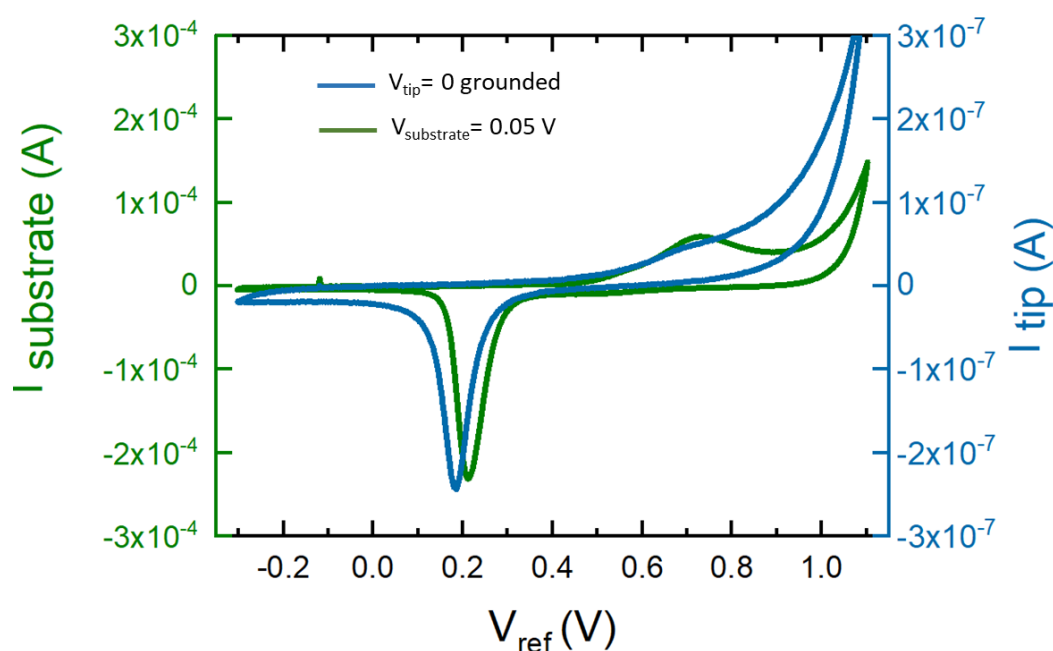


Figure 5.20. (a) CV of gold tip and substrate, obtained in HClO_4 solution 0.01 M, using two Pt wires as counter and reference electrodes. Note the independent current scale for each cycle, due to the different exposed area, and the shift of the reduction peak in the substrate cycle toward higher positive potentials due to the application of a 0.05 V_{bias} .

These results show that we have an experimental setup ready to study the properties of molecular junctions under electrochemical control. Although some preliminary tests have been performed, complete molecular studies with this setup have been left out of the content of this thesis, and contemplated for a future work.

5.3.2. Experiments with ferromagnetic electrodes under electrochemical conditions at the University of Bristol.

The experiments described in this section were conducted in the H.H. Wills Physics Laboratory, at the University of Bristol, in collaboration with the group of Professor Walther Schwarzacher, as part of a 3-month stay. This group has a wide experience in the use of the STM under electrochemical control for both, imaging redox-active surfaces,⁶² and conducting break-junctions experiments.^{42,43} Besides, they have previously used Ni and Co electrodes for creating ferromagnetic contacts for single-molecule experiments, in particular with the approach consisting in the application of an external magnetic field during the experiments.⁵⁰ Taking advantage of that, we planned a series of single molecule experiments for measuring the conductance of Ni-BDT-Ni junctions under electrochemical control, in order to provide a new perspective of this issue.

The setup, the electrode preparation and the functioning of the required electromagnet are described in the next sections.

5.3.2.1. University of Bristol setup

The experiments were performed using a commercial Agilent 5100 STM with a N9503A scanner, customized with a multichannel I - V converter.⁵⁰ The setup is allocated onto an anti-vibration table, rather than being suspended from the ceiling through a pole-and-rope system. The STM is controlled using the commercial PicoScan 5 software. Equivalently to our cell described in section 6.3.1.1, the electrochemical cell, depicted in Figure 5.21a, consists in a four-electrode configuration in which, the tip and the substrate are both acting as working electrode. A 0.25 mm diameter Pt wire was used as the counter electrode, and another Pt wire coated with PPy was used as reference. Ni tip and substrate were used as working electrodes. The cell, particularly designed to fit within the pole pieces of an electromagnet (Figure 5.21b), was made of politetrafluoroethylene (PTFE), generally known as “teflon”, which is chemically resistant and can be easily

RESULTS AND DISCUSSION

cleaned by immersion on concentrated acids. Different holes into the walls of the cell allow the convenient positioning of each electrode. The poles of the electromagnet are separated by a 8 mm gap, which is a compromise between the ability to obtain large magnetic fields and the space requirements for the STM-BJ experiments.⁵⁰ Figure 5.21c shows a real picture of the cell within the poles of the electromagnet, which has to be very carefully positioned, since the magnet should not come into contact with the sample plate or the electrochemical cell, as this may contribute to undesired vibrational noise in the system. The positioning of the STM scanner has also to be done carefully, avoiding the tip contacting the reference and counter electrodes, which is not trivial due to the reduced size of the cell.

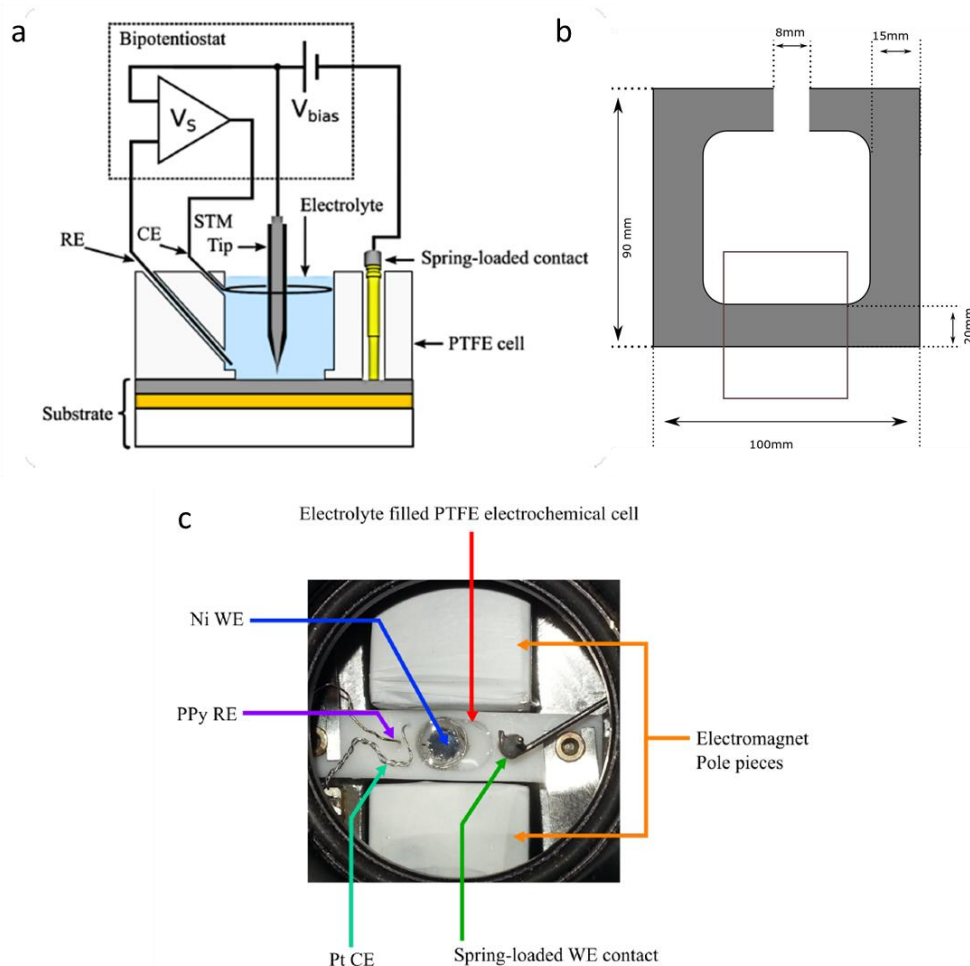


Figure 5.21. (a) Cell configuration for break-junction experiments with a STM under electrochemical conditions. (b) Schematic diagram of the electromagnet designed to produce *in-situ* magnetizing fields during the STM-BJ experiments in the plane of the substrate electrode. The experiment is performed between the pole pieces of the magnet, which are separated by an 8 mm gap. (c) Real picture of the setup. Reproduced from ref.⁵⁰ Both the cell and the electromagnet were designed by Dr. Richard Brooke, and manufactured by the University of Bristol workshop.

During the calibration of the electromagnet, it was found that a current of up to 2.5 A could be maintained continuously for up to 30 minutes without producing significant heating. Nevertheless, applying higher currents and applying currents longer than 30 minutes produced a heating of the system giving rise to not reliable results; and even being able to evaporate the electrolyte solution. Therefore, in order to collect the large data sets required for a proper statistical analysis, several measurement rounds of 30 minutes each should be performed.

It is also important to highlight that in this configuration, the magnetic field can be only applied in the plane of the substrate. In other words, perpendicular to the junction, as illustrated in Figure 5.22a. Interestingly, previous efforts in the group were made for developing another configuration for applying fields perpendicular to the substrate (Figure 5.22b). Unfortunately, it was found that too large noise was introduced to the current measured at the STM tip, due to the reduced dimensions of the hole for hosting it.

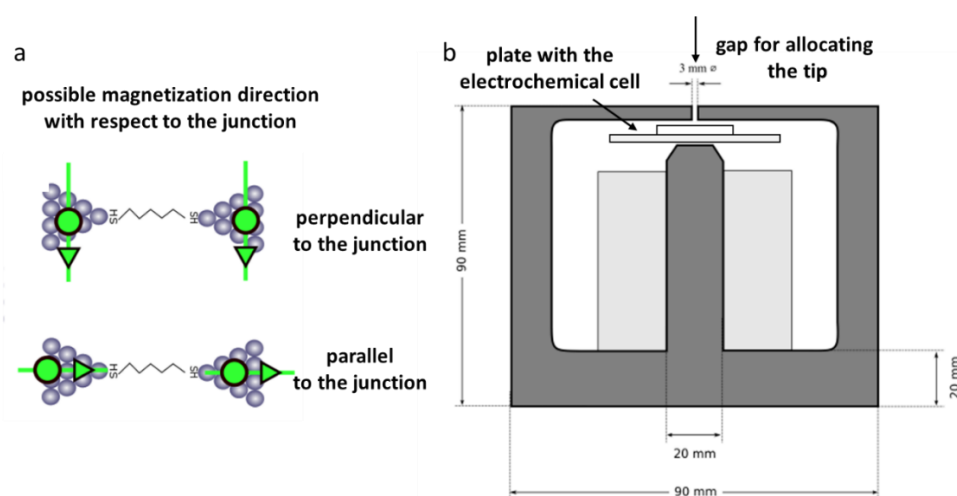


Figure 5.22. (a) Possible magnetization direction with respect to the junction. Adapted from ref.⁶³ (b) Electromagnet designed for applying a parallel field to the junction. Note the small gaps for positioning the plate with the electrochemical cell and the scanner with the tip. Adapted from ref.⁵⁰

5.3.2.2. Electrode preparation

For the preparation of Ni tips, an alternative to that explained in section 5.3.1.2 was employed. This method (Figure 5.23) consists in the formation of a meniscus into the Pt

RESULTS AND DISCUSSION

ring, when it is removed from the etching solution (KCl 2M). The Ni wire is introduced, carefully in the centre of the ring in order to avoid the rupture of the meniscus. Using this method, two completely functional tips can be etched since i) the piece of wire under the meniscus is not into the solution and no additional loss of material is produced; and ii) Ni is more resilient than gold, so the fall down does not cause any significant damage in the apex of the tip. This methodology can be used for preparing both, Ni and Co tips. The reaction occurring at the anode is the same that in the previous method, while the reaction occurring at the cathode involves formation of OH^- ions that forms $\text{Ni}(\text{OH})_2$ salts.

at the anode:
$$\text{Ni (solid)} + 2 \text{Cl}^- \rightarrow 1\text{e}^- + \text{NiCl}_2 \text{ (precipitate)}$$

at the cathode:
$$2 \text{H}_2\text{O} + 2 \text{e}^- \rightarrow \text{H}_2 \text{ (gas)} + 2 \text{OH}^-$$

Using this method a series of ten etched Ni tips were prepared and insulated with apiezon wax.

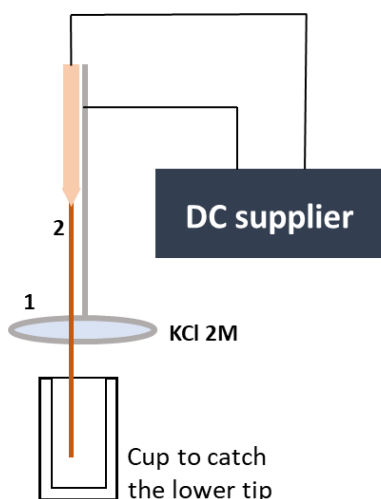


Figure 5.23. Setup for the electrochemical etching of Ni tips. The cathode electrode is a Pt ring (1), and the Ni wire acts as anode (2).

The preparation of Ni substrates were performed following a well-established protocol based on electrochemical deposition.⁵⁰ A three-electrode cell controlled by means of a potentiostat (Autolab PGSTAT302) was used (Figure 5.24). The reference was a SCE electrode, the counter a Pt foil, and an Au coated glass substrates was used as working electrode. The electrolyte was an aqueous 0.2 M NiSO_4 and 0.5 M H_3BO_3 solution. The

potential of the working electrode was set to -0.9 V versus the SCE reference.^c This potential is negative enough to promote the Ni deposition, but not negative enough to cause damage on the film by excessive hydrogen evolution. The role of H_3BO_3 is acting as a pH buffer, preventing local changes in pH taking place close to the working electrode where the consumption of protons by the hydrogen evolution reaction takes place. In this way, it prevents the precipitation of $\text{Ni}(\text{OH})_2$ near to the working electrode, which would have a negative impact on the film quality.

The Au substrates were cleaned immediately prior to electrodepositing Ni films by flame annealing followed by immersion in concentrated H_2SO_4 for 20 minutes. Good quality Ni films were obtained using both, commercial gold-on-glass plates and produced in-house gold substrates *via* Au evaporation onto glass microscope slides.

Obtaining a clean Au surface was important since it has a strong influence on the quality of the final metal deposit, which should be bright silver, with a mirror-like reflectance. Remarkably, when the electrodeposition was performed on Au surfaces not cleaned in acid, poor quality films were obtained, presenting cloudy or dark appearance.

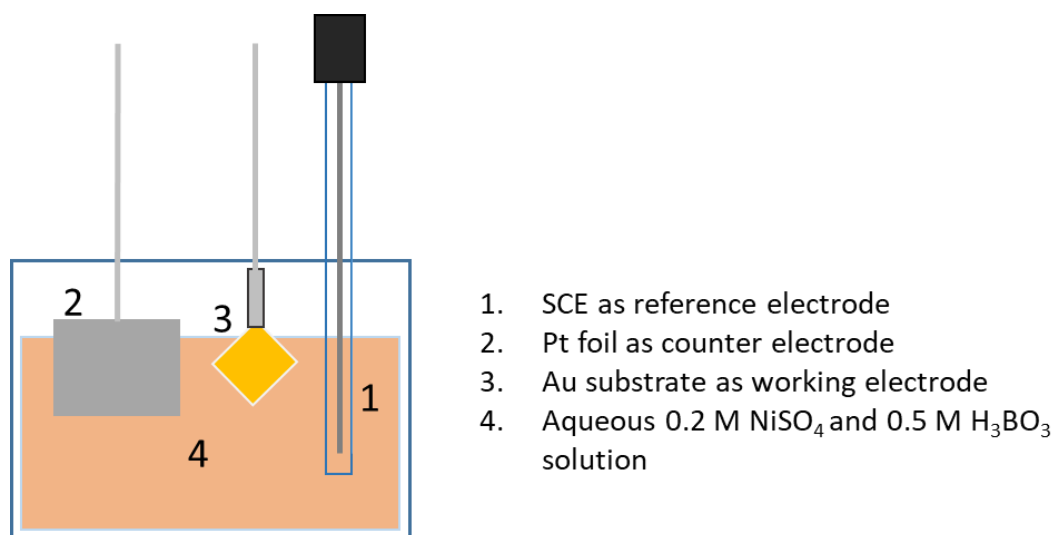


Figure 5.24. Three-electrode cell configuration for the electrodeposition of Ni films.

^c Interestingly, the same method can be used for fabricating Co electrodes, using CoSO_4 instead NiSO_4 .

RESULTS AND DISCUSSION

5.3.2.3. The experiments

Three different experiments were performed in order to become familiar with the setup including both, electrochemical control and *in-situ* magnetization of the electrodes.^d

- Firstly, Ni-Ni junctions without molecule neither magnetic field for ensuring a good functioning of the electrochemical control.
- Secondly, break-junction experiments with 1,4-benzenedithiol (BDT) without magnetic field, in order to ensure the detection of molecular signal.
- Finally, a third round of measurements applying the magnetic field, to be compared of those obtained in absence of magnetic field.

For all of them, the electrolyte was a pH 3, 50 mM Na₂SO₄ aqueous solution, in which the target molecule was found to be slightly soluble.

The electromagnet was typically powered by a Kepco BOP36-12D bipolar power supplier, using a current of 2.3 A, which produced a magnetic field of 2 kOe during the STM-BJ experiments. Nevertheless, several irregularities in its functioning forced a temporary replacement during the time of my stay at the lab. A Keithley 2400 supplier was then used, being 1 A the maximum current that it can provide. This meant a reduction in the maximum magnetic field available, going from 2 kOe to 1 kOe, according to the calibration of the electromagnet.

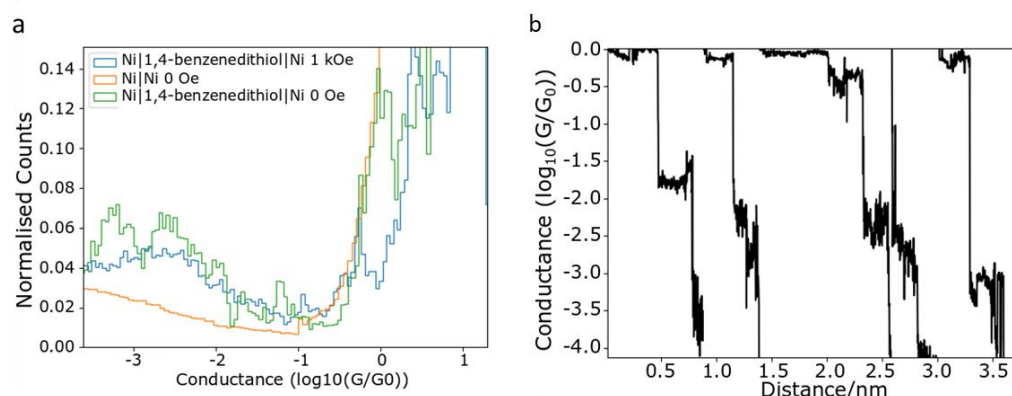


Figure 5.25. (a) 1D histograms of Ni-Ni contacts in the absence of field (orange line), Ni-1,4-benzenedithiol-Ni junctions in the absence of magnetic field (green line), and Ni-1,4-benzenedithiol-Ni junctions at 1kOe magnetic field perpendicular to the junction (blue line). The histograms were built from 254, 56 and 86 traces, respectively, with rates of success of ~20%. (b) Individual *G*-*z* traces for the Ni-BDT-Ni junction in the absence of magnetic field. The traces have been offset in *x* axis for clarity.

^d These experiments were performed in collaboration with Dr. Keisha Michael, and involve one of the main chapters of her PhD, successfully defended in May, 2020.

The 1D histograms obtained for the different experiments are collected in Figure 5.25a. As expected, in absence of molecule (orange line), no peaks at $G < G_0$ were detected. For the Ni-BDT-Ni junctions (green line), two different molecular signals were distinguished, at $(6.4 \pm 0.4) \times 10^{-4} G_0$ and $(2.5 \pm 0.3) \times 10^{-3} G_0$. These signals have been attributed to different conformations of the molecule in the junction, since the length of plateaus is quite similar for both sets of signals. Some individual G - z traces corresponding to Ni-BDT-Ni junctions displaying plateaus at different conductance are shown in Figure 5.25b. The 1D histogram corresponding to the junctions in presence of a magnetic field (blue line), presented a broad signal between -2 and $-3 G_0$, instead of the well-defined peaks previously observed. This phenomenon was attributed to the highly noisy data set obtained for those measurements. Several contributions to this noise were detected, all of them related with the functioning of the electromagnet. On the one hand, the noise clearly increased when the electromagnet was switched on, giving rise to noisy plateaus. On the other hand, as previously explained, the electromagnet promoted an increasing heating of the system, which produced a slight variation of the electrolyte volume along the measurement. This fact introduced certain instability on the electrochemical control system, which could be also contributing to the noisy G - z traces. As mentioned above, as consequence of such heating, the measurements in presence of magnetic field could be only performed in 30 minutes time slots. Considering all these factors, not conclusive results could be extracted concerning the Ni-BDT-Ni junctions, since more and cleaner data sets are still needed.

5.4. Conclusions

According to the conducted experimental tasks related with the electrochemical control and the measurements with magnetic electrodes, the following conclusions can be drawn:

- The elements needed for the implementation of the electrochemical control system into our homebuilt STM were defined, and the new configuration designed and implemented.
- The general protocol for preparing etched and electrochemically insulated Au, Ni and Co tips were tuned up, being the prepared tips able to read a tunnelling current as low as $G = 10^{-5} G_0$.
- A second I - V converter for the reading of the electrochemical current, as well as a bipotentiostat for the independent control of the potentials of tip and substrate was successfully built and assembled to the circuit.
- A preliminary round of single-molecule BDT experiments with Ni electrodes was carried out, applying an external magnetic field during the break-junction experiments. They revealed a series of practical difficulties, which makes this kind of experiments not trivial.

References

- (1) Wang, E. Electrochemical Scanning Tunneling Microscopy. *Anal. Sci.* **1994**, *10*, 155–156. <https://doi.org/10.2116/analsci.10.155>.
- (2) Picco, S.; Villegas, L.; Tonelli, F.; Merlo, M.; Rigau, J.; Diaz, D.; Masuelli, M. Electrochemical Scanning Tunneling Microscopy (ECSTM) – From Theory to Future Applications. *Intech* **2016**, 55–81.
- (3) Nagahara, L. A.; Thundat, T.; Lindsay, S. M. Characterization of Carbon Material as a Scanning Tunneling Microscopy Tip for in Situ Electrochemical Studies. *Rev. Sci. Instrum.* **1994**, *60*, 3128–3130. <https://doi.org/10.1063/1.1145146>.
- (4) Tao, N. J. Probing Potential-Tuned Resonant Tunneling through Redox Molecules with Scanning Tunneling Microscopy. *Phys. Rev. Lett.* **1996**, *76*, 4066–4069. <https://doi.org/10.1103/PhysRevLett.76.4066>.
- (5) Xu, B.; Tao, N. J. Single-Molecule Resistance Measured by Repeated Formation of Molecular Junctions. *Science* **2003**, *301*, 1221–1223. <https://doi.org/10.1557/mrs2003.223>.
- (6) Li, X.; Xu, B.; Xiao, X.; Yang, X.; Zang, L.; Tao, N. Controlling Charge Transport in Single Molecules Using Electrochemical Gate. *Faraday Discuss.* **2006**, *131*, 111–120. <https://doi.org/10.1039/b505666g>.
- (7) Xu, B.; Zhang, P.; Li, X.; Tao, N. Direct Conductance Measurement of Single DNA Molecules in Aqueous Solution. *Nano Lett.* **2004**, *4*, 1105–1108. <https://doi.org/10.1021/nl0494295>.
- (8) Sonnenfeld, R.; Hansma, P. K. Atomic-Resolution Microscopy in Water. *Science* **1986**, *232*, 211–213. <https://doi.org/10.1126/science.232.4747.211>.
- (9) Heben, M. J.; Dovek, M. M.; Lewis, N. S.; Penner, R. M.; Quate, C. F. Preparation of STM Tips for In-situ Characterization of Electrode Surfaces. *J. Microsc.* **1988**, *152*, 651–661. <https://doi.org/10.1111/j.1365-2818.1988.tb01434.x>.
- (10) Clark, R. A.; Ewing, A. G. Characterization of Electrochemical Responses in Picoliter

- Volumes. *Anal. Chem.* **1998**, *70*, 1119–1125. <https://doi.org/10.1021/ac970649v>.
- (11) Salerno, M. Coating of Tips for Electrochemical Scanning Tunneling Microscopy by Means of Silicon, Magnesium, and Tungsten Oxides. *Rev. Sci. Instrum.* **2010**, *81*. <https://doi.org/10.1063/1.3484191>.
- (12) Abelev, E.; Sezin, N.; Ein-Eli, Y. An Alternative Isolation of Tungsten Tips for a Scanning Tunneling Microscope. *Rev. Sci. Instrum.* **2005**, *76*, 1–4. <https://doi.org/10.1063/1.2075187>.
- (13) Zhu, L.; Claude-Montigny, B.; Gattrell, M. Insulating Method Using Cataphoretic Paint for Tungsten Tips for Electrochemical Scanning Tunneling Microscopy (ECSTM). *Appl. Surf. Sci.* **2005**, *252*, 1833–1845. <https://doi.org/10.1016/j.apsusc.2005.03.145>.
- (14) Thorgaard, S. N.; Buhlmann, P. Cathodic Electropaint Insulated Tips for Electrochemical Scanning Tunneling Microscopy. *Anal. Chem.* **2007**, *79*, 9224–9228. <https://doi.org/10.1021/ac071307k>.
- (15) Gorostiza, P.; Artés, J. M. Scanning Tunneling Microscopy Studies of Immobilized Biomolecules. In *Encyclopedia of Applied Electrochemistry*; SpringerReference, 2011. <https://doi.org/10.1007/springerreference>.
- (16) Liang, W.; Shores, M. P.; Bockrath, M.; Long, J. R.; Park, H. Kondo Resonance in a Single-Molecule Transistor. *Nature* **2002**, *417*, 725–729. <https://doi.org/10.1038/nature00790>.
- (17) Kubatkin, S.; Danilov, A.; Hjort, M.; Cornil, J.; Brédas, J. L.; Stuhr-Hansen, N.; Hedegård, P.; Bjørnholm, T. Single-Electron Transistor of a Single Organic Molecule with Access to Several Redox States. *Nature* **2003**, *425*, 698–701. <https://doi.org/10.1038/nature02010>.
- (18) Xu, B.; Xiao, X.; Yang, X.; Zang, L.; Tao, N. Large Gate Modulation in the Current of a Room Temperature Single Molecule Transistor. *J. Am. Chem. Soc.* **2005**, *127*, 2386–2387. <https://doi.org/10.1021/ja042385h>.
- (19) Xiao, X.; Nagahara, L. A.; Rawlett, A. M.; Tao, N. Electrochemical Gate-Controlled

REFERENCES

- Conductance of Single Oligo(Phenylene Ethynylene)S. *J. Am. Chem. Soc.* **2005**, *127*, 9235–9240. <https://doi.org/10.1021/ja050381m>.
- (20) Haiss, W.; Albrecht, T.; Van Zalinge, H.; Higgins, S. J.; Bethell, D.; Höbenreich, H.; Schiffrin, D. J.; Nichols, R. J.; Kuznetsov, A. M.; Zhang, J.; Chi, Q.; Ulstrup, J. Single-Molecule Conductance of Redox Molecules in Electrochemical Scanning Tunneling Microscopy. *J. Phys. Chem. B* **2007**, *111*, 6703–6712. <https://doi.org/10.1021/jp068692m>.
- (21) Osorio, H. M.; Catarelli, S.; Cea, P.; Gluyas, J. B. G.; Hartl, F.; Higgins, S. J.; Leary, E.; Low, P. J.; Martín, S.; Nichols, R. J.; Tory, J.; Ulstrup, J.; Vezzoli, A.; Milan, D. C.; Zeng, Q. Electrochemical Single-Molecule Transistors with Optimized Gate Coupling. *J. Am. Chem. Soc.* **2015**, *137*, 14319–14328. <https://doi.org/10.1021/jacs.5b08431>.
- (22) Kasibhatla, B. S. T.; Labonté, A. P.; Zahid, F.; Reifengerger, R. G.; Datta, S.; Kubiak, C. P. Reversibly Altering Electronic Conduction through a Single Molecule by a Chemical Binding Event. *J. Phys. Chem. B* **2003**, *107*, 12378–12382. <https://doi.org/10.1021/jp036715g>.
- (23) Xiao, X.; Xu, B.; Tao, N. Changes in the Conductance of Single Peptide Molecules upon Metal-Ion Binding. *Angew. Chem. Int. Ed.* **2004**, *43*, 6148–6152. <https://doi.org/10.1002/anie.200460886>.
- (24) Tao, N. J. Electron Transport in Molecular Junctions. *Nat. Nanotechnol.* **2006**, *1*, 173–181. <https://doi.org/10.1038/nnano.2006.130>.
- (25) White, H. S.; Kittlesen, G. P.; Wrighton, M. S. Chemical Derivatization of an Array of Three Gold Microelectrodes with Polypyrrole: Fabrication of a Molecule-Based Transistor. *J. Am. Chem. Soc.* **1984**, *106*, 5375–5377. <https://doi.org/10.1021/ja00330a070>.
- (26) Li, Z.; Han, B.; Meszaros, G.; Pobelov, I.; Wandlowski, T.; Błaszczuk, A.; Mayor, M. Two-Dimensional Assembly and Local Redox-Activity of Molecular Hybrid Structures in an Electrochemical Environment. *Faraday Discuss.* **2006**, *131*, 121–143. <https://doi.org/10.1039/b506623a>.

- (27) Li, Z.; Pobelov, I.; Han, B.; Wandlowski, T.; Błaszczak, A.; Mayor, M. Conductance of Redox-Active Single Molecular Junctions: An Electrochemical Approach. *Nanotechnology* **2007**, *18*, 044018. <https://doi.org/10.1088/0957-4484/18/4/044018>.
- (28) Leary, E.; Higgins, S. J.; Van Zalinge, H.; Haiss, W.; Nichols, R. J.; Nygaard, S.; Jeppesen, J. O.; Ulstrup, J. Structure-Property Relationships in Redox-Gated Single Molecule Junctions - A Comparison of Pyrrolo-Tetrathiafulvalene and Viologen Redox Groups. *J. Am. Chem. Soc.* **2008**, *130*, 12204–12205. <https://doi.org/10.1021/ja8014605>.
- (29) Zhang, W.; Gan, S.; Vezzoli, A.; Davidson, R. J.; Milan, D. C.; Luzyanin, K. V.; Higgins, S. J.; Nichols, R. J.; Beeby, A.; Low, P. J.; Li, B.; Niu, L. Single-Molecule Conductance of Viologen-Cucurbit[8]Uril Host-Guest Complexes. *ACS Nano* **2016**, *10*, 5212–5220. <https://doi.org/10.1021/acsnano.6b00786>.
- (30) Nichols, R. J.; Higgins, S. J. Single Molecule Nanoelectrochemistry in Electrical Junctions. *Acc. Chem. Res.* **2016**, *49*, 2640–2648. <https://doi.org/10.1021/acs.accounts.6b00373>.
- (31) Kay, N. J.; Higgins, S. J.; Jeppesen, J. O.; Leary, E.; Lycoops, J.; Ulstrup, J.; Nichols, R. J. Single-Molecule Electrochemical Gating in Ionic Liquids. *J. Am. Chem. Soc.* **2012**, *134*, 16817–16826. <https://doi.org/10.1021/ja307407e>.
- (32) Chen, F.; He, J.; Nuckolls, C.; Roberts, T.; Klare, J. E.; Lindsay, S. A Molecular Switch Based on Potential-Induced Changes of Oxidation State. *Nano Lett.* **2005**, *5*, 503–506. <https://doi.org/10.1021/nl0478474>.
- (33) He, J.; Chen, F.; Lindsay, S.; Nuckolls, C. Length Dependence of Charge Transport in Oligoanilines. *Appl. Phys. Lett.* **2007**, *90*, 1–4. <https://doi.org/10.1063/1.2472758>.
- (34) Xiao, X.; Brune, D.; He, J.; Lindsay, S.; Gorman, C. B.; Tao, N. Redox-Gated Electron Transport in Electrically Wired Ferrocene Molecules. *Chem. Phys.* **2006**, *326*, 138–143. <https://doi.org/10.1016/j.chemphys.2006.02.022>.
- (35) Zhou, X. S.; Liu, L.; Fortgang, P.; Lefevre, A. S.; Serra-Muns, A.; Raouafi, N.; Amatore, C.; Mao, B. W.; Maisonhaute, E.; Schöllhorn, B. Do Molecular

REFERENCES

- Conductances Correlate with Electrochemical Rate Constants? Experimental Insights. *J. Am. Chem. Soc.* **2011**, *133*, 7509–7516. <https://doi.org/10.1021/ja201042h>.
- (36) Kolivoska, V.; Moreno-García, P.; Kaliginedi, V.; Hong, W.; Mayor, M.; Weibel, N.; Wandlowski, T. Electron Transport through Catechol-Functionalized Molecular Rods. *Electrochim. Acta* **2013**, *110*, 709–717. <https://doi.org/10.1016/j.electacta.2013.02.003>.
- (37) Li, C.; Stepanenko, V.; Lin, M. J.; Hong, W.; Würthner, F.; Wandlowski, T. Charge Transport through Perylene Bisimide Molecular Junctions: An Electrochemical Approach. *Phys. Status Solidi B* **2013**, *250*, 2458–2467. <https://doi.org/10.1002/pssb.201350034>.
- (38) Ke, G.; Duan, C.; Huang, F.; Guo, X. Electrical and Spin Switches in Single-molecule Junctions. *InfoMat* **2020**, *2*, 92–112. <https://doi.org/10.1002/inf2.12068>.
- (39) Li, C.; Mishchenko, A.; Wandlowski, T. Charge Transport in Single Molecular Junctions at the Solid/Liquid Interface. *Top. Curr. Chem.* **2012**, *313*, 121–188. https://doi.org/10.1007/128_2011_238.
- (40) Capozzi, B.; Chen, Q.; Darancet, P.; Kotiuga, M.; Buzzeo, M.; Neaton, J. B.; Nuckolls, C.; Venkataraman, L. Tunable Charge Transport in Single-Molecule Junctions via Electrolytic Gating. *Nano Lett.* **2014**, *14*, 1400–1404. <https://doi.org/10.1021/nl404459q>.
- (41) Baghernejad, M.; Zsolt Manrique, D.; Li, C.; Pope, T.; Zhumaev, U.; Pobelov, I.; Moreno-García, P.; Kaliginedi, V.; Huang, C.; Hong, W.; Lambert, C.; Wandlowski, T. Highly-Effective Gating of Single-Molecule Junctions: An Electrochemical Approach. *Chem. Commun.* **2014**, *50*, 15975–15978. <https://doi.org/10.1039/c4cc06519k>.
- (42) Brooke, R. J.; Jin, C.; Szumski, D. S.; Nichols, R. J.; Mao, B. W.; Thygesen, K. S.; Schwarzacher, W. Single-Molecule Electrochemical Transistor Utilizing a Nickel-Pyridyl Spinterface. *Nano Lett.* **2015**, *15*, 275–280. <https://doi.org/10.1021/nl503518q>.
- (43) Brooke, R. J.; Szumski, D. S.; Vezzoli, A.; Higgins, S. J.; Nichols, R. J.; Schwarzacher,

- W. Dual Control of Molecular Conductance through PH and Potential in Single-Molecule Devices. *Nano Lett.* **2018**, *18*, 1317–1322. <https://doi.org/10.1021/acs.nanolett.7b04995>.
- (44) Weiss, E. A.; Kaufman, G. K.; Kriebel, J. K.; Li, Z.; Schalek, R.; Whitesides, G. M. Si/SiO₂-Templated Formation of Ultraflat Metal Surfaces on Glass, Polymer, and Solder Supports: Their Use as Substrates for Self-Assembled Monolayers. *Langmuir* **2007**, *23*, 9686–9694. <https://doi.org/10.1021/la701919r>.
- (45) Yoo, D.; Johnson, T. W.; Cherukulappurath, S.; Norris, D. J.; Oh, S. H. Template-Stripped Tunable Plasmonic Devices on Stretchable and Rollable Substrates. *ACS Nano* **2015**, *9*, 10647–10654. <https://doi.org/10.1021/acsnano.5b05279>.
- (46) Senthil Kumar, K.; Jiang, L.; Nijhuis, C. A. Fabrication of Ultra-Smooth and Oxide-Free Molecule-Ferromagnetic Metal Interfaces for Applications in Molecular Electronics under Ordinary Laboratory Conditions. *RSC Adv.* **2017**, *7*, 14544–14551. <https://doi.org/10.1039/c6ra27280k>.
- (47) Costa-Krämer, J. Conductance Quantization at Room Temperature in Magnetic and Nonmagnetic Metallic Nanowires. *Phys. Rev. B* **1997**, *55*, R4875–R4878. <https://doi.org/10.1103/PhysRevB.55.R4875>.
- (48) Ray, S. G.; Daube, S. S.; Leitus, G.; Vager, Z.; Naaman, R. Chirality-Induced Spin-Selective Properties of Self-Assembled Monolayers of DNA on Gold. *Phys. Rev. Lett.* **2006**, *96*, 1–4. <https://doi.org/10.1103/PhysRevLett.96.036101>.
- (49) Xie, Z.; Markus, T. Z.; Cohen, S. R.; Vager, Z.; Gutierrez, R.; Naaman, R. Spin Specific Electron Conduction through DNA Oligomers. *Nano Lett.* **2011**, *11*, 4652–4655. <https://doi.org/10.1021/nl2021637>.
- (50) Brooke, R. J. Ferromagnetic Contacts for Single-Molecule Devices, **2015**. Thesis dissertation, Bristol University.
- (51) Aragonès, A. C.; Medina, E.; Ferrer-Huerta, M.; Gimeno, N.; Teixidó, M.; Palma, J. L.; Tao, N.; Ugalde, J. M.; Giralt, E.; Díez-Pérez, I.; Mujica, V. Measuring the Spin-Polarization Power of a Single Chiral Molecule. *Small* **2016**, *13*. <https://doi.org/10.1002/sml.201602519>.

REFERENCES

- (52) Aragonès, A. C.; Aravena, D.; Cerdá, J. I.; Acís-Castillo, Z.; Li, H.; Real, J. A.; Sanz, F.; Hihath, J.; Ruiz, E.; Díez-Pérez, I. Large Conductance Switching in a Single-Molecule Device through Room Temperature Spin-Dependent Transport. *Nano Lett.* **2016**, *16*, 218–226. <https://doi.org/10.1021/acs.nanolett.5b03571>.
- (53) Yamada, R.; Noguchi, M.; Tada, H. Magnetoresistance of Single Molecular Junctions Measured by a Mechanically Controllable Break Junction Method. *Appl. Phys. Lett.* **2011**, *98*, 053110. <https://doi.org/10.1063/1.3549190>.
- (54) Horiguchi, K.; Sagisaka, T.; Kurokawa, S.; Sakai, A. Electron Transport through Ni/1,4-Benzenedithiol/Ni Single-Molecule Junctions under Magnetic Field. *J. Appl. Phys.* **2013**, *113*. <https://doi.org/10.1063/1.4800530>.
- (55) Lucier, A.-S. Preparation and Characterization of Tungsten Tips Suitable for Molecular Electronics Studies, **2004**. MA dissertation, McGill University,.
- (56) Van Well, T. L.; Redshaw, M.; Gamage, N. D.; Kandegedara, R. M. E. B. Electrochemical Etching and Characterization of Sharp Field Emission Points for Electron Impact Ionization. *J. Vis. Exp.* **2016**, *2016*, 1–9. <https://doi.org/10.3791/54030>.
- (57) Sørensen, A. H.; Hvid, U.; Mortensen, M. W.; Mørch, K. A. Preparation of Platinum/Iridium Scanning Probe Microscopy Tips. *Rev. Sci. Instrum.* **1999**, *70*, 3059–3067. <https://doi.org/10.1063/1.1149891>.
- (58) Chen, H.; Xiao, W.; Wu, X.; Yang, K.; Gao, H.-J. Electrochemically Etched Ni Tips in a Constant-Current Mode for Spin-Polarized Scanning Tunneling Microscopy. *J. Vac. Sci. Technol. B* **2014**, *32*, 061801. <https://doi.org/10.1116/1.4898865>.
- (59) Mészáros, G.; Li, C.; Pobelov, I.; Wandlowski, T. Current Measurements in a Wide Dynamic Range - Applications in Electrochemical Nanotechnology. *Nanotechnology* **2007**, *18*. <https://doi.org/10.1088/0957-4484/18/42/424004>.
- (60) Hamelin, A. Cyclic Voltammetry at Gold Single-Crystal Surfaces. Part 1. Behaviour at Low-Index Faces. *J. Electroanal. Chem.* **1996**, *407*, 1–11. [https://doi.org/10.1016/0022-0728\(95\)04499-X](https://doi.org/10.1016/0022-0728(95)04499-X).

- (61) Hamelin, A.; Martins, A. M. Cyclic Voltammetry at Gold Single-Crystal Surfaces. Part 2. Behaviour of High-Index Faces. *J. Electroanal. Chem.* **1996**, *407*, 13–21. [https://doi.org/10.1016/0022-0728\(95\)04500-7](https://doi.org/10.1016/0022-0728(95)04500-7).
- (62) Yang, C.; Huang, Y.; Golden, M. S.; Schwarzacher, W. Electrochemical Scanning Tunneling Microscopy Study of Bismuth Chalcogenide Single Crystals. *Langmuir* **2019**, *35*, 15100–15105. <https://doi.org/10.1021/acs.langmuir.9b03062>.
- (63) Michael, K. Single Molecule Electronics, **2020**. Thesis dissertation, University of Bristol.
- (64) Quek, S. Y.; Kamenetska, M.; Steigerwald, M. L.; Choi, H. J.; Louie, S. G.; Hybertsen, M. S.; Neaton, J. B.; Venkataraman, L. Mechanically Controlled Binary Conductance Switching of a Single-Molecule Junction. *Nat. Nanotechnol.* **2009**, *4*, 230–234. <https://doi.org/10.1038/nnano.2009.10>.
- (65) Kim, T.; Darancet, P.; Widawsky, J. R.; Kotiuga, M.; Quek, S. Y.; Neaton, J. B.; Venkataraman, L. Determination of Energy Level Alignment and Coupling Strength in 4,4'-Bipyridine Single-Molecule Junctions. *Nano Lett.* **2014**, *14*, 794–798. <https://doi.org/10.1021/nl404143v>.

CHAPTER 6: GENERAL CONCLUSIONS

6.1. General conclusions

According to the experimental research carried out during this thesis and the obtained results, the following conclusions can be drawn:

- A new strategy for obtaining multi-conductance state molecules, having well-defined and distinguishable states, has been developed. It consists on the introduction of an in-backbone linker in an asymmetric position of the molecular bridge, which opens two additional conduction channels to the end-to-end pathway. As proof-of-concept, an oligo-*para*-phenylethyne (*p*-OPE) derivative incorporating a pyrimidine ring in an asymmetric position, was synthesized, as well as the corresponding models for each proposed channel. Single-molecule experiments revealed three different conductance values for this pyrimidine based-OPE, which were in agreement with those of the model compounds. In this way, the asymmetric position of the in-backbone linker has proved to be responsible for easily distinguishable conductance values attributed to the three different channels.
- Single-molecule conductance of azaborine-acene derivatives was measured for the first time. Using a strategic synthetic design, BN-anthracene- and BN-pentacene-like derivatives were prepared, in which both, nitrogen and boron were forced to be placed unambiguously along the electron conduction pathway. It was found that the B-N substitution in the anthracene scaffold gives rise to slightly lower conductance values, but still in the same order of magnitude, than that of the all-C analogue. The lateral extension of the azaborine acene scaffolds, from anthracene to pentacene, resulted in a shift of the conductance towards lower values. Calculated aromaticity indexes related the decreases of conductance with the lower aromaticity of the central rings from anthracene to the BN-anthracene derivative, and from the latter to the BN-pentacene molecule.
- The unimolecular conductance of negatively curved polycyclic aromatic hydrocarbons (PAHs), incorporating 7-membered rings, was measured for the first time. A synthetic strategy previously developed in the group, for the preparation of heptagon-containing PAHs, was exploited in order to incorporate linker groups in the edges of these structures. A collection of curved PAHs with different linkers was

prepared and their conductance measured. The effect of the curvature on the conductance was evaluated by comparing the conductance value obtained for a curved PAHs having terminal acetylene groups as anchors, with that of its planar counterpart. For that, an exhaustive analysis of the behavior of this anchor was developed. The comparison revealed that the distortion does not involve a quantitative change of conductance with respect to the planar structure. Further comparison with the dendritic oligophenylene precursor of the curved PAH demonstrated that the formation of five C–C bonds, which occurs during the expansion of the aromatic surface, involves an increase in the conductance of more than one order of magnitude.

- The STM setup was redesigned in order to incorporate an electrochemical control system. A four-electrode configuration was developed, including a counter and a reference electrode, and considering both, STM tip and substrate, as working electrodes. Other required changes consisted on the incorporation of a second *I-V* converter-amplifier, for reading the electrochemical current flowing between the substrate and the counter electrode, in addition to the electric STM current between the tip and the substrate; and a bipotentiostat, for independently controlling the potential of tip and substrate respect the reference electrode. The general strategy for tips preparation was tuned up, achieving tips able to read tunneling current as low as $G = 10^{-5} G_0$. Simultaneous and independent cyclic voltammetry of both electrodes were recorded, demonstrating the adequate functioning of the system.
- Preliminary investigation for the break-junction experiments with magnetic electrodes was developed. A series of break-junction experiments, performed under electrochemical control and *in-situ* magnetization of the electrodes, demonstrated that the presence of an electromagnet during the measures introduces high levels of noise in the *G-z* traces. In order to overcome this limitation, we proposed the combination of electrochemical control with the prior magnetization of the electrodes as a future work.

Experimental Section

1. General information:

- Reagents and solvents: unless otherwise stated, all reagents and solvents were purchased from commercial sources. Anhydrous and non-anhydrous solvents such as hexane, DCM, EtOAc, toluene, *i*Pr₂NH and Et₃N were used without further purification. Anhydrous THF was an exception since it was freshly distilled over Na/benzophenone and cooled down to room temperature under inert atmosphere.
- Flash column chromatography: For product purification, silica gel 60 (230-400 mesh, Scharlab, Spain) or silica gel 40-63 μ m (230-400 mesh, SILICYCLE, Canada) was used as the stationary phase.
- Thin layer chromatography: reactions were monitored by TLC, carried out on aluminium sheets coated with silica gel with fluorescent indicator UV254 (purchased from Sigma-Aldrich) and observed under UV light (254 or 365 nm) and/or stained with phosphomolybdic acid (5% ethanol solution).
- Nuclear magnetic resonance spectroscopy: All ¹H and ¹³C NMR spectra were recorded on Varian 300, 400 or 500 MHz spectrometers, at a constant temperature of 298 K. Chemical shifts are reported in ppm and referenced to residual solvent. Coupling constants (*J*) are reported in Hertz (Hz). Standard abbreviations indicating multiplicity were used as follows: m = multiplet, quint. = quintet, q = quartet, t = triplet, d = doublet, s = singlet, b = broad. Assignment of the ¹³C NMR multiplicities was accomplished by DEPT techniques if possible. ¹H and ¹³C NMR spectra of molecules under study are collected in Annexe 1.
- Mass spectrometry: high resolution mass spectrometry measurements were performed on a Bruker ULTRAFLEX III spectrometer equipped with a matrix-assisted laser desorption ionization source coupled with a time of flight spectrometer as detection system (MALDI-TOF) or on a Waters XEVO GL-XS QToF mass spectrometer equipped with an electrospray ionization source coupled with a time of flight spectrometer as detection system (ESI-TOF).

2. Description of the main experimental setup: a home-built STM

The electron transport studies of this thesis have been conducted by means of the break junction technique described in Chapter 1, using two different home-built STMs. One of them is located in the Molecular Electronics Laboratory at *IMDEA Nanociencia* and the other one in the *Centro de Instrumentación Científica* of the *Universidad de Granada*. The first one was running prior to the development of this thesis, while the second one was successfully assembled and tuned up during this thesis. Both microscopes are practically identical, except of small geometry changes, the corresponding piezo-tube calibration parameters and the electronic parameters given by their specific electronic circuits (Figure E.1a).

Tips employed in these STMs are freshly cut metallic wires, generally of gold (0.25 mm diameter, 99.99% purity from Goodfellows). The wires are diagonally cut ($\approx 45^\circ$) in order to achieve a sharp apex and then, soldered to a tinny screw. This serves as a holder and is fastened to a nut fixed at the end of a piezo-tube (Figure E.1c).

The substrates are commercial gold on quartz squares (Arrandee), which are cleaned with ethanol and flame-annealed prior to be exposed to the molecules of interest.

Besides the electrodes, the following parts can be distinguished in our setup:

- A head containing the tip, the tip-holder and the piezo-tube, which includes the electrical connection between the tip and the rest of the electric circuit (Figure E.1c).
- A body, used to keep the head mechanically stable over the sample (Figure E.1a).
- A table (Figure E.1d), where the sample is held and connected to the electric circuit by means of a copper electrode. Three screws serve as support for the body and the head over the sample. They can be controlled by means of three micromanipulators, one of which is controlled by an electrical motor (Figure E.1a). This configuration involves several advantages over the four screw configuration, as i) it provides a more stable system and ii) a good control over the substrate-tip distance (z axis), allowing a fine approach between the electrodes. We use these screws for adjusting the distance within the displacement range that the piezoelectric permits for the tip.

- A made-in-house linear current-to-voltage (I - V) converter with two stages of amplification, which transforms the tunnelling current through the sample-tip junction to a voltage that can be read by a data acquisition system. This voltage (V_i) follows the expression $V_i = -A \times I$, where A is the amplification gain of the device and I is the input current
- An insulating system for mechanical and electrical noise reduction, consisting in a box hanged from the ceiling, where the STM table, head and circuit are assembled during the measurements (Figure E.1e). This box acts as a Faraday cage, since its metallic structure is grounded in order to isolate the STM from external electromagnetic signals. Besides, the box is covered by sponges and held by a pulley and elastic ropes that isolate the STM from mechanical vibrations.

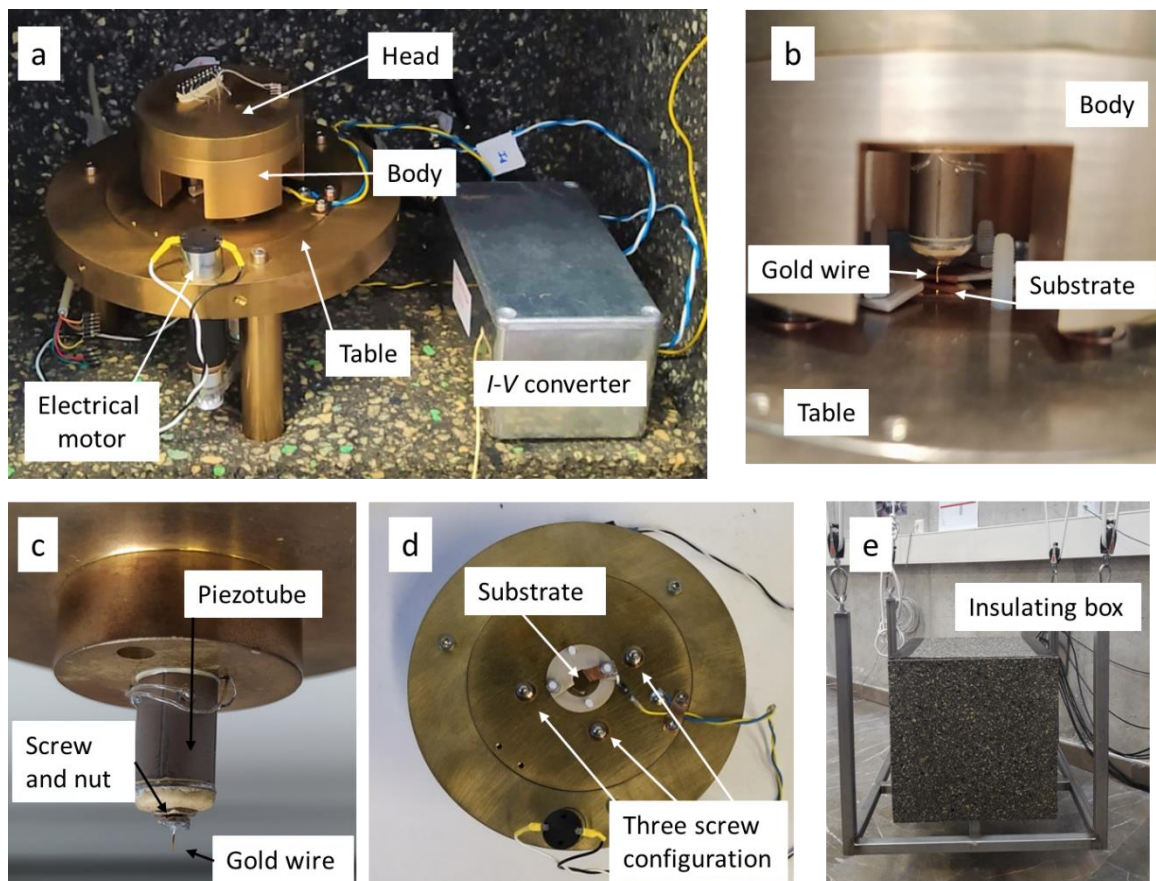


Figure E.1. Elements of the home-built STM.

EXPERIMENTAL SECTION

The electronics of the STM is shown in Figure E.2. A FPGA (Field Programmable Gate Array) card permits the communication between the STM and the computer, controlling the voltages needed for changing the position of the tip, the bias voltage applied to the sample and recording the tunneling current flowing between the tip and the substrate. Note that this current crossing the sample-tip junction is amplified and converted to a voltage before arriving to the FPGA card. The current-to-voltage amplifier circuit has an easily-exchangeable resistance, which allows adjusting the range of recorded conductance values depending on the experiment. This working window goes from conductance values higher than G_0 corresponding to tip-sample metallic contact^a down to conductance values that can reach down to $10^{-8} G_0$. This allows to explore a range in conductance $G=I/V$ up to 8 orders of magnitude. Importantly, a protector resistor is connected in series to the substrate, in order to limit the current flowing through the circuit, avoiding that high current levels cause damage on the circuit elements when the gap between the electrodes is small or closed, also avoiding the saturation of our I - V converter at those stages.. This resistor can also be varied according to the selected gain in the I - V converter. The bias voltage, gain and resistor in-series used for each particular experiment have been included in the corresponding chapters.

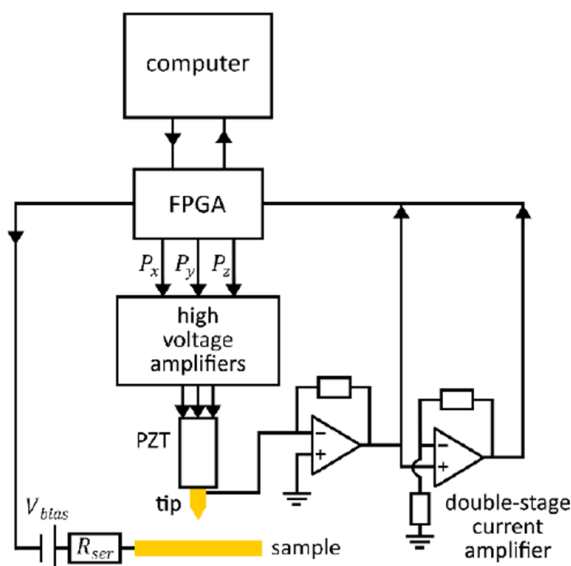


Figure E.2. Schematic representation of electronics of the home-built STMs used. Reproduced from ref.¹

^a As a reminder, atomic Au-Au contacts show a well-known conductance at $G_0=2e/h=77.5 \times 10^{-6}$ S, which is known as the quantum conductance, and which can be used as reference.

For the data acquisition and STM control, a Labview program previously developed in the group has been used, while the G - z and I - V curves were analyzed using an equally customized MATLAB program. The final data representation, shown along the thesis, has been carried out using both MATLAB and Origin.

2.1. Experimental details about data analysis and electrode preparation

Algorithm for plateau-detection:

The total of G - z traces recorded for each compound has been submitted to an automatic algorithm able to separate the traces displaying molecular signals, or plateau regions, from those displaying an exponential conductance decay due to tunneling current. The criterion for considering a trace containing plateau has been that a change in conductance of $\Delta \log(G/G_0) = x$ needs to be related with a displacement (Δz) larger than y nm. Importantly, the values of x and y have been modified according to the requirements of each compound. Further details about this algorithm are reported in reference 2.

Plateau-length distributions:

For building the plateau-length distributions, the plateau length for each individual trace was obtained as the distance from just after the gold contact breakage (in particular $0.5 G_0$). For the later, a reference conductance value was used, which was different for each compound, since it is selected as a conductance value just below the plateau (after the cloud in the 2D histograms).

Typical conductance value determination:

For extracting the experimental typical conductance value for the molecular junctions of each compound, a Gaussian distribution has been fitted to the corresponding peaks in the 1D histograms. The main value of the curve is the most probable conductance value, while the error is given as the half width at half maximum (HWHM) of the Gaussian fit.

Clustering-based analysis:

When a further analysis of the experimental data was needed, an additional unsupervised k-means clustering subdivision has been used. We have employed an algorithm similar to those described in literature,³ using the 2D histograms of the individual G - z traces

EXPERIMENTAL SECTION

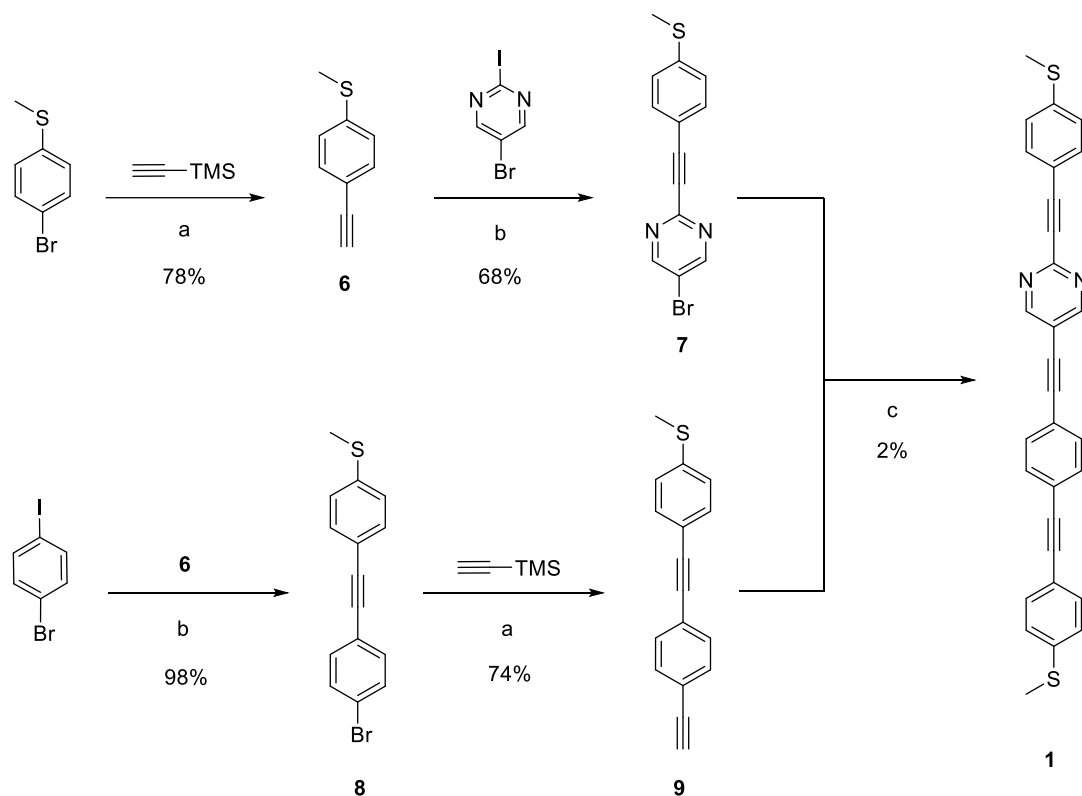
previously selected as displaying plateaus. During the analysis of each compound, different numbers of blind subdivisions in the algorithm were explored, obtaining so many final subdivision as the data required. This technique proved to be especially useful to separate traces with plateaus of similar conductance and different profiles.

Fabrication of polypyrrole electrodes:

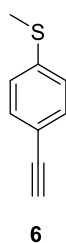
Polypyrrole (PPy) reference electrodes were fabricated for use in the STM-BJ experiments by the electrochemically induced polymerisation of pyrrole following the procedure previously reported in literature.⁴ A 0.25 mm diameter Pt wire (Goodfellow, 99.99%) was used as the working electrode in a three terminal electrochemical cell using a Pt foil counter electrode and a saturated calomel reference electrode. The solution consisted of 0.01 M pyrrole and 0.1 M tetrabutylammonium hexafluorophosphate using acetonitrile as the solvent. The Pt wire was cleaned immediately prior to use by heating in a propane flame. The polymerisation was carried out by performing cyclic voltammetry, sweeping the potential of the Pt wire from -0.6 V to 1.1 V vs. SCE over 50 times. After these scans the potential was held at 0.4 V for a few seconds in order to partially oxidize the film. This process resulted in black slightly iridescent films.

3. Synthesis and characterization of compounds of interest

Compounds prepared in Chapter 2.

Synthesis of compound 1:

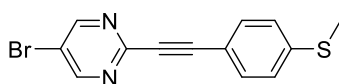
Scheme E1. (a) (i) $\text{Pd}(\text{CH}_3\text{CN})_2\text{Cl}_2$, $\text{PtBu}_3\cdot\text{HBF}_4$, CuI , $i\text{Pr}_2\text{NH}/\text{THF}$, rt, 16 h. (ii) Bu_4NF , THF , rt, 2 h; (b) $\text{Pd}(\text{PPh}_3)_2\text{Cl}_2$, CuI , $\text{Et}_3\text{N}/\text{THF}$, rt, 16 h; (c) $\text{Pd}(\text{CH}_3\text{CN})_2\text{Cl}_2$, $\text{PtBu}_3\cdot\text{HBF}_4$, CuI , $i\text{Pr}_2\text{NH}/\text{THF}$, rt, 16 h.



Trimethylsilyl acetylene (3.86 g, 40 mmol) dissolved in THF (10 mL) was added dropwise to a carefully degassed solution of $\text{Pd}(\text{CH}_3\text{CN})_2\text{Cl}_2$ (240 mg, 1 mmol), CuI (180 mg, 1 mmol), $\text{PtBu}_3\cdot\text{HBF}_4$ (460 mg, 2 mmol) and 4-bromothiobenzene (4 g, 20 mmol) in $i\text{Pr}_2\text{NH}$ (30 mL). Afterwards, the reaction was stirred at room temperature under Ar atmosphere during 24 h. The mixture was then diluted with EtOAc, washed with saturated NH_4Cl (aq) solution,

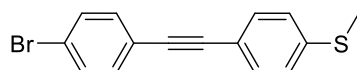
EXPERIMENTAL SECTION

dried over anhydrous Na_2SO_4 and the solvent was removed under reduced pressure. The residue was purified by flash chromatography (SiO_2 , Hexane) to give a yellow oil (4.16 g, 96%). It was dissolved (4.16 g, 18.9 mmol) in THF (20 mL) with 4-5 drops of water and Bu_4NF (8.9 g, 28.3 mmol) was added. The mixture was stirred at room temperature until complete consumption of the starting material (TLC, 1 h). The solution was then diluted with EtOAc, washed with brine, dried over anhydrous Na_2SO_4 , filtered and the solvent was removed under reduced pressure. The residue was purified by flash column chromatography (SiO_2 , Hexane) to give **6** (2.27 g, 82%, global yield = 78%) as a yellow oil. $^1\text{H NMR}$ (400 MHz, CDCl_3) δ 7.40 (d, $J = 8.1$ Hz, 2H), 7.18 (d, $J = 8.1$ Hz, 2H), 3.07 (s, 1H), 2.48 (s, 3H). $^{13}\text{C NMR}$ (101 MHz, CDCl_3) δ 140.2 (C), 132.5 (CH), 125.9 (CH), 118.5 (C), 83.6 (C), 77.3 (CH), 15.5 (CH_3). HRMS (EI): m/z $[\text{M}]^+$ calcd for $\text{C}_9\text{H}_8\text{S}$: 148.0347; found: 148.0346.



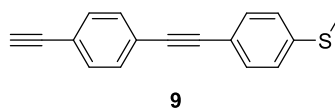
7

A solution of **6** (258 mg, 1.75 mmol) in THF (8 mL) was added dropwise to a carefully degassed solution of $\text{Pd}(\text{PPh}_3)_2\text{Cl}_2$ (62 mg, 0.09 mmol), CuI (17 mg, 0.09 mmol) and 5-bromo-2-iodopyrimidine (500 mg, 1.75 mmol) in Et_3N (5 mL). Afterwards, the reaction was stirred at room temperature under Ar atmosphere for 16 h. The mixture was then diluted with EtOAc, washed with saturated NH_4Cl (aq) solution, dried over anhydrous Na_2SO_4 , filtered and the solvent was removed under reduced pressure. The residue was purified by flash column chromatography (SiO_2 , EtOAc:Hexane, 3:7) to give **7** (360 mg, 68%) as a yellow solid. $^1\text{H NMR}$ (400 MHz, CDCl_3) δ 8.79 (s, 2H), 7.56 (d, $J = 8.5$ Hz, 2H), 7.22 (d, $J = 8.5$ Hz, 2H), 2.51 (s, 3H). $^{13}\text{C NMR}$ (101 MHz, CDCl_3) δ 158.2 (CH), 151.3 (C), 142.1 (C), 133.0 (CH), 125.7 (CH), 119.0 (C), 117.1 (C), 89.7 (C), 87.6 (C), 15.2 (CH_3). HRMS (ESI): m/z $[\text{M}+\text{H}]^+$ calcd for $\text{C}_{13}\text{H}_{10}\text{N}_2\text{SBr}$: 304.9748; found: 304.9748.



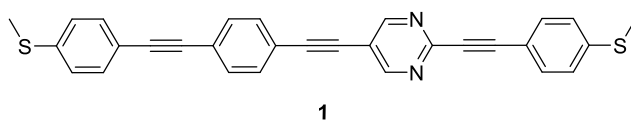
8

A solution of **6** (618 mg, 4.2 mmol) dissolved in THF (2 mL) was added dropwise during 1 h to a carefully degassed solution of Pd(PPh₃)₂Cl₂ (123 mg, 0.17 mmol), CuI (33 mg, 0.17 mmol) and 1-bromo-4-iodobenzene (1 g, 3.5 mmol) in Et₃N (8 mL). Afterwards, the reaction was stirred at room temperature under Ar atmosphere during 2 h. The mixture was then diluted with EtOAc, washed with saturated NH₄Cl (aq) solution, dried over anhydrous Na₂SO₄, filtered and the solvent was removed under reduced pressure. The residue was purified by flash column chromatography (SiO₂, Hexane) to give **8** (1.14 g, 99%) as a yellow solid. **¹H NMR (400 MHz, CDCl₃)** δ 7.48 (d, *J* = 8.6 Hz, 2H), 7.43 (d, *J* = 8.6 Hz, 2H), 7.37 (d, *J* = 8.5 Hz, 2H), 7.21 (d, *J* = 8.5 Hz, 2H), 2.50 (s, 3H). **¹³C NMR (101 MHz, CDCl₃)** δ 139.5 (C), 132.8 (CH), 131.7 (CH), 131.4 (CH), 125.7 (CH), 122.2 (C), 122.1 (C), 119.0 (C), 90.2 (C), 88.2 (C), 15.2 (CH₃). **HRMS (EI):** *m/z* [M]⁺ calcd for C₁₅H₁₁SBr: 301.9765; found: 301.9772.



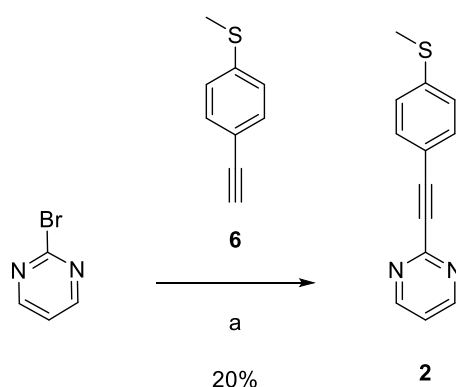
Trimethylsilyl acetylene (721 mg, 7.36 mmol) was added dropwise to a carefully degassed solution of Pd(CH₃CN)₂Cl₂ (48 mg, 0.18 mmol), CuI (35 mg, 0.18 mmol), PtBu₃·HBF₄ (107 mg, 0.37 mmol) and **8** (1.11 g, 3.68 mmol) in *i*Pr₂NH (10 mL) and THF (15 mL). Afterwards, the reaction was stirred at room temperature under Ar atmosphere during 24 h. The mixture was then diluted with EtOAc, washed with saturated NH₄Cl (aq) solution, dried over anhydrous Na₂SO₄ and the solvent was removed under reduced pressure. The residue was purified by flash column chromatography (SiO₂, Hexane) to give a yellow solid (1.44 g, 99%). It was dissolved (920 mg, 2.87 mmol) in THF (10 mL) with 4-5 drops of water. Bu₄NF (1.36 g, 4.3 mmol) was added and the mixture was stirred at room temperature until complete consumption of the starting material (TLC, 1 h). The solution was then diluted with EtOAc, washed with brine, dried over anhydrous Na₂SO₄, filtered and the solvent was removed under reduced pressure. The residue was purified by flash column chromatography (SiO₂, Hexane) to give **9** (536 mg, 75%, global yield = 74%) as a yellow solid. **¹H NMR (400 MHz, CDCl₃)** δ 7.46 (s, 4H), 7.43 (d, *J* = 8.6 Hz, 2H), 7.21 (d, *J* = 8.6 Hz, 2H), 3.17 (s, 1H), 2.50 (s, 3H). **¹³C NMR (101 MHz, CDCl₃)** δ 139.9 (C), 132.2 (CH), 132.0 (CH), 131.5 (CH), 126.0 (CH), 124.0 (C), 121.9 (C), 119.3 (C), 91.4 (C), 89.1 (C), 83.4 (C), 79.0 (CH), 15.5 (CH₃). **HRMS (EI):** *m/z* [M]⁺ calcd for C₁₇H₁₂S: 248.0660; found: 248.0666.

EXPERIMENTAL SECTION



A solution of **9** (293 mg, 1.18 mmol) dissolved in THF (5 mL) was added dropwise to a carefully degassed solution of Pd(CH₃CN)₂Cl₂ (31 mg, 0.12 mmol), CuI (23 mg, 0.12 mmol), PtBu₃·HBF₄ (70 mg, 0.24 mmol) and **7** (360 mg, 1.18 mmol) in *i*Pr₂NH (4 mL). Afterwards, the reaction was stirred at room temperature under Ar atmosphere during 24 h. The mixture was then diluted with DCM, washed with saturated NH₄Cl (aq) solution, dried over anhydrous Na₂SO₄, filtered and the solvent was removed under reduced pressure. The residue was purified by flash column chromatography (SiO₂, EtOAc/Hexane 2:8) and then DCM to give **1** (10 mg, 2%) as a light green solid. ¹H NMR (500 MHz, CD₂Cl₂) δ 8.84 (s, 2H), 7.56 (d, *J* = 3.2 Hz, 6H), 7.46 (d, *J* = 8.4 Hz, 2H), 7.26 (d, *J* = 8.5 Hz, 2H), 7.24 (d, *J* = 8.4 Hz, 2H), 2.52 (s, 3H), 2.51 (s, 3H). ¹³C NMR (126 MHz, CD₂Cl₂) δ 159.5 (CH), 151.4 (C), 142.8 (C), 140.9 (C), 133.3 (CH), 132.4 (CH), 132.3 (CH), 132.1 (CH), 126.3 (CH), 126.1 (CH), 125.0 (C), 122.1 (C), 119.4 (C), 118.2 (C), 117.6 (C), 97.6 (C), 92.3 (C), 90.1 (C), 89.3 (C), 87.3 (C), 85.1 (C), 15.6 (CH₃), 15.4 (CH₃). HRMS (ESI): *m/z* [M+H]⁺ calcd for C₃₀H₂₁N₂S₂: 473.1146; found: 473.1133.

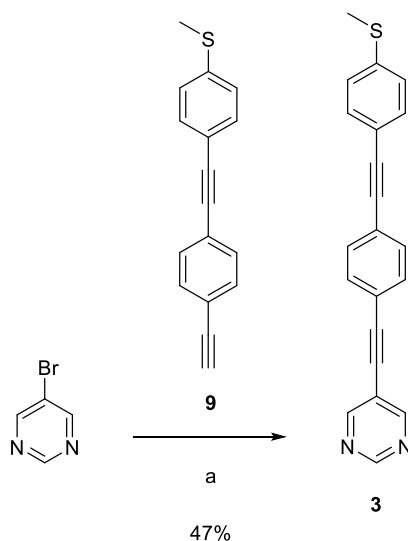
Synthesis of compound 2:



Scheme E.2. (a) Pd(CH₃CN)₂Cl₂, PtBu₃·HBF₄, CuI, *i*Pr₂NH/THF, rt, 16 h.

A solution of **6** (400 mg, 2.72 mmol), dissolved in THF (5 mL) was added dropwise to a carefully degassed solution of Pd(CH₃CN)₂Cl₂ (35 mg, 0.14 mmol), CuI (26 mg, 0.14 mmol), PtBu₃·HBF₄ (79 mg, 0.27 mmol) and 2-bromopyrimidine (432 mg, 2.72 mmol) in *i*Pr₂NH (5 mL). Afterwards, the reaction was stirred at room temperature under Ar atmosphere during 24 h. The mixture was then diluted with EtOAc, washed with NH₄Cl (aq) (x2), dried over anhydrous Na₂SO₄, filtered and the solvent was removed under reduced pressure. The residue was purified by flash column chromatography (SiO₂, EtOAc/Hexane 1:9) and then EtOAc to give **2** (120 mg, 20%) as a yellow solid. ¹H NMR (400 MHz, CD₂Cl₂) δ 8.72 (d, *J* = 5.0 Hz, 2H), 7.56 (d, *J* = 8.5 Hz, 2H), 7.25 (d, *J* = 8.5 Hz, 2H), 7.23 (t, *J* = 5.0 Hz, 1H), 2.51 (s, 3H). ¹³C NMR (101 MHz, CD₂Cl₂) δ 157.8 (CH), 153.8 (C), 142.4 (C), 133.2 (CH), 126.1 (CH), 120.2 (CH), 117.7 (C), 88.9 (C), 87.6 (C), 15.4 (CH₃). HRMS (ESI): *m/z* [M+H]⁺ calcd for C₁₃H₁₁N₂S: 227.0643; found: 227.0641.

Synthesis of compound 3:



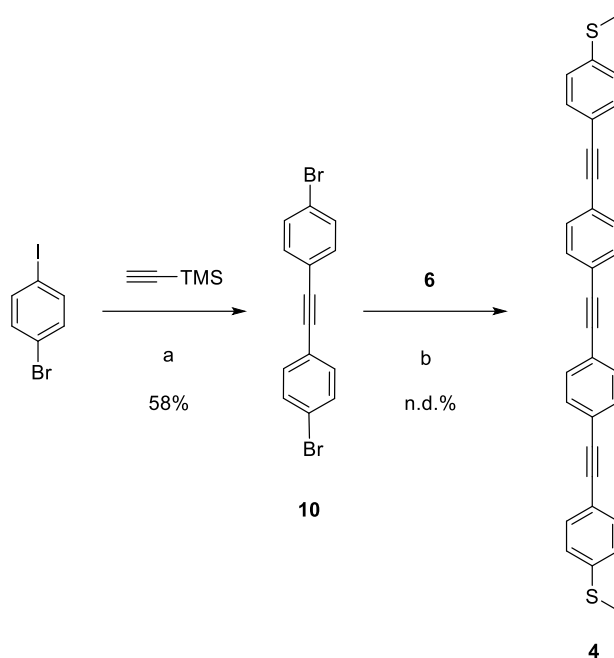
Scheme E.3. (a) Pd(CH₃CN)₂Cl₂, PtBu₃·HBF₄, CuI, *i*Pr₂NH/THF, rt, 16 h

A solution of **9** (408 mg, 1.64 mmol) dissolved in THF (6 mL) was added dropwise to a carefully degassed solution of Pd(CH₃CN)₂Cl₂ (21 mg, 0.08 mmol), CuI (16 mg, 0.08 mmol), PtBu₃·HBF₄ (47 mg, 0.16 mmol) and 5-bromopyrimidine (261 mg, 1.64 mmol) in *i*Pr₂NH (5 mL). Afterwards, the reaction was stirred at room temperature under Ar atmosphere during 24h. The mixture was then diluted with DCM, washed with NH₄Cl (aq) (x2), dried

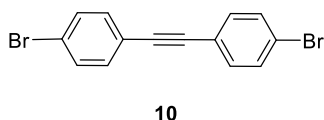
EXPERIMENTAL SECTION

over anhydrous Na_2SO_4 , filtered and the solvent was removed under reduced pressure. The residue was purified by flash column chromatography (SiO_2 , EtOAc/Hexane 1:9) to give **3** (250 mg, 47%) as a yellow solid. $^1\text{H NMR}$ (400 MHz, CD_2Cl_2) δ 9.12 (s, 1H), 8.86 (s, 2H), 7.55 (d, $J = 2.0$ Hz, 4H), 7.46 (d, $J = 8.4$ Hz, 2H), 7.24 (d, $J = 8.4$ Hz, 2H), 2.51 (s, 3H). $^{13}\text{C NMR}$ (101 MHz, CD_2Cl_2) δ 159.2 (CH), 157.4 (CH), 140.9 (C), 132.4 (CH), 132.3 (CH), 132.1 (CH), 126.3 (CH), 124.9 (C), 122.1 (C), 120.2 (C), 119.4 (C), 96.0 (C), 92.2 (C), 89.3 (C), 84.7 (C), 15.6 (CH_3). HRMS (ESI): m/z $[\text{M}+\text{H}]^+$ calcd for $\text{C}_{21}\text{H}_{15}\text{N}_2\text{S}$: 327.0956; found: 327.0950.

Synthesis of compound 4:

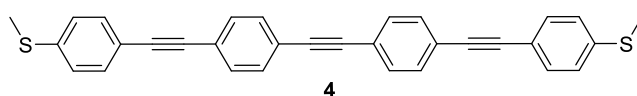


Scheme E.4. (a) $\text{Pd}(\text{PPh}_3)_2\text{Cl}_2$, CuI, DBU, H_2O , acetonitrile, 60°C , 16 h. (b) $\text{Pd}(\text{CH}_3\text{CN})_2\text{Cl}_2$, $\text{PtBu}_3\cdot\text{HBF}_4$, CuI, $i\text{Pr}_2\text{NH}/\text{THF}$, rt, 16 h;



1-bromo-4-iodobenzene (2 g, 7.1 mmol), $\text{Pd}(\text{PPh}_3)_2\text{Cl}_2$ (300 mg, 0.43 mmol), CuI (132 mg, 0.71 mmol) are dissolved in acetonitrile (15 mL). Then, DBU (6.28 g, 43 mmol) and trimethylsilyl acetylene (340 mg, 3.55 mmol) and 4 drops of water are added to the mixture

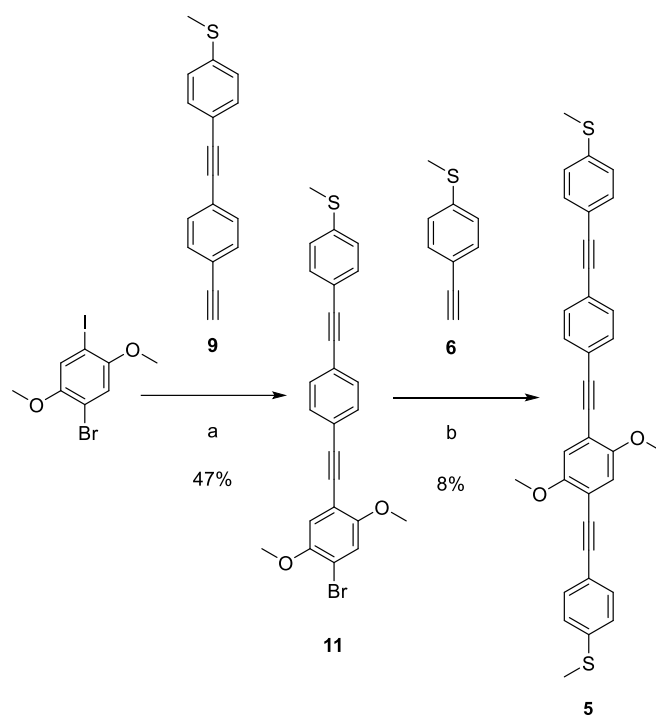
and heat up at 60 °C. Afterwards, the reaction was stirred under Ar atmosphere for 4 hours. The mixture was then diluted with diethylether, washed with HCl 10%, dried over anhydrous Na₂SO₄, filtered and the solvent was removed under reduced pressure. The residue was purified by flash column chromatography (SiO₂, Hexane) to give **10** (692 mg, 58%) as a white solid. ¹H NMR (400 MHz, CDCl₃) δ 7.49 (d, *J* = 8.2 Hz, 4H), 7.38 (d, *J* = 8.2 Hz, 4H). ¹³C NMR (101 MHz, CDCl₃) δ 133.1 (CH), 131.8 (CH), 122.9 (C), 122.0 (C), 89.6 (C). HRMS (EI): *m/z* [M]⁺ calcd for C₁₄H₈Br₂: 333.8993; found: 333.9006.



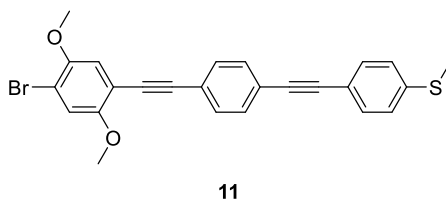
A solution of **6** (700 mg, 4.76 mmol) dissolved in THF (5 mL) was added dropwise to a carefully degassed solution of Pd(CH₃CN)₂Cl₂ (31 mg, 0.12 mmol), CuI (23 mg, 0.12 mmol), PtBu₃·HBF₄ (70 mg, 0.24 mmol) and **10** (360 mg, 1.18 mmol) in 5 mL of *i*Pr₂NH and 5 mL of THF. Afterwards, the reaction was stirred at room temperature under Ar atmosphere for 16 h. The mixture was then diluted with DCM and washed with NH₄Cl (aq) (x2). A grey solid was obtained and washed with DCM, AcOEt, methanol, acetonitrile, diethylether, toluene, cyclohexane, chloroform and THF. The washed solid was dispersed in DMF and heated at reflux during 1 hour. The residue was filtered and washed with DCM to give **4** as a grey insoluble solid (yield not determined). ¹H NMR (400 MHz, CD₂Cl₂) δ 7.52 (d, *J* = 4.5 Hz, 8H), 7.46 (d, *J* = 8.2 Hz, 4H), 7.23 (d, *J* = 8.2 Hz, 4H), 2.51 (s, 6H). HRMS (APCI): *m/z* [M+H]⁺ calcd for C₃₂H₂₃S₂: 471.1236; found: 471.1238.

EXPERIMENTAL SECTION

Synthesis of compound 5:



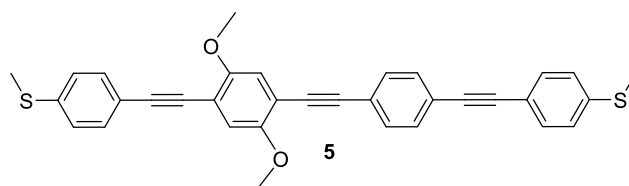
Scheme E.5. (a) Pd(PPh₃)₂Cl₂, CuI, Et₃N/THF, rt, 16 h; (b) Pd(CH₃CN)₂Cl₂, PtBu₃·HBF₄, CuI, *i*Pr₂NH/THF, rt, 16 h;



A solution of **9** (254 mg, 1.02 mmol) in THF (3 mL) was added dropwise to a carefully degassed solution of Pd(PPh₃)₂Cl₂ (35 mg, 0.05 mmol), CuI (19 mg, 0.1 mmol) and 1-bromo-4-iodo-2,5-dimethoxybenzene (318 mg, 3.5 mmol) in Et₃N (4 mL). Afterwards, the reaction was stirred at room temperature under Ar atmosphere for 16 h. The mixture was then diluted with EtOAc, washed with saturated NH₄Cl (aq) solution, dried over anhydrous Na₂SO₄, filtered and the solvent was removed under reduced pressure. The residue was purified by flash column chromatography (SiO₂, EtOAc:Hexane 1:9) to give **11** (202 mg, 47%) as a yellow solid. ¹H NMR (500 MHz, CDCl₃) δ 7.53 (d, *J* = 8.5 Hz, 2H), 7.49 (d, *J* = 8.5 Hz, 2H), 7.44 (d, *J* = 8.5 Hz, 2H), 7.21 (d, *J* = 8.5 Hz, 2H), 7.12 (s, 1H), 7.03 (s, 1H), 3.88 (s, 6H), 2.50 (s, 3H). ¹³C NMR (126 MHz, CDCl₃) δ 154.7 (C), 150.0 (C), 139.8 (C), 132.0 (CH), 131.7 (CH), 131.6 (CH), 126.0 (CH), 123.4 (C), 123.0 (C), 119.4 (C), 116.7 (CH), 116.5 (CH),

113.0 (C), 112.0 (C), 94.1 (C), 91.4 (C), 89.4 (C), 87.1 (C), 57.0 (CH₃), 56.8 (CH₃), 15.5 (CH₃).

HRMS (ESI): m/z [M+H]⁺ calcd for C₂₅H₂₀O₂SBr: 465.0347; found: 465.0330.



A solution of **6** (71 mg, 0.48 mmol) dissolved in THF (4 mL) was added dropwise to a carefully degassed solution of Pd(CH₃CN)₂Cl₂ (10 mg, 0.04 mmol), CuI (10 mg, 0.05 mmol), PtBu₃·HBF₄ (20 mg, 0.07 mmol) and **11** (202 mg, 0.44 mmol) in *i*Pr₂NH (5 mL). Afterwards, the reaction was stirred at room temperature under Ar atmosphere during 24 h. The mixture was then diluted with EtOAc, washed with NH₄Cl (aq) (x2), dried over anhydrous Na₂SO₄, filtered and the solvent was removed under reduced pressure. The residue was purified by flash column chromatography (SiO₂, EtOAc:Hexane 2:98) to give **5** (18 mg, 8%) as a white solid. ¹H NMR (500 MHz, CDCl₃) δ 7.54 (d, *J* = 8.5 Hz, 2H), 7.51–7.46 (m, 4H), 7.44 (d, *J* = 8.5 Hz, 2H), 7.21 (dd, *J* = 8.5, 2.2 Hz, 4H), 7.03 (s, 2H), 3.91 (s, 3H), 3.91 (s, 3H), 2.51 (s, 6H). ¹³C NMR (126 MHz, CDCl₃) δ 154.1 (C), 154.0 (C), 139.8 (C), 139.7 (C), 132.1 (CH), 132.0 (CH), 131.8 (CH), 131.6 (CH), 126.0 (CH), 125.9 (CH), 123.4 (C), 123.1 (C), 119.6 (C), 119.4 (C), 115.7 (CH), 113.8 (C), 113.2 (C), 95.2 (C), 94.9 (C), 91.4 (C), 89.4 (C), 87.7 (C), 85.9 (C), 56.6 (CH₃), 15.5 (CH₃). **HRMS (ESI):** m/z [M+H]⁺ calcd for C₃₄H₂₇O₂S₂: 531.1452; found: 531.1442.

Compounds prepared in Chapter 3.

General protocol for Buchwald-Hartwig cross-coupling reactions (GP1).

An oven-dried Schlenk tube was charged with Pd(dba)₂ (0.05 equiv), PtBu₃·HBF₄ (0.1 equiv.), *t*BuONa (1.5 equiv). The flask was deoxygenated and filled with Ar. Degassed toluene (0.5 M or 1 M) was added and then, the aniline derivative (1 equiv) and the iodoarene (1.2 equiv.) were also added sequentially. The stirring mixture was heated at 80 °C for 16 h. The cooled mixture was partitioned between EtOAc and water. The organic layer was separated and the aqueous layer was extracted with EtOAc (x2). The combined organic layers were washed with brine (x2), dried over Na₂SO₄, filtered and concentrated

EXPERIMENTAL SECTION

under reduced pressure. The crude was purified by flash column chromatography to give the corresponding final products.

General protocol for the synthesis of azaborine derivatives (GP2):

Method A.

An oven-dried flask was charged with the triarylaniline precursor (1 equiv.) and deoxygenated. Dry and degassed THF (0.45 M) was added and the solution was cooled to $-78\text{ }^{\circ}\text{C}$. *n*-BuLi (2.5 M in hexane, 2.2 equiv.) was slowly added and the mixture was stirred for 1 h at $-78\text{ }^{\circ}\text{C}$. Then $\text{B}(\text{OMe})_3$ (1.5 equiv.) was added dropwise and the mixture stirred for 1 h at $-78\text{ }^{\circ}\text{C}$. Then the reaction was removed from the cooling bath and stirred for further 2 h. This mixture was added dropwise over a $\text{Et}_2\text{O}:\text{THF}$ solution of the corresponding organolithium (2 equiv.) at $-70\text{ }^{\circ}\text{C}$. The reaction was stirred at this temperature for 30 min, then cooling bath was removed and the mixture stirred for further 30 min. The reaction was passed through a short silica pad using DCM as eluent and solvent was removed. The crude was purified by column chromatography to give the corresponding final products.

Note: The organolithium was previously prepared by dissolving the corresponding aryl halide (2.5 equiv.) in an $\text{Et}_2\text{O}:\text{THF}$ solution (3:1, 0.25 M) under Ar and adding *n*-BuLi (2.5 M in hexane, 2.0 equiv.) dropwise at $-70\text{ }^{\circ}\text{C}$. After 1h the organolithium is generated.

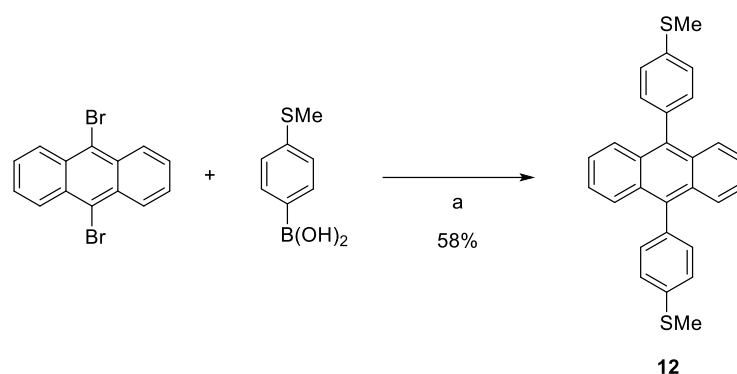
Method B.

The corresponding triarylaniline precursor (1 equiv.) was dissolved in dry Et_2O or a 8:1 mixture of dry $\text{Et}_2\text{O}:\text{THF}$ (0.015 M) under Ar and the solution was cooled to $-78\text{ }^{\circ}\text{C}$. *n*-BuLi (2.5 M in hexane, 2.1 equiv.) was added dropwise and the mixture stirred for 2 h. Then the boronic ester (1.1 equiv.) was added dropwise and the mixture stirred for further 3 h at $-78\text{ }^{\circ}\text{C}$. The cooling bath was removed and the mixture was allowed to reach room temperature. The reaction was quenched with NH_4Cl and the organic layer was separated. Aqueous layer was extracted with Et_2O and combined organic layers were dried over NaSO_4 , filtered and solvent removed under reduced pressure. The crude was dissolved in

DCM and hexane resulting in a precipitate. The liquid supernatant was removed and the solid was thoroughly washed with HPLC-grade hexane.

NOTE: The boronic ester was freshly prepared by mixing the corresponding boronic acid and trimethylorthoformate (2.2 equiv.) under Ar and adding a few drops of trifluoroacetic acid. After stirring for 1 h the mixture became homogeneous and volatiles were evaporated under reduced pressure.

Synthesis of compound 12:



Scheme E.6. (a) Pd(OAc)₂, K₂CO₃, Bu₄NBr, Toluene : H₂O (1:1), 70 °C, 18 h.

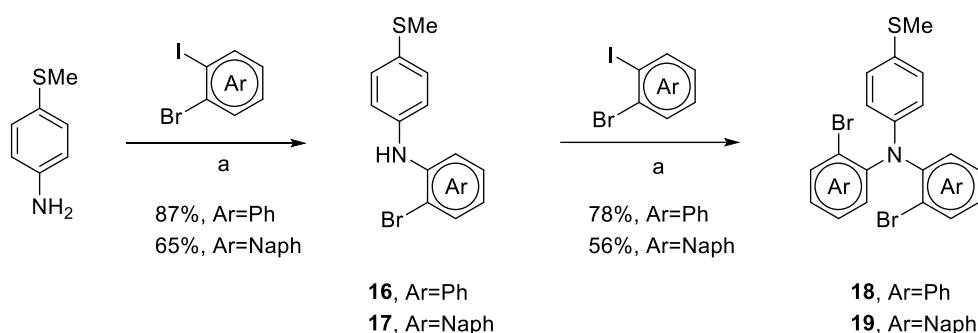
A degassed solution of K₂CO₃ (345 mg, 2.5 mmol) in H₂O (20 mL) was added to a deoxygenated mixture of 9,10-dibromoanthracene (167 mg, 0.5 mmol), (4-(methylthio)phenyl)boronic acid (252 mg, 1.5 mmol), Pd(OAc)₂ (6 mg, 0.05 mmol), and Bu₄NBr (321 mg, 1.0 mmol) in toluene (1.25 mL). The mixture was heated at 70 °C for 18 h. After cooling, phases were separated and aqueous phase extracted with EtOAc (x 2). The combined organic phases were dried over Na₂SO₄, filtered and solvent was removed under reduced pressure. The crude was re-dissolved in DCM and the resulting insoluble powder was filtered, washed with DCM and collected. Compound **12** was isolated pure as a pale yellow solid in 58% yield (123 mg, 0.29 mmol) .m.p. > 300 °C. IR ν_{max} (neat)/cm⁻¹: 2962, 1494, 1394, 1089, 809, 772, 670, 520. ¹H NMR (500 MHz, CDCl₃) δ (ppm) 7.72 (dd, *J* = 6.8, 3.3 Hz, 4H), 7.49 (d, *J* = 8.3 Hz, 4H), 7.40 (d, *J* = 8.2 Hz, 4H), 7.34 (dd, *J* = 6.9, 3.2 Hz, 4H), 2.63 (s, 6H). ¹³C NMR (125 MHz, CDCl₃) δ (ppm) 137.8 (C), 136.5 (C), 135.6 (C), 131.8 (C), 2.63 (s, 6H).

EXPERIMENTAL SECTION

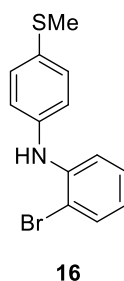
130.0 (CH), 126.9 (CH), 126.4 (CH), 125.1 (CH), 15.8 (CH₃). HRMS (ESI) calc'd for C₂₈H₂₂S₂ [M]⁺: 422.1163; found: 422.1166.

Synthesis of precursors **18** and **19**:

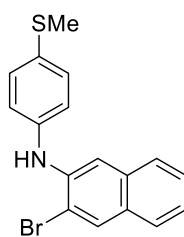
Firstly, precursors **18** and **19** were prepared by Buchwald-Hartwig amination reaction as shown in Scheme E.7.



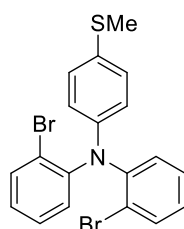
Scheme E.7. (a) Dihaloarene, Pd(dba)₂, PtBu₃.HBF₄, tBuONa, 80 °C, 16 h..



Compound **16** was prepared following GP1 from 4-(methylthio)aniline (600 mg, 4.32 mmol) and 1-bromo-2-iodobenzene (1830 mg, 6.47 mmol) using Pd(dba)₂ (124 mg, 0.22 mmol), PtBu₃.HBF₄ (125 mg, 0.43 mmol) and tBuONa (622 mg, 6.47 mmol) in 4.4 mL of toluene. After purification by flash column chromatography (SiO₂, Hex: EtOAc, 95:5), compound **16** was obtained as a colourless oil (1110 mg, 87%). IR ν_{max} (neat)/cm⁻¹: 3391, 2925, 1586, 1493, 1309, 741. ¹H NMR (400 MHz, CDCl₃) δ (ppm) 7.51 (dd, *J* = 7.9, 1.2 Hz, 1H), 7.26 (d, *J* = 8.6 Hz, 2H), 7.20-7.12 (m, 2H), 7.08 (d, *J* = 8.6 Hz, 2H), 6.72 (ddd, *J* = 8.0, 6.5, 2.3 Hz, 1H), 6.03 (bs, 1H), 2.47 (s, 3H). ¹³C NMR (100 MHz, CDCl₃) δ (ppm) 141.4 (C), 139.5 (C), 133.0 (CH), 131.5 (C), 129.2 (CH), 128.1 (CH), 121.1 (CH), 120.9 (CH), 115.7 (CH), 112.1 (C), 17.3 (CH₃). HRMS (ESI) calc'd for C₁₃H₁₂BrNS [M]⁺: 292.9874; found: 292.9875.

**17**

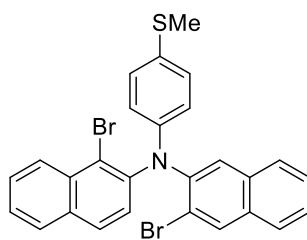
Compound **17** was prepared following GP1 from 4-(methylthio)aniline (174 mg, 1.25 mmol) and 2-bromo-3-iodonaphthalene⁵ (500 mg, 1.50 mmol) using Pd(dba)₂ (36 mg, 0.06 mmol), PtBu₃·HBF₄ (36 mg, 0.12 mmol) and tBuONa (180 mg, 1.88 mmol) in 2.5 mL of toluene. After purification by flash column chromatography (SiO₂, Hex: EtOAc, 95:5), compound **17** was obtained as a greenish solid (279 mg, 65%). **m.p.**: 94-96 °C. **IR** ν_{max} (neat)/cm⁻¹: 3395, 2961, 1260, 1092, 1018, 799. **¹H NMR (500 MHz, CDCl₃)** δ (ppm) 8.07 (s, 1H), 7.65 (dd, *J* = 8.3, 1.1 Hz, 1H), 7.56 (dd, *J* = 8.2, 1.1 Hz, 1H), 7.48 (s, 1H), 7.39 (ddd, *J* = 8.2, 6.8, 1.2 Hz, 1H), 7.32 (d, *J* = 8.6 Hz, 2H), 7.29 (ddd, *J* = 8.1, 6.7, 1.2 Hz, 1H), 7.22 (d, *J* = 8.6 Hz, 2H), 6.19 (s, 1H), 2.52 (s, 3H). **¹³C NMR (125 MHz, CDCl₃)** δ (ppm) 139.4 (C), 138.9 (C), 133.5 (C), 131.9 (CH), 129.2 (CH), 129.1 (C), 126.8 (CH), 126.7 (CH), 126.3 (CH), 123.9 (CH), 121.5 (CH), 114.2 (C), 109.8 (CH), 17.2 (CH₃). **HRMS (ESI)** calc'd for C₁₇H₁₄NSBr [M]⁺: 343.0030; found: 343.0033.

**18**

Compound **18** was prepared following GP1 from **16** (1100 mg, 3.77 mmol) and 1-bromo-2-iodobenzene (1279 mg, 4.52 mmol) using Pd(dba)₂ (108 mg, 0.19 mmol), PtBu₃·HBF₄ (109 mg, 0.38 mmol) and tBuONa (543 mg, 5.65 mmol) in 3.8 mL of toluene. After purification by flash column chromatography (SiO₂, Hexane:EtOAc, 95:5) followed by re-crystallization (DCM/Hexane), compound **17** was obtained as colourless needles (1315 mg, 78%). **m.p.**: 108-109 °C. **IR** ν_{max} (neat)/cm⁻¹: 3020, 2970, 1739, 1465, 1366, 1219, 755, 543, 510. **¹H NMR (400 MHz, CDCl₃)** δ (ppm) 7.61 (dd, *J* = 8.0, 1.5 Hz, 2H), 7.25 (ddd, *J* = 8.0, 7.3, 1.5 Hz, 2H),

EXPERIMENTAL SECTION

7.15 (d, $J = 8.7$ Hz, 2H), 7.11 (dd, $J = 8.0, 1.6$ Hz, 2H), 7.04 (ddd, $J = 8.0, 7.3, 1.6$ Hz, 2H), 6.65 (d, $J = 8.7$ Hz, 2H), 2.45 (s, 3H). ^{13}C NMR (100 MHz, CDCl_3) δ (ppm) 145.4 (C), 145.3 (C), 134.6 (CH), 130.2 (C), 129.3 (CH), 128.6 (CH), 128.4 (CH), 126.5 (CH), 122.0 (C), 121.5 (CH), 17.1 (CH_3). HRMS (ESI) calc'd for $\text{C}_{19}\text{H}_{15}\text{NSBr}_2$ $[\text{M}]^+$: 446.9292; found: 446.9286.

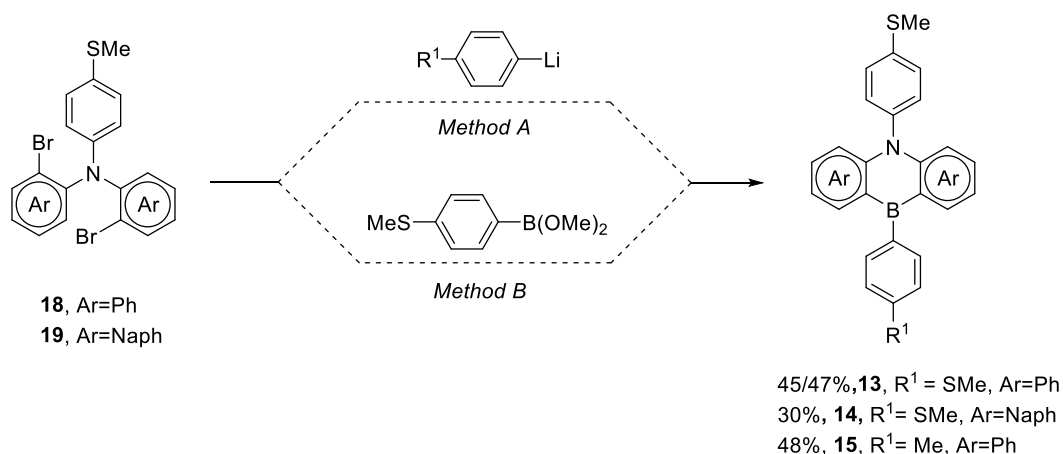


19

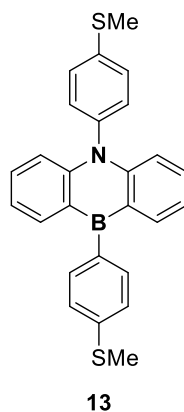
Compound **19** was prepared following GP1 from **17** (311 mg, 0.90 mmol) and 2-bromo-3-iodonaphthalene (362 g, 1.09 mmol) using $\text{Pd}(\text{dba})_2$ (26 mg, 0.04 mmol), $\text{PtBu}_3\cdot\text{HBF}_4$ (26 mg, 0.08 mmol) and $t\text{BuONa}$ (130 mg, 1.36 mmol) in 1.8 mL of toluene. After purification by column chromatography (SiO_2 , Hexane:EtOAc, 95:5) followed by re-crystallization (DCM/Hexane), compound **19** was obtained as a yellow-green solid (280 mg, 56%). m.p.: 179-180 °C. IR ν_{max} (neat)/ cm^{-1} : 2970, 1581, 1487, 1448, 1365, 1229, 1216, 749. ^1H NMR (500 MHz, CDCl_3) δ (ppm) 8.17 (s, 2H), 7.81–7.72 (m, 2H), 7.68–7.61 (m, 2H), 7.54 (s, 2H), 7.50–7.45 (m, 4H), 7.20 (d, $J = 8.8$ Hz, 2H), 6.78 (d, $J = 8.7$ Hz, 2H), 2.48 (s, 3H). ^{13}C NMR (125 MHz, CDCl_3) δ (ppm) 146.0 (C), 143.6 (C), 133.6 (CH), 133.1 (C), 132.1 (C), 128.3 (CH), 127.2 (CH), 126.7 (CH), 126.3 (CH), 122.5 (CH), 121.1 (C), 16.9 (CH_3). HRMS (ESI) calc'd for $\text{C}_{27}\text{H}_{20}\text{NSBr}_2$ $[\text{M}+\text{H}]^+$: 547.9683; found: 547.9659.

Synthesis of compounds 13, 14 and 15:

Two different methods were developed for the synthesis of azaborines **13-15** (Scheme E.8). Method A was successful for the preparation of **13** and **15**, but it failed for the synthesis of **14**. Method B was employed for the synthesis of **14** and it is also suitable for preparing **13**.



Scheme E.8. Method A: (i) *n*-BuLi, (ii) B(OMe)₃, (iii) lithiated arene; **Method B:** (i) *n*-BuLi, (ii) dimethyl (4-(methylthio)phenyl)boronate.

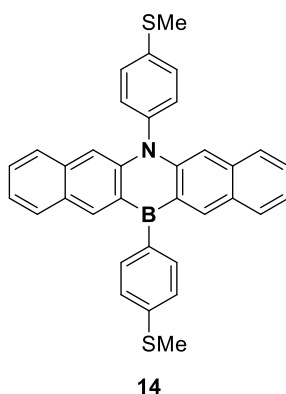


Compound **13** was prepared following GP2-Method A from **18** (200 mg, 0.45 mmol) using *n*-BuLi (0.39 mL, 0.98 mmol), B(OMe)₃ (0.08 mL, 0.67 mmol) in THF (1.5 mL) and (4-(methylthio)phenyl)lithium (0.89 mmol) in 3.7 mL of a 3:1 mixture Et₂O:THF. After purification by column chromatography (SiO₂, Hex: DCM, 8:2) followed by precipitation in HPLC-grade hexane, compound **13** was obtained as a white solid (85 mg, 45 %).

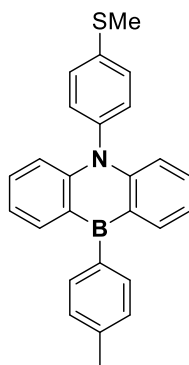
Alternatively, compound **13** was also prepared following GP1-Method B from **18** (150 mg, 0.33 mmol) using *n*-BuLi (0.28 mL, 0.70 mmol) and dimethyl (4-

EXPERIMENTAL SECTION

(methylthio)phenyl)boronate (72 mg, 0.37 mmol) in Et₂O (23 mL). After purification, compound **13** was obtained as a white solid (66 mg, 47%). **m.p.**: 221-222 °C. **IR** ν_{\max} (neat)/cm⁻¹: 1561, 1598, 1439, 1345, 1247, 1115, 1089, 804, 759, 619, 521. **¹H NMR (500 MHz, CD₂Cl₂)** δ (ppm) 8.16 (dd, *J* = 7.7, 1.8 Hz, 2H), 7.69 (d, *J* = 8.2 Hz, 2H), 7.62 (d, *J* = 8.5 Hz, 2H), 7.57 (ddd, *J* = 8.7, 6.9, 1.8 Hz, 2H), 7.49 (d, *J* = 8.1 Hz, 2H), 7.33 (d, *J* = 8.4 Hz, 2H), 7.22 (ddd, *J* = 7.7, 6.8, 1.0 Hz, 2H), 6.96 (d, *J* = 8.7 Hz, 2H), 2.67 (s, 3H), 2.63 (s, 3H). **¹³C NMR (125 MHz, CD₂Cl₂)** δ (ppm) 147.2 (C), 140.2 (C), 138.3 (C), 137.8 (C), 137.0 (CH), 134.2 (CH), 132.6 (CH), 130.5 (CH), 128.2 (CH), 125.4 (CH), 119.7 (CH), 117.0 (CH), 15.4 (CH₃). **¹¹B NMR (128 MHz, CD₂Cl₂)** δ 50.4. **HRMS (APCI)** calc'd for C₂₆H₂₃BNS₂ [M+H]⁺: 424.1359; found: 424.1362.



Compound **14** was prepared following GP2-Method B from **19** (70 mg, 0.12 mmol) using *n*-BuLi (0.10 mL, 0.25 mmol) and dimethyl (4-(methylthio)phenyl)boronate (26 mg, 0.13 mmol) in a 8:1 mixture Et₂O:THF (9 mL). After purification, compound **14** was obtained as a bright red solid (20 mg, 30%). **m.p.** > 300 °C. **IR** ν_{\max} (neat)/cm⁻¹: 2920, 1622, 1585, 1488, 1279, 1094, 809, 746. **¹H NMR (500 MHz, CDCl₃)** δ (ppm) 8.75 (s, 2H), 7.94 (d, *J* = 8.2 Hz, 2H), 7.83 (d, *J* = 7.9 Hz, 2H), 7.69 (d, *J* = 8.4 Hz, 2H), 7.68 (d, *J* = 8.4 Hz, 2H), 7.58 (d, *J* = 7.9 Hz, 2H), 7.48 (td, *J* = 7.8, 0.8 Hz, 2H), 7.45 (d, *J* = 8.4 Hz, 2H), 7.34 (td, *J* = 7.8, 0.8 Hz, 2H), 7.11 (s, 2H), 2.73 (s, 3H), 2.70 (s, 3H). **¹³C NMR (125 MHz, CD₂Cl₂)** δ (ppm) 140.3 (CH), 129.0 (CH), 134.1 (CH), 128.7 (CH), 127.1 (CH), 125.6 (CH), 128.1 (CH), 130.9 (CH), 123.1 (CH), 111.2 (CH), 15.1 (CH₃). Carbons were assigned from the HSQC (quaternary carbons are not shown). **HRMS (ESI)** calc'd for C₃₄H₂₆BNS₂ [M]⁺: 523.1600; found: 523.1606.

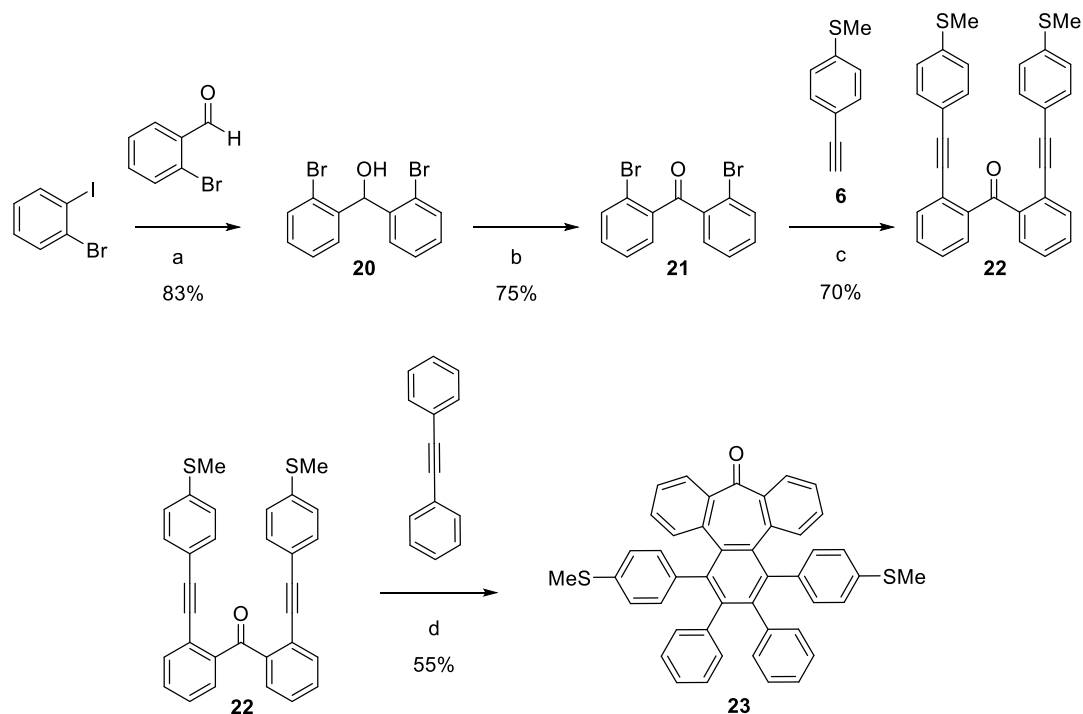
**15**

Compound **15** was prepared following GP2-Method A from **18** (250 mg, 0.56 mmol) using *n*-BuLi (0.49 mL, 1.22 mL mmol), B(OMe)₃ (0.09 mL, 0.83 mmol) in THF (2 mL) and (4-methyl)phenyllithium (1.11 mmol) in 4 mL of a 3:1 mixture Et₂O:THF. After purification by column chromatography (SiO₂, Hexane:DCM, 8:2) followed by precipitation in HPLC-grade hexane, compound **15** was obtained as a white solid (105 mg, 48%). **m.p.:** 231-233 °C. **IR** ν_{max} (neat)/cm⁻¹: 1563, 1598, 1440, 1346, 1250, 803, 758, 621, 523. **¹H NMR (500 MHz, CDCl₃)** δ 8.22 (dd, *J* = 7.7, 1.7 Hz, 1H), 7.67 (d, *J* = 7.9 Hz, 1H), 7.59 (d, *J* = 8.5 Hz, 1H), 7.54 (ddd, *J* = 8.7, 6.9, 1.8 Hz, 1H), 7.41 (d, *J* = 7.5 Hz, 1H), 7.32 (d, *J* = 8.4 Hz, 1H), 7.20 (ddd, *J* = 7.8, 6.8, 0.8 Hz, 1H), 6.92 (d, *J* = 8.7 Hz, 1H), 2.66, (s, 3H), 2.53 (s, 3H). **¹³C NMR (125 MHz, CDCl₃)** δ 147.2 (C), 140.0 (C), 138.5 (C), 137.4 (CH), 137.0 (C), 133.8 (CH), 132.6 (CH), 130.6 (CH), 128.3 (CH), 128.2 (CH), 119.7 (CH), 116.9 (CH), 21.6 (CH₃), 15.6 (CH₃). **¹¹B NMR (128 MHz, CDCl₃)** δ 51.4 (bs). **HRMS (ESI)** calc'd for C₂₆H₂₂BNS [M]⁺: 391.1566; found: 391.1579.

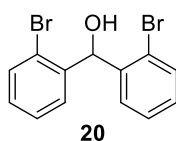
EXPERIMENTAL SECTION

Compounds prepared in Chapter 4.

Synthesis of compound 23:

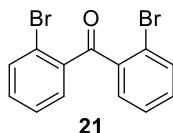


Scheme E.9. (a) *i*PrMgCl·LiCl, THF, -78 °C to rt, 16 h; (b) DMP, CH₂Cl₂, rt, 16 h; (c) **6**, PdCl₂(CH₃CN)₂, CuI, PtBu₃·HBF₄, THF, *i*Pr₂NH, rt, 16 h; (d) Co₂(CO)₈, dioxane, 100 °C, 16 h.

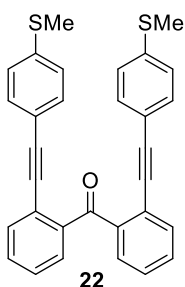


Procedure modified from literature.⁶ To a stirring solution of 2-bromoiodobenzene (3.67 mL, 29.27 mmol) in THF (80 mL) placed into an acetone bath at -15 °C was added *i*PrMgCl·LiCl (1.3 M in THF, 25 mL, 32.5 mmol) and stirred for 30 min at -15 °C. The reaction was cooled to -78 °C and 2-bromobenzaldehyde (4.17 mL, 36 mmol) was added dropwise. The cold bath was kept and the reaction was allowed to slowly warm up to room temperature for 16 h. The reaction mixture was quenched with HCl 2M (2 mL), diluted with water (100 mL) and extracted twice with DCM (2 × 100mL). The combined organic phases were dried with anhydrous Na₂SO₄, filtered and concentrated under reduced pressure. The

crude material was purified by flash column chromatography (SiO₂, Hexane:DCM, 4:1) affording compound **20** (8.31 g, 83%) as a colorless oil. ¹H NMR (300 MHz, CDCl₃): δ = 7.58 (d, *J*=7.9 Hz, 2H), 7.37–7.24 (m, 4H), 7.22–7.13 (m, 2H), 6.38 (d, *J*=3.8 Hz, 1H), 2.82 (d, *J*=4.0 Hz, 1H). Spectroscopic data are in accordance with those reported in literature.⁶



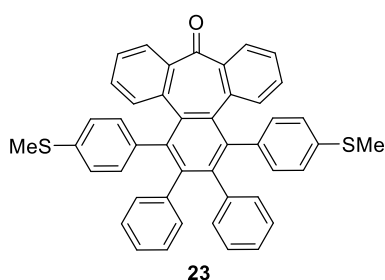
Compound **20** (4.20 g, 12.28 mmol) was dissolved in DCM (50 mL) and placed into an ice-water bath, then Dess-Martin periodinane (6.76 g, 15.93 mmol) was added slowly under vigorous stirring. The reaction mixture was allowed to warm to room temperature and stirred for 16 h. The reaction mixture was diluted with DCM (50 mL) and washed twice with Na₂S₂O₃ and NaHCO₃ (2 × 100 mL). The organic layer was dried over anhydrous Na₂SO₄, filtered and the solvent removed under reduced pressure. The crude was purified by flash column chromatography (SiO₂, Hexane:DCM, 4:1) giving rise to compound **21** (3.13 g, 75%) as a white solid. ¹H NMR (300 MHz, CDCl₃): δ = 7.69–7.59 (m, 2H), 7.49–7.42 (m, 2H), 7.42–7.30 (m, 4H). Spectroscopic data are in accordance with those reported in literature.⁷



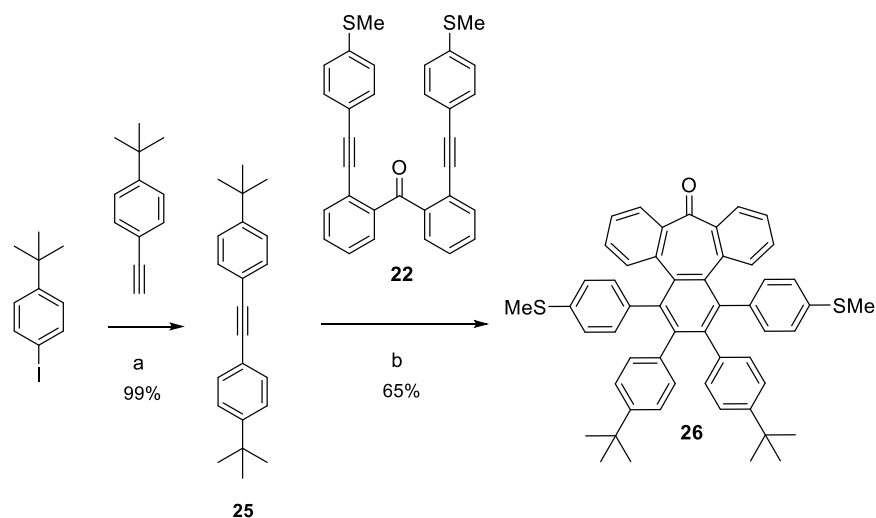
In a oven-dried round-bottom flask, compound **21** (540 mg, 1.58 mmol), PdCl₂(CH₃CN)₂ (60 mg, 0.24 mmol), CuI (45 mg, 0.24 mmol) and PtBu₃·HBF₄ (140 mg, 0.47 mmol) were placed and purged with Ar. The solids were suspended in THF (4 mL), *i*Pr₂NH (10 mL) was added and the suspension bubbled with Ar. A solution of **6** (0.63 mL, 4.28 mmol) in THF (2 mL) was added dropwise and the reaction mixture was stirred at room temperature for 3h. The solvent was removed under reduced pressure, diluted with DCM (100 mL) and washed with

EXPERIMENTAL SECTION

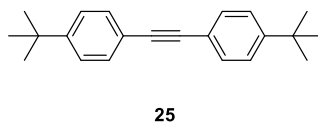
saturated NH_4Cl (aq) solution (x2). The organic layer was dried over anhydrous Na_2SO_4 , filtered and the crude purified by flash column chromatography (SiO_2 , Hexane:EtOAc 49:1) affording **22** (520 mg, 70%) as a yellow oil. ^1H NMR (300 MHz, CDCl_3): δ 7.72 (dd, $J = 7.4, 1.7$ Hz, 4H), 7.61 (dd, $J = 7.4, 1.6$ Hz, 4H), 7.53–7.38 (m, 4H), 7.16–7.08 (m, 4H), 2.49 (s, 6H).



In an oven-dried round-bottom flask, compound **22** (100 mg, 0.2 mmol) and $\text{Co}_2(\text{CO})_8$ (95 mg, 0.27 mmol) were dissolved in dry dioxane (8 mL) under Ar atmosphere. The mixture was heated at 100 °C and stirred for 30 min. Then, diphenylacetylene (56 mg, 0.31 mmol) was added during 30 min and finally the mixture was heated at 100 °C for 16 h. The solvent was removed under reduced pressure and the crude material purified by flash column chromatography (SiO_2 , Hexane:DCM, 6:4) affording a brown solid. The solid was precipitated in HPLC-grade hexane (8 mL) obtaining **23** (85 mg, 56%) as a white solid. ^1H NMR (300 MHz, CDCl_3): δ 7.40 (d, $J = 7.6$ Hz, 2H), 7.32 (d, $J = 7.8$ Hz, 2H), 7.11 (t, $J = 7.5$ Hz, 2H), 7.05–6.94 (m, 6H), 6.90–6.77 (m, 6H), 6.69 (dd, $J = 9.9, 7.1$ Hz, 4H), 6.41–6.34 (m, 4H), 2.31 (s, 6H).

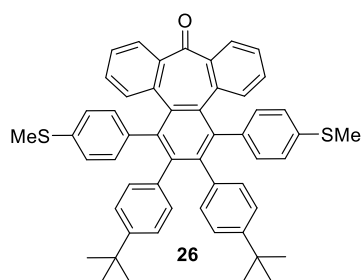
Synthesis of compound 26:

Scheme 10. (a) $\text{PdCl}_2(\text{PPh}_3)_2$, CuI, Et_3N , THF, rt, 16 h; (b) $\text{Co}_2(\text{CO})_8$, toluene, 110 °C, 16 h



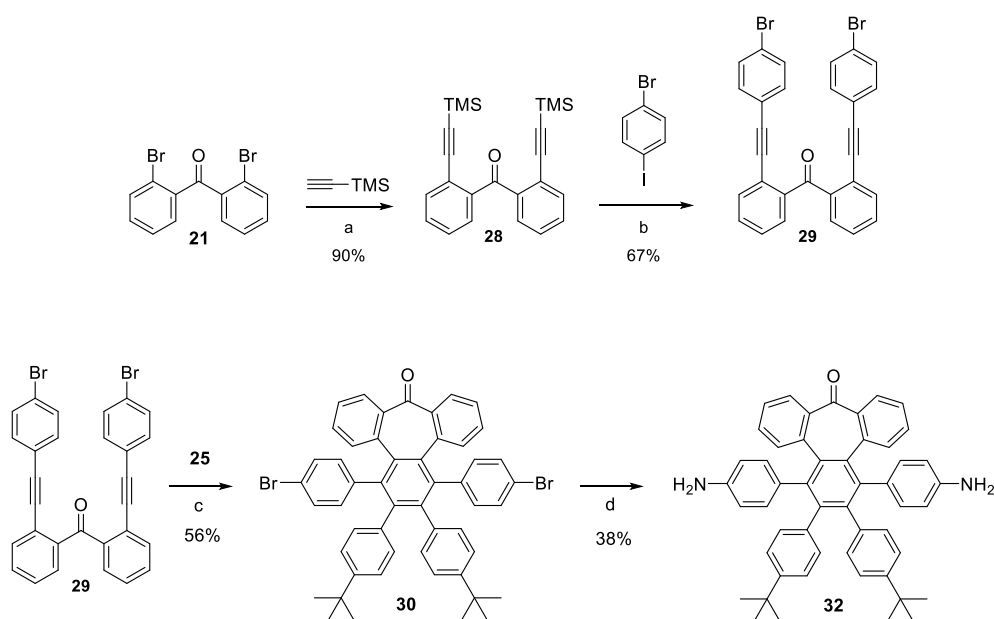
Into a properly degassed and oven-dried round-bottom flask, $\text{PdCl}_2(\text{PPh}_3)_2$ (40 mg, 0.06 mmol) and CuI (40 mg, 0.20 mmol) were placed and purged with Ar. The solids were suspended in a 1:2 mixture of THF and Et_3N (9 mL) and bubbled with Ar. 4-*tert*-butyliodobenzene (0.7 mL, 3.95 mmol) was added to the reaction mixture and then 4-*tert*-butylphenylacetylene (0.9 mL, 7.55 mmol) was added dropwise. The reaction mixture was stirred at room temperature for 16 h. The mixture was diluted with DCM (100 mL) and washed with saturated NH_4Cl (aq) solution (x2). The organic layer was separated and dried over anhydrous Na_2SO_4 , filtered and the solvent removed under reduced pressure. The crude was purified by flash column chromatography (SiO_2 , Hexane) giving rise to **25** (1.08 g, 94%) as a white solid. $^1\text{H NMR}$ (300 MHz, CDCl_3): δ = 7.48 (d, J = 8.1 Hz, 4H), 7.38 (d, J = 8.2 Hz, 4H), 1.34 (s, 18H). $^{13}\text{C NMR}$ (125 MHz, CDCl_3): δ = 152.0 (C), 131.8 (CH), 125.9 (CH), 120.9 (C), 89.4 (C), 35.2 (C), 31.5 (CH_3).

EXPERIMENTAL SECTION

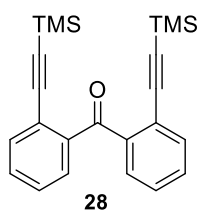


In an oven-dried round-bottom flask, compound **22** (140 mg, 0.3 mmol) and $\text{Co}_2(\text{CO})_8$ (100 mg, 0.3 mmol) were dissolved in dry toluene (8 mL) under Ar atmosphere. The mixture was heated at 110 °C and stirred for 30 min. Then, a solution of **25** (128 mg, 0.45 mmol) in degassed dry toluene (4 mL) was added during 30 min and finally the mixture was heated at 110 °C for 16 h. The solvent was removed under reduced pressure and the crude material purified by flash column chromatography (SiO_2 , Hexane:DCM, 6:4) affording a brown solid. The solid was precipitated in HPLC-grade hexane (8 mL) obtaining **26** (150 mg, 65%) as a white solid. $^1\text{H NMR}$ (300 MHz, CDCl_3): δ 7.43 (d, $J = 7.6$ Hz, 2H), 7.22 (d, $J = 8.2$ Hz, 2H), 7.17–6.99 (m, 10H), 6.93–6.84 (m, 4H), 6.75–6.67 (m, 2H), 6.41 (d, $J = 8.3$ Hz, 2H), 6.26 (d, $J = 8.1$ Hz, 2H), 2.33 (s, 6H), 1.10 (s, 18H).

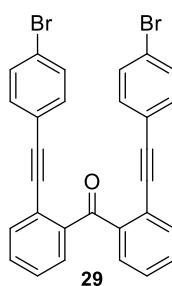
Synthesis of compound 32:



Scheme 11. (a) $\text{PdCl}_2(\text{CH}_3\text{CN})_2$, CuI, $\text{PtBu}_3\text{-HBF}_4$, $i\text{Pr}_2\text{NH}/\text{THF}$, rt, 16 h; (b) $\text{PdCl}_2(\text{PPh}_3)_2$, CuI, Et_3N , DBU, THF, H_2O , 70 °C, 16 h; (c) $\text{Co}_2(\text{CO})_8$, toluene, 110 °C, 16 h; (d) (i) *t*butyl carbamate, $\text{Pd}(\text{dba})_2$, $\text{PtBu}_3\text{-HBF}_4$, $t\text{BuONa}$, toluene, 115 °C, 16 h; (ii) TFA, CH_2Cl_2 , 30 min.



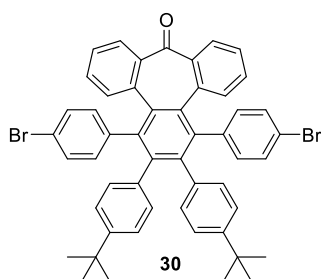
In a oven-dried round-bottom flask, compound **21** (500 mg, 1.47 mmol), PdCl₂(CH₃CN)₂ (57 mg, 0.22 mmol), CuI (42 mg, 0.22 mmol) and PtBu₃·HBF₄ (127 mg, 0.44 mmol) were placed and purged with Ar. The solids were suspended in THF (4 mL), *i*Pr₂NH (10 mL) was added and the suspension bubbled with Ar. Trimethylsilylacetylene (0.61 mL, 4.41 mmol) was added dropwise and the reaction mixture was stirred at room temperature for 3h. The solvent was removed under reduced pressure, diluted with DCM (100 mL) and washed with saturated NH₄Cl (aq) solution (x2). The organic layer was dried over anhydrous Na₂SO₄, filtered and the solvent removed under reduced pressure. The crude was purified by flash column chromatography (SiO₂, Hexane:EtOAc 49:1) affording **28** (497 mg, 90%) as a yellow oil. IR ν_{max} (neat)/cm⁻¹: 3069, 2964, 2155, 1667, 840 cm⁻¹. ¹H NMR (500 MHz, CDCl₃): δ = 7.56 (dd, *J*=7.6 Hz, 1.4, 2H), 7.51 (dd, *J*=7.6 Hz, 1.4, 2H), 7.43 (td, *J*=7.5 Hz, 1.6, 2H), 7.37 (td, *J*=7.5 Hz, 1.6, 2H), 0.04 (s, 18H). ¹³C NMR (126 MHz, CDCl₃): δ = 196.9 (C), 141.9 (C), 133.9 (CH), 131.0 (CH), 129.9 (CH), 128.4(CH), 122.7 (C), 102.5 (C), 100.9 (C), -0.1 (CH₃). HRMS (ESI): *m/z* calc. for C₂₃H₂₇OSi₂ [M+H]⁺: 375.1600; found: 375.1604.



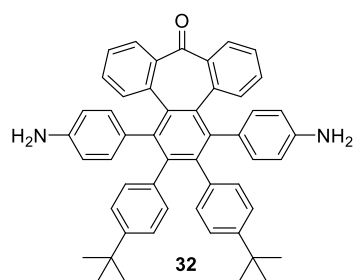
28, 1-bromo-4-iodobenzene (2.51 g, 8.86 mmol), PdCl₂(PPh₃)₂ (141 mg, 0.20 mmol) and CuI (77mg, 0.40 mmol) were placed in a round-bottom flask and purged with Ar. Then, THF (32 mL), DBU (10 mL), Et₃N (5mL) and H₂O (3 mL) were added, and the mixture was heated at 70 °C under Ar atmosphere for 16 h. The mixture was diluted with EtOAc (120 mL) and washed with saturated NH₄Cl (aq) solution (x2) and brine, the organic layer was separated,

EXPERIMENTAL SECTION

dried over anhydrous Na_2SO_4 and the solvent removed under reduced pressure. The crude was purified by flash column chromatography (SiO_2 , Hexane:EtOAc 19:1) affording **29** (1.46 g, 67%) as an orange foam. IR ν_{max} (neat)/ cm^{-1} : 3060, 2960, 2213, 1489, 822 cm^{-1} . $^1\text{H NMR}$ (500 MHz, CDCl_3): δ = 7.72 (d, J = 7.1 Hz, 2H), 7.62 (d, J = 7.1 Hz, 2H), 7.56–7.44 (m, 4H), 7.41 (d, J = 8.0 Hz, 4H), 7.09 (d, J = 8.0 Hz, 4H). $^{13}\text{C NMR}$ (126 MHz, CDCl_3): δ = 196.7 (C), 141.1 (C), 133.3 (CH), 133. (CH), 131.4 (CH), 131.3 (CH), 130.1 (CH), 128.6 (CH), 122.8 (C), 122.4 (C), 121.7 (C), 94.3 (C), 88.7 (C). HR-MS (ESI): m/z calc. for $\text{C}_{29}\text{H}_{17}\text{OBr}_2$ $[\text{M}+\text{H}]^+$: 538.9646; found: 538.9641;

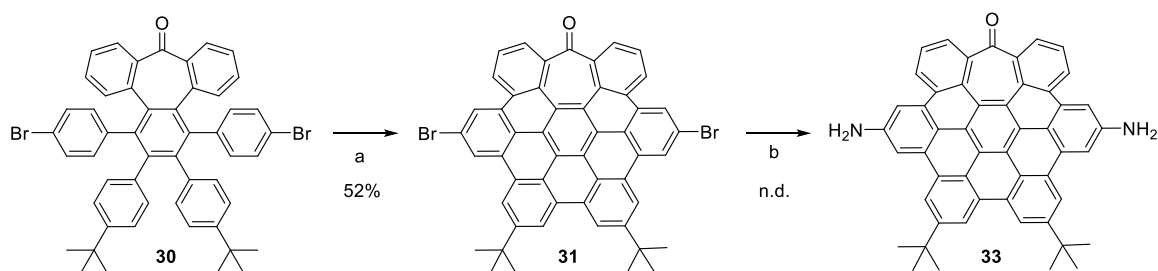


Compound **29** (375 mg, 0.70 mmol) and $\text{Co}_2(\text{CO})_8$ (308 mg, 0.90 mmol) were dissolved in dry toluene (7 mL) under Ar atmosphere. The mixture was heated at 110 °C and stirred for 30 min. Then, a solution of **25** (305 mg, 1.05 mmol) in degassed dry toluene (4 mL) was added during 30 min and finally the mixture was heated at 110 °C for 16 h. The solvent was removed under reduced pressure and the crude material purified by flash column chromatography (SiO_2 , Hexane:DCM, 13:7) affording a brown solid. The solid was precipitated in hexane (5mL) obtaining **30** (325 mg, 56%) as a white solid. IR ν_{max} (neat)/ cm^{-1} : 3028, 2961, 1738, 758 cm^{-1} . $^1\text{H NMR}$ (500 MHz, CDCl_3): δ = 7.44 (d, J = 7.6 Hz, 2H), 7.2–7.1 (m, 4H), 7.06 (d, J = 7.9 Hz, 2H), 7.01 (dd, J = 8.4 Hz, 2.1, 4H), 6.98–6.83 (m, 6H), 6.71 (d, J = 8.1 Hz, 2H), 6.36 (d, J = 8.4 Hz, 2H), 6.24 (d, J = 8.1 Hz, 2H), 1.11 (s, 18H). $^{13}\text{C NMR}$ (126 MHz, CDCl_3): δ = 200.1 (C), 148.4 (C), 146.0 (C), 143.3 (C), 140.4 (C), 139.8 (C), 136.6 (C), 135.2 (C), 134.5 (C), 134.1 (CH), 133.1 (CH), 132.2 (CH), 131.2 (CH), 130.3 (CH), 129.7 (CH), 129.6 (CH), 128.9 (CH), 127.4 (CH), 124.4 (CH), 123.9 (CH), 122.8 (CH), 119.7 (C), 34.1 (C), 31.1 (CH₃). HRMS (ESI): m/z calc. for $\text{C}_{51}\text{H}_{43}\text{Br}_2\text{O}$ $[\text{M}+\text{H}]^+$: 851.1500; found: 851.1521.



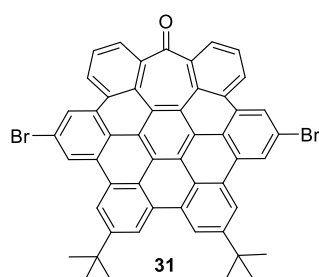
An oven-dried Schlenk tube was charged with Pd(dba)₂ (40 mg, 0.07 mmol), PtBu₃·HBF₄ (25 mg, 0.12 mmol), NaOtBu (87 mg, 0.1 mmol), **30** (250 mg, 0.3 mmol) and *t*butyl carbamate (106 mg, 0.9 mmol). The flask was deoxygenated and filled with Ar. Degassed toluene (10 mL) was added and then, the mixture was heated at 115 °C and stirred for 16 h. The cooled mixture was partitioned between EtOAc and water. The organic layer was separated and the aqueous layer was extracted with EtOAc (x2). The combined organic layers were washed with brine (x2), dried over Na₂SO₄, filtered and concentrated under reduced pressure. The crude was purified by flash column chromatography (SiO₂, Hexane:DCM, 6:4). Then it was dissolved in DCM (2mL) and the mixture deoxygenated. TFA (1 mL) was then added dropwise to the stirring mixture. The reaction was followed by TLC until the consumption of the starting material (30 min). The solvent was removed under reduced pressure and the residue was precipitated in HPLC-grade hexane, obtaining **32** (80 mg, 38%) as a white solid. ¹H NMR (400 MHz, THF-*d*₈) δ 7.28 (d, *J* = 7.6 Hz, 4H), 7.22 (d, *J* = 8.0 Hz, 2H), 7.07–6.98 (m, 6H), 6.89 (d, *J* = 7.7 Hz, 2H), 6.83 (t, *J* = 7.6 Hz, 2H), 6.67 (d, *J* = 6.6 Hz, 2H), 6.29 (d, *J* = 7.0 Hz, 4H), 6.18–6.09 (m, 2H), 4.7–4.6 (s, 4H) 1.08 (s, 18H).

Synthesis of compound 33

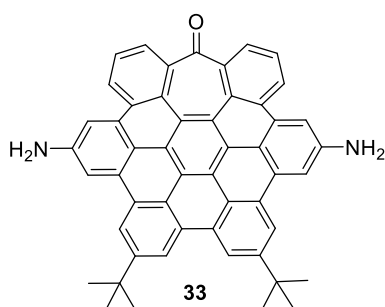


Scheme 12. (a) DDQ, CF₃SO₃H, CH₂Cl₂, 0 °C, 10 min; (b) (i) *t*butyl carbamate, Pd(dba)₂, PtBu₃·HBF₄, *t*BuONa, toluene, 115 °C, 16 h; (ii) TFA, CH₂Cl₂, 30 min.

EXPERIMENTAL SECTION



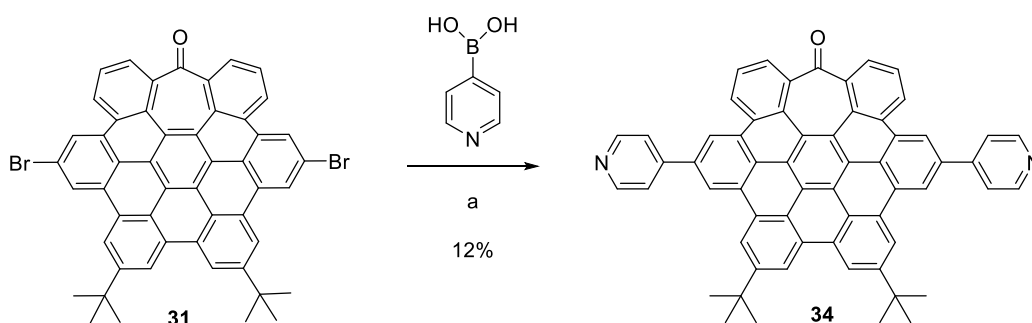
In a round bottom flask, compound **30** (115 mg, 0.14 mmol) and DDQ (173 mg, 0.76 mmol) were dissolved in dry DCM (5 mL) under Ar atmosphere. The mixture was cooled down to 0°C, then trifluoromethanesulfonic acid (0.25 mL) was added and the mixture stirred at 0 °C for 10 min. The mixture was then diluted with DCM (10 mL) and silica gel was added. The solvent was removed under reduced pressure and the crude material purified by flash column chromatography (SiO₂, DCM:Hexane, 6:4) affording **31** (59 mg, 52%) as a yellow solid. IR ν_{max} (neat)/cm⁻¹: 3064, 2957, 1681, 1364, 759 cm⁻¹. ¹H NMR (400 MHz, CDCl₃): δ = 9.06 (s, 2H), 8.47 (d, J = 8.0 Hz, 2H), 8.36 (s, 2H), 7.99 (t, J =7.7 Hz, 2H), 7.85 – 7.67 (m, 6H), 1.91 (s, 18H). ¹³C NMR (101 MHz, CDCl₃): δ = 202.0 (C), 149.9 (C), 141.7 (C), 130.8 (C), 129.4 (C), 129.0 (C), 128.9 (C), 128.3 (C), 127.4 (CH), 126.7 (CH), 125.0 (CH), 124.3 (CH), 122.8 (C), 122.4 (CH), 122.2 (C), 121.7 (C), 121.5 (C), 121.2 (C), 120.1 (C), 119.0 (CH), 118.9 (CH), 36.0 (C), 32.2 (CH₃). HRMS (ESI): m/z calc. For C₅₁H₃₂Br₂ONa [M+Na]⁺: 843.0697; found: 843.0708.



An oven-dried Schlenk tube was charged with Pd(dba)₂ (70 mg, 0.12 mmol), PtBu₃·HBF₄ (36 mg, 0.18 mmol), NaOtBu (115 mg, 1.2 mmol), **31** (190 mg, 0.23 mmol) and *t*butyl carbamate (140 mg, 1.2 mmol). The flask was deoxygenated and filled with Ar. Degassed toluene (15 mL) was added and then, the mixture was heated at 115 °C and stirred for 16 h. The cooled mixture was partitioned between EtOAc and water. The organic layer was

separated and the aqueous layer was extracted with EtOAc (x2). The combined organic layers were washed with brine (x2), dried over Na₂SO₄, filtered and concentrated under reduced pressure. The crude was purified by flash column chromatography (SiO₂, DCM:Hexane, 7:3). Then it was dissolved in DCM (4 mL) and the mixture deoxygenated. TFA (1 mL) was then added dropwise to the stirring mixture. The reaction was followed by TLC until the consumption of the starting material (30 min). The solvent was removed under reduced pressure and the residue was precipitated in HPLC-grade Hexane, obtaining 20 mg of a white solid. This solid resulted highly sensitive to the presence of oxygen, being impossible to carry out a proper confirmation of the structure by NMR.

Synthesis of compound 34:



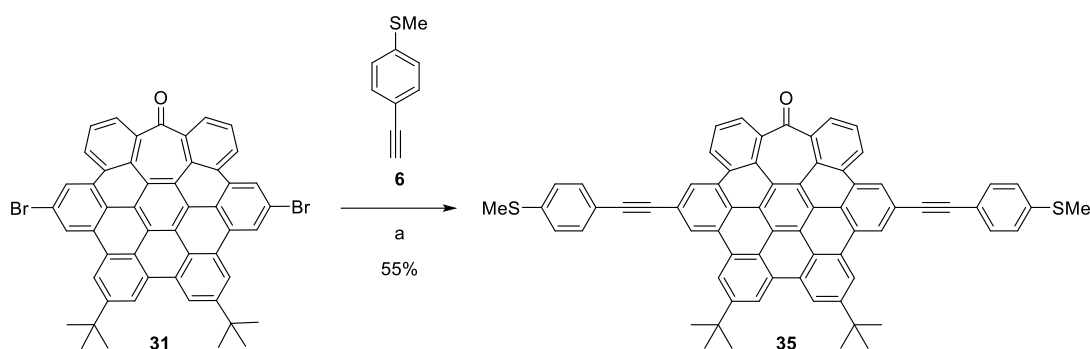
Scheme 13. (a) 4-pyridine-boronic acid, K₂CO₃, Pd(PPh₃)₄, toluene, H₂O, 100 °C, 16 h.

A round-bottom flask was charged with compound **31** (80 mg, 0.098 mmol), K₂CO₃ (135 mg, 0.98 mmol), 4-pyridine-boronic acid (60 mg, 0.49 mmol) and Pd(PPh₃)₄ (45 mg, 0.04 mmol). The flask was sealed and purged with Ar. Anhydrous toluene (10 mL) was added and the solution bubbled with Ar for 10 minutes. Then H₂O (3 mL) was added and the flask heated at 100 °C for 16 h. The solution was allowed to reach room temperature and diluted with DCM. The organic phase was washed with brine, dried over anhydrous Na₂SO₄, filtered and the solvent was removed under reduced pressure. The residue was purified by flash chromatography (SiO₂, Hexane:DCM, 6:4), to give compound **34** (10 mg, 12%). ¹H NMR (500 MHz, CDCl₃) δ 9.18 (s, 2H), 8.89 (s, 2H), 8.81 (s, 2H), 8.76–8.66 (m, 6H), 8.61 (s, 2H), 7.70 (s, 8H), 1.77 (s, 18H). Aromatic signals are not well-resolved. ¹³C NMR (126 MHz, CDCl₃) δ

EXPERIMENTAL SECTION

216.1 (C), 150.5 (CH), 142.2 (C), 137.5 (C), 137.1 (C), 136.9 (C), 136.5 (C), 131.1 (C), 130.6 (C), 130.0 (C), 129.7 (C), 129.3 (C), 127.7 (CH), 127.4 (C), 126.7 (CH), 125.3 (C), 124.8 (C), 124.6 (CH), 122.8 (C), 122.2 (CH), 121.6 (CH), 121.1 (C), 119.8 (CH), 119.4 (CH), 119.1 (CH), 35.9 (C), 32.1 (CH₃). **HRMS (ESI)** calc'd for C₆₁H₄₀N₂O [M]⁺ : 817.3200; found: 817.3204.

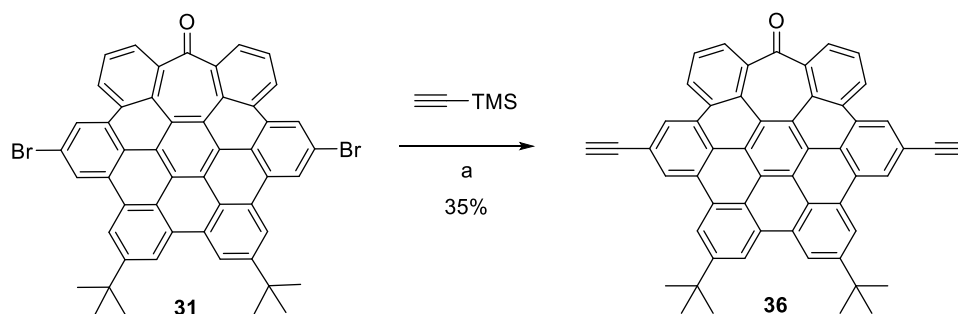
Synthesis of compound 35:



Scheme 14. (a) Pd(CH₃CN)₂Cl₂, PtBu₃·HBF₄, CuI, *i*Pr₂NH, THF, 70 °C, 16 h.

An oven-dried round-bottom flask was charged with **31** (110 mg, 0.135 mmol), Pd(CH₃CN)₂Cl₂ (18 mg, 0.069 mmol), CuI (15 mg, 0.078 mmol) and PtBu₃·HBF₄ (20 mg, 0.068 mmol). The flask was sealed and purged with Ar. Freshly distilled THF (2 mL) and *i*Pr₂NH (6 mL) were added and bubbled with Ar for 10 min. The reaction mixture was heated to 60 °C and a solution of **6** (99 mg, 0.669 mmol) in freshly distilled THF (1 mL) was then added dropwise. The reaction mixture was stirred at 70 °C for 16 h. The mixture was then cooled to room temperature, diluted with DCM and washed with saturated NH₄Cl (aq) solution (x2). The organic layer was separated, dried over anhydrous Na₂SO₄ and filtered. The solvent was removed under reduced pressure. The crude was purified by flash column chromatography (SiO₂, Hexane:DCM, 7:3), to give compound **35** (70 mg, 55%). **¹H NMR (500 MHz, CDCl₃)** δ 9.02 (s, 2H), 8.74 (d, *J* = 8.1 Hz, 2H), 8.47 (s, 2H), 8.05 (t, *J* = 7.6 Hz, 2H), 7.99 (s, 2H), 7.93 (s, 2H), 7.82 (d, *J* = 8.5 Hz, 4H), 7.79 (d, *J* = 7.4 Hz, 2H), 7.45 (d, *J* = 8.8 Hz, 4H), 2.64 (s, 6H), 1.91 (s, 18H). **¹³C NMR (126 MHz, CDCl₃)** δ 202.40 (C), 149.49 (C), 141.85 (C), 140.04 (C), 132.06 (CH), 129.06 (C), 128.86 (C), 128.73 (C), 127.23 (CH), 126.25 (C), 124.76 (CH), 124.67 (CH), 121.53 (C), 121.46 (C), 121.15 (C), 119.64 (C), 118.75 (CH), 90.91 (C), 35.86 (C), 32.22 (CH₃), 15.48 (CH₃). **HRMS (ESI)** calc'd for C₆₉H₄₆ONaS₂ [M+Na]⁺:977.2906; found: 977.2888.

Synthesis of compound 36

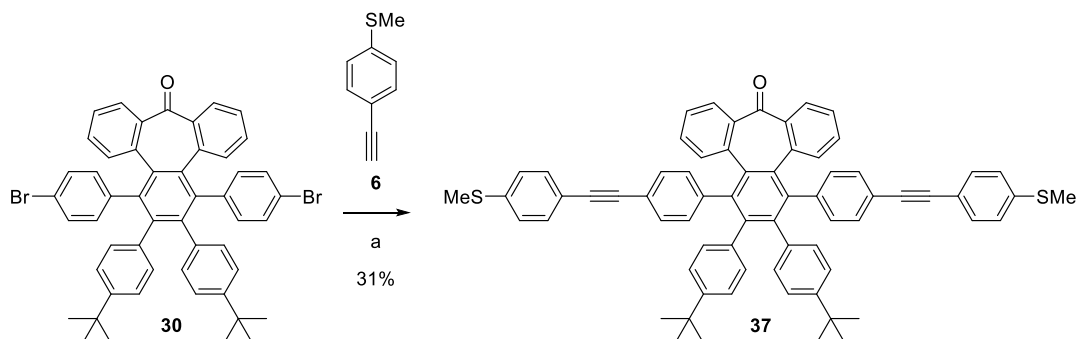


Scheme 15. (a) (i) $\text{PdCl}_2(\text{CH}_3\text{CN})_2$, CuI , $\text{PtBu}_3\cdot\text{HBF}_4$, THF, $i\text{Pr}_2\text{NH}$, rt, 16 h; (ii) TBAF, THF, 2 h.

An oven-dried round-bottom flask was charged with compound **31** (50 mg, 0.061 mmol), $\text{Pd}(\text{CH}_3\text{CN})_2\text{Cl}_2$ (2 mg, 0.092 mmol), CuI (2 mg, 0.011 mmol) and $\text{PtBu}_3\cdot\text{HBF}_4$ (5 mg, mmol). The flask was sealed and purged. Freshly distilled THF (2mL) and $i\text{Pr}_2\text{NH}$ (6mL) were added to the flask. The solution was bubbled with Ar. Trimethylsilylacetylene (TMSA) (90 mg, 0.996 mmol) was added dropwise over the reaction mixture for 30 min. The solution was stirred at room temperature for 16 h. Then, it was diluted with DCM and washed with saturated NH_4Cl (aq) solution (x2). The organic layer was separated, dried over anhydrous Na_2SO_4 , filtered and the solvent removed under reduced pressure. The crude was purified by flash column chromatography (SiO_2 , Hex:DCM, 2:8). The purified product was diluted in THF (20 ml) with 4-5 drops of water, and tetrabutylammonium fluoride (TBAF) (50 mg, 0.191 mmol) was added. The reaction mixture was stirred and the alkyne deprotection followed by TLC until the consumption of the starting material. The solution was then diluted with EtOAc, washed with brine, dried over anhydrous Na_2SO_4 , filtered and the solvent was removed under reduced pressure. The residue was purified by flash chromatography (SiO_2 , Hexane:DCM, 35:65), to give **36** (15 mg, 35%). $^1\text{H NMR}$ (400 MHz, CDCl_3) δ 9.03 (s, 2H), 8.57 (d, $J = 8.4$ Hz, 2H), 8.42 (s, 2H), 7.99 (t, $J = 7.7$ Hz, 2H), 7.84 (s, 2H), 7.83 (s, 2H), 7.78 (dd, $J = 7.3, 1.3$ Hz, 2H), 3.56 (s, 2H), 1.90 (s, 18H). $^{13}\text{C NMR}$ (101 MHz, CDCl_3) δ 202.3 (C), 149.8 (C), 141.8 (C), 129.9 (C), 129.02 (C), 128.97 (C), 128.7 (C), 127.5 (C), 127.4 (C), 126.73 (CH), 126.66 (C), 125.2 (CH), 124.9 (CH), 123.5 (C), 123.33 (CH), 123.28 (C), 121.5 (C), 120.1 (C), 119.9 (CH), 119.3 (C), 118.9 (CH), 85.2 (C), 78.8 (CH), 36.0 (C), 32.2 (CH_3). **HRMS (ESI)** calc'd for $\text{C}_{55}\text{H}_{34}\text{ONa}$ $[\text{M}+\text{Na}]^+$: 733.2499; found: 733.2507.

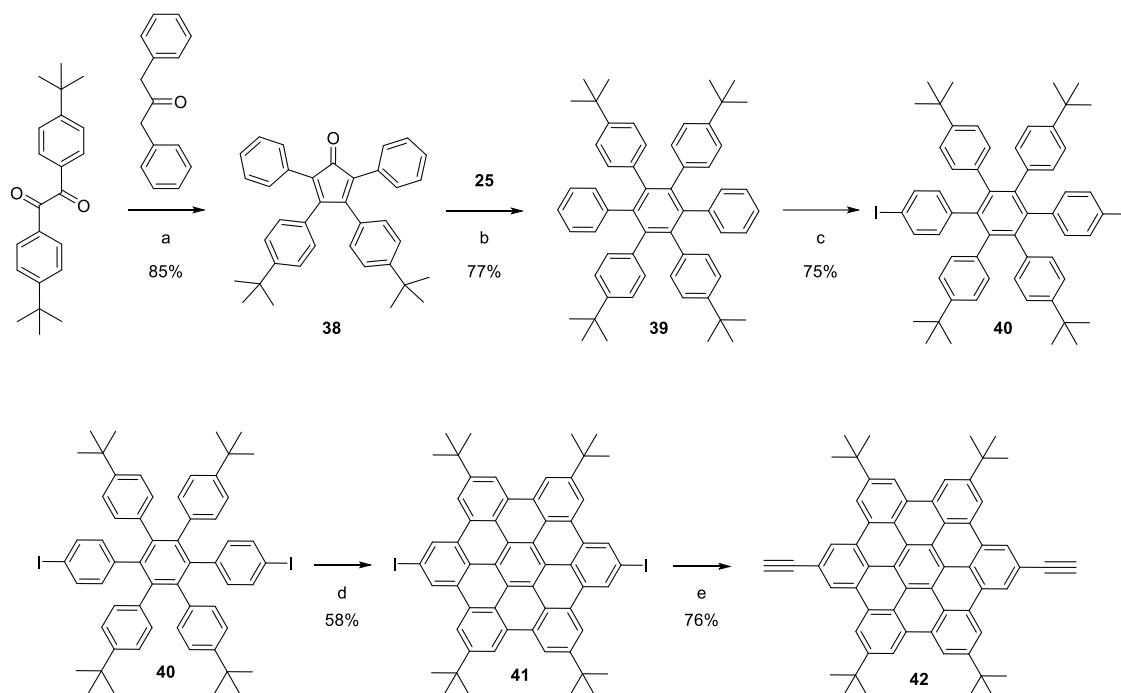
EXPERIMENTAL SECTION

Synthesis of compound 37:

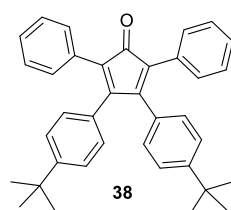


Scheme 16. (a) Pd(CH₃CN)₂Cl₂, CuI, PtBu₃·HBF₄, *i*Pr₂NH, THF, 70 °C, 16 h

An oven-dried round-bottom flask was charged with **30** (85 mg, 0.102 mmol), Pd(CH₃CN)₂Cl₂ (8 mg, 0.030 mmol), CuI (7 mg, 0.037 mmol) and PtBu₃·HBF₄ (9 mg, 0.031 mmol). The flask was sealed and purged with Ar. Freshly distilled THF (2 mL) and *i*Pr₂NH (4 mL) were added and bubbled with Ar for 10 min. The reaction mixture was heated to 70 °C and a solution of **6** (40 mg, 0.270 mmol) in freshly distilled THF (1 mL) was then added dropwise. The reaction mixture was stirred at 70 °C for 16 h. The mixture was then cooled to room temperature, diluted with DCM and washed with saturated NH₄Cl (aq) solution (x2). The organic layer was separated, dried over anhydrous Na₂SO₄ and filtered. The solvent was removed under reduced pressure. The crude was purified by flash column chromatography (SiO₂, Hexane:DCM, 8:2), to give compound **37** (30 mg, 31%). ¹H NMR (400 MHz, CDCl₃) δ 7.42 (d, *J* = 7.7 Hz, 2H), 7.36 (d, *J* = 8.4 Hz, 4H), 7.20 (d, *J* = 8.2 Hz, 2H), 7.17 (d, *J* = 8.4 Hz, 4H), 7.15–7.08 (m, 6H), 7.02–6.94 (m, 6H), 6.88 (t, *J* = 7.6 Hz, 2H), 6.67 (d, *J* = 8.1 Hz, 2H), 6.47 (d, *J* = 8.0 Hz, 2H), 6.24 (d, *J* = 8.1 Hz, 2H), 2.48 (s, 6H), 1.07 (s, 18H). ¹³C NMR (101 MHz, CDCl₃) δ 200.3 (C), 148.3 (C), 146.0 (C), 143.4 (C), 141.1 (C), 140.9 (C), 139.2 (C), 136.7 (C), 135.3 (C), 134.7 (C), 133.2 (CH), 132.5 (CH), 131.8 (CH), 131.3 (CH), 130.7 (CH), 130.5 (CH), 129.8 (CH), 129.7 (CH), 128.9 (CH), 127.3 (CH), 125.9 (CH), 124.3 (CH), 123.8 (CH), 122.8 (CH), 120.1 (C), 119.6 (C), 89.8 (C), 88.9 (C), 31.1 (CH₃), 15.4 (CH₃). HRMS (ESI) calc'd for C₆₉H₅₆ONaS₂ [M+Na]⁺: 987.3698; found: 987.3670.

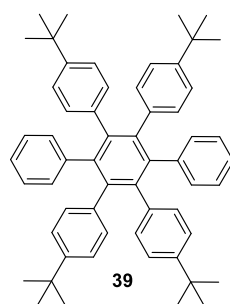
Synthesis of compound 42:

Scheme 17. (a) KOH, EtOH, reflux, 15 min; (b) Ph₂O, reflux, 16 h; (c) PIFA, I₂, CH₂Cl₂, rt, 72 h; (d) FeCl₃, CH₂Cl₂, CH₃NO₂, 0 °C to rt, 16 h; (e) (i) TMSA, Pd(PPh₃)₄, CuI, Et₃N, THF, 16 h; (ii) TBAF, THF, 2 h.

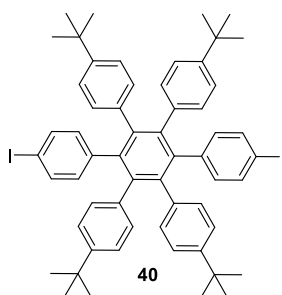


Procedure modified from literature.⁸ In a round bottom flask were placed 1,3-bis-phenyl-2-propanone (290 mg, 1.39 mmol) and 1,2-bis-(*p*-*tert*-butyl)phenylethane-1,2-dione (450 mg, 1.39 mmol) and dissolved in EtOH absolute (10 mL). The reaction mixture was heated to reflux and then a KOH 2 M solution in EtOH absolute (0.5 mL) was added. The reaction mixture was refluxed for 15 min and then cooled to 0 °C. The solid was filtered affording **38** (600 mg, 85%) as a deep purple solid. ¹H NMR (400 MHz, CDCl₃) δ 7.27–7.19 (m, 10H), 7.15 (d, *J* = 8.5 Hz, 4H), 6.82 (d, *J* = 8.5 Hz, 4H), 1.26 (s, 18H). The obtained spectroscopic data were in accordance with those reported in literature.⁸

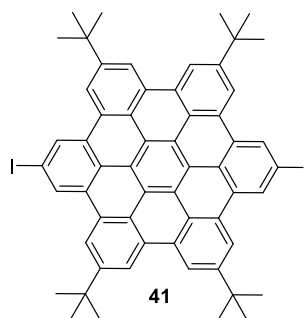
EXPERIMENTAL SECTION



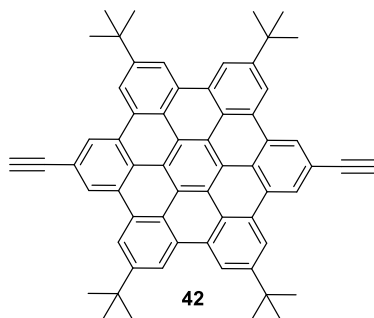
An equimolar amount of **38** (120 mg, 0.24 mmol) and **25** (70 mg, 0.24 mmol) were placed in a Schlenk tube, dissolved in diphenyl ether (2 mL) and bubbled with Ar. The reaction mixture was placed in a sand bath and refluxed for 16 h. The crude material was allowed to cool to room temperature and diluted with hexane (10 mL) and purified by flash column chromatography (SiO₂, Hexane) to afford **39** (146 mg, 77%) as a white solid. ¹H NMR (400 MHz, CDCl₃) δ 6.82–6.78 (m, 18H), 6.65 (d, *J* = 8.3 Hz, 8H), 1.08 (s, 36H). The obtained spectroscopic data were in accordance with those reported in literature.⁸



Compound **39** (120 mg, 0.16 mmol) was dissolved in DCM (10 mL) and degassed with Ar. PIFA (172 mg, 0.40 mmol) and iodine (102 mg, 0.40 mmol) were added and the mixture was stirred for 72 h without light exposure. The reaction mixture was washed with 10% Na₂S₂O₃ solution (20 mL), dried over anhydrous Na₂SO₄ and filtered. After removal of the solvent, the residue was purified by flash column chromatography (SiO₂, Hexane) affording **40** (121 mg, 75%) as a white solid. ¹H NMR (400 MHz, CDCl₃) δ 7.15 (d, *J* = 8.4 Hz, 4H), 6.83 (d, *J* = 8.4 Hz, 8H), 6.62 (d, *J* = 8.4 Hz, 8H), 6.55 (d, *J* = 8.4 Hz, 4H), 1.11 (s, 36H). The obtained spectroscopic data were in accordance with those reported in literature.⁸



Compound **40** (40 mg, 40 μ mol) was dissolved in DCM (20 mL) and degassed via bubbling Ar through the solution for 15 min. A solution of anhydrous FeCl_3 (206 mg, 1.27 mmol) in CH_3NO_2 (0.6 mL) was added and the Ar bubbling was maintained for further 30 min. The reaction was stirred for 16 h at rt, quenched via the addition of MeOH (20 mL) and the solvent removed under reduced pressure. The residue was purified by flash column chromatography (SiO_2 , Hexane:DCM, 8:2) giving rise to **41** (23 mg, 58%) as a pale yellow solid. $^1\text{H NMR}$ (400 MHz, CDCl_3) δ 8.94 (s, 4H), 8.71 (s, 4H), 8.52 (s, 4H), 1.93 (s, 36 H). The obtained spectroscopic data were in accordance with those reported in literature.⁸



An oven-dried round-bottom flask was charged with compound **41** (20 mg, 0.02 mmol), $\text{Pd}(\text{PPh}_3)_4$ (2 mg, 0.092 mmol) and CuI (2 mg, 0.011 mmol). The flask was sealed and purged. Freshly distilled toluene (2 mL) and Et_3N (0.5 mL) were added to the flask and it was bubbled with Ar. The mixture was heated to 60°C and TMSA (24 mg, 0.24 mmol) was added dropwise for 30 min. The reaction mixture was stirred for 16 h at 60 °C. Then, it was diluted with DCM and washed with saturated NH_4Cl (aq) solution (x2). The organic layer was separated, dried over anhydrous Na_2SO_4 , filtered and the solvent removed under reduced

EXPERIMENTAL SECTION

pressure. The crude was purified by flash column chromatography (SiO₂, Hexane:DCM, 1:1). The purified product was diluted in THF (20 mL) with 4-5 drops of water, and TBAF (50 mg, 0.191 mmol) was added. The reaction mixture was stirred and the alkyne deprotection followed by TLC until completion of the reaction. The solution was then diluted with DCM, washed with brine, dried over anhydrous Na₂SO₄, filtered and the solvent was removed under reduced pressure. The residue was purified by flash chromatography (SiO₂, Hexane:DCM, 7:3) to give compound **42** (11 mg, 70%). ¹H NMR (400 MHz, CDCl₃) δ 8.96 (s, 4H), 8.62 (s, 4H), 8.57 (s, 4H), 3.67 (s, 2H), 1.94 (s, 36H). HRMS (ESI) calc'd for C₆₂H₅₀ [M]⁺ : 795.3995; found: 795.3990

References

- (1) Rincón García, L. Conductance, Thermopower and Thermal Conductance Measurements in Single-Molecule Junctions and Atomic Contacts, **2019**. Thesis dissertation, Universidad Autónoma de Madrid.
- (2) Arroyo, C. R.; Leary, E.; Castellanos-Gómez, A.; Rubio-Bollinger, G.; González, M. T.; Agraït, N. Influence of Binding Groups on Molecular Junction Formation. *J. Am. Chem. Soc.* **2011**, *133*, 14313–14319. <https://doi.org/10.1021/ja201861k>.
- (3) Cabosart, D.; El Abbassi, M.; Stefani, D.; Frisenda, R.; Calame, M.; Van der Zant, H. S. J.; Perrin, M. L. A Reference-Free Clustering Method for the Analysis of Molecular Break-Junction Measurements. *Appl. Phys. Lett.* **2019**, *114*. <https://doi.org/10.1063/1.5089198>.
- (4) Ghilene, J.; Haplot, P.; Bard, A. J. Metal/Polypyrrole Quasi-Reference Electrode for Voltammetry in Nonaqueous and Aqueous Solutions. *Anal. Chem.* **2006**, *78*, 6868–6872. <https://doi.org/10.1021/ac060818o>.
- (5) Cottet, F.; Castagnetti, E.; Schlosser, M. The Metalation of 1- and 2-(Trifluoromethyl)Naphthalenes: Noteworthy Site Selectivities. *Synthesis*. **2005**, *5*, 798–803. <https://doi.org/10.1055/s-2005-861814>.
- (6) Wood, T. K.; Piers, W. E.; Keay, B. A.; Parvez, M. 9-Boraanthracene Derivatives Stabilized by N-Heterocyclic Carbenes. *Angew. Chem. Int. Ed.* **2009**, *48*, 4009–4012. <https://doi.org/10.1002/anie.200901217>.
- (7) Gao, Q.; Xu, S. Palladium-Catalyzed Synthesis of Fluorenes from Bis(2-Bromophenyl)Methanols. *Org. Biomol. Chem.* **2018**, *16*, 208–212. <https://doi.org/10.1039/c7ob02895d>.
- (8) Martin, M. M.; Lungerich, D.; Haines, P.; Hampel, F.; Jux, N. Electronic Communication across Porphyrin Hexabenzocoronene Isomers. *Angew. Chem. Int. Ed.* **2019**, *58*, 8932–8937. <https://doi.org/10.1002/anie.201903654>.

ACRONYMS AND ABBREVIATIONS

1D	One-Dimension(al)
2D	Two-Dimension(al)
3D	Three-Dimension(al)
BJ	Break Junction
BPy	Bipyridine
BSD	Benzoselenadiazole
BDT	Benzenedithiol
BTD	Benzothiadiazole
CD	Constrained Dihedral Angles
Cp	Cyclopentadienyl
CNTs	Carbon Nanotubes
CV	Cyclic Voltammetry
D-A	Donor-Acceptor
DC	Direct current
DCM	Dicloromethane
DDQ	2,3-Dichloro-5,6-dicyano-p-benzoquinone
DFT	Density Functional Theory
DMF	Dimethylformamide
DNA	Deoxyribonucleic Acid
ECSTM	Electrochemical Scanning Tunneling Microscope/Microscopy
EDS	Energy Dispersive Spectroscopy
EEF	External Electric Field

E_F	Fermi Energy
FET	Field-Effect Transistors
Fe-PP	Fe(III)–Protoporphyrin
FR	Fully Relaxed
FVP	Flash Vacuum Pyrolysis
G	Conductance
G_0	Quantum Conductance
GQDs	Graphene Quantum Dots
GNRs	Graphene Nanoribbons
HBC	Hexa- <i>peri</i> -Hexabenzocoronene
HOMO	Highest Occupied Molecular Orbital
HOPG	Highly ordered pyrolytic graphite
HR-ESI	High-resolution Electrospray Ionization
/	Intensity/Current
LUMO	Lowest Unoccupied Molecular Orbital
MCBJ	Mechanically Controllable Break-Junction
$M_{ii'}$	Magic Integers
MRR	Magic Ratio Rule
MSE	Mercury Sulfate Electrode
NEGF	Nonequilibrium Green's Functions
NMR	Nuclear Magnetic Resonance
OFETs	Organic Field-Effect Transistors
PAHs	Polycyclic Aromatic Hydrocarbons

PEEK	Polyether Ether Ketone
PIFA	Phenyliodine(III) Bis(trifluoroacetate)
PmPV	Poly(m-phenylene-co-2,5-dioctoxy-p-phenylenevinylene)
PTCDI	Perylene Tetracarboxylic Diimide
<i>p</i> -OPE	<i>para</i> -Olygophenylene Ethylene
PP	Protoporphyrin
PPy	Polypyrrole
<i>R</i>	(Electrical) Resistance
RR	Rectification Ratio
<i>S</i>	Seebeck Coefficient
SCE	Saturated Calomel Electrode
SEM	Scanning Electron Microscope/Microscopy
SQUID	Superconductor Quantum Interference Device
STM	Scanning Tunneling Microscope/Microscopy
STMBJ	Scanning Tunneling Microscope Break Junction
<i>T</i>	Transmission
TBAF	Tetrabutylammonium Fluoride
TFA	Trifluoroacetic acid
THF	Tetrahydrofuran
TMSA	Trimethylsilylacetylene
TMSCHN ₂	Trimethylsilyldiazomethane
UHV	Ultra-High Vacuum
UV	Ultraviolet

UV-PES	UV-Photoelectron Spectroscopy-Mass Spectrometry
UV-Vis	Ultraviolet-Visible
V	Voltage
V _{bias}	Bias Voltage
V _{gate}	Gate Voltage

List of publications

Thesis publications:

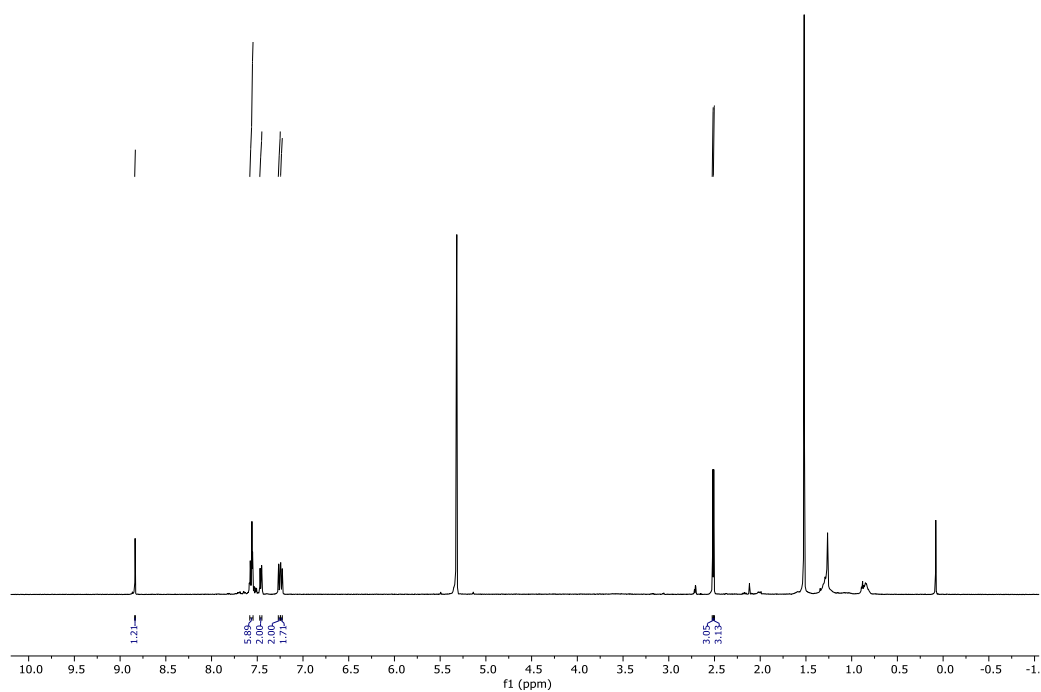
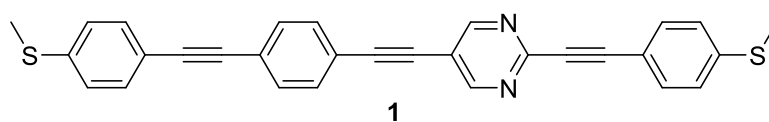
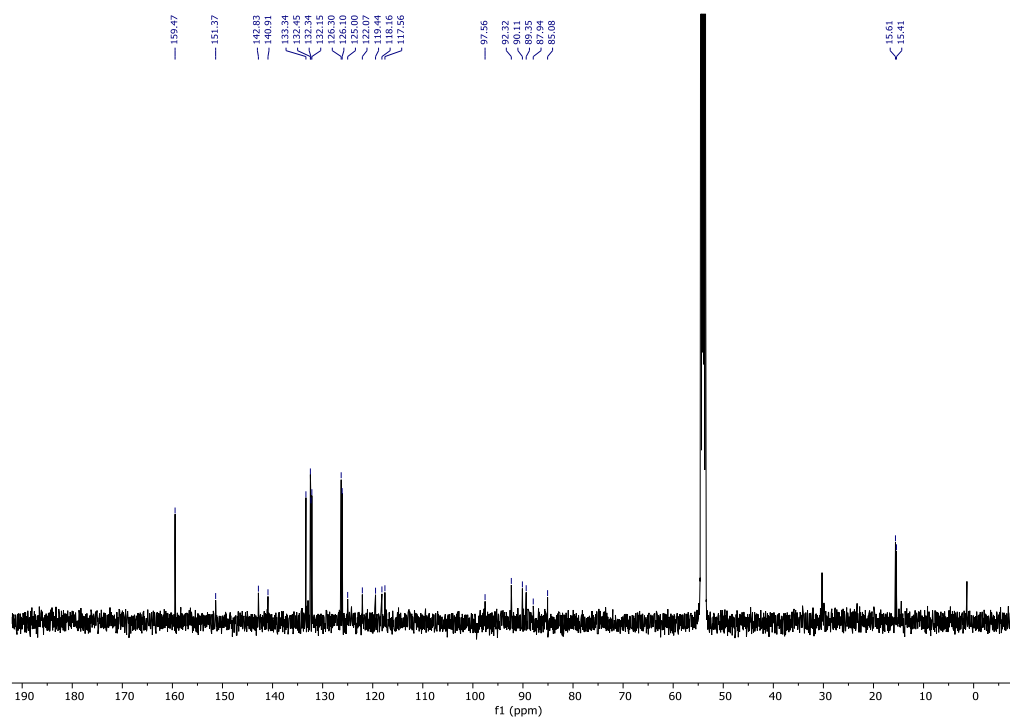
- Palomino-Ruiz, L.; Rodríguez-González, S.; Fallaque, J. G.; Márquez, I. R.; Agraït, N.; Díaz, C.; Leary, E.; Cuerva, J. M.; Campaña, A. G.; Millán, A.; González, M. T. Single-Molecule Conductance of 1,4-Azaborine Derivatives as Models of BN-doped PAHs. *Angew. Chem. Int. Ed.* **2021**. <https://doi.org/10.1002/anie.202014194>

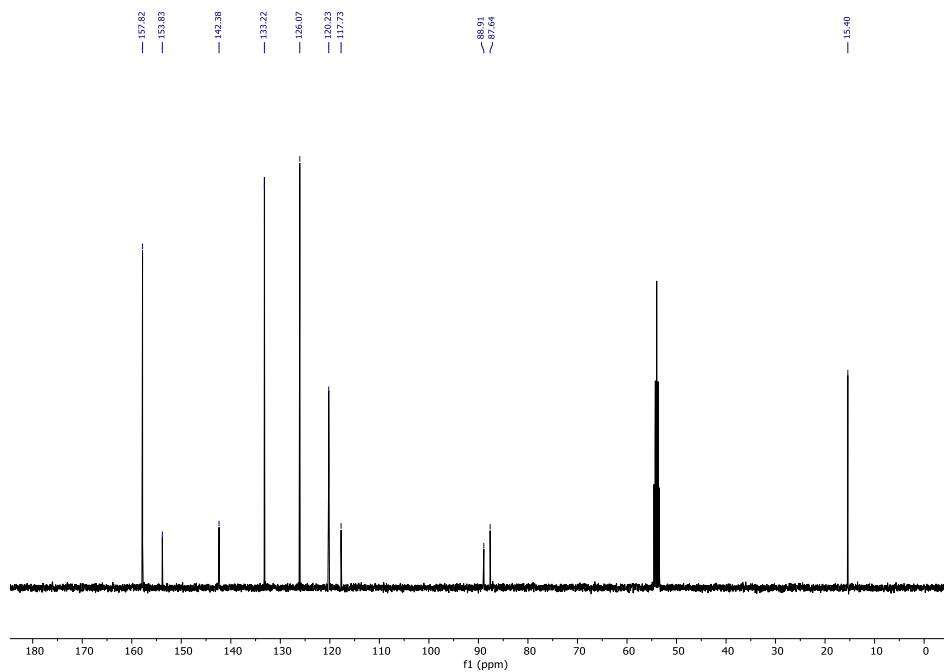
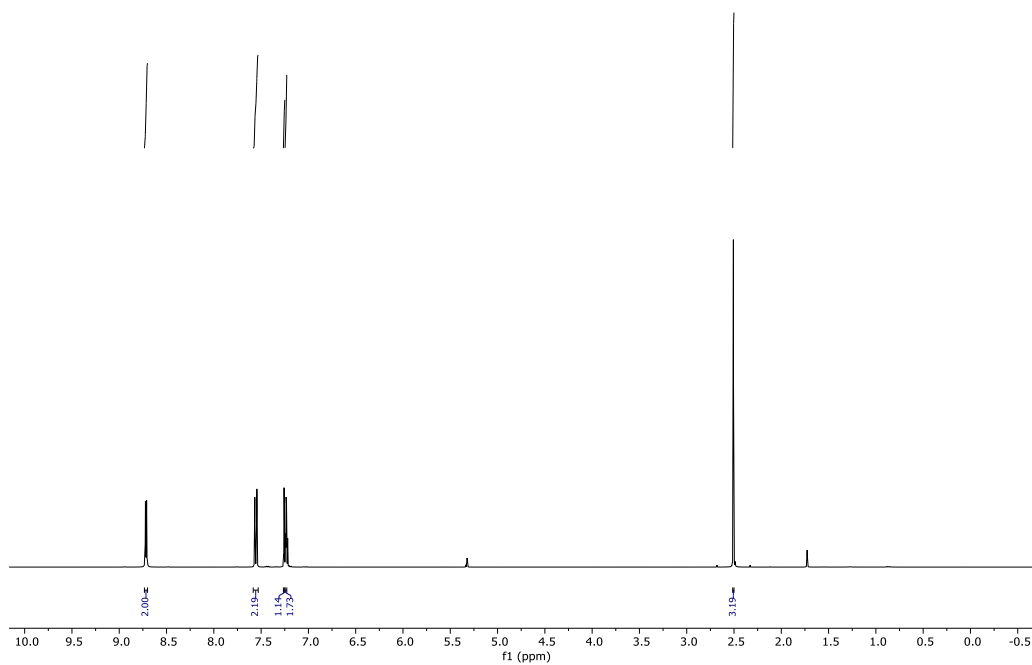
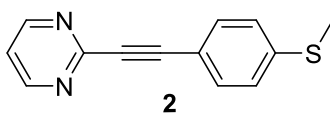
Other publications:

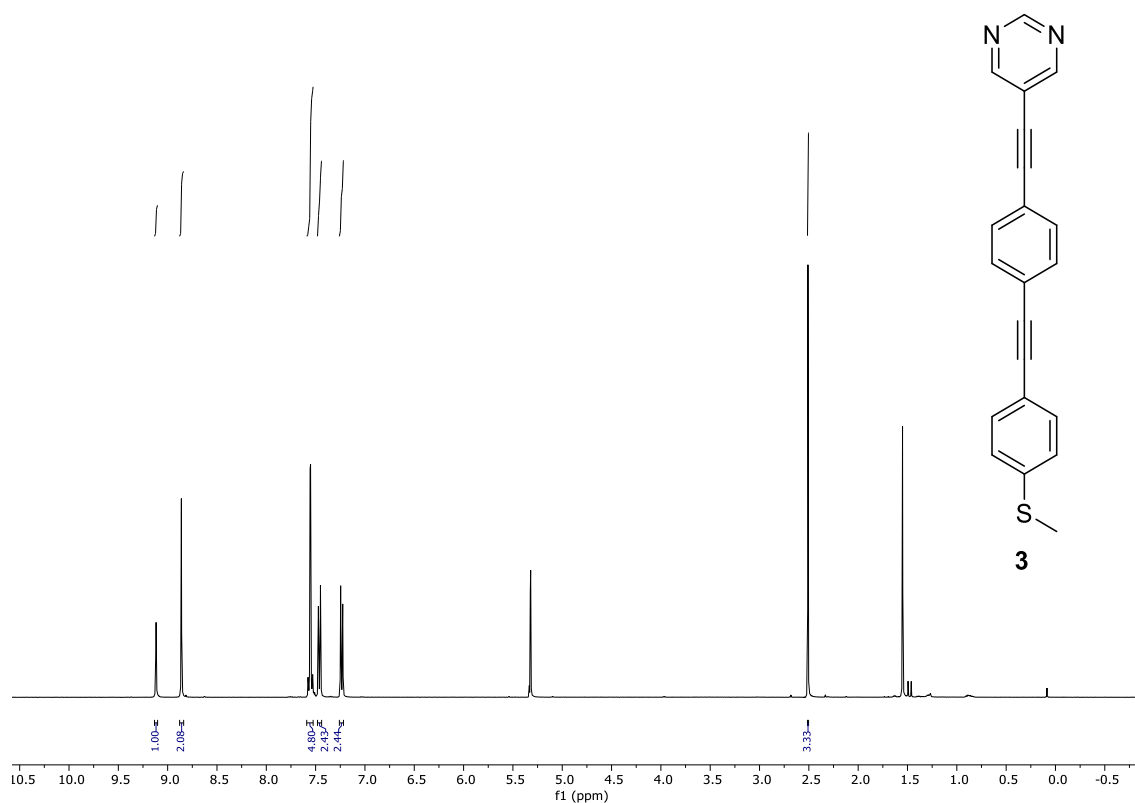
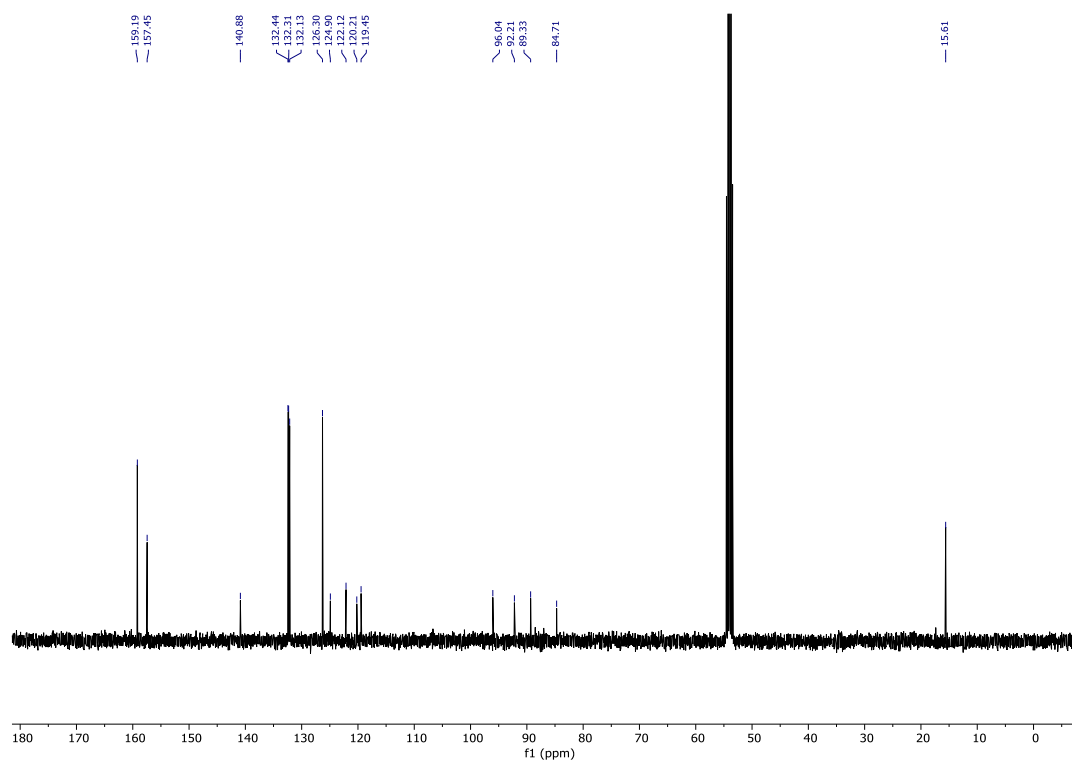
- Leary, E.; Zotti, L. A.; Miguel, D.; Márquez, I. R.; Palomino-Ruiz, L.; Cuerva, J. M.; Rubio-Bollinger, G.; González, M. T.; Agraït, N. The Role of Oligomeric Gold-Thiolate Units in Single-Molecule Junctions of Thiol-Anchored Molecules. *J. Phys. Chem. C* **2018**. <https://doi.org/10.1021/acs.jpcc.7b11104>
- Sacchetti, V.; Ramos-Soriano, J.; Illescas, B. M.; González, M. T.; Li, D.; Palomino-Ruiz, L.; Márquez, I. R.; Leary, E.; Rubio-Bollinger, G.; Pauly, F.; Agraït, N.; Martín, N. Effect of Charge-Assisted Hydrogen Bonds on Single-Molecule Electron Transport. *J. Phys. Chem. C* **2019**, *123*, 29386–29393. <https://doi.org/10.1021/acs.jpcc.9b06850>
- Castro-Fernández, S.; Cruz, C. M.; Mariz, I. F. A.; Márquez, I. R.; Jiménez, V. G.; Palomino-Ruiz, L.; Cuerva, J. M.; Maçôas, E.; Campaña, A. G. Two-Photon Absorption Enhancement by the Inclusion of a Tropone Ring in Distorted Nanographene Ribbons. *Angew. Chem. Int. Ed.* **2020**, *132*, 7205-7211. <https://doi.org/10.1002/anie.202000105>

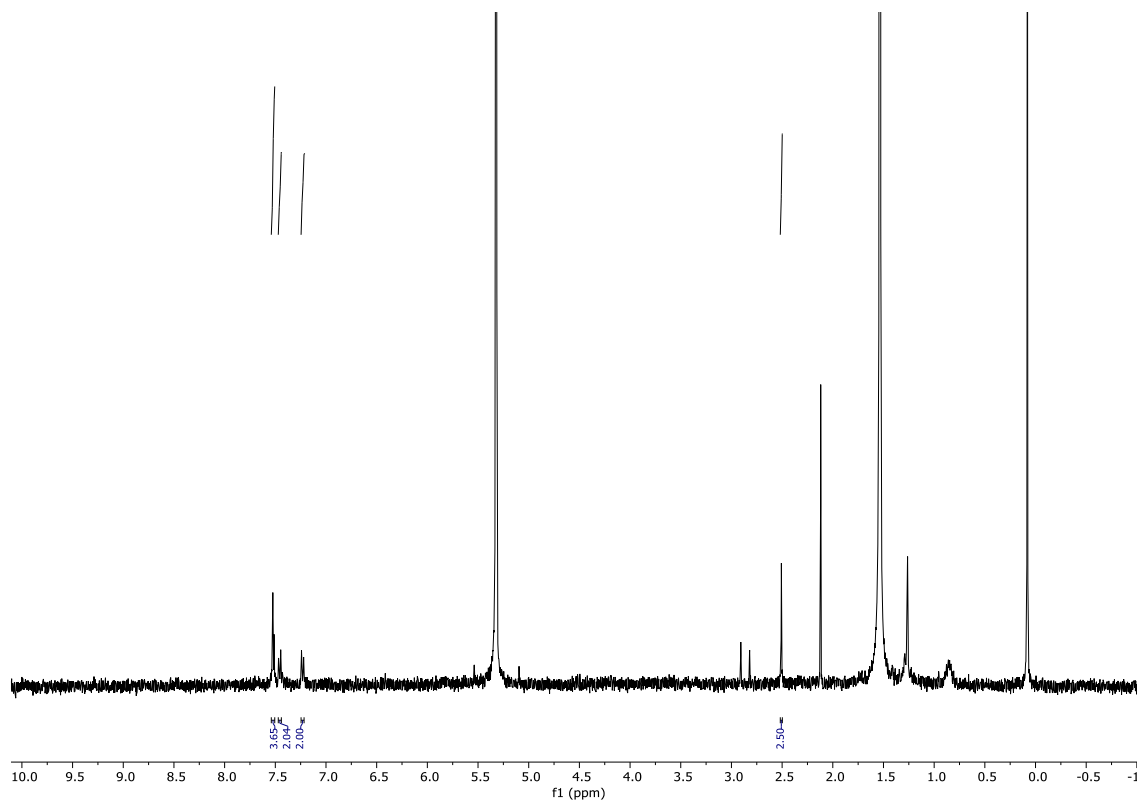
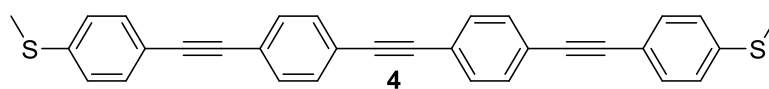
Annexes

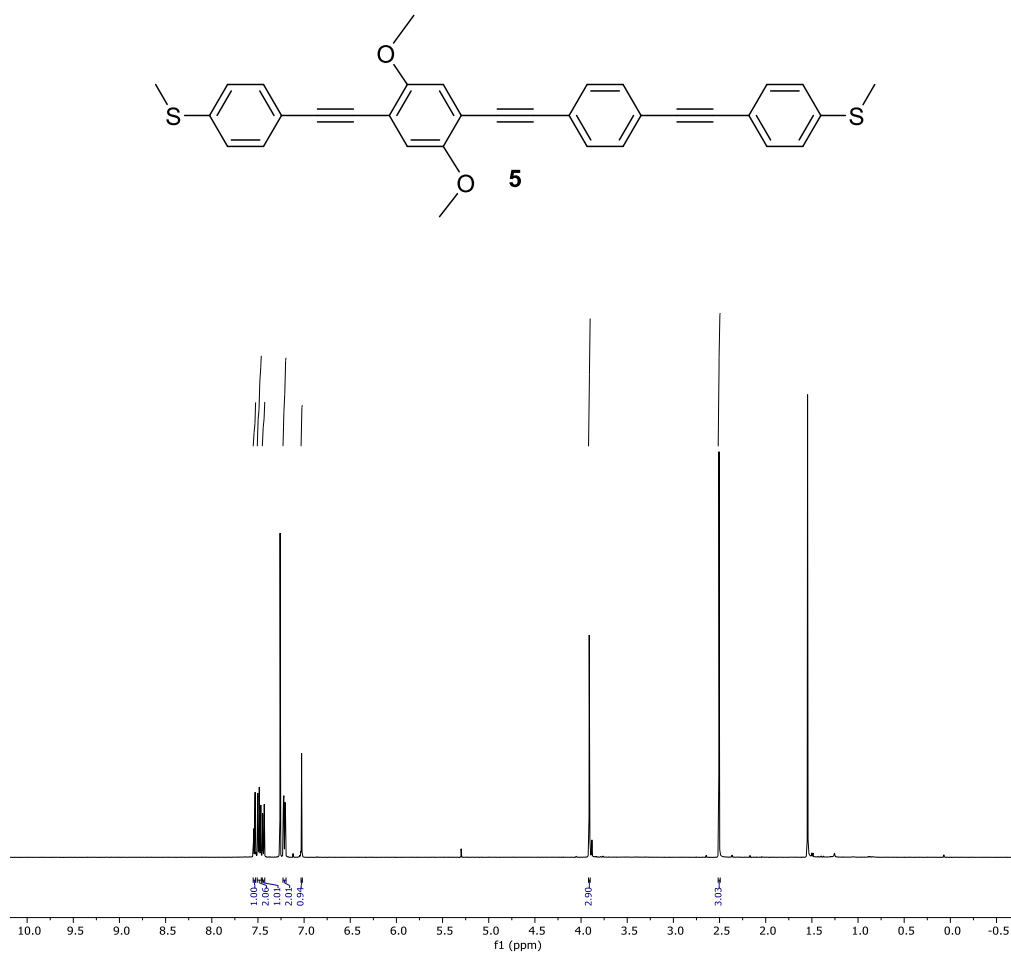
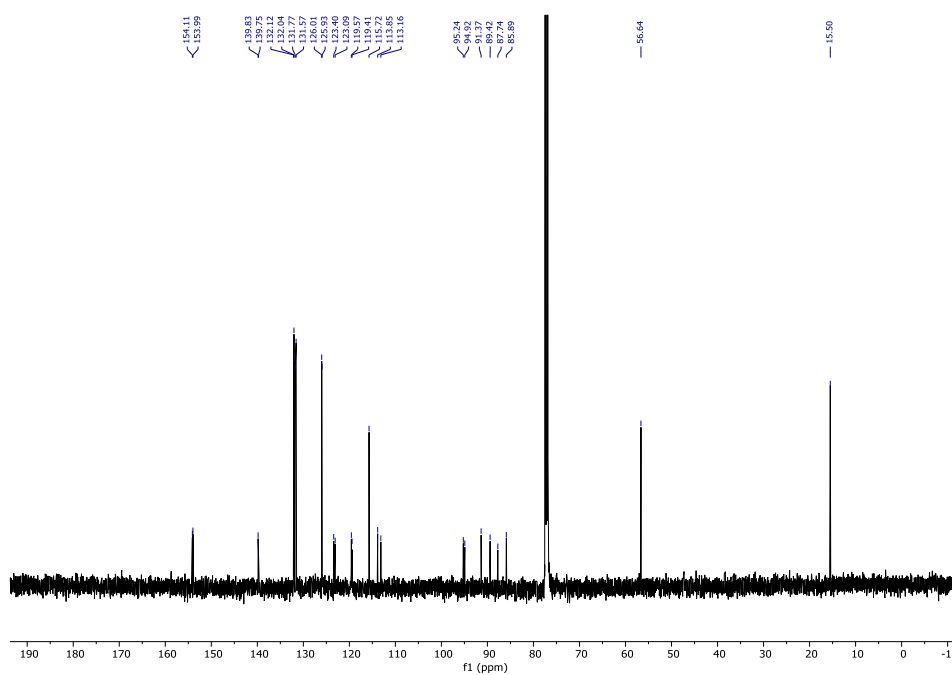
^1H and ^{13}C NMR spectra

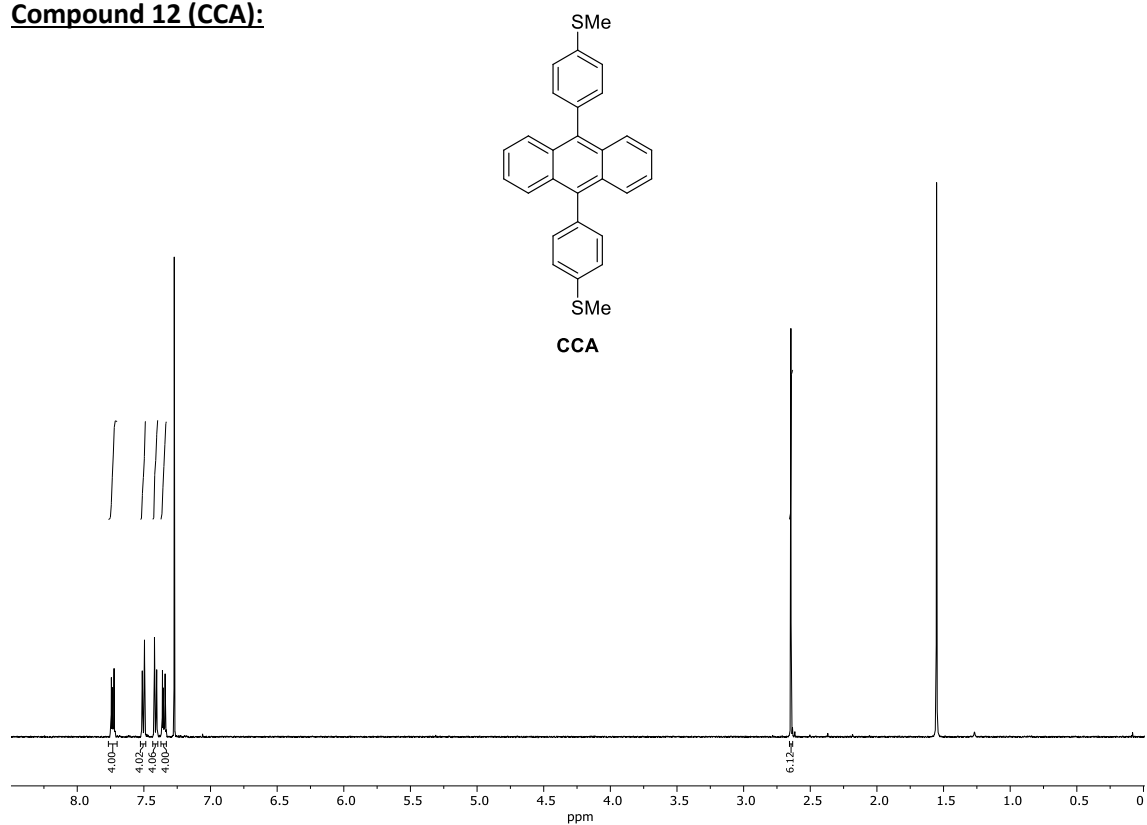
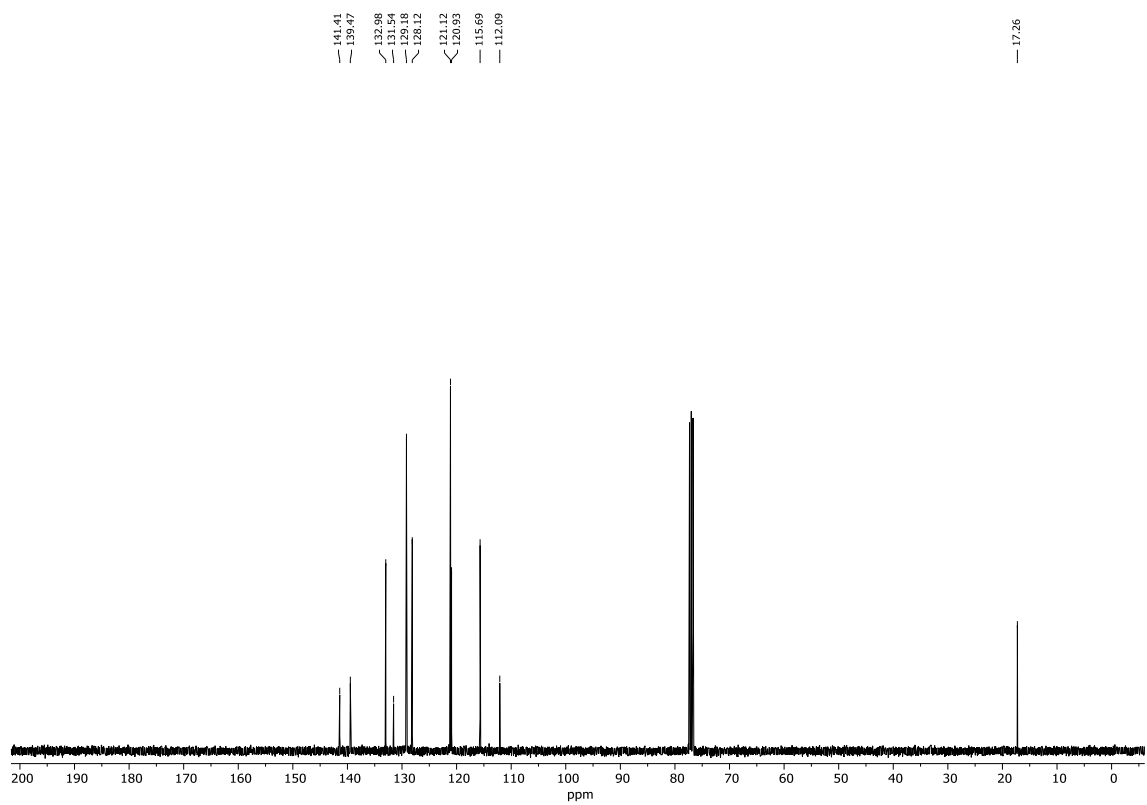
Compound 1 (OPE4-pym).Figure 1. ^1H NMR (500 MHz, CD_2Cl_2) spectrumFigure 2. ^{13}C NMR (126 MHz, CD_2Cl_2) spectrum

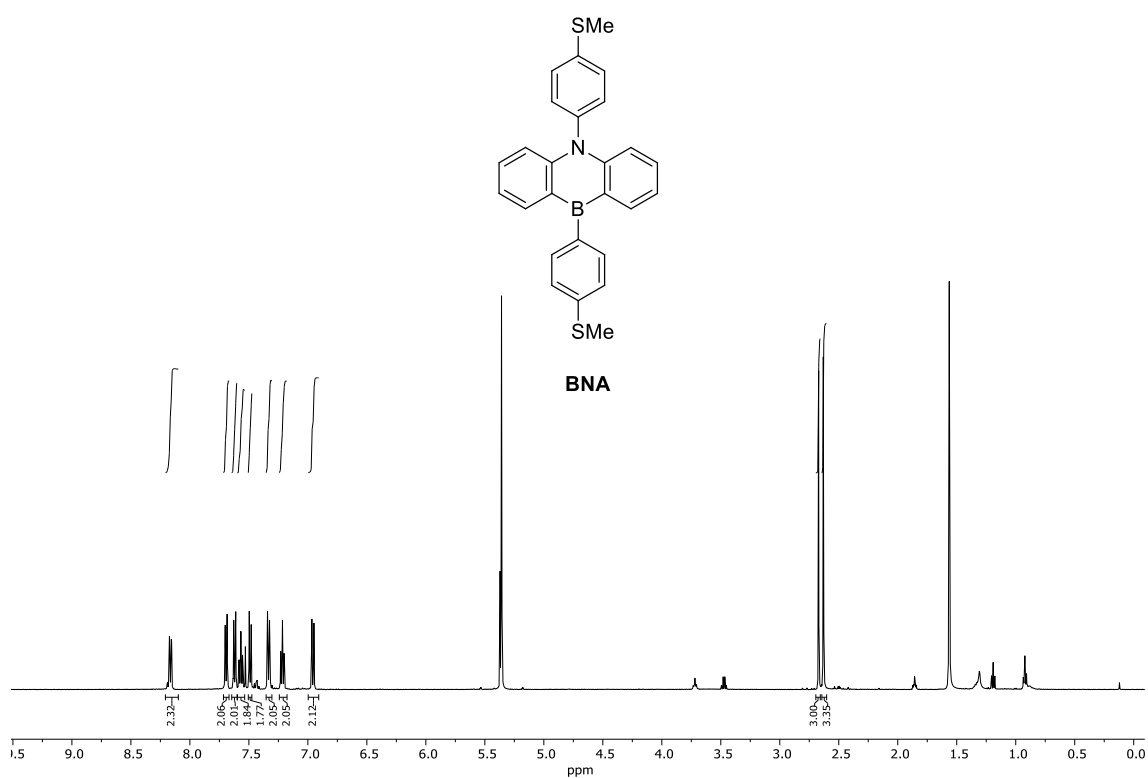
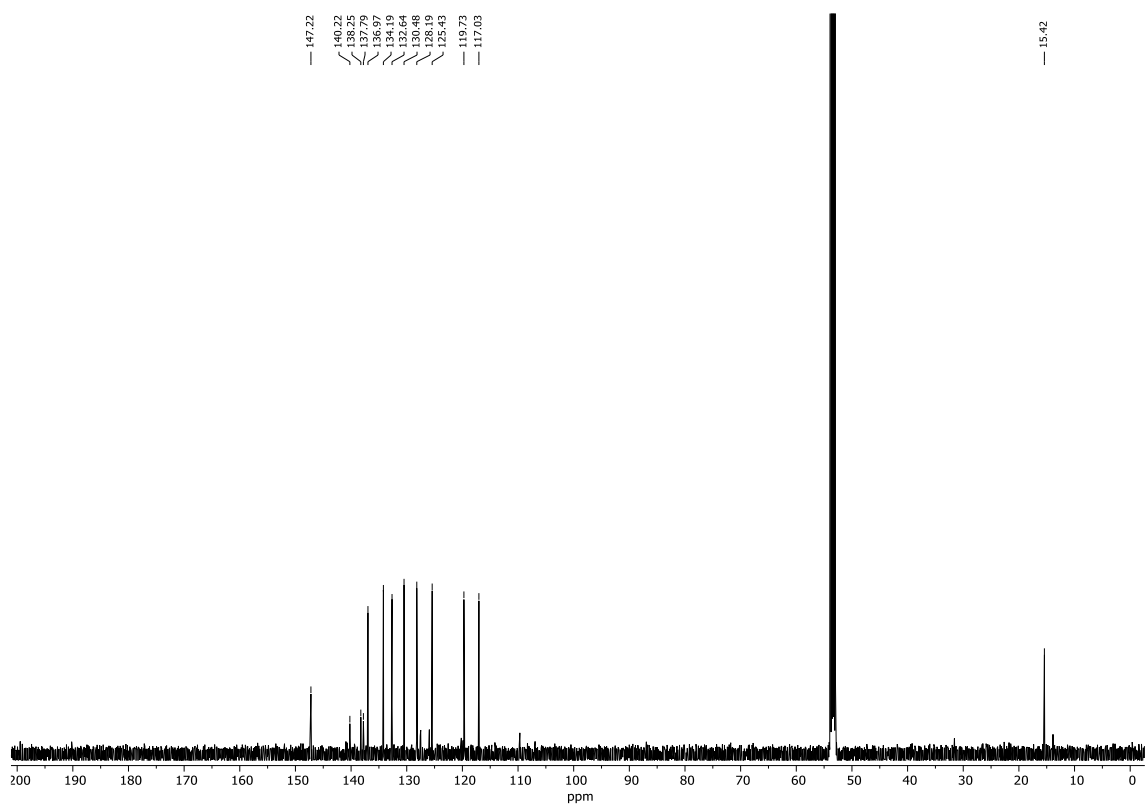
Compound 2 (OPE2/S-pym).

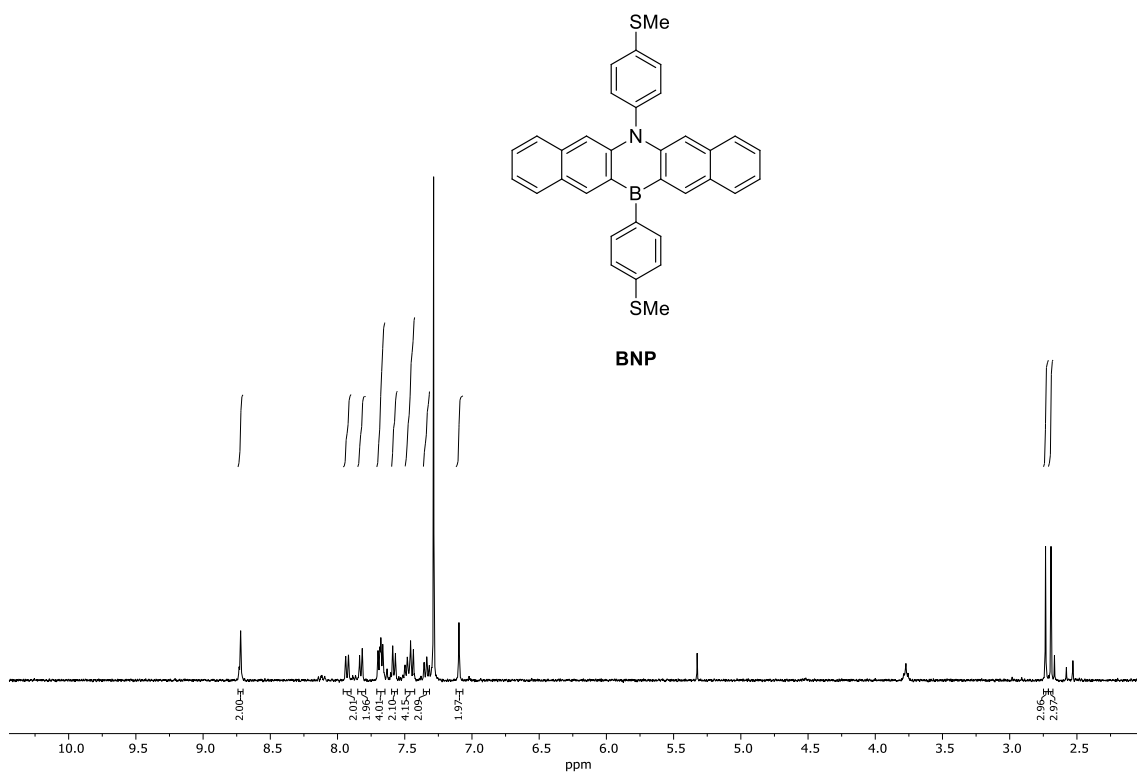
Compound 3 (OPE3/S-pym).Figure 5. ^1H NMR (500 MHz, CD_2Cl_2) spectrumFigure 6. ^{13}C NMR (126 MHz, CD_2Cl_2) spectrum

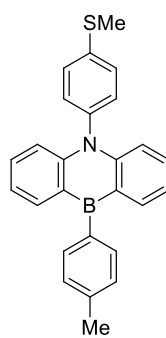
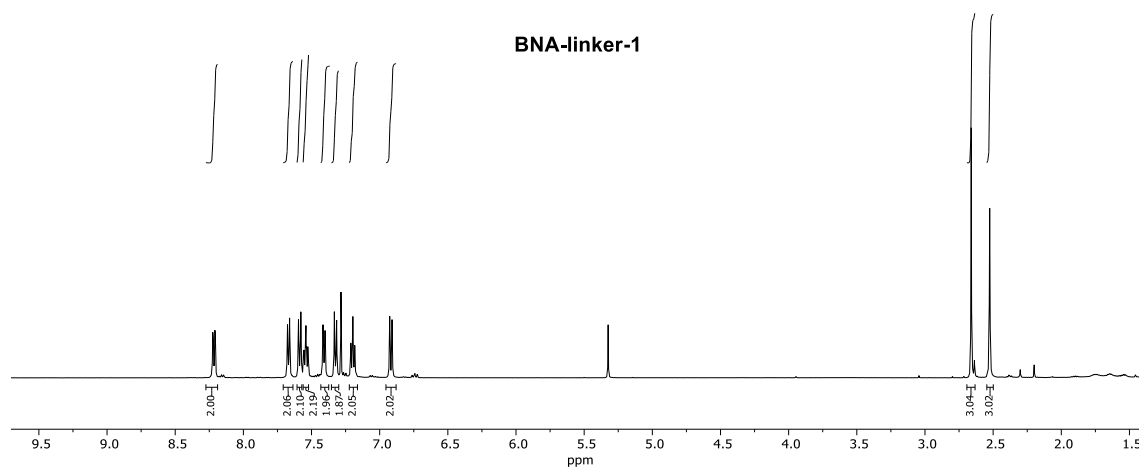
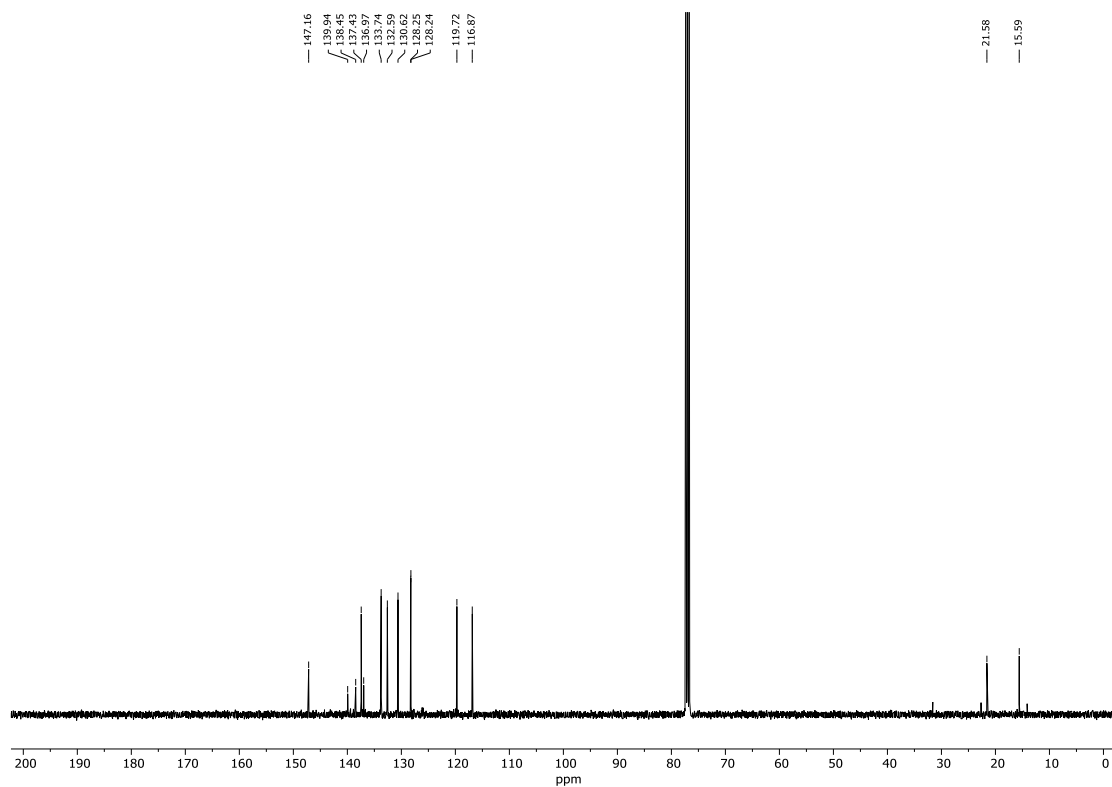
Compound 4 (OPE4).Figure 7. ¹H NMR (500 MHz, CDCl₃) spectrum

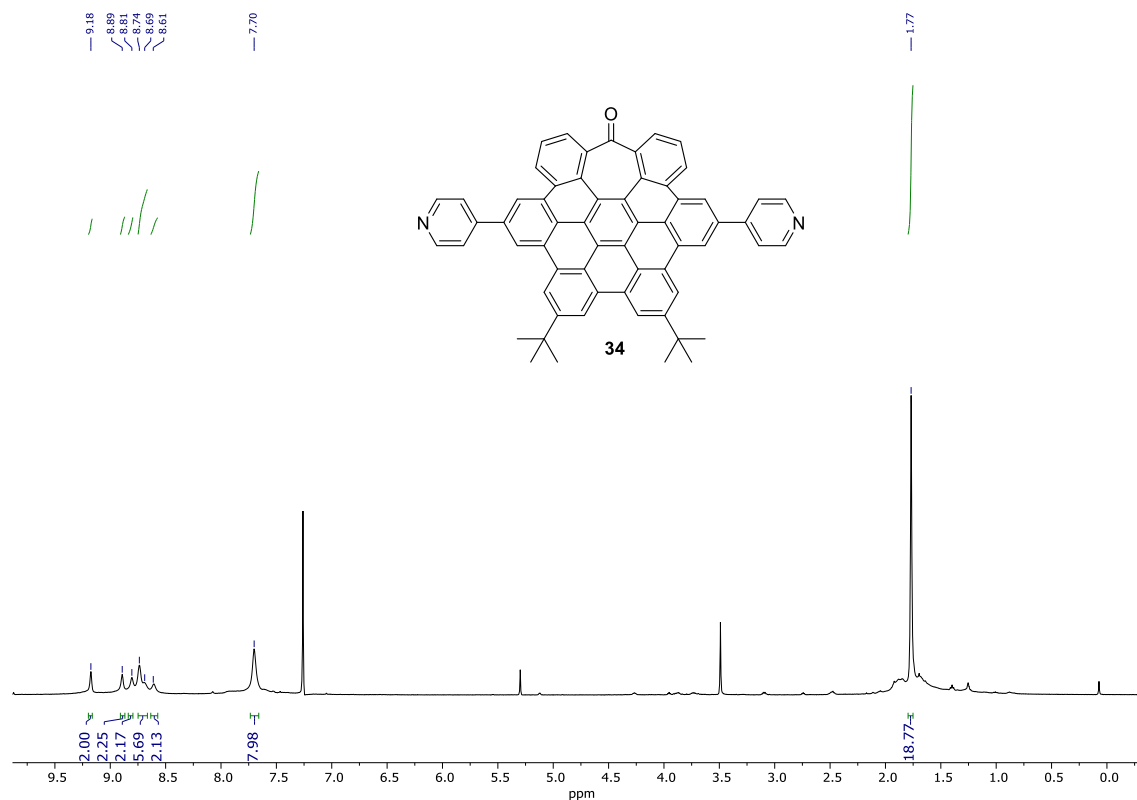
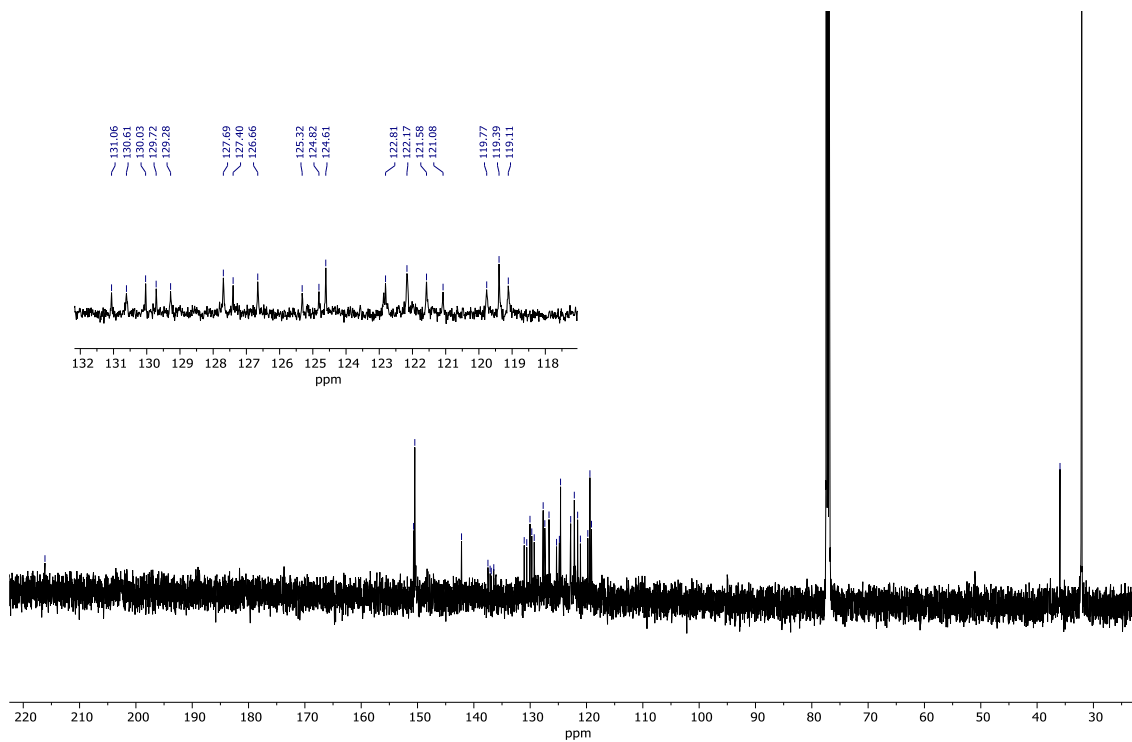
Compound 5 (OPE4/OMe):Figure 8. ¹H NMR (500 MHz, CDCl₃) spectrumFigure 9. ¹³C NMR (126 MHz, CDCl₃) spectrum

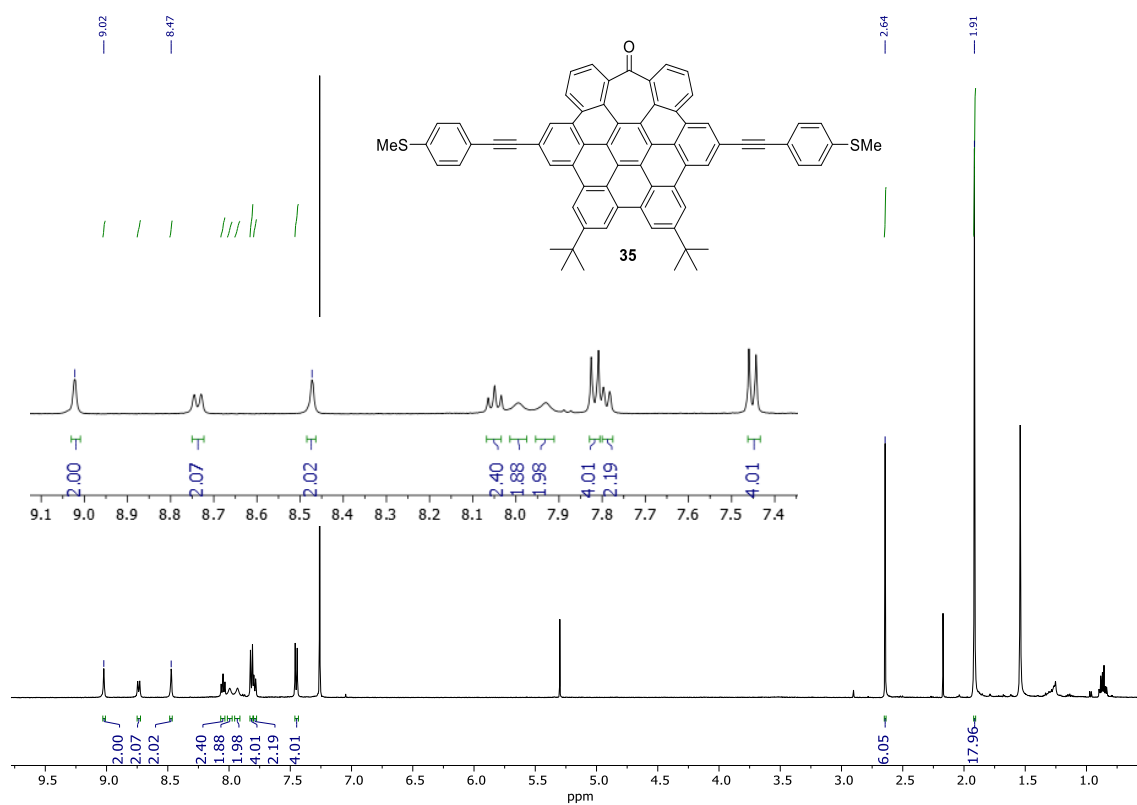
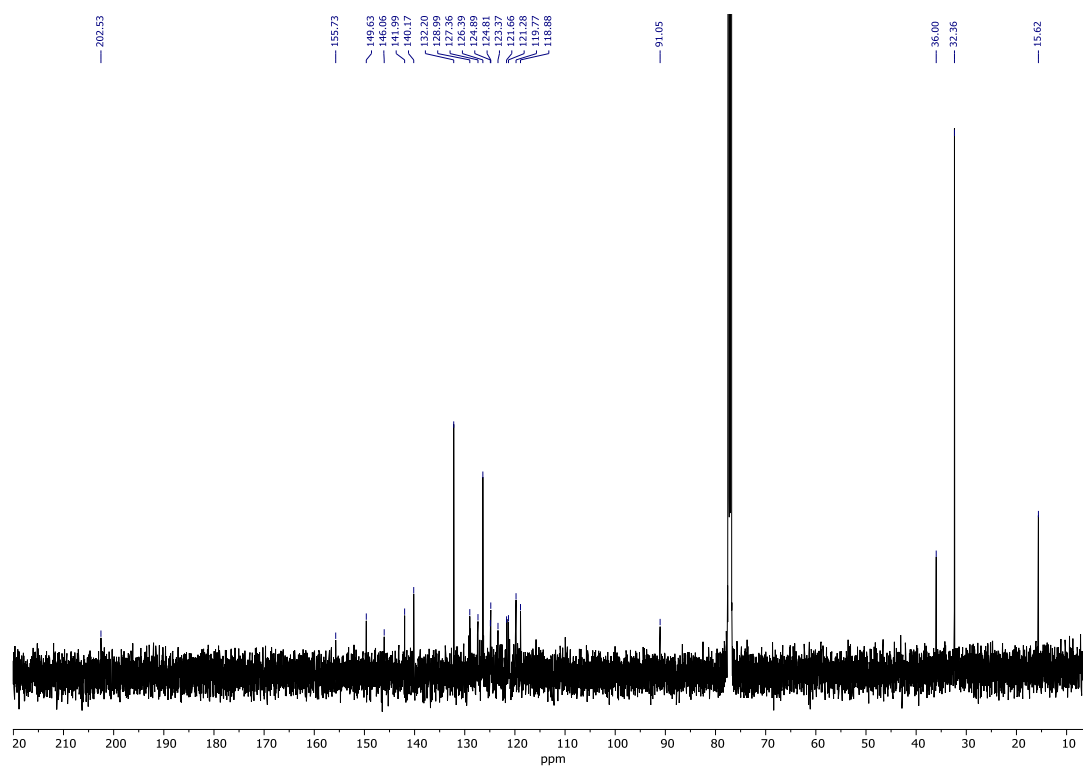
Compound 12 (CCA):Figure 10. ^1H NMR (500 MHz, CDCl_3)Figure 11. ^{13}C NMR (126 MHz, CDCl_3)

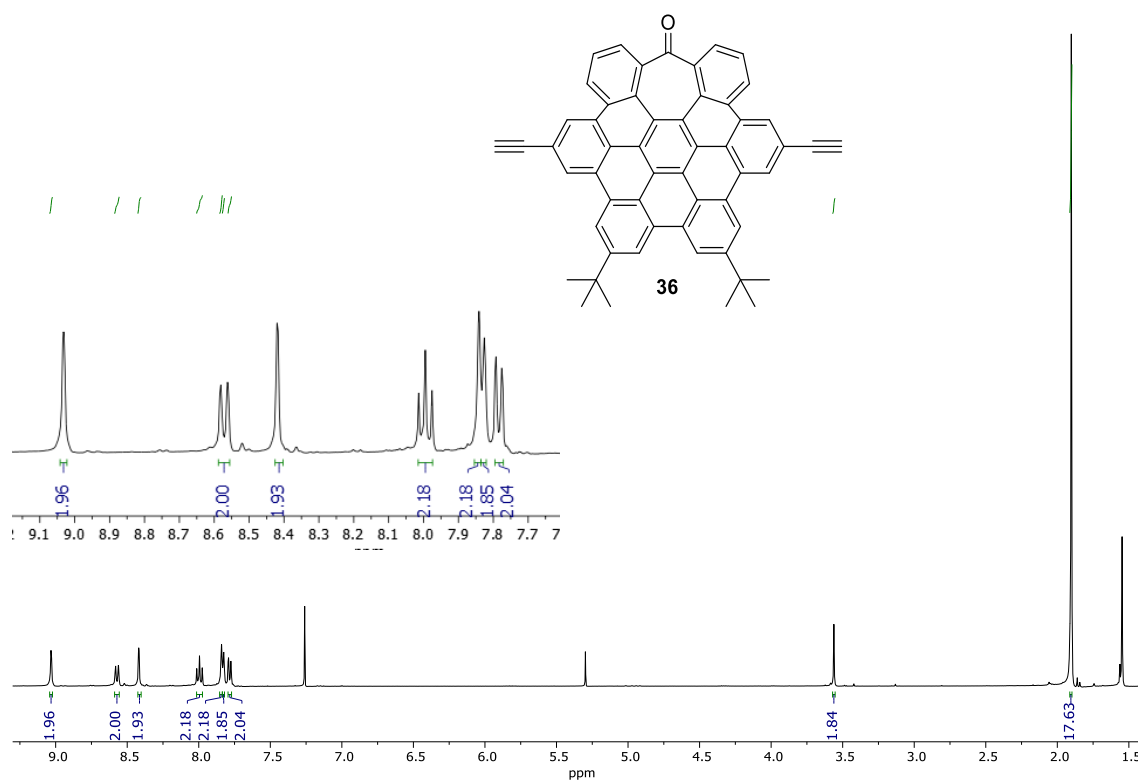
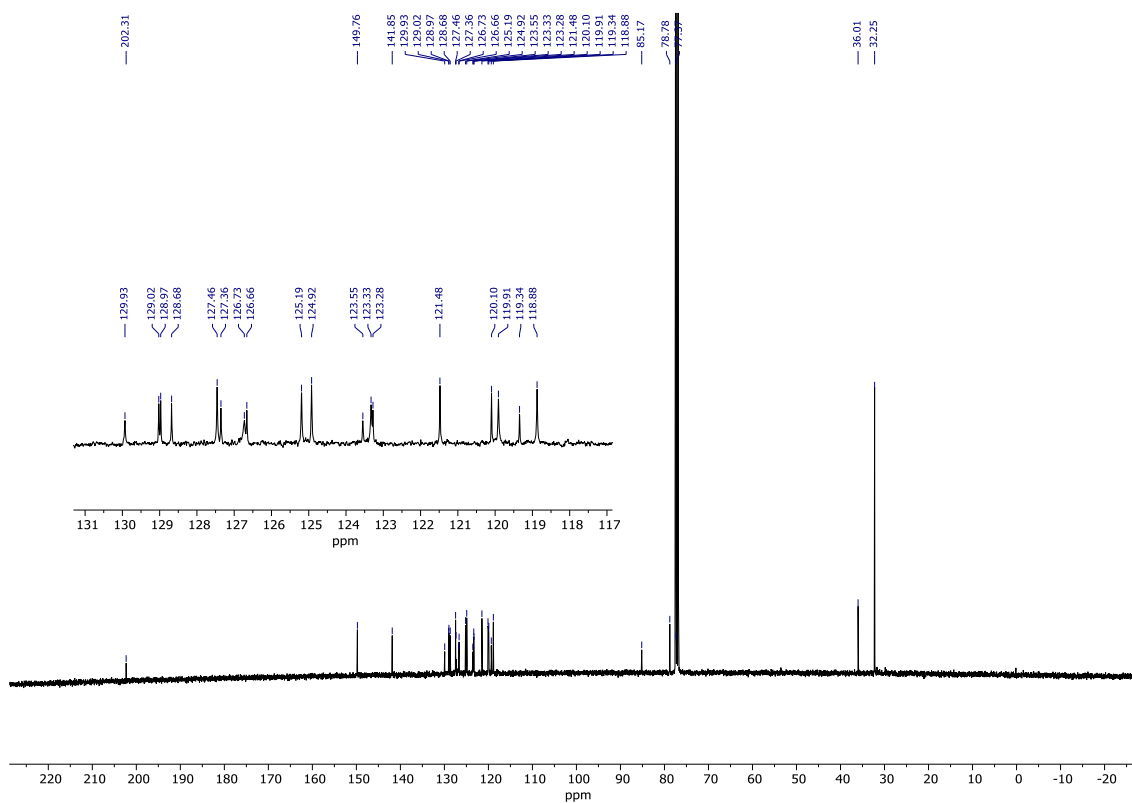
Compound 13 (BNA):**Figure 12.** ¹H NMR (500 MHz, CD₂Cl₂)**Figure 13.** ¹³C NMR (126 MHz, CD₂Cl₂)

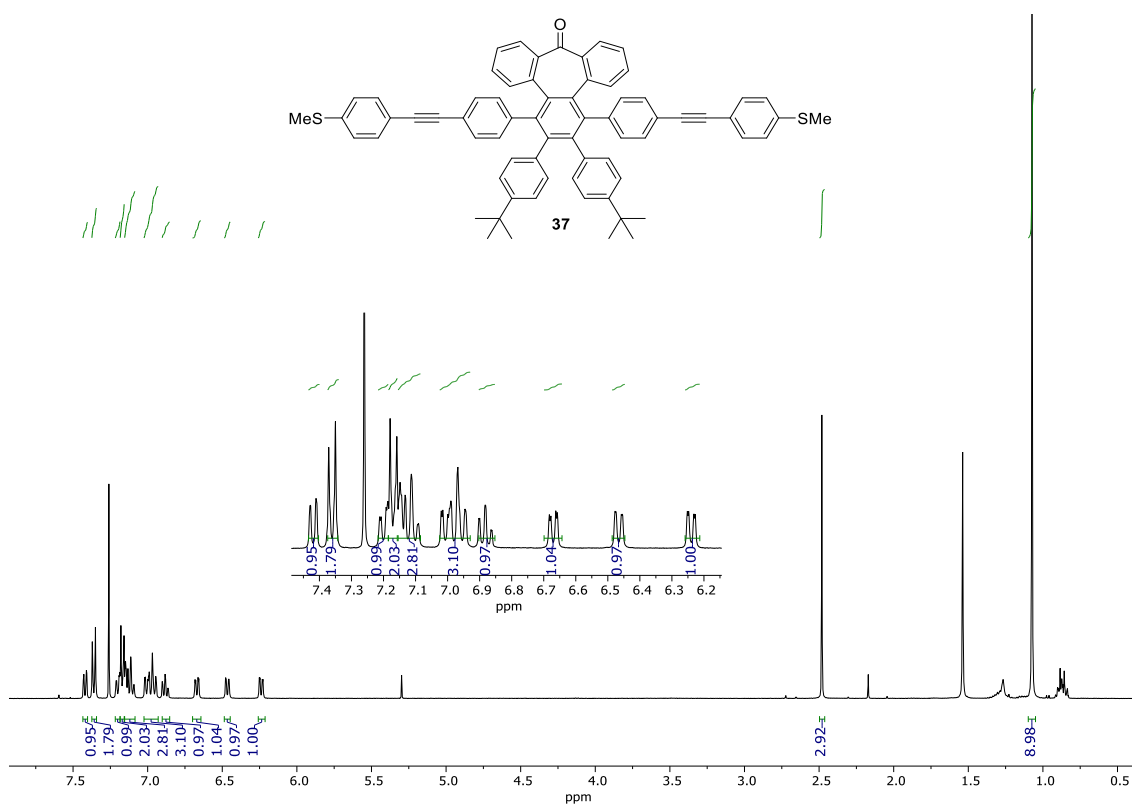
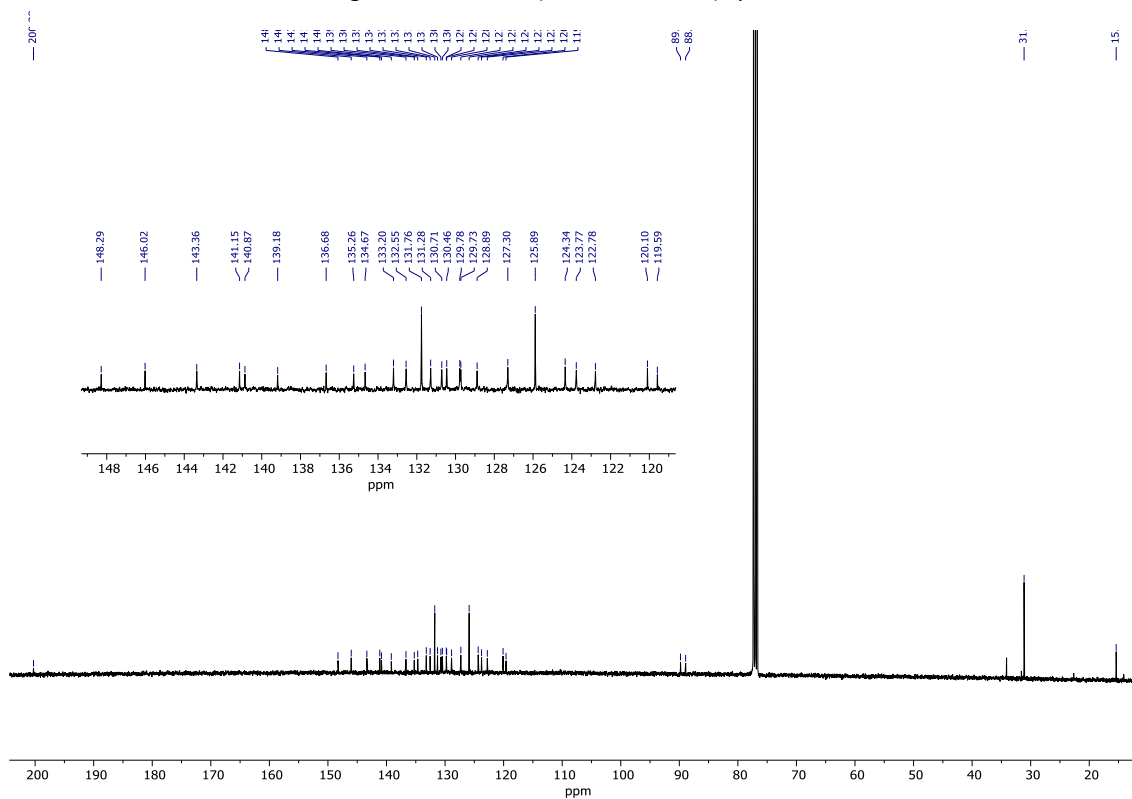
Compound 14 (BNP):**Figure 14.** ¹H NMR (500 MHz, CDCl₃)

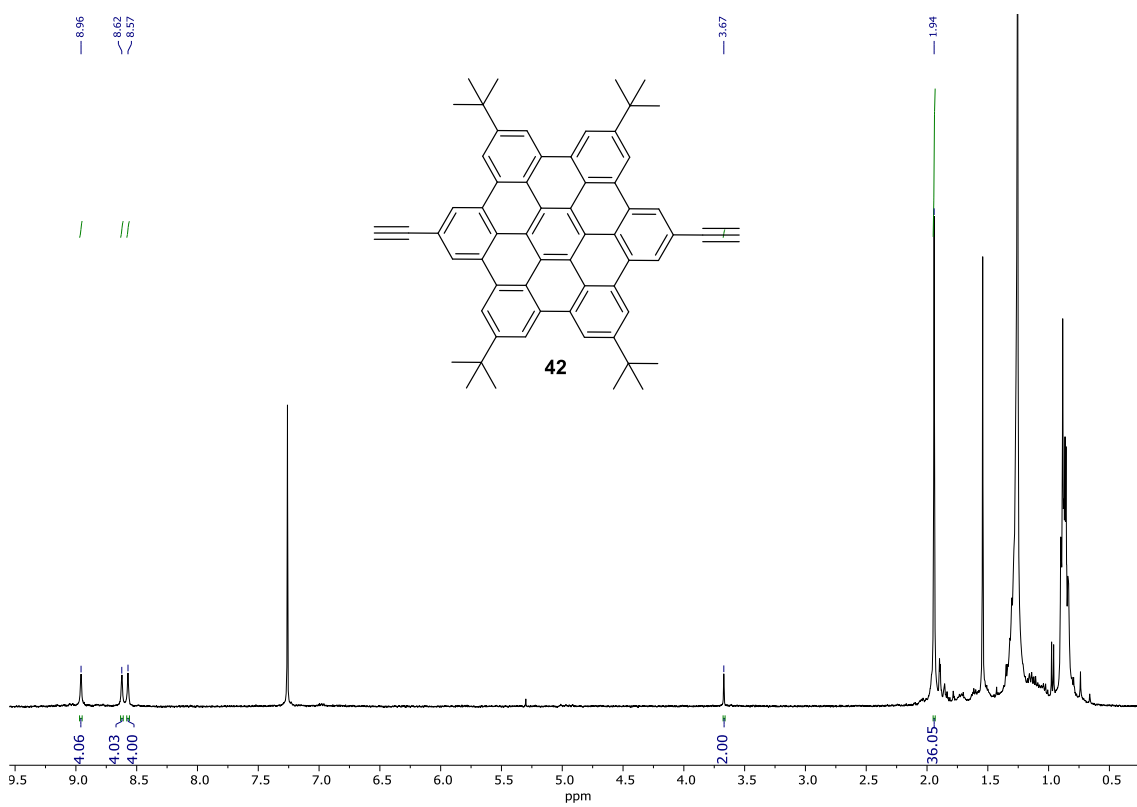
Compound 15 (BNA-1linker):**BNA-linker-1****Figure 15.** ^1H NMR (500 MHz, CDCl_3)**Figure 16.** ^{13}C NMR (126 MHz, CDCl_3)

Compound 34 (7-HBC-py):Figure 17. ^1H NMR (500 MHz, CDCl_3) spectrumFigure 18. ^{13}C NMR (126 MHz, CDCl_3) spectrum

Compound 35 (7-HBC-SMe):Figure 19. $^1\text{H NMR}$ (500 MHz, CDCl_3) spectrum

Compound 36 (7-HBC-alk):Figure 20. ¹H NMR (500 MHz, CDCl₃) spectrumFigure 21. ¹³C NMR (126 MHz, CDCl₃) spectrum

Compound 37 (7-olphe-SMe):Figure 22. ^1H NMR (500 MHz, CDCl_3) spectrumFigure 23. ^{13}C NMR (126 MHz, CDCl_3) spectrum

Compound 42 (HBC-alk)Figure 24. ¹H NMR (500 MHz, CDCl₃) spectrum

